Investigation of the Stratospheric Inorganic Bromine Budget for 1996-2000: Balloon-Borne Measurements and Model Comparisons

Dissertation
von
Richard Fitzenberger

Heidelberg, September 2000

INAUGURAL – DISSERTATION
zur
Erlangung der Doktorwürde

der
Naturwissenschaftlich – Mathematischen
Gesamtfakultät

der
Ruprecht – Karls – Universität
Heidelberg

vorgelegt von
Dipl.-Phys. Richard Fitzenberger
aus Friedberg(Hessen)

Tag der mündlichen Prüfung: 8.November 2000

Investigation of the Stratospheric Inorganic Bromine Budget for 1996-2000: Balloon-Borne Measurements and Model Comparisons

Gutachter: Prof. Dr. Ulrich Platt
Prof. Dr. Konrad Mauersberger

DISSERTATION
submitted to the
Combined Faculties for the Natural Sciences and for Mathematics
of the
Rupertus Carola University of
Heidelberg, Germany
for the degree of
Doctor of Natural Sciences

Investigation of the Stratospheric Inorganic Bromine Budget for 1996-2000: Balloon-Borne Measurements and Model Comparisons

presented by
Diplom-Physicist: Richard Fitzenberger
born in : Friedberg(Hessen)

Heidelberg, 8.November 2000

Referees: Prof. Dr. Ulrich Platt
Prof. Dr. Konrad Mauersberger

Zusammenfassung

Anorganische Bromverbindungen spielen eine bedeutende Rolle in katalytischen Ozonabbauzyklen der Stratosphäre. Im Rahmen dieser Doktorarbeit wurden ballongetragene DOAS (Differentielle Optische Absorptions Spektroskopie) *BrO* Vertikalprofilmessungen mittels direkten Sonnenlichts mit bisher nicht erreichter Genauigkeit (±12%) durchgeführt. Die spektroskopischen Messungen fanden während acht erfolgreicher Flüge mit der gemeinsamen deutsch-französischen Nutzlast LPMA/DOAS unter sehr verschiedenen geophysikalischen Bedingungen in den Jahren 1996-2000 statt. Dabei ergaben sich völlig neue Einblicke in die Chemie und das Budget des stratosphärischen Broms. Die neuartigen Erkenntnisse umfassen (1) eine genaue und vollständige Erfassung des stratosphärischen Bromgehaltes der letzten vier Jahre, (2) ein verbessertes Verständnis der Chemie des stratosphärischen anorganischen Broms, und (3) den erstmaligen Nachweis und die Messung von Höhenprofilen der *BrO* Konzentration in der freien Troposphäre. Mit Hilfe der *BrO* Messungen konnte der stratosphärische Gehalt an anorganischem Brom zu Br_y^{in}=(21.5±3) ppt in 5.6 Jahre alter Luft für 1999 bestimmt werden. Hingegen zeigt die erstmalige gleichzeitige Bestimmung des stratosphärischen Bromgehaltes aus Messungen organischer Bromverbindungen nur Br_y^{org}=(18.4±1.8) ppt. Die Übereinstimmung des Gesamtbrommischungsverhältnisses ist befriedigend, jedoch deutet das konsistent größere Br_y^{in} darauf hin, daß vermutlich anorganisches Brom (3.1±3.5 ppt) aus der Troposphäre in die Stratosphäre eingetragen wird. Diese Vermutung wird durch den Befund (3) und den kürzlich erfolgten Nachweis von im Aerosol der oberen Troposphäre gebundenem, anorganischem Brom von etwa 1 ppt qualitativ gestützt.

Als weiterer Teil der Arbeit wurde ein Algorithmus zur Auswertung der vom Ballon aus gemessenen Sonnenspektren für den Nachweis von Chlordioxid (*OClO*) neu entwickelt. *OClO* konnte in allen arktischen Winterflügen auch bei geringer Chloraktivierung detektiert werden. Überraschenderweise wurde *OClO* auch während eines Ballonfluges über Spanien im Herbst 1996 nachgewiesen (5-10 ppt in 20-30 km Höhe bei einem Sonnenzenitwinkel von 88-93^o). Zur Interpretation der erhöhten *OClO* Werte wurden Ergebnisse des 3-D CTM Modells SLIMCAT und des dafür eigens entwickelten Lagrange Boxmodells LABMOS mit den Messungen verglichen. Dabei stellte sich heraus, daß sich die arktischen *OClO* Messungen im Winter gut verstehen lassen, während die in mittleren Breiten gemessenen *OClO* Konzentrationen deutlich höher sind als mit der bisherigen Theorie der stratosphärischen Chemie erklärt werden kann.

Summary

Inorganic bromine plays an important role in catalytic ozone depletion in the stratosphere at high and mid-latitudes. This study reports and discusses in detail stratospheric DOAS (Differential Optical Absorption Spectroscopy) *BrO* vertical profile measurements with direct sunlight, that were conducted aboard the french-german LPMA/DOAS (Laboratoire de Physique Moléculaire et Application) balloon gondola at mid and high northern latitudes during the years 1996 to 2000. The unprecedented high accuracy (±12%) of the *BrO* measurements together with 3-D CTM and Lagrangian photochemical modelling provided new insights into the budget and chemistry of atmospheric bromine. These include (1) a thorough investigation of the present and recent budget of stratospheric bromine, (2) an improved understanding of the chemistry of stratospheric bromine, and (3) the first measurements of free tropospheric *BrO* concentration profiles. The total inorganic bromine (in 5.6 year old air in 1999) determined from *BrO* measurements (Br_y^{in}=(21.5±3) ppt) was tested for the first time against the total stratospheric bromine inferred from the organic bromine method (Br_y^{org}=(18.4±1.8) ppt). The agreement of total bromine found with both methods is good, however, the consistently larger Br_y^{in} suggests an influx (3.1±3.5 ppt) of inorganic bromine from the troposphere. This conclusion is supported by finding (3) and qualitatively by the recent detection of inorganic bromine at a 1 ppt level in the upper tropospheric aerosol. Thus this thesis could establish a more complete budget of stratospheric bromine.

Also, a new DOAS retrieval algorithm was developed for the detection of chlorine dioxide (*OClO*) in the balloon-borne direct sun spectra. In all Arctic winter flights *OClO* could be detected - even at low chlorine activation. Surprisingly, *OClO* could also be measured in significant amounts (5-10 ppt at 20-30 km and a solar zenith angle (SZA) of 88-93^o) during a fall 1996 mid-latitude balloon flight. The *OClO* measurements were inter compared with results from a 3-D CTM (SLIMCAT) and a Lagrangian trajectory box model (LABMOS), which was implemented for this purpose as a part of this study. While the *OClO* detected at high latitudes during winter corresponds well to the model predictions, the *OClO* detected at mid-latitudes cannot be explained by the presently known stratospheric photochemistry.

Contents

Chapter 1

Introduction

The chemical composition and dynamics of the atmosphere are vital for human, animal, and plant life on Earth. On a global scale, the system atmosphere-biosphere-ocean is in an equilibrium steady-state, where small short-term variations of the climate and the chemical composition of the different compartments are smoothed by the relatively long transport processes and therefore generally of small amplitude.

Since the beginning of industrialisation mankind has released large amounts of gases into the atmosphere and influenced thereby the natural cycles of material transport between the different reservoirs. One of the most important examples of this influence was the discovery of the Antarctic ozone hole by Farman et al. [1985], where nowadays at some altitude levels up to 100% of the stratospheric ozone can be depleted within a few weeks simultaneously reducing the total column of ozone by more than 70%. This observation was not expected and provoked a lot of concern among scientists and politicians, because the stratospheric ozone layer is protecting life on Earth against harmful UV radiation[1]. Research on this phenomenon led to the installation of a series of international political agreements on the ban of ozone depleting species like the CFCs, halons and halogenated hydrocarbons[WMO 1998].

Concern that some halogenated hydrocarbons may destroy ozone in the upper atmosphere was first raised in the 1970s [Molina and Rowland 1974; Stolarski and Cicerone 1974] predicting a global ozone reduction of 10-20% during the next 50-100 years. Acknowledging the realisation that these man-made chemicals are threatening the ozone layer, the Vienna Convention for the Protection of the Ozone layer was adopted by 28 countries in 1985. This committed signatories to a general obligation to take appropriate actions to protect the ozone layer and to co-operate on research. Shortly after the Vienna meeting, the ozone hole over the Antarctic was discovered, reinforcing the pressure to control potential ozone depleting substances. In 1987, the Montreal Protocol on Substances that Deplete the Ozone Layer was agreed and has since been ratified by over 160 countries. Initially, the Protocol imposed clear limits on the future production of CFCs and halons only and committed Parties to cutting down production by 50% by the year 2000. There were several amendments to the Montreal Protocol (London, 1990; Copenhagen, 1992; Montreal, 1997) thus strengthening the control of ozone depleting substances. The phase-out of substances already regulated was accelerated, and other chemicals found to cause ozone depletion were included, i.e. carbon tetrachloride, methyl chloroform, HCFCs and methyl bromide (CH_3Br).

Because of the long lifetime of CFCs and halons ('organic' F, Cl and Br) in the atmosphere, these species can reach the stratosphere where they are photolysed by sunlight (or attacked by

---

[1] UV-A: $320-400nm$ (biologically relatively uncritical), UV-B: $290-320nm$ (biologically critical), UV-C: $\lambda \leq 290nm$ (biologically extremely critical). The basic biological molecule DNA is most sensitive to UV-C radiation meaning that enhancements of this part of the electromagnetic spectrum can lead to changes in heritable information.

chemical radicals like OH or O), thereby setting free active[2] chlorine and bromine, which reacts nearly instantaneously with ozone. While the political actions taken world-wide do already show a decrease of the chlorine loading of the lower atmosphere [WMO 1998], the bromine containing halons are still increasing. As bromine and chlorine chemistry in the stratosphere are coupled together, the impact of bromine on the ozone budget is largest, where chlorine is activated - like in the Arctic and Antarctic winter. There have been a series of intensive measurement field campaigns during the last 10 years also studying the Arctic ozone layer and the occurrence of an Arctic ozone hole(e.g. EASOE, SESAME, THESEO, THESEO2000-EuroSolve)[3], which was observed during 3-5 of the Arctic winters in the 1990s [Goutail et al. 2000].

Although the abundance of active bromine is about 200 times less than the one of active chlorine, the efficiency of the bromine related catalytic cycles can be as high as the efficiency of the chlorine cycles. This is due to the lower stability of the bromine reservoir species in comparison with the chlorine reservoir species. During daytime inorganic stratospheric bromine is mainly present in the form of BrO, so that the balloon-borne DOAS[4] measurement of BrO is an efficient method to investigate the inorganic bromine budget of the stratosphere. Using model studies to predict the behaviour of the measured species during the time of the measurements allows to derive the total amount of inorganic bromine [Fitzenberger et al. 2000; Fitzenberger et al. 2000; Harder et al. 2000; Pfeilsticker et al. 2000]. Thus the eight LPMA/DOAS[5] balloon flights conducted between 1996 and 2000 provide the unique possibility to measure total inorganic bromine (Br_y^{in}) directly and compare it to the increase of organic precursors in the troposphere and lower stratosphere.

There are different methods to measure BrO in the stratosphere. The in-situ chemical conversion resonance-fluorescence instruments measure BrO indirectly within a certain air sample, while the remote sensing DOAS instruments (Zenith Scattered Light (ZSL) [Platt et al. 1997], direct sunlight DOAS from ground, satellite or balloon platform [Ferlemann et al. 2000]) directly measure the absorption bands in the UV part in the sunlight associated to BrO. The in-situ resonance-fluorescence technique performs well only in the stratosphere, while under certain conditions direct sunlight and scattered light DOAS can be sensitive to the troposphere and lower stratosphere [Friess et al. 1999; Fitzenberger et al. 2000; Fitzenberger et al. 2000]. The remote sensing instruments using zenith-sky or other scattered sunlight apply the same absorption technique as balloon-borne direct sunlight DOAS, but suffer from a more complicated radiative transport in the atmosphere, which has to be well known to retrieve the vertical distribution of the measured species. Therefore balloon-borne DOAS with direct sunlight allows to measure accurately the profiles of chemical species and by SCD[6] comparison it is also possible to check its photochemical variation.

The chemical species $OClO$ is an indicator for chlorine activation as it is believed to be predominantly produced by the reaction of ClO and BrO in the stratosphere. During the measurements presented in this thesis it could be detected in the Arctic winter as well as at mid-latitudes in autumn under undisturbed conditions. Nevertheless, it was only possible to predict the activation seen in the Arctic by the models used in this thesis - the 3-D Chemical Transport Model(CTM) SLIMCAT [Chipperfield 1999], which is well established in the scientific community, and a Lagrangian box model

---

[2] The short-lived chlorine species, which react very fast, are called active chlorine ($ClO_x = ClO + Cl + 2Cl_2O_2$). For bromine the same characterization is used ($BrO_x = Br + BrO$).

[3] EASOE : European Arctic Stratospheric Ozone Experiment, SESAME : Second European Stratospheric Arctic and Mid-latitude Experiment, THESEO : THird European Stratospheric Experiment on Ozone, THESEO2000-EuroSolve : as THESEO but within the US led SOLVE(SAGEIII Ozone Loss and Validation Experiment) campaign

[4] DOAS: Differential Optical Absorption Spectroscopy

[5] The LPMA/DOAS balloon payload is a French-German collaboration between LPMA/Paris (Laboratoire de Physique Moléculaire et Application) and the IUP/Heidelberg (Institut für Umweltphysik).

[6] SCD: Slant Column Density

on isentropic trajectories (LABMOS) especially implemented as a part of this thesis. The mid-latitude measurements cannot be explained with the standard gas phase and heterogeneous chemistry used in both models.

Chapter 2 gives an overview about the chemistry of the stratosphere and especially highlight the importance of halogens in the atmosphere. Chapter 3 proceeds with a description of the direct sunlight balloon-borne DOAS measurement technique which was used to retrieve the concentrations of the chemical species of interest in this thesis. Then an overview of the results of the eight LPMA/DOAS balloon flights conducted so far is presented in chapter 4. Chapter 5 covers the additional results of first free tropospheric BrO profile measurements which were stimulated by the combination of different measurement platforms (balloon, satellite, and ground-based). In chapter 6, the first comparison of the total inorganic bromine method with the standard organic bromine method is shown. Then, chapter 7 outlines two case studies made to understand the observation of enhanced $OClO$ amounts. Finally the thesis concludes with an outlook in chapter 8.

Chapter 2

Halogen species and their importance in atmospheric chemistry

Stratospheric ozone depletion through catalytic chemistry involving man-made chlorofluorocarbons is an area of focus in the study of geophysics and one of the global environmental issues of the twentieth and twenty-first century. It has been shown by several theoretical and experimental studies that catalytic cycles involving oxygen, hydrogen, nitrogen and last but not least halogens can affect fundamentally the abundance of ozone in the stratosphere, as well as in the troposphere.

2.1 Stratospheric Ozone

Although it was already proposed in 1974 that stratospheric ozone could be depleted in chemical reactions involving the degradation products of chlorofluorocarbons(CFCs), it was not until 1985 that unequivocal evidence of ozone loss was reported in the scientific literature. In that year, scientists from the British Antarctic Survey [Farman et al. 1985] described the polar ozone depletion, now known as the ozone hole, in which during six weeks in the spring the total ozone column decreases by more than half. It was subsequently shown that in the lower stratosphere almost all the ozone is removed from a layer at altitudes between about 13 and 20 km. These observations attracted great public interest, and aroused considerable scientific debate. At that time, photochemical theory had predicted ozone loss in the upper stratosphere by catalytic cycles involving the chlorine monoxide radical(ClO) and oxygen atoms. As the Antarctic ozone loss occurs in the lower stratosphere, it cannot be explained by that mechanism.

The unique role of ozone in absorbing certain wavelengths of incoming solar ultraviolet light was recognized in the latter part of the nineteenth century by Cornu [1879] and Hartley [1880]. Interest in ozone stems from the fact that such absorption of solar radiation is important in determining not only the thermal structure of the stratosphere but also the ecological framework for life on the Earth's surface. Decreased ozone results in increased ultraviolet transmission, which can affect the health of humans, animals, and plants.

Observations of the total integrated column ozone based on ultraviolet absorption began in the first few decades of the twentieth century [Fabry and Buisson 1913; Dobson 1968]. Systematic measurements of this type have revealed that the total abundances over many regions of the globe have decreased markedly since about 1980, as is illustrated in the data presented in Figure 2.1 - the total integrated ozone column is given generally in Dobson[1] units (DU).

Downward trends are evident in the time series of spatially or time-averaged spring column ozone

---

[1] Dobson unit (DU) is the common unit for expressing the total vertical column content of ozone in the atmosphere. 1 cm column of ozone at standard conditions (1013 mbar,273.15 K) corresponds to 1000 DU. The typical total ozone column is between 250 and 400 DU.

observations shown in Figure 1. Ozone varies from year to year at all locations, but the behaviour seen in recent decades in Antarctic spring lies very far outside of the historical variability.

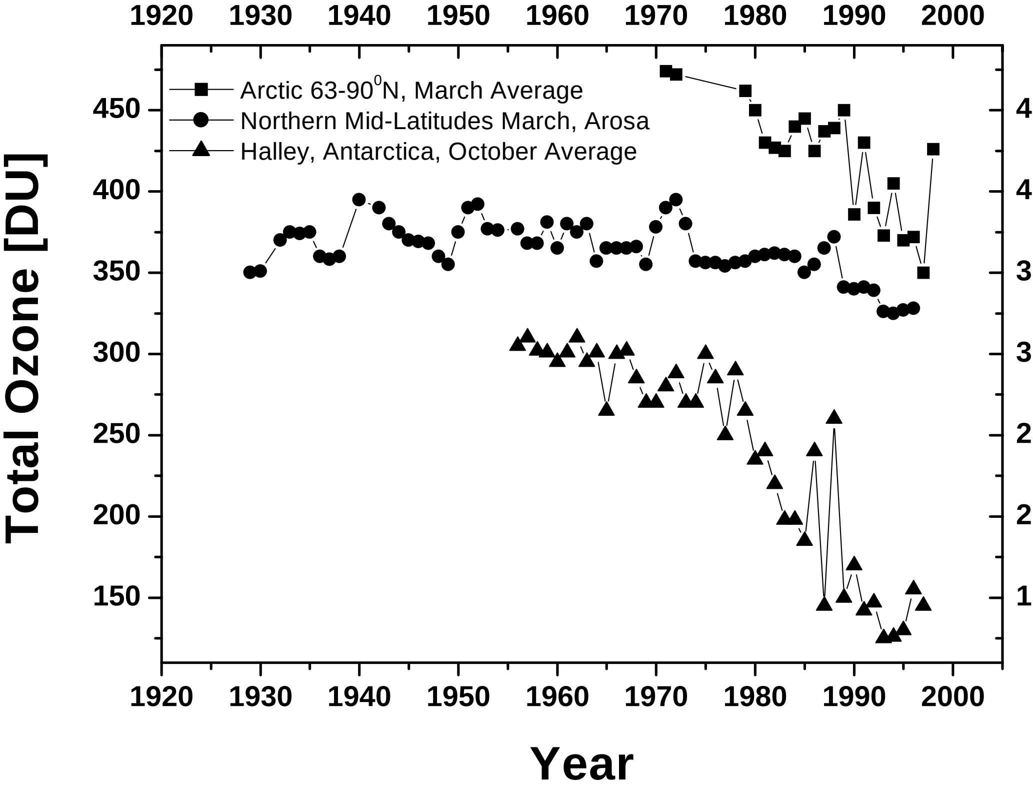

Figure 2.1: Observations of total ozone at various locations and its trends. The Arctic data from satellite observations [Newman et al. 1997] display the March average total ozone, while the Antarctic data from Halley [Farman et al. 1985] show the October average total ozone. The data from Arosa are 3 yr. running means of the March measurements [Staehelin et al. 1998]. Adapted from [Solomon 1999].

As the chlorofluorocarbons have very long atmospheric residence times, they will continue to deplete ozone even after a phase-out. Figure 2.2 shows the key processes controlling chlorofluorocarbon lifetimes in the Earth's atmosphere. These species are not significantly soluble in water; nor do they react with ocean or soil surfaces or with any chemical species present in the troposphere. Their chemical destruction depends upon the ultraviolet light found in the stratosphere. This radiation breaks up the chlorofluorocarbon molecules, yielding Cl atoms that can go on to destroy ozone in catalytic cycles as they move through the stratosphere.

Dobson [1930] inferred the existence of a large-scale stratospheric circulation cell characterized by rising motion in the tropics and descending motion at mid and high latitudes on the basis of his observations of the latitude gradients in ozone. Brewer [1949] reached a similar conclusion based upon an elegant analysis of early water vapour measurements. Recent studies have used observations of very long-lived gases with known tropospheric trends such as CO_2 [Schmidt and Khedim 1991] to show that the timescale for the overturning of this *Brewer-Dobson* circulation cell is 5 years. About 90% of the total atmospheric mass resides in the troposphere, and 10% resides in the stratosphere.

The Brewer-Dobson circulation illustrates only the key net processes that transport CFCs and other gases in a zonally averaged flow pattern. Waves mix trace gases when they break down, particularly in the winter hemisphere.

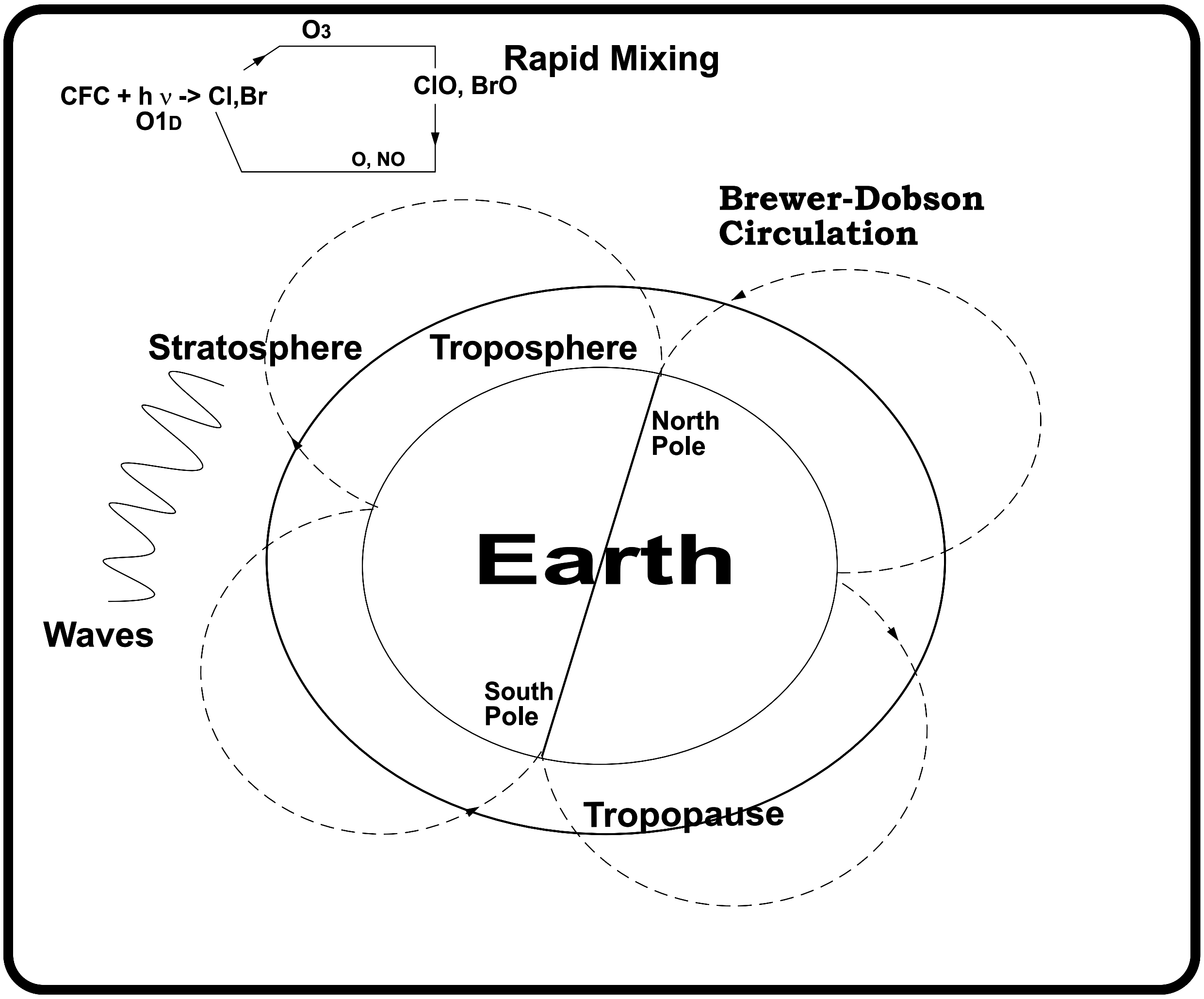

Figure 2.2: Schematic diagram showing the breakdown of CFCs and catalytic destruction of ozone in the middle and upper stratosphere. As the stratosphere contains only 10% of the mass of the total atmosphere, the atmosphere must turn over many times to destroy all of the CFCs present, resulting in long atmospheric residence times of these gases. Adapted from [Solomon 1999].

2.2 Tropospheric Ozone

In the beginning of the 20th century all ozone in the troposphere was believed to be of stratospheric origin, because the short-wave solar radiation required ($\lambda \leq 240\,nm$) for the primary production of O_3 by photolysis of the oxygen molecule is already absorbed in the stratosphere.
However, in the mid 1940s, it became clear that tropospheric ozone production could also take place. It was shown that plant damage can be produced by ozone (in the Los Angeles(USA) area heavy damage had repeatedly occurred to vegetable crops). Haagen-Smit et al. [1952] proposed in the early 1950s that ozone could be formed as a result of photochemical reactions involving nitrogen species and reactive non-methane hydrocarbons, NMHC, present in automobile exhaust (like ethylene, butane, etc.). Sometimes the NMHC are also called NMOC, non-methane organic compounds. The overall reaction identified to produce O_3 was as follows

$$NMOC + NO_x + h\nu \rightarrow O_3 + other \quad pollutants \tag{2.1}$$

NO_x represents nitric oxide(NO) plus nitrogen dioxide (NO_2); NO, however, generally forms the greatest fraction of directly emitted NO_x.

Since hydrocarbons and NO_x are major constituents of the exhaust from uncontrolled motor vehicles and Los Angeles has year-round intense sunlight, appropriate meteorological and geographical characteristics, it is clear why photochemical air pollution was first identified there.
The following are the principal reactions leading to ozone production and destruction in the troposphere.

$$\begin{array}{cccll} NO_2 & \overset{h\nu}{\rightarrow} & NO+O(^3P) & \lambda \leq 420\,\mathrm{nm} & J(NO_2) \\ O(^3P)+O_2 & \overset{M}{\rightarrow} & O_3 & k_1 = 1.5*10^{-14}\frac{cm^3}{molecule*sec} \\ NO+O_3 & \rightarrow & NO_2+O_2 & k_2 = 1.8*10^{-12}\frac{cm^3}{molecule*sec} \end{array} \tag{2.2}$$

When there is a photostationary state established between the NO_x and O_x species, we can calculate the O_3 concentration

$$[O_3] = \frac{J(NO_2)*[NO_2]}{k_2*[NO]} \Longleftrightarrow \frac{[NO]}{[NO_2]} = \frac{J(NO_2)}{[O_3]*k_2} \tag{2.3}$$

The ratio of NO to NO_2 is also called *Leighton ratio*. During the night different other reactions become important involving NO_3, which is photolysed during the day (the photolysis rates are given for solar zenith angle (SZA) of O^o).

$$\begin{array}{cccl} NO_2+O_3 & \rightarrow & NO_3+O_2 & k_3 = 1.2*10^{-13}\frac{cm^3}{molecule*sec} \\ NO_3 & \overset{h\nu(580\,nm \leq \lambda \leq 635\,nm)}{\rightarrow} & NO+O_2 & J_1(NO_3) = 0.022s^{-1} \\ NO_3 & \overset{h\nu(\lambda \leq 635\,nm)}{\rightarrow} & NO_2+O & J_2(NO_3) = 0.18s^{-1} \\ NO_3+NO & \rightarrow & 2NO_2 & k_4 = 2.6*10^{-11}\frac{cm^3}{molecule*sec} \\ NO_3+NO_2 & \overset{M}{\rightarrow} & N_2O_5 & k_5 = 2.5*10^{-11}\frac{cm^3}{molecule*sec} \\ NO_3+RH & \rightarrow & HNO_3+R & \text{RH=hydrocarbons} \end{array} \tag{2.4}$$

The main sink of NO_x is nitric acid (HNO_3).

$$\begin{array}{cccl} NO_2+OH & \rightarrow & HNO_3 & k_6 = 1.1*10^{-11}\frac{cm^3}{molecule*sec} \\ NO_3+RH & \rightarrow & R+HNO_3 & \\ NO_3+RCHO & \rightarrow & RCO+HNO_3 & \end{array} \tag{2.5}$$

Photochemical ozone production in polluted urban areas can be explained by the following reaction schemes - the $O(^1D)$ to $O(^3P)$ transition is forbidden, so that $O(1D)$ reacts with other species

$$\begin{array}{cccl} O_3 & \overset{h\nu(\lambda \leq 315\,nm)}{\rightarrow} & O(^1D)+O_2 & \\ O_3 & \overset{h\nu(315\,nm \leq \lambda \leq 1100\,nm)}{\rightarrow} & O(^3P)+O_2 & \\ O(^1D) & \overset{M}{\rightarrow} & O(^3P) & k_7 = 2*10^{-11}\frac{cm^3}{molecule*sec} \\ O(^1D)+H_2O & \rightarrow & 2OH & k_8 = 2.2*10^{-11}\frac{cm^3}{molecule*sec} \\ CO+OH & \overset{O_2}{\rightarrow} & CO_2+HO_2 & \\ HO_2+NO & \rightarrow & OH+NO_2 & k_9 = 8.6*10^{-12}\frac{cm^3}{molecule*sec} \\ RH+OH & \rightarrow & R+H_2O & \\ R+O_2 & \rightarrow & RO_2 & \\ RO_2+NO & \rightarrow & RO+NO_2 & \\ & \rightarrow & RONO_2 & \end{array} \tag{2.6}$$

The newly generated $RO = R`CHO$ radicals react with O_2 producing HO_2, which itself is again producing a OH radical, closing this catalytic O_3 production cycle.
In the free troposphere and the remote oceanic boundary layer, NMHC/NMOC concentrations are

relatively small. Under such conditions the ozone production is dominated by oxidation of CO and CH_4 instead of NMHC [Crutzen 1974].

$$\begin{array}{ccc} CO+OH & \rightarrow & CO_2+H \\ H+O_2 & \overset{M}{\rightarrow} & HO_2 \\ CH_4+OH & \rightarrow & CH_3+H_2O \\ CH_3+O_2 & \overset{M}{\rightarrow} & CH_3O_2 \\ HO_2+NO & \rightarrow & OH+NO_2 \\ HO_2+O_3 & \rightarrow & OH+2O_2 \\ CH_3O_2+NO & \rightarrow & CH_3O+NO_2 \\ CH_3O+O_2 & \rightarrow & HO_2+HCHO \end{array} \tag{2.7}$$

The ozone concentration can then be estimated to

$$[O_3]=\frac{k_{HO_2+NO}}{k_{HO_2+O_3}}\times[NO]\approx 4300\times[NO] \tag{2.8}$$

For background O_3 values of typically 40 ppb, this corresponds to a threshold of 10 ppt NO for the production of ozone. The fast ozone depletion (within a few days) in the polar regions observed during spring cannot be explained by a decrease in NO, but is related to the appearance of tropospheric boundary layer BrO [Hausmann and Platt 1994].

The photochemical production of OH is possible via photolysis of ozone ($\lambda \leq 310nm$), so that O_3 is largely influencing the oxidation capacity of the atmosphere. The fundamental importance of the oxidation by the hydroxyl radical is the conversion of non-soluble compounds into highly soluble ones which are removed from the atmosphere very efficiently by wet deposition.

2.3 Stratospheric gas phase chemistry related to ozone

2.3.1 Chapman Chemistry

A photochemical theory for formation and destruction of ozone based on an oxygen-only chemical scheme was first proposed by Chapman [1930]. Chapman noted that ozone and atomic oxygen rapidly interchange with each other, while the sum of the two is linked to much slower chemical processes. This work laid the foundation for the understanding of *odd oxygen* chemistry, which allows a clear distinction to be drawn between net and gross production and loss of ozone over a chosen timescale.

$$O_2 \overset{h\nu}{\rightarrow} 2O \qquad \lambda \leq 242\,\mathrm{nm} \tag{2.9}$$

$$O+O_2 \overset{M}{\rightarrow} O_3 \tag{2.10}$$

$$O_3 \overset{h\nu}{\rightarrow} O(^1D)+O_2 \qquad \lambda \leq 320\,\mathrm{nm} \tag{2.11}$$

$$O(^1D) \overset{M}{\rightarrow} O(^3P) \tag{2.12}$$

$$O_3 \overset{h\nu}{\rightarrow} O(^3P)+O_2 \qquad \lambda \leq 1100\,\mathrm{nm} \tag{2.13}$$

$$O+O \overset{M}{\rightarrow} O_2 \tag{2.14}$$

$$O(^3P)+O_3 \rightarrow 2O_2 \tag{2.15}$$

Ozone photolysis below 50 km represents a gross but not net loss process over timescales of the order of minutes, since nearly all of the atomic oxygen thus produced reforms ozone in just a few seconds or less. Ozone and atomic oxygen thereby cycle very rapidly between one another in the stratosphere. A very small fraction of the oxygen atoms produced from ozone photolysis can react with ozone, yielding a net loss of the sum of the two over extended timescales. Hence it is conceptually useful to consider atomic oxygen together with ozone as an *odd oxygen family* distinct from the much longer-lived form of *even oxygen*, O_2.

2.3.2 Catalytic Cycles

After Chapman's groundbreaking theory, it became clear that stratospheric ozone was chemically destroyed not solely by reaction with atomic oxygen, but also by hydrogen[Bates and Nicolet 1950] and nitrogen oxide chemistry[Crutzen 1970]. Each of these species may also be considered in terms of their own odd hydrogen and odd nitrogen families, the members of which can interchange chemically with one another. Hydrogen and nitrogen oxides can destroy odd oxygen in a catalytic fashion wherein the initiating active species (e.g. OH, NO) are regenerated, so that even small amounts of these gases can influence the much greater ozone abundances.

$$\begin{array}{rcllr}
O + OH & \rightarrow & O_2 + H & \text{Odd Hydrogen Catalytic Cycles} & (2.16) \\
H + O_2 & \overset{M}{\rightarrow} & HO_2 & & (2.17) \\
O + HO_2 & \rightarrow & O_2 + OH & & (2.18) \\
\hline
Net \quad Cycle \quad 1 : O + O & \overset{M}{\rightarrow} & O_2 & & (2.19) \\
OH + O_3 & \rightarrow & HO_2 + O_2 & & (2.20) \\
HO_2 + O_3 & \rightarrow & OH + 2O_2 & & (2.21) \\
\hline
Net \quad Cycle \quad 2 : \quad 2O_3 & \rightarrow & 3O_2 & & (2.22)
\end{array}$$

$$\begin{array}{rcllr}
NO + O_3 & \rightarrow & NO_2 + O_2 & \text{Odd Nitrogen Catalytic Cycle} & (2.23) \\
O + NO_2 & \rightarrow & NO + O_2 & & (2.24) \\
\hline
Net \quad Cycle \quad 3 : O + O_3 & \rightarrow & 2O_2 & & (2.25)
\end{array}$$

$$\begin{array}{rcllr}
Cl + O_3 & \rightarrow & ClO + O_2 & \text{Odd Chlorine Catalytic Cycles} & (2.26) \\
ClO + O & \rightarrow & Cl + O_2 & & (2.27) \\
\hline
Net \quad Cycle \quad 4 : O + O_3 & \rightarrow & 2O_2 & & (2.28) \\
Cl + O_3 & \rightarrow & ClO + O_2 & & (2.29) \\
Cl + O_3 & \rightarrow & ClO + O_2 & & (2.30) \\
ClO + ClO & \overset{M}{\rightarrow} & Cl_2O_2 & & (2.31) \\
Cl_2O_2 & \overset{h\nu}{\rightarrow} & Cl + ClO_2 & & (2.32) \\
ClO_2 & \overset{M}{\rightarrow} & Cl + O_2 & & (2.33) \\
\hline
Net \quad Cycle \quad 5 : \quad 2O_3 & \rightarrow & 3O_2 & & (2.34)
\end{array}$$

$$
\begin{aligned}
Cl + O_3 &\rightarrow ClO + O_2 \quad \text{Odd Cl-Br Catalytic Cycle} && (2.35)\\
Br + O_3 &\rightarrow BrO + O_2 && (2.36)\\
BrO + ClO &\rightarrow Br + ClO_2 && (2.37)\\
ClO_2 &\overset{M}{\rightarrow} Cl + O_2 && (2.38)
\end{aligned}
$$

$$Net \quad Cycle \quad 6: \quad 2O_3 \rightarrow 3O_2 \qquad (2.39)$$

The following reactions illustrate how one family of gases can couple to another (such as the formation of $ClONO_2$ through reaction of ClO with NO_2; $ClONO_2$ is thus a member of both the *odd chlorine and odd nitrogen families*) and how relatively long-lived reservoirs ($HCl, ClONO_2, HNO_3$) form, which can strongly influence the abundances of the ozone-destroying gases.

$$
\begin{aligned}
ClO + NO &\rightarrow Cl + NO_2 \quad \text{Coupling and Reservoir Reactions} && (2.40)\\
Cl + CH_4 &\rightarrow HCl + CH_3 && (2.41)\\
HO_2 + ClO &\rightarrow HOCl + O_2 && (2.42)\\
ClO + NO_2 &\overset{M}{\rightarrow} ClONO_2 && (2.43)\\
OH + NO_2 &\overset{M}{\rightarrow} HNO_3 && (2.44)
\end{aligned}
$$

$$
\begin{aligned}
HCl + ClONO_2 &\rightarrow Cl_2 + HNO_3 \quad \text{Key Heterogeneous Reactions} && (2.45)\\
N_2O_5 + H_2O &\rightarrow 2HNO_3 && (2.46)\\
H_2O + ClONO_2 &\rightarrow HOCl + HNO_3 && (2.47)\\
HCl + HOCl &\rightarrow H_2O + Cl_2 && (2.48)\\
BrONO_2 + H_2O &\rightarrow HNO_3 + HOBr && (2.49)\\
HCl + BrONO_2 &\rightarrow HNO_3 + BrCl && (2.50)\\
HCl + HOBr &\rightarrow H_2O + BrCl && (2.51)
\end{aligned}
$$

The natural abundances of odd hydrogen can also be affected through human modifications of sources gases such as H_2O and CH_4, while natural odd nitrogen can be perturbed through direct emissions of high-flying aircraft, by nuclear explosions, or by changes in its primary source gas, N_2O.

Stolarski and Cicerone [1974] pointed out the importance of chlorine engaging in a catalytic cycle resulting in ozone destruction and Molina and Rowland [1974] identified man-made chlorofluorocarbons as the major source of ozone-destroying stratospheric chlorine. Wofsy et al. [1975], Yung et al. [1980], Tung et al. [1986] and McElroy et al. [1986] showed that bromocarbons could also contribute to ozone depletion, especially through the coupling of bromine and chlorine chemistry. Figure 2.3 and Figure 2.4 show the relative importance of the different ozone destruction cycles with respect to the height in the stratosphere. As can be seen in the figures, the bromine cycle - which is of special interest within this thesis - plays a non-negligible role in the lower stratosphere, where most of the stratospheric ozone resides.

2.3.3 Nitrogen chemistry in the stratosphere

The daytime evolution of NO_2 is determined by the reactions with NO, NO_3 and N_2O_5. During the night NO is converted via the reaction with O_3 to NO_2, which itself can react again with O_3 to form NO_3, whose photolysis during the day is very fast (lifetime = 3 sec).

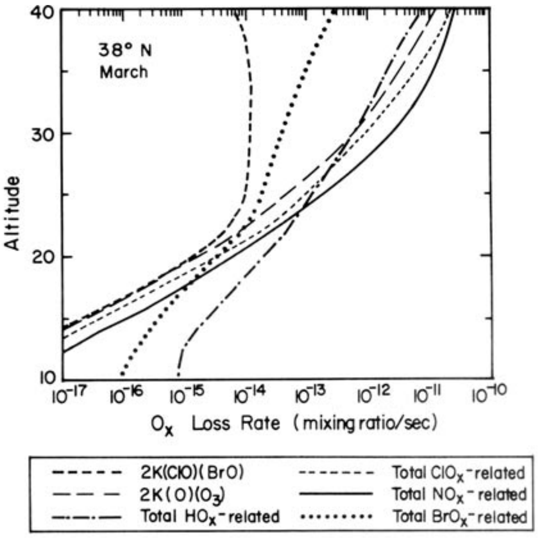

Figure 2.3: Modelled vertical distribution of the ozone depletion potential of different catalytic cycles - time integration of 24 h - for 38°N in March [Garcia and Solomon 1994]

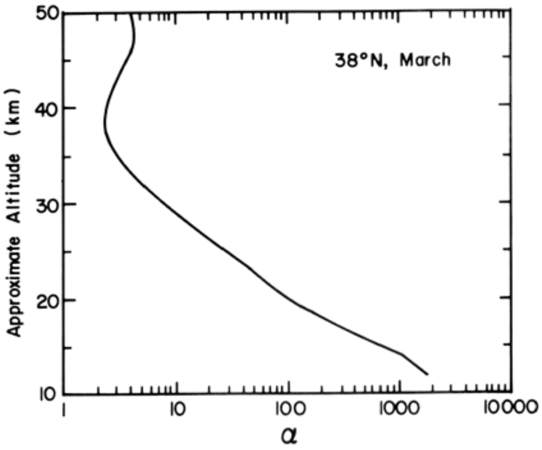

Figure 2.4: Modelled vertical distribution of the ozone depletion potential of bromine versus chlorine - time integration of 24 h - for 38°N in March [Garcia and Solomon 1994]

$$NO + O_3 \rightarrow NO_2 + O_2 \qquad (2.52)$$

$$NO_2 + O_3 \rightarrow NO_3 + O_2 \qquad (2.53)$$

The next step is the formation of N_2O_5 by reaction of NO_2 with NO_3. N_2O_5 is a reservoir gas, which is relatively stable in the stratosphere, especially when the temperatures are low as in the polar stratosphere, when thermal decay is no more effective.

$$NO_2 + NO_3 \overset{M}{\leftrightarrow} N_2O_5 \qquad (2.54)$$

$$NO_2 \overset{h\nu}{\rightarrow} NO + O \qquad J_{NO_2} = 1.4 * 10^{-2} sec^{-1} \qquad (2.55)$$

$$NO_3 \overset{h\nu}{\rightarrow} NO_2 + O \qquad or \qquad NO + O_2 \qquad J_{NO_3} = 0.36 sec^{-1} \qquad (2.56)$$

$$N_2O_5 \overset{h\nu}{\rightarrow} NO_2 + NO_3 \qquad J_{N_2O_5} = 3 * 10^{-5} sec^{-1} \qquad (2.57)$$

In the sunlit stratosphere NO_2, NO_3 and N_2O_5 are photolysed, but the photolysis of N_2O_5 proceeds some orders of magnitude more slowly than the one of NO_2. That is why the measured NO_2 slant column densities (SCDs) are smaller in the morning than in the evening for the same solar zenith angle (SZA), because in the morning NO_2 is first photolysed very fast, while it is increasing slowly during the day - as N_2O_5 is photolysed slowly during the day - and very fast in the evening when NO_2 photolysis decreases with SZA.

These reactions are responsible both for the seasonal variation of the NO_2 slant column (maximum in the summer and minimum in the winter) and for the latitudinal NO_2 gradient (*Noxon-Cliff*) in the winter hemisphere with reduced NO_2 columns towards the pole [Noxon 1979]. This reduction of NO_2 in the dark polar stratosphere is strongest during mid winter in the polar vortex, where the temperatures become lowest, and is called *denoxification*. The gradient is even reinforced through the reduced airmass exchange along the border of the polar vortex.

Besides N_2O_5, HNO_3 is another important reservoir of the inorganic nitrogen family (NO_y). It is formed in the gas phase by the reaction of OH with NO_2 and heterogeneously by the hydrolysis of N_2O_5 on PSCs or sulphate aerosols.

$$NO_2 + OH \overset{M}{\rightarrow} HNO_3 \quad (2.58)$$

$$N_2O_5 \overset{het,H_2O}{\rightarrow} 2HNO_3 \quad (2.59)$$

The main sink of HNO_3 is the photolysis (resulting in NO_2 and OH) and the reaction with OH.

$$HNO_3 + OH \rightarrow NO_3 + H_2O \quad (2.60)$$

Both the formation of HNO_3 and its destruction are relatively slow, so that it does not influence the NO_2 daytime evolution. But the former reactions are very important for the *renoxification* of the polar stratosphere in spring, when the NO_x concentrations are increasing again and reactive chlorine is bound again in its reservoirs.

2.3.4 Halogen chemistry in the stratosphere

Halogens belong to the seventh main group of the periodic table of chemical elements. These are fluorine(F), chlorine(Cl), bromine(Br), iodine(I) and astatine(At).[2] Fluorine has only the oxidation number -1, while the other halogens have primarily the number -1 and +7. The valences +5, +3 and +1 are more and more unstable.

These elements are all non-metals, but the metallic character becomes more and more intense going from F to At. Hydroxides are only known to exist for Cl, Br and I. As in the 6th main group, the acidity decreases from Cl to I. While $HClO_4$ is the strongest acid, H_5IO_6 is only weakly acid. The aqueous solutions of the halogens are acids and their acidity increases strongly from HF(medium) to HI(very strong).

In the stratosphere chemical partitioning processes play a major role in ozone destruction that is dramatically illustrated by the contrasts between F, Cl and Br gas phase chemistry. Briefly, the halogen atoms released in the stratosphere from chlorocarbon, bromocarbon, and fluorocarbon source gases can form acids (through abstraction of a hydrogen atom) and nitrates (through reaction with NO_2). In the case of fluorine, the acid HF is quickly formed and so tightly bound that essentially all fluorine released from fluorine source gases in the stratosphere is irreversibly and rapidly *neutralized* as HF [Rowland and Molina 1975]. The amount of atomic fluorine and FO available to participate in ozone-destroying catalytic cycles (or, in chemical terms, the catalytic chain length) is hence extremely short, and fluorine has a negligible impact on ozone [Lary 1998].

Chlorine forms both HCl and $ClONO_2$ reservoirs. These gases can be reconverted to chlorine atoms by gas phase chemistry (i.e., by reaction with OH and photolysis, respectively). The amount of Cl and ClO available to participate in ozone-destroying catalytic chemistry therefore is critically dependent on the partitioning of chlorine between these *active chlorine* radicals and the non-ozone-destroying *reservoirs* HCl and $ClONO_2$.

Bromine is less tightly bound than chlorine, so that relatively little of the bromine released from bromocarbons is tied up in HBr and $BrONO_2$, rendering this atom quite effective for ozone loss [Wofsy et al. 1975; Yung et al. 1980; Lary 1996; Lary et al. 1996], especially in combination with chlorine [Tung et al. 1986; McElroy et al. 1986]. Although there are significant human sources of bromine, the contemporary abundances of total stratospheric bromine are about 200 times smaller than those of chlorine [Schauffler et al. 1998; Wamsley 1998; Harder et al. 2000].

Iodine may also participate in ozone-destroying catalytic cycles with bromine and chlorine [Solomon et al. 1994] but its stratospheric abundance is believed to be much smaller than those of bromine and chlorine [Pundt et al. 1998], and its primary sources are believed to be natural rather than largely or partly man-made as in the case of fluorine, chlorine, and bromine.

---

[2] *Halogens* means salt generators

Stratospheric Chlorine Chemistry

While many natural processes produce chlorine at ground level (including for example, sea salt and volcanic emissions HCl), these compounds are efficiently removed in precipitation (rain and snow) owing to high solubility. The removal of HCl emitted by volcanoes is extremely efficient, rendering even the most explosive volcanic plumes ineffective at providing significant inputs of chlorine to the stratosphere.

In contrast, airborne observations of the suite of chlorofluorocarbons at the base of the tropical stratosphere [Schauffler et al. 1998] show that the total chlorine content in air entering the lowermost stratosphere due to chlorofluorocarbons in 1992 was about 3.0 ppb, compared with only 0.1-0.2 ppb from concurrent measurements of HCl and 0.5-0.6 ppb from CH_3Cl, which is the sole stratospheric chlorocarbon that has significant natural sources. Observations have confirmed that the temporal trends in global surface level abundances of chlorofluorocarbons are consistent with the known industrial emissions [Montzka et al. 1996], both in terms of the buildup of these gases in past decades and the slower accumulation in the 1990s following reductions in global use (see Figure 2.14).

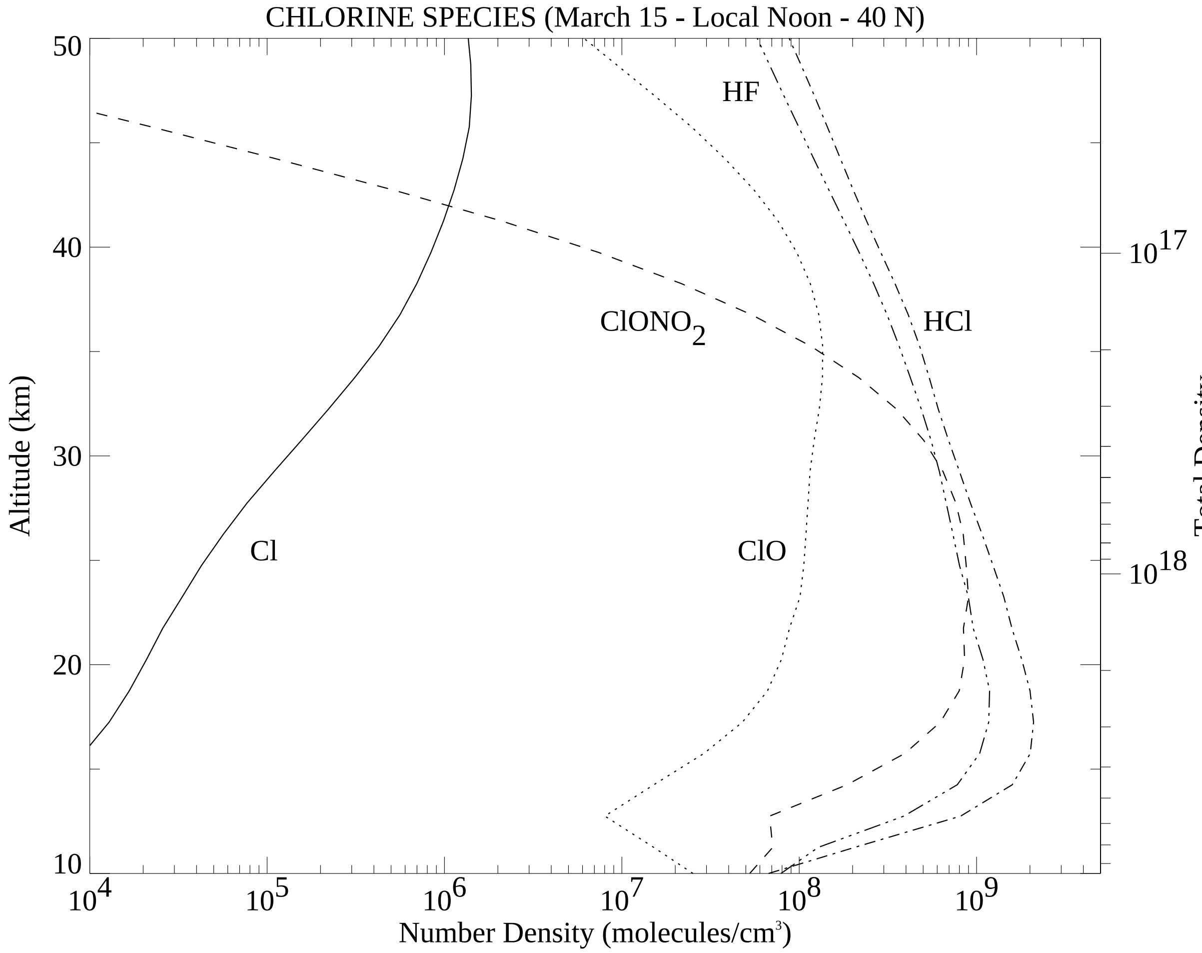

Figure 2.5: Typical number densities for chlorine species for mid-latitudes and spring local noon. Adapted from [DeMore et al. 1997].

The typical chlorine partitioning is shown in Figure 2.5. In the uppermost stratosphere above 45 km, nearly all of the chlorine released from source molecules such as CFCs (Cl_y) is sequestered in the HCl reservoir, owing largely to the efficacy of the reaction of $Cl + CH_4$ at warm temperatures and high Cl/ClO ratios there. Recent studies [Lipson et al. 1997] suggest that a small yield of HCl in the reaction of ClO with OH also affects the HCl/ClO partitioning in this region.

Stratospheric Bromine Chemistry

The other important halogen ozone-destruction catalytic cycle is the bromine cycle involving the bromine oxide radical BrO. Here an overview about the bromine gas phase and heterogeneous chemistry according to Lary [1996], Lary et al. [1996] is be given.

Bromine does not have such a photochemically stable reservoir as chlorine. The most important reservoir species are HBr and $BrONO_2$ with photochemical lifetimes, which are 100 times shorter than the lifetimes of HCl and $ClONO_2$, respectively. In comparison with chlorine the ratio of reactive bromine (BrO_x) is by far larger than in the case of chlorine, so that the ozone depletion potential of bromine is comparable to that one of chlorine, although the BrO concentration is 10-200 times smaller than the one of ClO [McKinney et al. 1997; Harder et al. 1998].

The impact of bromine is most effective during high chlorine activation like for example in the polar vortex. There, the combined cycle of BrO and ClO can effectively destroy ozone

$$ClO + BrO \rightarrow BrCl + O_2 \qquad (\ 7\%) \tag{2.61}$$

$$\rightarrow Br + ClOO \qquad (\ 38\%) \tag{2.62}$$

$$\rightarrow Br + OClO \qquad (\ 55\%) \tag{2.63}$$

The branching ratios of this reaction are given for $T = 210$ K. Both the generation of $BrCl$ and $ClOO$ lead to a coupled catalytic bromine-chlorine ozone-destruction cycle [McElroy et al. 1986], because of the fast photolysis of $BrCl$ and the impact-induced decay of $ClOO$ to Cl and molecular oxygen.

The third pathway is the only known production channel of $OClO$ in the lower stratosphere, because the reaction of ClO and NO_3 [Toumi 1994] can be neglected there.

The main sink of $OClO$ is the fast photolysis

$$OClO \xrightarrow{h\nu} ClO + O \tag{2.64}$$

which prevents the buildup of noteworthy amounts of $OClO$ during the day. The formation of $OClO$ is not depleting O_3 - because of the formation of one O_3 molecule after the photolysis - but it is an indicator for chlorine activation, as well as for ozone depletion [Solomon et al. 1987; Sanders et al. 1989; Sessler et al. 1995].

BrO has a short lifetime (≈ 1 sec) during the day. Still between 40-70% of the total inorganic bromine (Br_y) can be in the form of BrO, because atomic bromine (Br) does react very fast with O_3. The most important sinks of BrO are the photolysis and the reactions with NO, ClO and NO_2. During the sunset the BrO concentrations decrease very fast, as the reservoir species become more and more abundant.

$BrONO_2$ is formed by the reaction of BrO and NO_2

$$BrO + NO_2 \xrightarrow{M} BrONO_2 \tag{2.65}$$

It is under non-denoxification conditions (out of the polar vortex) the most important bromine reservoir species and has a photolytic lifetime of a few minutes

$$BrONO_2 \xrightarrow{h\nu} Br + NO_3 \tag{2.66}$$

Another important heterogeneous loss reaction of $BrONO_2$ is the $BrONO_2$ hydrolysis on PSC (polar stratospheric clouds) and sulphuric acid aerosol surfaces - the latter are subject of another special section of this thesis.

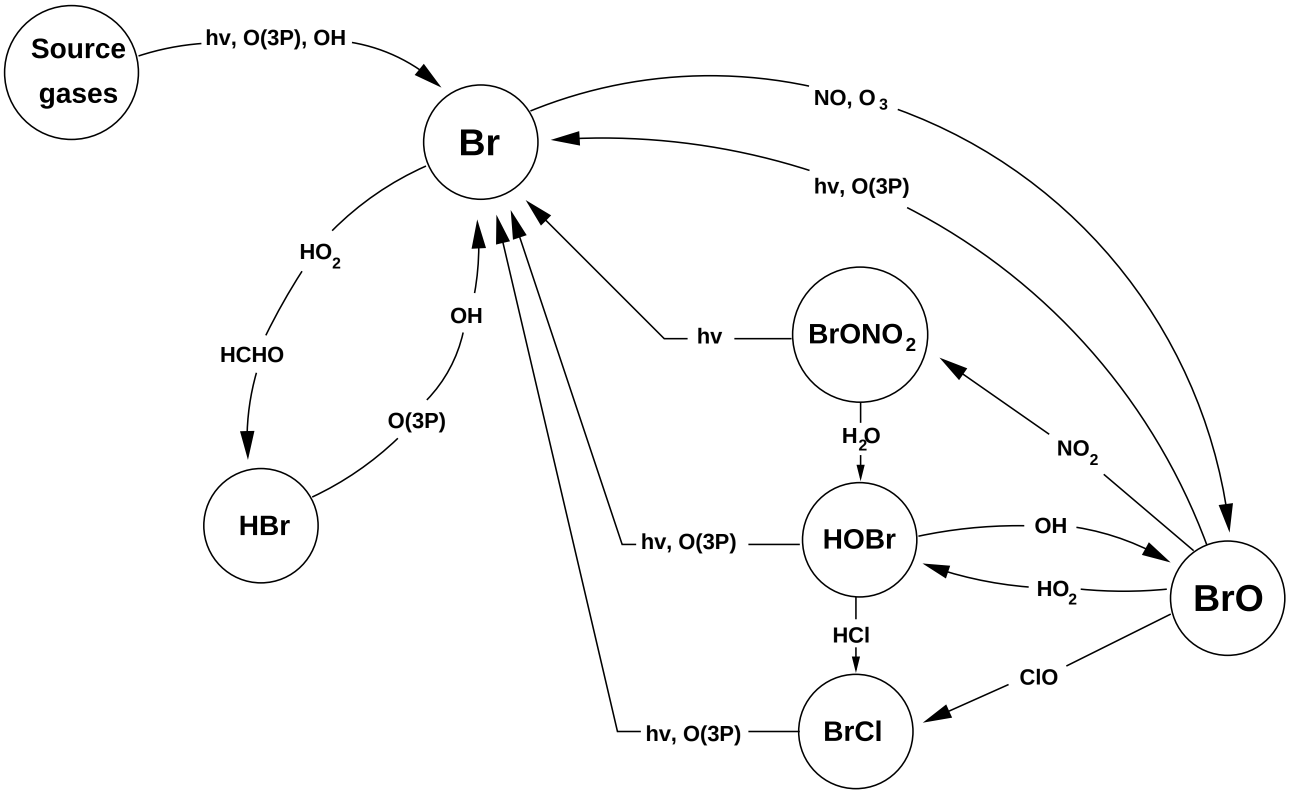

Figure 2.6: Stratospheric bromine chemistry [Lary 1996; Lary et al. 1996]

$$BrONO_2 \overset{aerosol,H_20}{\rightarrow} HOBr + HNO_3 \tag{2.67}$$

$HOBr$ can also be formed by the reaction of BrO and HO_2

$$BrO + HO_2 \rightarrow HOBr + O_2 \tag{2.68}$$

Because of this reaction and the lower photolytic stability of $HOBr$, ($J_{HOBr} = 1.6 \times J_{BrONO_2}$) in comparison with $BrONO_2$ (lifetime = 500 sec) $HOBr$ can form up to 30% of the total inorganic bromine (Br_y) during daytime and can be the most important bromine reservoir during the night taking into account the increased importance of $BrONO_2$ hydrolysis on sulphuric acid background aerosols.

$BrCl$ is the product of the reaction of BrO and ClO and has the largest photolysis frequency of the bromine reservoirs (lifetime=$30sec$, at 67^oN, noon). In general, the ratio $BrCl/Br_y$ is very small, but it can increase noticeably because of heterogeneous bromine reactions, especially during the polar night.

HBr is formed by the reaction of atomic Br with the peroxy radical HO_2 and formaldehyde, $HCHO$

$$Br + HO_2 \rightarrow HBr + O_2 \tag{2.69}$$

$$Br + HCHO \rightarrow HBr + HCO \tag{2.70}$$

However, as measured HBr mixing ratios of 1-2 ppt [Nolt et al. 1997] are much larger than that calculated by models, there are suggestions that there is a HBr channel in the reaction of BrO with HO_2 or the reaction of BrO with OH - a 1-2% yield of HBr in the latter reaction would reconcile measurements and model[Chipperfield et al. 1997].

The main sink of HBr is the reaction with OH

$$HBr + OH \rightarrow Br + H_2O \tag{2.71}$$

so that HBr has the longest lifetime of all inorganic bromine species in the stratosphere ($1h - 1day$). Following this reaction scheme, it is possible to explain the annual evolution of the BrO SCD. In summer the higher NO_2 concentrations lead to a larger $BrONO_2$ formation, which means less BrO in accordance with observations and models [Richter et al. 1999; Fish and Jones 1995; Danilin and McConnell 1995].

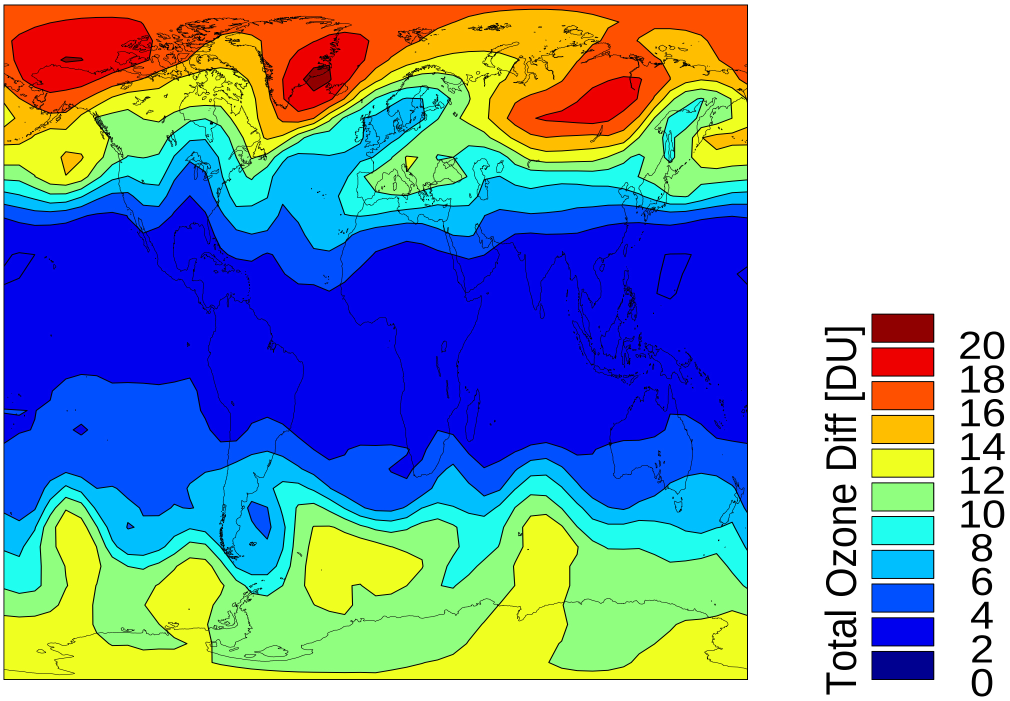

Figure 2.7: Global change in Dobson units of total O_3 column as a function of total bromine for March 13, 1995. The first model run included 10 ppt Br_y and the second 20 ppt. Kindly provided by Sinnhuber and Chipperfield [2000].

Because of the different catalytic reaction cycles, where stratospheric bromine is involved, the impact of an increase of bromine is not the same throughout the world. To investigate the impact of bromine on stratospheric ozone Sinnhuber and Chipperfield [2000] conducted two 1-year long model runs for the years 1994/1995 with the 3-D CTM model SLIMCAT [Chipperfield 1999] - one with 10 ppt total inorganic bromine (Br_y) and one with 20 ppt Br_y. The difference in Dobson units (DU) and percent change is shown in Figure 2.7 and 2.8. It can be observed that the influence of increasing bromine levels in the stratosphere is the largest in the polar stratosphere. This is mainly due to the coupling of bromine and chlorine chemistry in the chlorine activated polar stratosphere. As the two figures show case model results for March 13, 1995, the largest effect can be seen in the Arctic winter polar stratosphere, while the equivalent figures for October 1995 show the enhanced effect in the Antarctic polar stratosphere.

2.4 Heterogeneous chemistry on PSCs leading to the *Ozone Hole*

It was known long before the advent of the *Ozone Hole* that there exist *Polar Stratospheric Clouds* (PSCs) in polar regions. The name of the PSCs was coined by [McCormick et al. 1982], who first presented satellite observations of high-altitude clouds in the Antarctic and Arctic stratosphere. The

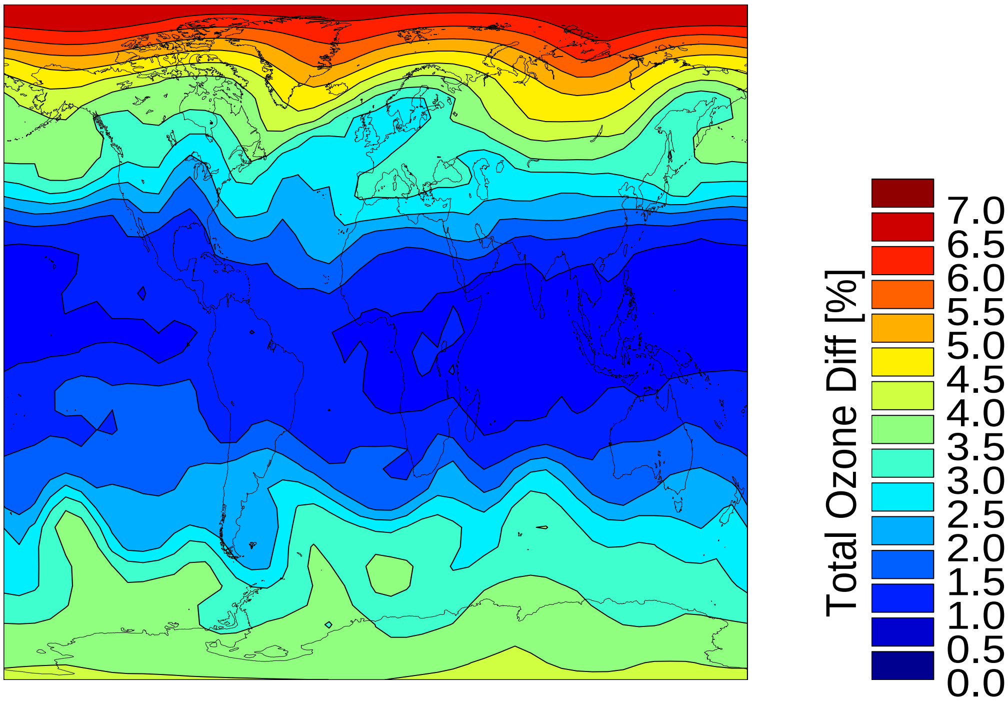

Figure 2.8: Global change in % of total O_3 column as a function of total bromine for March 13, 1995. The first model run included 10 ppt Br_y and the second 20 ppt. Kindly provided by Sinnhuber and Chipperfield [2000].

data showed that the Antarctic clouds were present from June to September that they were associated with cold temperatures below 200 K, and that they occurred between 12 and 25 km.

Solomon et al. [1986] suggested that HCl and $ClONO_2$ might react on the surfaces of PSCs, perturbing gas phase chlorine partitioning in a manner that could greatly accelerate ozone loss in the Antarctic lower stratosphere.

$$HCl + ClONO_2 \overset{het,PSC}{\rightarrow} Cl_2 + HNO_3 \tag{2.72}$$

$$H_2O + ClONO_2 \overset{het,PSC}{\rightarrow} HOCl + HNO_3 \tag{2.73}$$

The Cl_2 formed would photolyze rapidly in sunlit air and form ClO. They also pointed out that this and related heterogeneous reactions would suppress the concentration of NO_2 by forming HNO_3, so that the released ClO could not readily reform the $ClONO_2$ reservoir. Thus it was recognized that rapid ozone loss via chlorine chemistry would require (1) the heterogeneous *activation* of chlorine from both the HCl and $ClONO_2$ reservoirs and (2) the suppression of NO_2, an essential element in keeping the chlorine active.

Molina and Molina [1987] showed that very rapid ozone depletion can occur through a previously unrecognized catalytic cycle involving formation and photolysis of a ClO dimer, Cl_2O_2. Following a period of some uncertainty regarding the kinetics and photochemistry of the dimer, laboratory studies confirmed its importance [Sanders et al. 1989]. This process is now well recognized as the primary catalytic process responsible for about 75% of the ozone removal in the *Ozone Hole*. McElroy et al. [1986] emphasized the role of bromine chemistry in ozone hole formation (in particular, its coupling to chlorine through the reaction between ClO and BrO); this cycle is now known to contribute about 20% to the annual formation of the Antarctic *Ozone Hole* [Anderson et al. 1989].

In early studies after the detection of the Antarctic *Ozone Hole* it was generally assumed that the particles of which the observed PSCs were composed were mainly water ice. Stratospheric ice clouds are frequently optically thick and brilliant in colour. Such clouds form when temperatures drop below the frost point and are now referred to as *type 2 PSCs*. However, more sensitive satellite measurements suggested that optically thinner PSCs were also present at warmer temperatures [McCormick et al. 1982].

Toon et al. [1986] and Crutzen and Arnold [1986] pointed out that the PSC particles might be composed not only of water ice but also of solid nitric acid trihydrate (NAT). Laboratory studies by Hanson and Mauersberger [1988] showed that the NAT crystal is stable a few degrees above the frost point (T_{ice}) under stratospheric conditions. Both studies noted that such composition could affect the impact on ozone in two ways: (1) by reducing the amount of nitrogen oxide that could be present (i.e., not only by forming nitric acid but also by removing it from the gas phase) and (2) by raising the temperature at which clouds could form, since thermodynamic analyses suggested that NAT could condense at temperatures well above the frost point. These clouds became to be known as *type 1 PSCs*.

In addition, Toon et al. [1986] suggested that sedimentation of large particles could result in *denitrification* of the stratosphere. The removal of nitric acid not only from the gas phase but from the stratosphere altogether would have a potential to further reduce NO_2 concentrations and hence enhance $ClO/ClONO_2$ ratios and attendant chlorine-catalysed ozone loss. McElroy et al. [1986] also considered the possibility of nitric acid-water particles, suggesting that nitric acid monohydrate (NAM) was likely to form, but these particles are not believed to be stable under stratospheric conditions [Carslaw et al. 1999].

Measurements of the vertical profile of aerosols with LIDAR[3] demonstrate that PSCs sometimes consist of solid, depolarizing (non-spherical, type Ia PSCs) particles, or additionally liquid, non-depolarizing (spherical, type Ib PSCs). Figure 2.9 shows potential formation mechanisms of NAT PSCs. For decreasing temperatures the sulphuric acid content of sulphate aerosols is also decreasing, leading to ternary solutions of $HNO_3/H_2SO_4/H_2O$ with measured H_2O/HNO_3 ratios between 4:1 and 10:1. Nitric acid hydrates (NAH) could nucleate heterogeneously on water ice crystals below the ice frost point, leading to the release of NAH particles upon subsequent ice evaporation (shown as scenario 1). The nucleation of nitric acid hydrate particles might also occur in non-equilibrium $HNO_3/H_2SO_4/H_2O$ droplets in mountain waves, without ice formation - scenario 2. Tabazadeh et al. [1995] and Tabazadeh et al. [1996] suggested that nucleation of solid HNO_3/H_2O phases might occur in air parcels that have spent sufficiently long time below the nitric acid trihydrate (NAT) equilibrium temperature. They postulated the existence of a new phase with a higher H_2O to HNO_3 ratio than either NAT or $HNO_3 - H_2SO_4 - H_2O$ droplets, so called type 1c PSCs (scenario 3). Zhang et al. [1996] have suggested (scenario 4) that nitric acid hydrates may form on frozen sulphuric acid aerosols (sulphuric acid tetrahydrate (SAT)) after their surfaces have become activated by an initial deposition of NAT. The supersaturation required for NAT nucleation on preactivated SAT particles corresponds to about 2-3 K cooling below the NAT equilibrium temperature. Koop and Carslaw [1996] have shown that SAT particles can deliquesce to form $HNO_3 - H_2SO_4 - H_2O$ droplets upon cooling to temperatures a few K above the ice frost point (typically 3-4 K below the NAT equilibrium temperature). They suggested that this mechanism might lead to the heterogeneous nucleation of NAT. The formation pathways can be summarized as follows:

$$SSA \underset{T\downarrow}{\rightarrow} STS \underset{T\downarrow}{\rightarrow} ICE \underset{T\uparrow}{\rightarrow} NAT \underset{T\uparrow}{\rightarrow} SAT. \tag{2.74}$$

In the Arctic type II PSCs are often induced on the lee side of mountains [Carslaw et al. 1998]. When air is streaming across mountains, gravity waves (Rossby Waves) can be generated on the lee side. The perturbance can even propagate into the stratosphere decreasing there locally the temperatures below the frost point of NAT or water and enhancing to potential of PSC formation.

Just recently first mass-spectrometric in-situ measurements of the composition of mountain lee wave

---

[3] LIDAR: LIght Detecting And Ranging; a measurement system using lasers at different wavelengths often used for the detection of PSCs.

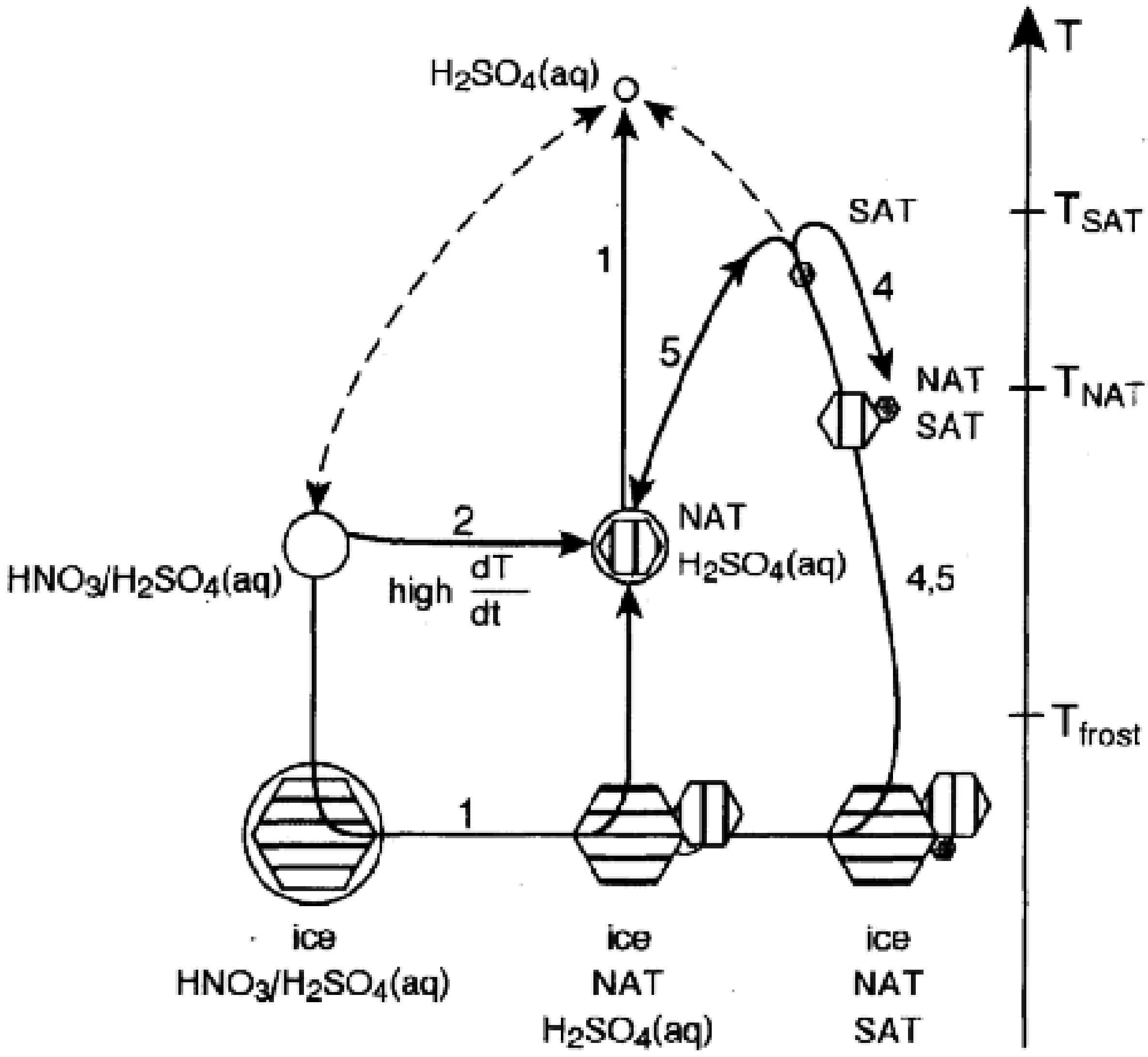

Figure 2.9: Possible generation mechanisms of PSCs: Particle phase transitions leading to the formation of solid PSC type I particles (NAT). Altogether there are five scenarios of NAT formation given in this plot. Circular symbols denote liquid particles, while square symbols are denoting solid particles. Adapted from [Carslaw et al. 1999].

induced PSCs have been performed by Schreiner et al. [1999] showing H_2O/HNO_3 ratios to be above 10 at atmospheric temperatures between 189 and 192 K. The presented high ratios indicate ternary solution particles of H_2O, HNO_3 and H_2SO_4 rather than the presence of solid hydrates.

An important reaction removing NO_x from the gas phase is the hydrolysis of N_2O_5 on PSCs [Solomon et al. 1986] - as described in the preceding section about the NO_x chemistry. There are more important reactions occurring on the surface of PSCs, like the $BrONO_2$ hydrolysis and heterogeneous reactions with HCl[4]

---

[4] The heterogeneous reactions of $HOBr$, $HOCl$, $ClONO_2$, $BrONO_2$ and N_2O_5 with HBr are less important because of the low concentration of HBr.

$$HOCl + HCl \overset{het,PSC}{\rightarrow} Cl_2 + H_2O \tag{2.75}$$

$$BrONO_2 + HCl \overset{het,PSC}{\rightarrow} BrCl + HNO_3 \tag{2.76}$$

$$HOBr + HCl \overset{het,PSC}{\rightarrow} BrCl + H_2O \tag{2.77}$$

$$N_2O_5 + HCl \overset{het,PSC}{\rightarrow} ClONO + HNO_3 \tag{2.78}$$

When the polar stratosphere reaches the end of the polar night (see Figure 2.10) and it is again sunlit, then the weakly bound halogen species (e.g. Cl_2 and $HOCl$) are quickly photolysed

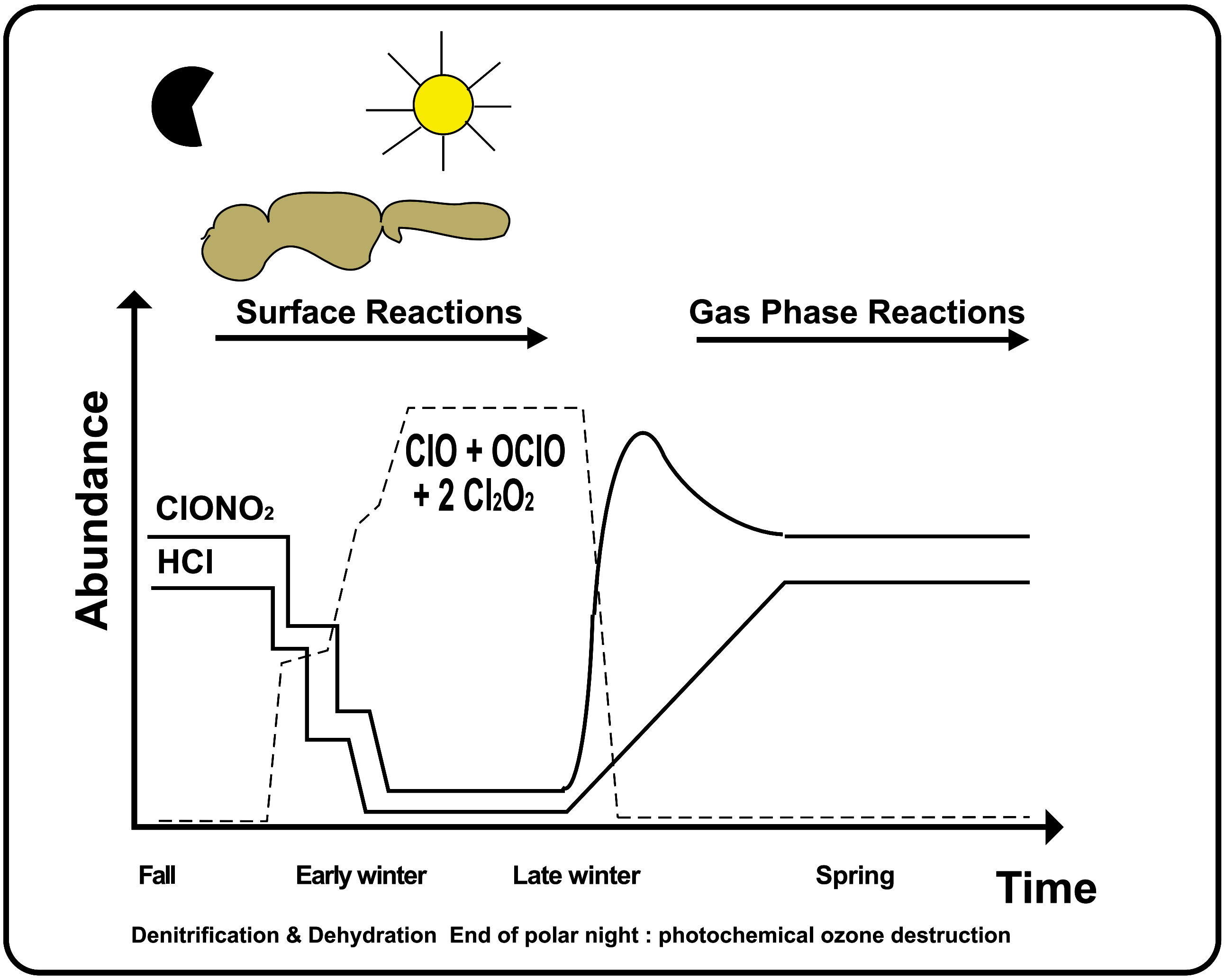

Figure 2.10: The schematic evolution of the polar *Ozone Hole* during the polar night and spring. Adapted from [Wagner 1999].

$$Cl_2 \overset{h\nu}{\rightarrow} 2Cl \tag{2.79}$$

$$HOCl \overset{h\nu}{\rightarrow} Cl + OH \tag{2.80}$$

$$Cl + O_3 \rightarrow ClO + O_2 \tag{2.81}$$

and the liberated atomic chlorine is beginning to deplete ozone. For high concentrations of ClO the catalytic ClO-dimer-cycle is very effective [Molina and Molina 1987]:

$$2(Cl + O_3 \rightarrow ClO + O_2) \tag{2.82}$$

$$ClO + ClO \overset{M}{\rightarrow} Cl_2O_2 \tag{2.83}$$

$$Cl_2O_2 \overset{h\nu}{\rightarrow} Cl + ClO_2 \tag{2.84}$$

$$ClOO \overset{M}{\rightarrow} Cl + O_2 \tag{2.85}$$

$$\text{Net}: \quad 2O_3 \rightarrow 3O_2 \tag{2.86}$$

The rate limiting step of this cycle is the self reaction of ClO, so that the ozone depletion potential (ODP)[5] of this cycle is proportional to the square of the ClO concentration. As already mentioned above, this cycle is responsible for 75% of the ozone destruction in the Antarctic spring, while the rest is mainly due to the coupled bromine-chlorine-cycle.

The strength of the ozone depletion depends mainly on the time, after which the NO_x concentration is again high enough to bind the reactive chlorine in its reservoir species. Because of the denoxification and the denitrification the nitric acid concentration tied up on the PSC particles can be very low in the early spring, so that the ozone depletion can go on for a very long time. NO_x from lower latitudes can mix with the polar airmasses not until the decay of the polar vortex, which takes place in mid spring or even later.

The Antarctic ozone holes of the 1990s have been long-lasting [Pyle et al. 1999]. Those in 1995, 1996 and 1998, remained evident until mid-December. In 1998 the minimum ozone column observed south of 40^oS did not rise above 160 DU until early December. The ozone holes are long-lasting because the radiative heating of air in which ozone has been almost completely destroyed is very slow, and flow across isentropic surfaces is largely inhibited. The vortex in the lower stratosphere is thus now more stable than it was in the 1960s to 1980s, when the breakdown of the vortex took place in some years in early October.

The mean ozone column in the Arctic region during winter exhibits large interannual variability. This variability is linked with interannual differences in meteorology, which influences ozone both through varying transport and through varying temperatures, which modulate chemistry. A method for deriving the chemical loss based on ground-based, balloon-borne and satellite measurements uses a 3-D CTM model for removing the transport contribution in the ozone field variations [Goutail et al. 2000]. The largest column reduction - within the time period 1993 to 2000 - of 32% has occurred in 1995, while the lowest of 5% was recorded in 1999. 3-D CTM simulations are found to be in good agreement with observations during the coldest winters when chlorine is fully activated. In contrast, significant disagreement is found during the winters when temperatures marginally reach PSC formation thresholds, suggesting that in those conditions the activation of the Arctic vortex is not captured correctly. The ozone column loss reported in 1999/2000 (23%) is smaller than the record values of 31-32% observed in the mid-1990's because the chemical loss was restricted to altitudes below 600 K (21 km) during that winter, while in 1995 the 60% loss extended up to 700 K (24 km). Though the profiles of O_3 on March 22, 2000 show a record loss of 66% at 470 K.

2.4.1 Heterogeneous chemistry on sulphate aerosols

Also in mid-latitudes there was statistically significant ozone loss during the 1990s of 5-10% [WMO 1998] and it was clear that this loss could not be attributed to dilution of polar airmasses with low

---

[5] An index called the Ozone Depletion Potential (ODP) has been adopted for regulatory purposes under the Montreal Protocol. The ODP of a compound is an estimate of the total ozone depletion due to 1 Kg of the compound divided by the total ozone depletion due to 1 Kg of CFC-11. Thus, the ODP shows relative effects of comparable emissions of the various compounds. Model calculated values for ODPs of individual compounds change as the basic understanding of their interaction with the ozone layer changes.

ozone at the end of the polar winter/spring [Sze et al. 1989].
Fahey et al. [1993] explained these phenomena in mid-latitudes with heterogeneous chemistry on liquid stratospheric sulphuric acid aerosols, the latter being dramatically increased after volcanic eruptions [Avallone et al. 1993; Solomon et al. 1996]. After the eruption of Mount Pinatubo in June 1991, it was possible to study the effect of enhanced aerosol loading of the PSC-free stratosphere in terms of chlorine activation on the background aerosols.
The stratospheric *Junge-Layer* in altitudes of 10-30 km consists mainly of H_2SO_4/H_2O droplets, which are distributed globally in the lower stratosphere (*background aerosol*) [Roedel 1992].
Sulphuric species are emitted anthropogenically (direct SO_2 emissions, fossil fuel burning) as well as naturally (organic sulphur species, dimethyl sulfid (DMS) and H_2S from the ocean, volcanic eruptions). Direct entry of SO_2 into the stratosphere is negligible, while long-lived sulphur species can get to the stratosphere, where they lead to the production of sulphuric acid

$$
\begin{aligned}
SO_2 + OH &\overset{M}{\rightarrow} HSO_3 && (2.87)\\
HSO_3 + O_2 &\rightarrow HO_2 + SO_3 && (2.88)\\
SO_3 + H_2O &\rightarrow H_2SO_4 && (2.89)
\end{aligned}
$$

then forming together with water the hydrate aerosols [Roedel 1992]. Typical aerosol surfaces are about 1-10 $\mu m^2 cm^{-3}$ in the lower stratosphere under non-perturbed conditions, which was the case during the time of our balloon-borne measurements.
The N_2O_5 hydrolysis was the first reaction to be experienced to be relevant not only on PSCs but also on sulphuric acid aerosol surfaces [Mozurkewich and Calvert 1988; Tolbert et al. 1988]. This reaction leads to a reduction of NO_x and is therefore indirectly responsible for an increase in reactive chlorine. The same is true for the $BrONO_2$ hydrolysis, but it has also a large influence on the bromine chemistry, because it changes $BrONO_2$ to $HOBr$, the latter photolysing faster. After the eruption of Mount Pinatubo and El Chichon it was shown by model studies [Rodriguez et al. 1991; Brasseur and Granier 1992; Lary 1996; Tie and Brasseur 1996] and measurements [Johnston et al. 1992; Solomon et al. 1996; Slusser et al. 1997], how important these reactions are both at high and mid-latitudes.
Besides the N_2O_5 and $BrONO_2$ hydrolysis the above mentioned heterogeneous reactions play an important role in polar areas [Portmann et al. 1996] and also at mid-latitudes [Solomon et al. 1996; Solomon et al. 1998]. Figure 2.11 summarizes the reaction probabilities for the different reactions.

The loss of $ClONO_2$, $BrONO_2$, $HOCl$ and $HOBr$ on HCl becomes not important for temperatures above 200K and background aerosol conditions. It is possible to calculate the time constant (or lifetime) for the different heterogeneous reactions from the aerosol surface area A, the mean thermal velocity v_{th}[6] and the reaction coefficient γ

$$
\begin{aligned}
\tau &= \frac{4}{\gamma \times v_{th} \times A} && (2.90)\\
k_{het} &= \tau^{-1} && (2.91)
\end{aligned}
$$

The $ClONO_2$ hydrolysis has a time constant of 3 weeks for typical aerosol surface areas ($A = 1 \mu m^2 cm^{-3}$) and $\gamma = 0.01$. Therefore it is clear that nearly all heterogeneous reactions do not lead to chlorine activation at temperatures above 210 K. However, they cannot be neglected for T=200-210 K, when aerosol levels are slightly increased. But the bromine reaction coefficients are higher by 1-3 orders of magnitude than the respective chlorine reactivities, explaining why the effect of bromine is comparable to that one of chlorine, while bromine is about 100 times less abundant than chlorine.

---

[6] $v_{th} = \sqrt{\frac{8k_bT}{\pi m}}$ where k_b is the Boltzmann constant, T the temperature and m the molecular mass. (e.g. for T=210 K $\longrightarrow v_{th} = 214 ms^{-1}$)

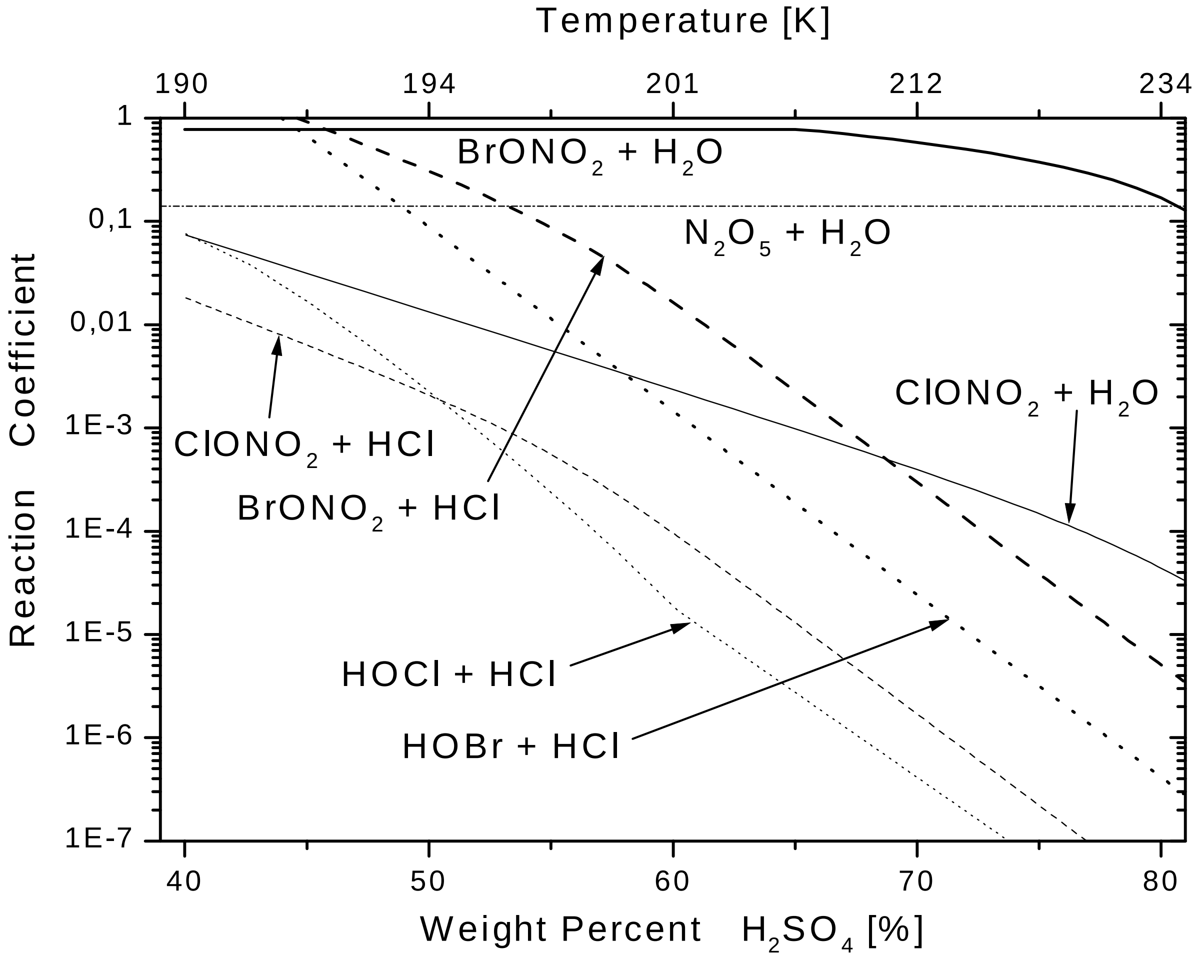

Figure 2.11: Reaction coefficients for the most important heterogeneous reactions on sulfuric acid aerosol surfaces (for a H_2O partial pressure of 2.5×10^{-4} mbar and a HCl mixing ratio of 500 ppt). Adapted from [Erle 1999].

The reaction coefficients of the heterogeneous bromine reactions were measured only recently in the laboratory [Hanson and Ravishankara 1995; Hanson et al. 1996; Waschevsky and Abbatt 1999] and point to higher atmospheric relevance than assumed previously.

2.5 Fundamental Stratospheric Dynamics

The distribution of most chemical species in the middle atmosphere result from the influences of both dynamical and chemical processes. In particular, when the rates of formation and destruction of a chemical species are comparable to the rate at which it is transported by physical processes, then transport can play a major role in determining the constituent distribution. This transport can be produced both by the prevailing winds (also called advection) and by turbulent mixing (diffusion). On the other hand, the distribution of some photochemical species, especially ozone, can influence the thermal structure of the atmosphere [Chipperfield 1999].

The major sources of heat in the middle atmosphere are provided by absorption of ultraviolet radiation, particularly by ozone and to a lesser extent by molecular oxygen. Radiative cooling occurs through infrared emissions associated with the vibrational relaxation of CO_2, H_2O and O_3. The large radiative heating rates (summer : 0.5-6 K/day with a maximum around 50 km) found the stratosphere are due primarily to the large amounts of ozone found there. The observed increase in temperature

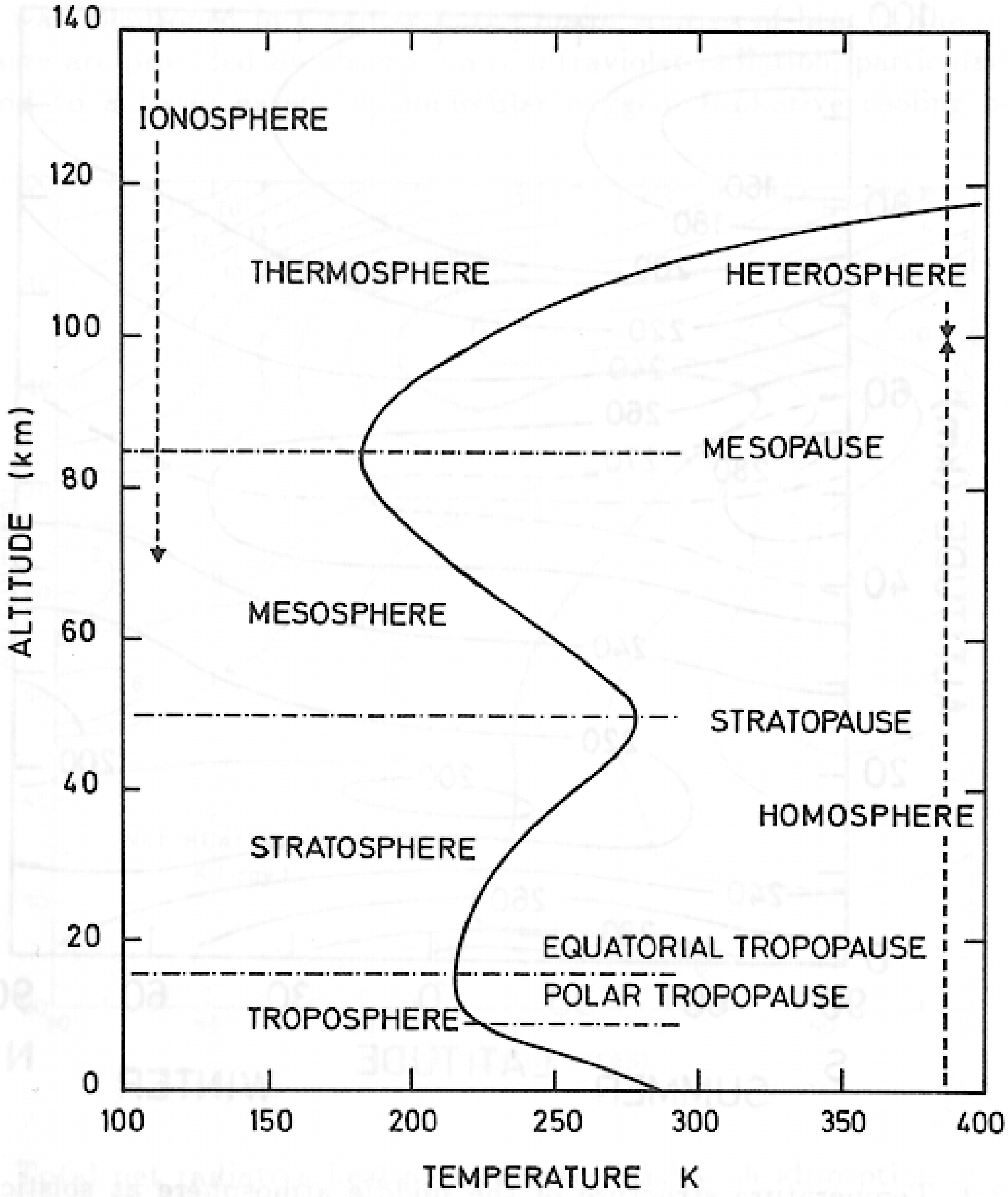

Figure 2.12: General vertical structure of the atmosphere [Brasseur and Solomon 1986].

with altitude in the stratosphere is a result of heating by ozone.

It is common to distinguish between zonal mean motions and fluctuations about the zonal mean (called the *eddies*). These fluctuations can be of varied spatial scale - from a few metres to thousands of kilometers. Any such fluctuation can be described in terms of waves, as can be shown by three-dimensional spectral models. The eddy terms describe the effects of the ensemble of atmospheric waves. In the stratosphere, observed wave structure indicates that most of the waves are of large scales, of zonal

wavenumber three or less.
Brewer [1949] suggested that the dryness (1 ppm) of the stratosphere was determined primarily by condensation of water vapour from the upper troposphere(1%) and that the content of an air parcel rising from the troposphere to the stratosphere would therefore be determined by the lowest temperature experienced by the parcel corresponding to the tropopause. He noted that tropopause temperatures were low enough to yield stratospheric water vapour densities as low as observed, while the middle and high latitude tropopause was much too warm to explain the observed dryness. Thus he suggested a circulation with rising motion only in the tropics, and descending motion at extra-tropical latitudes (*Brewer-Dobson circulation* or *Hadley cell*). Similarly, Dobson [1968] noted that although the region of maximum ozone production is found in the tropical upper stratosphere, the largest observed total column densities were observed at high latitudes, suggesting that a downward-poleward transport was also required.

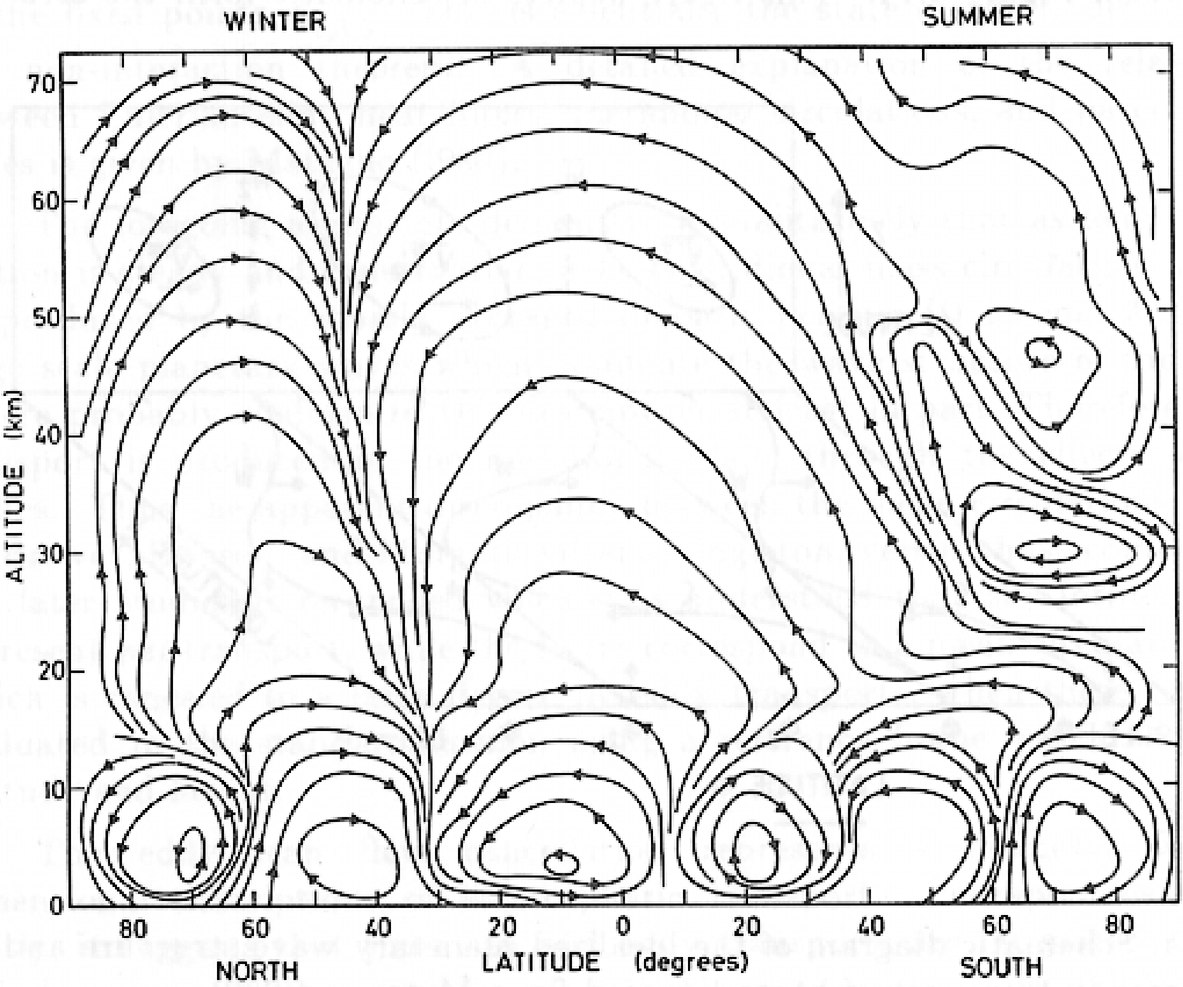

Figure 2.13: Meridional circulation deduced by the theoretical study of [Cunnold et al. 1975].

Figure 2.13 shows the mean meridional circulation deduced by theoretical studies, which is far more complicated than the primitive picture using only the *Brewer-Dobson circulation.* The heating due to eddy transport was shown to be much larger than that due to radiation in the stratosphere. As long as wave motion is steady and conservative, a net meridional mass circulation can only be produced by the zonally averaged diabatic heating. The large scale planetary waves which dominate the wave structure of the stratosphere probably conform to this description at least in part. Therefore no net transport is produced in the meridional plane through the effects of these eddies. Thus the discrepancy between the mean circulations derived by Brewer and Dobson, versus those computed by theoretical studies is reconciled when it is understood that the former studies represent net transport, while the latter correspond to a mean circulation only, which is cancelled to a large degree by eddy transports, when these terms are evaluated in the standard fashion using a reference frame which is fixed in latitude and height.

While the summer stratosphere is near to radiative equilibrium, stratospheric temperatures are in general higher than the equilibrium temperatures in wintertime. Reasons for that are stationary planetary waves, which originate from the troposphere with typical wavelengths near to the Earth's diameter (wave numbers of 1-3). These waves are mainly driven within the tropopause (i.e. when high pressure and low pressure systems lead to a change of the tropopause). They only propagate into the stratosphere, when there are westerly winds. As only the winter stratosphere displays west winds, this explains the deviation of the polar stratospheric temperatures in comparison with the equilibrium temperatures.

During the polar winter the stratosphere is cooling off strongly. Like in a tropospheric low-pressure system the air is descending so that the gradient of the isobar surfaces between the subtropics and the Arctic is increasing. As the strength of the wintertime westerly is proportional to the gradient of the isobars, these winds are getting stronger and the *polar vortex* is developing with cyclonal motion of the airmasses. Because of the high velocities at the edge of the vortex ($50\frac{m}{s}$) the exchange of airmasses with air outside of the vortex is very limited [Waugh et al. 1994].

As the distribution of land and water surfaces is very different for the two hemispheres, the planetary waves in the northern hemisphere are much more intensive and frequent there. This leads to increased meridional heat transport and therefore to higher temperatures in the northern polar vortex. During sudden *minor warmings* of the polar vortex the planetary waves play an important role. Rarely however, this may lead to strong perturbations or even to the total breakdown of the polar vortex already in wintertime (*major warming*) [Pawson and Naujokat 1999]. In spring the stratospheric dynamics of the sunlit polar stratosphere is changing again to summer circulation with easterly winds. This process is called *final warming* and features extreme increase of planetary wave activity. The polar vortex is split into different parts which are then being transported to mid-latitudes. In the northern hemisphere this breakdown takes place in March/April and in the southern hemisphere around October/November/December.

2.6 The atmospheric halogen budget

Organic compounds containing bromine, chlorine, fluorine, and iodine are released at the Earth's surface, mix rapidly, and are exchanged between the hemispheres in the troposphere. Whereas most of these compounds originate predominantly from human activities, natural biological and chemical processes can also contribute to the total organic budget. Some of these organics (e.g.,$CH_3CCl_3, CH_3Br, CH_3Cl, HFCs, HCFCs$) that contain hydrogen are destroyed by reaction with the hydroxyl radical (OH) in the troposphere. For these compounds their atmospheric lifetimes and their effect on stratospheric ozone depletion are reduced compared to similar compounds (i.e., $CFCs$ and halons) that are fully halogenated. Transport time scales are important in describing when stratospheric ozone losses can be expected to occur and can be estimated from observations of long-lived trace gases (like CO_2, SF_6 and CFC-115 [Elkins et al. 1996]) and from atmospheric models. Mixing within a hemisphere occurs in the troposphere on time scales of a few weeks to three months, whereas exchange between hemispheres occurs between 1.1 and 1.7 years [Levin and Hesshaimer 1996]. The halocarbons are also transported into the stratosphere, where photolysis and reaction with OH lead to the formation of inorganic species of bromine, chlorine, and fluorine. Mixing between the troposphere and the lower and middle stratosphere, where most of the ozone depletion

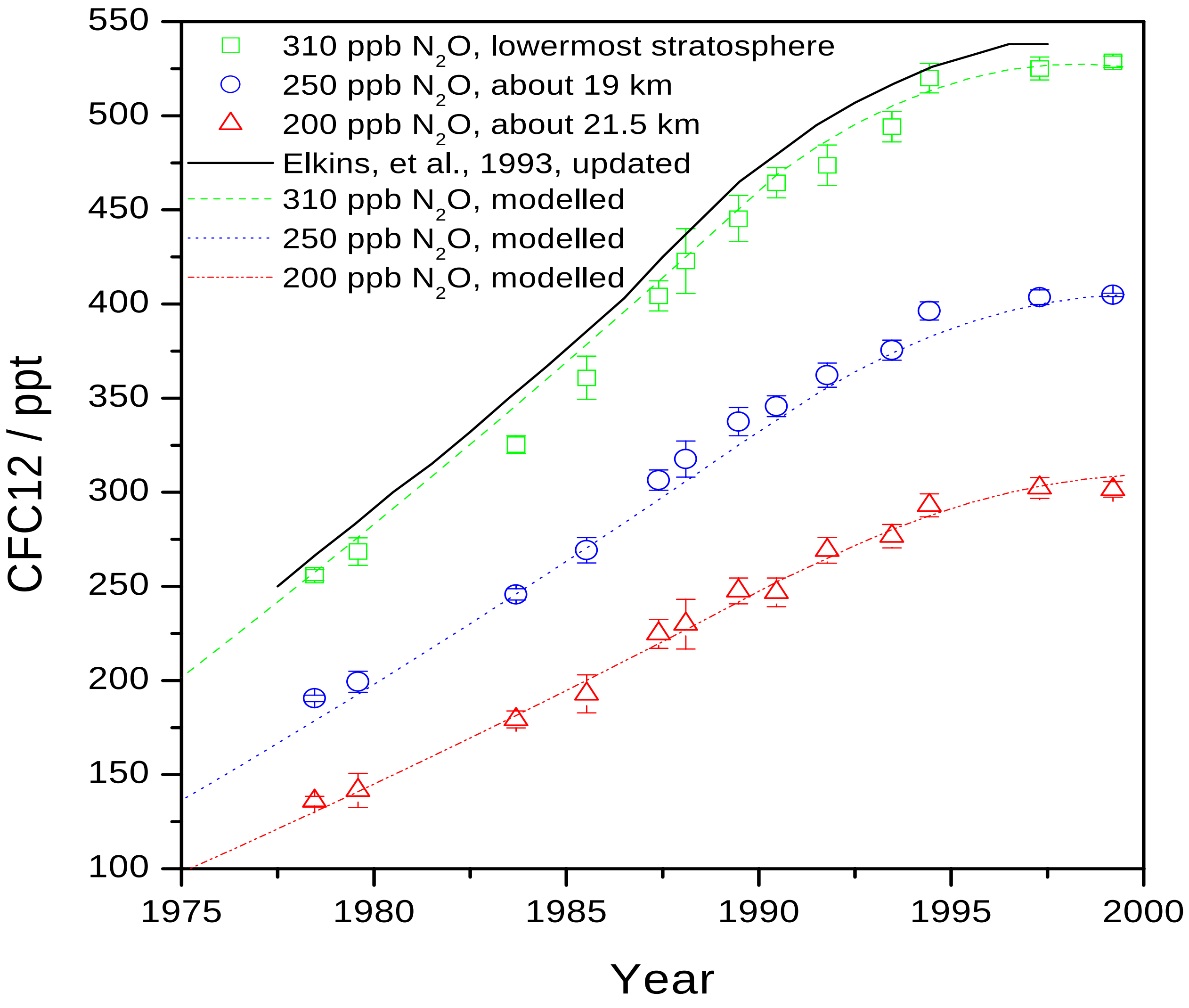

Figure 2.14: Observed temporal increase in stratospheric CFC12 mixing ratios. The solid lines are calculated trends based on the correlation observed in 1997 and the tropospheric trends of NOAA/CMDL [Elkins et al. 1993]. For the detrending and the retrending the age correction by Plumb et al. [1999] and the SF_6 derived age [Strunk et al. 2000] was used. Adapted from [Engel 2000].

occurs, takes place within 1-3 years in the tropics and between 3-6.5 years at mid-latitudes and in the polar regions at altitudes of 21 km and below [Elkins et al. 1996; Wamsley 1998].

Figure 2.14 shows the increase of the most abundant chlorofluorocarbon, CFC-12, whose concentration has already peaked in the troposphere in 1995. The peak in the different height layers of the stratosphere is expected in 1999-2001 and after that time the chlorine loading of the stratosphere is expected to decrease more slowly than it increased since the 1950s - see Figure 2.15. One can observe the time lag of about 5 years between the troposphere and stratosphere and also the effect of a broadening of the tropospheric peak because of the age spectrum of the stratospheric airmasses smoothing the peak in the stratosphere.

Still reaching a maximum of chlorine loading in the stratosphere followed by a slow decrease does not necessarily mean a fast recovery of the ozone layer [Dvortsov et al.], but will depend on the increase of other important species like bromine and nitrogen. Also, for current and future levels of stratospheric chlorine during the next 10-20 years, potential increases of stratospheric aerosols by volcanic eruptions could lead to even more enhanced ozone depletion at mid and high latitudes [Dvortsov et al.].

Table 2.6 gives an overview of the most important halogen species as they are measured in the atmosphere and indicates also their lifetimes in the troposphere and stratosphere, as well as their growth rate [WMO 1998]. There are the long-lived, fully halogenated $CFCs$ and halons reaching the stratosphere before being destroyed and the short-lived species like $HCFCs$, $HFCs$ and some others, which are depleted within the troposphere and therefore do not constitute input to the stratosphere. From the growth rates, it is also visible that the tropospheric chlorine loading has reached its maximum and is decreasing again, while it is still maximal in the stratosphere.

As can be seen from measurements and future extrapolations presented in Figure 2.15 there is a time lack of the chlorine peak of about 5 years between the troposphere and the stratosphere and the peak is broadening in the stratosphere because of the age distribution of the air reaching the upper levels of the stratosphere.

Figure 2.16 shows the increase in the primary halons, which are still increasing in the troposphere, so that the bromine loading is still expected to rise during the next years.

Species	trivial name	Stratospheric lifetime	Tropospheric lifetime	Tropospheric Concentration (1996)	Growth
		[years]	[years]	[ppt]	$\% year^{-1}$
CFCs					
$CFCl_3$	CFC-11	45	∞	263.6	-0.3
CF_2Cl_2	CFC-12	100	∞	529.7	0.85
$CClF_3$	CFC-13	640	∞	4	5
$CF_2ClCFCl_2$	CFC-113	85	∞	83	0.05
CF_2ClCF_2Cl	CFC-114	220	∞	15	8
CF_3CF_2Cl	CFC-115	550	∞	5	8
HCFCs					
CHF_2Cl	HCFC-22	240	17	122	4.2
CF_3CHCl_2	HCFC-123	47	2		
CF_3CHFCl	HCFC-124	129	7		
CH_3CFCl_2	HCFC-141b	76	13	5.4	43
CH_3CF_2Cl	HCFC-142b	215	25	7.6	15
$CF_3CF_2CHCl_2$	HCFC-225ea	120	3		
CF_2ClCF_2CHClF	HCFC-225cb	120	9		
CH_2FCl	HCFC-31	1.5			
HFCs					
CH_2F_2	HFC-32	7			
CF_3CF_2H	HFC-125	40	400		
CF_3CFH_2	HFC-134a	16	210	3.0	59
CF_3CH_3	HFC-143a	70			
CH_3F	HFC-41	4			
CH_3CHF_2	HFC-152a	1.7	62		
CH_2FCH_2F	HFC-152	0.4			
CHF_3	HFC-23	243		10.7	
HALONS					
CF_3Br	H-1301	77	∞	2.29	1.95
CF_2ClBr	H-1211	11	2.3	3.4	6.35
CF_2Br_2	H-1202		3.3	0.037	18
CF_2BrCF_2Br	H-2402	20	3.4	0.48	1.9
CF_2HBr	H-1201		5		
CF_3CHFBr	H-2401		2.8		
$CF_3CHClBr$	H-2311		0.8		
Other Halo Carbons					
CH_3Br	methyl bromide		0.7	9-11	
CH_2Br_2	dibromomethane		0.2	0.6-1.0	
$CHBr_3$	bromoform		0.03-0.1	0.2-0.6	
CH_2BrCl	bromochloro-methane		<1	0.1-0.2	
$CHBr_2Cl$	dibromochloro-methane		0.4	0.1	
$CHBrCl_2$	bromodichloro-methane		0.4	0.1-0.2	
CH_2BrCH_2Br	1,2-dibromoethane		0.4	0.1	
CCl_4	carbon tetrachloride	35	∞	99.7	-1.1
$CHCl_3$	chloroform	0.55			
CH_3CCl_3	methyl chloroform	6	7	93	-14
$COCl_2$				20	
CH_3Cl	methyl chloride		1.3	550	
Others					
N_2O	nitrous oxide	124±49	120	311.75	0.3
SF_6	sulphur hexafluoride			3.7	6.3
CH_4	methane		8.9		
Total Halogen					
Cl	chlorine			3580	-0.7
Br	bromine			20.2	1.1
F	fluorine			2370	1.8

Table 2.1: Overview of lifetimes of some important halogen compounds in the atmosphere. The lifetime is defined as the total amount of a compound in the atmosphere divided by its total rate of removal [WMO 1998; Brasseur]. The newest data is used [WMO 1998], when available.

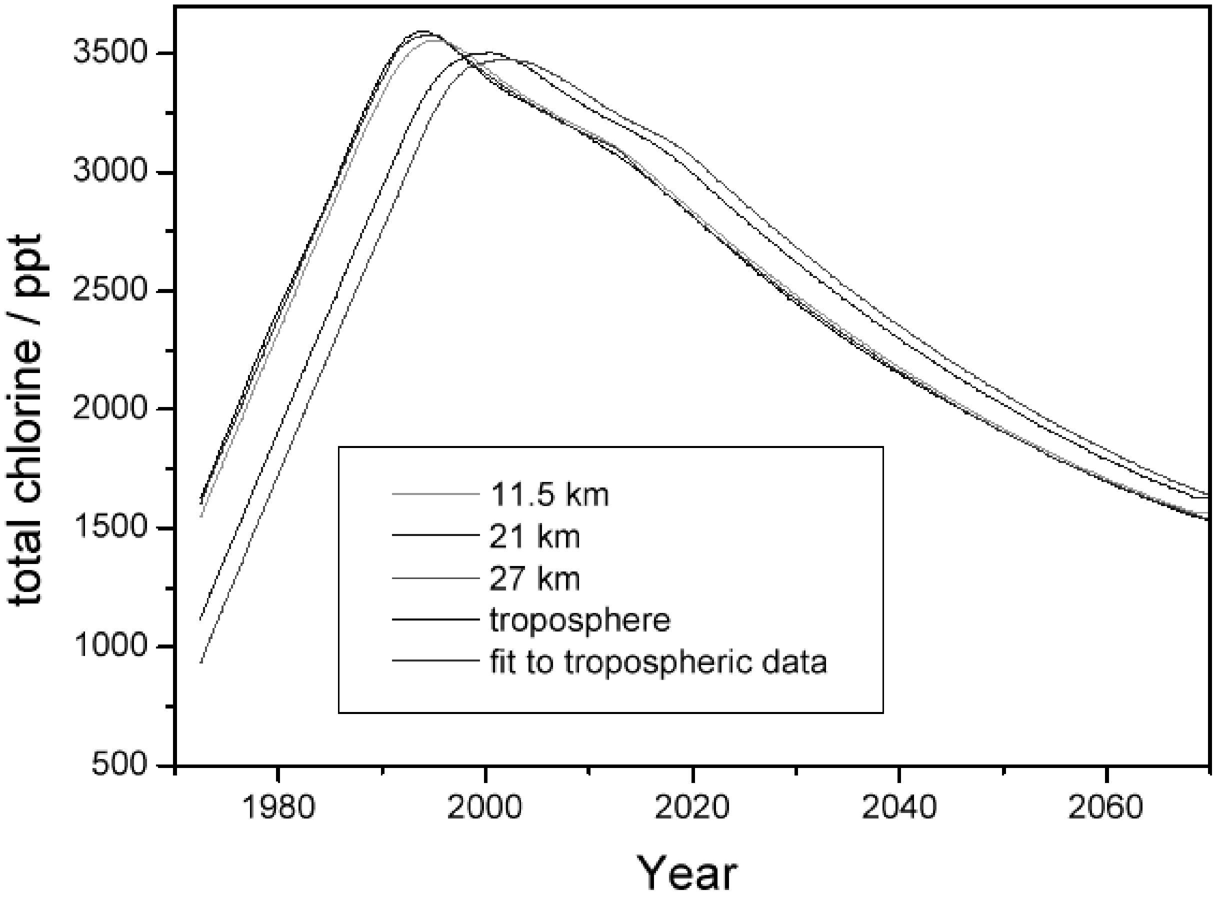

Figure 2.15: Observed and modelled evolution of total stratospheric chlorine at three different altitude levels - in the troposphere, near the tropopause, at 21 km and 27 km altitude. Adapted from [Engel 2000].

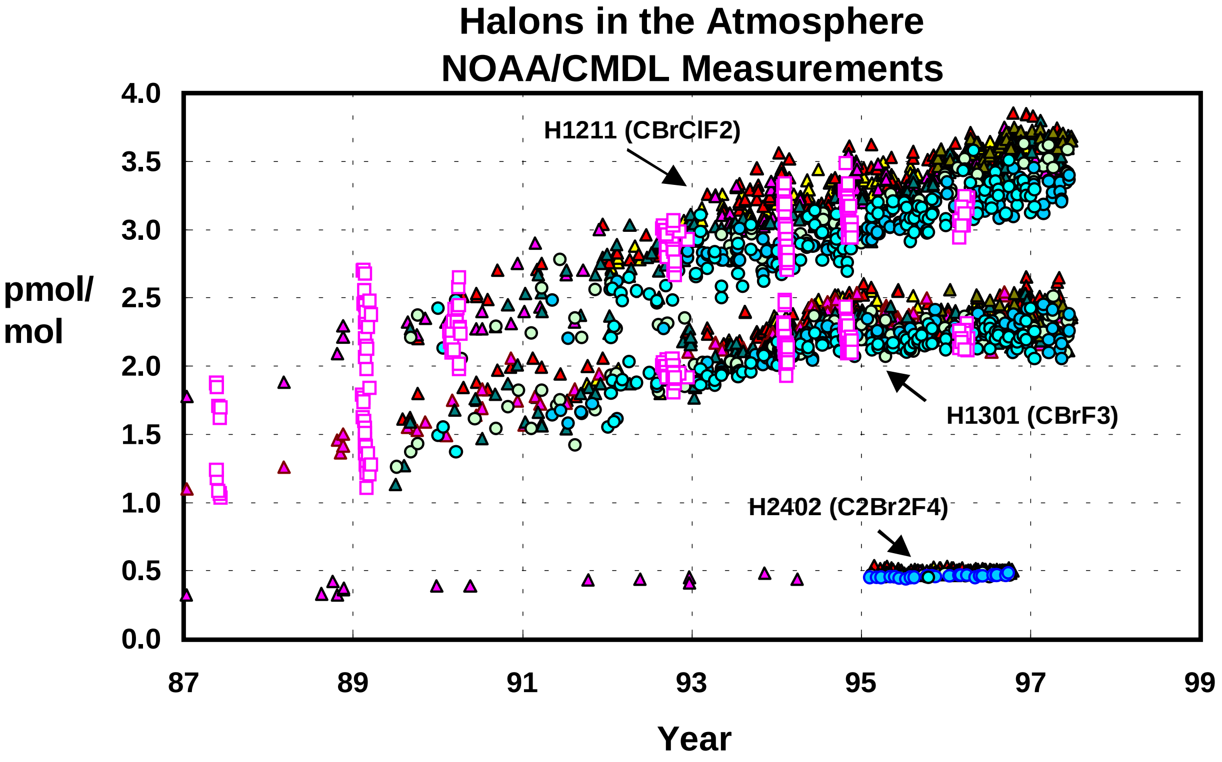

Figure 2.16: Global increase of halons [WMO 1998; Butler et al. 1998].

Chapter 3

Measurement Technique : Direct Sunlight Balloon Borne DOAS (Differential Optical Absorption Spectroscopy)

This chapter will deal with the principles of the measurement technique used during this thesis and the measurement system specially designed at the IUP(Institut für Umweltphysik). It will also give an overview about the numerical retrieval algorithms for the SCD (Slant Column Density) and profile retrieval from the raw spectra measured with the balloon-borne spectrograph.

3.1 Solar Radiation and the Solar Spectrum

Light reaching the earth from the sun is essential for life. The detailed balance between the inflow and outflow of solar energy establishes the temperature of the earth's surface and atmosphere. The absorption of solar light by the photosynthetic pigments drives a unique energy conversion process that enables plants, algae and a variety of photosynthetic bacteria to store solar energy into chemical free energy for later use.

The emission spectrum of the sun can be approximated by a black body radiation spectrum for a temperature of 5900 K but the fine structure of the spectrum is determined by the absorption of the solar radiation within the sun's atmosphere, mainly the photosphere [Sonett et al. 1991], and also the atmospheric absorptions within the Earth's atmosphere. Besides the solar spectrum outside the atmosphere, Figure 3.1 shows the specific absorption of the Earth's atmospheric gases. The O_3 absorption of UV light between 200-400 nm is noticeable - mainly due to the Hartley and Huggins absorption bands[1] - as well as the strong absorptions of H_2O in the near infrared and the strong infrared transitions of CO_2.

This spectrum clearly demonstrates that the spectral distribution and intensity of sunlight reaching the earth's surface are to a large extent determined by the absorption and the light scattering properties of the earth's atmosphere. Similarly, the amount of light absorbed by the surface in a certain frequency interval is determined by the distribution and spectral properties of the pigments of the vegetation and the scattering properties of the surface.

3.1.1 Interaction of light with matter

When light impinges on a medium containing a variety of atoms and/or molecules a number of processes may occur. First of all, due to the interaction between the electromagnetic wave and the matter energy

---

[1] Hartley bands of O_3: 220-310 nm, Huggins bands of O_3: 310-350 nm, Herzberg continuum of O_2: 190-220 nm, Schumann-Runge bands of O_2: $\leq$ 190 nm and the Schumann continuum (O_2): $\leq$ 170 nm

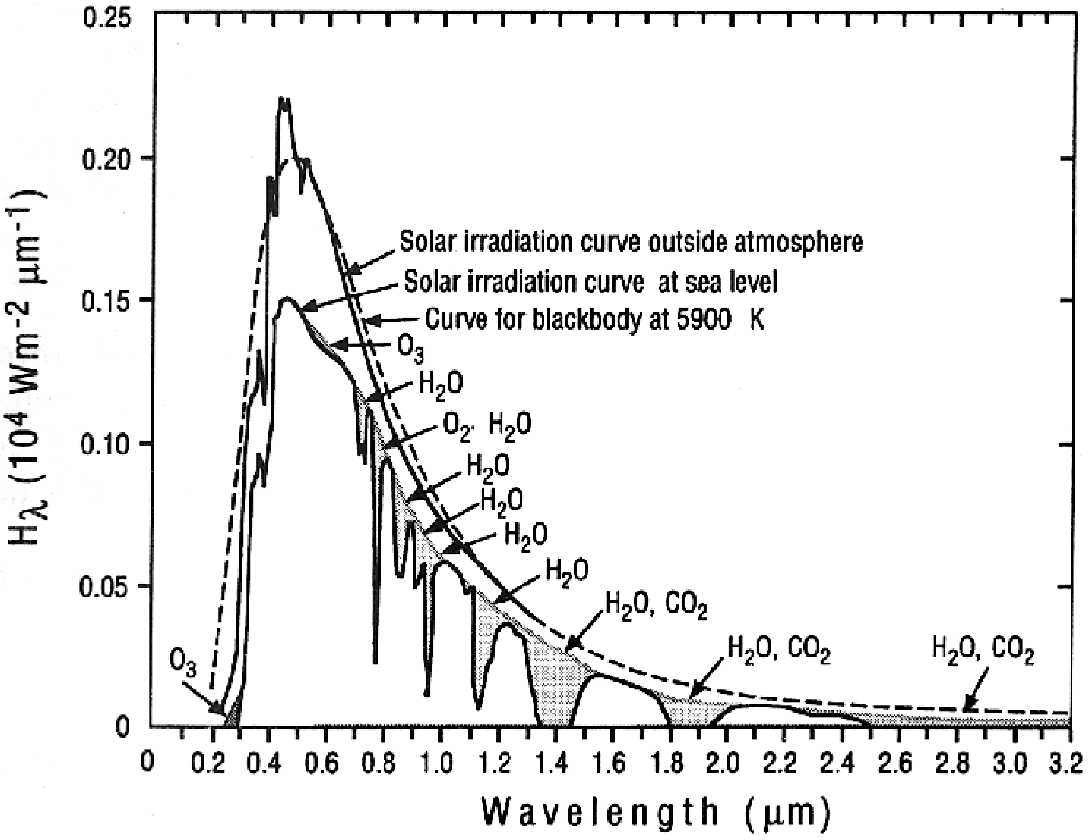

Figure 3.1: Spectral distribution of incident solar radiation outside the atmosphere and at sea level. Major absorption bands of the most important atmospheric gases are indicated. Adapted from [Boeker and van Grondelle 1995].

may be absorbed or released. This can be described by introducing the *Einstein coefficients.*
There exist two energy levels, E_1 and E_2, populated by N_1 and N_2 atoms/molecules, respectively. Three possible radiative processes which connect levels 1 and 2 are shown in Figure 3.2. Absorption and stimulated emission only occur with the light on and their rates are summarized by $B_{12}W(\omega)$ and $B_{21}W(\omega)$, in which B_{12} is the Einstein coefficient for absorption and B_{21} the Einstein coefficient for stimulated emission. A_{21} defines the Einstein coefficient for spontaneous emission from level 2 to level 1, which is a dark process.

For the rate of population of level 1 we have

$$\frac{dN_1}{dt} = -B_{12}WN_1 + B_{21}WN_2 + A_{21}N_2 \tag{3.1}$$

Assuming a steady state, i.e. $dN_1/dt = 0$, it directly follows

$$W(\omega) = \frac{A_{21}}{B_{12}(N_1/N_2) - B_{21}} \tag{3.2}$$

If we now take the situation that there is no external radiation field and that the system is in thermal equilibrium at a temperature T, then the ratio N_1/N_2 follows from the Boltzmann equation

$$\frac{N_1}{N_2} = e^{\hbar\omega/kT} \tag{3.3}$$

Under these conditions the energy density distribution as a function of frequency is given by Planck's radiation law - after averaging over polarizations

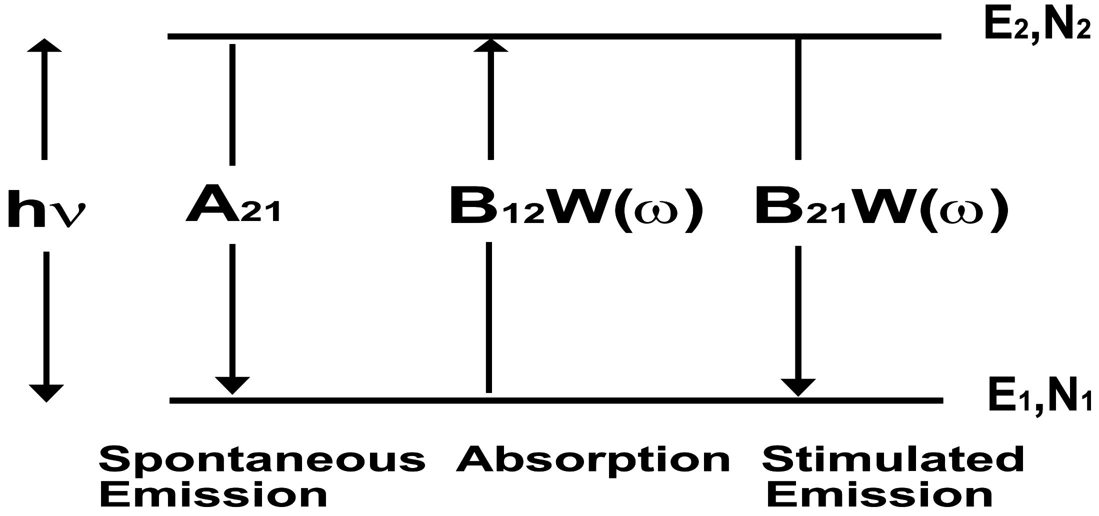

Figure 3.2: The three basic types of radiative processes. Indicated are the Einstein coefficients and the transition rates for the two levels with energy E_1, E_2 and occupation N_1, N_2. Adapted from [Boeker and van Grondelle 1995].

$$W(\omega) = \frac{\hbar\omega^3}{\pi^2 c^3} \times \frac{1}{e^{\hbar\omega/kT} - 1} \tag{3.4}$$

From the above equations it follows

$$\begin{aligned} B_{21} &= B_{12} && (3.5) \\ \frac{A_{21}}{B_{21}} &= \frac{\hbar\omega^3}{\pi^2 c^3} && (3.6) \end{aligned}$$

From quantum mechanics we know that

$$\frac{dP_2}{dt} = \frac{\pi}{3\epsilon_0\hbar}||\vec{\mu_{21}}||^2 W(\omega) = B_{21}W(\omega) \tag{3.7}$$

where $\vec{\mu}$ is the dipole operator $\vec{\mu} = \sum_i q_i\vec{r_i}$, so that we finally obtain

$$A_{21} = \frac{\omega^3}{3\pi c^3 \epsilon_0}||\vec{\mu_{21}}||^2 \tag{3.8}$$

The importance of this result is that the same quantity $\vec{\mu_{21}}$ determines the rates of all radiative processes and consequently common selection rules apply to them.

3.1.2 Lambert-Beer's Law - Optical Absorption Spectroscopy

The microscopic quantities $\vec{\mu_{21}}, B_{12}, B_{21} and A_{21}$ are connected to the macroscopic phenomenon of absorption by Lambert-Beer's law. When a beam of light passes through a sample of material, the light beam is usually absorbed, but sometimes amplified (in a laser). Absorption dominates when most of the atoms/molecules are in their ground states ($N_1 \gg N_2$) and when the intensity of the light beam is weak. In that case the rate for transitions between states 1 and 2 is given by

$$\frac{dN_1}{dt} = -B_{12}WN_1 + A_{21}N_2 \tag{3.9}$$

In a steady state $dN_1/dt = 0$ and $A_{21}N_2 = B_{12}WN_1$ is precisely the rate at which light energy is removed from the incident light beam. Let the light beam be propagated along the z axis. Since the beam is attenuated its energy W will be a function of z. Considering a small slice of thickness dz and surface a, the amount of beam energy in this slice in the frequency interval $(\omega, \omega + d\omega)$ is given by $W(\omega)d\omega adz$. It then follows that in the case of energy balance the rate of decrease of the beam energy equals the rate at which the light energy is removed from the beam by absorption.

$$-\frac{\partial W}{\partial t} a\, dz\, d\omega = N_1 B_{12} W(\omega) \hbar\omega \frac{adz}{V} F(\omega) d\omega \tag{3.10}$$

in which $a\, dz/V$ represents the fraction of atoms/molecules in the selected slice $a\, dz$ where V is the volume of the sample. Moreover, it is assumed that not all the atoms absorb precisely at the frequency ω_{21}, but that some statistical spread in transition frequencies exists at which the atoms/molecules can absorb light. To account for this, we introduced $F(\omega)d\omega$, the fraction of transitions that occur in the frequency interval $(\omega, \omega + d\omega)$ with

$$\int F(\omega) d\omega = 1 \tag{3.11}$$

If we consider $W = I/cn$, with the speed of light c, the index of refraction n and the intensity I in Wm^{-2} and $-\partial W/\partial t = -\partial I/\partial z$, we get

$$\frac{\partial I}{\partial z} = -\frac{N_1 B_{12} \hbar\omega F(\omega)}{Vnc} I \tag{3.12}$$

The solution of this differential equation is straightforward and gives Lambert-Beer's law:

$$I(z) = I(z_0) e^{-Kz} \tag{3.13}$$

with the absorption coefficient $K = \frac{N_1 B_{12} \hbar\omega F(\omega)}{Vnc}$. It is common practice to use the following expression for the dependence of I on passage through a material with pathlength l:

$$I(l) = I(l_0) e^{-OD} \tag{3.14}$$

with the optical density defined as $OD = \sigma l n_i$. Here $\sigma(\lambda)$ is the absorption cross section, l is the light path through the absorbing medium and n_i is the concentration of the sample medium i.
When light is passing through the Earth's atmosphere, it encounters several species of different concentrations. The light intensity is also changed by single and multiple scattering. As the extinction because of aerosols and the *real* light path length cannot be determined with the desired accuracy for all wavelengths, it is impossible to apply the Lambert-Beer law directly in atmospheric absorption spectroscopy looking only at one distinct wavelength. Generally, the observed intensity $I(l, \lambda)$ depends on a series of species with different concentrations along the light path.

$$I(l, \lambda) = I_0(\lambda) \mathrm{e}^{-\int_0^L \sum_i^{Species} \sigma_i(\lambda, p, T) n_i(l) dl} \tag{3.15}$$

$$SCD_i = \int_0^L n_i(l) dl \tag{3.16}$$

The variable SCD_i is called the Slant Column Density of species i, which is often used to describe the amount of a chemical species along a certain light path through the atmosphere.

3.2 Differential Optical Absorption Spectroscopy (DOAS)

The Differential Optical Absorption Spectroscopy (DOAS) takes advantage of the specific spectral signatures of each molecule in the atmosphere. As the molecular absorption bands are typical for each species and often of higher frequency than scattering characteristics or aerosol extinction, it is possible to separate the molecular absorption features from extinction effects of aerosols and scattering. Detailed descriptions of the application of the DOAS method in atmospheric science can be found in [Noxon 1975; Perner and Platt 1979; Platt 1994].
The principle of DOAS is the separation of the extinction features in broad-band/low-frequency structures and small-scale/high-frequency structures. While the former structures belong to extinction effects of aerosols, Rayleigh-, Mie-scattering and broad-band structures of the absorption cross sections (σ_l), the latter high-frequency structures (σ_h) refer to the molecular differential absorption bands. This is important, because it is often not possible to do absolute measurements referring to a distinct intensity I_0 - especially when using the sun as light source.

$$\sigma(\lambda) = \sigma_l(\lambda) + \sigma_h(\lambda) \tag{3.17}$$

The quantity SCD (slant column density) - as defined in the above equations - gives the amount of a chemical species along the light path through the atmosphere. By linearizing the numerical problem and assuming temperature and pressure independence of the absorption cross sections, we get to the equation

$$ln(I(l,\lambda)) = ln(I_0(\lambda)) - \sum_i^{Absorber} SCD_i(l)\sigma_i(\lambda) \tag{3.18}$$

so that the whole light path information is within the $SCD_i(l)$. We use the nonlinear Levenberg-Marquardt least square fitting algorithm of Stutz and Platt [1996] to fit the absorption spectra of the trace gases absorbing in the respective spectral range and a polynomial of a specified degree to account for the low-frequency part of the spectrum belonging to the aerosol extinction and the Rayleigh- and Mie-scattering. Also the broad-band structures of the absorption cross sections are included in the polynomial fit coefficients by the fit procedure. The fitting algorithm generates the best estimates for $SCD_i(l)$ by minimizing the mean square difference - $\chi^2 = \sum_{i=0}^{Channels}[ln(I(\lambda_i)_{measured}) - ln(I(\lambda_i)_{modelled})]^2$ - between the measured spectrum and the sum of the absorption spectra multiplied with the $SCDs$ plus the polynomial as well as an approximation for $ln(I_0(\lambda))$.
After linearization of the problem we can apply different linear filtering techniques without changing the resulting fit coefficients, the SCDs. That is why we can apply for example a binomial filter to the spectra to reduce the photo-electron noise of the spectra, which is the most important statistical noise source during the measurements.

$$\| \sum_i^{Channels} [ln(I(\lambda_i)) - ln(I_0(\lambda_i) + \sum_k^{Species} SCD_k(l)\sigma_k(\lambda_i) + \sum_j^{Pol.Degree} p_j\lambda_i^j] \quad \| \rightarrow 0 \tag{3.19}$$

Using the polynomial to detach the low-frequency part of the spectrum represents the principal spectral structure separation of DOAS in the case of our measurements when using differential absorption cross sections. For the evaluation of balloon-borne measurements it is best not to use a convolution of a high-resolution solar spectrum [Kurucz et al. 1984] as an approximation for $ln(I_0)$ - the so called Fraunhofer spectrum[2] - but to use a measured spectrum during the float of the balloon when the atmospheric absorptions are minimal. This is because the slit function of the spectrograph is non-gaussian

---

[2] From now on the reference spectrum $ln(I_0(\lambda))$ will be called **Fraunhofer spectrum**

and asymmetric, so that small errors in the high-resolution spectrum can change the convoluted low-resolution spectrum significantly. Also the absorption cross sections or reference spectra have to be shifted and squeezed with regard to their wavelength calibration and - the wavelength shifts during a typical balloon flight are of the order of ≤0.03 nm and there is also a nonlinear squeeze of the spectra - it is not possible to generate a sufficiently accurate approximation for the Fraunhofer reference for each measured spectrum.

3.3 The DOAS double spectrograph for balloon-borne measurements

For the measurements presented in this thesis a newly developed UV/Vis instrument for DOAS measurements of atmospheric trace gases from balloon platforms was used [Ferlemann 1998; Ferlemann et al. 2000; Harder 1999]. Direct solar light in day time in the near ultraviolet (320.6 - 422.6 nm) and visible (417.6 - 670.7 nm) spectral range can be simultaneously analyzed for the atmospheric abundances or profiles of O_3, NO_2, NO_3, BrO, $OClO$, O_4, H_2O and possibly other species such as HNO_2, IO, CH_2O - see Figure 3.4-3.5.

Compared to previously used balloon-borne UV/Vis spectrometers, the instrument is especially optimized with respect to low mass (42 kg), low power consumption (30 W), low spectral drift of the optical imaging system due to temperature and pressure changes, low detector dark current, and low spectrometer stray light. The latter three characteristics are achieved by enclosing the entire spectrometer in a pressurized and thermostated container and separately thermostated photodiode array detectors. The weight is reduced by a simplified optical set-up. The spectral stray light is reduced by suppressing the higher order and zero order grating reflections using light traps and in the UV by adding a dispersive prism-preanalyzer.

The spectrometer forms an instrument package together with the Fourier transform interferometer on the LPMA(Laboratoire Physique Moléculaire et Applications) balloon gondola as described by [Camy-Peyret et al. 1995].

The wavelength range of the DOAS double spectrograph was chosen to be able to measure the absorptions of as many as possible key species of stratospheric chemistry. Figure 3.4 and 3.5 shows the cross sections of the most important species, which can principally be measured with the balloon spectrograph - the UV wavelength region is extended down to 285 nm to show the differential absorption cross sections of SO_2 and ClO.

The optical components of the DOAS spectrograph consist of two transfer optics with quartz diffusers, filters and aperture stops (see Figure 3.6 and Figure 3.7), two quartz fibre bundles also forming the entrance slits of the spectrograph, two holographic gratings and two windowless photodiode array detectors. The input beam is stabilized by a sun-tracker installed on the balloon gondola as described by Hawat et al. [1995].

An evacuated stainless steel housing is used for the complete optics to minimize shifts and squeezes by changing ambient pressure. Thermal stabilisation of the optical components is provided by embedding the housing into a water-ice reservoir, which has a nearly constant temperature of 0^oC during the whole flight - please see Figure 3.3.

The photodiode arrays are stabilized at $(-10.0 \pm 0.03)^oC$ with on chip peltier elements, the cooling of the warm side of the peltier elements (about 4 W each) is provided by a refrigerant cycled through the reservoir.

The linearity of the detector was checked by recording Fraunhofer lines at different saturation levels. The ratio of selected channels over detector saturation should remain constant at different saturation levels (see Figure 3.8). A fit including ratios within saturation levels below 80% gives a slope of $(2.7 \pm 3.3)\ 10^{-5}(1\sigma)$ making a possible detector nonlinearity insignificant.

The electronic offset of the 16 Bit read-out electronics is shown in Figure 3.9. Typical offset drift during the flights is about 4 counts ($\sim 10^{-4}$ of signal) thus not interfering with the trace gas signals in the DOAS measurement.

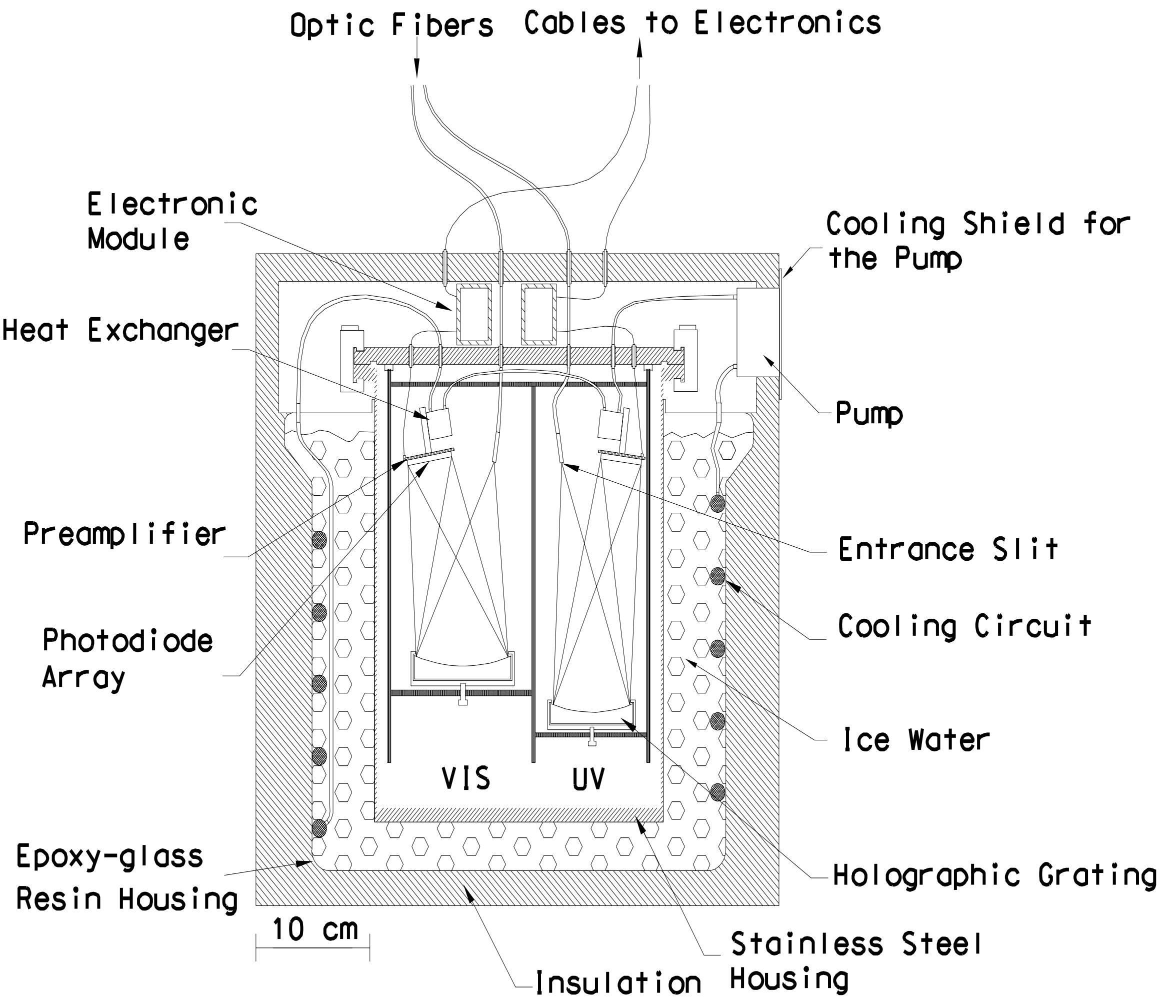

Figure 3.3: The DOAS double spectrograph for balloon-borne measurements of atmospheric trace species. Two holographic grating spectrometers (denoted UV and VIS) are integrated into a vacuum sealed stainless steel container. The light enters the spectrometers via two quartz fibre bundles. The exits of the fibre bundles form a rectangular slit and direct the light on the holographic gratings. The light detection is performed with two photodiode array detectors. The whole spectrometer container is thermostated by a liquid water/ice filled vessel, which surrounds it. In addition a refrigerant is circulated in a cooling circuit to thermostate the optical components and to cool the warm side of the photodiode peltier elements. The total weight of the instrument, including 10 liters of water/ice mixture is approximately 42 kg, and the total size is 45x45x55 cm^3.

Figure 3.10 and 3.11 show a typical offset spectrum and the difference of two offset spectra. These were taken applying an exposure time which was as small as possible - e.g. exposure time 0.1 sec and 1000 scans. The overall standard deviation σ of the unsystematic noise amounts to only $2.025\frac{counts}{\sqrt{scans}}$ leading to a 3σ noise in the differential optical density of $5 * 10^{-4}$.

The primarily measured intensity spectra are firstly corrected for the offset and the dark current. The offset is electronically added to the detector signal to make sure that the A/D conversion (16 bit) does not get negative signals as input. It has to be subtracted again before the DOAS retrieval. Also the dark current of the PDA detector, which depends mainly on temperature and is reduced by holding the PDA at a temperature of $(-10.0\pm0.03)^0$C, has to be subtracted from the measured solar spectra.

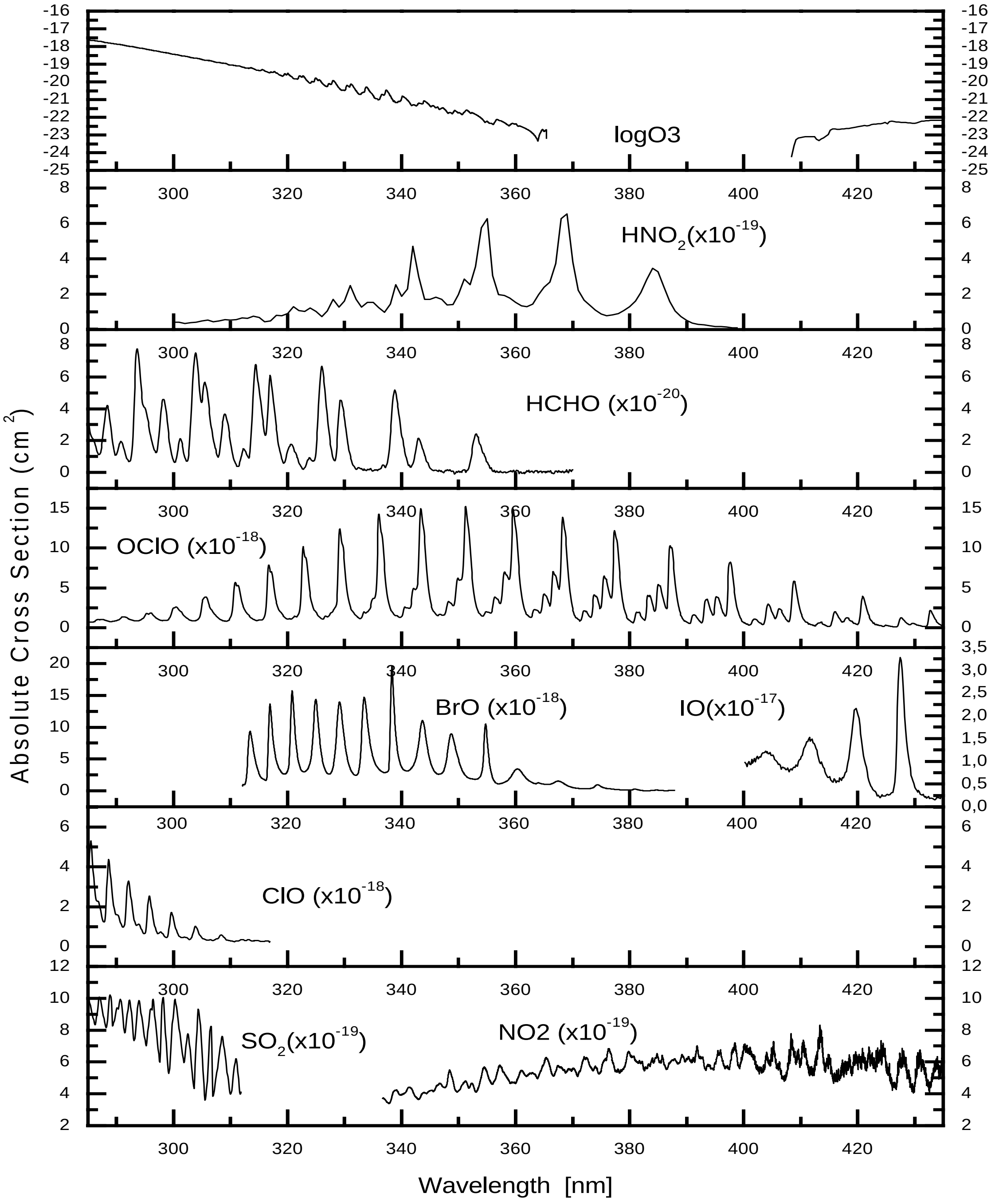

Figure 3.4: Absolute cross sections of the chemical species in the UV balloon double spectrograph wavelength range (320.6 - 422.6 nm). Adapted from [Bauer 1997].

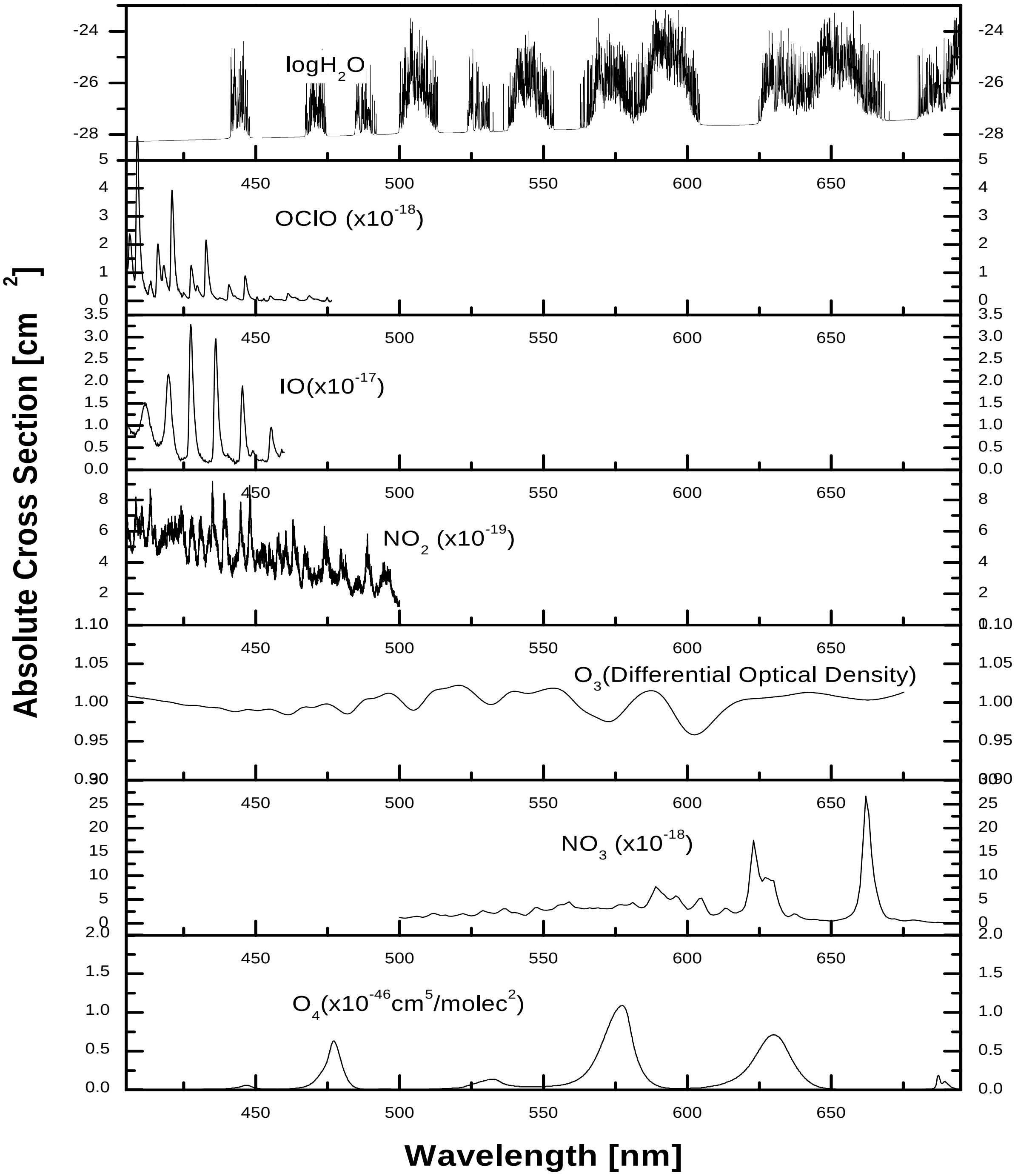

Figure 3.5: Absolute cross sections of the chemical species in the Vis balloon double spectrograph wavelength range (417.6 - 670.7 nm). Adapted from [Bauer 1997].

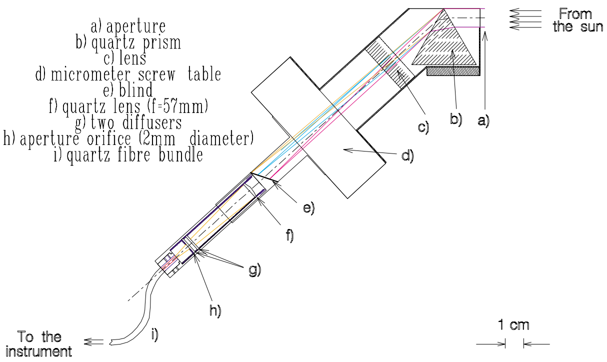

Figure 3.6: Schematic of the UV entrance optics with pre-analyzer. The f number of the UV spectrograph is 5.7 (10^o field of view).

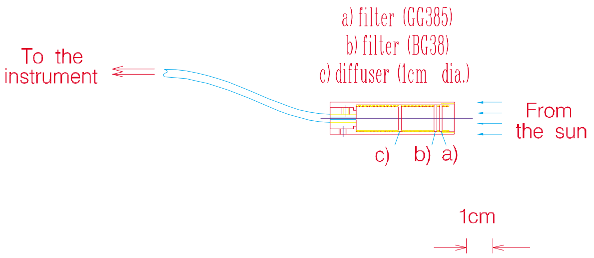

Figure 3.7: Schematic of the Vis entrance optics with filters. The f number of the VIS spectrograph is 3.5 (16^o field of view).

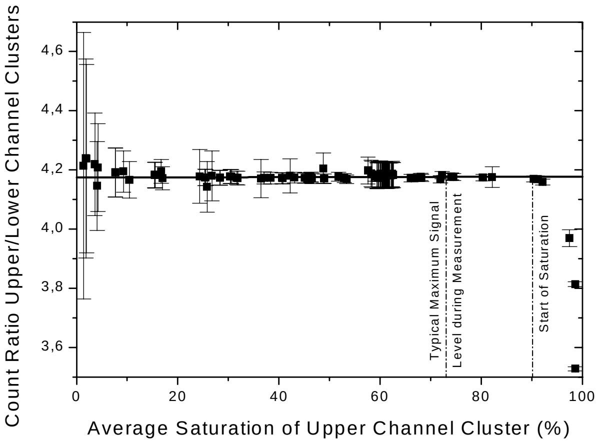

Figure 3.8: Linearity of detector arrays. Adapted from [Ferlemann 1998].

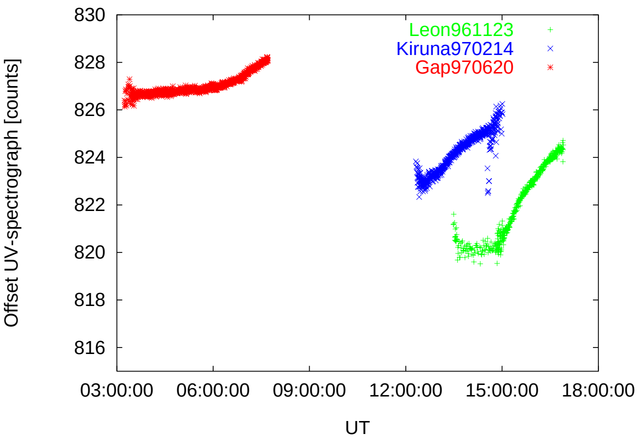

Figure 3.9: Offset of detector. Adapted from [Ferlemann 1998].

3.3.1 Noise sources of the measurements

The noise of the detector is an important parameter for the DOAS evaluation of the spectra. Table 3.1 shows the respective fractions of the detector noise.
During full conduction the photo electron noise of $N_{photoelectron} = 5.4BU^3$ represents the biggest fraction of the noise. Less important is the slightly temperature dependent diode reset noise. As there are two shifts of the clock line during a readout process, the parasitic capacity C_{VC} between video and clock line has double impact on the noise - as well as the photo diode capacity C_{diode}.

The voltage and current noise of the preamplifier ($\frac{4.5nV}{\sqrt{Hz}}$ and $\frac{1.6fA}{\sqrt{Hz}}$) is negligible because of the length of the integration window ($20\mu s$ frequency band width: 50 kHz). The noise fractions labelled with (*) occur both for video and dummy diode line^4 and have hence to be considered four times.
In general the photoelectron noise becomes most important for exposure intensities of more than 7000 BU. So an improvement of the detector electronics is only worthwhile for short exposure times, which is not necessary in direct sunlight spectroscopy where the detector noise is negligible.

---

[3] BU = binary unit describing the digitized video signal.

[4] The dummy diode is read out and preamplified in a similar way as the active diodes to separate the video signal from switching pulses and external interfering signals

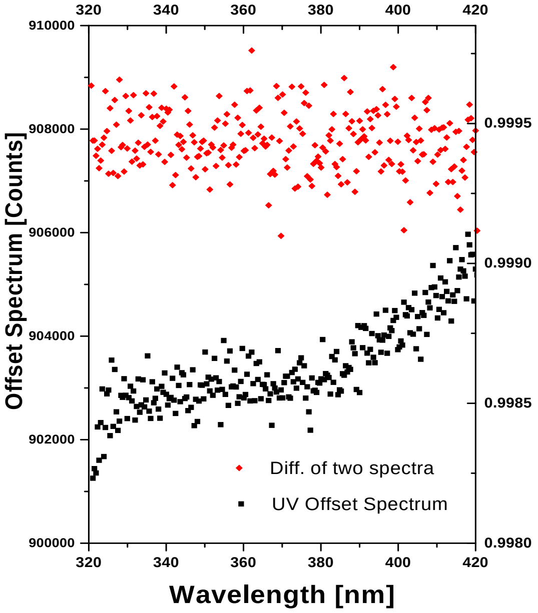

Figure 3.10: UV offset and difference spectrum.

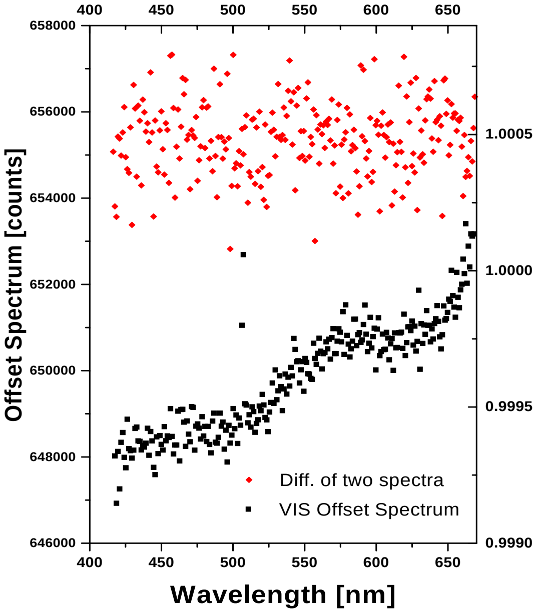

Figure 3.11: VIS offset and difference spectrum.

Noise source		electrons	BU
photo electron noise	$\sqrt{N_{photoelectrons}}$	0 – 11173	0 – 5.38
diode reset noise(*)	$1/q_e \cdot \sqrt{k \cdot T \cdot (2 \cdot C_{diode} + 2 \cdot C_{VC})}$	1843	0.88
voltage noise(*)	$1/q_e \cdot V_{noise} \cdot (C_{diode} + C_{readout})$	249	0.12
current noise(*)	$1/q_e \cdot I_{noise} \cdot T_{integration}$	45	0.02
noise of differential amplifier, integrator and AD-converter	experimental	1804	0.87
Sum of all noise sources without exposure	calculated	4124	1.99
Sum of all noise sources without exposure	experimental	3940	1.90

Table 3.1: Estimation of sources of noise of the detector. The experimentally determined total detector noise is 5% smaller than the calculated noise. For the calculations it was assumed: photo diode capacity C_{diode}=10 pF ([Hamamatsu Photonics 1995]), full conduction at 62000 BU, detector temperature T=263 K, reference voltage 2.06 V, capacity from video- to clock line C_{VC}=2 pF, capacity of the readout line 30 pF, input capacity of the operational amplifier inclusive capacity of video line on the detector printed circuit board 5 pF, and 4.7 pF for the capacity of the readout capacitor. Adapted from [Ferlemann 1998].

3.4 The LPMA/DOAS balloon payload

Figure 3.12 shows the schematic setup of the french-german LPMA/DOAS balloon experiment, which has already successfully been flown during eight flights at different latitudes and during different geophysical conditions. The gondola is equipped with the french Fourier transform infrared interferometer (LPMA-FTIR) and the german UV/Vis DOAS spectrometer, which was designed and built at the Institut für Umweltphysik (IUP).

The gondola used to accommodate the instruments results from the established expertise of Geneva Observatory in the operation of stratospheric payloads for astrophysical studies and from experience with an analogous gondola used for atmospheric studies [Camy-Peyret et al. 1993]. For atmospheric spectroscopy in absorption it is necessary to have the capability to stabilize the gondola in azimuth

in the proper direction. The azimuth suspension shaft of the present gondola is mounted on a thrust ball-bearing and driven DC servo-motor and gear-box. A torque limiter prevents overtwisting of the flight chain and parachutes. The motorized azimuth swivel is coupled to the upper beam of the gondola by a torquemeter and a universal joint. The signal from the torquemeter is fed to a regulator which produces a fast and linear response of the swivel over more than two decades of torque and reduces the dry friction of the azimuth thrust bearing by a factor of 50. With a good gyrocompass reference, the stability is around 1 degree in the troposphere, except during occasional wind gusts, 0.5 to 0.1 degrees in the lower stratosphere, and $1'$ or better at a float altitude of 33 km or higher. These performances are degraded by a factor of 3 when the azimuth reference is a magnetometer, due to a strong coupling between axes inherent to this type of device.
Both optical instruments share the same light input beam provided by the sun tracker Heliostat [Hawat et al. 1995].

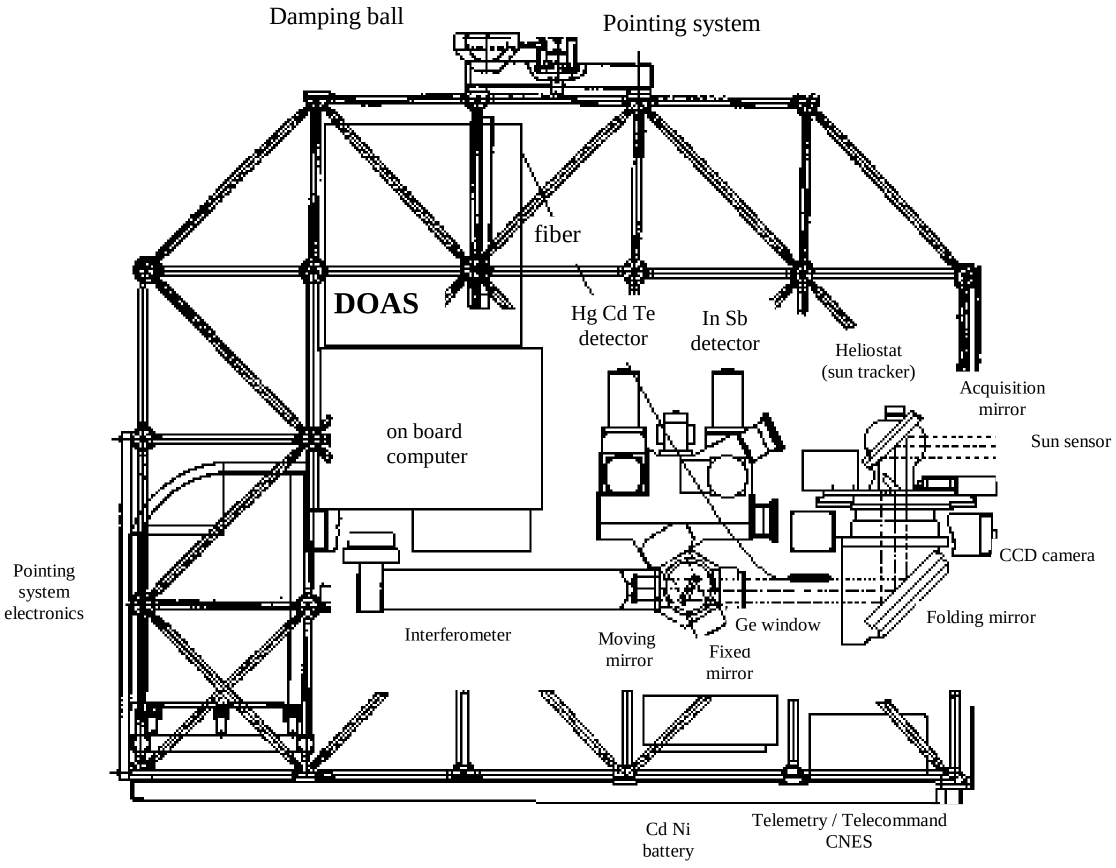

Figure 3.12: Schematic drawing of the LPMA/DOAS balloon payload. The sun tracker (Heliostat) [Hawat et al. 1995] follows the sun with a precision of 1/60 deg and feeds the direct sunlight into the evacuated Fourier transform IR interferometer(LPMA) and the telescopes of the UV/Vis DOAS spectrometer.

The measured chemical species by the joint LPMA/DOAS payload are shown in Table 3.2. With the combination of two independent optical techniques (UV/Vis DOAS and FTIR) using light with the same line of sight it is possible to study several key species of interest for the ozone chemistry in the stratosphere. This thesis will concentrate on the bromine species *BrO* and the chlorine species *OClO*.

A typical balloon sunset flight consists of three different phases : balloon ascent, balloon float and solar occultation. During the first phase (*ascent*) - see Figure 3.13 - the balloon is rising up to the

Chemical Species Measured		
Family	DOAS(UV/Vis)	LPMA(FTIR)
O_x	O_3, O_4	O_3, O_2
NO_x	NO_2, NO_3	NO, NO_2
NO_y	$HONO$	$HNO_3, ClNO_3$
ClO_y	$OClO$	$ClNO_3, HCl$
BrO_x	BrO	
IO_x	IO	
$Others$	H_2O, CH_2O	$HF, F_2CO, N_2O, CH_4, C_2H_6, F-11, F-12$

Table 3.2: Measured chemical species by the joint French-German LPMA/DOAS balloon payload.

height, where the buoyancy because of the weight difference between the light hydrogen in the balloon and the air outside is balanced by the weight of the whole balloon.[5] After reaching the float altitude the balloon remains at nearly constant altitude and begins only to sink a little bit during occultation, when the hydrogen in the balloon is cooling. During the float and the occultation part of the flight, the balloon scans again through the profile - see Figure 3.14. At the beginning of the measurements (balloon ascent) the instruments see nearly the whole profile of the interesting species, while during the latter parts of the flight (float, occultation) only higher lying parts of the profiles are probed. During the occultation most of the absorption takes place at the tangent point, where the light path is perpendicular to the Earth radius vector and the pressure is largest.

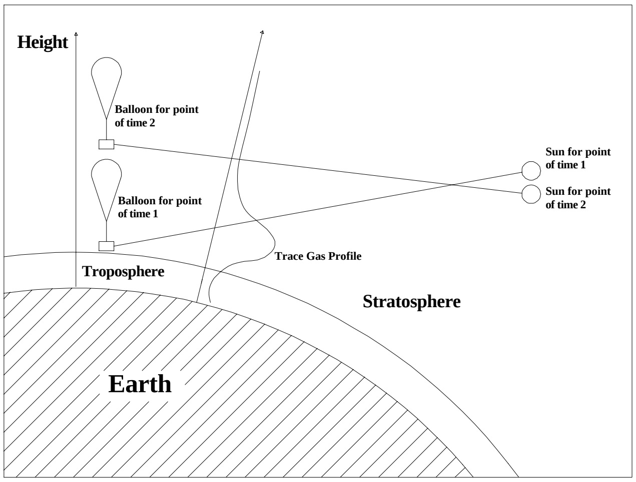

Figure 3.13: Balloon observation geometry during balloon ascent - refraction is not taken account of. For details see text.

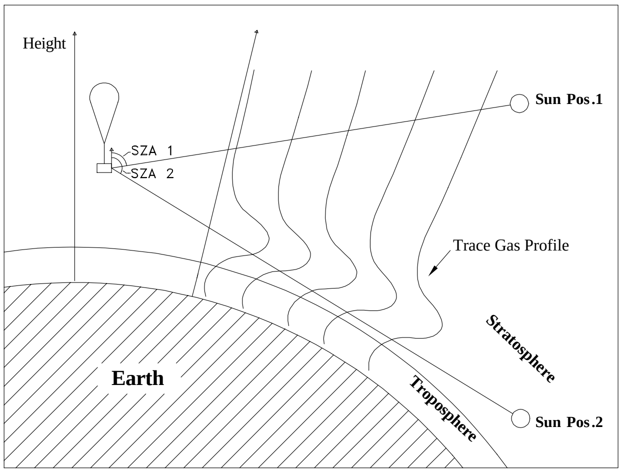

Figure 3.14: Balloon observation geometry during balloon float and occultation - refraction is not taken account of. For details see text.

After having reached the float altitude the balloon is oscillating around the equilibrium altitude, which can be explained by the fact that the hydrogen in the balloon is not yet in thermal equilibrium with the air. These oscillations are called Brunt-Väisälä oscillations - see Figure 3.15 - and depend on the relative gradient of the potential temperature. Their frequency is given by

$$\nu = \frac{1}{2\pi}\sqrt{\frac{g}{\theta}\frac{d\theta}{dz}} \tag{3.20}$$

---

[5] $\rho_{air}(z) = M_{Balloon}/(1 - \frac{m_{H_2}}{m_{air}})/V_{Balloon}$ is the minimal air density until the balloon stops rising; this is at a height of 28.5 km for our flight at Kiruna on Feb. 10, 1999 ($M_{Balloon} \cong$ 800 kg, $V_{Balloon} \cong$ 100 000 m^3) and also depends on pressure and temperature.

The cycle duration of these internal gravity oscillations is around 5 minutes for isothermal stratification of the airmasses but can be much shorter for stronger gradients of the potential temperature.

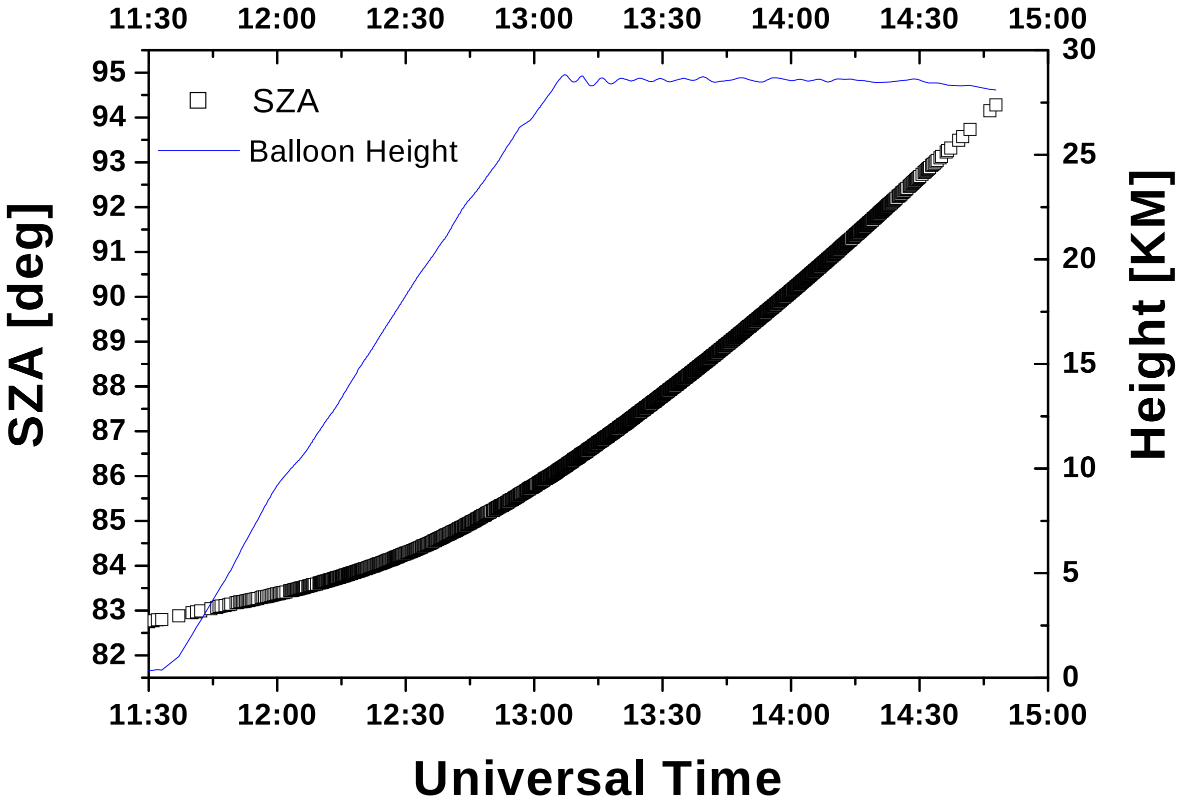

Figure 3.15: Balloon height during a typical flight.

When the sun is setting the solar heating of the balloon cover and hydrogen is decreasing so that the balloon height is slightly decreasing, too. During that phase of the flight the altitude of the balloon is nearly fixed, while the sun is setting, so that with increasing solar zenith angle (SZA) the measured light has passed lower parts of the atmosphere.

3.4.1 The behaviour of the DOAS spectrograph during the balloon flights and its impact on the BrO evaluation

The spectral shifts of the spectra during all of the eight flights performed so far from León, Kiruna and Gap - relative to a Fraunhofer spectrum taken at balloon float, respectively - are shown in Figure 3.16. The instrument withstood the impacts without degradation and no readjustments of the main optical set-up between all of the eight flights had to be undertaken.

The pressure induced shift detected at León and Kiruna ascent amounts to 0.019 nm/bar - it is largest in Kiruna 99, because we have measurements there beginning at ground level, while the measurements during the other flights began in the upper troposphere or at the tropopause - a small temperature induced shift is seen during sunset/sunrise for the Gap flights and the morning part of the Kiruna 98 flight.

The relative wavelength alignment of the reference spectra is not exactly known and thus may introduce errors in the retrieval [Aliwell et al. 1997]. But the effect of possibly misaligned reference spectra can be estimated taking all the shift-induced deviations of the SCD together (Fig. 3.17). The error of

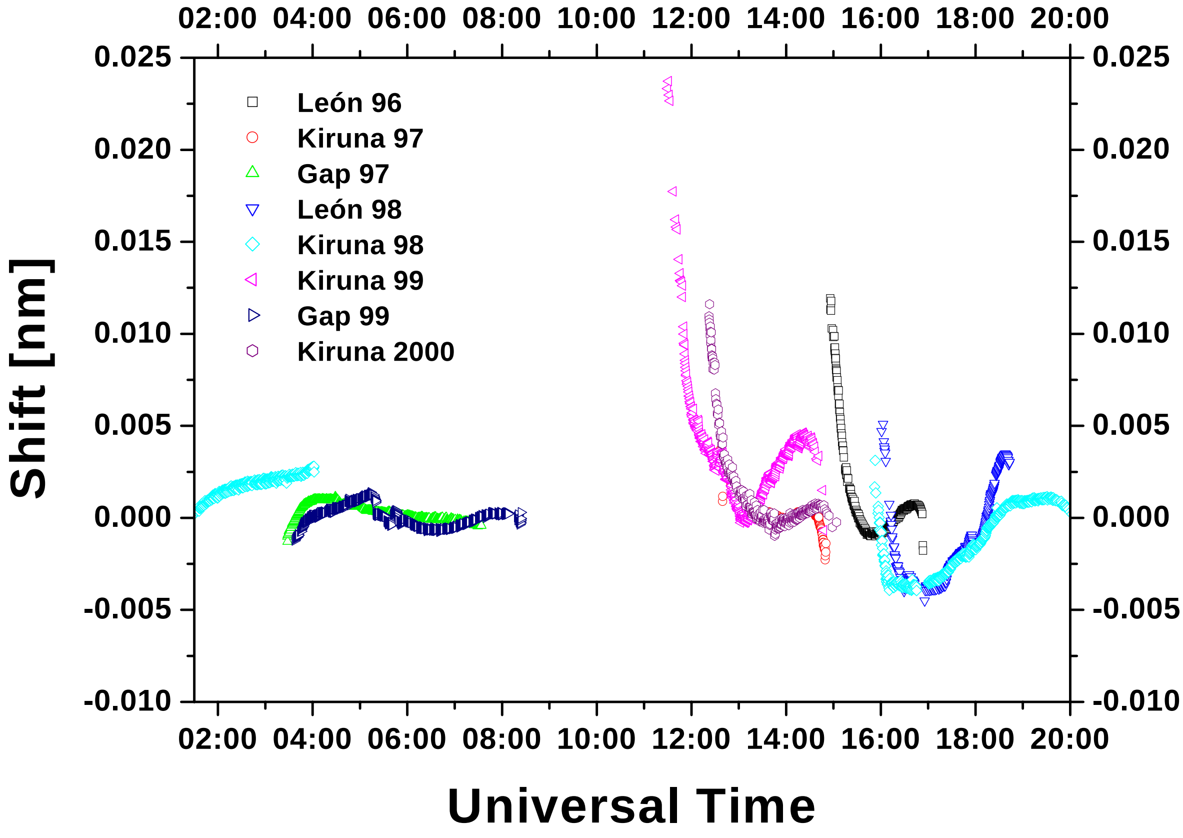

Figure 3.16: Spectral shifts during all eight flights conducted so far from León, Kiruna and Gap in the interesting BrO retrieval wavelength range (346-360 nm).

possible misalignments of the reference spectra can thus be assessed to be in the range of 3% in the case of BrO.

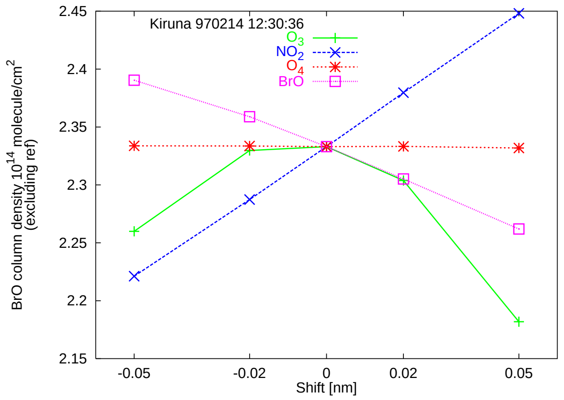

Figure 3.17: Sensitivity of the retrieved BrO SCD to misalignments of individual reference spectra. Adapted from [Ferlemann 1998]

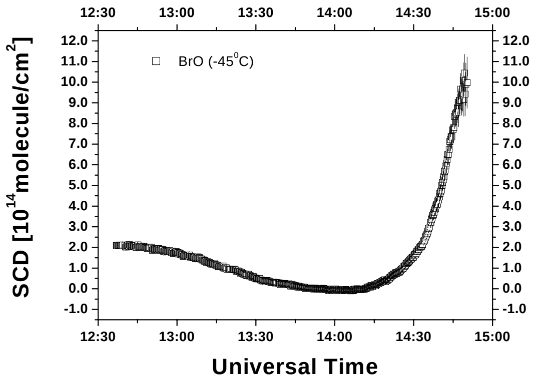

Figure 3.18: BrO column densities during the flight from Kiruna on Feb.14, 1997.

Figure 3.18 shows the BrO slant column densities during the flight from Kiruna 1997 with SZA 83° to 94° (Error bars denote statistical fit errors). During the balloon ascent the BrO $SCDs$ are decreasing after having passed the concentration maximum, which results from the fact that during the ascent in the troposphere the SZAs are increasing as well as the airmass factors. When the balloon reaches the float altitude, the smallest amount of BrO is observed. Therefore we take the so called *Fraunhofer spectrum* at this altitude as a reference spectrum for the DOAS fit. When the SZAs are getting larger than 90^o the instrument is looking down to lower altitudes and the most of the atmospheric absorption takes place at the *tangent point*, where the local SZA is 90^o.

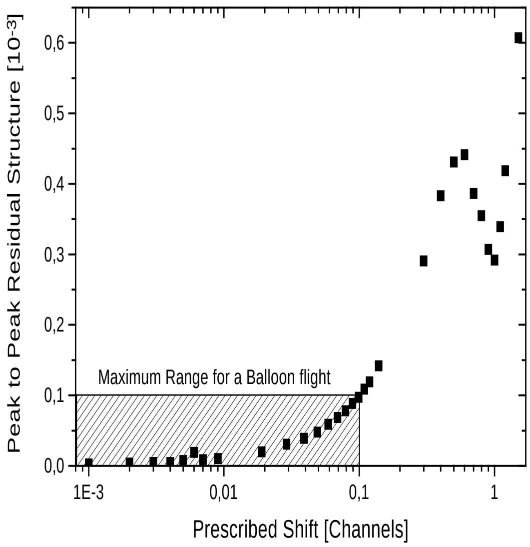

Figure 3.19: Peak-To-Peak residual structure as a function of the prescribed spectral shift. Adapted from [Vradelis 1998].

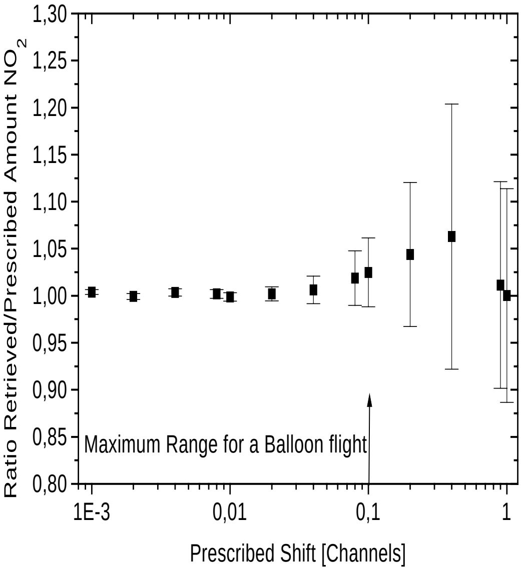

Figure 3.20: Ratio of the fit coefficient of NO_2 before and after shift as a function of the prescribed shift. Adapted from [Vradelis 1998].

Tests have been performed to study the influence of some important steps of the evaluation. Figure 3.19 shows the error propagation of misalignments of high resolution spectra, e.g., a sunlight spectrum [Kurucz et al. 1984]. The difference of a shifted and the original spectrum depends strongly on the shift itself, which can be seen when calculating the Peak-To-Peak residual. For real conditions this effect is smaller than 0.01%.

Another test is to fit a NO_2 and a solar spectrum to the sum of these two spectra after having shifted the solar spectrum and to look at the resulting NO_2 fit coefficient (Fig. 3.20).

For the different DOAS evaluations of the different flights, it is necessary to include the information about the real shifts of the spectrograph between the measurement flights, because otherwise the DOAS fit routine shifts the reference spectra to positions, which are by far larger than the physical shifts observed and improve the fit only because of numerical correlations of the absorption reference spectra. The atomic mercury lines measured before and after each flight are shown in Figure 3.21. It can be seen that the wavelength shift of the mercury lines is of the order of 0.1 nm and the shift was negative during the first flights (-0.1 nm), positive afterwards (+0.1 nm) and after the last flight in Kiruna 2000 the position of the lines was approximately the same as before the first flight in León 96. This is a very amazing result taking into account the eight rough landings of the up to 600 kg weighing balloon gondola and landing accelerations of up to 7G. Finally this comparison displays the robustness of the instrument specially designed for balloon-borne measurements.

The instrument condition (e.g., temperatures of photo diode array, peltier currents) is recorded together with the spectra and can be monitored remotely via telemetry on a ground station. A newly included GPS can track the location of the balloon (Fig. 3.22) with an accuracy of at least 100 m in height and

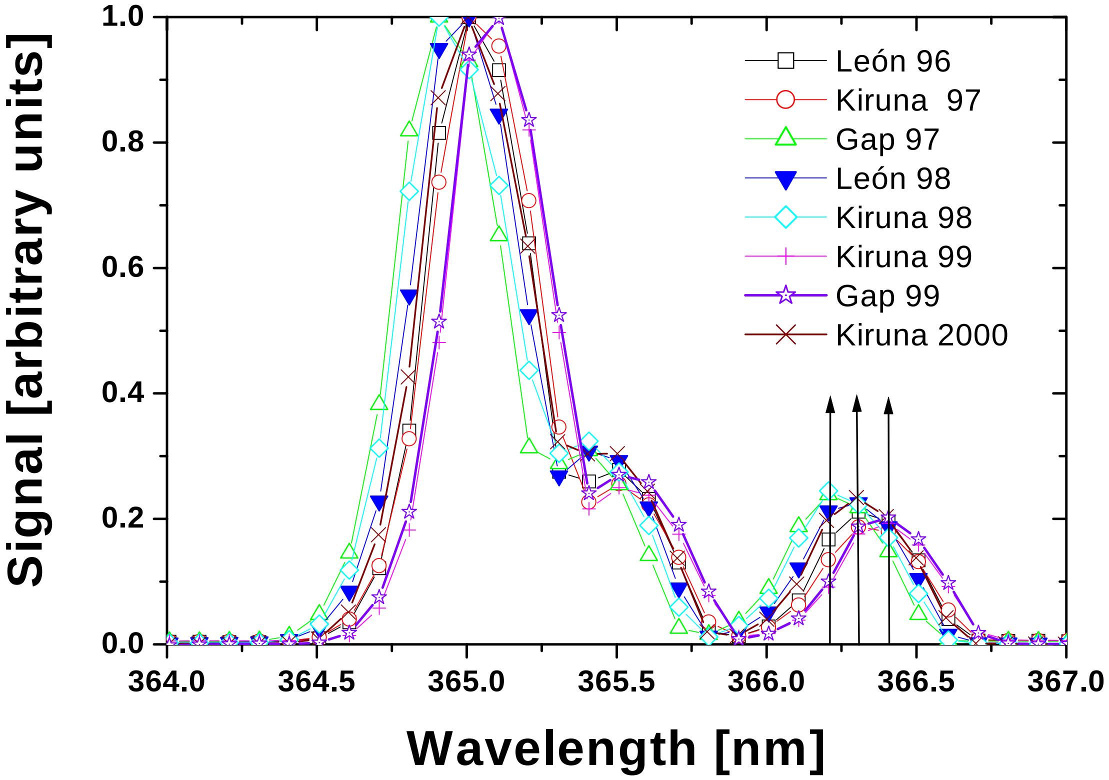

Figure 3.21: Shift and change of the atomic mercury lines at 365.02, 365.48 and 366.33nm. The atomic lines are used to image the slit function of the spectrograph, which is possible because the line width of the atomic lines ($\approx 0.001nm$) is much smaller than the resolution of the spectrograph (0.3-0.4 nm).

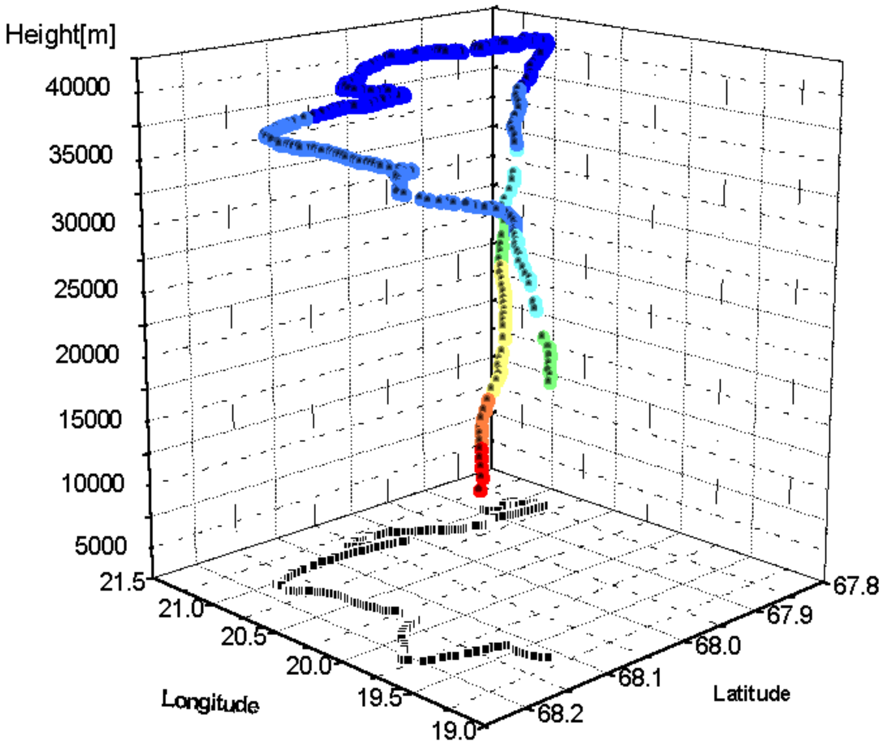

Figure 3.22: Trajectory - 3-D plot + projection - during the flight at Kiruna in Aug. 98.

100 m with respect to latitude/longitude[6]. Also the time of the onboard PC is synchronized with the GPS Time.

3.4.2 The BrO DOAS evaluation

The temperature and pressure independence of the absorption cross section is a good approximation for the interesting chemical radical species $BrO, OClO$ in the UV region, while it is not so well suited for O_3, O_4, NO_2 (see Figure 3.23). But from laboratory measurements of the cross sections it is clear that the pressure dependence plays only an insignificant role for the species measured and the temperature dependence is most important, because different temperatures means different populations of the energy levels of the molecules leading to different transition probabilities within them. That is why for the retrieval of the O_3 $SCDs$ and NO_2 $SCDs$ we use different wavelength ranges like the Chappuis Band region $(400-500\,nm)$ where the temperature dependence is only weak.

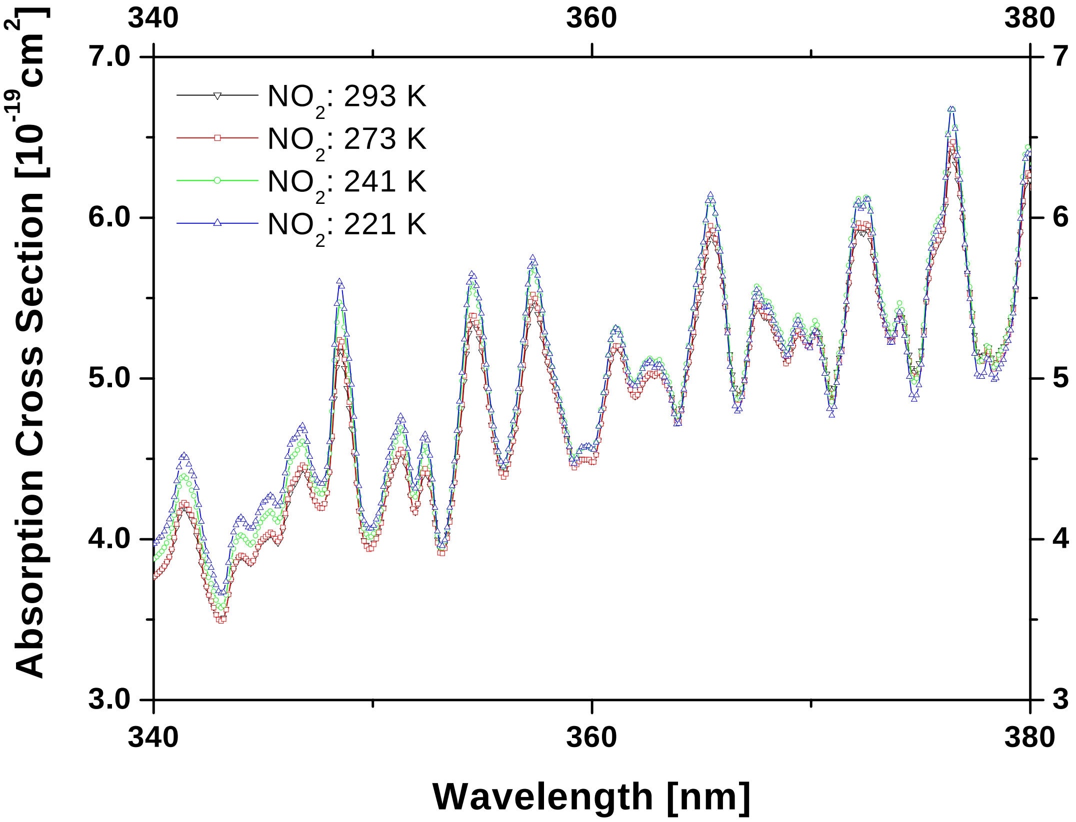

Figure 3.23: Temperature dependence of the NO_2 absorption cross sections in the BrO and $OClO$ retrieval wavelength range (346-380 nm). The cross sections were measured by Burrows et al. [1998].

A typical BrO DOAS evaluation of a measured spectrum - after correction of the dark current and the offset - from balloon in the interesting BrO retrieval spectral range is shown in Figure 3.24. Here, the UV vibrational absorption bands (4-0 at 354.7 nm, and 5-0 at 348.8 nm) of the $A(^2\pi)\leftarrow X(^2\pi)$ electronic transition of BrO are used. The reference spectra used for the BrO retrieval were measured in a cooled reference cell in the laboratory [Harder 1999]. O_3 at different temperatures, NO_2 and BrO

---

[6] In spring 2000 the US decided to reduce the jitter on the GPS signal which artificially made it impossible to achieve a better accuracy in realtime - from now on the accuracy will be ten times better (10 m). Still the onboard recorded satellite positions can be used after the flight to increase the accuracy of the position data to an even higher accuracy.

were measured independently with the balloon spectrograph and the reference spectra were calculated, respectively. For the O_4 absorptions the measured laboratory spectrum of Greenblatt et al. [1990] was used. The O_4 reference spectrum is not an absolute cross section but a collision pair absorption cross section[7] of the $O_2 - O_2$ dimer state of molecular oxygen. The BrO reference used is the absolute cross section measured by Wahner et al. [1988], which had been measured with a spectral resolution of 0.4 nm and the wavelength calibration was taken from our own laboratory measurements. As observed in the laboratory spectra the Wahner spectrum has to be shifted by 0.19 nm, which is in accordance with the FTUV measurements of Wilmouth et al. [1999], who deduced a shift for the 4-0 and 5-0 vibrational absorption bands of 0.07-0.19 nm.
It is obvious that the numerical retrieval algorithm - based on a nonlinear Levenberg-Marquardt least-square fitting algorithm [Stutz and Platt 1996; Van Roozendael and Fayt 2000] - has to be able to detect trace gas differential optical densities as small as 10^{-3} within a highly structured solar line spectrum with optical densities as large as 0.1-1, which it clearly does.

For the DOAS evaluation of the measured dark current and offset corrected raw spectra - which will be called from now on the *measured spectra* - we used two different software packages. The MFC [Gomer et al. 1996] based fit is a nonlinear Levenberg-Marquardt fit of the reference spectra to the measured spectrum allowing the reference spectra to shift and squeeze to better fit the wavelength grid of the measured spectra. In addition a polynomial of 3rd degree is included in the fit to account for the broad band structures like Rayleigh scattering. During the first three flights no optical preanalyzer was used in the UV to suppress geometrical stray light, which produced a nonlinear socket in the spectra. With the MFC package it was only possible to correct for this by including a stray light socket as a further reference in the fit procedure, which was identified by measurements of the stray light, when there was no UV light entering the UV spectrograph but only IR light [Bauer 1997].

$$ln(I(\lambda) + I_s(\lambda)) = ln(I(\lambda)) + ln(1 + \frac{I_s(\lambda)}{I(\lambda)}) \approx ln(I(\lambda)) + \frac{I_s(\lambda)}{I(\lambda)} \tag{3.21}$$

The further reference to include in the fit can be approximated by $\frac{I_s(\lambda)}{I(\lambda)}$, where $I_s(\lambda)$ is the stray light socket and $I(\lambda)$ is the measured spectrum itself [Ferlemann 1998].
With the second software package WINDOAS [Van Roozendael and Fayt 2000] it is possible to fix a fit coefficient - needed for example to keep the fit coefficient of the Fraunhofer reference fixed to 1 - and to include a polynomial of degree 2 into the nonlinear fit procedure, which means that it is not fitted as a reference but as an offset to the intensity spectrum. This is a good way to account for the geometrical spectrograph stray light without making the assumption of very small stray light like in the case of the MFC fit. Figure 3.24 shows such a DOAS fit using the WINDOAS package.
When comparing the root mean square (RMS) of the two different DOAS evaluations (see Figure 3.25), we recognize that the WINDOAS evaluation is better in minimizing the χ^2 of the fit. That is why from now on only the WINDOAS evaluation will be used for the DOAS fit.

Still the difference in the retrieved BrO $SCDs$ is very small and can be neglected, if we consider the error of our SCD measurements, which is about 12%. Figure 3.26 shows that the retrieved $SCDs$ are very much the same in the occultation part of the flight, while there seems to be a slight systematic discrepancy during the ascent of the balloon.
So the second WINDOAS based stray light correction technique will be used in the following, when evaluating the measured spectra.

Ring-effect

Inelastic rotational Raman scattering is filling in Fraunhofer lines in solar spectra, when the light is scattered inelastically at least once in the atmosphere. It was shown to be very crucial for DOAS spec-

---

[7] From measurements in the laboratory it is known that the absorption of O_4 can be written as $A = \alpha \times [O_2]^2$ with the collision pair absorption cross section α in units of $\frac{cm^5}{molecule^2}$

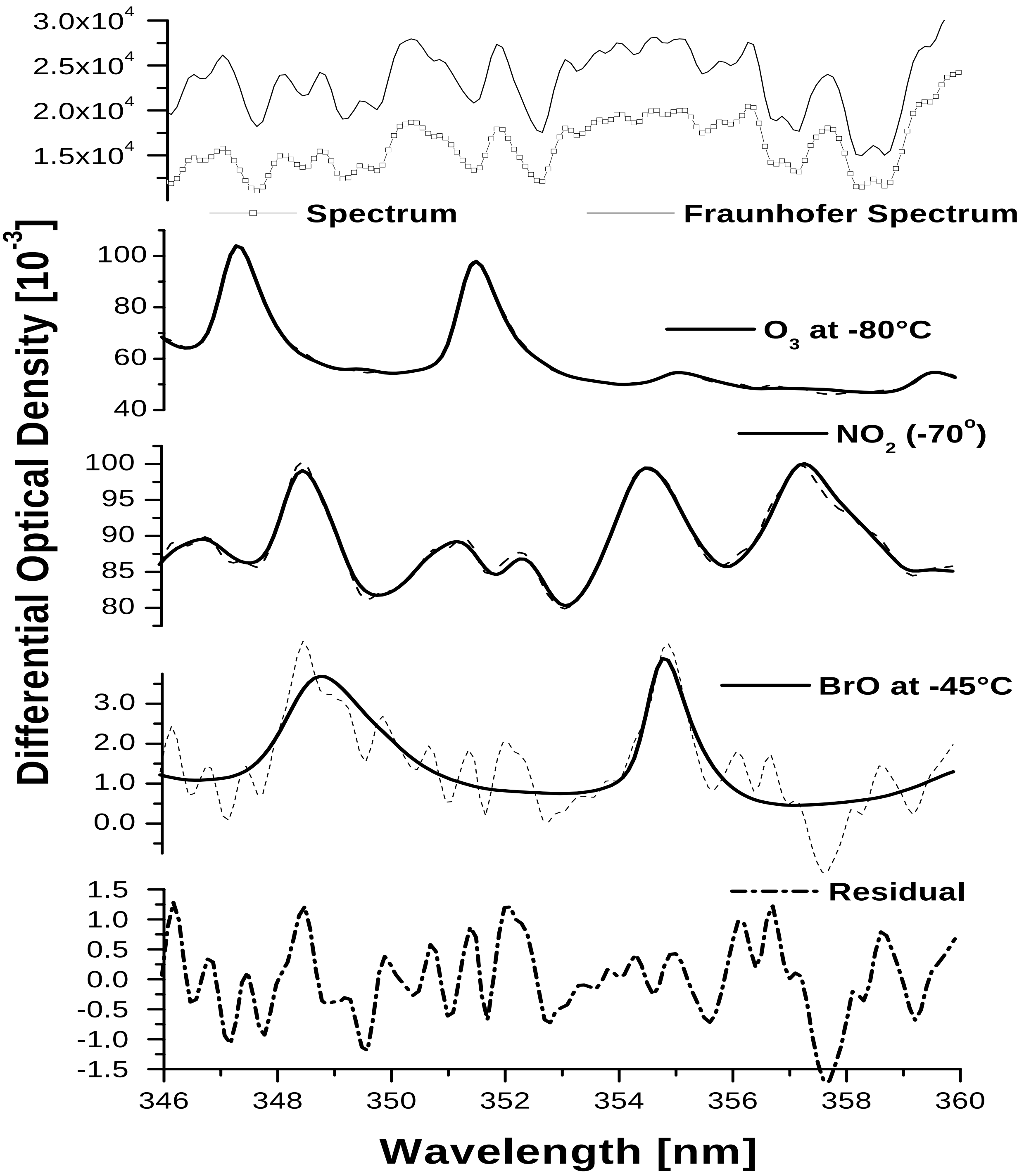

Figure 3.24: Example DOAS evaluation in the interesting BrO retrieval wavelength range (346-360 nm). The fit included O_3 at -80^{o}C and -20^{o}C(not shown), NO_2 at -70^{o}C(not shown), O_4(not shown) and BrO at -45^{0}C and a polynomial of degree 3. The last spectrum is the residual which cannot be explained by the fit but is due partly to statistical noise and to systematic errors.

troscopy using zenith-scattered sunlight [Bussemer 1993; Wagner 1999]. There the inelastic portion of light reaching the spectrograph can amount up to a few percent. For direct sunlight DOAS spectroscopy it is much less important, as only a very small portion of the analysed light is scattered, while the greatest portion is direct sunlight. When using a so called Ring reference spectrum ($\approx I_{inelastic}/I_{elastic}$)

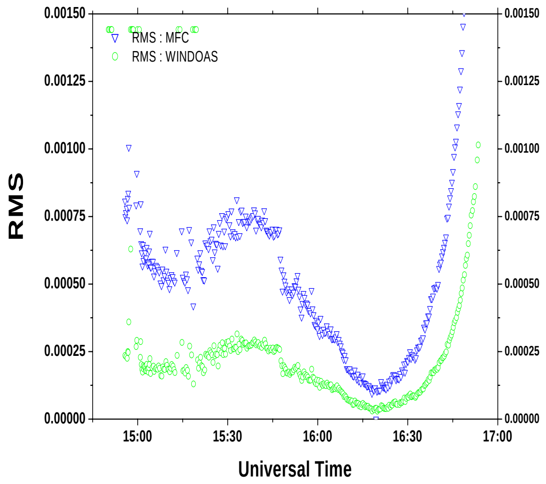

Figure 3.25: Comparison of the root mean square of the residual of the DOAS fit with MFC and WINDOAS software as a function of time. The WINDOAS fit is better reducing the residual.

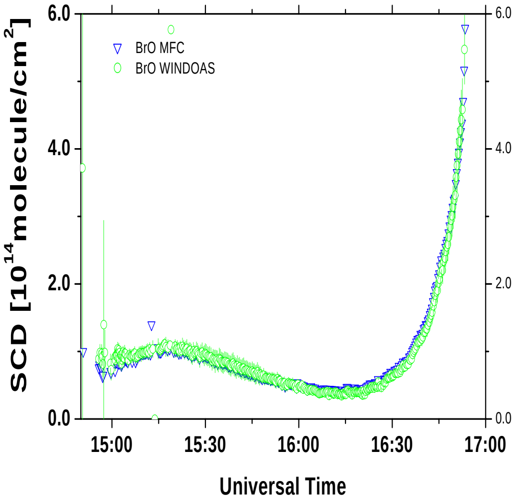

Figure 3.26: Comparison of the retrieved BrO $SCDs$ from the DOAS fit with the MFC and WINDOAS software as a function of time. The difference is in the range of the estimated error of 12% for this flight.

a problem is that it correlates very much with the stray light correction - which is also proportional to $1/I_{elastic}$ in a first approximation - so that applying a Ring correction would correct also for the stray light and vice versa. In accordance with former investigations and evaluations [Bauer 1997; Ferlemann 1998; Harder 1999] and after tests using a Ring spectrum - which did not improve the fit significantly and did not change the resulting fit coefficients of the other species - it was decided, generally not to apply a Ring correction.

Spectral resolution and the *solar* I_0 *effect*

Another problem of the DOAS evaluation may arise from the finite spectral resolution of the imaging spectrograph. In the case of our balloon-borne double spectrograph, this resolution is between 0.4-1.0 nm - for details see section 3.21 - which is about 10-100 times higher than the typical line width of the atomic Fraunhofer lines and high resolution absorption cross section bands like the ones of NO_2.

$$I(l,\lambda) = \int_0^{\mathrm{inf}} T(\lambda',\lambda) \times [I_0(\lambda')\mathrm{e}^{-\sum_i^{Species}\sigma_i(\lambda')SCD_i}]d\lambda' \tag{3.22}$$

The finite spectral resolution of our optical setup can be described by convolution of the incoming light with an optical slit function $T(\lambda',\lambda)$, which is normalized by $\int_0^{\mathrm{inf}} T(\lambda',\lambda)d\lambda' = 1$.
The first approximation of our DOAS evaluation is that we use measured spectra and absorption cross sections in the linearized version of the model, which means permutation of logarithm and integration, which is only allowed when the light source $I_0(\lambda)$ is nearly constant within a certain spectral range and the trace gas absorptions are small. This has been numerically tested for the BrO spectral retrieval region by Huppert [2000] and the respective error in the determination of the $SCDs$ was found to be $\leq 0.1\%$.
The second problem arises from taking absorption cross sections which were convoluted to the spectrograph resolution or have been measured with the same instrument. When we use a highly structured light source like the sun it is obvious that there is a difference between the absorption cross section convoluted to our spectrograph resolution and the natural logarithm of the ratio of a sunlight spectrum

measured with absorption of the chemical species ($S_i(\lambda)$) and without it ($S_o(\lambda)$). This is called the *solar I_0 effect* [Johnston 1996].

$$R_i(\lambda) = \frac{S_i(\lambda)}{S_o(\lambda)} = \frac{\int_0^{\inf} T(\lambda',\lambda) \times I_0(\lambda') \mathrm{e}^{-\sigma_i(\lambda')SCD_i} d\lambda'}{\int_0^{\inf} T(\lambda',\lambda) \times I_0(\lambda') d\lambda'} \tag{3.23}$$

This representation of the so called *solar I_0 corrected reference spectrum* is suitable to correct the fit error, which has been tested numerically (see Figure 3.27).

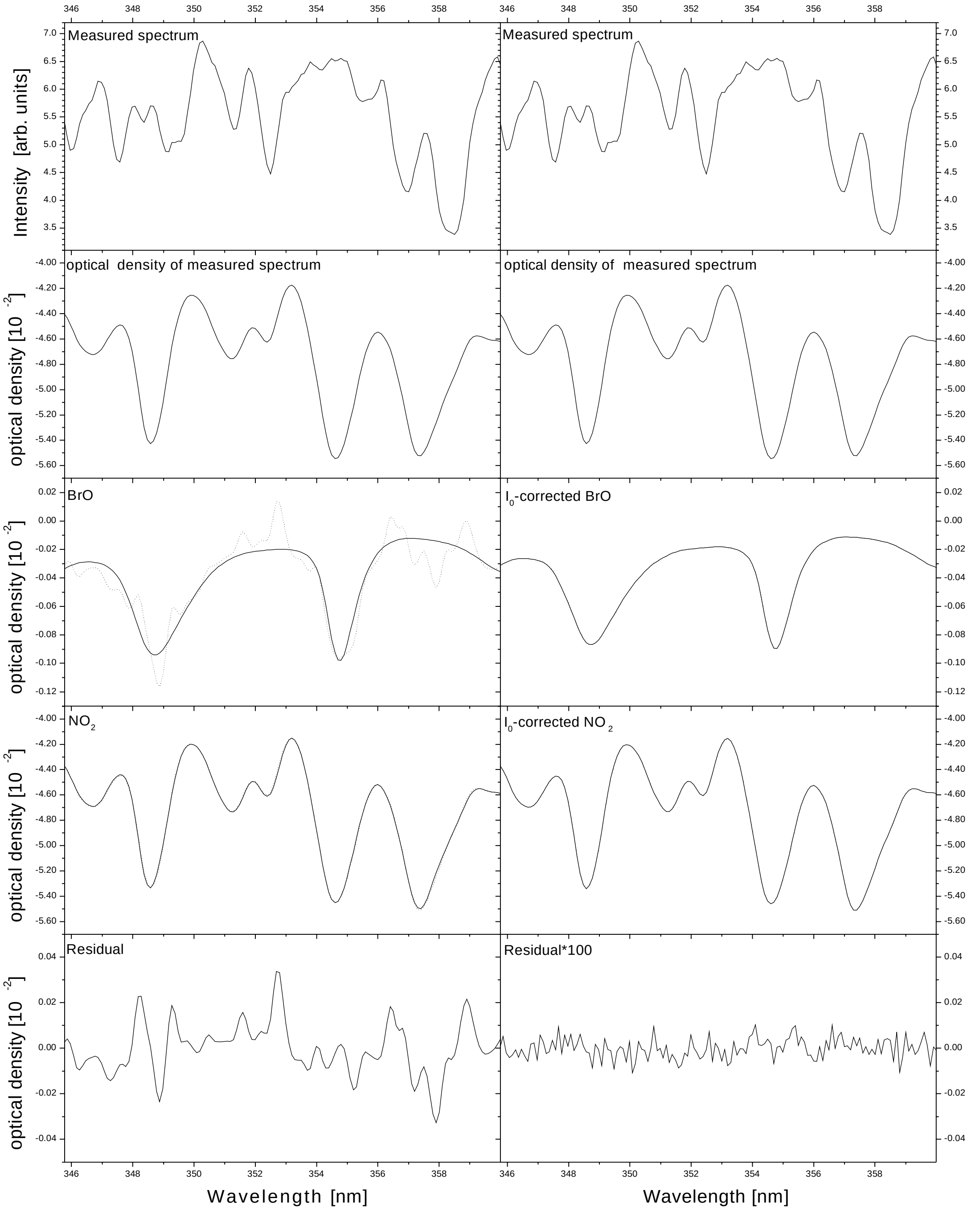

Figure 3.27: Example of a numerical I_0 correction of spectra generated by convolution using the slit function of the UV spectrograph in the interesting BrO retrieval wavelength range (346-360 nm).

For the BrO retrieval it has been shown that the strongest impact of the solar I_0 effect results from NO_2 and it could also be shown theoretically as well as practically that it is possible to correct the error in the determination of the $BrO\ SCD$ by a linear relation between the SCD error and the $NO_2\ SCD$. Overall the $BrO\ SCD$ error induced by the solar I_0 effect is smaller than the fit error resulting mainly from the residual of the fit. As it was shown by Huppert [2000] that the introduction of I_0 corrected spectra does not improve the residual but even worsens it - this is attributed to interpolation errors, when using convoluted reference spectra - only laboratory reference spectra will be used throughout this thesis.

3.4.3 The $OClO$ DOAS evaluation

$OClO$ is only expected to be measurable during balloon flights with enhanced chlorine activation - as in wintertime in the polar Arctic vortex.

In the $OClO$ DOAS fit - using the vibrational and rotational absorption bands of the $\tilde{A}^2\mathrm{A}_2 \longleftarrow \tilde{X}^2\mathrm{B}_1$ electronic transition - a convoluted $OClO$ spectrum is applied, which is based on the high resolution FTUV absorption cross section measured with a resolution of 0.005-0.006 nm at the Institut für Umweltphysik of the University of Bremen, Germany [Kromminga et al. 1999]. The other reference spectra used in the fitting procedure are taken from our own laboratory measurements using the balloon spectrograph.

Figure 3.28 shows a typical DOAS evaluation in the $OClO$ wavelength range (362-390 nm). This is the range, where it is only necessary to include $OClO$ (convoluted, measured at 213 K), NO_2 (measured at 203 K) and O_4 into the fit as absorbers. A polynomial of degree 5 is also used for this DOAS fit region. As there are three $OClO$ absorption bands included in this fit window ($OClO\,range$), this spectral range will be used further on - if not otherwise stated - to retrieve SCDs and to calculate profiles which are then compared to model predictions. In the following chapter also an $OClO$ DOAS evaluation in the wavelength region, where BrO and O_3 cannot be neglected, will be presented. There it will be shown that the different evaluations in the different wavelength ranges result in the same amounts of $OClO$ and NO_2, which is also used in all tested wavelength windows.

The error of the absorption cross section is estimated by to be about 10% [Wahner et al. 1987; Kromminga et al. 1999] and the temperature dependence of the cross section is 10-20% between 204 and 298 K, so that using a cross section measured at 213 K for the evaluation of stratospheric spectra (205-230 K) introduces a temperature error of less than 5%. Tests of the fit window and shifts of the other reference spectra, etc. generated variations of the $OClO$ SCD between 5 and 10%, so that the overall error of the $OClO$ SCD measurements is estimated to be ≈15%.

3.5 Determination of the SCD offset in the Fraunhofer reference - Langley Plot

As we take a spectrum with minimal atmospheric absorption to fit it together with the references to the measured spectrum, it is essential to determine the atmospheric column within the Fraunhofer reference to be able to calculate the absolute amount of the measured species.

$$SCD_{real} = SCD_{fit} + SCD_{offset} \tag{3.24}$$

There is an offset (SCD_{offset}) necessary to be determined for retrieving the real, absolute SCD (SCD_{real}), which is equal to the column amount in the Fraunhofer spectrum. We use the *Langley reference plot* technique - or shortly the Langley plot - to extract the SCD offset from our measurements. As we know from models and measurements that the mixing ratio of species like BrO is nearly constant in the middle and upper stratosphere - once the Br_y maximum is reached - we can write for

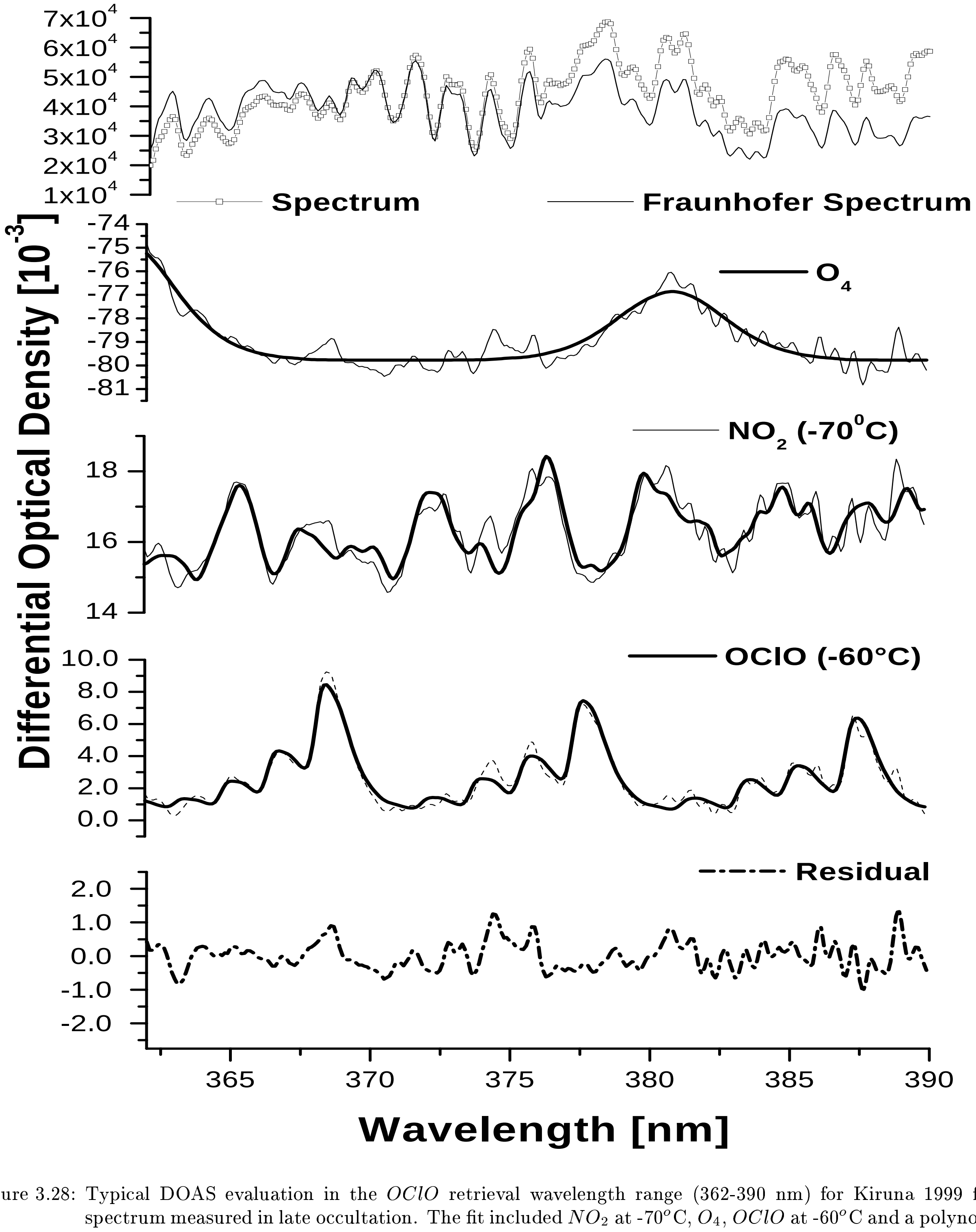

Figure 3.28: Typical DOAS evaluation in the *OClO* retrieval wavelength range (362-390 nm) for Kiruna 1999 for a spectrum measured in late occultation. The fit included NO_2 at -70^{o}C, O_4, $OClO$ at -60^{o}C and a polynomial of degree 5. The last spectrum is the residual of the fit which cannot be explained by the fit but is due partly to statistical noise and to systematic errors. All spectra have been filtered with a binomial filter of degree 3 before the fit.

the results of the DOAS fit for our spectra recorded at balloon float altitude and for SZAs smaller than 90^o

$$SCD_{fit} = AMF * VCD_{air} * VMR - SCD_{offset} \tag{3.25}$$

where AMF is the so called *airmass factor*, VMR is the mixing ratio of the interesting species and VCD_{air} the vertical column density of air molecules above balloon float altitude. The airmass factor is defined as the ratio of volume column density and slant column density

$$AMF = SCD/VCD \tag{3.26}$$

We get the SCD offset from fitting the measured $SCDs$ (SCD_{fit}) as a function of the air slant column density ($AMF * VCD_{air}$), which is a linear function in the case of constant mixing ratios above float altitude. The SCD offset is the axis intercept for an air slant column density of zero and the VMR is given by the slope of the linear function. Figure 3.29 shows the Langley plot for our flight at Kiruna 1999.

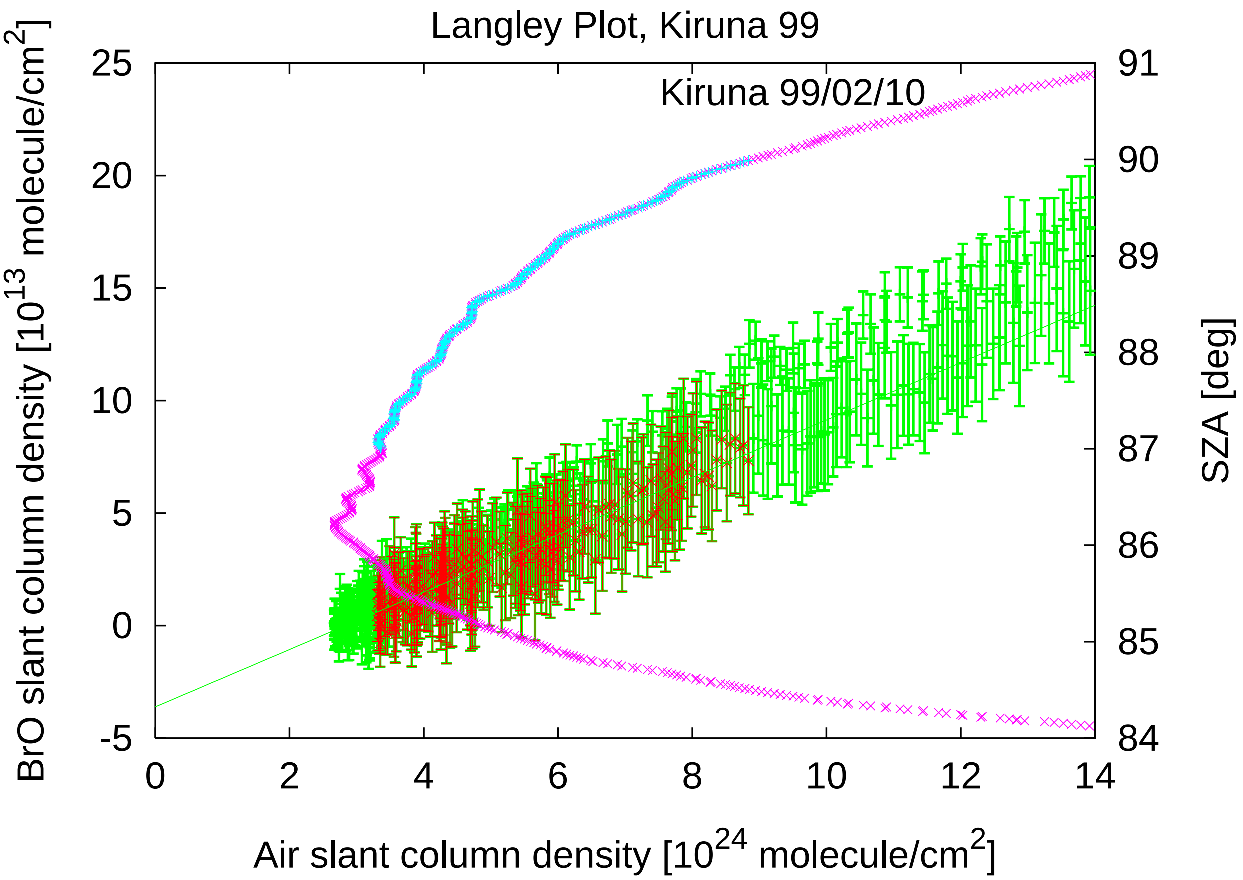

Figure 3.29: *BrO* Langley plot for determining the SCD offset during the flight at Kiruna on Feb. 10, 1999. The $SCDs$ are denoted by bars and the solar zenith angle (SZA) is also plotted (crosses). For the fit of the SCDs only measurements for SZAs between 87 and 90^o are used.

3.6 Summary of the error sources of the bromine oxide SCD measurements

This section summarizes the different error sources of the BrO SCD measurements.
The DOAS fit procedure minimizes the mean quadratic difference χ^2 of the model description and the measurements for all channels of the detector in a certain wavelength range. As the resulting SCD error is calculated as a 1σ error of the linear fit by the fit routine plus the error induced by the wavelength alignment error calculated by the nonlinear part of the Levenberg-Marquardt fit, the possibly occurring systematic errors are not taken account of by the fit.
As shown in Figure 3.17 the possible physical misalignment of the reference spectra has been tested to be about 3%. After performing several numerical tests of the fit procedure varying the boundary conditions (e.g. polynomial degree, wavelength alignment of the reference spectra, fit wavelength range, influence of the smoothing filter mask, use of I_0 corrected reference spectra) it could be stated a systematic uncertainty of 10%.
A crucial parameter of the BrO DOAS evaluation is the absolute cross section measured in the laboratory. As it was recently shown by new measurements of Wilmouth et al. [1999], the different FTUV and grating spectrometer measurements fall in a range of ±7%, when corrected for the different temperatures and the different resolutions of the respective instruments. The newest measurements with FTUV do only differ from the first measurement of Wahner et al. [1988] by less than 2%.
The temperature dependence of the BrO cross section [Gilles et al. 1997] shows a $20-30\%$ difference of the absolute cross sections between $223K$ and $298K$. As we observed in the stratosphere and troposphere temperatures between $200K$ and $250K$, we can estimate the maximum temperature error of the SCD by 10%. Still is has to be recognized that we are almost always integrating the BrO concentrations along the whole range of temperatures, so that the use of a mean temperature BrO reference at $228K$ is a good approximation.
Also the SCD measurements have a statistical scatter around a mean time evolution, which can be estimated to be $4-8\%$ depending on the Signal-To-Noise ratio (SNR) during the respective flights. In general, sunset flights at high latitudes have a much better SNR than the sunset or sunrise flights at mid-latitudes. This is mainly because of the lower tropopause at high latitudes and in winter the large SZAs are the predominant factor for high SNRs.
Taking all error sources together it is possible to estimate the total SCD error by $SCD_{tot} = \sqrt{3^2+10^2+2^2+10^2+6^2}\% \approx 16\%$, when using the gaussian error propagation law to calculate it. This is a conservative estimate and it can be smaller for some flights (12%).

3.7 Profile Retrieval

To numerically retrieve the vertical distribution of a chemical species from our measurements, we have to use a discrete model of our SCD measurement. We measure SCDs, which is the integrated amount of molecules along the line of sight through the atmosphere. If we think of a vector $\overrightarrow{VCD}_n$ with dimension n, where n is the discretization of our model atmosphere, it should describe the vertical column density within a certain height segment. We can now describe our SCD measurements by a vector $\overrightarrow{SCD}_m$ of dimension m - m is the total number of SCD measurements - which is given by a multiplication of $\overrightarrow{VCD}_n$ with the so called *airmass factor* matrix $\tilde{AMF}$

$$\overrightarrow{SCD}_m = \begin{pmatrix} AMF_{11} & \cdots & AMF_{1n} \\ \vdots & \ddots & \vdots \\ AMF_{m1} & \cdots & AMF_{mn} \end{pmatrix} \cdot \overrightarrow{VCD}_n \tag{3.27}$$

In the easiest case of a model atmosphere with plane and parallel layers and constant pressure and temperature throughout the atmosphere the airmass factors for all measurements and all layers would be $1/cos(SZA)$. But because of the pressure and temperature dependent refraction index of the atmosphere and the spherical geometry, we have to use a raytracer to calculate the airmass factor matrix. The program *damf* [Schulte 1996] was used to calculate AMF and to retrieve the profiles by inverting the airmass factor matrix (AMF matrix). It makes the following assumptions:

- Homogeneity of the chemical composition of each segment up to a weighting factor, which permits to take into account the SZA dependence of the photochemical equilibria - *chemical enhancement factors*
- Constancy of the physical parameters except for the SZA during the observation

3.7.1 Raytracing

The central symmetry of the problem suggests to choose polar coordinates (r, ϕ). The choice of the division of the atmosphere into segments of constant trace gas concentration should not influence the calculation of the optical path. Accordingly, the refraction of the light is treated as a continuous process.

A differential equation for the light rays is derived easily from Fermat's principle:

$$\delta \int n(\vec{x}) ds = 0 \tag{3.28}$$

where n is the index of refraction and ds is the infinitesimal path element. With the line element in polar coordinates

$$\begin{aligned} ds = \sqrt{dr^2 + (rd\phi)^2} &= \sqrt{(\frac{dr}{d\phi})^2 + r^2} d\phi \qquad (3.29) \\ \delta \int n(r) \sqrt{r'^2 + r^2} d\phi &= 0 \qquad (3.30) \end{aligned}$$

Then, designating the integrand by F, the Euler-Lagrange equation for the variational problem is

$$\frac{d}{d\phi} \frac{\partial F}{\partial r'} - \frac{\partial F}{\partial r} = 0 \tag{3.31}$$

Differentiating leads to a differential equation of second order in $r(\phi)$:

$$r'' = \frac{dn}{dr} \frac{1}{n} (r'^2 + r^2) + r + 2\frac{r'^2}{r} \tag{3.32}$$

Since the solution (the path of the light) is smooth and only little bent, a Runge-Kutta-algorithm (here of fourth order [Bronstein and Semendjajew 1991]) is sufficient. For the same reason the stepsize can be chosen constant. Further the light path can be weighted with the photochemical correction factor. Besides, the entrance into another segment as well as the escape into space and the absorption by the earth has to be considered.

3.7.2 AMF matrix inversion

To ensure a stable treatment even of nearly singular matrices the singular value decomposition (SVD)[8] method is used for inverting the airmass factor matrix [Press et al. 1995]. The SVD algorithm represents a generalization of the principal axis transformation to arbitrary real matrices. It is the method of choice for solving most *linear least-squares* problems, because in most cases we have much

---

[8] A set of linear equations that is degenerate is called singular

more measurements than height segments.
SVD methods are based on the following theorem of linear algebra : any $M \times N$ matrix $\mathbf{A}$ whose number of rows M is greater than or equal to its number of columns N, can be written as the product of a $M \times N$ column-orthogonal matrix $\mathbf{U}$, a $N \times N$ diagonal matrix $\mathbf{W}$ with positive or zero elements (the singular values), and the transpose of a $N \times N$ orthogonal matrix $\mathbf{V}$.

$$\mathbf{A} = \mathbf{U} \times \begin{pmatrix} w_1 & & & & \\ & w_2 & & & \\ & & \cdots & & \\ & & \cdots & & \\ & & & & w_N \end{pmatrix} \times \mathbf{V^T} \tag{3.33}$$

The matrices $\mathbf{U}$ and $\mathbf{V}$ are each orthogonal in the sense that their columns are orthonormal,

$$\sum_{i=1}^{M} U_{ik} U_{in} = \delta_{kn} \qquad 1 \leq k \leq N, 1 \leq n \leq N \tag{3.34}$$

$$\sum_{j=1}^{N} V_{jk} V_{jn} = \delta_{kn} \qquad 1 \leq k \leq N, 1 \leq n \leq N \tag{3.35}$$

Since $\mathbf{V}$ is square, it is also row-orthonormal, $V \cdot V^T = 1$.
The SVD decomposition can also be carried out when $M < N$. In this case the singular values $w_j, j = M+1, ..., N$ are all zero, and the corresponding columns of $\mathbf{U}$ are also zero.
If the matrix $\mathbf{A}$ is square, N say, then $\mathbf{U}$, $\mathbf{V}$, and $\mathbf{W}$ are all square matrices of the same size. Their inverses are easy to calculate: $\mathbf{U}$, $\mathbf{V}$ are orthogonal, so their inverses are equal to their transposes; $\mathbf{W}$ is diagonal, so its inverse is the diagonal matrix whose elements are the reciprocals of the elements w_j.

$$\mathbf{A}^{-1} = \mathbf{V} \cdot [diag(1/w_j)] \cdot \mathbf{U^T} \tag{3.36}$$

The only thing that can go wrong with this construction is for one of the w_j's to be zero, or (numerically) for it to be so small that its value is dominated by roundoff error and therefore unknowable. Formally the *condition number* is defined as the ratio of the largest of the w_j's to the smallest of the w_j's. A matrix is singular if its condition number is infinite, and it is *ill-conditioned* if its condition number is too large that is, if its reciprocal approaches the machine's floating-point precision (for example, less than 10^{-6} for single precision or 10^{-12} for double).
For singular matrices, the concepts of *nullspace* and *range* are important. If we take

$$\mathbf{Ax} = \mathbf{b} \tag{3.37}$$

where $\mathbf{A}$ is a square matrix, **b**,**x** are vectors. If $\mathbf{A}$ is singular, then there is some subspace of $\mathbf{x}$, called the nullspace, which is mapped to zero. Now, there is some subspace of $\mathbf{b}$ that can be reached by $\mathbf{A}$ - it is called range of $\mathbf{A}$. The dimension of the range is called *rank* of $\mathbf{A}$. It can be shown that *rank plus nullity equals N.* When the vector $\mathbf{b}$ on the right-hand side is not zero, the important question is wether it lies in the range of $\mathbf{A}$ or not. If it does, then the singular set of equations does have a solution $\mathbf{x}$; in fact it has more than one solution, since any vector in the nullspace (any column of $\mathbf{V}$ with a corresponding zero w_j) can be added to $\mathbf{x}$ in any linear combination.
Using SVD we single out the vector with the smallest length $|\mathbf{x}|^2$ by replacing $1/w_j$ by 0 if $w_j = 0$. If $\mathbf{b}$ is not in the range of $\mathbf{A}$, then SVD gives us the best estimate of a solution in the least squares sense.

$$\mathbf{x} \qquad which \qquad minimizes \qquad r = |\mathbf{A} \cdot \mathbf{x} - \mathbf{b}| \tag{3.38}$$

In the case of an overdetermined set of linear equations - which is the case for our measurements - SVD gives - as described above for square matrices - the least-squares solution vector $\mathbf{x}$.

3.7.3 Errors of the inversion technique

The main source of error is the SCD error. When the SCD is mapped onto the VCD vector each of its components is amplified by the reciprocal of the corresponding singular value. Therefore the contribution of a component corresponding to a relatively large singular value might be hidden among the noise amplified from the contributions of the directions of small singular values. Hence the relative error of the SCD measurements is amplified by the condition of the AMF matrix, where the condition of a matrix is defined by the ratio of its biggest to its smallest singular value. So it is reasonable to artificially confine it to a certain maximum which the user can choose. This is done by setting the reciprocals of the too small singular values to zero. Calculating the resulting VCD error is then straightforward

$$\Delta VCD_i = \sqrt{\sum_j (\sum_k V_{ik} \frac{1}{w_k} U^T_{jk})^2 (\Delta SCD_j)^2} \tag{3.39}$$

If SCD measurements with relatively large errors are abundant, it might be advantageous to combine some of them to reduce the statistical error. Of course this is a trade-off between statistical and systematical error. The latter increases as the former decreases, because the differences in the light paths are neglected, but it can still be worthwhile when the height resolution is fairly rough.

3.7.4 Differential Onion Peeling technique

For the ascent part of the flight, we can also use another approximation for retrieving the profile corresponding to our SCD measurements. The main idea about the *differential onion peeling technique* is that the decrease of the measured SCD while flying through the profile can directly be attributed to the concentration of the last layer.
As the light path is only little bent during ascent measurements, we can approximate the VCD by

$$VCD = SCD \cdot cos(SZA) \tag{3.40}$$

The difference of the VCD for each SCD can now be identified as the concentration of the last height layer, where the balloon has been flying through.

$$Profile(h) = \frac{\partial VCD}{\partial h} = \frac{\Delta VCD}{\Delta h} \tag{3.41}$$

This approximation is only good for SZAs smaller than $\approx 80^o$, where the airmass factor can be approximated by $1/cos(SZA)$. Figure 3.30 shows the comparison of this approximation with the output of the raytracer for the highest height segment of the raytracing model.

The limiting factor for the height resolution is the statistical noise of the SCDs, which is around 4%. This leads to a typical height resolution of 1000-2000 m. Furthermore real profile filaments are smoothed and only its altitude position can be retrieved, but the absolute amplitude cannot be determined. When the height segmentation is too fine, it is necessary to filter the calculated $VCDs$ with a gaussian filter to suppress oscillatory artifacts in the profile.
Figure 3.31 shows the typical performance of the two profile retrieval methods for an in-situ measured O_3 sonde profile. Both methods perform well by reproducing the prescribed profile - even in the case where statistical gaussian noise has been added to the prescribed SCDs. But it is not possible to reproduce strong fluctuations of the profiles - like the big dip at 18 km - because of the height

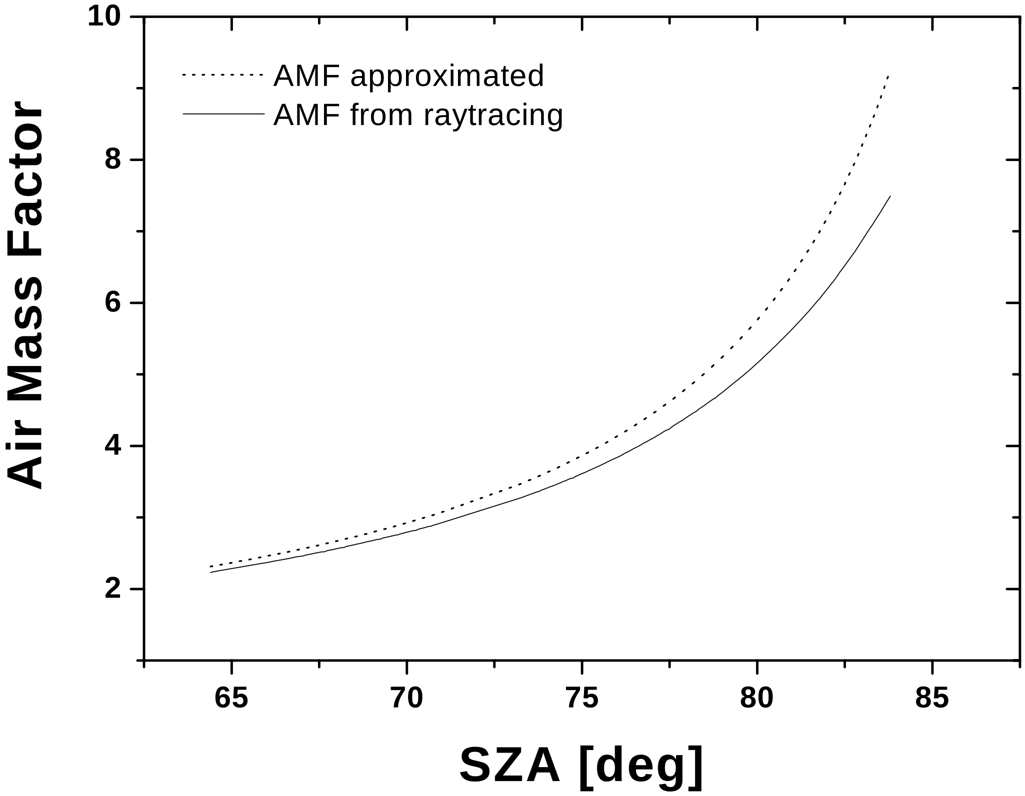

Figure 3.30: Comparison of the AMF approximation (differential onion peeling) with the AMF calculated by the raytracer for the highest height segment of the model.

resolution in the case of the inversion technique and the gaussian filter needed for differential onion peeling.

3.8 Modelling of SCDs

Principally it is possible to use any model - 3-D CTM or Lagrangian trajectory model - to simulate so called model SCDs, which we can then compare with our own measurements. This is especially important for photochemically active species like BrO and $OClO$, which are the central species of interest in this thesis.

The concentration of these species depends on the height, longitude, latitude and most important the SZA, which can be modelled taking into account the meteorological situation and solar illumination. To get the modelled $SCDs$ we simply integrate the concentration of the species along the line of sight - the light path through the atmosphere.

Figure 3.32 shows such a situation for our first balloon flight at León on Nov. 23, 1996. The model data was produced by the 3-D Chemical Transport Model (3-D CTM) SLIMCAT[9] [Chipperfield 1999], which will be used for comparison for most of the flights. The model concentration field of BrO is shown in colour code as a function of height and SZA.

For the understanding of the figure it is essential to recognize that because of the spherical geometry for SZAs larger than 90^o the light is passing the height layers between the balloon height and the height

---

[9] SLIMCAT : Single Layer Isentropic Model for Chemistry And Transport

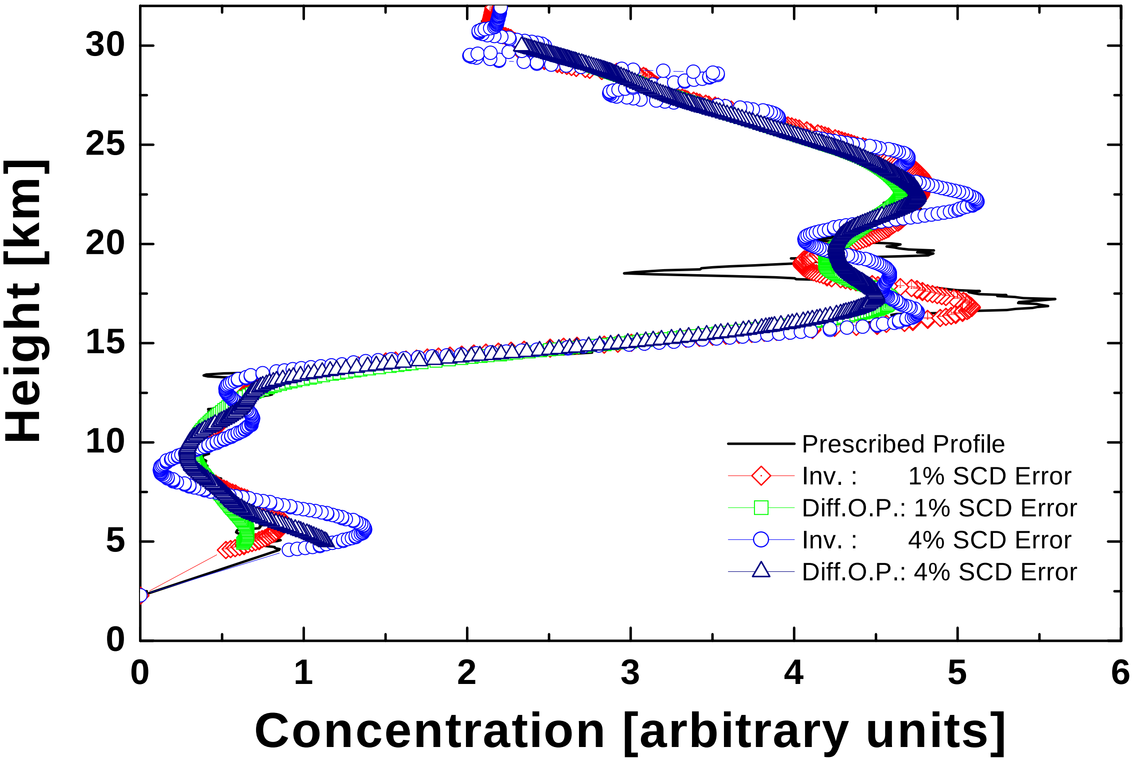

Figure 3.31: The O_3 sonde profile was prescribed and the $SCDs$ were calculated. Then the profile was retrieved from the $SCDs$ by inversion and also by differential onion peeling. In addition statistical gaussian noise (1% and 4%) was added to the $SCDs$ to determine the sensitivity of the profile retrieval to statistical noise. The flight geometry used for this test was from the balloon flight at León on Nov. 23, 1996.

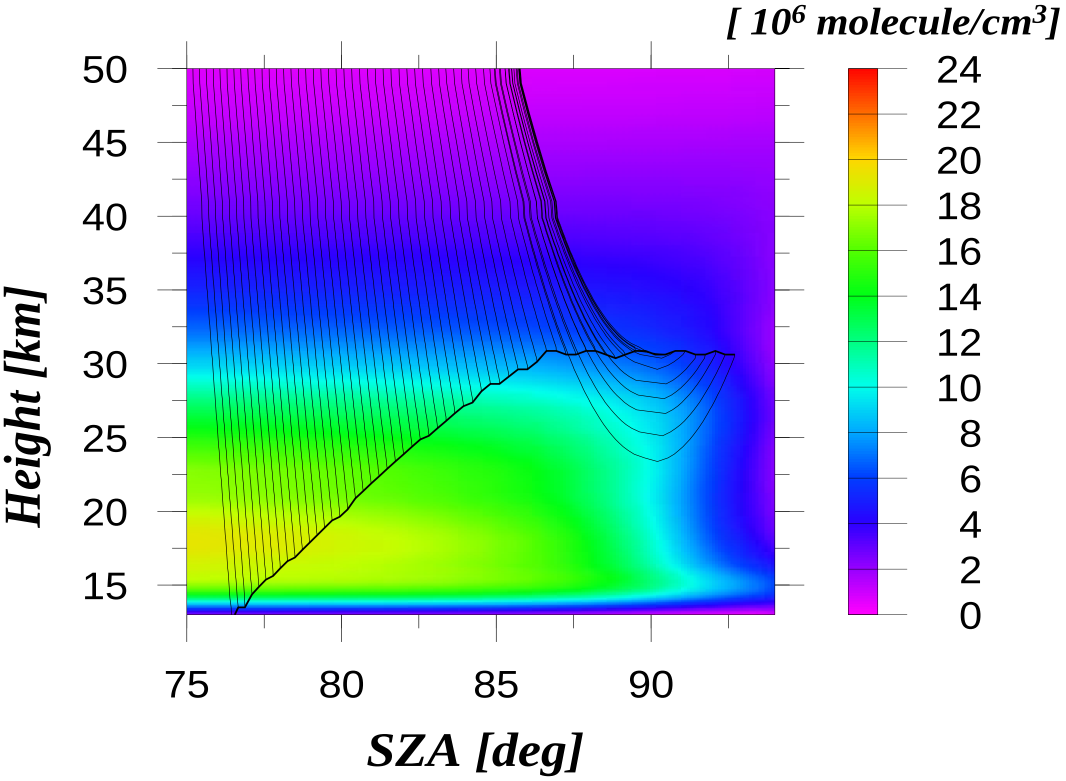

Figure 3.32: Modelling of BrO $SCDs$ by integration of the concentration along the light path through the atmosphere. The model field is colour-coded as a function of height and SZA. Both the trajectory of the balloon (thick line) and the light rays from the sun (fine lines) reaching the balloon instrument are shown in the plot.

of the tangent point two times. That is why the light rays are parallel to the SZA axis for 90^o SZA. During the occultation measurements (SZA $\geq 90^o$) most of the absorption takes place at the tangent point, where the pressure is the largest as well as the airmass factor.

Chapter 4

Results and Discussion of the LPMA/DOAS balloon flights

In this chapter the results of the eight balloon flights will be presented, which we already conducted with the LPMA/DOAS balloon payload between end of 1996 until beginning of 2000. Table 4.1 shows a summary of all balloon flights presenting a considerable stratospheric record of measurements for all different seasons at mid and high latitudes (different geophysical conditions) during a time range of nearly 4 years. The campaigns took place within the framework of different EU sponsored field campaigns to study the stratosphere or to validate a new satellite-borne instrument (ADEOS ILAS validation). Also the GOME (Global Ozone Monitoring Experiment), which started measurements in 1995, will be used for data comparison, as well as a ground-based DOAS instrument located at IRF[1] (Kiruna).
For the BrO evaluation the standard retrieval range (346-360 nm) and for the $OClO$ retrieval different ranges ($BrO - OClO$: 345-370 nm, $OClO$: 362-382 nm or 362-390 nm) will be used in this chapter.

LPMA/DOAS Balloon flights					
No.	Location			Date	Campaign
1	León	$42.6^o N$	$5.7^o W$	23. Nov. 96	CHORUS
2	Kiruna	$67.9^o N$	$21.1^o E$	14. Feb. 97	ADEOS
3	Gap	$44.0^o N$	$6.1^o E$	20. Jun. 97	CHELOSBA
4	León	$42.6^o N$	$5.7^o N$	19. Mar. 98	CHELOSBA
5	Kiruna	$67.9^o N$	$21.1^o E$	19./20. Aug. 98	SABINE/CHELOSBA
6	Kiruna	$67.9^o N$	$21.1^o E$	10. Feb. 99	THESEO
7	Gap	$44.0^o N$	$6.1^o E$	25. Jun. 99	THESEO
8	Kiruna	$67.9^o N$	$21.1^o E$	18. Feb. 2000	THESEO2000/SOLVE

Table 4.1: Summary of the balloon flights at different latitudes and seasons conducted so far. The launch stations for big balloons operated by the french balloon launching company CNES (Centre National d'Etudes Spatiales) are in the case of our flights León(Spain), Gap(France) and Kiruna(Sweden).

4.1 The sunset flight at León on November 23, 1996

The first flight of the LPMA/DOAS payload took part from León(Spain) on Nov. 23, 1996. Figure 4.1 shows the trajectory of the balloon and the probed airmass during the occultation of the sun, when the tangent points are floating away from the balloon trajectory towards the sun. That means during the solar occultation we are probing different airmasses and integrating the column over possible horizontal

---

[1] Institutet för rymdfysik

gradients while during the ascent of the flight the remote sensing instrument probes only airmasses within an area of less than 100x100km^2.

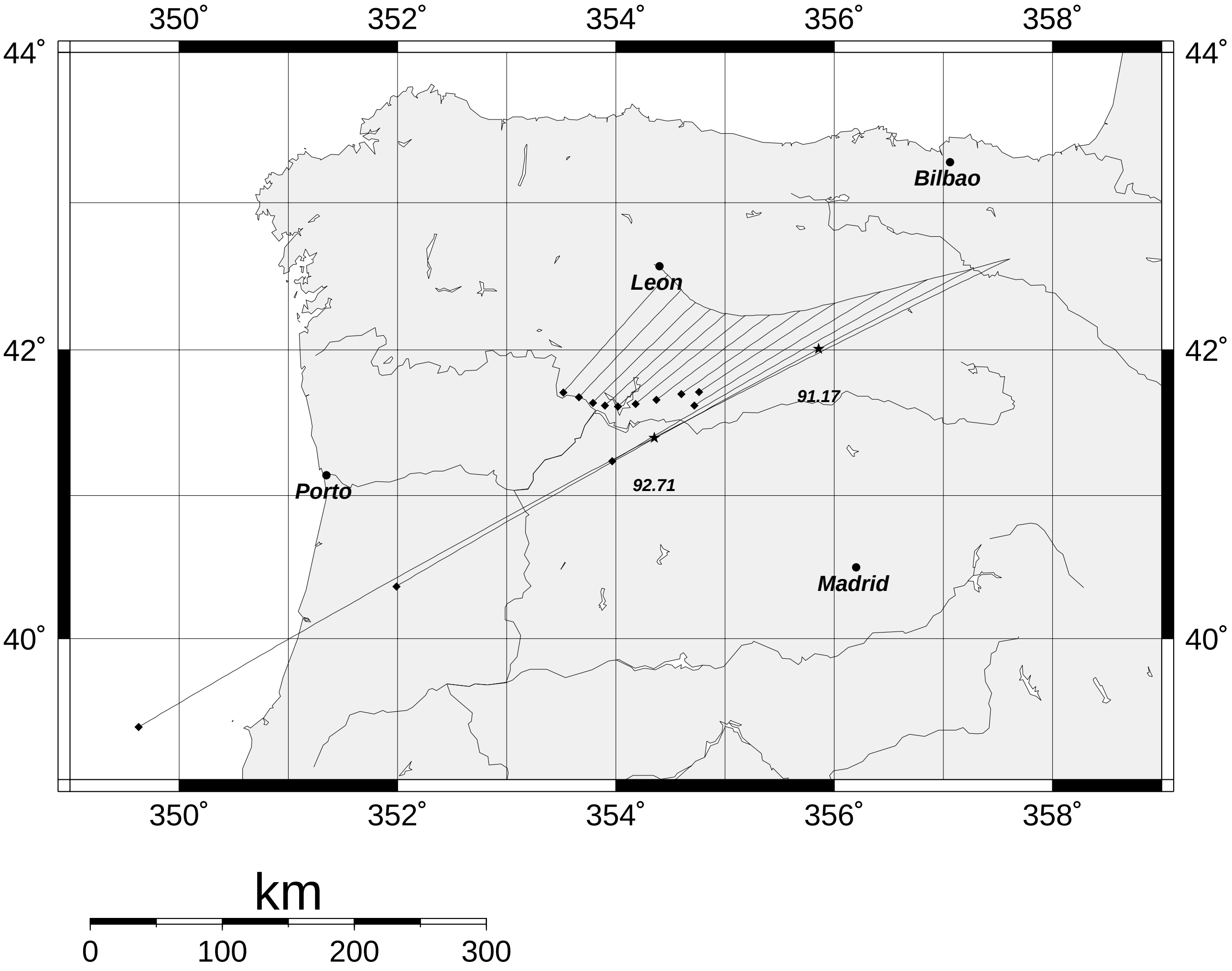

Figure 4.1: Balloon trajectory during the flight at León (Spain) on Nov. 23, 1996. The trajectory is the curved line towards the east, while the lines ending with a point denote the light rays and the end points(◇) show the location of the tangent points - that is the main area of atmospheric absorption.

In Figure 4.2 the balloon height as a function of time as well as the SZA at the balloon position (latitude, longitude) is presented. As the balloon is flying in easterly direction the SZA is increasing faster than it would if the position of the balloon was fixed.

For the DOAS fit - see Figure 4.3 - reference spectra measured in the laboratory of $O_3(-80^oC, -20^oC)$ and $NO_2(-70^oC)$ were used. The O_4 reference spectrum is not an absolute cross section but a collision pair absorption cross section. Only the BrO absorption cross section is an absolute cross section taken from [Wahner et al. 1988] and adapted to the spectrograph resolution by laboratory reference measurements. The reference spectra were aligned with the Fraunhofer reference and fitted altogether to the measured spectra. The respective shifts and squeezes of the reference spectra ensemble during the flight are shown in Figure 4.12 and Figure 4.13.

In a second DOAS evaluation an absolute $OClO$ reference spectrum was included in the fit and the wavelength range of the fit was enlarged. The $OClO$ reference spectrum used is a high resolution FTUV spectrum measured by Kromminga et al. [1999], which was convoluted to the spectrograph resolution. The $OClO$ reference was measured at a temperature of 213 K. As $OClO$ is photolysed very fast during the daytime, one cannot expect large $OClO$ absorption during the ascent of the balloon, but it was investigated, if there is some $OClO$ absorption in the occultation measurements. The first

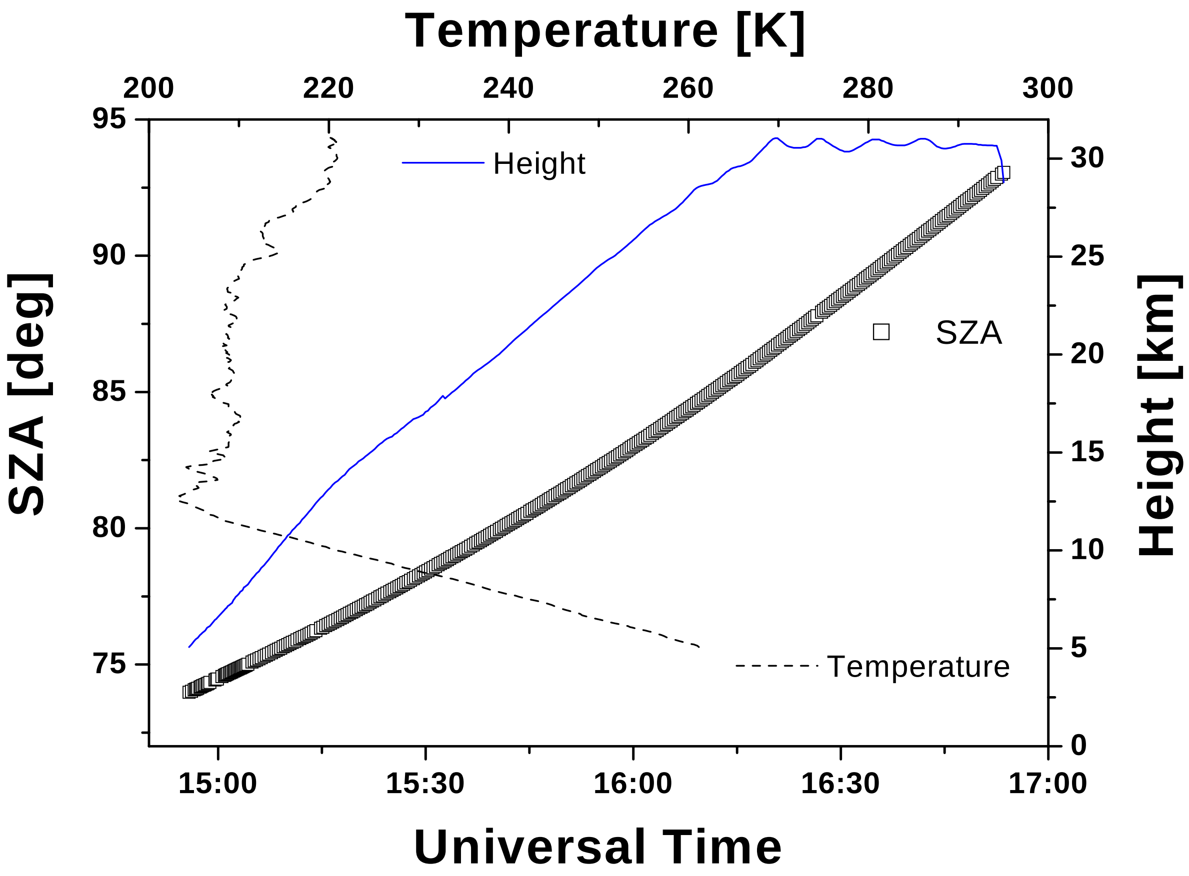

Figure 4.2: Balloon trajectory, temperature and SZA at balloon position (latitude,longitude) during the flight at León (Spain) on Nov. 23, 1996.

fit window was 345-370 nm, where the same reference spectra have to be included in the fit as used in the BrO retrieval. The respective example evaluation is shown in Figure 4.4.

A cross-check for the $OClO$ retrieved is to extract it from another DOAS fit in a different wavelength region. The fit of NO_2, O_4 and $OClO$ in the 362-382 nm wavelength region is shown in Figure 4.5. A polynomial of degree 5 was chosen after having recognized O_4 to change substantially with the polynomial degree. When determining the O_4 fit coefficient by a pre-fit in the 375-385 nm range, it became clear that it is necessary to use a polynomial degree of 5 in the 362-382 nm range to reproduce the fit coefficient.

Figures 4.6-4.13 show the time evolution of the SCDs of the different absorbers. Only the BrO and $OClO$ SCDs are given in absolute units ($\frac{molecule}{cm^2}$), because temperature and pressure dependence of the BrO and $OClO$ cross section is negligible for the retrieval, when we use a cross section measured at -45^oC or -60^oC, respectively. The absolute difference in the cross section is less than 10% in the case of BrO and 5% in the case of $OClO$ for the stratospheric temperatures encountered during this flight.

For a comparison the BrO SCDs retrieved in the two different BrO retrieval wavelength ranges are shown. The BrO range is the standard 346-360 nm range, while the $BrO-OClO$ range is from 345 to 370 nm. The latter range includes $OClO$, which is compared to the results of the $OClO$ retrieval in the 362-382 nm range.

The agreement between the BrO SCDs retrieved in the different wavelength ranges is very good, while the discrepancy of the $OClO$ SCDs is small during the occultation and very large in the ascent part, where no $OClO$ is expected at all. As the $OClO$ absorption cross section correlates with the O_3

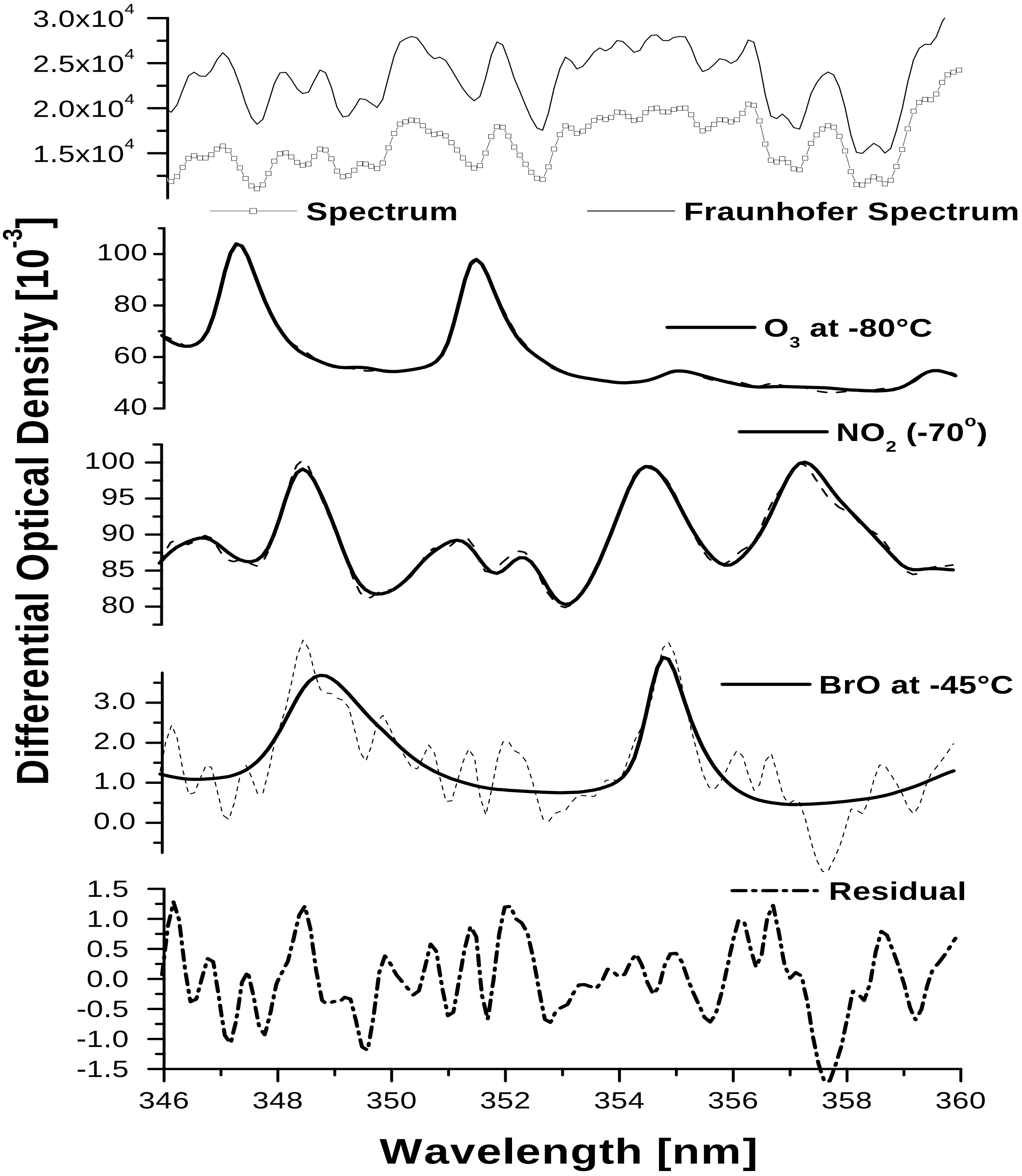

Figure 4.3: Typical DOAS evaluation in the interesting BrO retrieval wavelength range (346-360 nm) for León 1996. The fit included O_3 at -80^oC and -20^oC(not shown), NO_2 at -70^oC, O_4(not shown) and BrO at -45^oC and a polynomial of degree 3. The last spectrum is the residual of the fit which cannot be explained by the fit but is due partly to statistical noise and to systematic errors. All spectra have been filtered with a binomial filter of degree 3 before the fit.

absorptions, the $OClO$ SCDs from the retrieval in the 362-382 nm ($OClO$) range will be used for the inter comparison with modelled SCDs in the succeeding parts of this section.

We used two O_3 reference spectra for two different temperatures (-80^o and -20^oC) to allow for

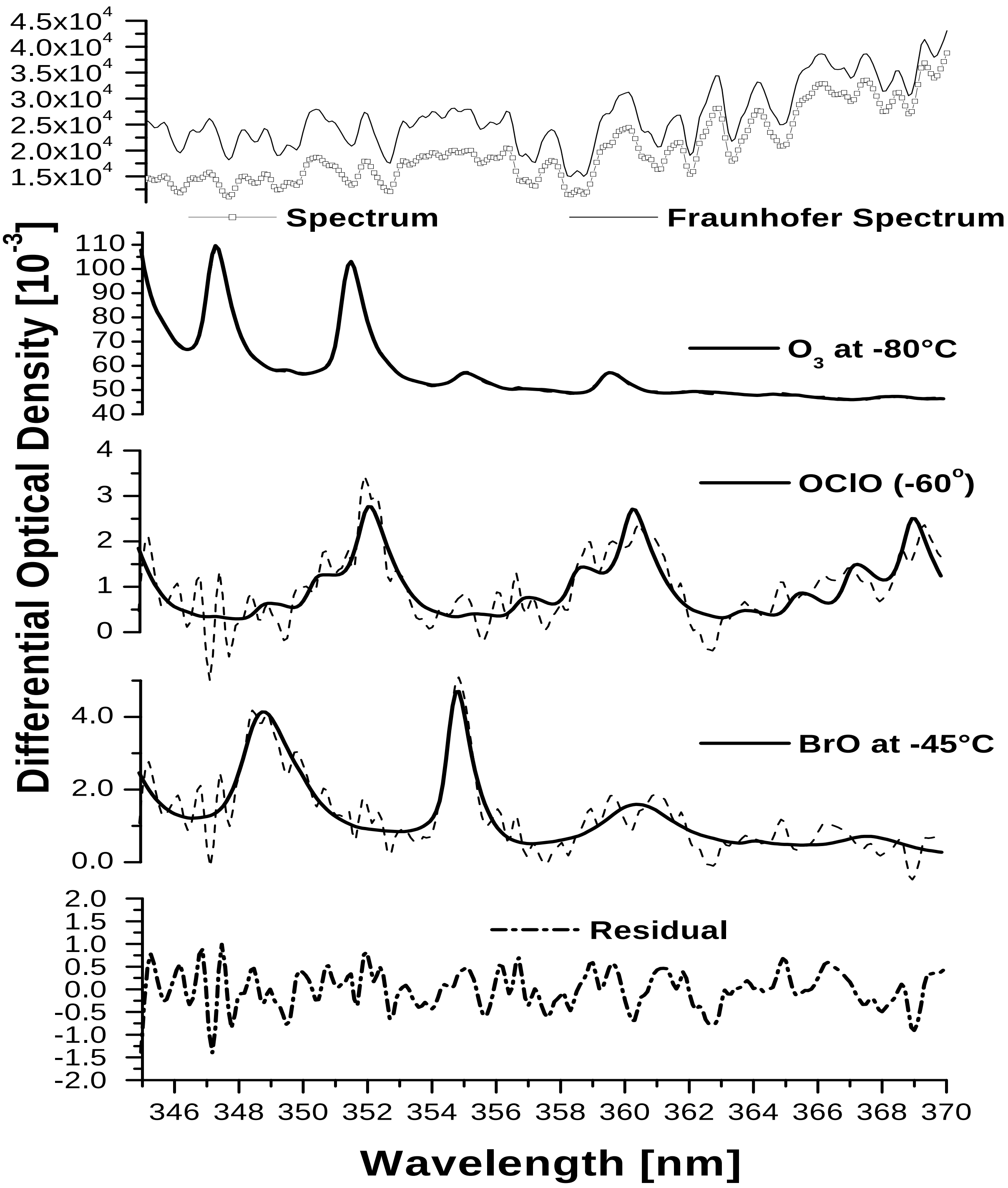

Figure 4.4: Typical DOAS evaluation in the interesting $BrO - OClO$ retrieval wavelength range (345-370 nm) for León 1996 using the software *Windoas*. The fit included O_3 at -80^oC and -20^oC(not shown), NO_2 at -70^oC(not shown), O_4(not shown), $OClO$ at -60^oC and BrO at -45^oC and a polynomial of degree 5. The last spectrum is the residual of the fit which cannot be explained by the fit but is due partly to statistical noise and to systematic errors. All spectra have been filtered with a binomial filter of degree 3 before the fit.

the strong temperature dependence of the form of the ozone cross section. The NO_2 temperature dependence in the BrO retrieval wavelength range is less pronounced and therefore we included only one reference spectrum at -70^oC.

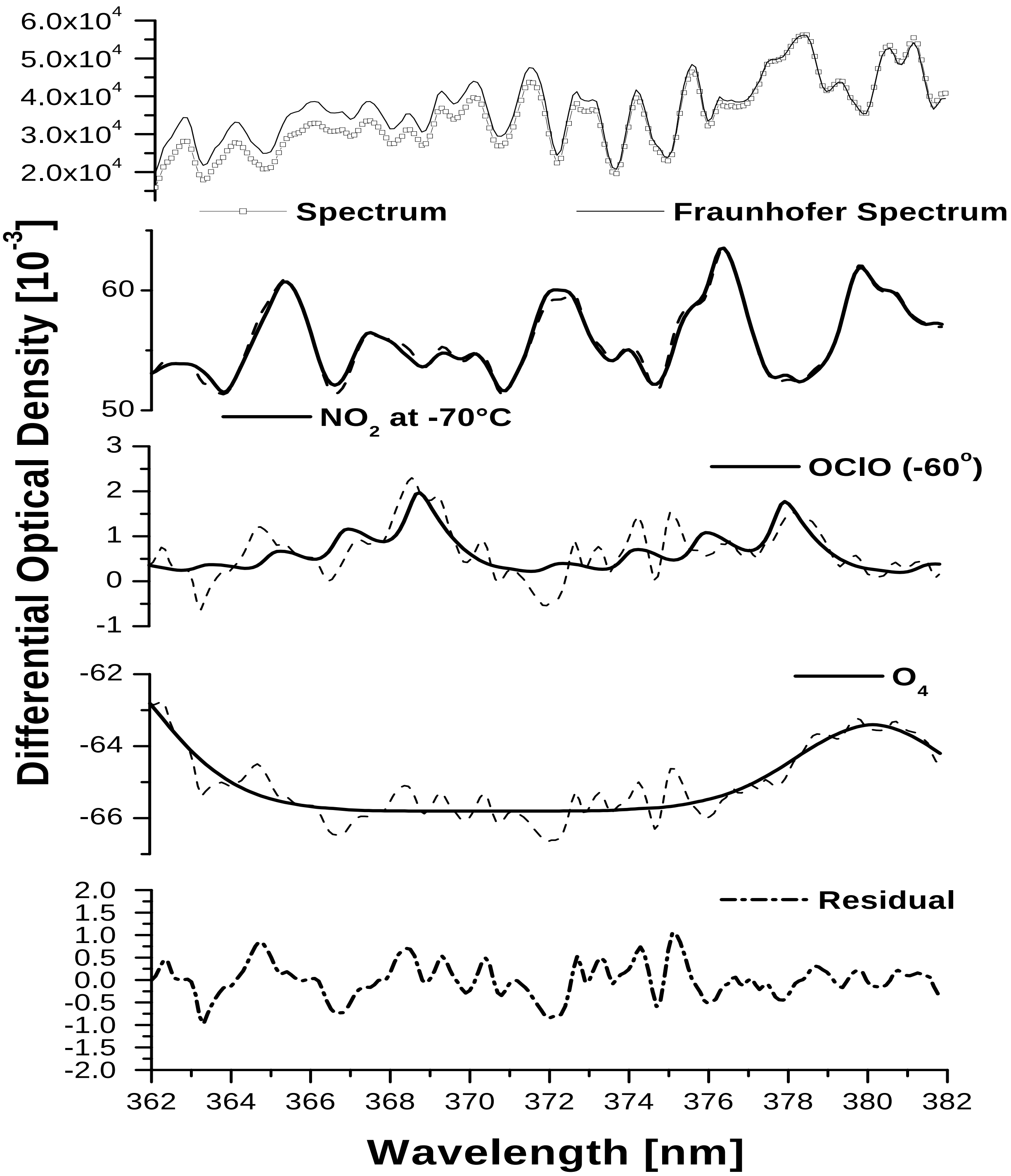

Figure 4.5: Typical DOAS evaluation in the interesting $OClO$ retrieval wavelength range (362-382 nm) for León 1996. The fit included NO_2 at -70^oC, NO_2 at -30^oC (not shown), O_4 and $OClO$ at -60^oC and a polynomial of degree 5. The last spectrum is the residual of the fit which cannot be explained by the fit but is due partly to statistical noise and to systematic errors. All spectra have been filtered with a binomial filter of degree 3 before the fit.

Figure 4.9 shows the absolute BrO SCDs, which have been corrected for the column offset in the Fraunhofer reference. The respective Langley Plot is shown in Figure 4.14. The SCD offset of the $OClO$ SCDs is negligible in the occultation, where the largest SCDs are observed, as can be seen in

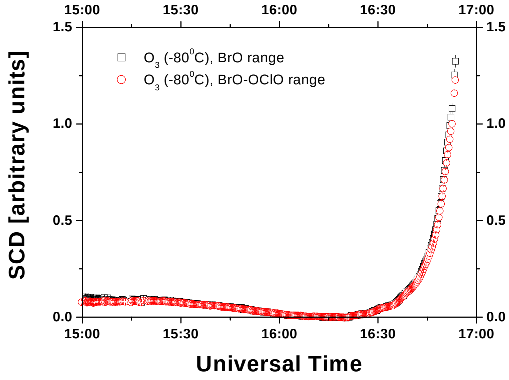

Figure 4.6: Time evolution of the $O_3(-80^oC)$ SCDs during the flight.

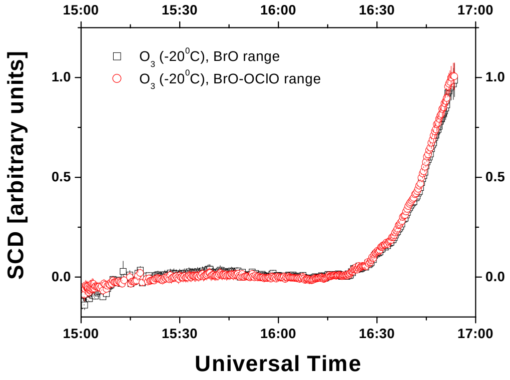

Figure 4.7: Time evolution of the $O_3(-20^oC)$ SCDs during the flight.

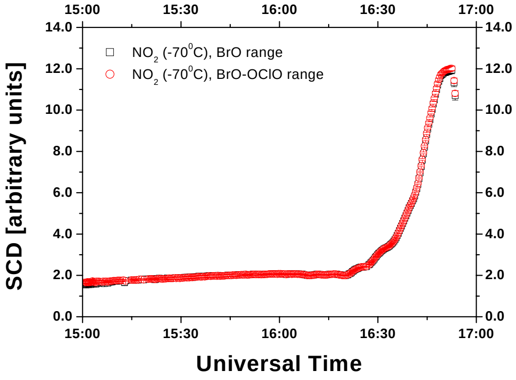

Figure 4.8: Time evolution of the $NO_2(-70^oC)$ SCDs during the flight.

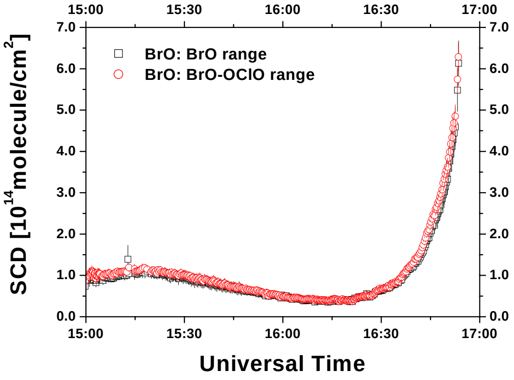

Figure 4.9: Time evolution of the $BrO(-45^oC)$ SCDs during the flight.

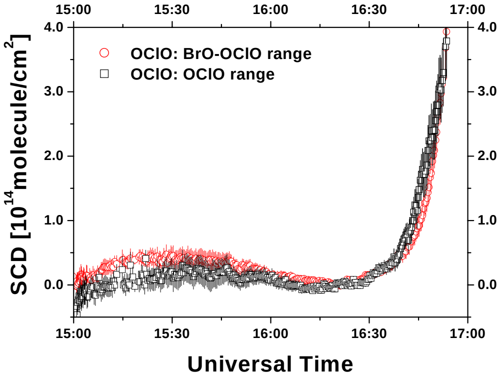

Figure 4.10: Time evolution of the $OClO$ SCDs during the flight.

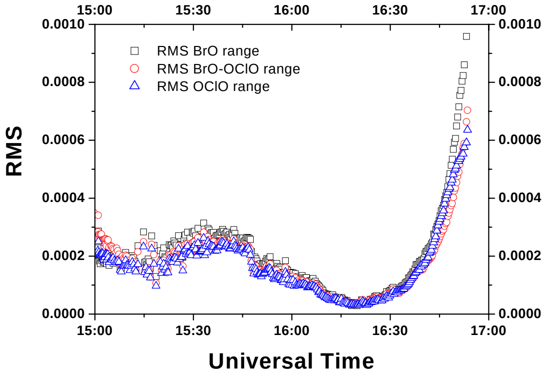

Figure 4.11: Time evolution of the RMS of the DOAS fit during the flight.

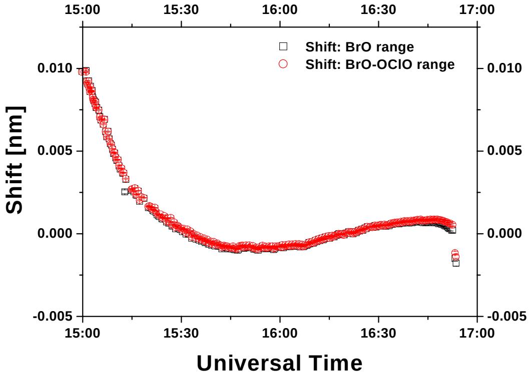

Figure 4.12: Time evolution of the shift of the reference spectra ensemble during the flight.

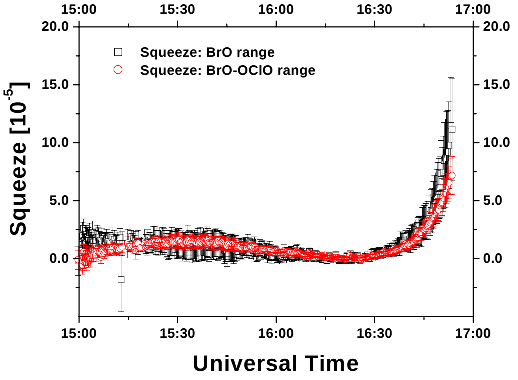

Figure 4.13: Time evolution of the squeeze of the reference spectra ensemble during the flight.

the model SCD time evolution presented in the following. Model results also suggest that there is almost no $OClO$ at 86^o SZA, when the Fraunhofer spectrum was measured.

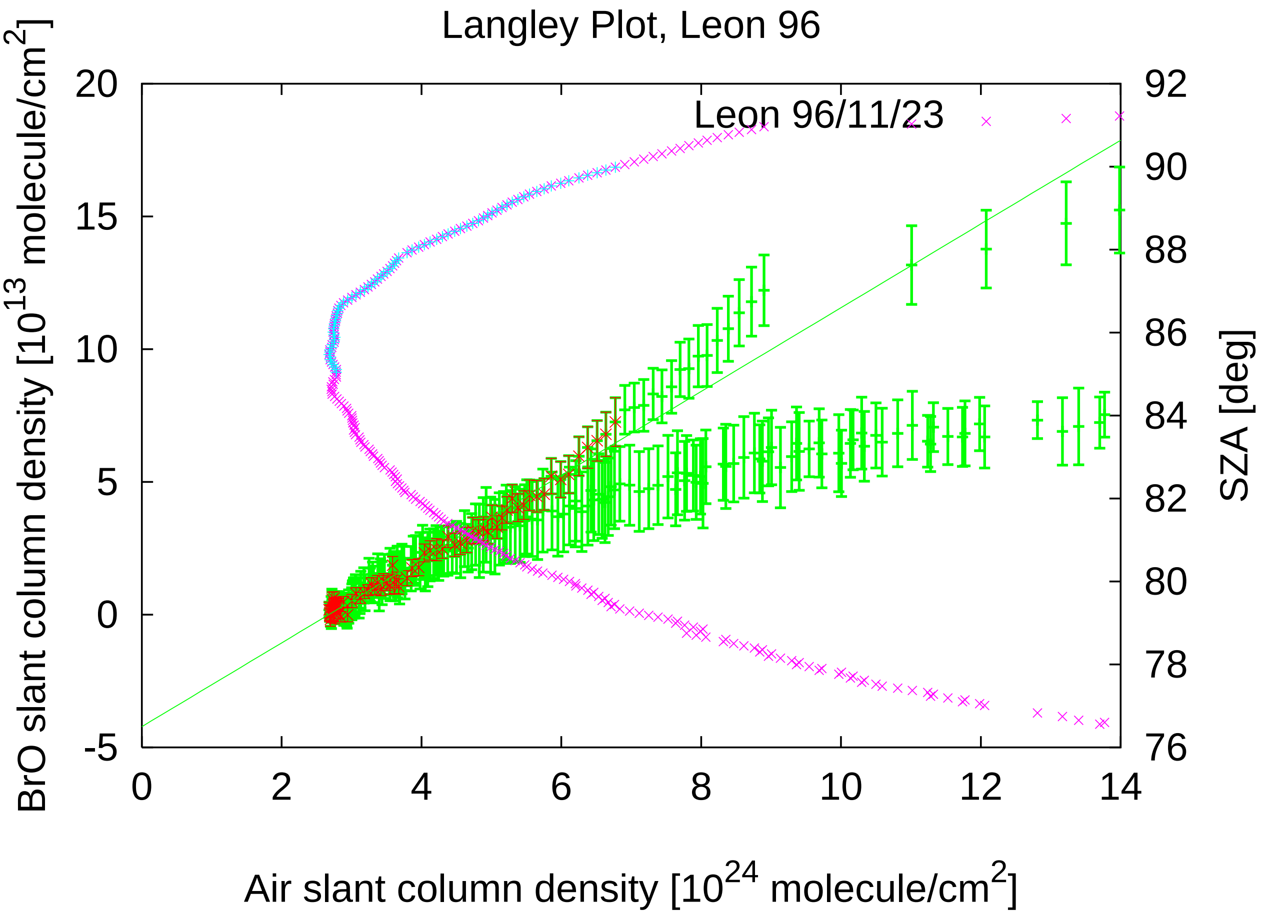

Figure 4.14: Langley plot for the flight at León using the float SCDs for SZAs between 86.5^o and 89.0^o. The Fraunhofer reference spectrum was measured at a balloon height of 30.8 km and a SZA of 86.5^o. The resulting SCD offset is $(4.2 \pm 0.5)e13\frac{molecule}{cm^2}$ and the mean mixing ratio above float (15.8 ± 2.5) ppt.

4.1.1 BrO profile and SCD model comparison

After performing the matrix inversion and the onion peeling technique for profile extraction, we get the respective profiles, which are shown in Figure 4.15 and 4.16.

The retrieved profiles agree very well, but the onion peeling profile tends to underestimate the BrO maximum, which can be explained by the overestimation of the airmass factor during the AMF approximation. Especially at the end of the ascent, the onion peeling technique is not able to reproduce the constant mixing ratio near to and above float, which can be seen in the inverted profile and in the profile modelled by the 3-D CTM model SLIMCAT.

In the figures two profiles modelled by SLIMCAT for two different SZAs (74^o and 86.5^o) are shown to emphasize the photochemical change of the BrO profile even during the relatively short time period of the balloon ascent. The model profiles overestimate slightly the BrO near to the tropopause and underestimate it around the profile concentration maximum, while the model-measurement agreement is quite good in the middle stratosphere.

A reason for that can be the way how the SLIMCAT model allows for the organic bromine precursors,

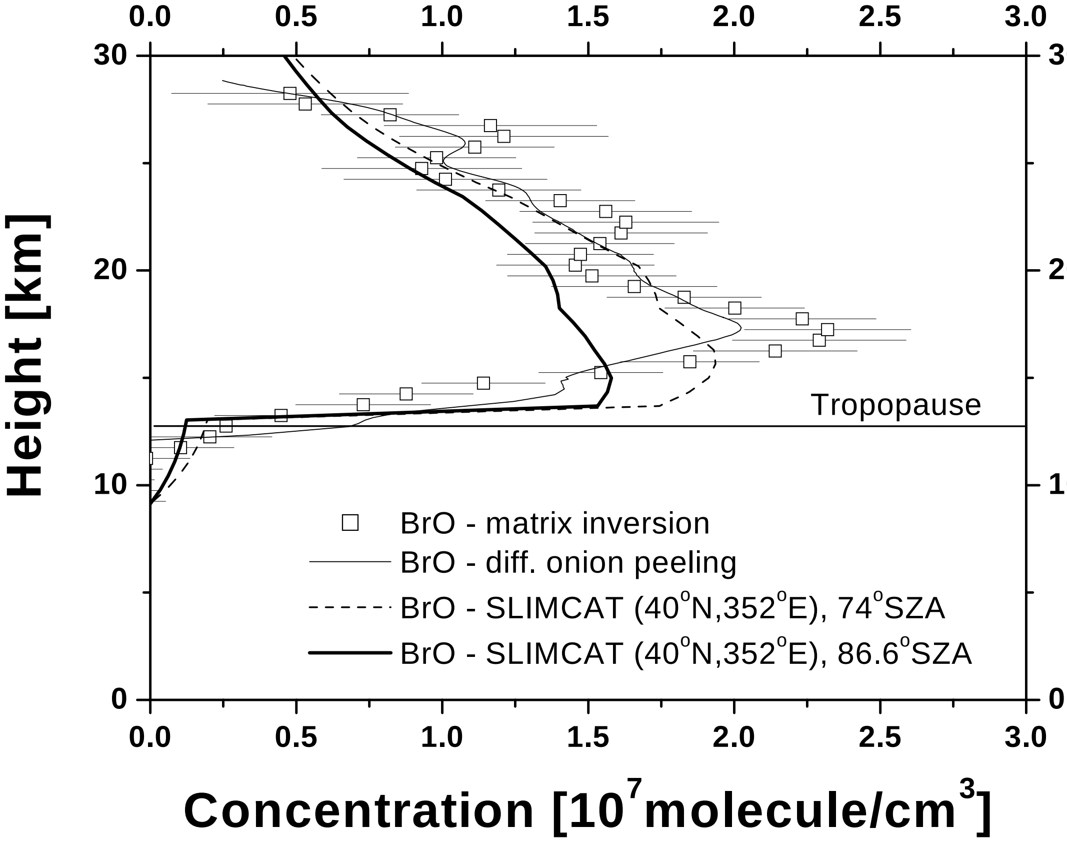

Figure 4.15: *BrO* concentration profiles from the ascent part of the balloon flight retrieved by AMF matrix inversion and Differential Onion Peeling. The ascent took place during a SZA interval of $74.0 - 86.5^o$.

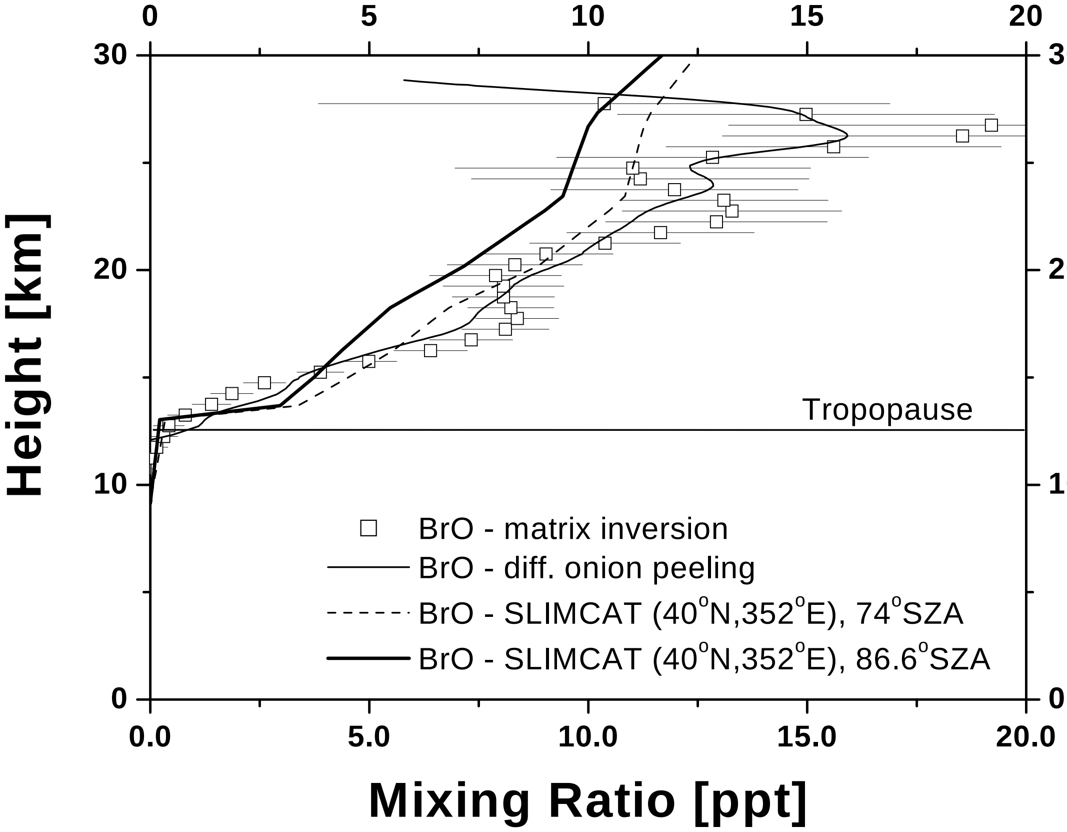

Figure 4.16: *BrO* mixing ratio profiles from the ascent part of the balloon flight retrieved by AMF matrix inversion and Differential Onion Peeling. The ascent took place during a SZA interval of $74.0 - 86.5^o$.

because actually SLIMCAT only takes into account the main organic bromine species CH_3Br, which accounts for about 50% of total bromine at the tropopause [Wamsley 1998]. Methyl bromide has a relatively short lifetime of ≈1 year in the atmosphere and is mainly destroyed by photolysis in the lower and middle stratosphere. As the model overestimates CH_3Br, it also overestimates the release of inorganic bromine from the organic precursors, as the other 50% of total organic Br_y (like the halons) have all much longer lifetimes in the stratosphere. A second possible reason for the discrepancy in the lower stratosphere may be a wrong partitioning of the inorganic bromine species, which will be investigated in further detail for the other flights.

The presented profiles are only from the balloon ascent, as the photochemical change is quite small during that SZA range. For larger SZAs the photochemical change will be larger, so that it is necessary to compare modelled SCDs with our measured ones.

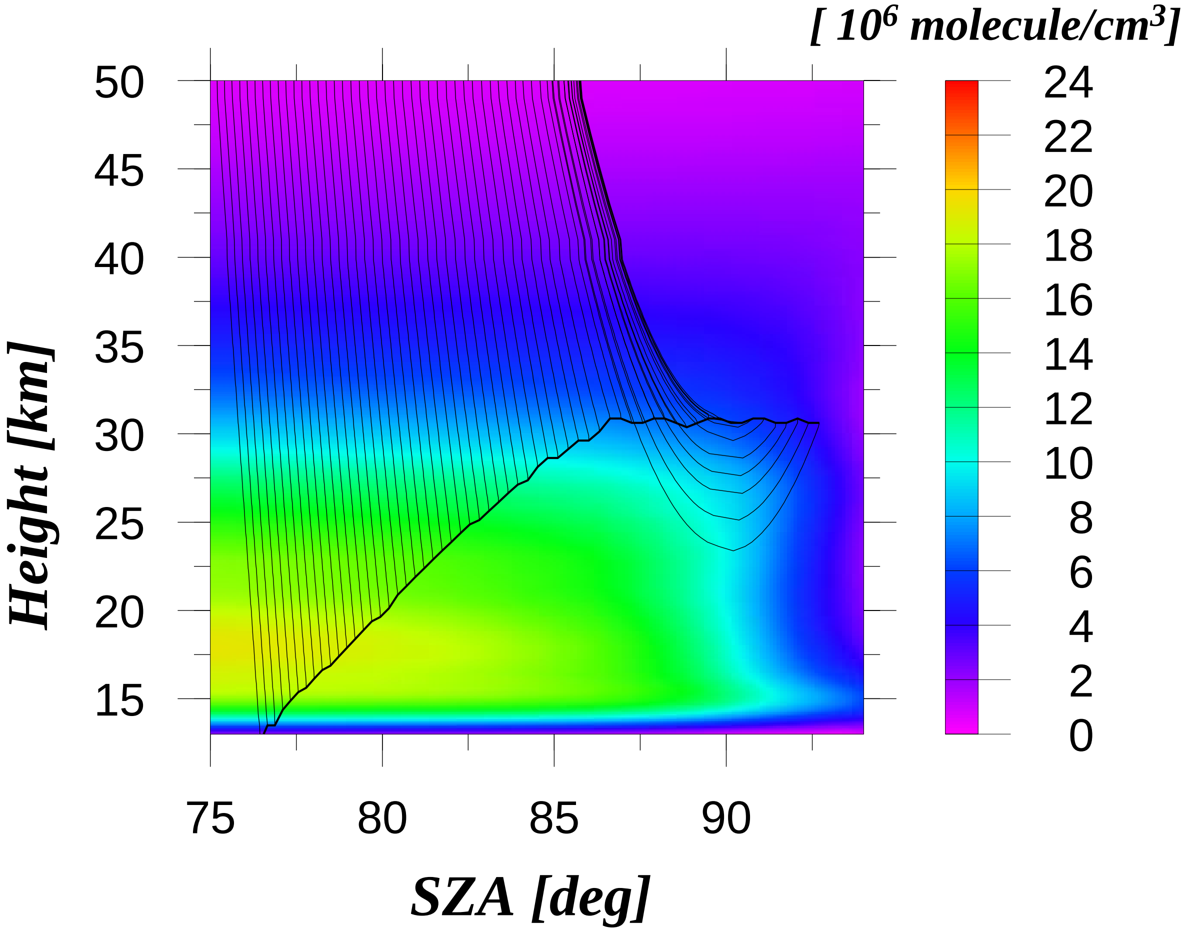

Figure 4.17: Modelling of BrO SCDs by integration of the concentration along the light path through the atmosphere. The model concentration field is color-coded as a function of height and SZA. Both the trajectory of the balloon (thick line) and the light rays from the sun (fine lines) reaching the balloon instrument are shown in the plot.

Therefore we use the 3-D CTM SLIMCAT concentration of BrO with respect to height and SZA for the airmasses encountered during our flight. Figure 4.17 shows the BrO model concentration field in colour code and also the trajectory of the balloon as well as the light rays from the sun to the balloon.

When integrating the model concentrations along the line of sights throughout the atmosphere for each measurement, we can calculate the modelled BrO SCD and compare it directly to the measured ones.

Figure 4.18 shows the evolution of the measured and modelled SCDs as a function of time.

In order to separate the different phases of the flight and check the linear correlation between modelled and measured BrO SCDs in detail, also the modelled SCDs versus the measured SCDs were plotted. In addition, the results for the different model runs (Br_y = 17, 20 and 23 ppt) are shown. See Figure 4.19.

From the variation of the total inorganic bromine in the model runs it is possible to deduce a new estimate for the stratospheric inorganic bromine content. As we believe our BrO SCDs to be accurate to 12%, we get an estimate for Br_y of 20 ± 2.5 ppt [Harder et al. 2000].

The BrO concentration is generally decreasing with SZA, so that we have to make sure to compare profiles and SCDs for the right SZA. This is particularly important when comparing the vertically integrated BrO column (VCD) from the balloon ascent profile to the VCD measured by satellite-borne instruments like GOME[2]. At the day of the flight at León it was passing the balloon flight area at a SZA of 65.4^o. When we want to compare the vertical columns of BrO (VCD) measured by different instruments, we have to take account of the SZA dependence of the VCDs. This is illustrated in Figure 4.20 for the comparison of the measurements at León.

Figure 4.21 shows the comparison of three different GOME pixels with different distances from the balloon measurement site to examine the horizontal variation of the BrO VCDs. The discrepancy between satellite and balloon measurements cannot be explained by errors of the retrieval and neither the SZA dependence nor the horizontal variability of the VCDs can explain the difference of at least a factor of 2.

So the only realistic explanation for the systematic VCD difference is the existence of $2 - 3 \cdot 10^{13}$ molecule/cm^2 tropospheric column, which would correspond to a mean mixing ratio of 1.5 ppt if homogeneously distributed within the tropospheric air column ($1.7 \cdot 10^{25}$ molecule/cm^2).

Wether this is a special event during the first flight or a more common phenomenon has to be examined in the next sections.

4.1.2 *OClO* profile and SCD model comparison

Like it was shown in Figure 4.4 and 4.5 the measured $OClO$ is only during the occultation above the detection limit. That is why here only profiles retrieved from the occultation SCDs are shown. Figure 4.22 shows such an occultation profile of $OClO$. It was retrieved from the SCDs belonging to SZAs between 85^o and 93^o. The measured profile does not show the modelled profile structure with a minimum around 27 km and maxima at 23 km and 37 km altitude. Also the measured profile is a factor of $5 - 10$ larger than the modelled one. Still one has to take into account that the measured profile is a mixture of profiles at different SZAs.

As the $OClO$ amount is highly depending on the photolysis and therefore the SZA it is necessary to compare the measured SCDs directly to modelled SCDs using the 3-D CTM model SLIMCAT. The photochemical model $OClO$ concentration field is shown in Figure 4.23.

After integrating the model $OClO$ concentration along the line of sight, we get the modelled SCD which we can compare to our measurements. The respective comparison of the time evolution is shown in Figure 4.24. It is again obvious that the occultation measurements are between a factor of $5 - 10$ larger than the model predictions.

As $OClO$ is formed mainly via the pathway $ClO + BrO$, it is necessary to check the model concentrations of ClO to find out more about the observed discrepancy. Figure 4.25 shows the measurements of ClO by Stroh [1999], which were done at Nov.14, 1996 during a flight starting from León. The measurement technique used is the resonance fluorescence technique [Anderson et al. 1989], which was

---

[2] *Global Ozone Monitoring Experiment* on the ERS-2 satellite is flying at an altitude of about 780 km at a sun-synchronous polar orbit with an equator crossing time around local noon. It is an UV/Vis DOAS spectrometer with four separate channels from 240 to 790 nm with a moderate spectral resolution of 0.17 to 0.33 nm.

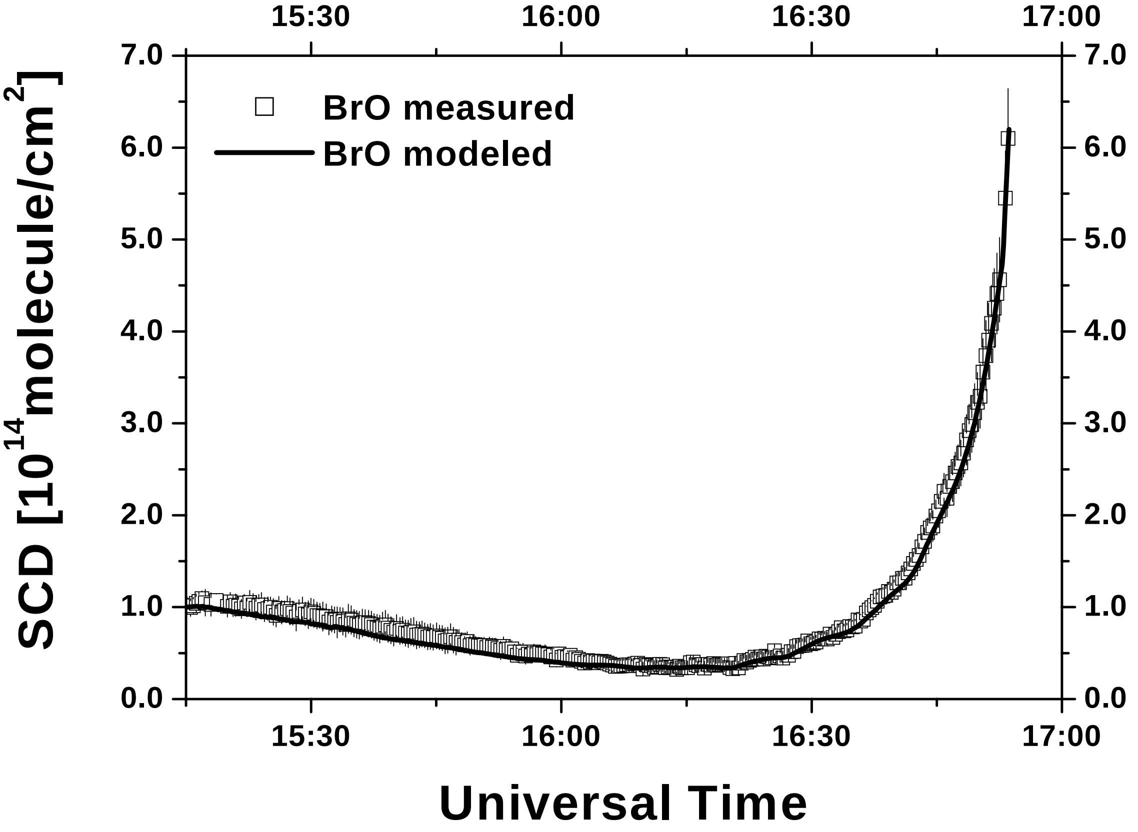

Figure 4.18: Time evolution of measured and modelled BrO SCDs for the León 96 flight.

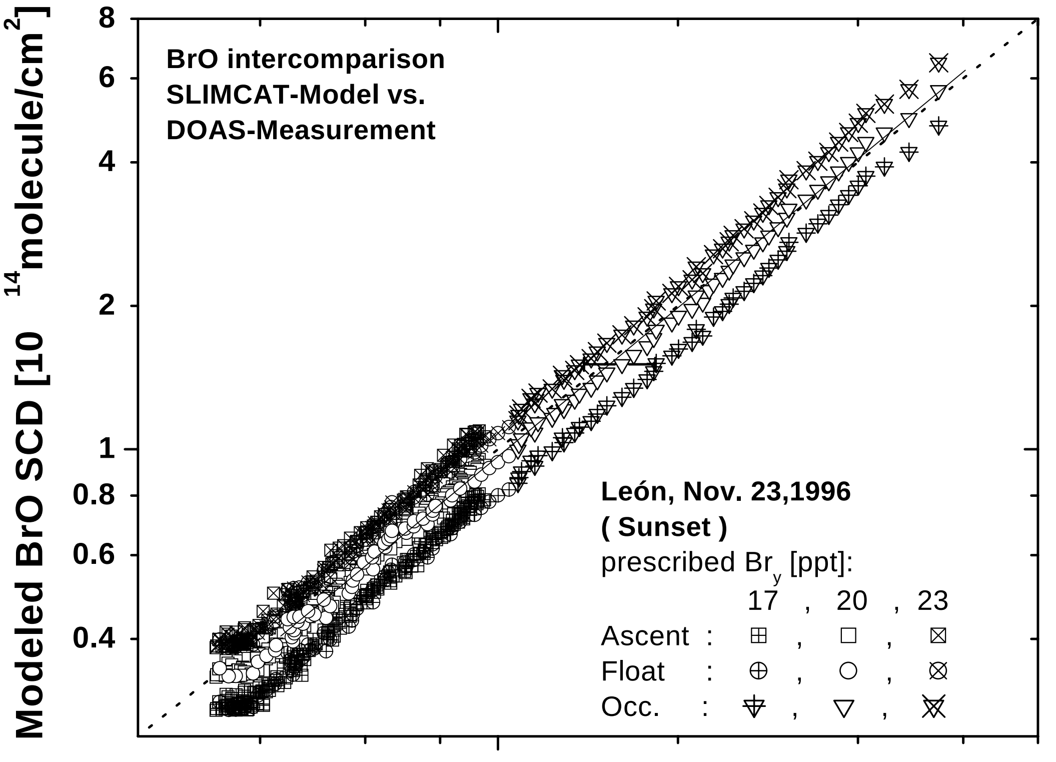

Figure 4.19: Correlation plot of measured and modelled BrO SCDs for the León 96 flight. The different model runs with different total inorganic bromine content are also shown (Br_y = 17, 20 and 23 ppt).

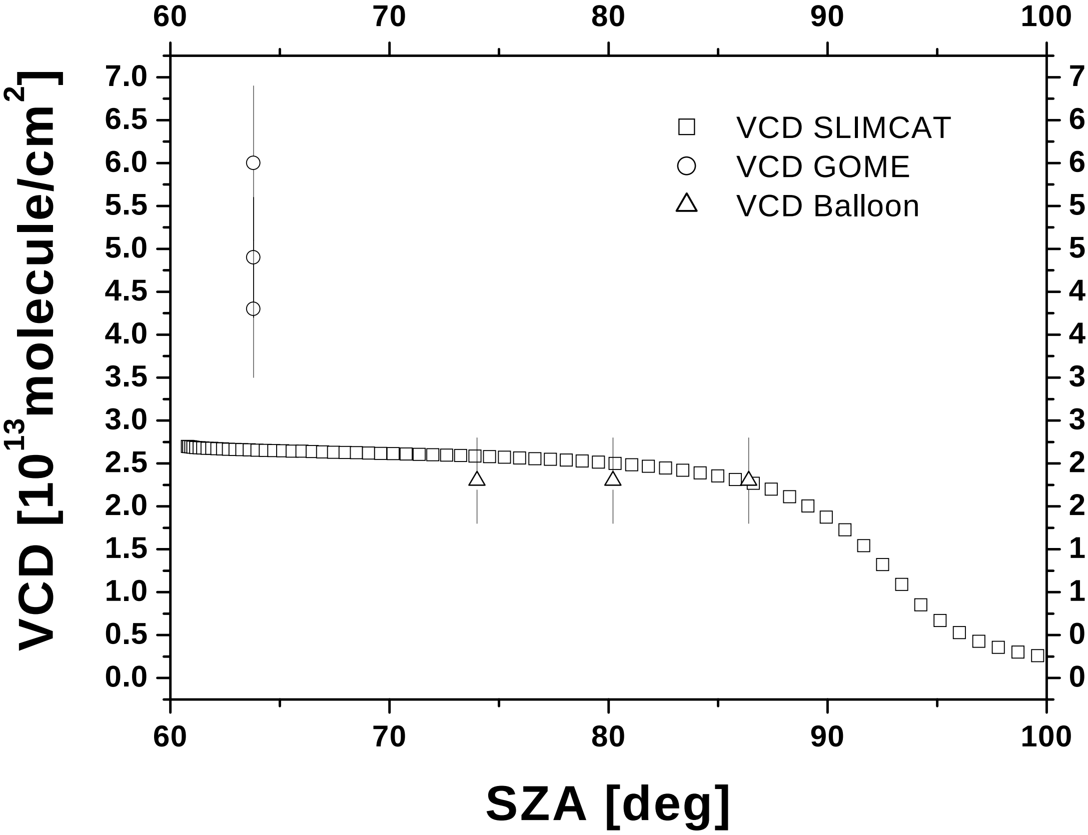

Figure 4.20: Comparison of the measured *BrO* VCDs by balloon and GOME satellite instrument as a function of SZA.

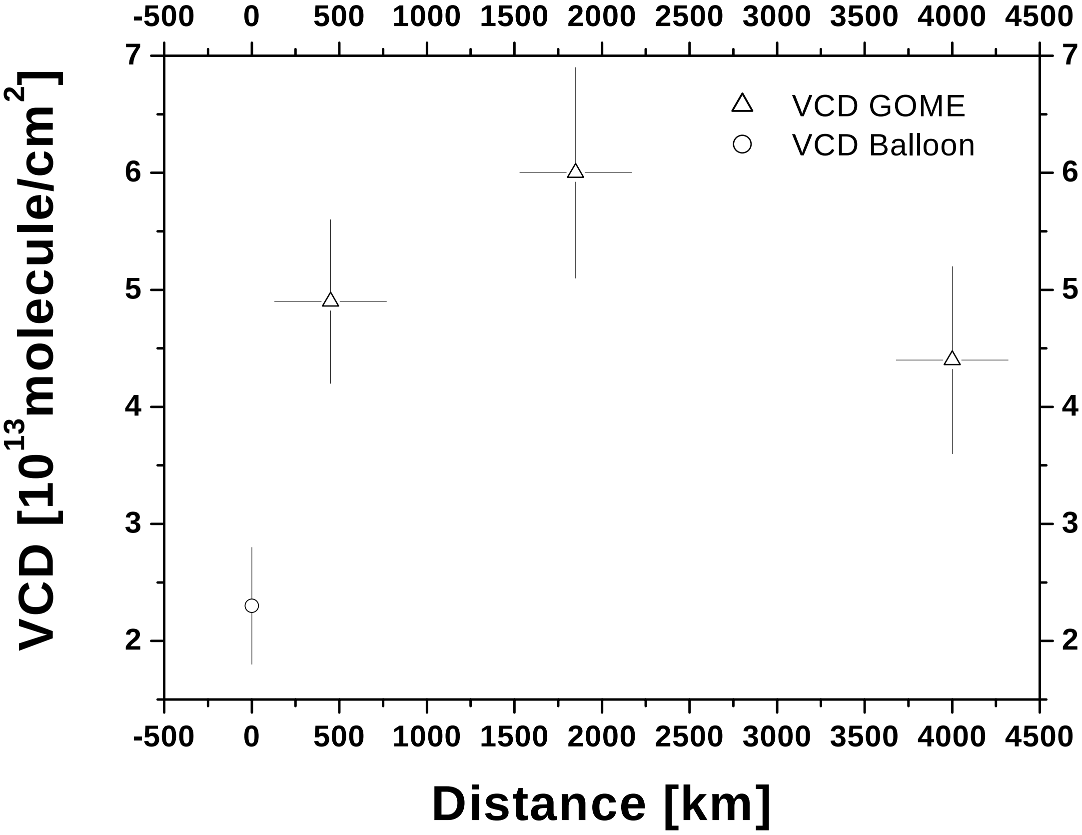

Figure 4.21: Comparison of the measured total vertical column densities (VCDs) by balloon and GOME satellite-borne instrument as a function of position. The GOME pixel measurements belong to the same SZA range (62.5-65.1^o) and the same latitude range (41.1-43.9^{o}N). Adapted from [Harder 1999].

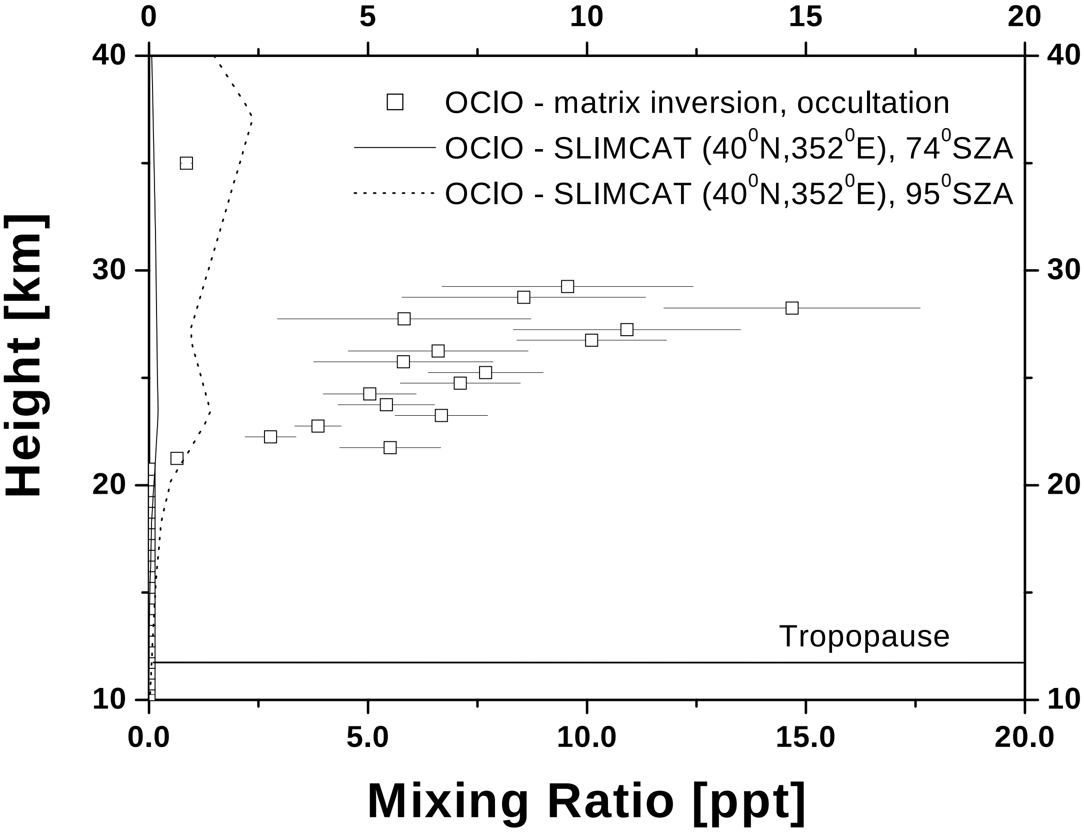

Figure 4.22: *OClO* mixing ratio profiles from the ascent part of the balloon flight retrieved by AMF matrix inversion from the occultation SCDs. The occultation measurements took place between 85 – 93^o SZA.

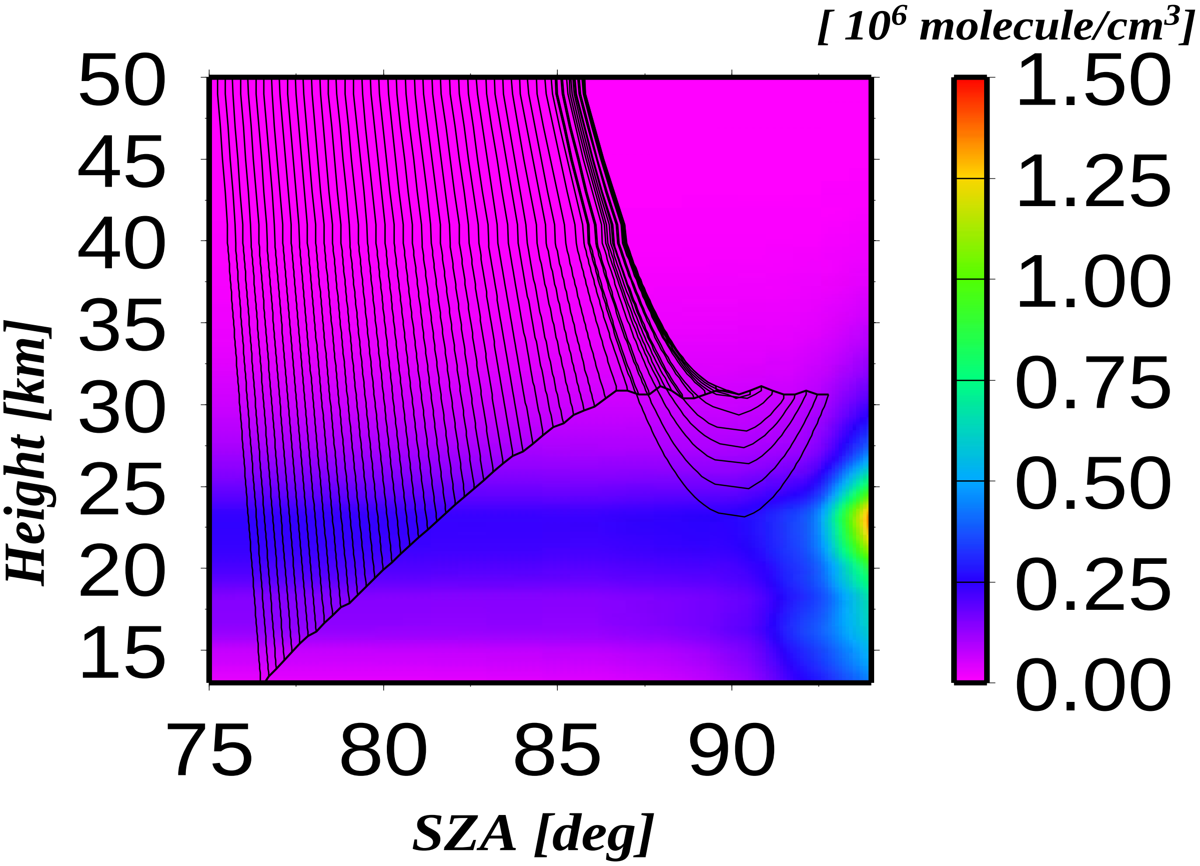

Figure 4.23: Modelling of *OClO* SCDs by integration of the concentration along the light path through the atmosphere. The model field is color-coded as a function of height and SZA. Both the trajectory of the balloon (thick line) and the light rays from the sun (fine lines) reaching the balloon instrument are shown in the plot.

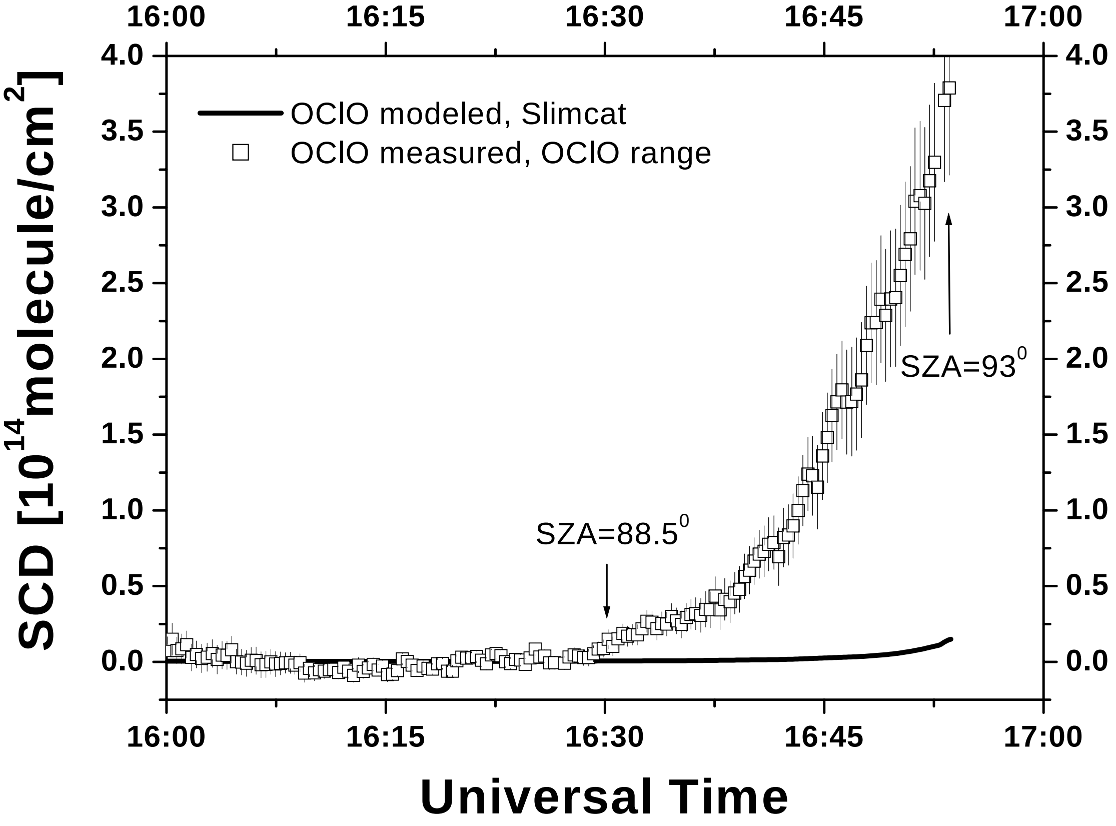

Figure 4.24: Time evolution of measured and modelled *OClO* SCDs for the León 96 flight.

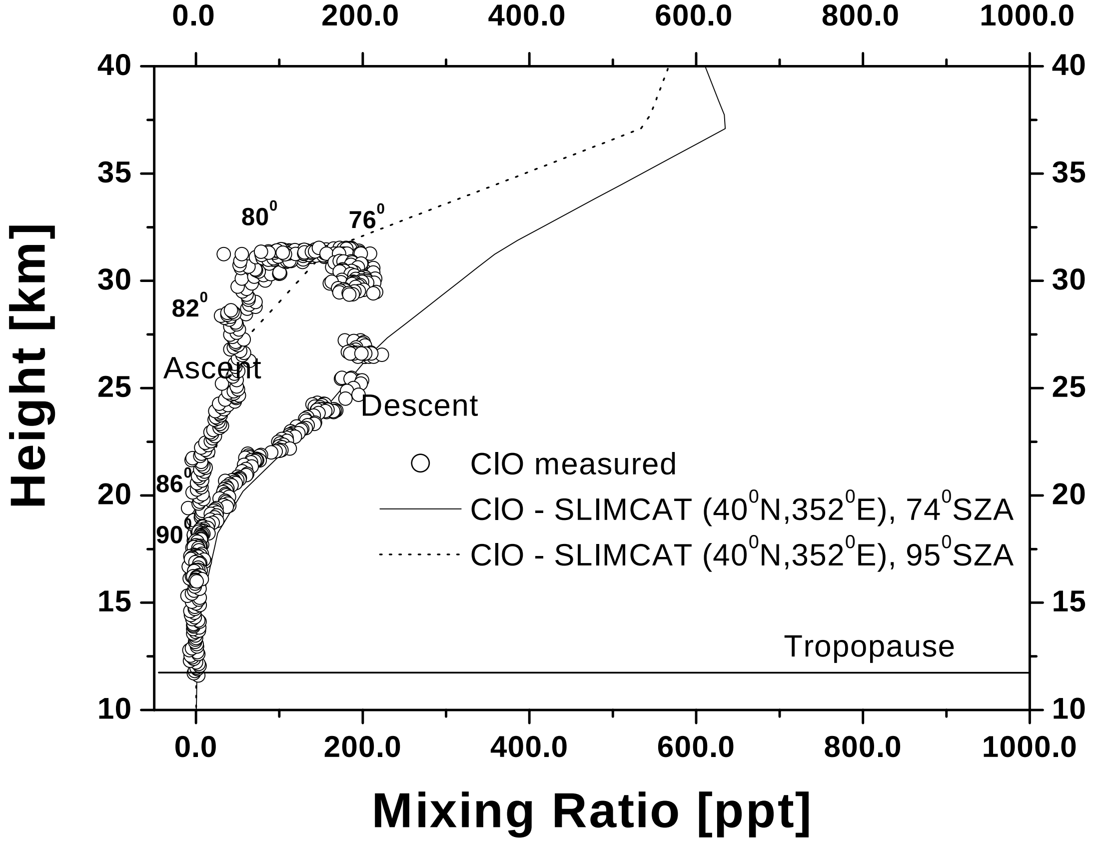

Figure 4.25: *ClO* profiles measured by Stroh [1999] at Nov.14,1996 from León using the resonance fluorescence technique. The ascent of the balloon flight took place in the night reaching the float at 80^o SZA and descending in the morning. For an inter comparison the *ClO* profiles modelled by SLIMCAT - but on Nov.23, 1996 - for 74^o and 95^o SZA are also shown.

applied during balloon-borne measurements onboard the TRIPLE[3] gondola.
For an inter comparison the ClO profiles modelled by SLIMCAT for 74^o and 95^o SZA are also shown in the plot. The agreement is rather good although the model results are for Nov.23, 1996. But as the measurements took all place under undisturbed geophysical conditions, one does not expect large variations of the ClO distribution during that time interval.
As the measured BrO and ClO profiles are in good agreement with the 3-D CTM SLIMCAT, it has still to be clarified, what are the reasons for the large underestimation of the $OClO$ amounts. This issue will be dealt with in the following chapter 7 about lagrangian case studies.

4.2 The sunset flight at Kiruna on February 14, 1997

While the first flight was an autumn mid-latitude flight, the next flight took place in winter at high latitudes starting from Kiruna (Sweden) on Feb. 14, 1997. In Figure 4.26 it is shown the trajectory of the balloon and the directions of the line of sight during the flight. While the balloon is moving to the east the line of sight direction changes from south to south west. Again during the sunset/solar occultation the tangent points are moving away from the balloon. As we are looking through the edge of the vortex, it is clear that during the different phases of the flight the instrument is probing different airmasses with different photochemical history. This has to be taken account of when comparing to models.

In Figure 4.27 the balloon height as a function of time as well as the SZA at the balloon position (latitude, longitude) is displayed. As the balloon is flying in easterly direction the SZA is increasing faster than it would, if the position of the balloon was fixed.

The temperatures at the edge of the vortex are not as low as in the centre of the vortex. They remain above $205K$, while the minimum temperatures at that day in the vortex are as low as $190K$ (see Figure 4.28 [ECMWF 1999]).

A typical DOAS evaluation for this flight is shown in Figure 4.29. This time an $OClO$ reference spectrum is included in the fit procedure in the BrO range, because it is expected to form within the polar vortex, when denoxification and chlorine activation have taken place, so that $OClO$ production can become significant, mainly during the night.

$OClO$ is also evaluated in the 362-380 nm wavelength range, where the absorbers with the strongest differential absorption cross sections are $OClO$, NO_2 and O_4. Figure 4.30 shows a typical DOAS evaluation in the $OClO$ wavelength range, where the references used are the Fraunhofer reference, NO_2, O_4, $OClO$ and a polynomial of degree 5.
The residual structures in the $OClO$ wavelength range are slightly larger than in the BrO range, mainly because the measured NO_2 reference at -70^oC [Harder 1999] does not fit as well as in the BrO range and the Fraunhofer lines are stronger.
Figures 4.31-4.38 show the time evolution of the different SCDs during the flight as they are retrieved by the DOAS fit in the BrO and the $OClO$ evaluation range, respectively. The evolutions for $O_3(-80^oC, -20^oC)$, $OClO$ and BrO look very similar: they decrease during the ascent in the stratosphere until the float height of the balloon is reached and they increase again during the occultation of the sun. The NO_2 SCDs do also increase during the beginning of the solar occultation but at the end they decrease again. This can be explained by the fact that the balloon float altitude is below the maximum of the NO_2 concentration and that the tangent points of the line of sight do decrease during the occultation.
At 13:38:20 UT there was a change in the photodiode cooling system leading to an increase of the temperature of the detector (from -10^oC to -2.54^oC), which can be seen in the small gaps in the shift and squeeze of the reference spectra ensemble. Still this small malfunction did not decrease the

---

[3] A balloon experiment combining an in-situ chemical conversion resonance fluorescence instrument for ClO and BrO (FZ Jülich, Germany) with a cryogenic whole air sampler (Univ.Frankfurt, Germany), a Lyman-α water vapour instrument (FZ Jülich, Germany), a laser scatter aerosol counter (LMD, Palaiseau, France) and an ozone sonde.

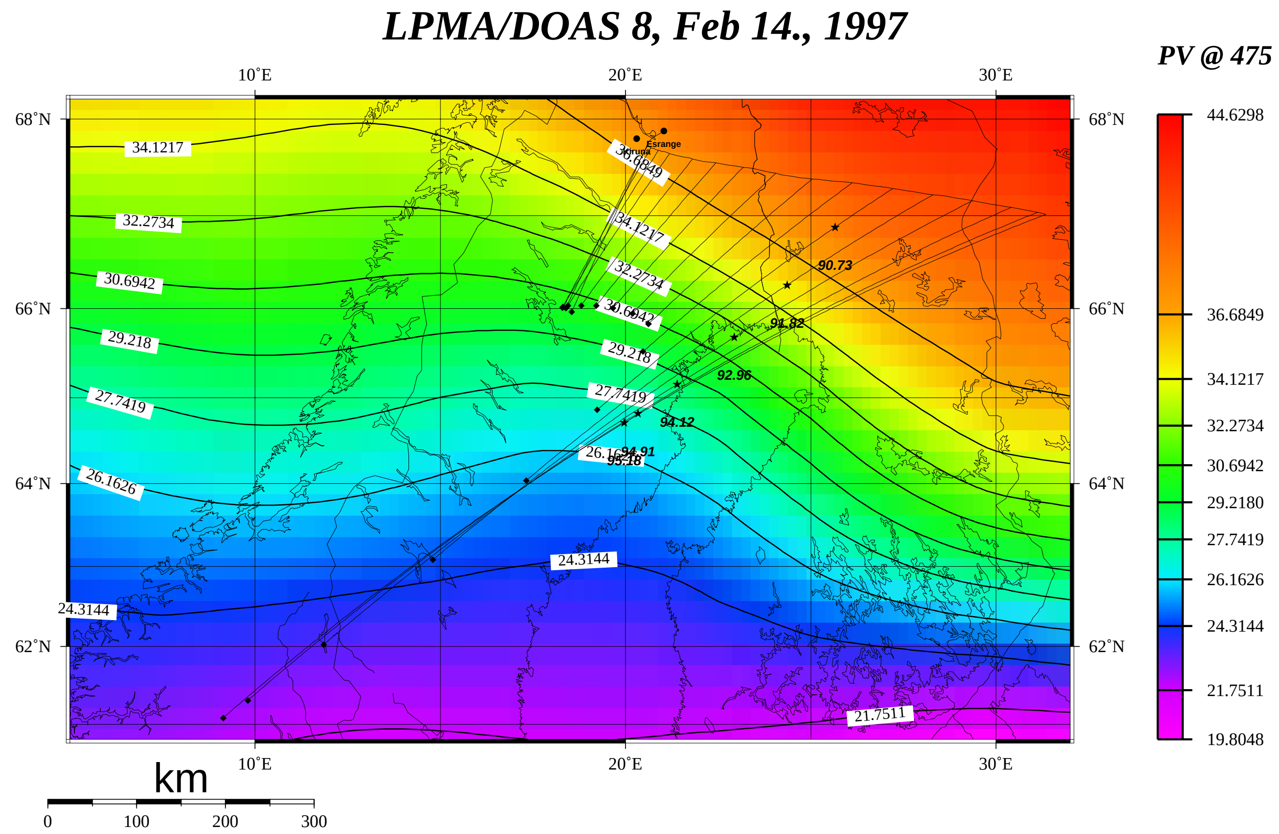

Figure 4.26: Balloon trajectory during the flight at Kiruna (Sweden) on Feb. 14, 1997. The trajectory is the curved line towards the east, while the lines ending with a point denote the light rays and the end points show the location of the tangent points - that is the main area of atmospheric absorption. The potential vorticity determines the strength of the vortex and is shown in color code in units of 10^{-6}K m^2/(kg·sec). Adapted from [Harder 1999].

precision of the DOAS evaluation significantly.
Concerning the different BrO and $OClO$ DOAS retrieval ranges, it is only possible to compare the SCD evolutions for $OClO$, NO_2, O_4 as well as the evolution of the RMS, the shift and the squeeze of the respective reference data sets. The $OClO$ SCDs agree very well in the occultation part of the flight, but there is a slight difference in the ascent. For the NO_2 SCDs it is different. The agreement is best during the ascent, float and main part of the occultation, while the NO_2 SCDs are about 10% larger in the $OClO$ range at the end of the occultation. To retrieve the absolute NO_2 and O_3 SCDs with the highest possible accuracy, it is necessary to make the DOAS evaluation in the visible part of the spectrum ($\geq$ 400 nm), where the temperature dependence is less significant [Bösch et al. 1999].

4.2.1 BrO profile and SCD model comparison

As the balloon reached the float altitude during that flight at a SZA of 89^o, there is only a small number of SCDs available to do the Langley plot to determine the BrO content of the Fraunhofer reference spectrum. That is why the Fraunhofer spectrum of the León 96 flight was used to determine the SCD offset by comparing the respective SCDs as it is shown in Figure 4.39.

After performing the matrix inversion and the onion peeling technique for profile extraction, we get the respective profiles, which are shown in Figure 4.40 and 4.41. Despite the inhomogeneities of the polar vortex boundary, where the measurements took place, there is a quite good agreement between

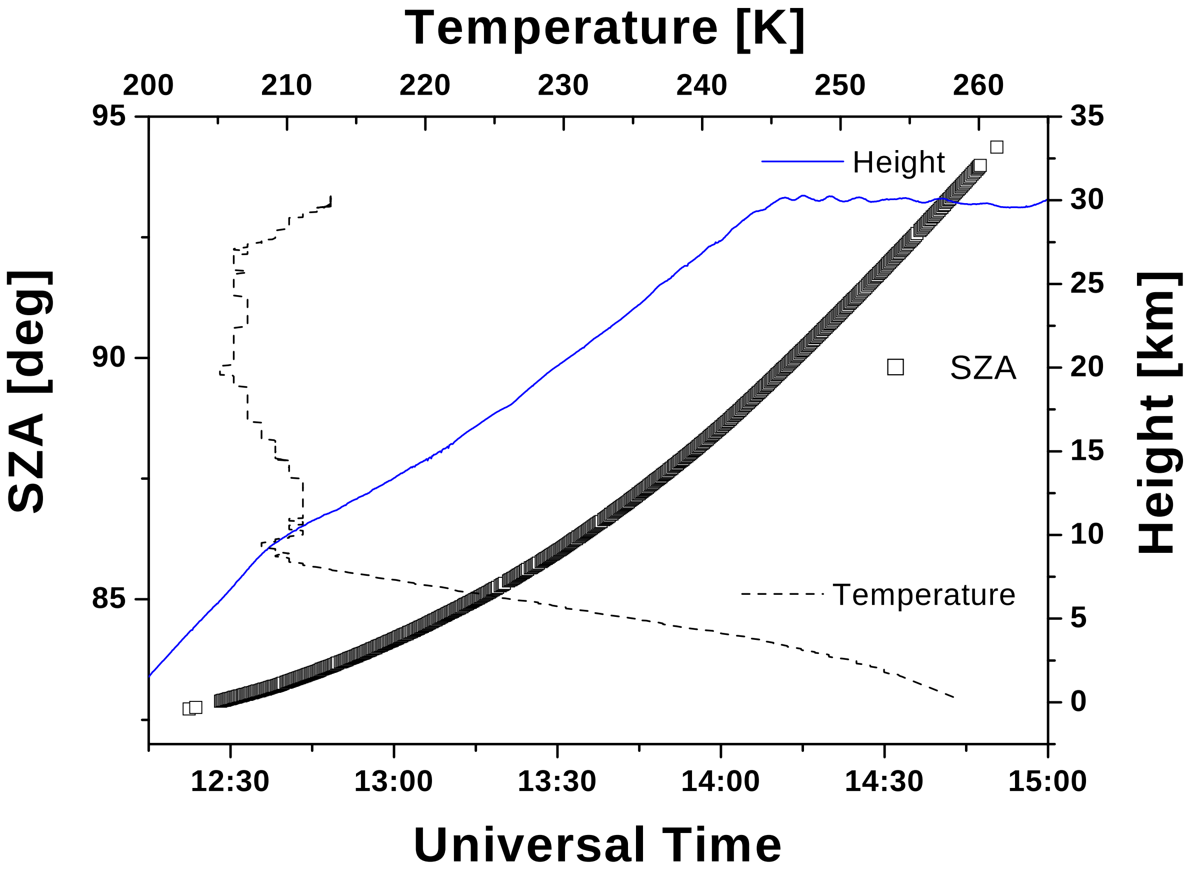

Figure 4.27: Balloon trajectory, temperature and SZA at balloon position (latitude, longitude) during the flight at Kiruna (Sweden) on Feb.14, 1997.

the model and the measurement.

Still the onion peeling profile tends to underestimate the BrO profile, which can be explained by the overestimation of the airmass factor during the AMF approximation, which is most important for large SZAs as observed during this flight. Especially at the end of the ascent, the onion peeling technique is not able to reproduce the constant mixing ratio near to and above float, which can be seen in the inverted profile and in the profile modelled by the 3-D CTM model SLIMCAT.
The model profile for 82.4^o SZA is smaller by $15 - 20\%$ in the altitude range around the BrO concentration maximum, while it agrees very well with the measurements above, where the BrO mixing is maximal and nearly constant.
At 88.6^o SZA the model sees already much less BrO - about $20 - 25\%$ in comparison with 82.4^o - because BrO is effectively converted during the sunset to its reservoir species $BrONO_2$ and $HOBr$, as well as $OClO$ in the case of low NO_x - as it can be observed during denoxification in the Arctic and Antarctic polar vortex.

Again we use the 3-D CTM SLIMCAT concentration field of BrO with respect to height and SZA for the airmasses encountered during our flight for comparison. Figure 4.42 shows the BrO model field in colour code and also the trajectory of the balloon as well as the light rays from the sun to the balloon. And in Figure 4.43 the evolution of the measured and modelled SCDs as a function of time is displayed.
The different phases of the flight are separated and the linear correlation between modelled and measured BrO SCDs is checked in detail by plotting the modelled SCDs versus the measured SCDs. In addition, the results for different model grid points (and for different total Br_y = 17, 20 and 23 ppt)

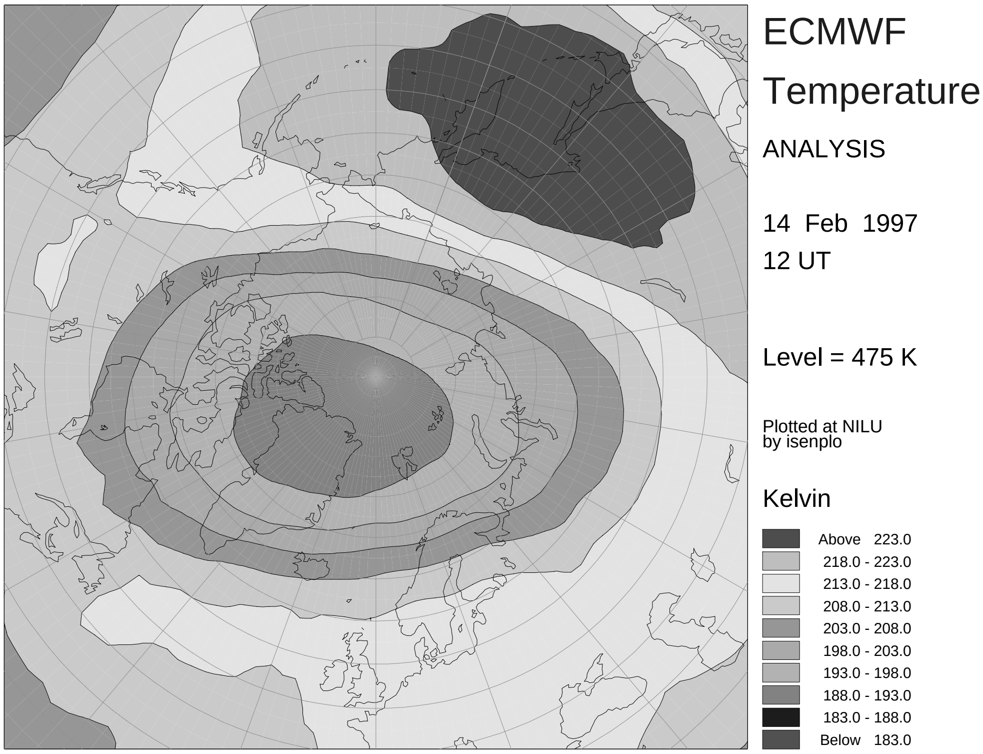

Figure 4.28: Temperatures of the polar arctic vortex at the day of the flight for the potential temperature level 475 K [ECMWF 1999].

are shown - see Figure 4.44. It is evident that there is nearly no difference between the neighbour grid points ($65N, 19E$ and $65N, 22E$). As we have seen in the comparison of the ascent profiles with the respective model profiles, there is a large discrepancy between model and measurement for the smaller SCDs corresponding to measurements including the BrO profile maximum, while the agreement is fairly good in the later occultation part. There, the airmasses seen by the instrument are above the BrO maximum. Taking into account the different model runs with 17-23 ppt total Br_y, we can at least state a lower limit for this case of (20±2.5) ppt, which agrees well with the value derived from the first flight.

Figure 4.45 shows the comparison of the integrated BrO VCDs measured by the balloon instrument, the ground-based zenith-scattered light DOAS spectrograph [Otten et al. 1997] and the satellite instrument GOME. The satellite (GOME) was measuring in the 320x40 km^2 area around Kiruna for a SZA of 81.7^o, which is near to the SZAs encountered during the balloon flight. GOME is not only averaging over the whole pixel area but also over the different SZAs (the SZA change in this area is about 0.8^o). It is again obvious that there is a striking discrepancy between the total vertical columns measured by GOME and the ground-based spectrograph on the one hand and the stratospheric BrO VCD measured by the balloon instrument on the other hand. This VCD difference again provides indirect evidence for a tropospheric BrO VCD of $1-2\times 10^{13}$ molecule/cm^2.
This becomes even more evident, if we look at the spatial distribution of BrO as measured by the GOME satellite instrument - see Figure 4.46. On the day before the balloon flight there are significant amounts of BrO visible next to Northern Scandinavia - comparable to the amounts measured above Northern Canada, where a lot of tropospheric measurements [Hausmann and Platt 1994] have shown that there are periods of nearly full ozone depletion in the tropospheric boundary layer linked to high

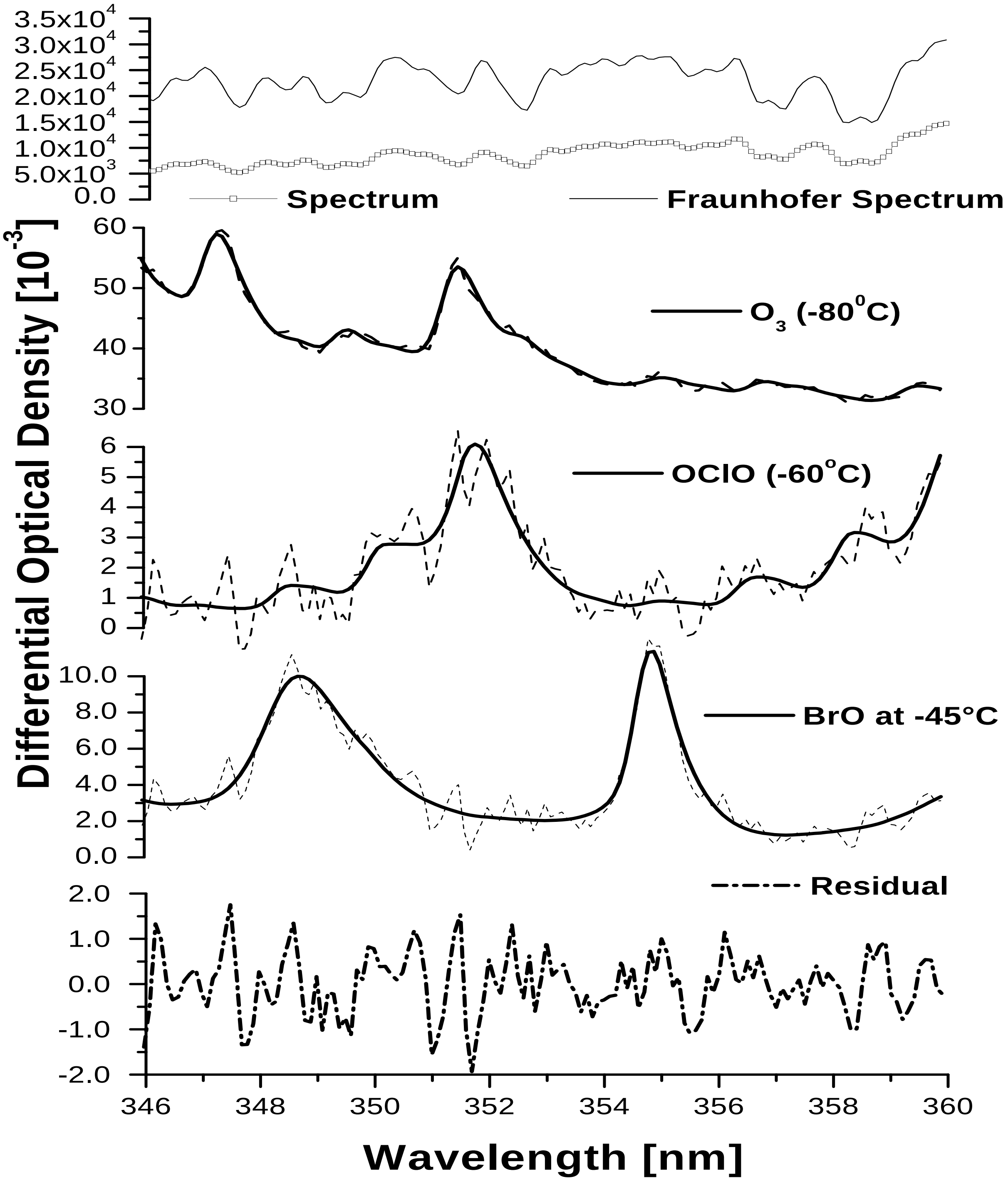

Figure 4.29: Typical DOAS evaluation in the BrO retrieval wavelength range (346-360 nm) for Kiruna 1997. The fit included O_3 at -80^oC and -20^oC(not shown), NO_2 at -70^oC (not shown), O_4 (not shown), $OClO$ at -60^oC, BrO at -45^oC and a polynomial of degree 3. The last spectrum is the residual of the fit which cannot be explained by the fit but is due partly to statistical noise and to systematic errors. All spectra have been filtered with a binomial filter of degree 3 before the fit.

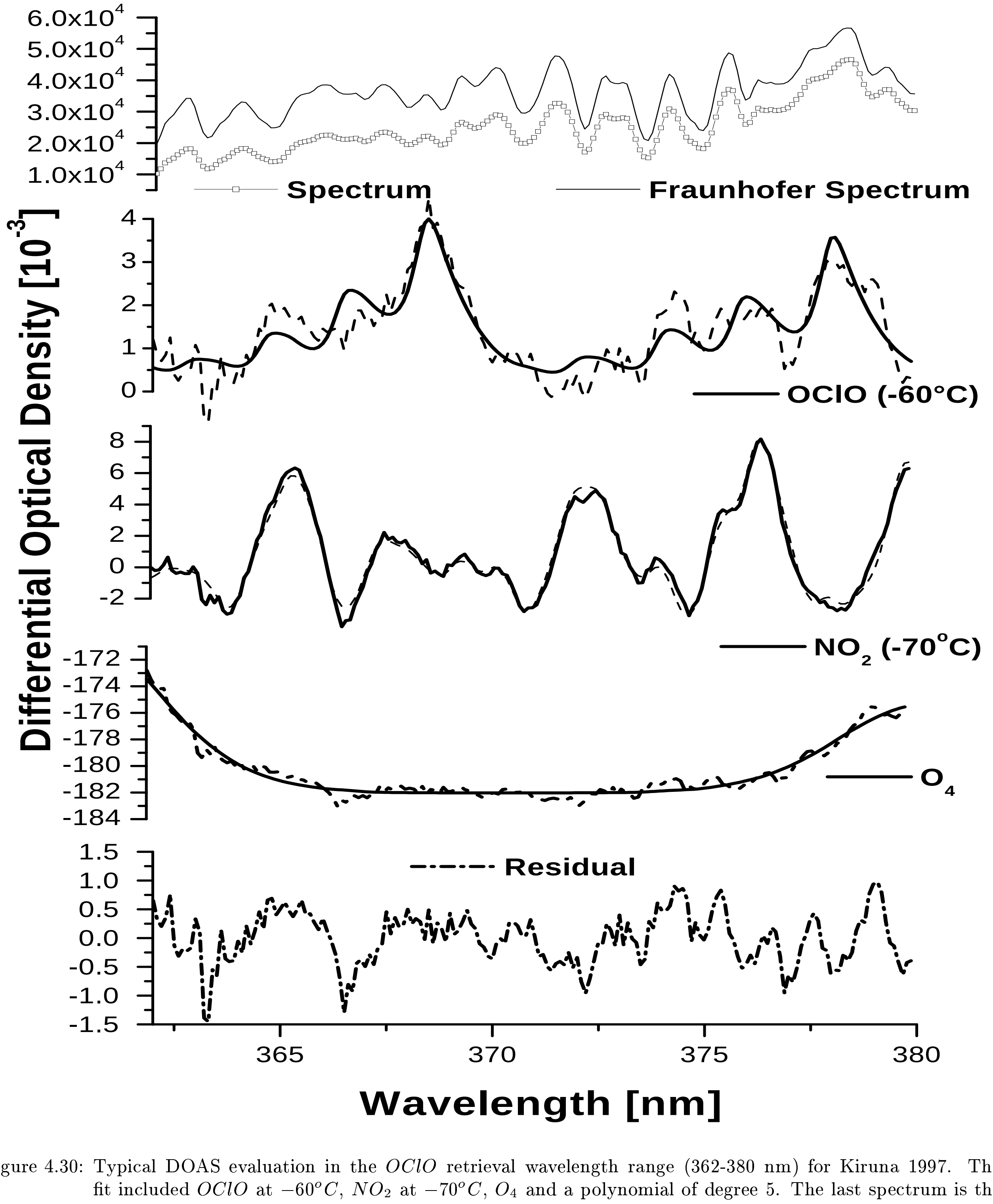

Figure 4.30: Typical DOAS evaluation in the *OClO* retrieval wavelength range (362-380 nm) for Kiruna 1997. The fit included *OClO* at -60^oC, NO_2 at -70^oC, O_4 and a polynomial of degree 5. The last spectrum is the residual of the fit which cannot be explained by the fit but is due partly to statistical noise and to systematic errors. All spectra have been filtered with a binomial filter of degree 3 before the fit.

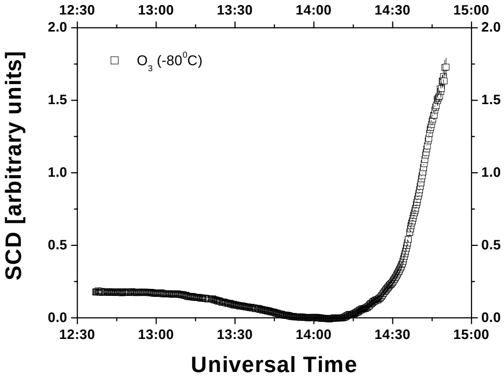

Figure 4.31: Time evolution of the $O_3(-80^oC)$ SCDs during the flight.

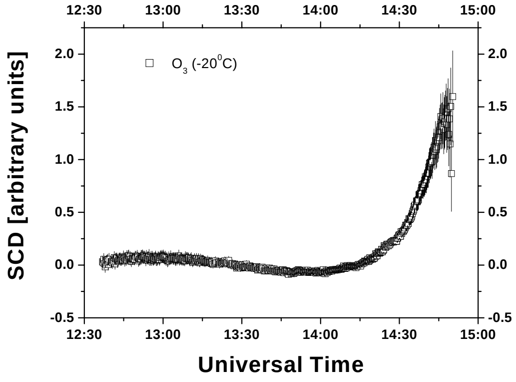

Figure 4.32: Time evolution of the $O_3(-20^oC)$ SCDs during the flight.

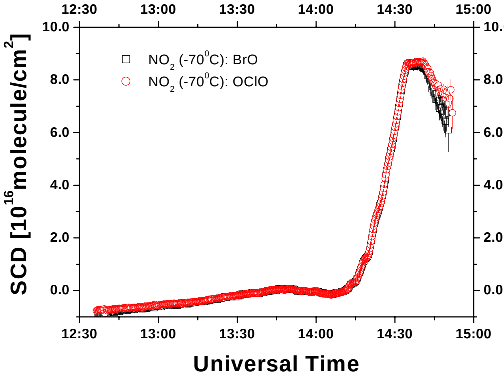

Figure 4.33: Time evolution of the $NO_2(-70^oC)$ SCDs during the flight.

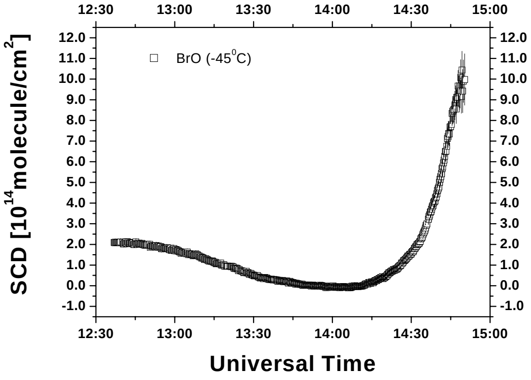

Figure 4.34: Time evolution of the $BrO(-45^oC)$ SCDs during the flight.

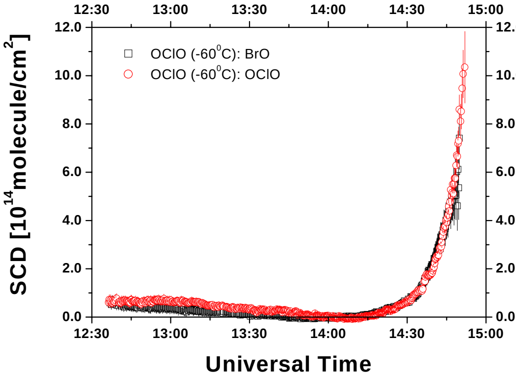

Figure 4.35: Time evolution of the $OClO$ SCDs during the flight.

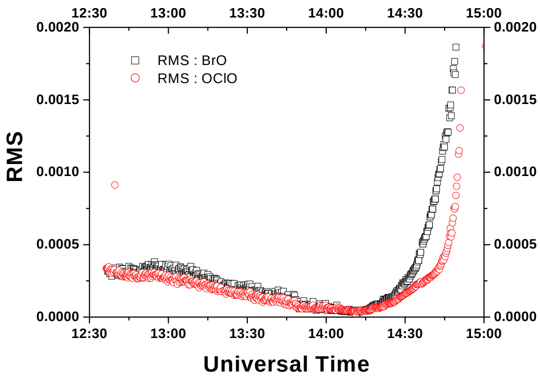

Figure 4.36: Time evolution of the RMS of the DOAS fit during the flight.

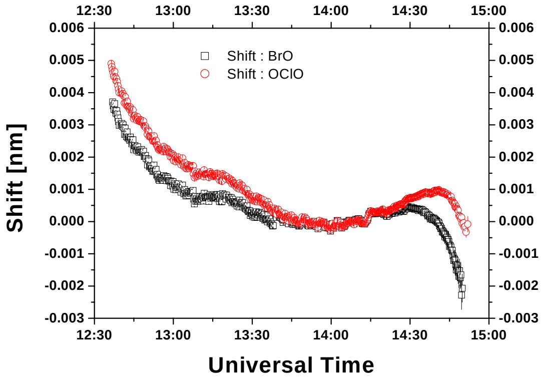

Figure 4.37: Time evolution of the shift of the reference spectra ensemble during the flight.

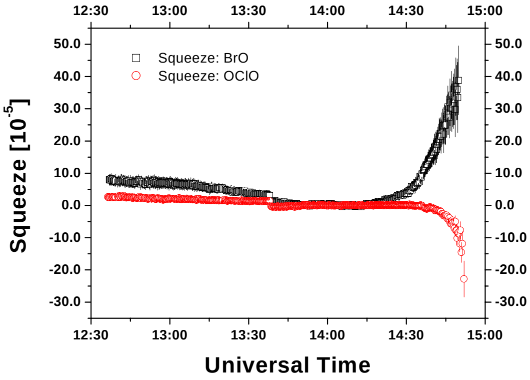

Figure 4.38: Time evolution of the squeeze of the reference spectra ensemble during the flight.

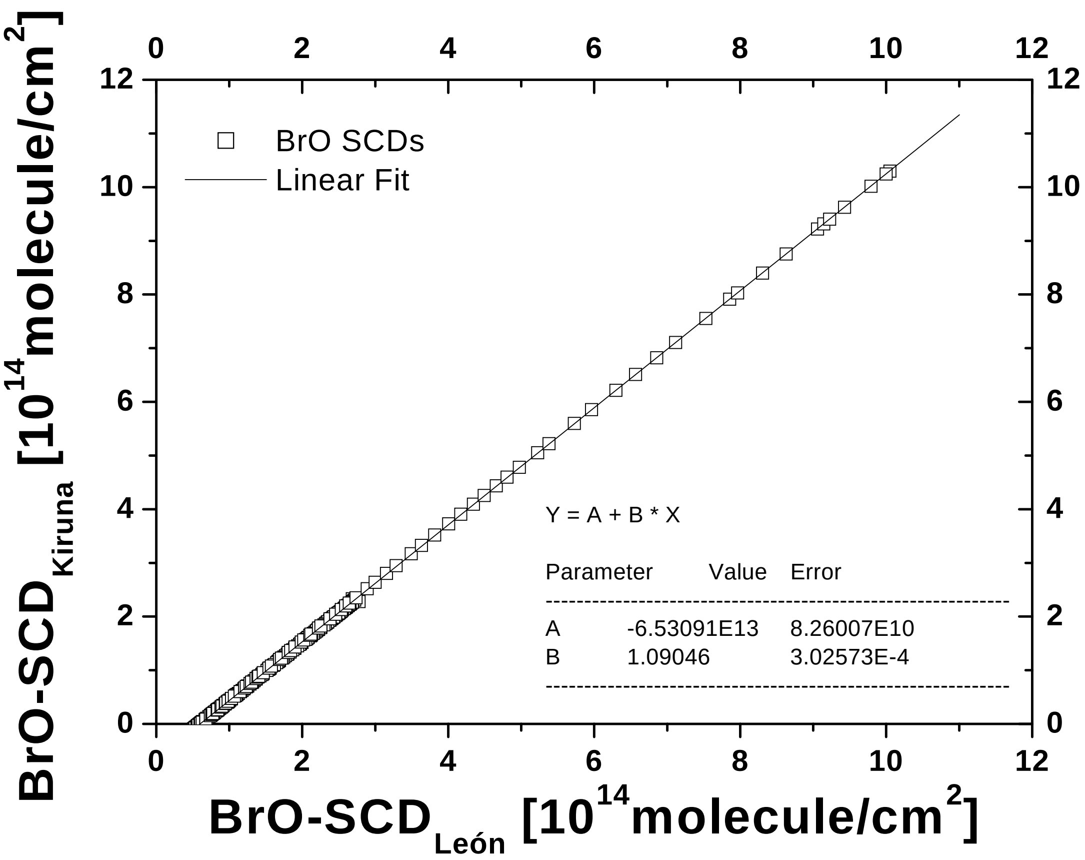

Figure 4.39: Comparison of the *BrO* SCDs for two DOAS evaluations using the Fraunhofer reference spectrum from Kiruna 97 and León 96, respectively. The linear fit gives the difference in the SCD of the two Fraunhofer reference spectra, so that the SCD offset of the Kiruna Fraunhofer reference can be determined to be $10.7 \pm 0.5 \cdot 10^{13}$ molecule/cm^2. If we use this SCD offset as input in the Langley plot we get a Mixing Ratio above float of 15.6 ± 2 ppt.

values of tropospheric *BrO*.

Strong local spatial gradients in the *BrO* distribution can be noticed, which are most probable of tropospheric origin, because the inhomogeneities are not correlated with the large-scale potential vorticity and temperature pattern in the stratosphere - see Figure 4.28. Also the *BrO* VCD values in the vicinity of the balloon measurement area are consistently above the 6×10^{13} molecule/cm^2 and there is an area east of the balloon trajectory, where VCD values even in the range of $8 - 10 \times 10^{13}$ molecule/cm^2 can be observed, like they appear during tropospheric *BrO* events in the planetary boundary layer in northern Canadian spring.

4.2.2 *OClO* profile model comparison

The retrieved profiles of *OClO* are shown in Figure 4.48 and 4.49. In these plots of the concentration and the mixing ratio, also the respective SLIMCAT model profiles for different model grid points and SZAs can be seen. It is obvious that the model sees much less *OClO* than the actual measurement.

This is also the case, when looking at the *OClO* profiles more inside the vortex, where strong chlorine activation has been observed - for example by GOME measurements; see Figure 4.47. However, the conversion of the *OClO* SCD measured by GOME requires radiative transport modelling; thus only a qualitative comparison is possible. Still we can try to compare the GOME SCDs to our total atmospheric VCD deduced from the stratospheric profile. The VCD of the balloon measurements is

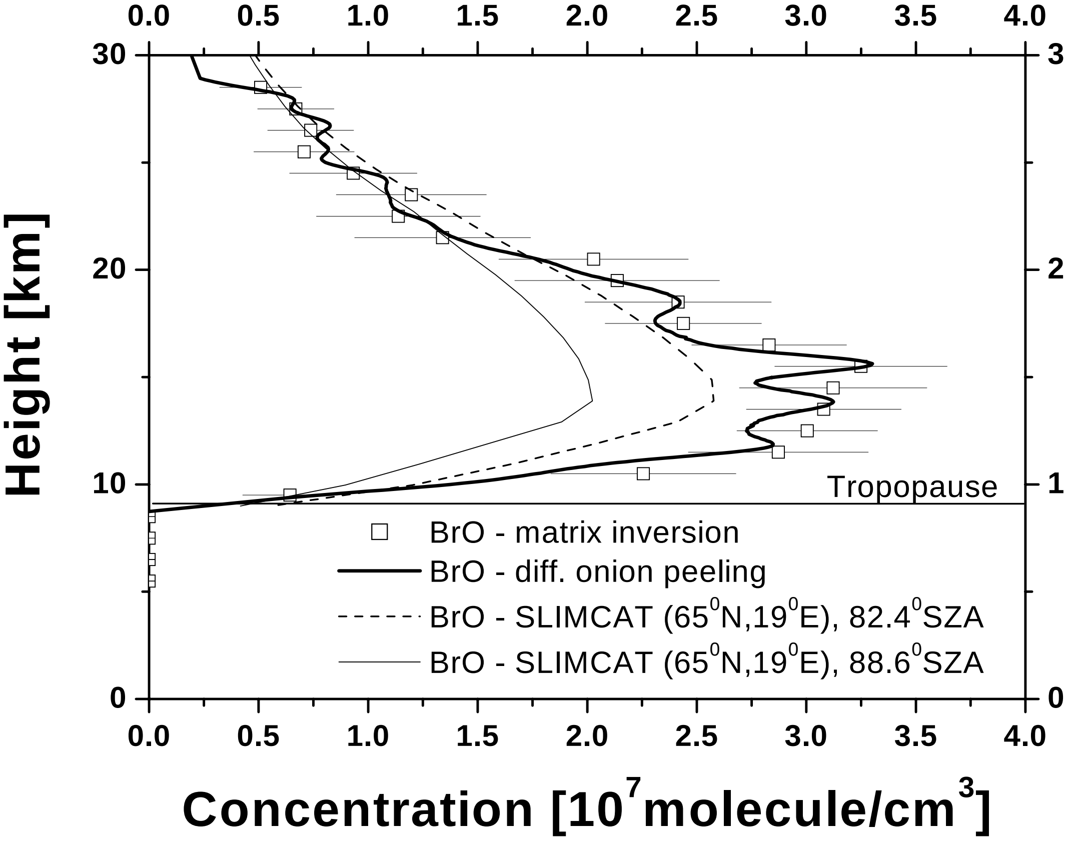

Figure 4.40: *BrO* concentration profiles from the ascent part of the balloon flight retrieved by AMF matrix inversion and Differential Onion Peeling. The ascent took place during a SZA interval of $82.9 - 88.9^o$.

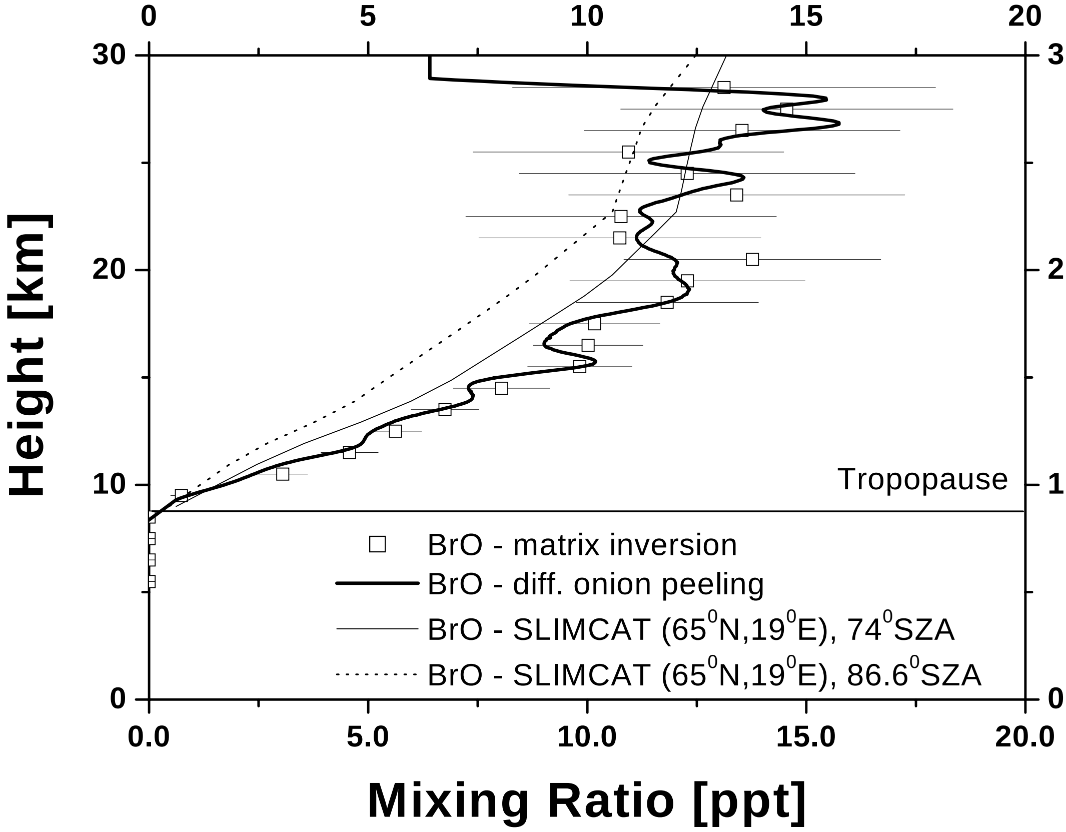

Figure 4.41: *BrO* mixing ratio profiles from the ascent part of the balloon flight retrieved by AMF matrix inversion and Differential Onion Peeling. The ascent took place during a SZA interval of $82.9 - 88.9^o$.

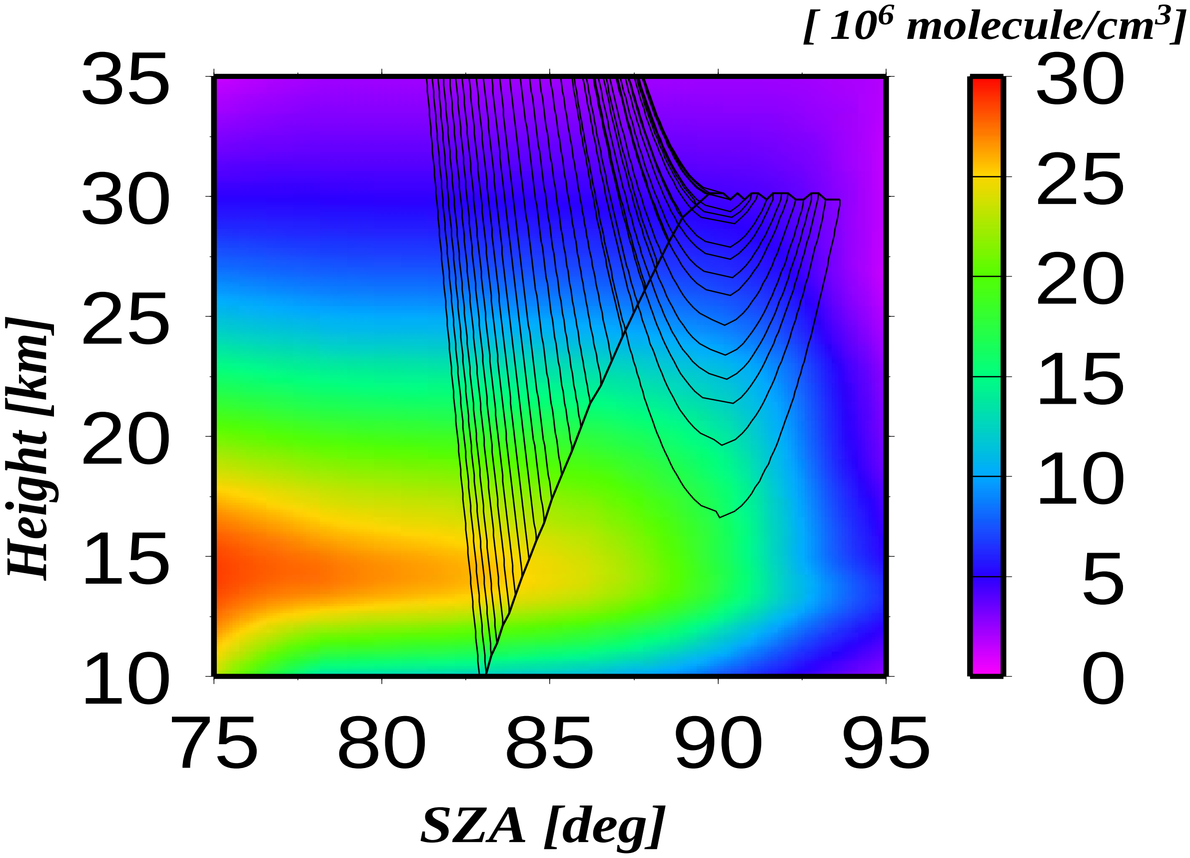

Figure 4.42: Modelling of BrO SCDs by integration of the concentration along the light path through the atmosphere. The model field is color-coded as a function of height and SZA. Both the trajectory of the balloon (thick line) and the light rays from the sun (fine lines) reaching the balloon instrument are shown in the plot.

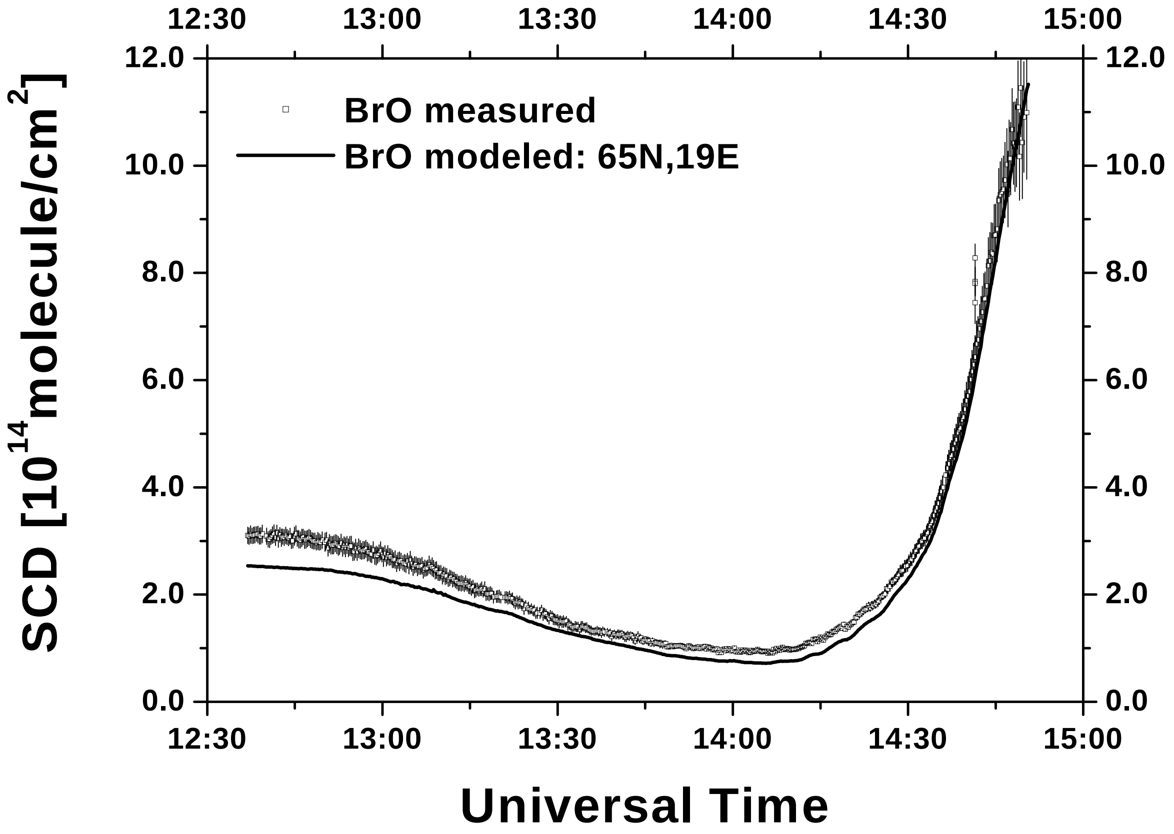

Figure 4.43: Time evolution of measured and modelled BrO SCDs for the Kiruna 97 flight.

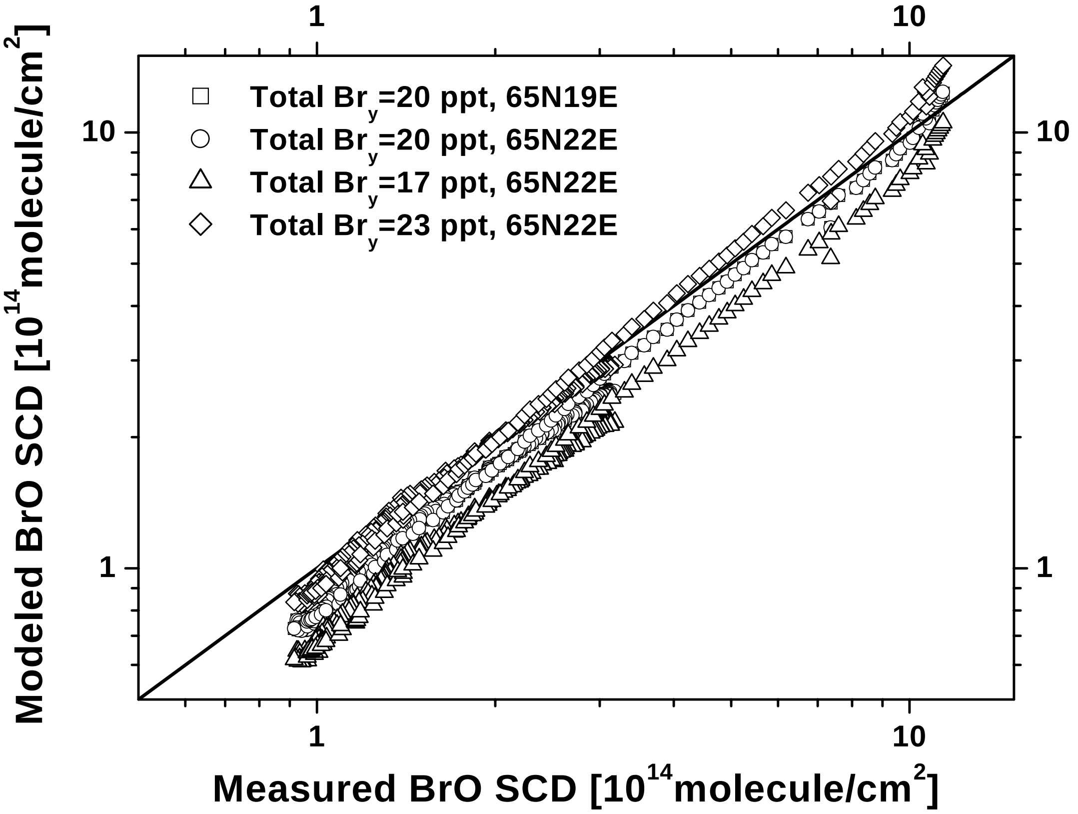

Figure 4.44: Correlation plot of measured and modelled *BrO* SCDs for the Kiruna 97 flight. The different model runs with for different locations ($65N, 19E$ and $65N, 22E$) with the same total inorganic bromine content are also shown ($Br_y = 20$ ppt).

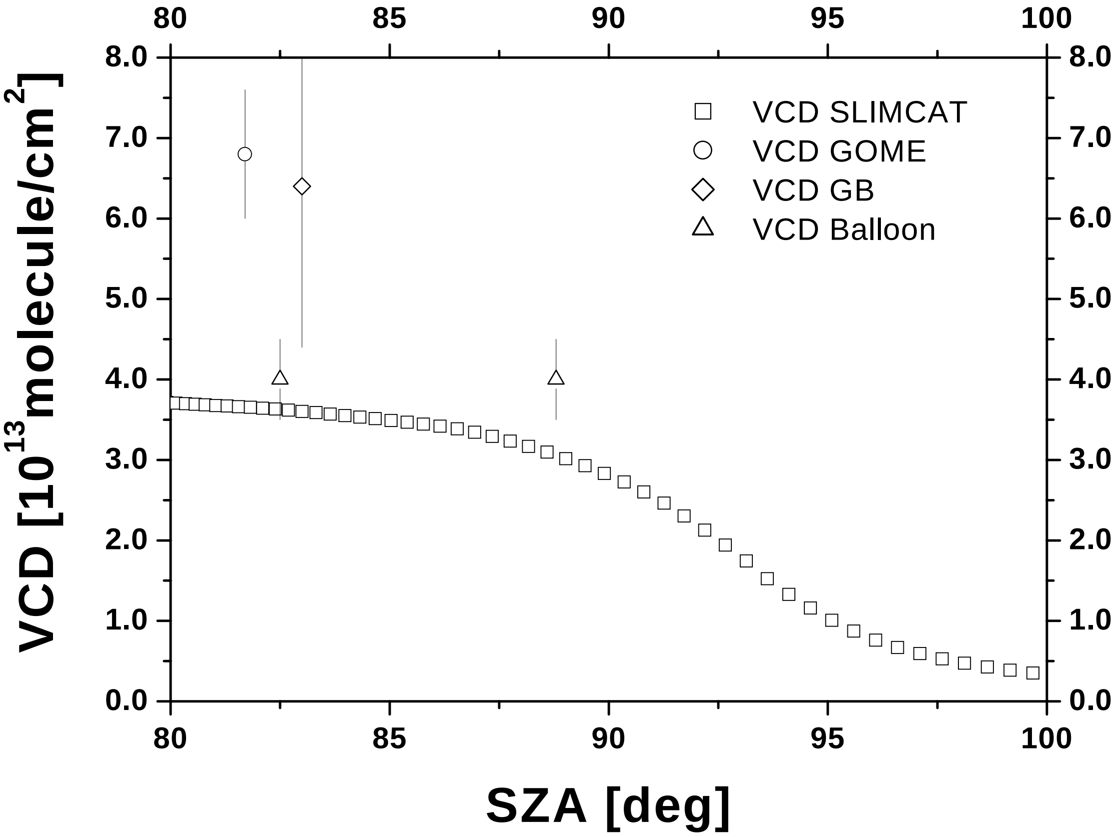

Figure 4.45: *BrO* VCD comparison between balloon-borne, ground-based and satellite-borne instruments (GOME). The VCD derived from the balloon profile belongs to a SZA range from $82.5 - 88.8^o$, while the GOME measurement refers to SZA of 81.7^o and the ground-based VCD measurement took place at a SZA of 82^o.

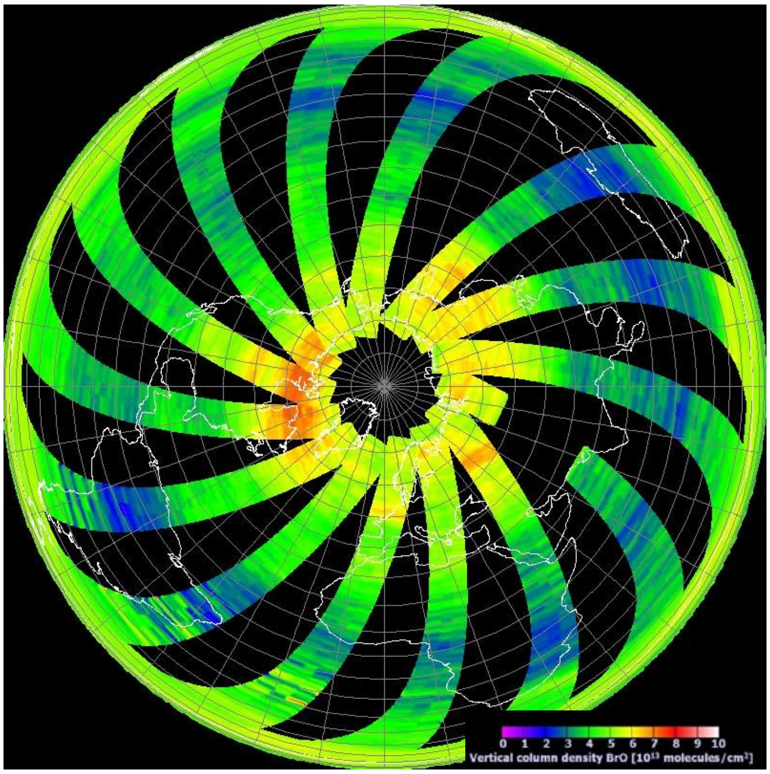

Figure 4.46: *BrO* VCDs measured by the satellite instrument GOME on ERS-2 on Feb. 13, 1997. The instrument has a spatial resolution of 320x40 km^2 and a global coverage of the pole area - latitudes$>75^o$ - is possible daily. There are no SCD values available for the center arctic pole pixels, because there is no sunlight reaching these areas Adapted from [Wagner and Leue 1999].

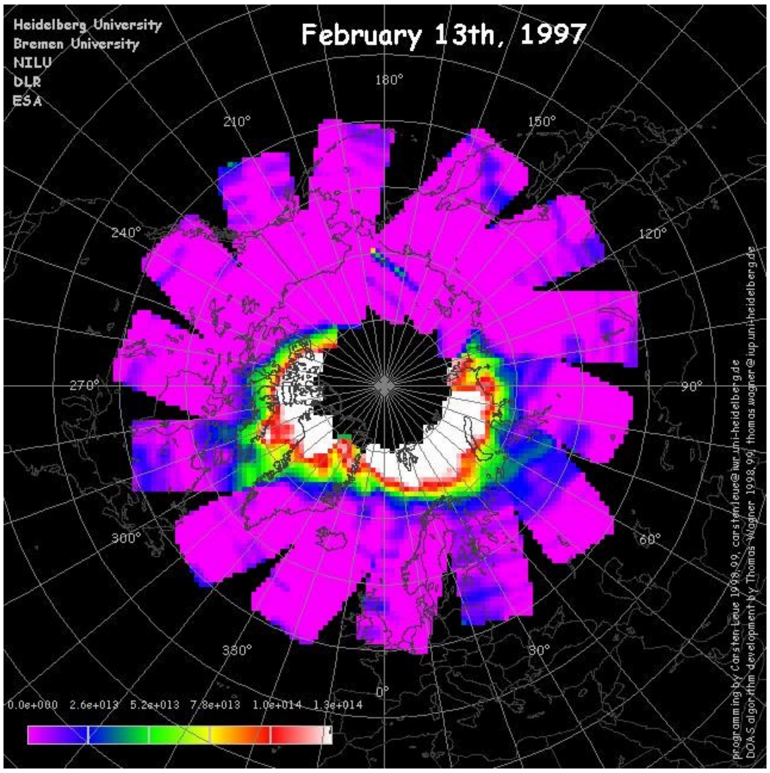

Figure 4.47: *OClO* SCDs measured by the satellite instrument GOME on ERS-2. The instrument has a spatial resolution of 320x40 km^2 and a global coverage of the pole area - latitudes$>75^o$ - is possible daily. There are no SCD values available for the center arctic pole pixels, because there is no sunlight reaching these areas. Adapted from [Wagner and Leue 1999].

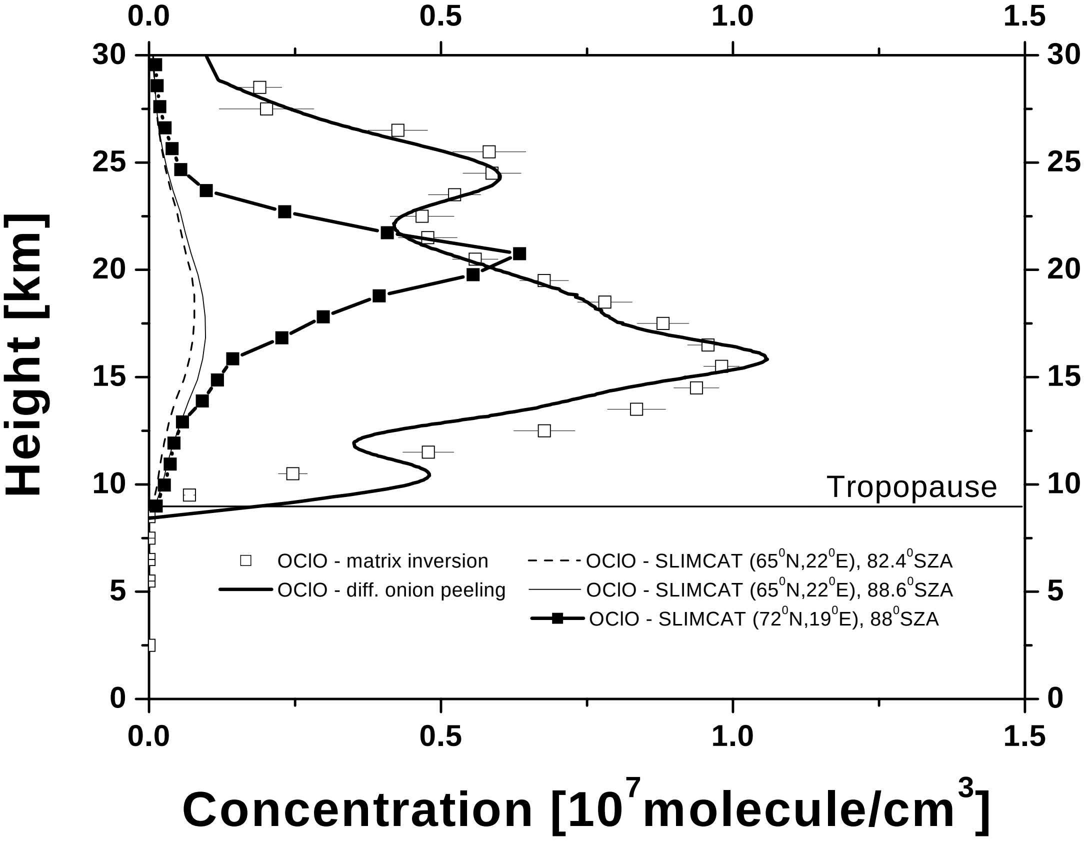

Figure 4.48: *OClO* concentration profile comparison with SLIMCAT profiles for different grid points and different SZAs. The measured profile corresponds to a SZA range of 82.5 − 88.5^o. The total atmospheric *OClO* VCD determined is 1.3 10^{13} molecule/cm^2

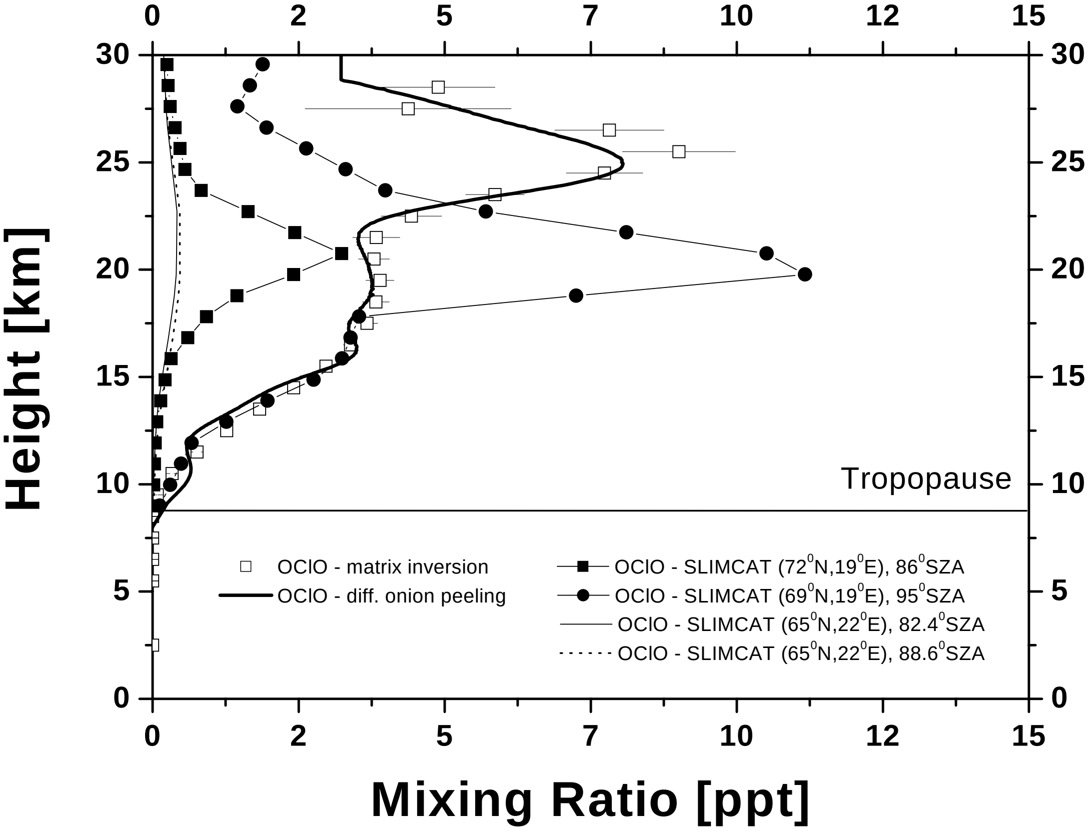

Figure 4.49: *OClO* mixing ratio profile comparison with SLIMCAT profiles for different grid points and different SZAs. The measured profile corresponds to a SZA range of 82.5 − 88.5^o.

$(1.3 \pm 0.5) \times 10^{13}$ molecule/cm^2 for $\approx 85^o$ SZA. In the $OClO$ map a strong chlorine activation in the inner vortex can be seen, while the values at the vortex boundary are much smaller. The estimated GOME $OClO$ AMF for 80-85^o is 6-8, so that vortex boundary SCDs of $(2\pm1)\times10^{13}$ molecule/cm^2 result in a VCD of $(0.2 - 0.5) \times 10^{13}$ molecule/cm^2, which deviates not too much from the measured VCD from balloon - especially when taking account of the assumptions made about the profile when calculating the GOME AMF [Wagner 1999].

4.2.3 O_3 profile model comparison

Another interesting check of the model is the comparison of the O_3 profiles, which should depend strongly on the model grid point position relative to the vortex boundary. Figure 4.50 shows the O_3 profiles measured by our DOAS balloon instrument and the ozone sonde launched from Sodankyla $(67.4N, 26.7E)$ at 7:00 UT on the same day. Also the model profiles for two grid points are shown in this plot - one nearest to the trajectory of the balloon $(65N, 19E)$ and one within the polar vortex $(72N, 19E)$. The in-situ ozone sonde measures even the fine structure of the O_3 profile - the typical height resolution of these sondes is a few metres - while the model and the remote sensing method DOAS averages the profiles over a large area. The agreement between DOAS and the model is good, while the point measurement of the ozone sonde shows a smaller maximum. Still the model overestimates the O_3 profile maximum around 25km - in comparison with the ascent as well as the occultation profile. For O_3 it is possible to retrieve profiles by inversion even in occultation, because the photochemical change of O_3 is negligible.

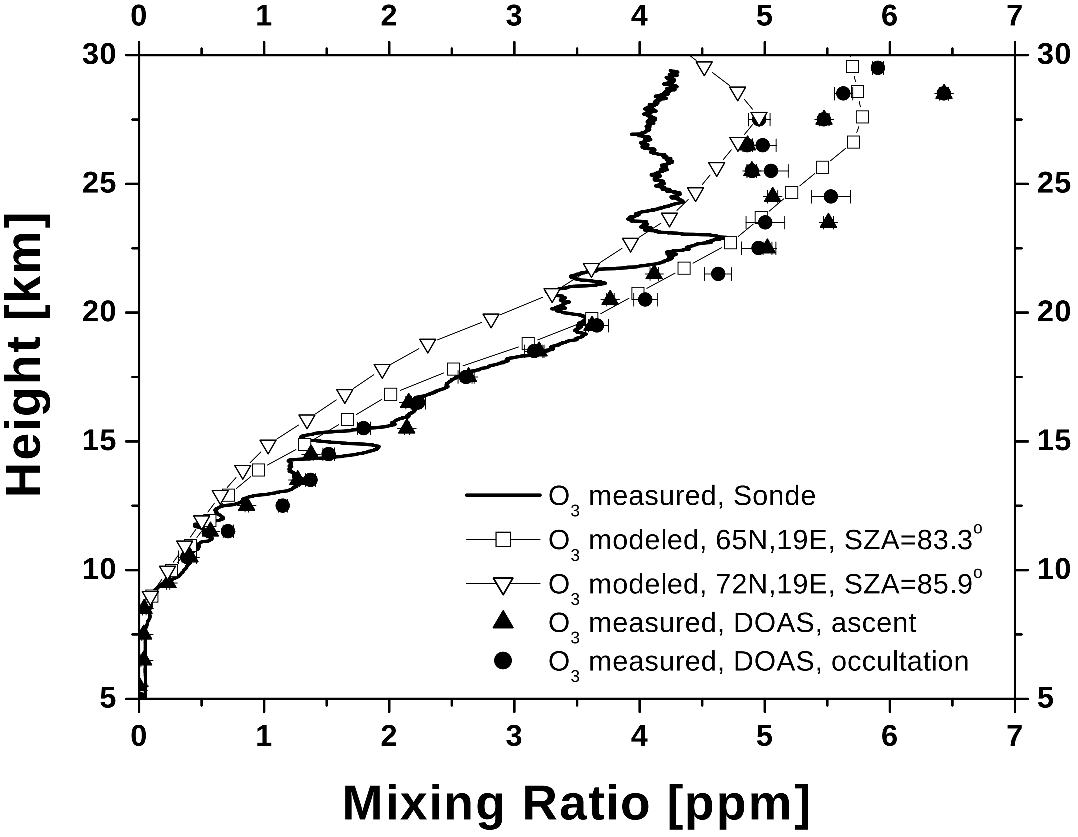

Figure 4.50: O_3 mixing ratio profile comparison with Ozone sonde/SLIMCAT profiles. The O_3 profile was retrieved from the spectra of the VIS spectrograph in the 550-620 nm wavelength region [Harder 1999; Bösch et al. 1999], where the temperature dependence of the absorption cross section is small compared to the UV.

4.2.4 NO_2 profile model comparison

Figure 4.51 show the comparison of measured and modelled NO_2 profiles. The NO_2 profiles measured by the LPMA instrument, the DOAS instrument and another satellite instrument (**ILAS**[4]) are displayed here. The campaign in Kiruna was within the **ADEOS/ILAS** validation balloon campaign [Kanzawa et al. 1997]. The agreement between the LPMA/DOAS measurements is quite good and also the modelled profiles fit well. The discrepancies around the maximum of the profile are difficult to interpret, because in the case of NO_2 the measurements took all place with the instruments being below the profile maximum. The ILAS profile data have very big error bars and agree within these error bars with the balloon measurements.

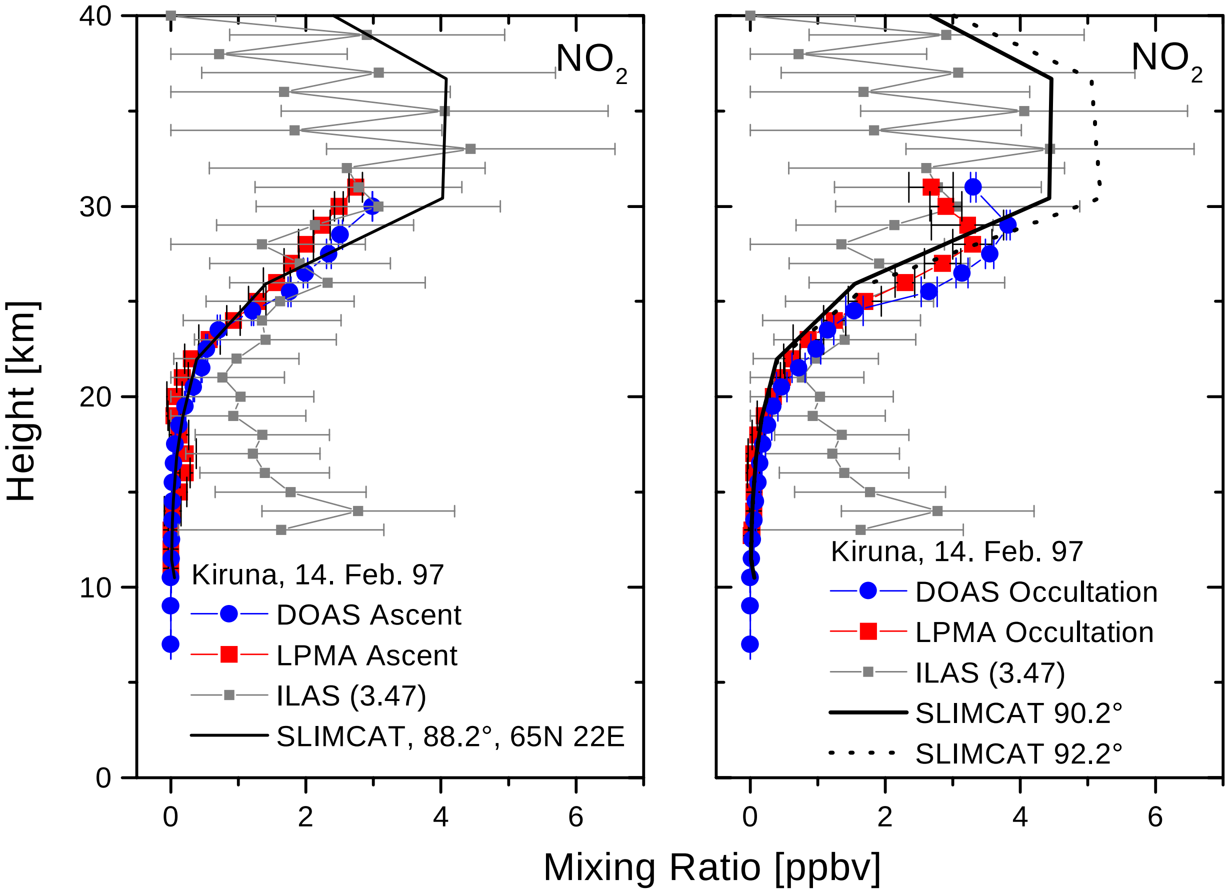

Figure 4.51: Measured NO_2 mixing ratio profile comparison with SLIMCAT profiles and ILAS data. The NO_2 profile was retrieved from the spectra of the VIS spectrograph in the 550-620 nm wavelength region [Schneider 1997; Harder 1999; Bösch et al. 1999], where the temperature dependence of the absorption cross section is small compared to the UV.

The NO_2 profiles are about a factor of 2 smaller than the ones measured during the first flight at mid-latitudes and this can be explained by the lack of actinic flux, which leads to enhanced formation of N_2O_5 and less photolytic production of NO_2. The N_2O_5 can react again to HNO_3 by hydrolysis on the stratospheric aerosol or on PSC particles, which is especially important when temperatures are low enough to decrease the thermal decay of N_2O_5 - leading to denoxification.

---

[4] **ILAS**: Improved Limb Atmospheric Spectrometer, a japanese solar occultation infrared satellite sensor, which was launched in August 1996 and operated until June 1997.

4.2.5 Summary of the model comparison

As can be seen in the trajectory plot at the beginning of this section, the airmasses probed by the balloon instrument during this flight were very heterogeneous concerning potential vorticity and temperatures. That is why it is not easy to compare the different measured species to the 3-D model SLIMCAT, which has a very rough spatial resolution of $7.5x7.5^o$ using synoptic scale meteorological data. The model is not able to see the fine structure of the vortex boundary, which cannot only be seen in the $OClO$ measurements showing chlorine activation, but also in the HCl measurements of LPMA - see Figure 4.52.

The ascent profile of HCl is pertaining to inside vortex - see Figure 4.52. There is a dip around 20 km indicating a depletion of HCl through heterogeneous reactions during the previous days along the trajectory of the air parcel probed during the ascent measurements [Pfeilsticker 1999; Payan et al. 1998]. The SLIMCAT model produces a quite different profile, which is smaller than the measured profile in the middle stratosphere. It also sees the dip in the 20 km altitude region denoting 300-500 ppt of chlorine activation.

The profile of N_2O is shown in Figure 4.53 together with the respective SLIMCAT profile. The agreement is rather good indicating that the diabatic descent of the airmasses in the polar vortex is properly modelled for this flight - there are situations when this is not true, see the next sections. So this error possibility can be ruled out when searching for the reason for the observed chlorine activation at the edge of the vortex.

4.3 The sunrise flight at Gap on June 20, 1997

The next flight was a sunrise flight at mid-latitudes starting from Gap(France) on June 20, 1997. In Figure 4.54 you can see the trajectory of the balloon and the directions of the line of sight during the flight. While the balloon is moving to the west the line of sight direction changes from north-east to east. During the sunrise the tangent points of the light rays are moving away from the balloon. As we are in summer at mid-latitudes, we encounter a quite homogeneous pattern of stratospheric air streams, which are flowing to the west.

In Figure 4.55 you can see the balloon height as a function of time as well as the SZA at the balloon position. As the balloon is flying in westerly direction the SZA is decreasing more slowly than it would if the position of the balloon was fixed.

The balloon remained at approximately the same altitude when the sun was rising. After the sunrise the valve of the balloon was opened to release some of the hydrogen to make the balloon sink. Unfortunately the balloon decreased only to an altitude of 31 km before the measurements had to be stopped because of security reasons above western France, so that it was not possible to retrieve profiles of BrO from the descent measurements. Still it is interesting to examine the occultation SCDs and to compare them again to modelled SCDs.

Figure 4.56 shows a typical DOAS evaluation for that flight. Here it was not possible to fix the reference spectra data set by fitting it to a spectrum with strong absorptions - e.g. an occultation spectrum at the beginning of the measurements. Instead it was necessary to fix the BrO reference wavelength alignment by shifting the León 96 BrO reference by the wavelength shift observed between these two flights ($\delta\lambda \approx$0.1 nm). The shift between the two flights can be determined by comparing the slit function position or the Fraunhofer spectra.

The spectral residuals are larger during this flight because of the lower Signal-To-Noise ratio, which is a result of the observation geometry. Even at the beginning of the measurements, the BrO SCDs remain at least a factor of 2 smaller than in the occultation for example during the first flight at León. The reason for that is mainly the height of the balloon - this becomes very clear when looking at Figure 4.66, because the light rays are not passing the maximum layer of the BrO profile during the day.

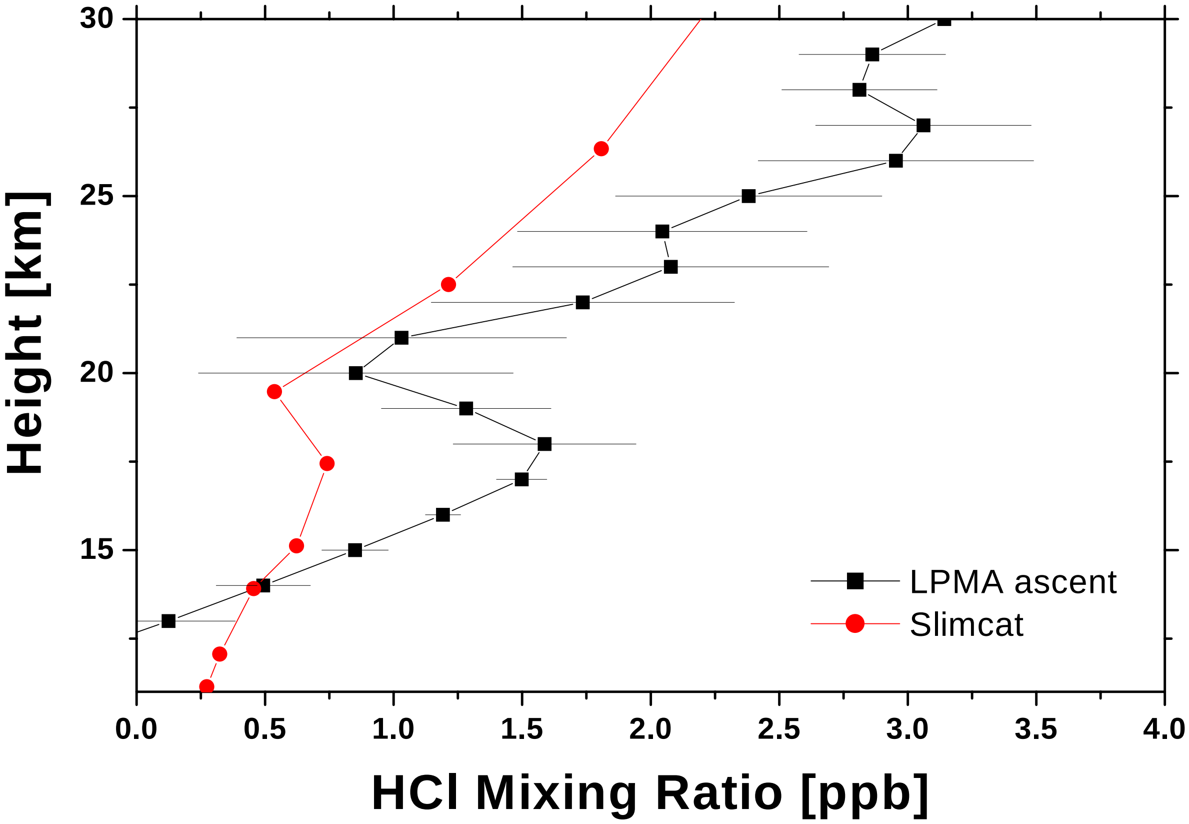

Figure 4.52: HCl comparison between LPMA measurements and SLIMCAT model. The LPMA instrument sees a dip around 20 km indicating depletion of HCl through heterogeneous reactions [Payan et al. 1998].

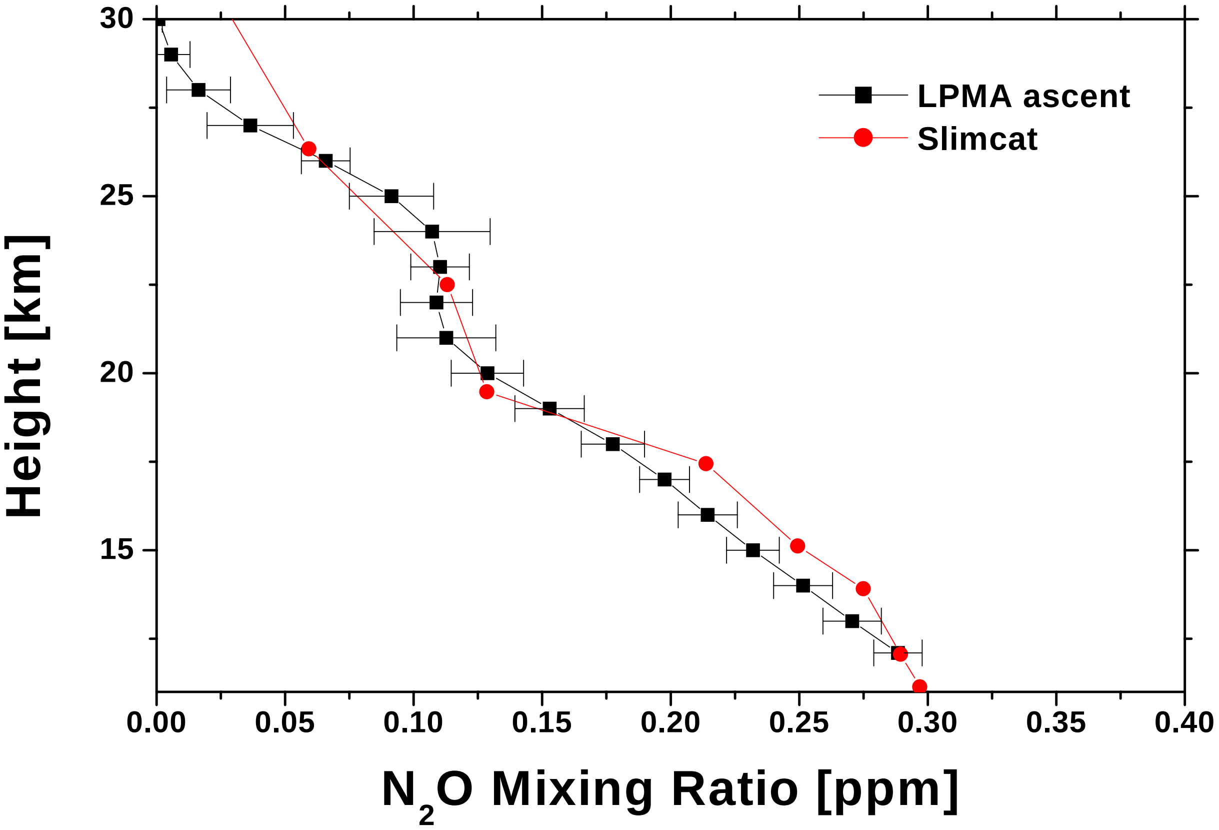

Figure 4.53: N_2O comparison between LPMA measurements and SLIMCAT model. Adapted from [Pfeilsticker 1999].

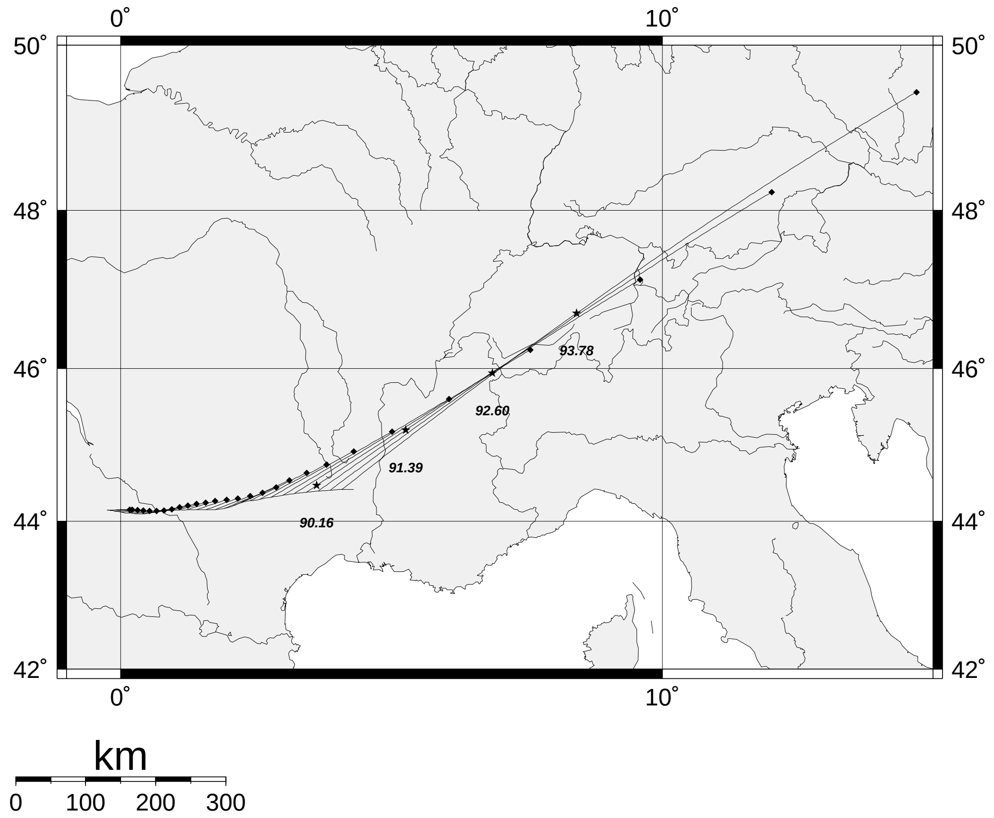

Figure 4.54: Balloon trajectory during the flight at Gap(France) on June 20, 1997. The trajectory is the curved line towards the west, while the lines ending with a point denote the light rays and the end points show the location of the tangent points - that is the main area of atmospheric absorption.

As the balloon instrument started the measurements in occultation and the SZA is decreasing with time the SCD time evolution looks inverse in comparison with the evolution for the first two sunset flights. All SCDs are first decreasing until the descent of the balloon is initiated; then some of the SCDs are increasing slightly again, especially the ones belonging to species whose profile maximum is just below the float altitude of the balloon, e.g. NO_2 and O_3. BrO SCDs are not increasing significantly during the descent, as the BrO maximum is not passed and the small increase because of the descent is compensated by the decrease of the SZA reducing the AMFs.

The Langley plot technique is here again used to determine the SCD offset amount in the Fraunhofer reference spectrum, which was in Gap taken at a height of 37 km and a SZA of 70^o. That is why the expected SCD offset is much smaller than in the case of the first two flights. Figure 4.57 shows the Langley plot for BrO. The mixing ratio determined for the airmasses above the float is (16.4 ± 2.5) ppt and the SCD offset $(6 \pm 5) \times 10^{12}$ molecule/cm^2, which is almost the detection limit of the BrO SCDs $(5.0 \times 10^{12}$ molecule/cm$^2)$.

4.3.1 BrO profile and SCD model comparison

When we compare our observation geometry with the photochemical model concentration field - as shown in Figure 4.66 - it becomes very clear that we were during that flight only able to probe the model field boundaries. Still the special situation about that flight is that we were probing the sunrise photochemical field, and this is very interesting for BrO, whose time evolution is not symmetric with respect to SZA. BrO is expected to be mostly converted to $BrONO_2$ during sunset, so that heterogeneous conversion of bromine nitrate can than make $HOBr$ the predominant source of BrO in

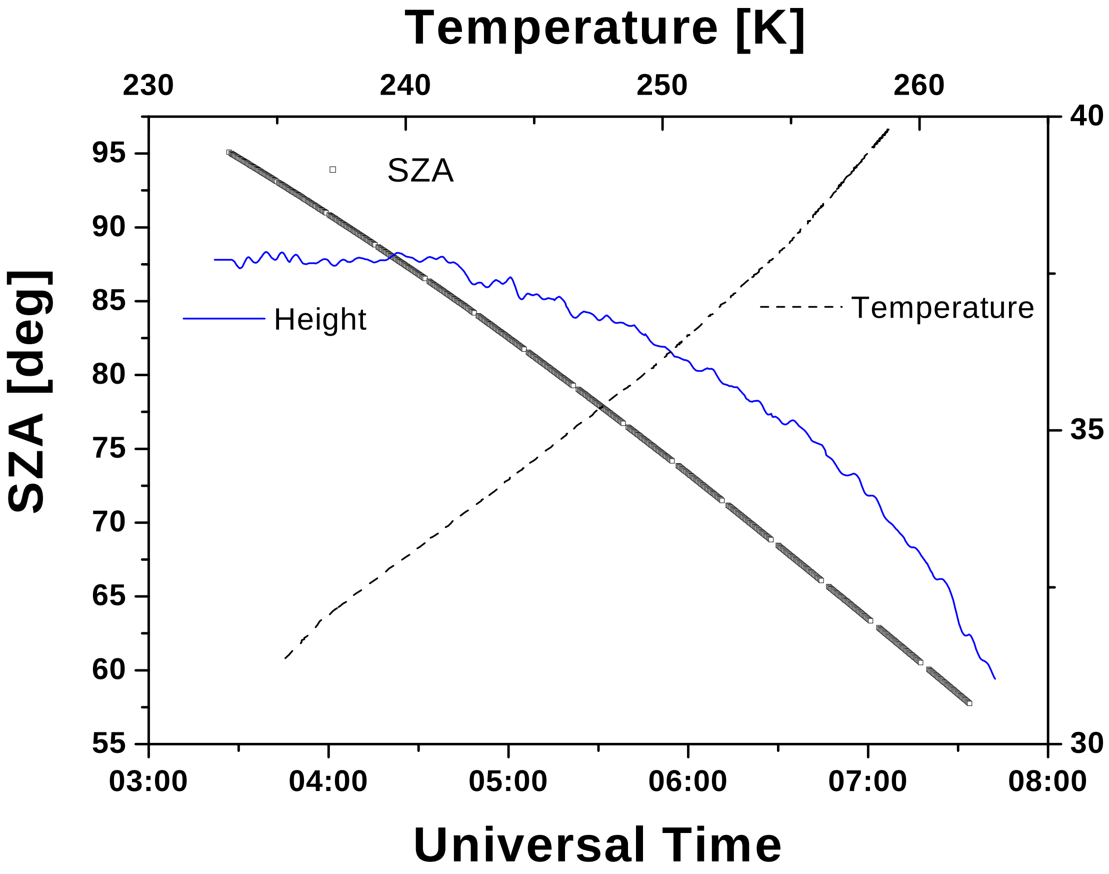

Figure 4.55: Balloon trajectory, temperature and SZA at balloon position (latitude, longitude) during the flight at Gap(France) on June 20, 1997.

the morning. As the photolysis of $HOBr$ is faster than the one of $BrONO_2$, the dawn BrO is released faster than it is taken up at dusk.

First a comparison of modelled profiles for different SZAs and the measured profile will be shown, which was retrieved by matrix inversion - differential onion peeling is not possible for the observation geometry of that flight. For the matrix inversion measured SCDs for SZAs between $85-95^o$ were used, so that the resulting profile is only an average of the different SZA dependent instantaneous profiles seen in the light path.

From the profile comparison it becomes clear that during the sunrise/occultation the balloon instrument does predominantly see the lower part of profiles belonging to large SZAs ($\approx 90^o$) and the upper part of all profiles for a large range of SZAs. Hence, the lower part of the measured profile is determined by small profile values at large SZAs. This and the photochemical change of BrO are the reasons, why the position of the maximum in the measured and modelled profile differ as much as observed.
From that point of view it is best to check the model by calculating modelled SCDs from the SLIMCAT model field. The comparison of the time evolution of the measured and modelled BrO SCDs is shown in Figure 4.69.
There is a strong discrepancy between the model and the measurements at the beginning of the measurements. This gap closes during the course of the flight - especially when taking into account the error bars of the measurements.
The correlation plot between the modelled and measured BrO SCDs - see Figure 4.70 - shows the model-measurement correlation for model runs with total inorganic Br_y of 17, 20 and 23 ppt. In the occultation the model tends to underestimate the SCDs, whereas the agreement is better in the float

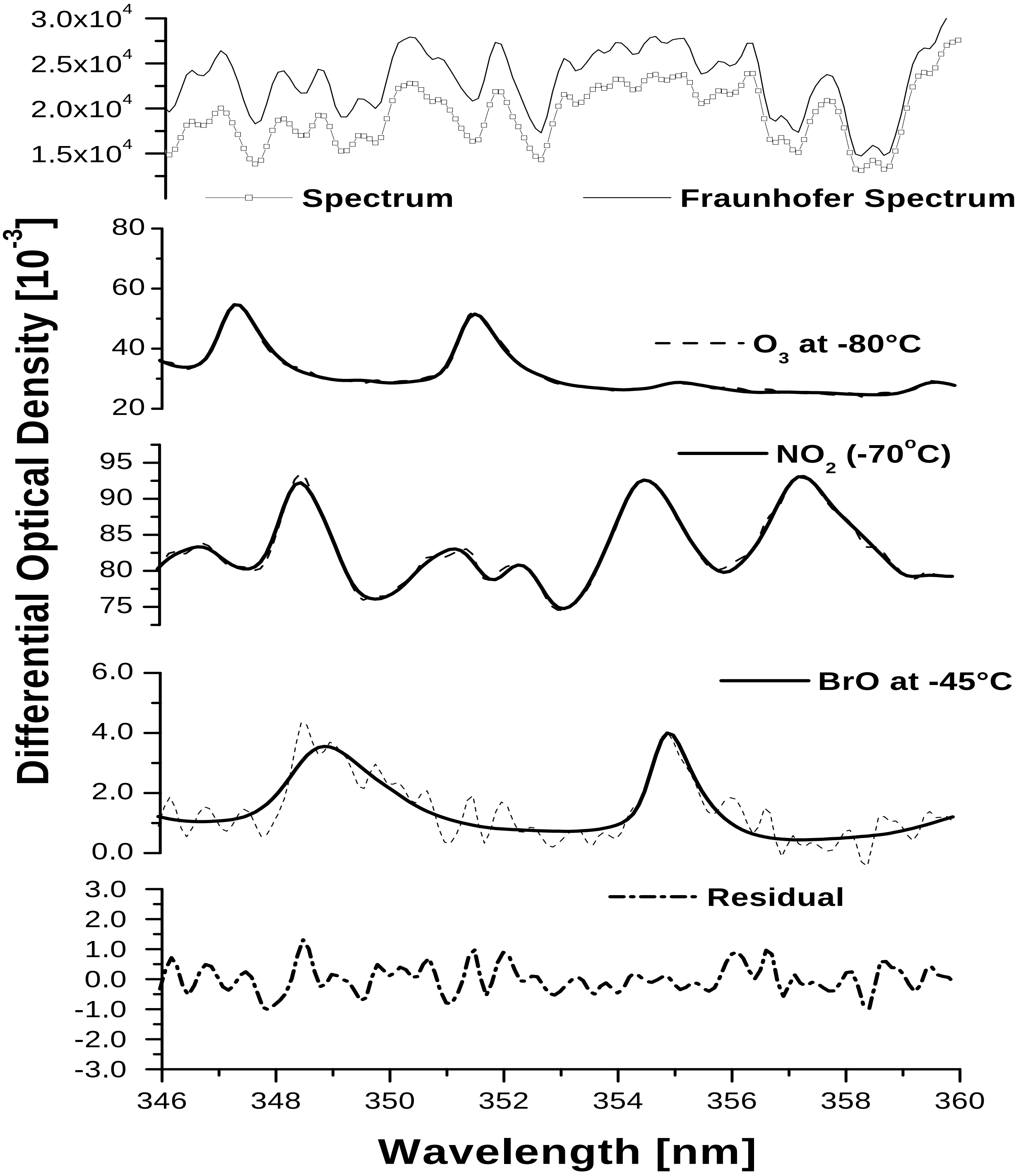

Figure 4.56: Typical DOAS evaluation in the BrO retrieval wavelength range (346-360 nm) for Gap 1997. The fit included O_3 at -80^oC and -20^oC(not shown), NO_2 at -70^oC, O_4(not shown), BrO at -45^oC and a polynomial of degree 3. The last spectrum is the residual of the fit which cannot be explained by the fit but is due partly to statistical noise and to systematic errors. All spectra have been filtered with a binomial filter of degree 1 before the fit.

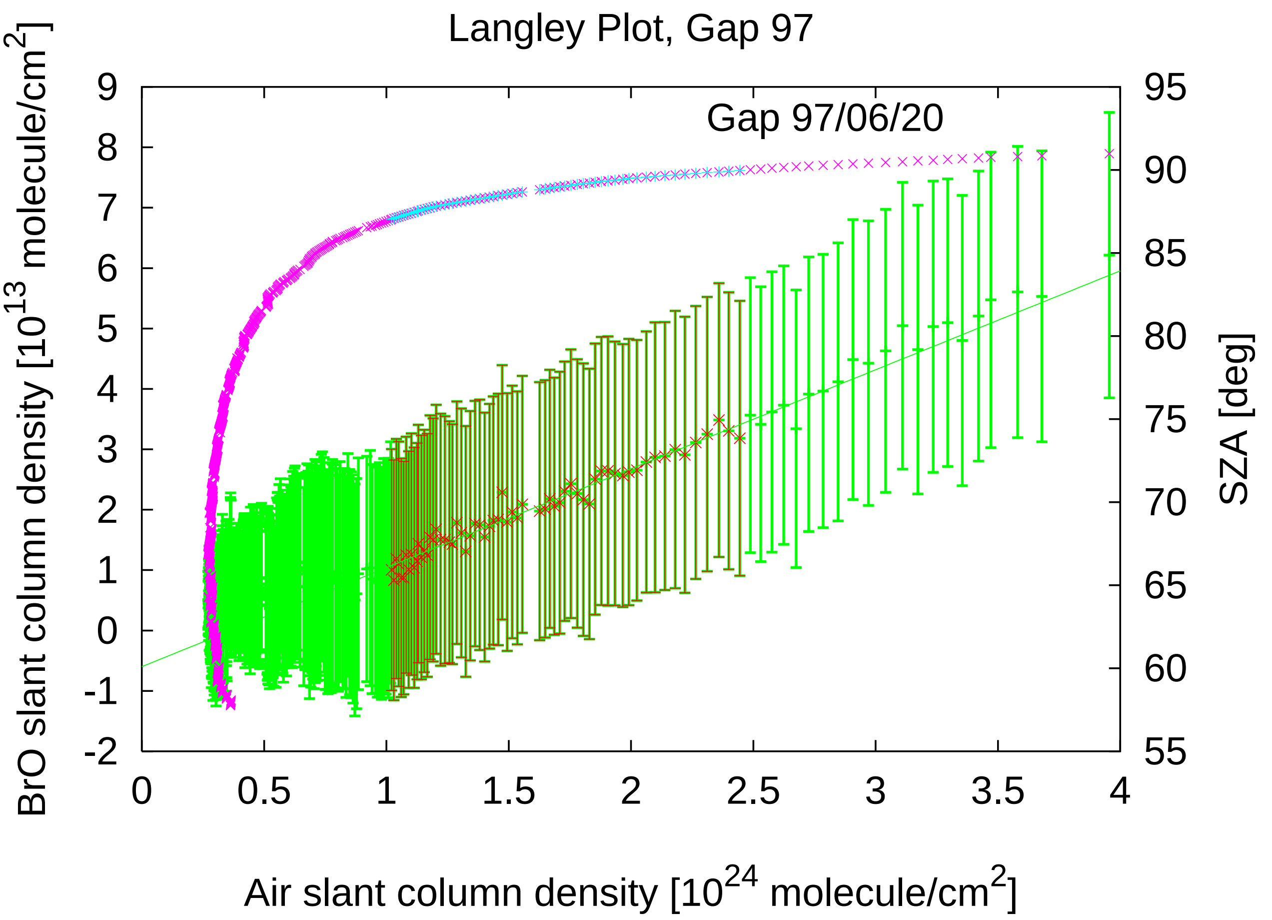

Figure 4.57: Langley plot for the flight at Gap using the float SCDs for SZAs between 87^o and 90.0^o. The Fraunhofer reference spectrum was measured at a balloon height of $37km$ and a SZA of 70^o. The resulting SCD offset is $(6 \pm 5) \times 10^{12}$ molecule/cm^2 and the mean mixing ratio above float (16.4 ± 2.5) ppt.

and descent part of the flight. Still it is important to notice that the SCDs measured at the end of the flight begin to scatter significantly around the detection limit.

The underestimation of the dawn BrO SCDs could be explained by a too slow release of BrO from its nighttime reservoir species (mainly $HOBr$). This was also proposed by [Friess et al. 1999], who recognized a large discrepancy between modelled and measured SCD evolution at 'high NO_2' days and dawn, while the comparison for the dusk SCDs was fine.

Despite the discrepancies it is possible to derive from this SCD comparison - mainly taking into account the float and descent SCDs - an estimate of total inorganic bromine of 20 ± 2.5 ppt, as observed in León 96 and Kiruna 97.

For this flight it was not possible to make a VCD comparison with the satellite instrument GOME, as the observation geometry did not allow the non-ambiguous derivation of a BrO profile.

4.4 The sunset flight at León on March 19, 1998

The following flight was a spring sunset flight again at mid-latitudes starting from León(Spain) on March 19, 1998. In Figure 4.71 you can see the trajectory of the balloon and the directions of the line of sight during the flight. While the balloon is moving to the east the line of sight direction changes

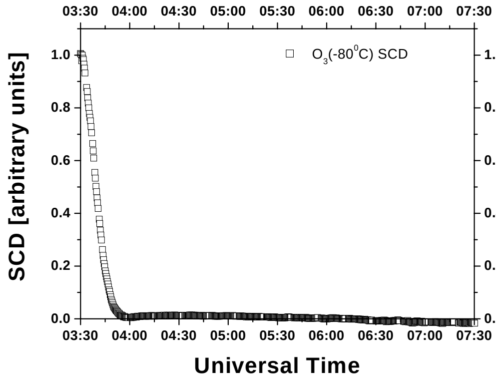

Figure 4.58: Time evolution of the $O_3(-80^oC)$ SCDs during the flight.

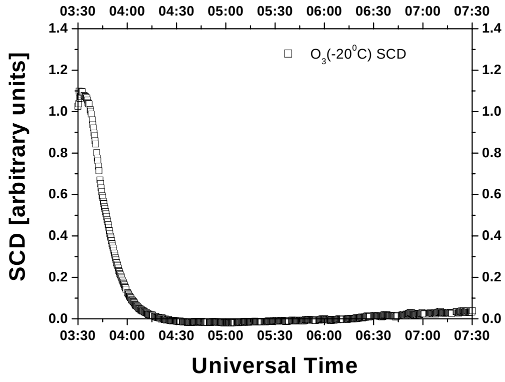

Figure 4.59: Time evolution of the $O_3(-20^oC)$ SCDs during the flight.

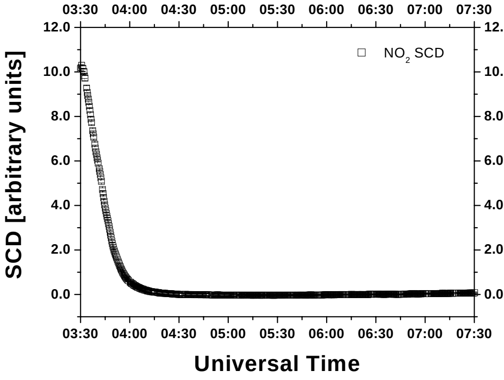

Figure 4.60: Time evolution of the $NO_2(-70^oC)$ SCDs during the flight.

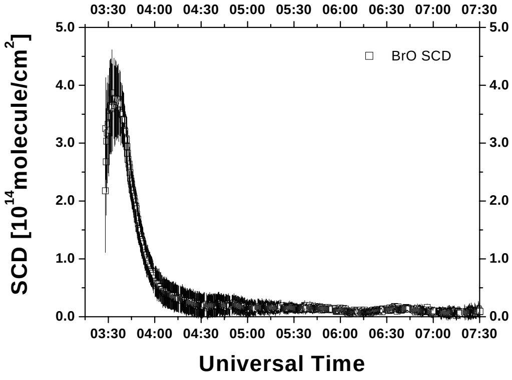

Figure 4.61: Time evolution of the $BrO(-45^oC)$ SCDs during the flight.

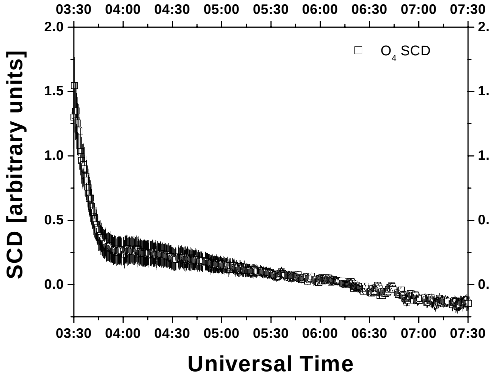

Figure 4.62: Time evolution of the O_4 SCDs during the flight.

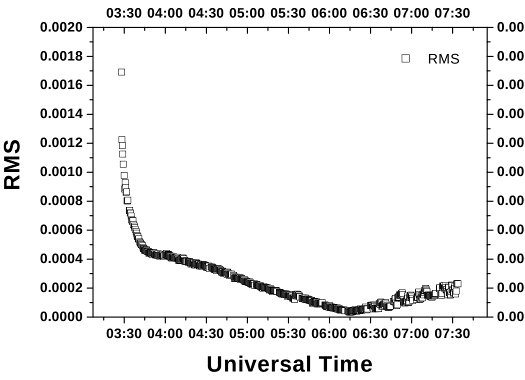

Figure 4.63: Time evolution of the RMS of the DOAS fit during the flight.

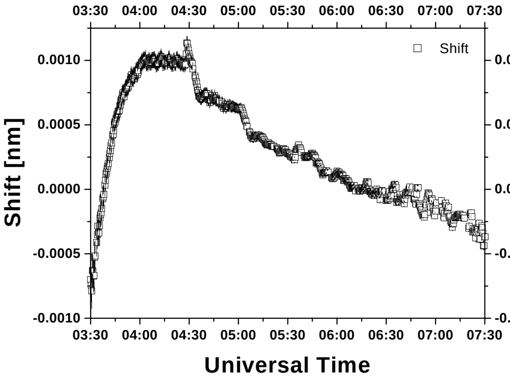

Figure 4.64: Time evolution of the shift of the reference spectra ensemble during the flight.

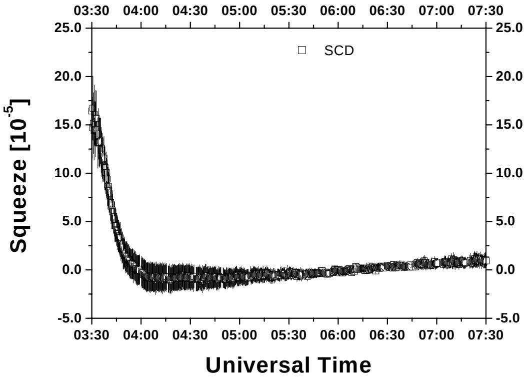

Figure 4.65: Time evolution of the squeeze of the reference spectra ensemble during the flight.

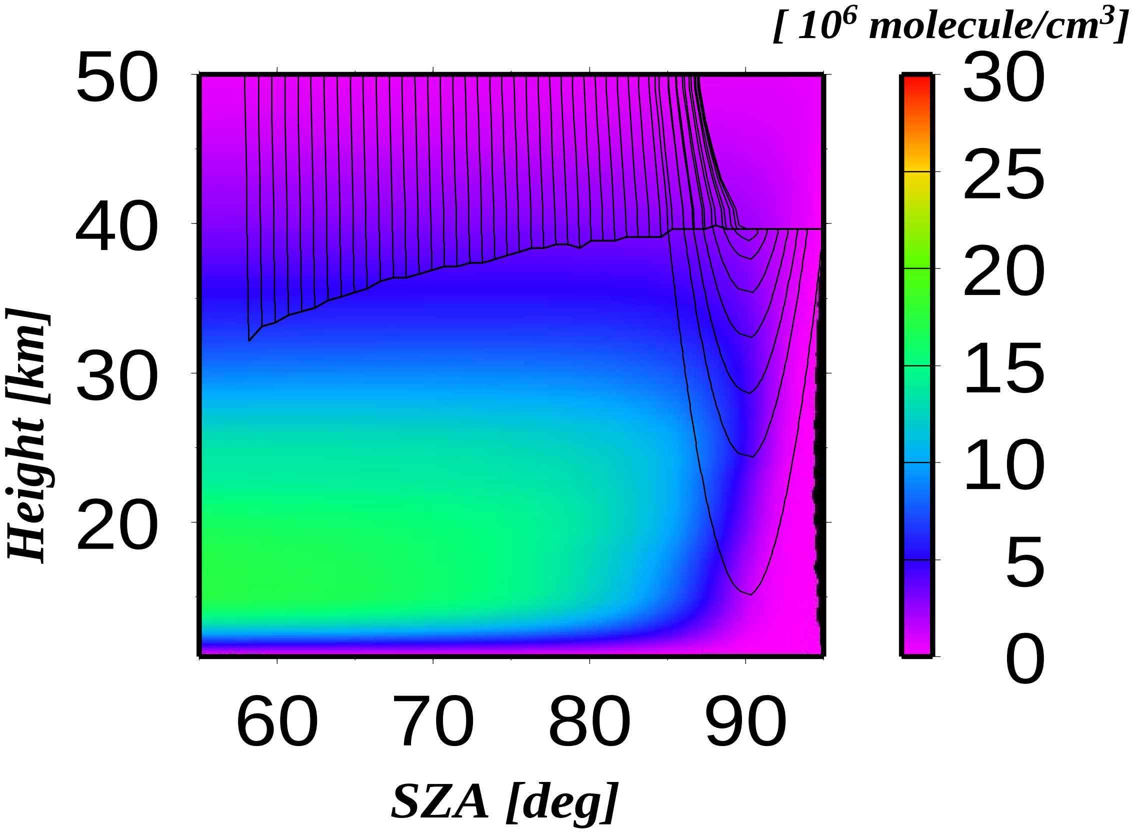

Figure 4.66: Modelling of BrO SCDs by integration of the concentration along the light path through the atmosphere. The model field $(47N, 7E)$ is color-coded as a function of height and SZA. Both the trajectory of the balloon (thick line) and the light rays from the sun (fine lines) reaching the balloon instrument are shown in the plot.

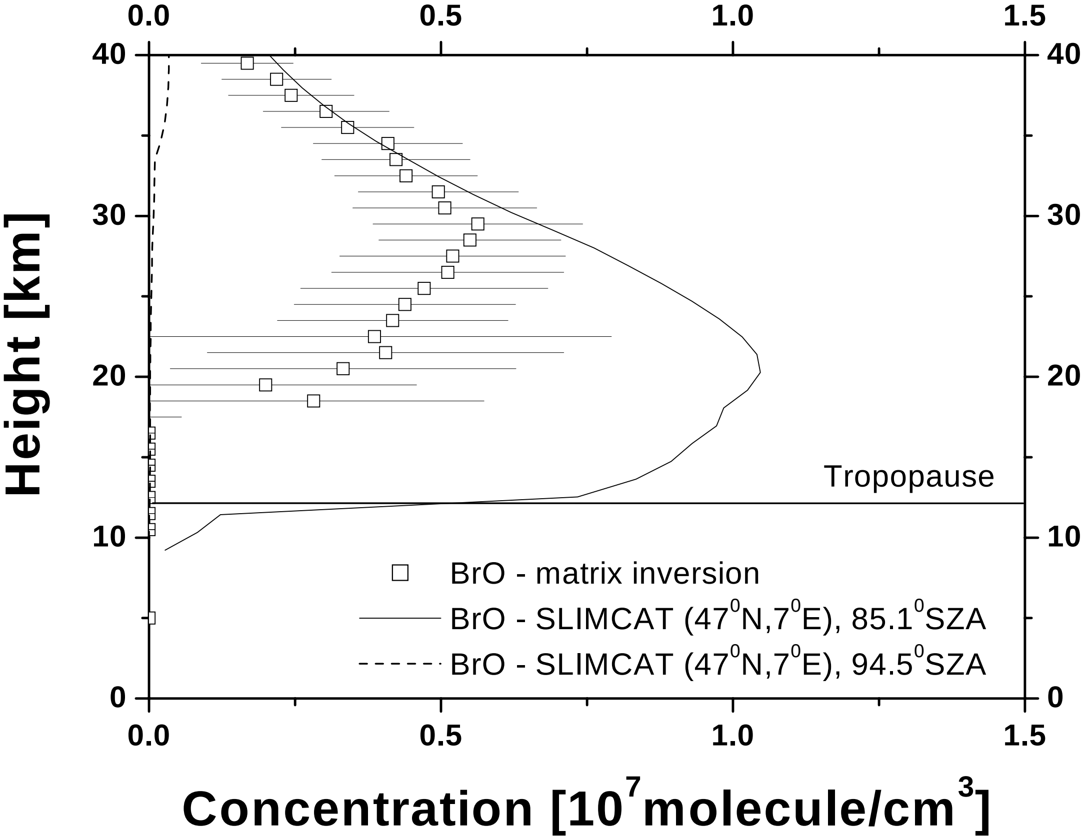

Figure 4.67: BrO concentration profile comparison between with SLIMCAT profiles for different grid points and different SZAs. The measured profile corresponds to a SZA range of $85 - 95^o$.

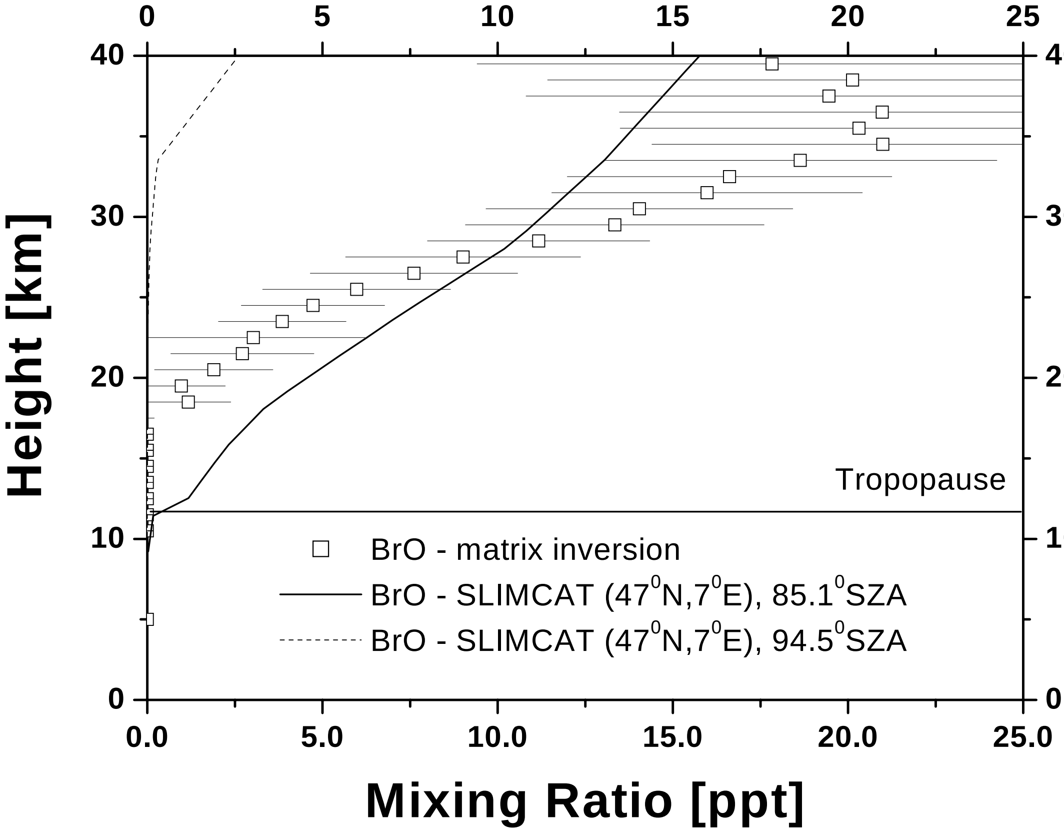

Figure 4.68: *BrO* mixing ratio profile comparison between with SLIMCAT profiles for different grid points and different SZAs. The measured profile corresponds to a SZA range of $85 - 95^o$.

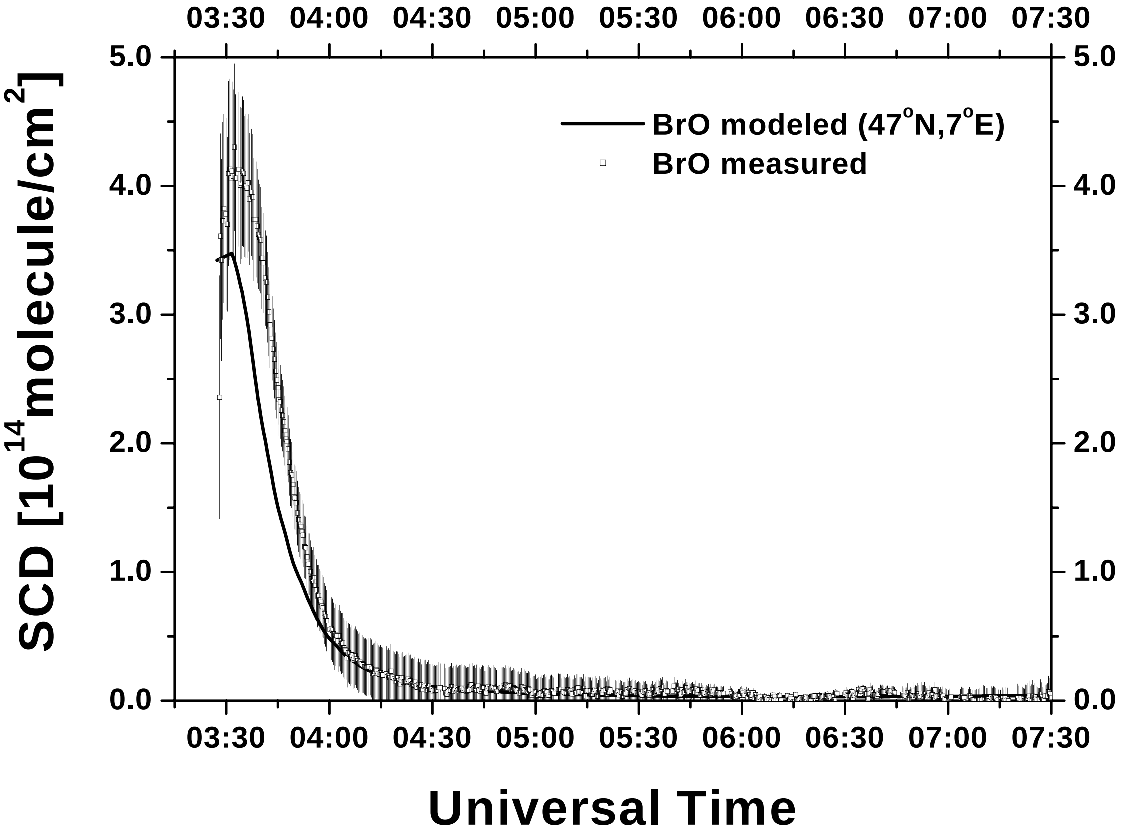

Figure 4.69: Time evolution of measured and modelled *BrO* SCDs for the Gap 97 flight.

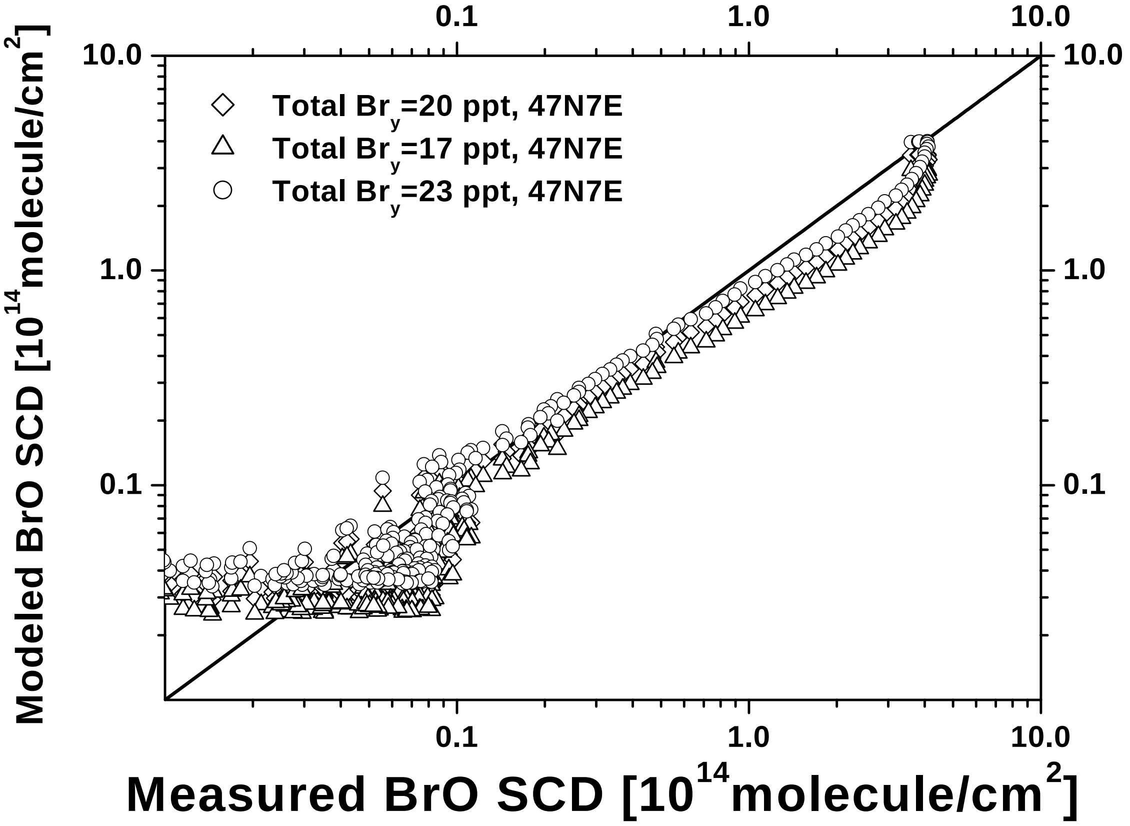

Figure 4.70: Correlation plot of modelled and measured BrO SCDs for the Gap 97 flight. The different model runs ($47N, 7E$) with different total inorganic bromine contents are shown (Br_y = 17, 20 and 23 ppt).

from south to south-west. During the sunset the tangent points of the light rays are moving away from the balloon in westerly direction. As we are in spring at mid-latitudes, we encounter a quite homogeneous pattern of stratospheric air streams, which are flowing to the east. In comparison with the first flight at León, the balloon is moving nearly as fast as one and a half years before, so that the cut point of the balloon is almost at the same location ($\pm 0.1^o$ longitude/latitude).

In Figure 4.72 you can see the balloon height as a function of time as well as the SZA at the balloon position. As the balloon is flying in easterly direction the SZA is decreasing faster than it would if the position of the balloon was fixed.

During this flight the balloon was launched very early because the float altitude aimed at was higher up than in the previous sunset flights (up to 38.5 km). This was also the first time we used an onboard GPS module incorporated in our instrument electronics box, which is able to track the height of the balloon with an accuracy of 100 m and a time resolution of 1 sec. In the former flights the height resolution was about a factor of 2 worse and the sampling rate was only 0.1 Hz.
The potential vorticity map on the $475K$ level shows that there was a vortex at the time of the flight above the Arctic Pole, but it also indicates that there was no influence on the mid-latitudes - e.g. by filaments of the vortex. That is why we expect to see no enhanced BrO concentrations or chlorine activation in the data sets.
The temperatures in the stratosphere are well above the PSC formation threshold and they are nearly constant (215 ± 10 K) around the expected BrO profile maximum. That is why using a 228 K BrO reference spectrum is again a good approximation.
Figure 4.73 shows a typical DOAS evaluation in the standard BrO retrieval range for that flight. The

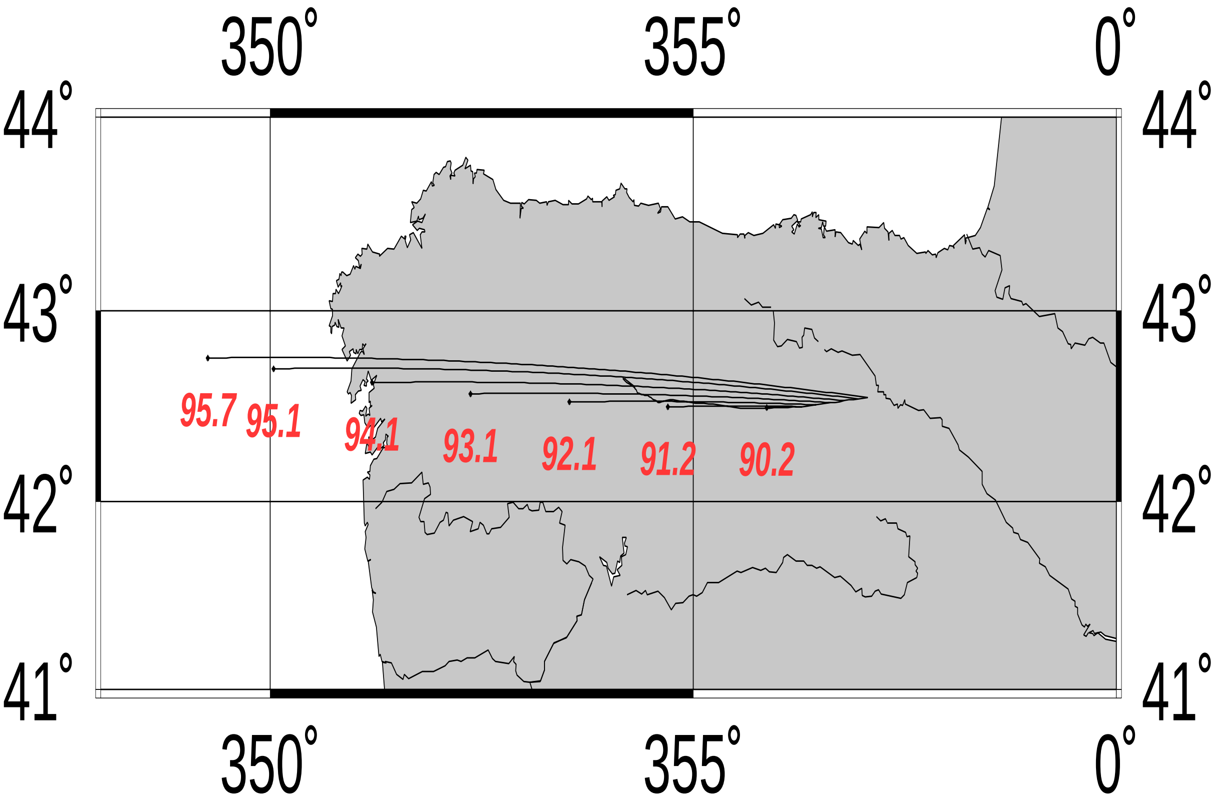

Figure 4.71: Balloon trajectory during the flight at León(Spain) on March 19, 1998. The trajectory is the curved line towards the east, while the lines ending with a point denote the light rays for SZAs larger than 90^o and the end points show the location of the tangent points - that is the main area of atmospheric absorption.

wavelength range chosen includes two BrO absorption lines (346-360 nm).

In Figure 4.74-4.81 the time evolution of all species used in the fitting process is shown for the whole flight. The SCDs of the species show the typical evolution as observed in the sunset flights before. There is a measurement gap between 16:45 and 16:52 UT, when the strong shear winds in the 16-18 km altitude range prevented a proper function of the sun tracking unit. For the profile retrieval it will be necessary to extrapolate the existing data in this altitude range to avoid numerical artifacts in the retrieved profile.

4.4.1 BrO profile and VCD comparison with GOME

Figure 4.82 shows the Langley plot for BrO for that flight. From the Langley plot fit follows a mean mixing ratio of BrO above 39 km float altitude of 11.4 ± 2 ppt and a SCD offset of $(2.0 \pm 0.5) \times 10^{13} \frac{molecule}{cm^2}$. The SZA range used for the fit is $[84, 90]^o$.

From the time evolution plot of the BrO SCDs it is clear that the SCDs are only a factor of 2-4 above the detection limit so that the profile retrieval is more difficult than in the case of the first flight at León, where the measurements started at a SZA of 74^o, while the measurements here began at a SZA of 65^o. The relative small SZAs lead to small airmass factors and in turn to small SCDs. Another technical complication was the measurement gap between 16:45 and 16:52 UT, which has to filled up by extrapolation to reduce numerical artifacts of the matrix inversion or onion peeling.

Still it is possible to retrieve a profile by matrix inversion and by differential onion peeling, which is shown in the Figure 4.83 and 4.84. The ascent profiles retrieved with the matrix inversion and onion peeling technique, as well as an occultation profile retrieved with the matrix inversion are shown in

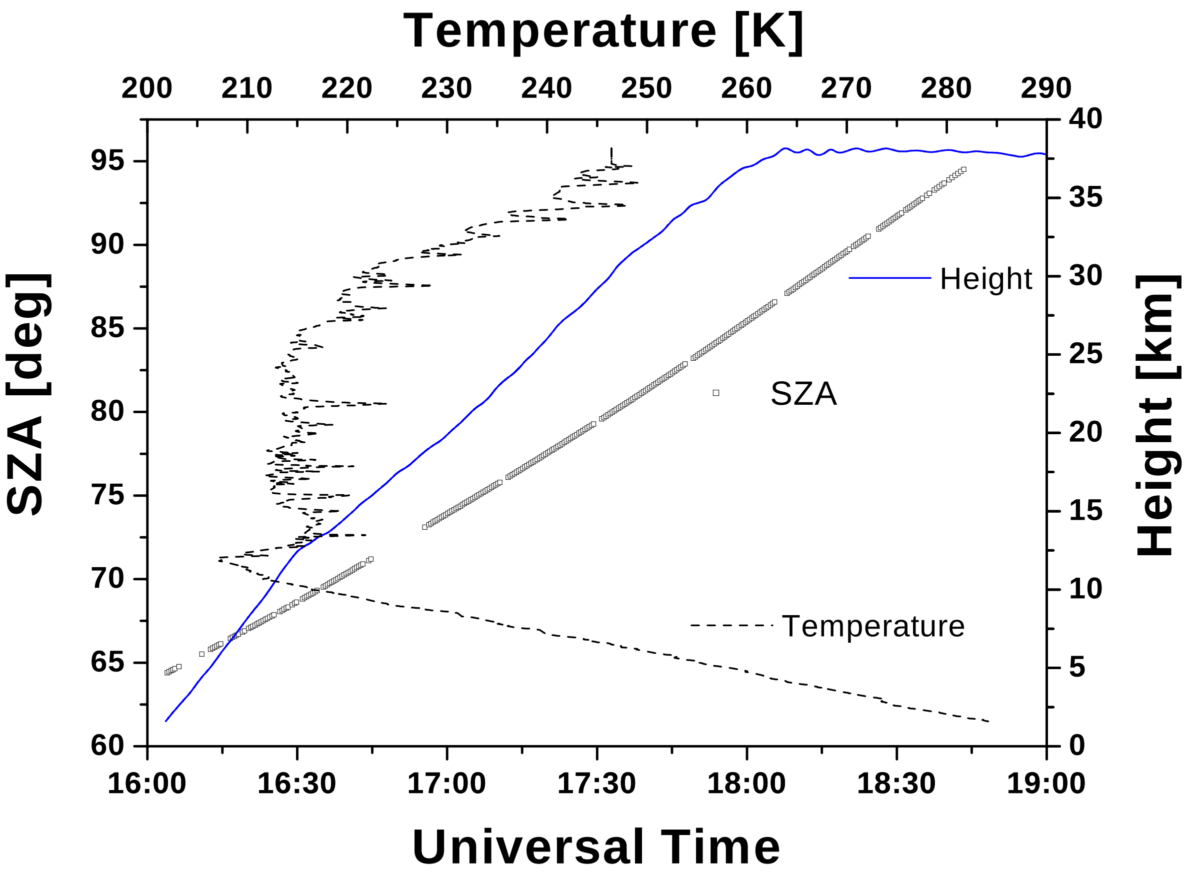

Figure 4.72: Balloon trajectory, temperature and SZA at balloon position (latitude, longitude) during the flight at León(Spain) on March 19, 1998.

these plots.

The BrO profile amounts up to ≈ 12 ppt at maximum, which agrees well with the value determined by the Langley plot method. Although the matrix inversion technique produces artificial oscillations in the retrieved profile, together with the differential onion peeling technique a good approximation of the real profile can be found. The bad Signal-To-Noise ratio - which is ≤ 2 and often even ≤ 1 - is not the only reason for the profile retrieval discrepancies in comparison with the other flights, but the small airmass factors - corresponding to small SZAs - make the Singular Value Decomposition of the matrix inversion nearly impossible, as the large errors even propagate into the profile retrieval, when only the biggest singular values are taken into account. Therefore and because of the fact that for small SZAs the onion peeling technique is most accurate, the onion peeling profile is considered the best approximation of the real profile. The profile values above 35 km are oscillating very much, as there is almost no information in the measured SCDs there. So the scatter there is an artifact.

Using this profile for the determination of the total stratospheric VCD we find a value of $(2.0 \pm 0.5) \times 10^{13}$molecule/cm^2, which we can compare with the total atmospheric VCD of $(4.4 \pm 0.5) \times 10^{13}$molecule/cm^2 measured by GOME for a SZA of 45.5^o. As the stratospheric profile was measured between $65 - 87^o$ SZA and as there is a good agreement between the integrated profile stratospheric VCD and the stratospheric VCD determined from the SCD measurements just above the tropopause again a tropospheric background of $(2.4{\pm}1) \times 10^{13}$molecule/cm^2 can be found. The SCD at tropopause level is $SCD_{tropopause} = (6{\pm}1) \times 10^{13}$molecule/cm^2, the airmass factor $AMF = 2.7$, so that the VCD at tropopause level results in $VCD_{tropopause} = SCD_{tropopause}/AMF = (2.2 \pm 0.25) \times 10^{13}$molecule/cm^2. The photochemical change of the BrO VCD between the two measurements (45.5^o and 70^o SZA)

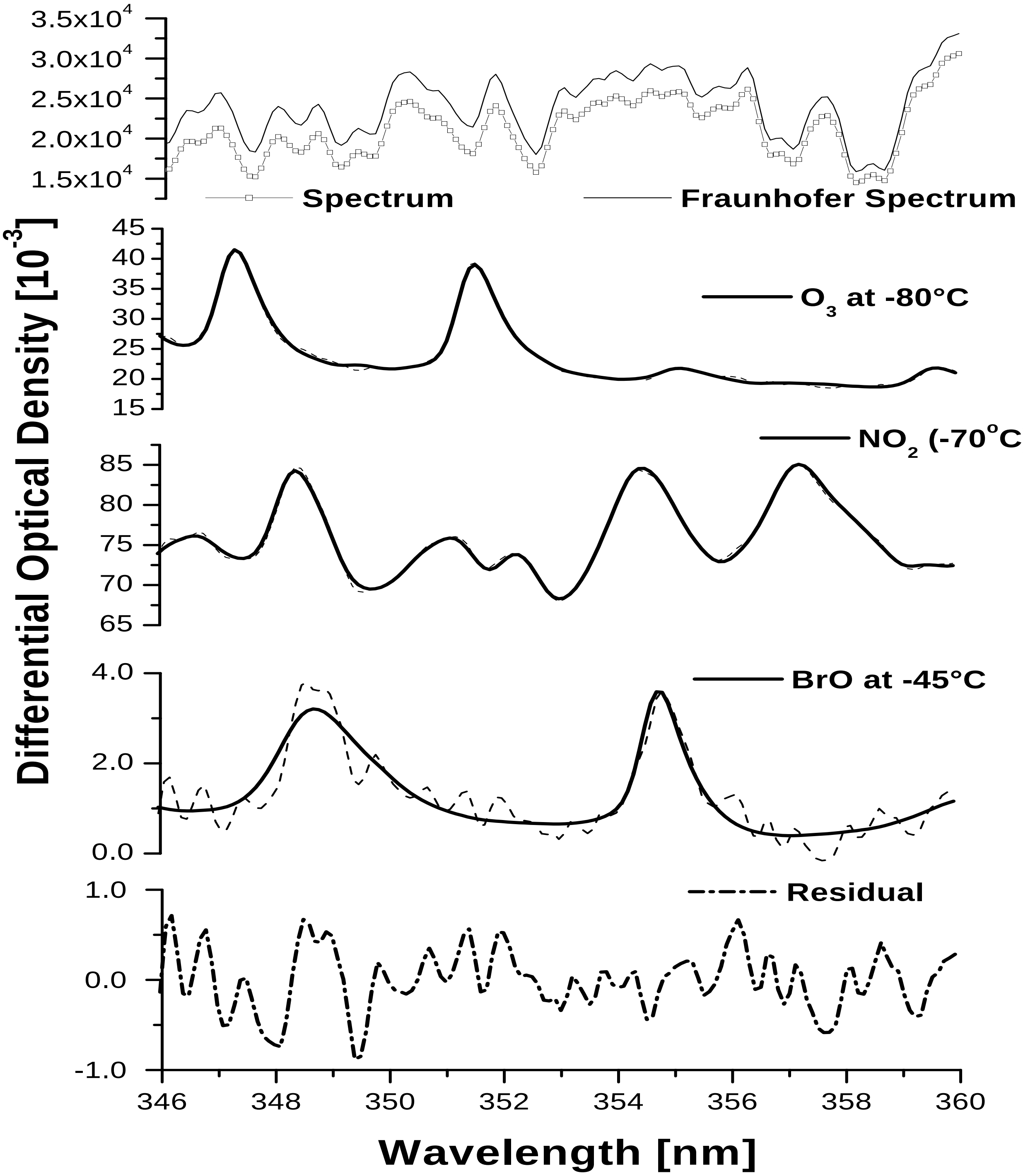

Figure 4.73: Typical DOAS evaluation in the BrO retrieval wavelength range (346-360 nm) for León 1998. The fit included O_3 at -80^oC and -20^oC(not shown), NO_2 at -70^oC, O_4(not shown), BrO at -45^oC and a polynomial of degree 3. The last spectrum is the residual of the fit which cannot be explained by the fit but is due partly to statistical noise and to systematic errors. All spectra have been filtered with a binomial filter of degree 3 before the fit.

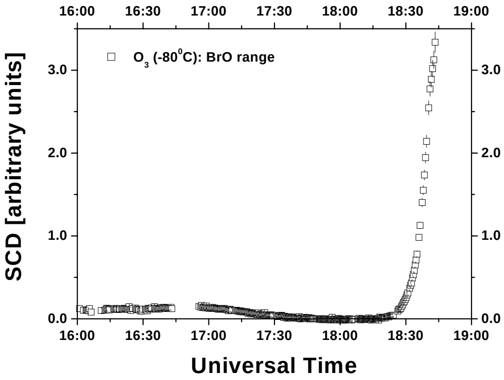

Figure 4.74: Time evolution of the $O_3(-80^oC)$ SCDs during the flight.

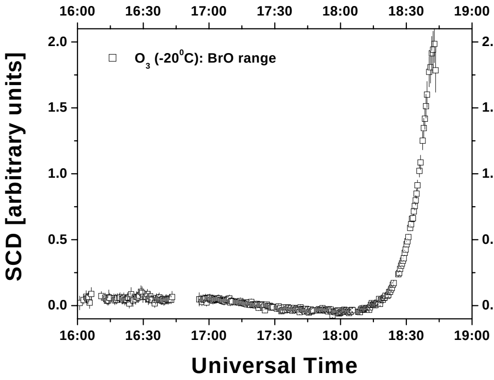

Figure 4.75: Time evolution of the $O_3(-20^oC)$ SCDs during the flight.

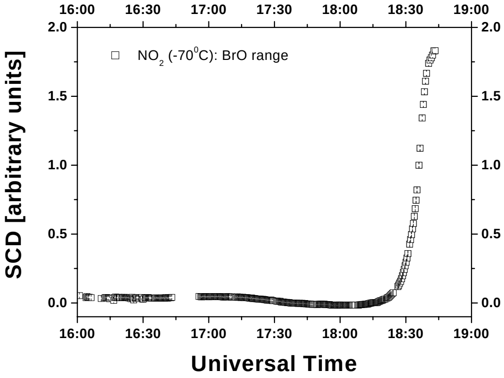

Figure 4.76: Time evolution of the $NO_2(-70^oC)$ SCDs during the flight.

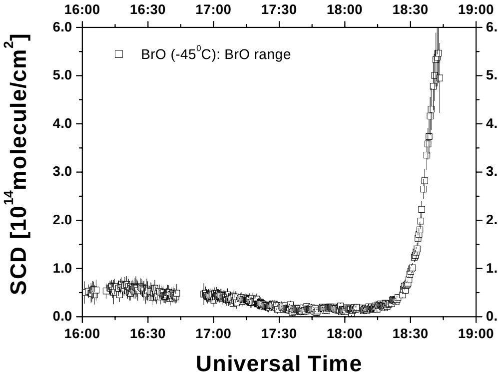

Figure 4.77: Time evolution of the $BrO(-45^oC)$ SCDs during the flight.

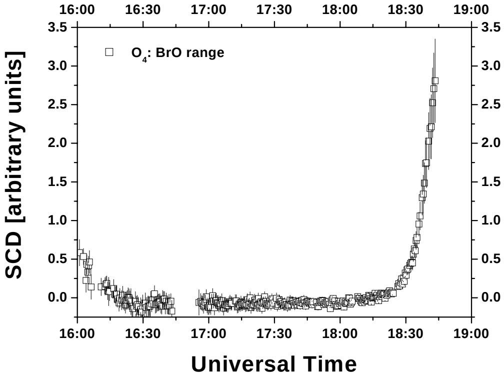

Figure 4.78: Time evolution of the O_4 SCDs during the flight.

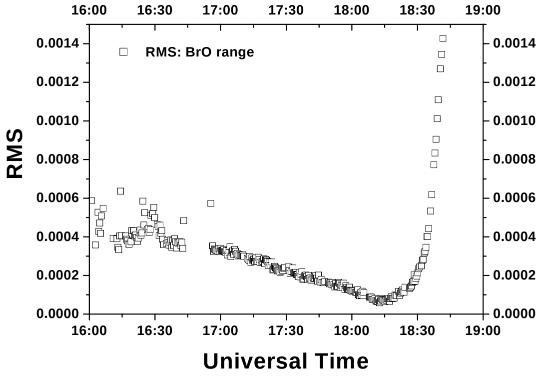

Figure 4.79: Time evolution of the RMS of the DOAS fit during the flight.

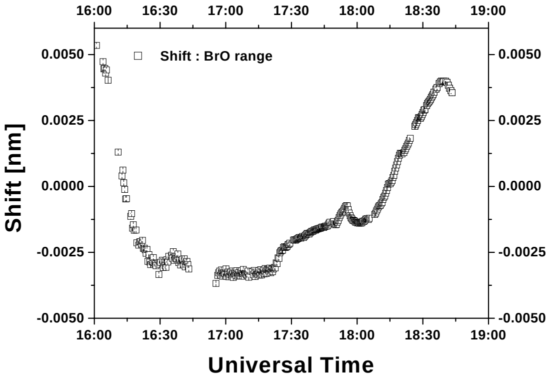

Figure 4.80: Time evolution of the shift of the reference spectra ensemble during the flight.

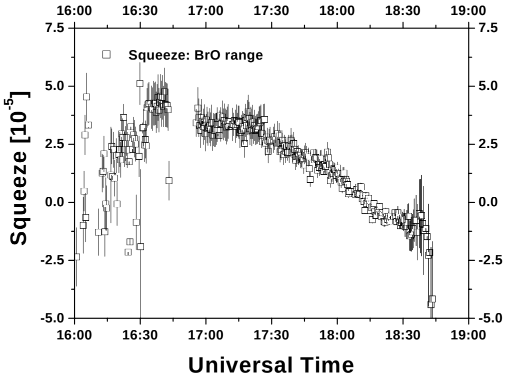

Figure 4.81: Time evolution of the squeeze of the reference spectra ensemble during the flight.

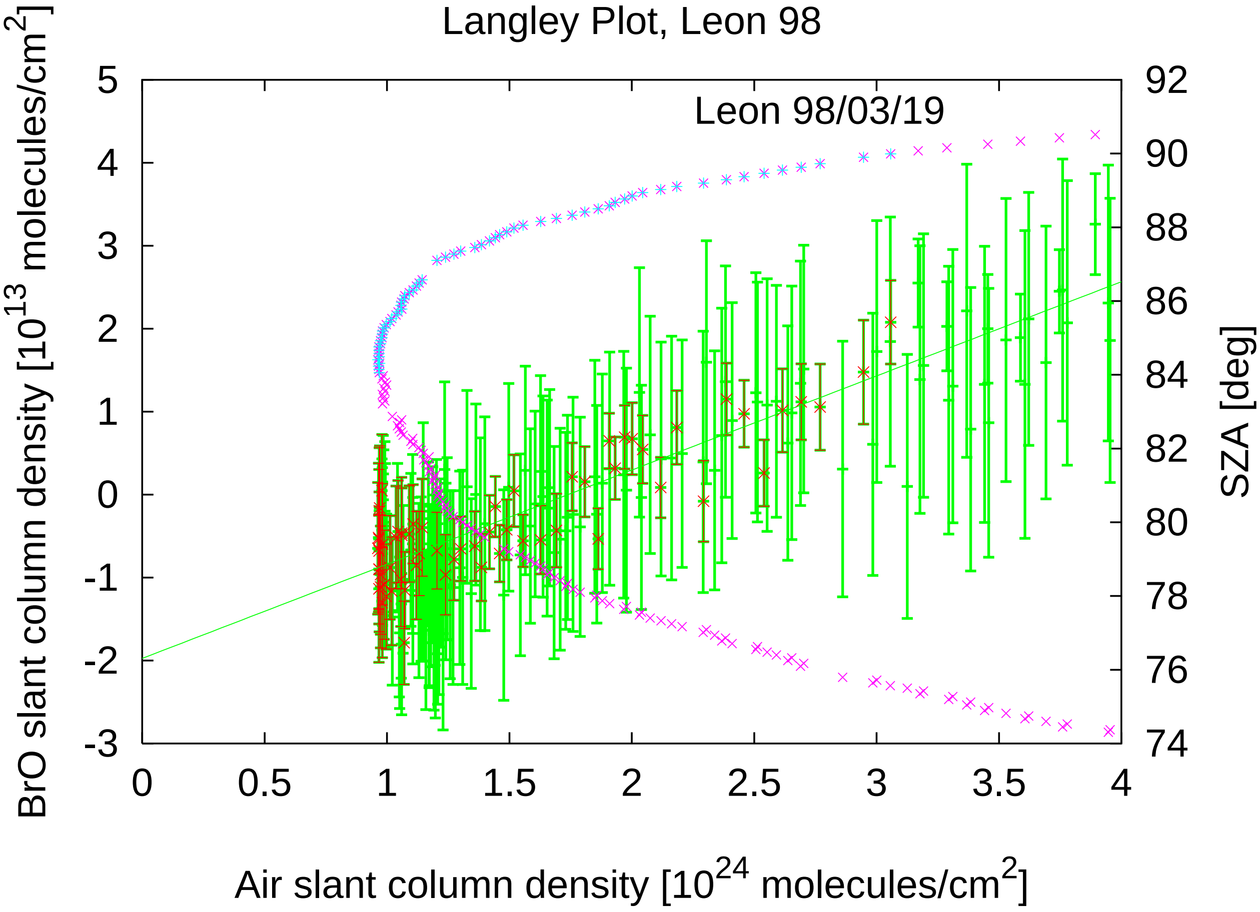

Figure 4.82: Langley plot for the flight at León 98 using the float SCDs for SZAs between 84^o and 90.0^o. The Fraunhofer reference spectrum is the average of 30 spectra measured at a balloon height of $37.9 - 38.2km$ and a SZA of $87.1 - 89.4^o$. The resulting SCD offset is $(2.0 \pm 0.5) \times 10^{13} \frac{molecule}{cm^2}$ and the mean mixing ratio above float (11.4 ± 2) ppt.

cannot explain more than 25% of the observed difference, so that tropospheric BrO must have been present during the balloon flight.

The occultation profile cannot provide information below 22 km, because the lowest tangent point is at this altitude. Still it shows a good agreement with the ascent profile in the altitude range above. The constantly smaller values can be attributed to the photochemical decrease of BrO during the occultation.

4.5 The sunset and sunrise flight at Kiruna on August 19/20, 1998

The next flight was an Arctic summer sunset/sunrise flight starting from Kiruna(Sweden) on August 19/20, 1998. This was the first and up to now only flight, when we could measure both during the sunset and the following sunrise at nearly the same location. This was only possible because the measurement campaign took place at the time, when the stratospheric winds were not as strong as for example during the winter, when the cyclonic vortex is turning around the Arctic Pole.

In Figure 4.85 you can see the trajectory of the balloon and the directions of the line of sight during the flight. While the balloon is nearly fixed in position above Northern Scandinavia the line of sight direction changes from south-west to north-west. During the sunset the tangent points of the light

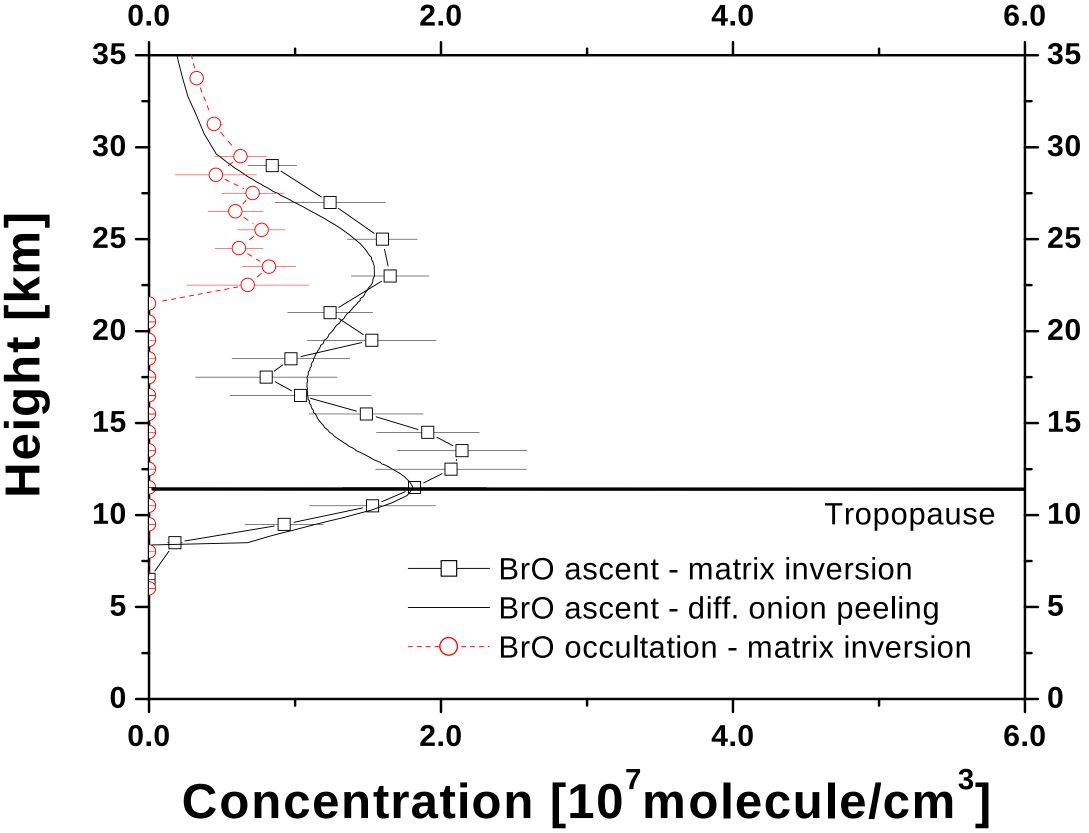

Figure 4.83: *BrO* concentration profiles measured during the ascent and the occultation. The measured ascent profile corresponds to a SZA range of $65 - 87^o$ and the occultation profile to $90 - 94^o$ SZA.

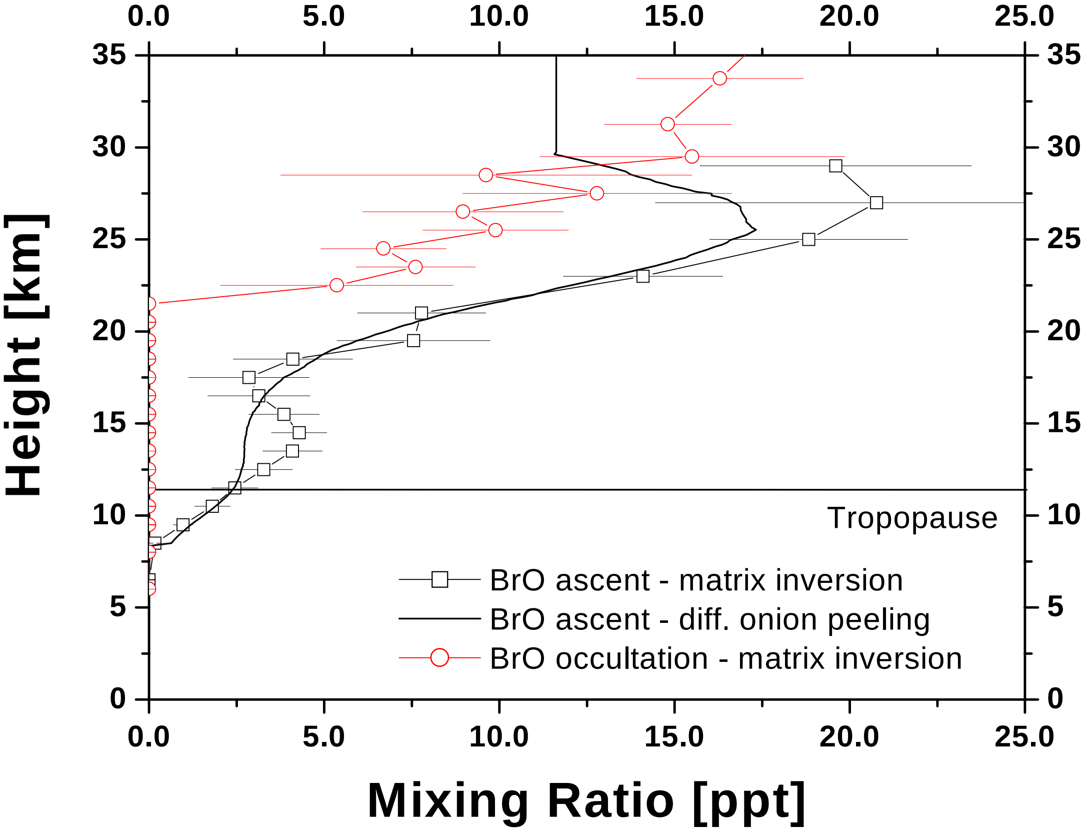

Figure 4.84: *BrO* mixing ratio profiles measured during the ascent and the occultation. The measured ascent profile corresponds to a SZA range of $65 - 87^o$ and the occultation profile to $90 - 94^o$ SZA.

rays are moving away from the balloon in north-westerly direction and they are continuing to turn clockwise during the sunrise at the next day. As we are in summer at high latitudes, we encounter a quite homogeneous pattern of stratospheric air streams, which are flowing slowly to the west. In comparison with the winter flights at Kiruna the meridional exchange of airmasses is less important, as the summer air streams in the stratosphere are uniform and there are less instabilities compared to the vortex in winter. At the time of our flight the stratosphere was in the state of turning from summer circulation to winter circulation, why the stratospheric winds were so weak and the flight could be as long as it was.

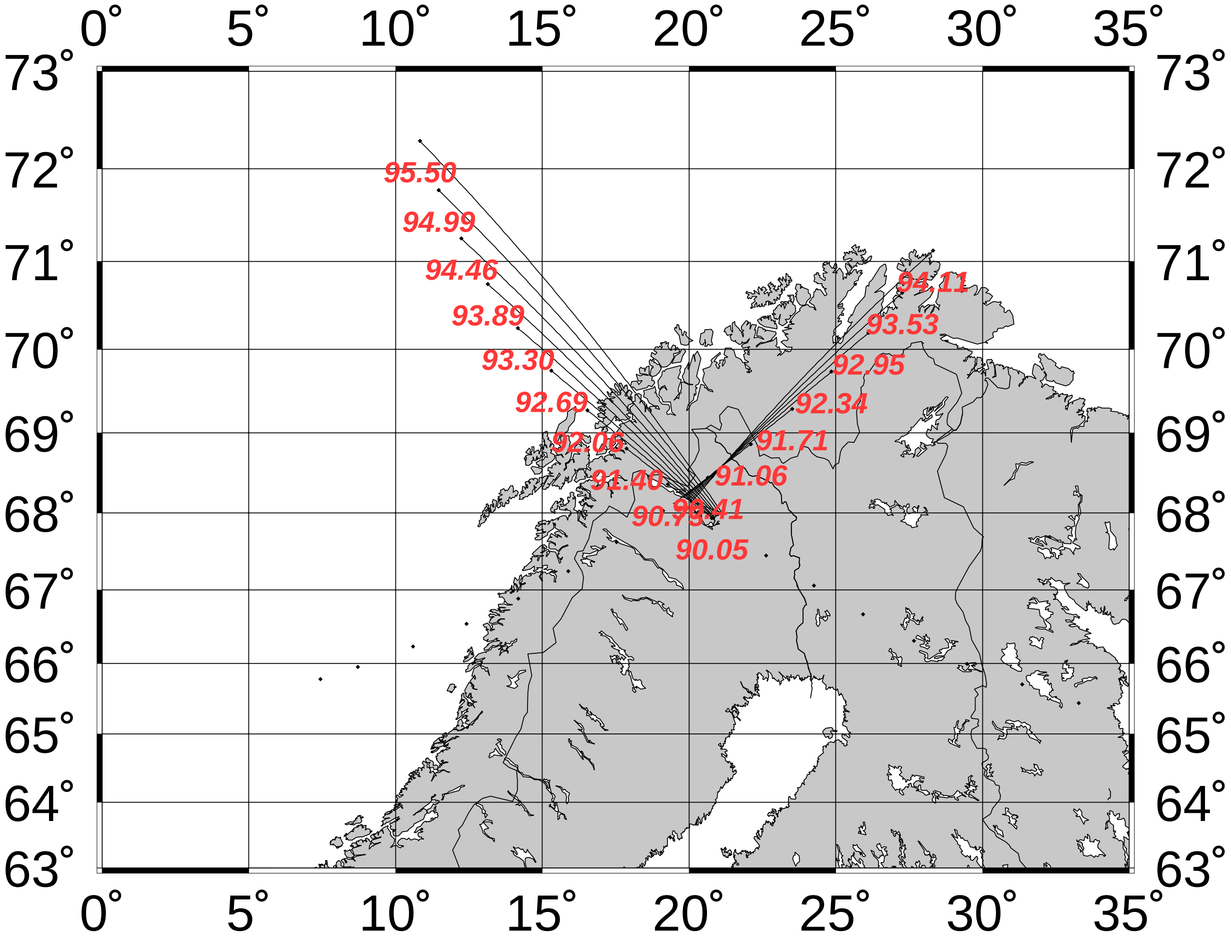

Figure 4.85: Balloon trajectory during the flight at Kiruna(Sweden) on Aug. 19/20, 1998. The trajectory is the curved line towards the east, while the lines ending with a point denote the light rays for SZAs larger than 90^o and the end points show the location of the tangent points - that is the main area of atmospheric absorption during occultation.

Figure 4.86 displays the balloon height as a function of time as well as the SZA at the balloon position (latitude, longitude) during the time when measurements were taken. As the balloon is remaining at the same position ($\pm 0.2^o \times 0.2^o$ latitude×longitude) the SZA is decreasing/increasing almost as if the position of the balloon was fixed.

From the plot of the temperature as a function of height it is clear that the temperature at the balloon position is not changing significantly from day to night and again from night to day.

Figure 4.87 shows a typical DOAS evaluation in the BrO retrieval range for that flight. The wavelength range chosen for this flight includes the two typically used BrO absorption lines (346-360

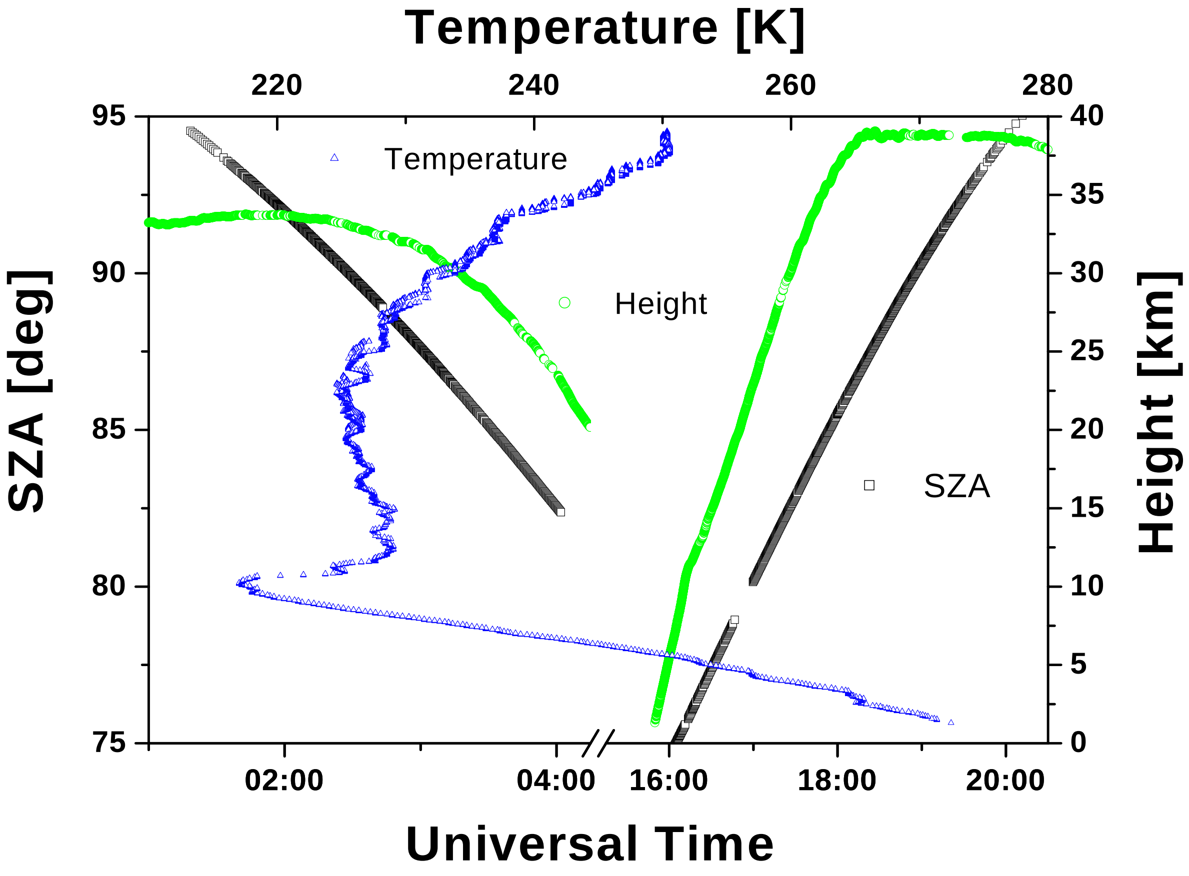

Figure 4.86: Balloon trajectory, temperature and SZA at balloon position (latitude, longitude) during the flight at Kiruna(Sweden) on August 19/20, 1998. The first part of the flight (sunset) is shown in the right part of the figure and the sunrise is shown in the left part of the figure.

nm).

To compare the resulting evolution of the SCDs and the fit coefficients the respective SCDs were plotted as a function of time in Figure 4.88-4.95 first for the sunset part of the flight and in Figure 4.96-4.103 for the sunrise part of the flight.

The evening SCDs of all measured species show the same well-known time evolution of the ascent flights and the morning SCDs behave like during a typical sunrise flight.

In Figure 4.104 and 4.105 you can see the resulting Langley plots for the evening and morning BrO SCDs. Both Langley plots used the float SCDs between 86 and 90^o SZA at the evening and morning, respectively. The evening Langley plot gives a mean mixing ratio above float of 17 ± 3 ppt and a SCD offset of $(2.7 \pm 1) \times 10^{13}$molecule/cm^2, while the morning Langley plot yields a mean mixing ratio above float of 13 ± 2 ppt and a SCD offset of $(0 \pm 2) \times 10^{13}$molecule/cm^2. Despite the discrepancies of the two different Langley fits, there are good reasons to take the evening Langley plot for the most realistic one, because the morning Langley plot uses measurements, when the balloon was sinking, while the altitude of the balloon was fixed during the float measurements. In addition the RMS of the residual structures of the DOAS fit are much larger in the morning.

4.5.1 BrO profile and SCD model comparison for the sunset

As the SZAs during the ascent of the balloon were relatively small and the tropopause lies higher than in the winter the respective SCDs are smaller than during the first measurement at Kiruna during wintertime. That is why the relative scatter and error of the SCD measurements is larger compared

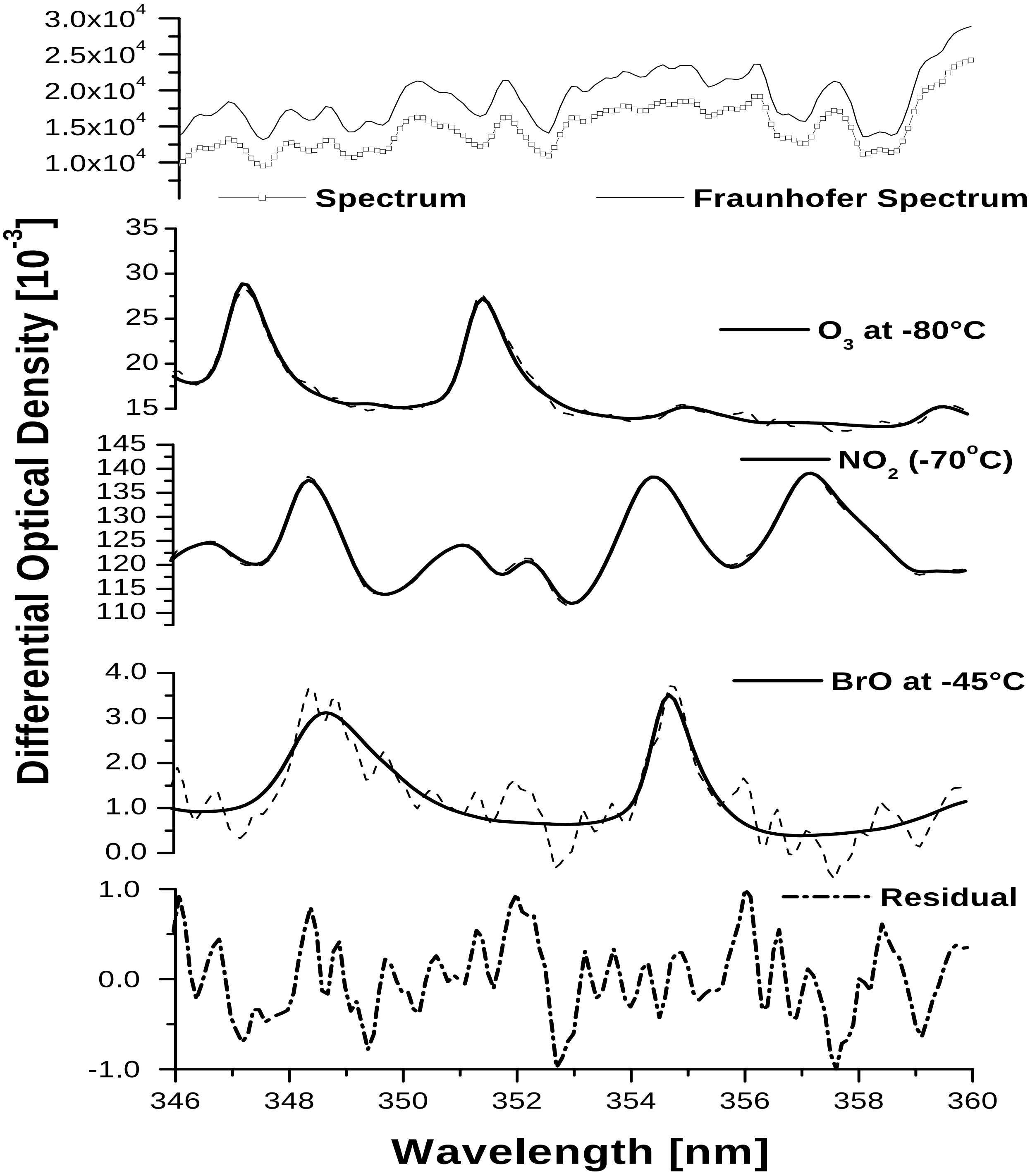

Figure 4.87: Typical DOAS evaluation in the BrO retrieval wavelength range (346-360 nm) for Kiruna 1998. The fit included O_3 at -80^oC and -20^oC(not shown), NO_2 at -35^oC, O_4(not shown), BrO at -45^oC and a polynomial of degree 3. The last spectrum is the residual of the fit which cannot be explained by the fit but is due partly to statistical noise and to systematic errors. All spectra have been filtered with a binomial filter of degree 3 before the fit.

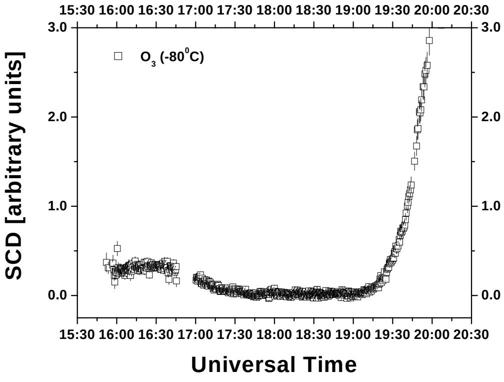

Figure 4.88: Time evolution of the $O_3(-80^oC)$ SCDs during the sunset.

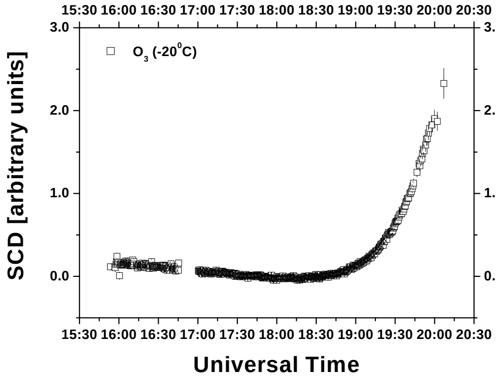

Figure 4.89: Time evolution of the $O_3(-20^oC)$ SCDs during the sunset.

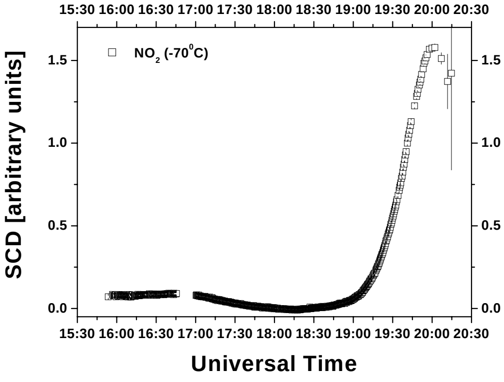

Figure 4.90: Time evolution of the $NO_2(-70^oC)$ SCDs during the sunset.

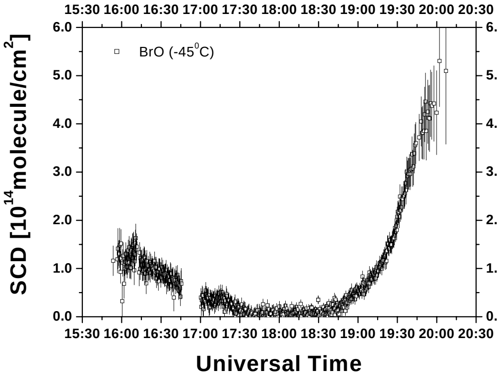

Figure 4.91: Time evolution of the $BrO(-45^oC)$ SCDs during the sunset.

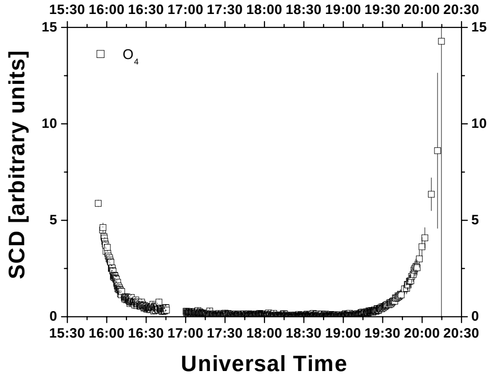

Figure 4.92: Time evolution of the O_4 SCDs during the sunset.

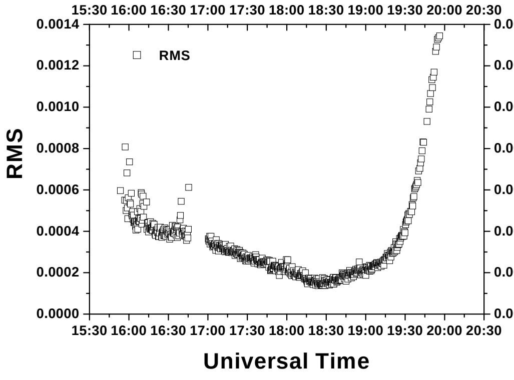

Figure 4.93: Time evolution of the RMS of the DOAS fit during the sunset.

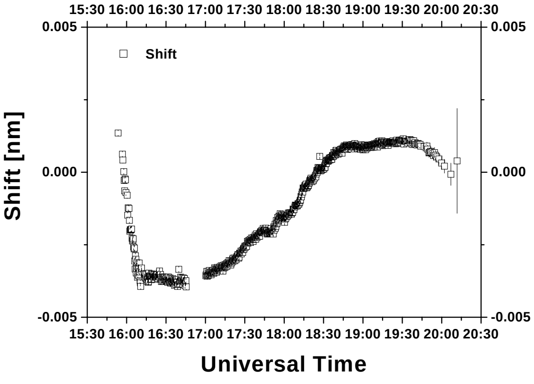

Figure 4.94: Time evolution of the shift of the reference spectra ensemble during the sunset.

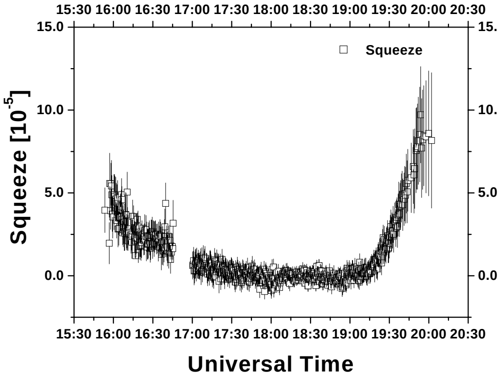

Figure 4.95: Time evolution of the squeeze of the reference spectra ensemble during the sunset.

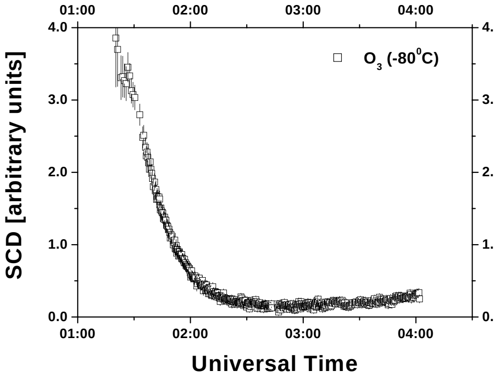

Figure 4.96: Time evolution of the $O_3(-80^oC)$ SCDs during the sunrise.

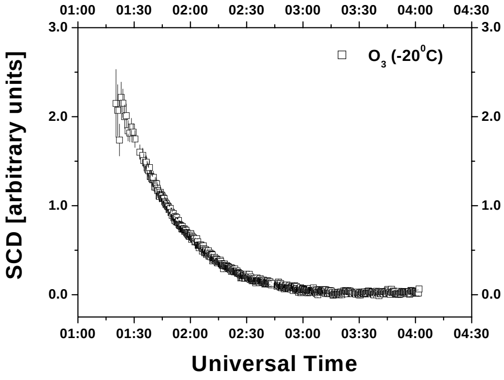

Figure 4.97: Time evolution of the $O_3(-20^oC)$ SCDs during the sunrise.

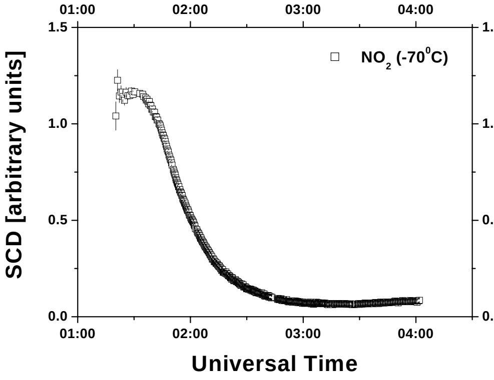

Figure 4.98: Time evolution of the $NO_2(-70^oC)$ SCDs during the sunrise.

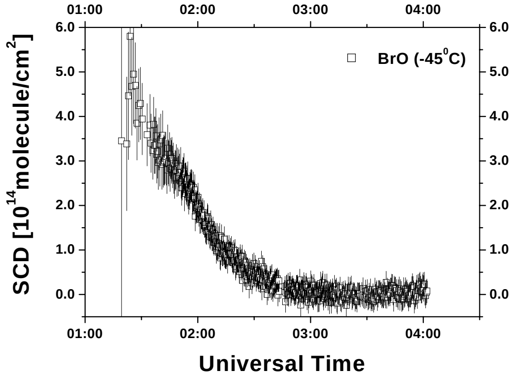

Figure 4.99: Time evolution of the $BrO(-45^oC)$ SCDs during the sunrise.

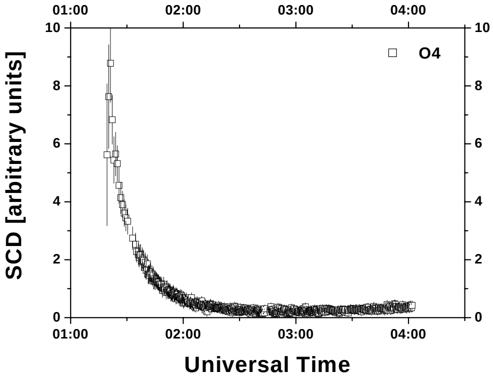

Figure 4.100: Time evolution of the O_4 SCDs during the sunrise.

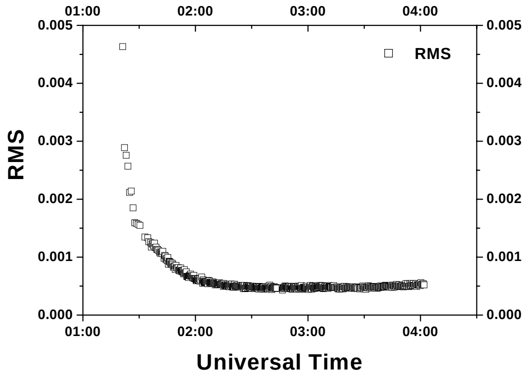

Figure 4.101: Time evolution of the RMS of the DOAS fit during the sunrise.

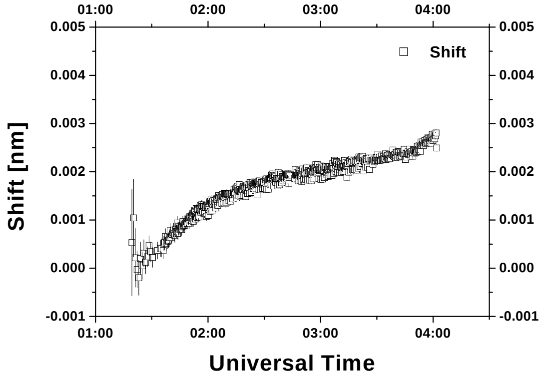

Figure 4.102: Time evolution of the shift of the reference spectra ensemble during the sunrise.

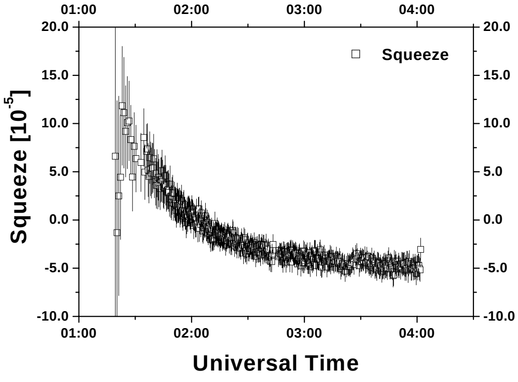

Figure 4.103: Time evolution of the squeeze of the reference spectra ensemble during the sunrise.

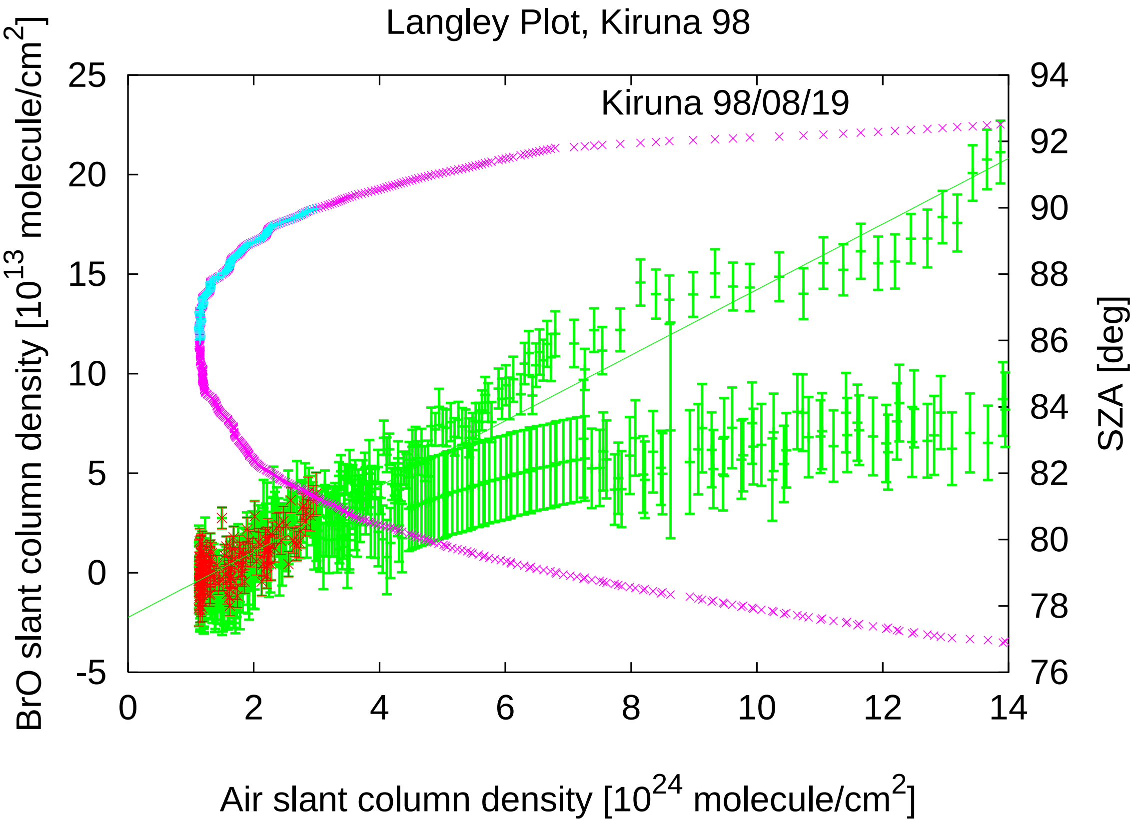

Figure 4.104: Langley plot for the flight at Kiruna 98 using the evening float SCDs for SZAs between 86^o and 90.0^o. The Fraunhofer reference spectrum is the average of 30 spectra measured at a balloon height of 38-39 km and a SZA of $87.9 - 88.4^o$. The resulting SCD offset is $(2.7 \pm 1) \times 10^{13} \frac{molecule}{cm^2}$ and the mean mixing ratio above float (17 ± 3) ppt.

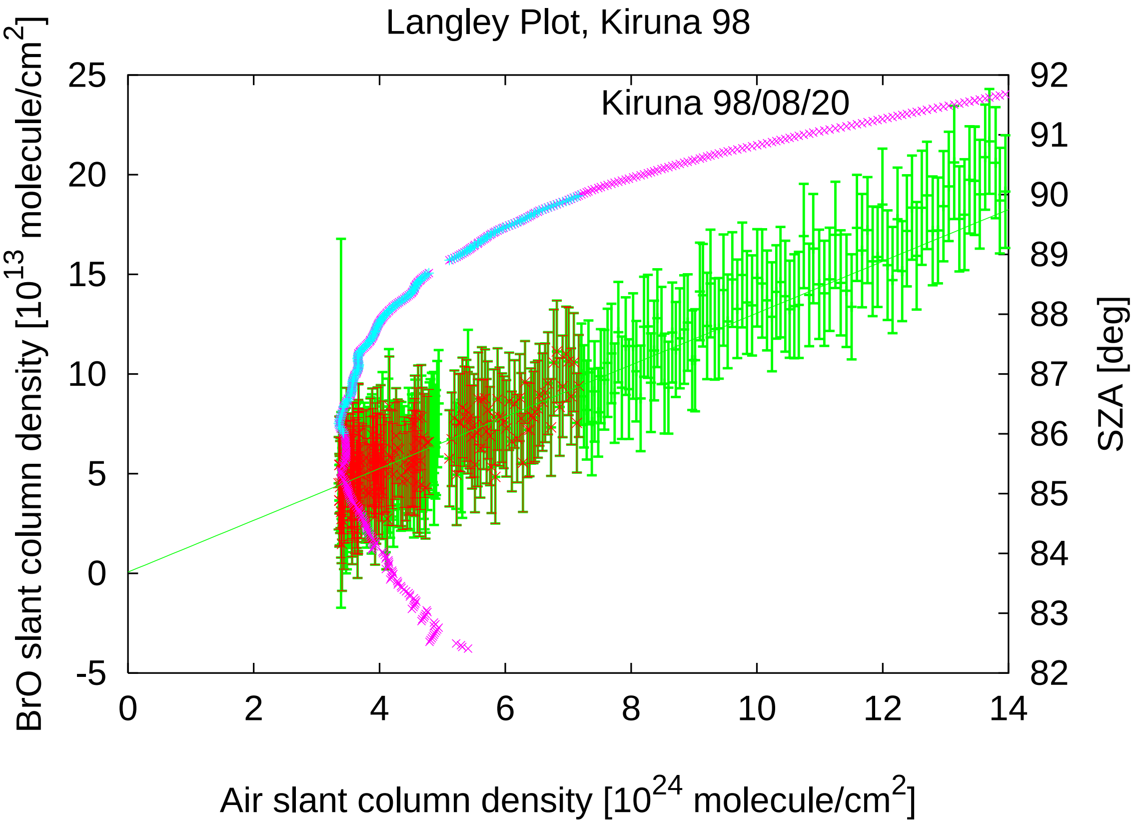

Figure 4.105: Langley plot for the flight at Kiruna 98 using the morning float SCDs for SZAs between 86^o and 90.0^o. The Fraunhofer reference spectrum is the average of 30 spectra measured at a balloon height of 38-39 km and a SZA of $87.9 - 88.4^o$. The resulting SCD offset is $(0 \pm 2) \times 10^{13} \frac{molecule}{cm^2}$ and the mean mixing ratio above float (13 ± 2) ppt.

to the winter flight. Still it is possible to retrieve profiles and to compare them to the model output of the 3-D CTM model SLIMCAT. This is shown in Figures 4.106 and 4.107.

The profiles refer to the ascent SCDs for SZAs between $75 - 87^o$ and to altitudes of 6-35 km. Both the matrix inversion and the differential onion peeling technique provides the same profile information. The stratospheric BrO concentration maximum is reached near the tropopause. There seems to be a local maximum of BrO at 30 km altitude, which is seen in both different profile retrievals. Looking at the modelled profiles for the two boundary SZAs of our measurement, it is obvious that the amount of BrO is changing dramatically during the course of the ascent, so that a SCD comparison is much more appropriate in this case. It can be seen that the position of the BrO model concentration maximum is also near to the tropopause as it was measured. Still the measured profile is - in both retrievals - much more structured than during previous flights. This is partly due to the scatter of the BrO signal - the SNR is smaller than during previous flights - but most of the scatter has been removed by filtering the SCDs applying a gaussian mask with a σ of 3 km and 0.5 km in the case of the matrix inversion and the differential onion peeling, respectively.

The peak in the onion peeling profile at about 20 km altitude is clearly linked to the gap in measurements - between 18-22 km altitude the pointing system was not working fine because of very strong shear winds[5]. This peak can even be seen in the matrix inversion profile, but it is less pronounced. The local maximum around 30 km altitude is seen in both profile retrievals and cannot be explained by a misalignment of the pointing system. Clearly, this structure of the profile cannot be reproduced by the SLIMCAT model. On the other hand, it is not clear, wether this structure is a filament of different airmasses, because there is only a small horizontal gradient, which can be seen e.g. on the GOME BrO map of that day. In the occultation measurements it is not possible to see such a structure, which could be explained by the larger area which the instrument is seeing by that time. The probed area during balloon ascent is only about 100x100 km^2.

It is also possible to retrieve a profile of BrO in the troposphere, but this observation and its consequences will be dealt with in the next chapter.

The modelled photochemical BrO concentration field for this flight (gridpoint $68N, 15E$) is shown in Figure 4.108. When we make the SCD model comparison (see Figure 4.109), we can again find a very good agreement between the measured and modelled BrO SCDs after the middle stratosphere is reached by the balloon and during most of the occultation measurements. Still there is a significant discrepancy in the troposphere and lower stratosphere. As the tropospheric measurements will be subject of the next chapter, the lower stratospheric discrepancy will be investigated here. It clearly corresponds the observed profile difference, which is the largest just above the tropopause. This finding could be explained by the underestimation of the inorganic bromine calculated by the model in the lower stratosphere.

There are also small discrepancies between measurement and model, where the measured SCDs show a small-scale structure, while the modelled SCDs are very smooth - corresponding to the smooth profiles. As these profile structures are only seen in the BrO profile and SCD time evolution, it is not consistent with the other species. Still there is no indication of a numerical artifact, which should be observed in one of the other species, the residual or other fit parameters, too.

The modelled late occultation SCDs are smaller than observed, which can again be explained by the profile discrepancy in the lower stratosphere, as the tangent points for SZAs larger than 93.5^o are even reaching altitudes as low as 13.8 km.

The correlation plot between the modelled and measured BrO SCDs - see Figure 4.110 - shows the model-measurement correlation for different model runs with total inorganic Br_y of 17, 20 and 23 ppt. In the occultation part the model tends to underestimate the SCDs, whereas the agreement is better in the float and ascent part of the flight. Still it is important to notice that the SCDs measured at the end

---

[5] Unfortunately, during the launch of the balloon one the two auxiliary balloons used to hold the balloon gondola above the ground did not fall down to the earth when they were cut by remote control, but it snarled around the pivot (primary pointing system), which made the pointing system more vulnerable to shear winds.

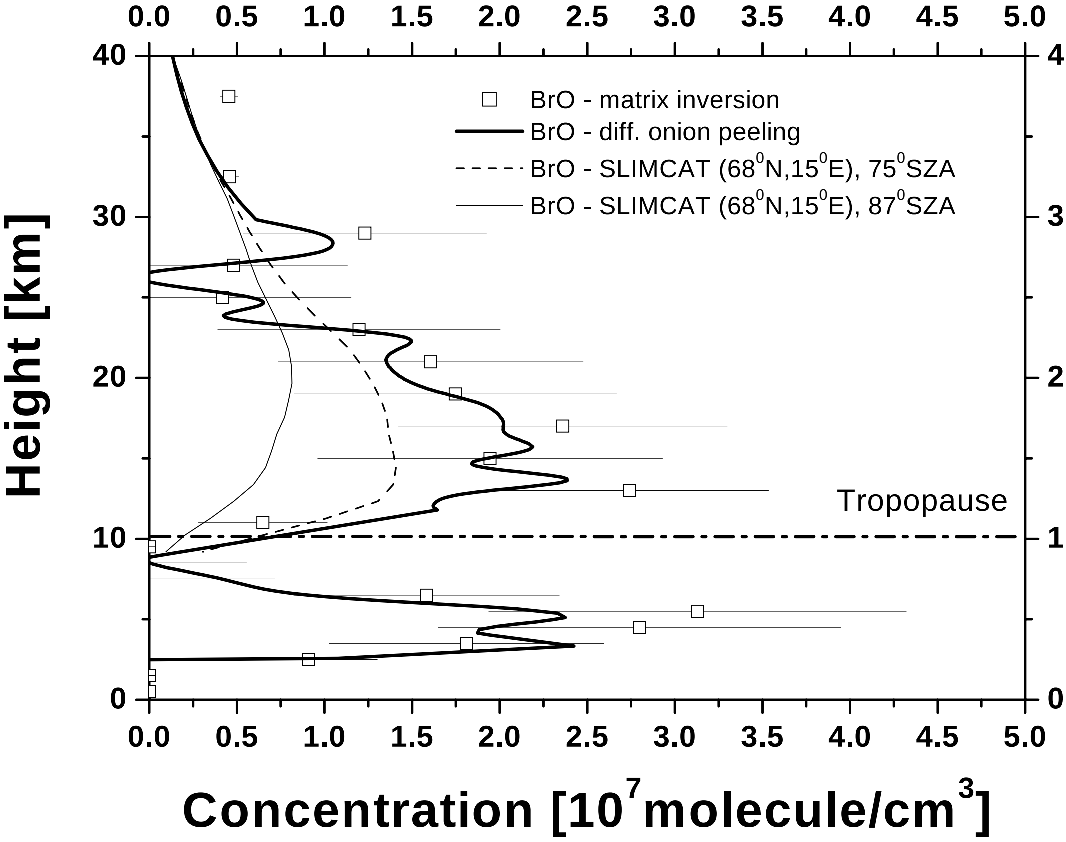

Figure 4.106: *BrO* concentration profile. The measured profile corresponds to a SZA range of $75 - 87^o$.

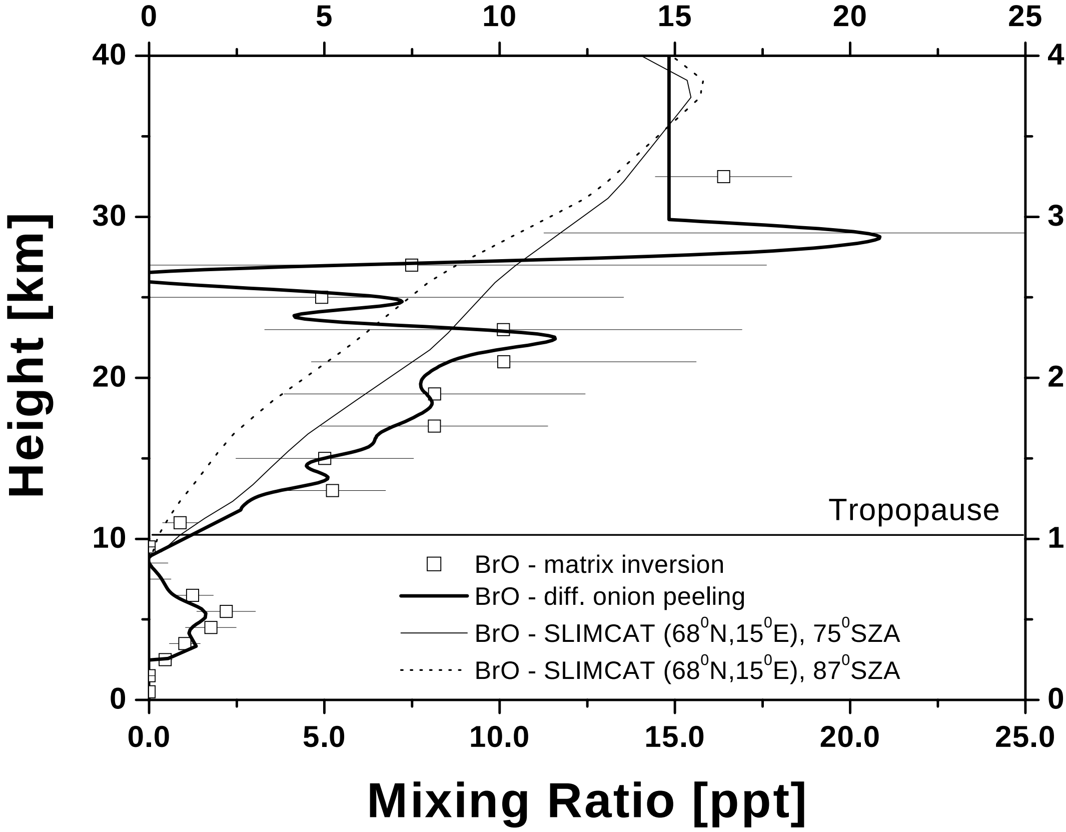

Figure 4.107: *BrO* mixing ratio profile. The measured profile corresponds to a SZA range of $75 - 87^o$.

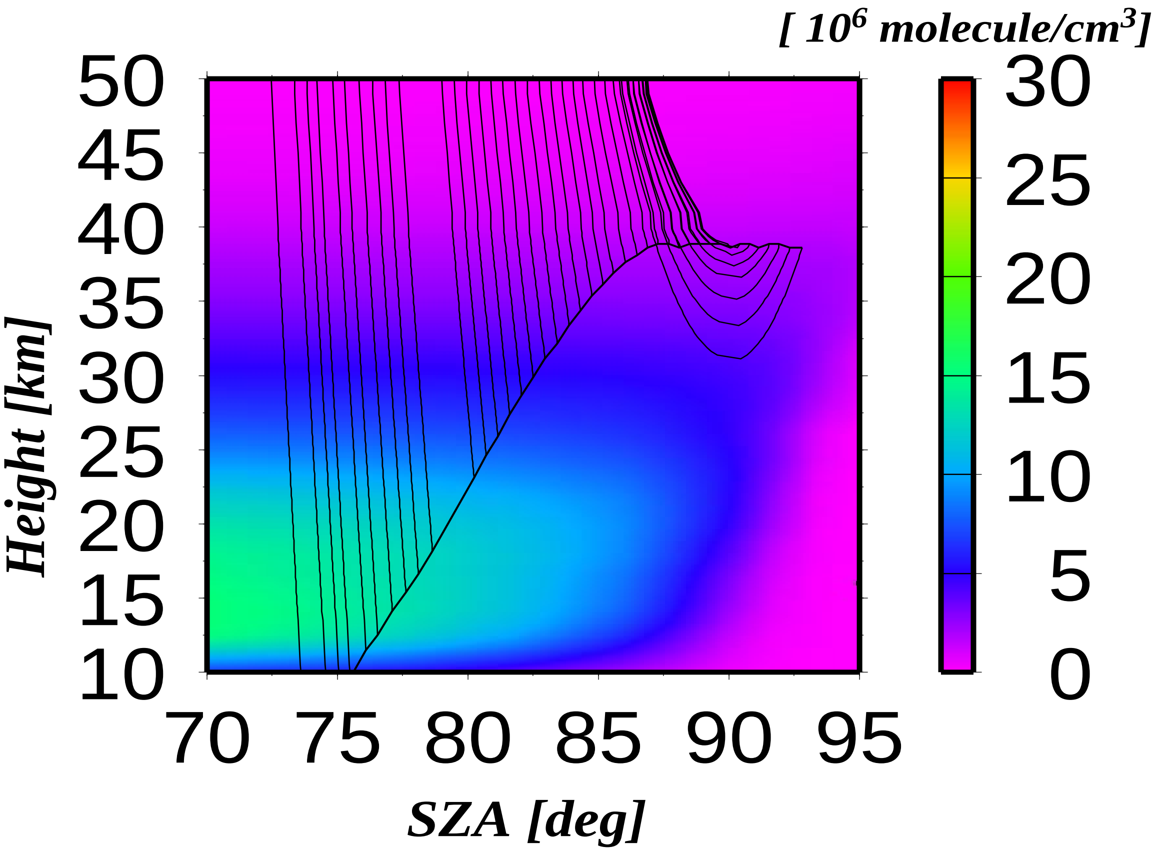

Figure 4.108: Modelling of BrO SCDs by integration of the concentration along the light path through the atmosphere. The model field for the evening measurements on Aug. 19 is color-coded as a function of height and SZA. Both the trajectory of the balloon (thick line) and the light rays from the sun (fine lines) reaching the balloon instrument are shown in the plot.

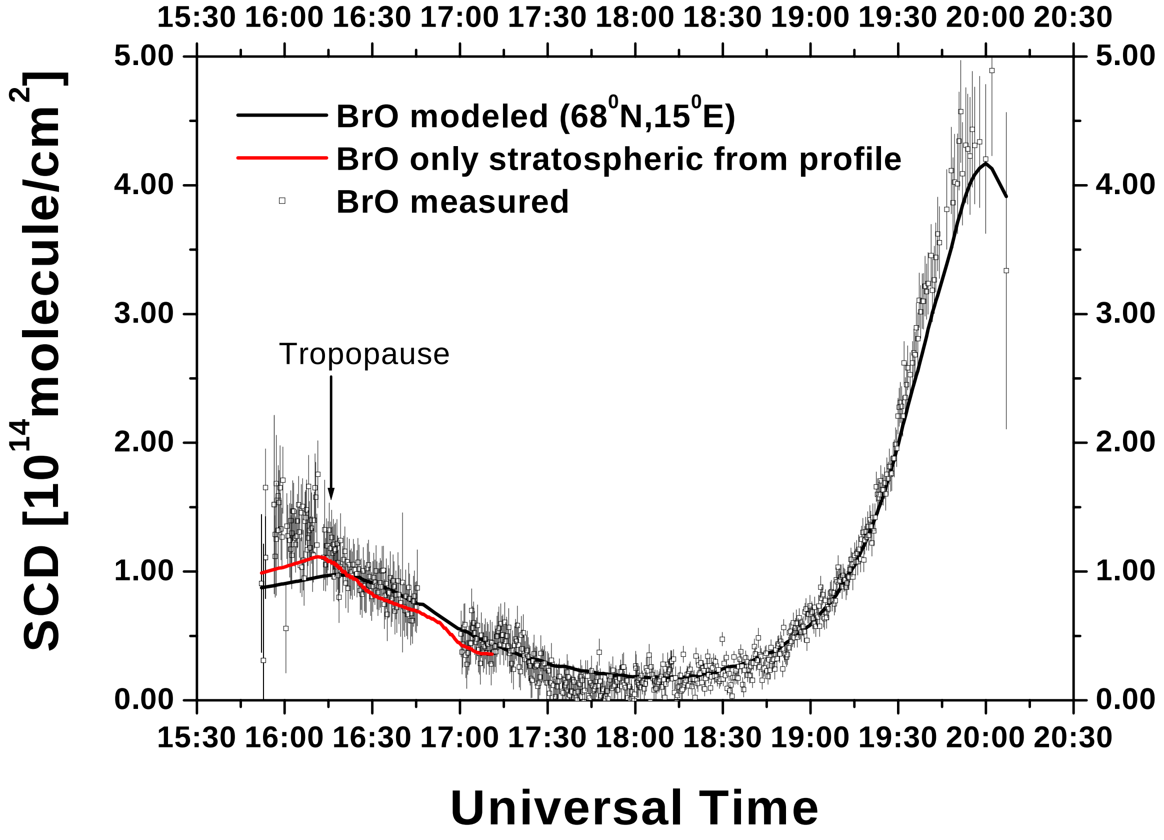

Figure 4.109: Time evolution of measured and modelled BrO SCDs for the Kiruna 98 flight on Aug.19.

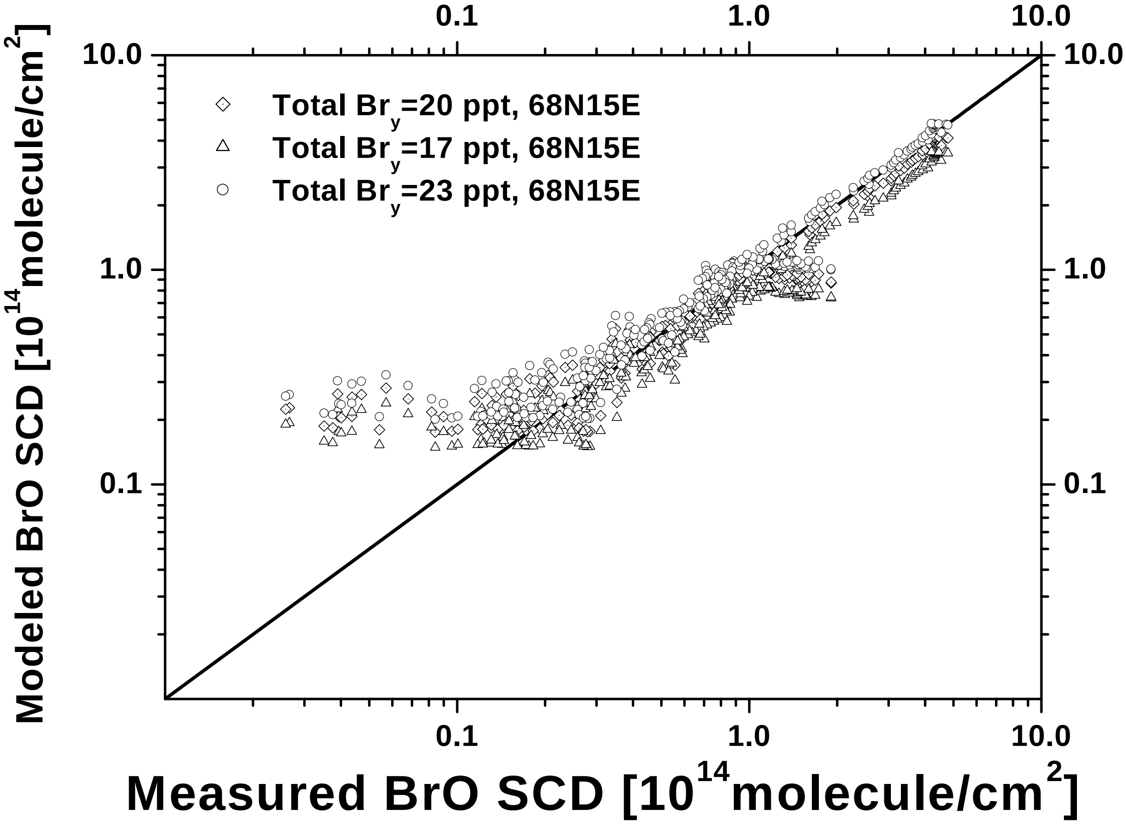

Figure 4.110: Correlation plot of modelled and measured BrO SCDs for the Kiruna 98 flight: evening. The different model runs $(68N, 15E)$ with different total inorganic bromine contents are shown (Br_y = 17, 20 and 23 ppt).

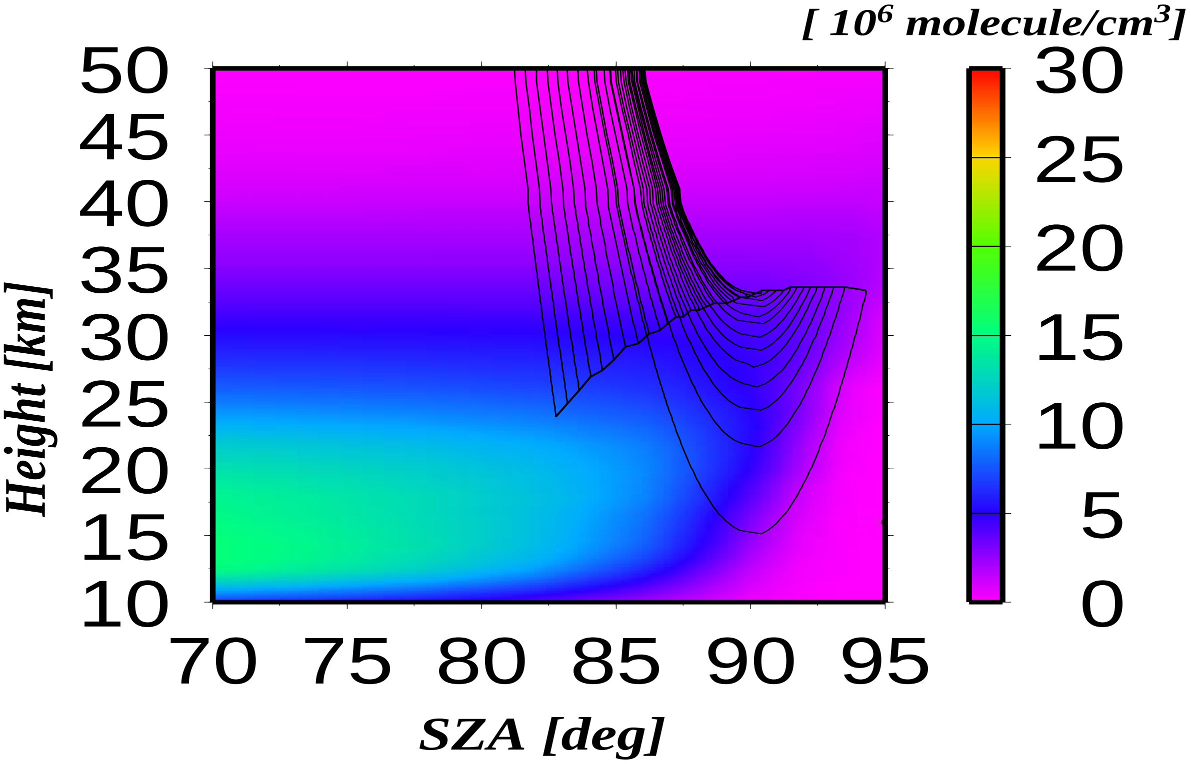

Figure 4.111: Modelling of BrO SCDs by integration of the concentration along the light path through the atmosphere. The model field for the morning measurements on Aug. 20 is color-coded as a function of height and SZA. Both the trajectory of the balloon (thick line) and the light rays from the sun (fine lines) reaching the balloon instrument are shown in the plot.

of the ascent and during the float scatter significantly around the detection limit, thus deteriorating the correlation.

4.5.2 BrO SCD model comparison for the sunrise

As the measurements during the sunrise at the next day of the flight took place mainly during solar occultation, it was not possible to retrieve non-ambiguously a profile, which could be compared to the model estimate. The photochemical change of the profile in the atmospheric layers probed by the light is very large and so the different measurements belong to different profiles - as can be seen in Figure 4.111.

When making the SCD model inter comparison (see Figure 4.112), we can again find a very good agreement between the measured and modelled BrO SCDs during most of the occultation measurements. Though there is a significant discrepancy in the lower stratosphere, which leads to an underestimation of the BrO SCDs at the beginning of and at the end of the measurements. As for the evening measurements the SCD discrepancy clearly corresponds to the observed profile difference, which is the largest just above the tropopause. This can be seen for the largest SZAs, when the tangent points reach the lowest altitudes and during the descent of the balloon. We again interpret this finding by the underestimation of the total inorganic bromine calculated by the model in the lower stratosphere.

The correlation plot between the modelled and measured BrO SCDs - see Figure 4.110 - shows the model-measurement correlation for modelled total inorganic Br_y of 17, 20 and 23 ppt in the maximum. Generally the agreement between model and measurement is very good and the total inorganic Br_y can be determined to 21.5 ± 2.5 ppt, as the best agreement is observed for a 20-23 ppt model case study.

4.6 The sunset flight at Kiruna on February 10, 1999

In the framework of the THESEO[6] campaign we had a flight in the Arctic starting from Kiruna(Sweden) on Feb. 10, 1999. This was the first flight of the LPMA/DOAS gondola taking place completely in the polar vortex, so that it was possible to observe the measured species during chlorine activation and denoxification.

In Figure 4.114 the trajectory of the balloon and the directions of the line of sight during the flight are plotted. While the balloon is moving in north-easterly direction the line of sight direction changes from south to south-west. During the sunset the tangent points of the light rays are moving away from the balloon in south-westerly direction. As can be seen from the potential vorticity map at 475 K potential temperature level, which is plotted in the figure in colour-code, the measurements all took place within the polar Arctic vortex.

Figure 4.115 shows the balloon height as a function of time as well as the SZA at the balloon position (latitude, longitude) during the time when measurements were taken. As the balloon is moving to the east during the sunset the SZA is decreasing faster than if the position of the balloon was fixed.

The temperatures are slightly above the formation threshold of PSCs. But the following chapter 7 will contain a detailed analysis of the chlorine activation, where lagrangian model case studies will show, by which kind of chlorine activation the observations can be explained.

Figure 4.116 and 4.117 show typical DOAS evaluations in two different BrO retrieval ranges for that flight. The first wavelength range ($BrO\,range$) includes the two typically used BrO absorption lines (346-360 nm). In the second case ($BrO - OClO\,range$) two $OClO$ absorption lines were included in the fit to get a better signature of $OClO$ (346-365 nm). For both fits $OClO$ was included, which minimized the residual. Still in these wavelength ranges the $OClO$ absorption bands interfere with

---

[6] Third European Stratospheric Experiment on Ozone - sponsored by the European Union; see also *http://www.nilu.no/projects/theseo2000.*

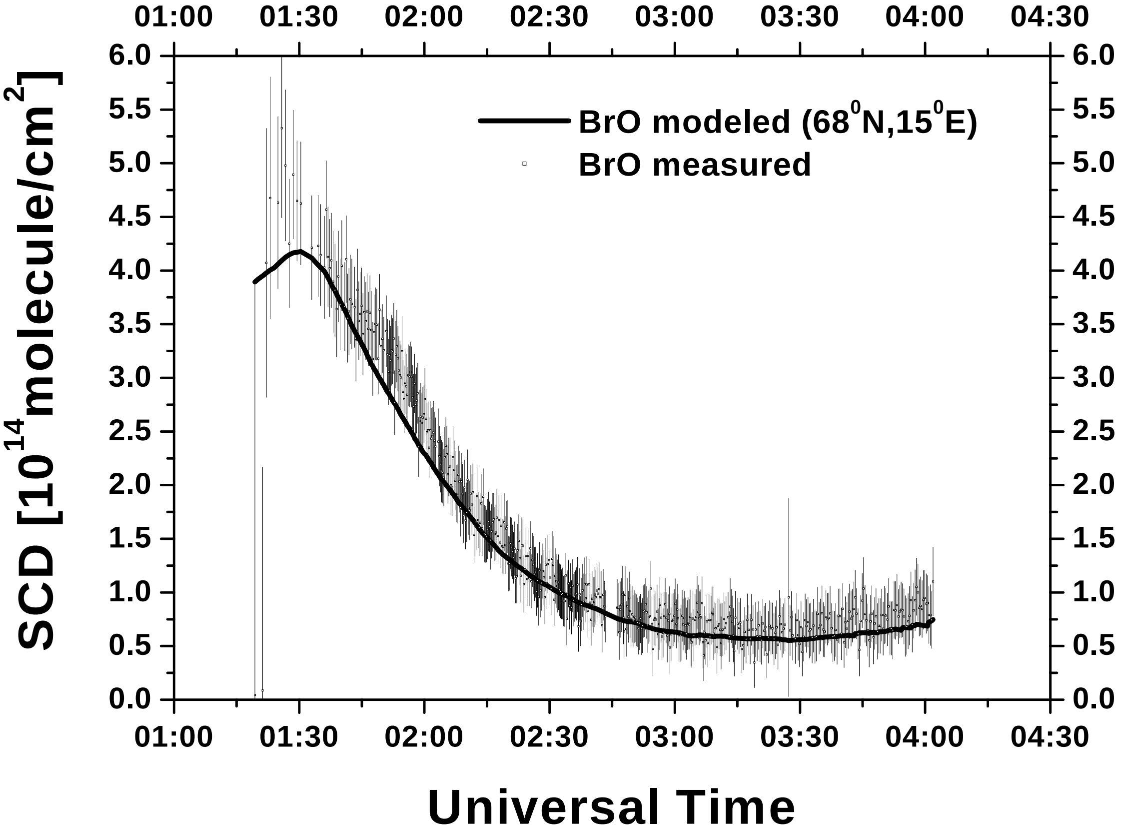

Figure 4.112: Time evolution of measured and modelled *BrO* SCDs for the Kiruna 98 flight on Aug.20.

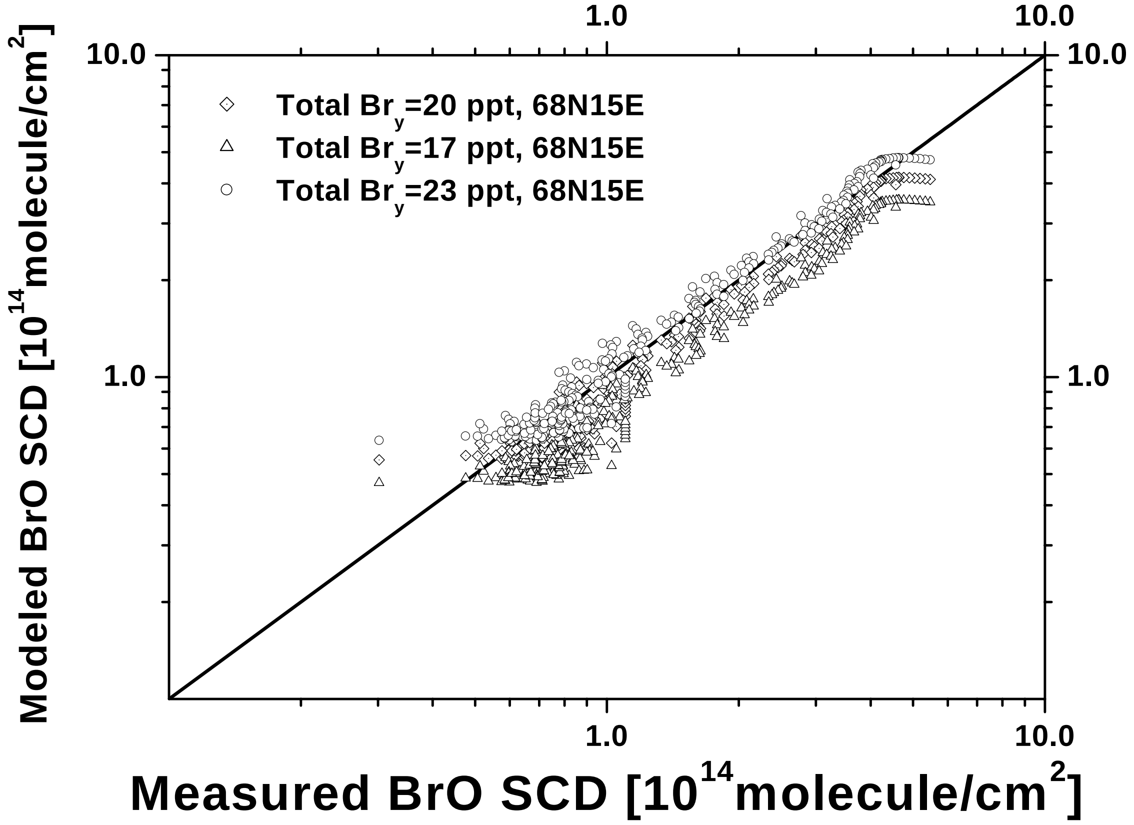

Figure 4.113: Correlation plot of modelled and measured *BrO* SCDs for the Kiruna 98 flight: morning. The different model runs $(68N, 15E)$ with different total inorganic bromine contents are shown $(Br_y = 17, 20$ and 23 ppt).

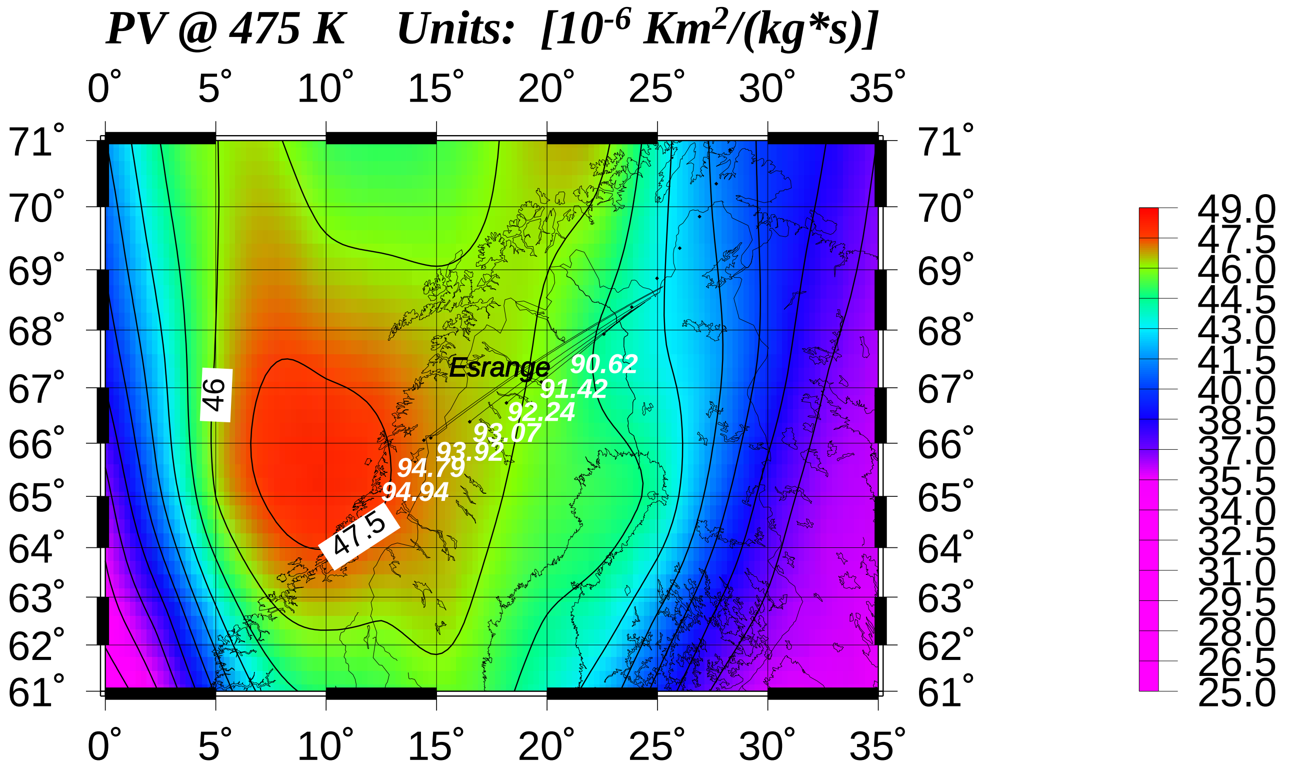

Figure 4.114: Balloon trajectory during the flight at Kiruna(Sweden) on Feb. 10, 1999. The trajectory is the curved line towards the east, while the lines ending with a point denote the light rays for SZAs larger than 90^o and the end points show the location of the tangent points - that is the main area of atmospheric absorption during occultation. The PV map at $475K$ potential temperature level is given in colour-code.

some of the other absorbers and so the finding of $OClO$ has to be checked also in a larger wavelength window, especially in a window where O_3 and BrO do not absorb.

Figure 4.118 shows a typical DOAS evaluation in the $OClO$ wavelength range (362-390 nm). This is the range, where it is only necessary to include $OClO$, NO_2 and O_4 into the fit as absorbers. A polynomial of degree 5 is also used for this DOAS fit region. As there are three absorption lines included in this fit window ($OClO\,range$), the resulting $OClO$ SCDs will be used further on to retrieve a profile and to compare them to model predictions.

The time evolution of the measured species in the three different wavelength ranges (BrO, $BrO-OClO$ and $OClO$ range) is shown in Figure 4.119-4.126. From the different evaluations and the variations of the respective fit coefficients it can be deduced that the wavelength range 345-365 nm is well suited for the evaluation of BrO, while the exact retrieval of absolute O_3 and NO_2 SCDs is not possible in this wavelength range. For $OClO$ the best range is the third one including three absorption lines and being not influenced by O_3 or BrO. Still this wavelength range displays large scatter of the retrieved SCDs as well as of the RMS of the DOAS fit. A possible explanation for this is the large size of the wavelength window, where a higher degree of the non-linear fitted offset may be necessary to describe the stray light or other broad-band intensity variations during the flight.
In the case of BrO it can be said that the two absorption band evaluation ($BrOrange$) shows the smallest RMS and residual structures and the largest discrepancies in the troposphere, where the SNR is the smallest - though the agreement of the BrO SCDs even in the troposphere is remarkable and within the stated error interval. After performing several *spectral window tests* for the tropospheric measurements, which all increased the RMS and also slightly the tropospheric BrO SCDs compared to the two band DOAS evaluation, it was concluded that the old $BrO\,range$ is best suited to determine the tropospheric amount of BrO. The resulting profile and its interpretation will be discussed in detail

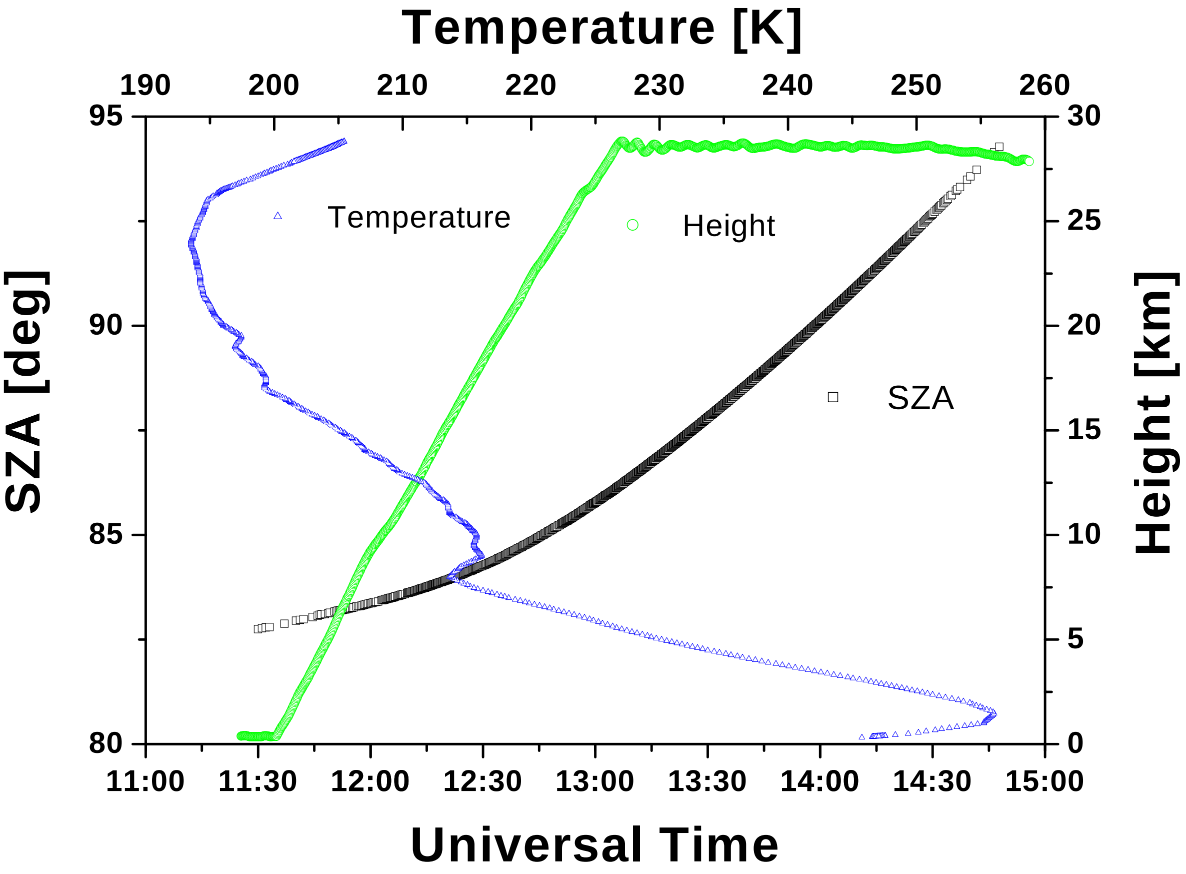

Figure 4.115: Balloon trajectory, temperature and SZA at balloon position (latitude, longitude) during the flight at Kiruna(Sweden) on Feb. 10, 1999. The first part of the flight (sunset) is shown in the right part of the figure and the sunrise is shown in the first part of the figure.

in the following chapter.

The differences in O_4, NO_2, $OClO$ and O_3 - mainly during the balloon ascent - can be explained by possible correlations of the absorption spectra between each other and the polynomial used in the fit, as well as by the temperature dependence of NO_2 and O_3, which is the largest in the UV region. As the NO_2 absorption in the spectra is smaller than during the previously conducted flights, the SNR for NO_2 is much smaller. In the lower stratosphere and troposphere, where the temperatures are changing very much in comparison with the middle stratosphere, the NO_2 SCDs show a quite large scatter depending on the fit window, which could be explained either by the large temperature dependence of NO_2 or the bad SNR. Though, the BrO SCDs are not affected by this scatter of the NO_2 SCDs and their temperature dependence is much less pronounced. For O_4 the variability is the largest, as its correlation with the polynomial is the strongest. This is again a reason for the $BrO\,range$ being the best fit range for the retrieval of BrO, because the change of the tropospheric BrO SCDs is mainly due to the O_3 anticorrelation and the O_4 correlation. The O_3 at -20^{o}C SCDs are not shown here, because they are nearly zero and almost all of the O_3 absorption can be described by the -80^{o}C reference, which is proved by the comparison with the O_3 SCDs retrieved in the VIS (Chappuis bands) range - see Figure 4.119.

4.6.1 BrO profile and SCD model comparison

Figure 4.127 shows the Langley plot for BrO for this flight. The resulting SCD offset is $(3.6\pm0.5)\times10^{13}$ molecule/cm^2 and the mixing ratio determined above float is (13 ± 2) ppt, which agrees well with the

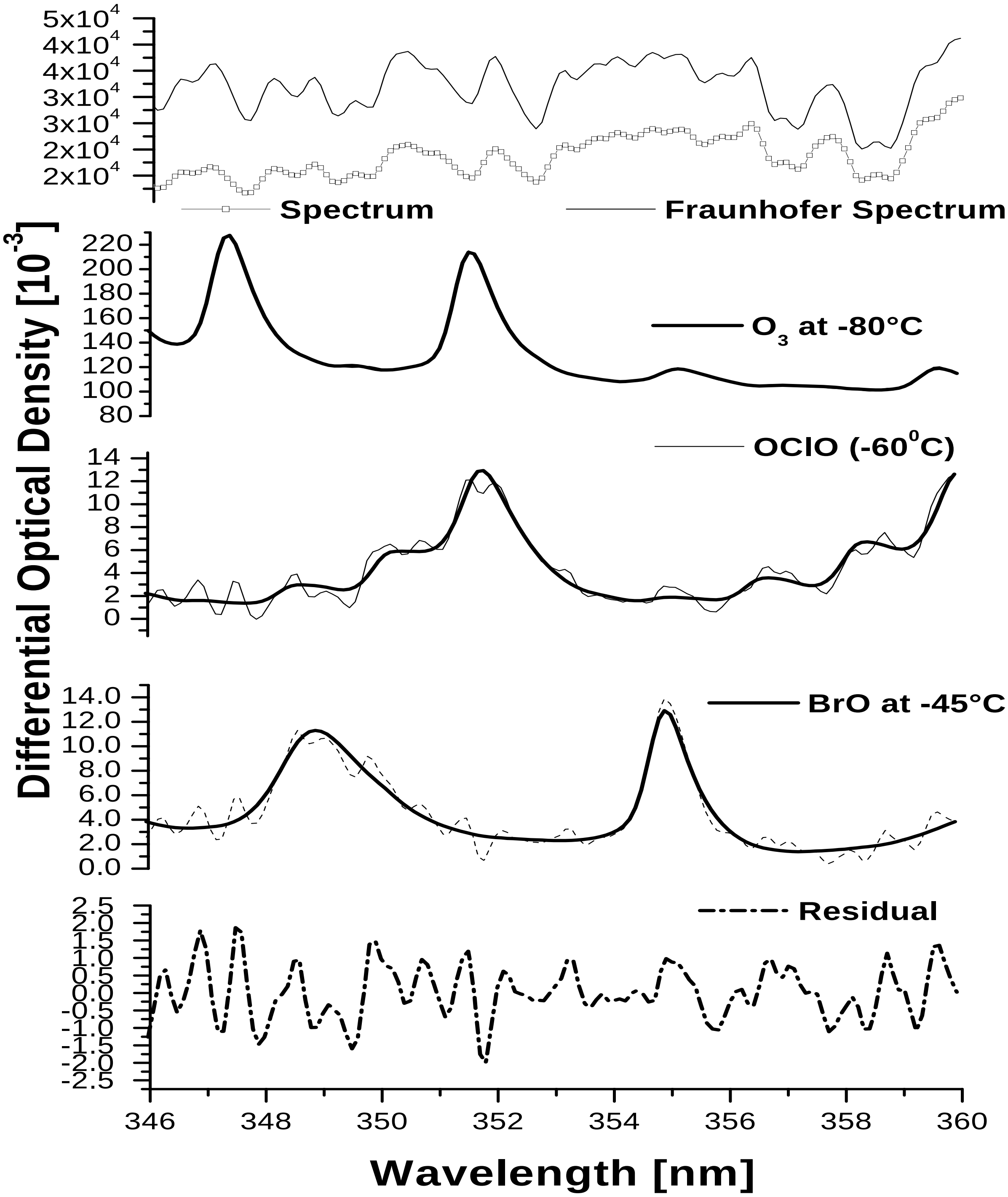

Figure 4.116: Typical DOAS evaluation in the BrO retrieval wavelength range (346-360 nm) for Kiruna 1999 for a spectrum measured at the tropopause. The fit included O_3 at -80^oC and -20^oC(not shown), NO_2 at -70^oC (not shown), O_4(not shown), BrO at -45^oC, $OClO$ at -60^oC and a polynomial of degree 3. The last spectrum is the residual of the fit which cannot be explained by the fit but is due partly to statistical noise and to systematic errors. All spectra have been filtered with a binomial filter of degree 3 before the fit.

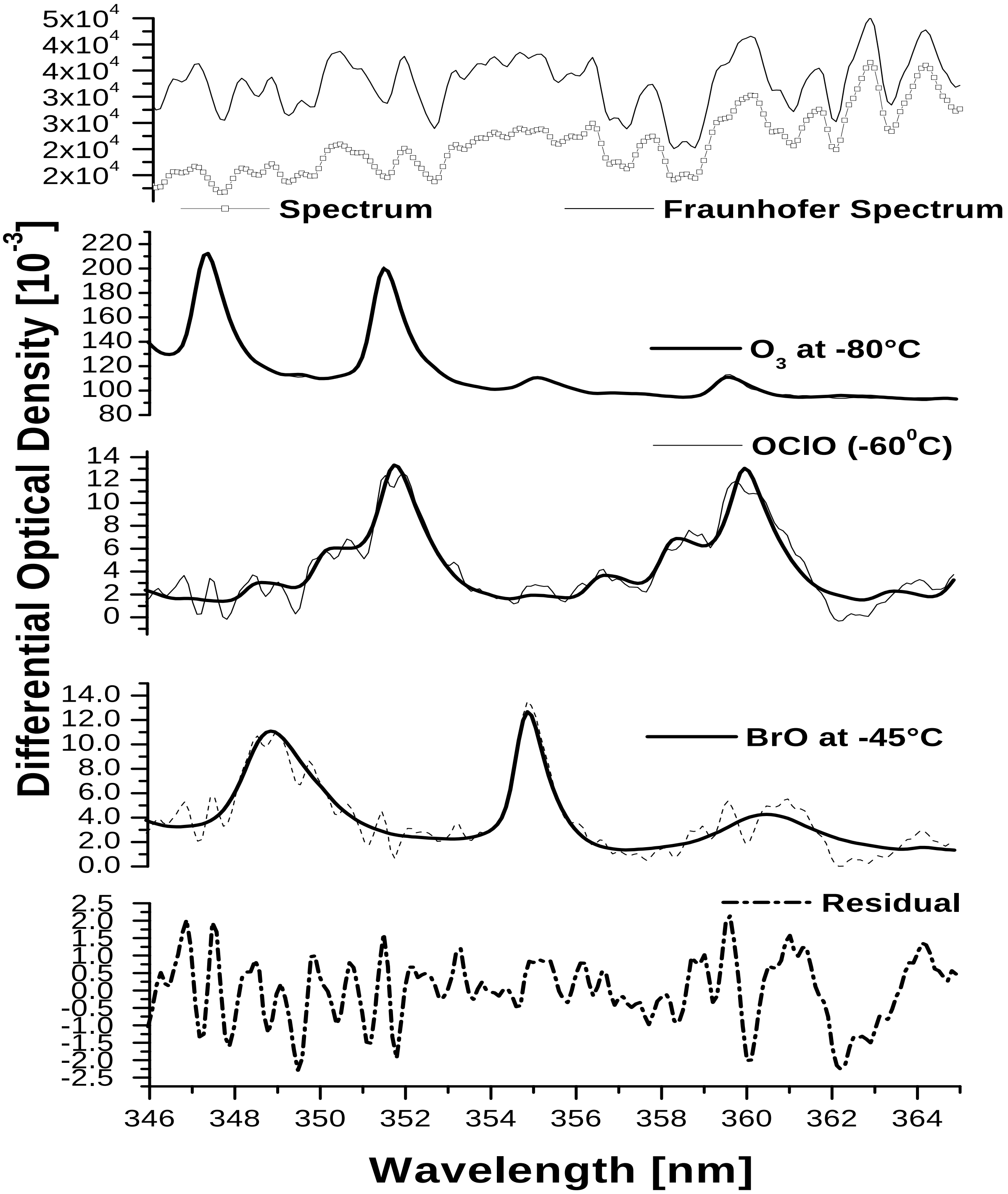

Figure 4.117: Typical DOAS evaluation in the BrO retrieval wavelength range (346-365 nm) for Kiruna 1999 for a spectrum measured in late occultation. The fit included O_3 at -80^oC and -20^oC(not shown), NO_2 at -70^oC(not shown), O_4(not shown), BrO at -45^oC, $OClO$ at -60^oC and a polynomial of degree 3. The last spectrum is the residual of the fit which cannot be explained by the fit but is due partly to statistical noise and to systematic errors. All spectra have been filtered with a binomial filter of degree 3 before the fit.

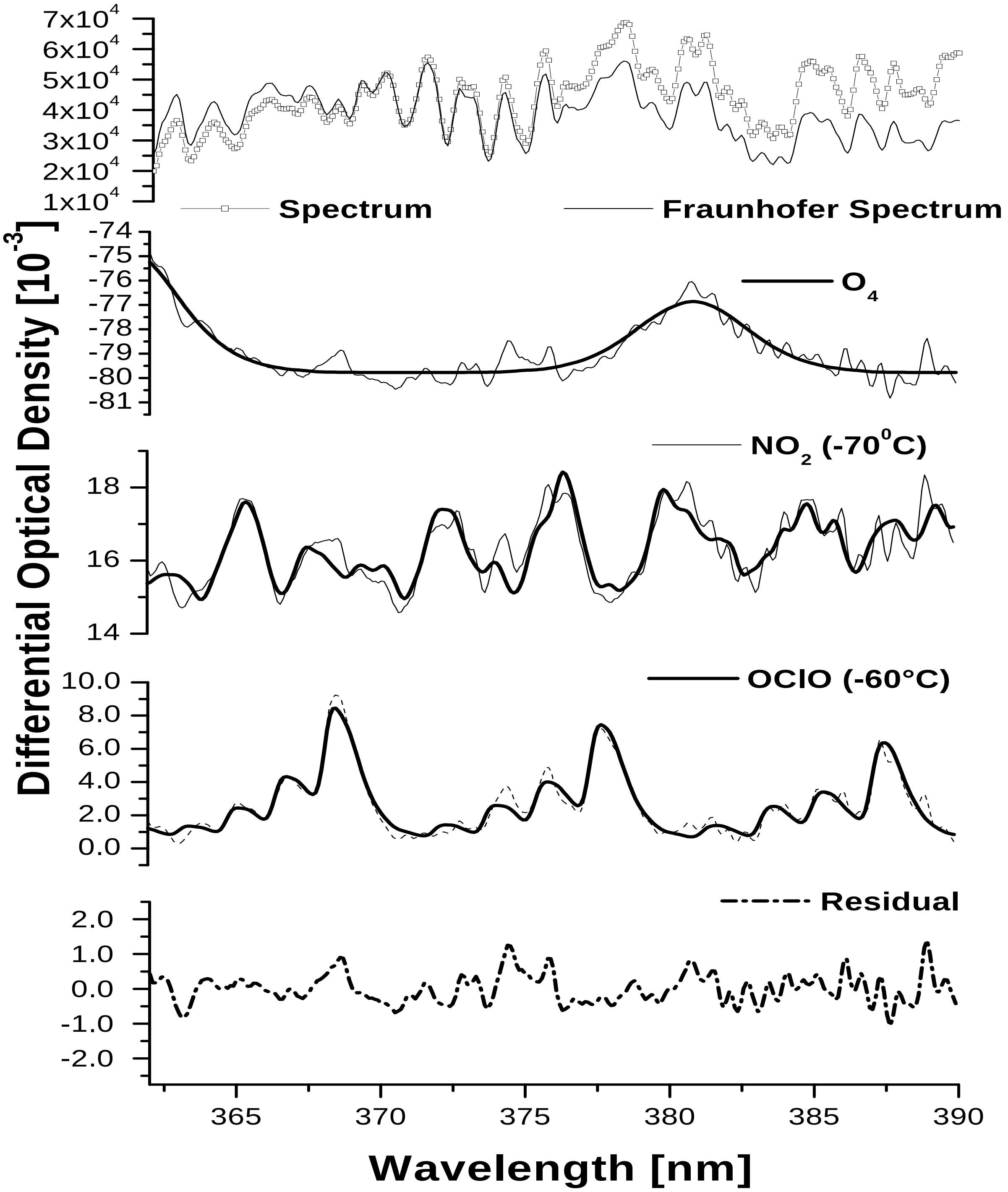

Figure 4.118: Typical DOAS evaluation in the *OClO* retrieval wavelength range (362-390 nm) for Kiruna 1999 for a spectrum measured in late occultation. The fit included NO_2 at -70^oC, O_4, *OClO* at -60^oC and a polynomial of degree 5. The last spectrum is the residual of the fit which cannot be explained by the fit but is due partly to statistical noeise and to systematic errors. All spectra have been filtered with a binomial filter of degree 3 before the fit.

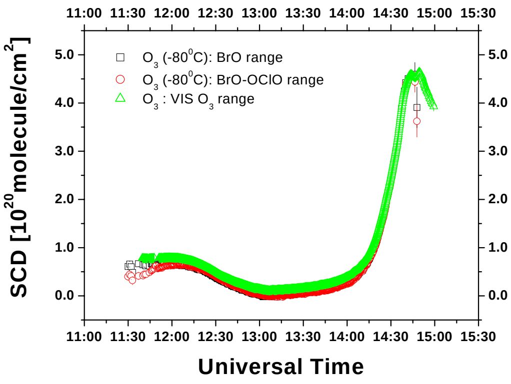

Figure 4.119: Time evolution of the $O_3(-80^oC)$ SCDs during the flight.

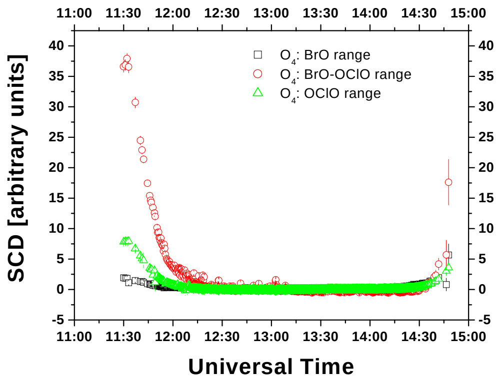

Figure 4.120: Time evolution of the O_4 SCDs during the flight.

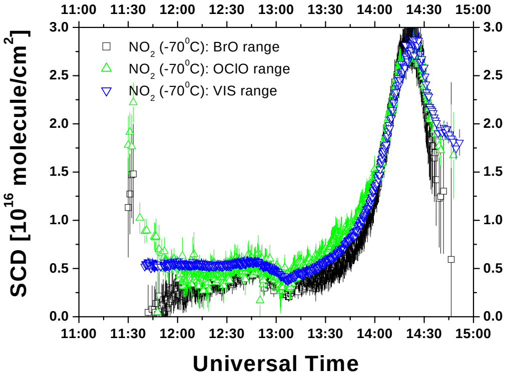

Figure 4.121: Time evolution of the $NO_2(-70^oC)$ SCDs during the flight.

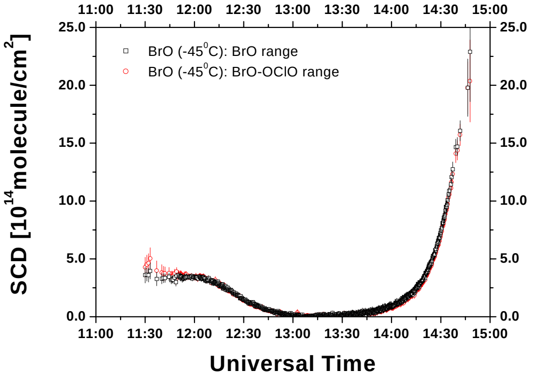

Figure 4.122: Time evolution of the $BrO(-45^oC)$ SCDs during the flight.

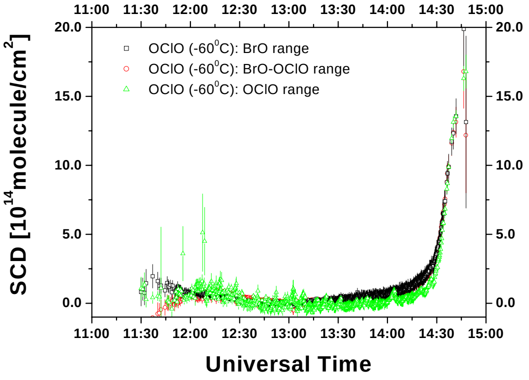

Figure 4.123: Time evolution of the $OClO$ SCDs during the flight.

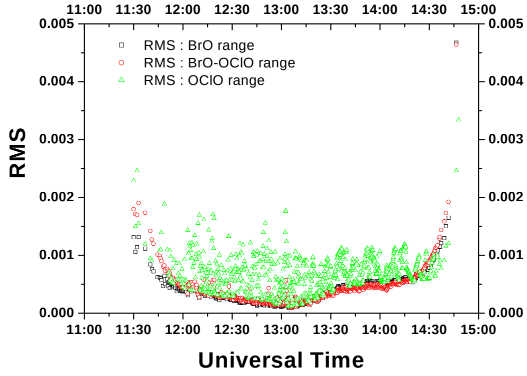

Figure 4.124: Time evolution of the RMS of the DOAS fit during the flight.

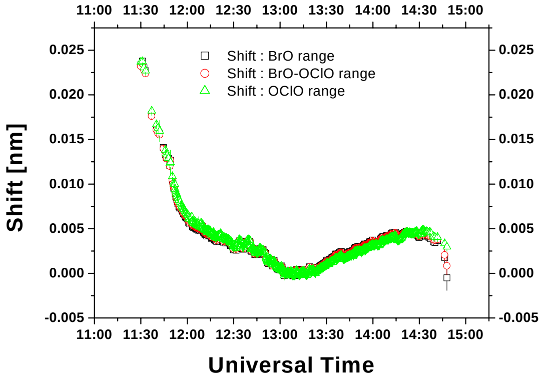

Figure 4.125: Time evolution of the shift of the reference spectra ensemble during the flight.

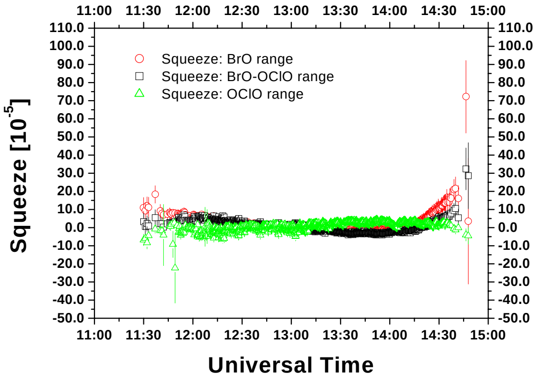

Figure 4.126: Time evolution of the squeeze of the reference spectra ensemble during the flight.

profile retrieved from the ascent SCDs, which will be shown in the following.

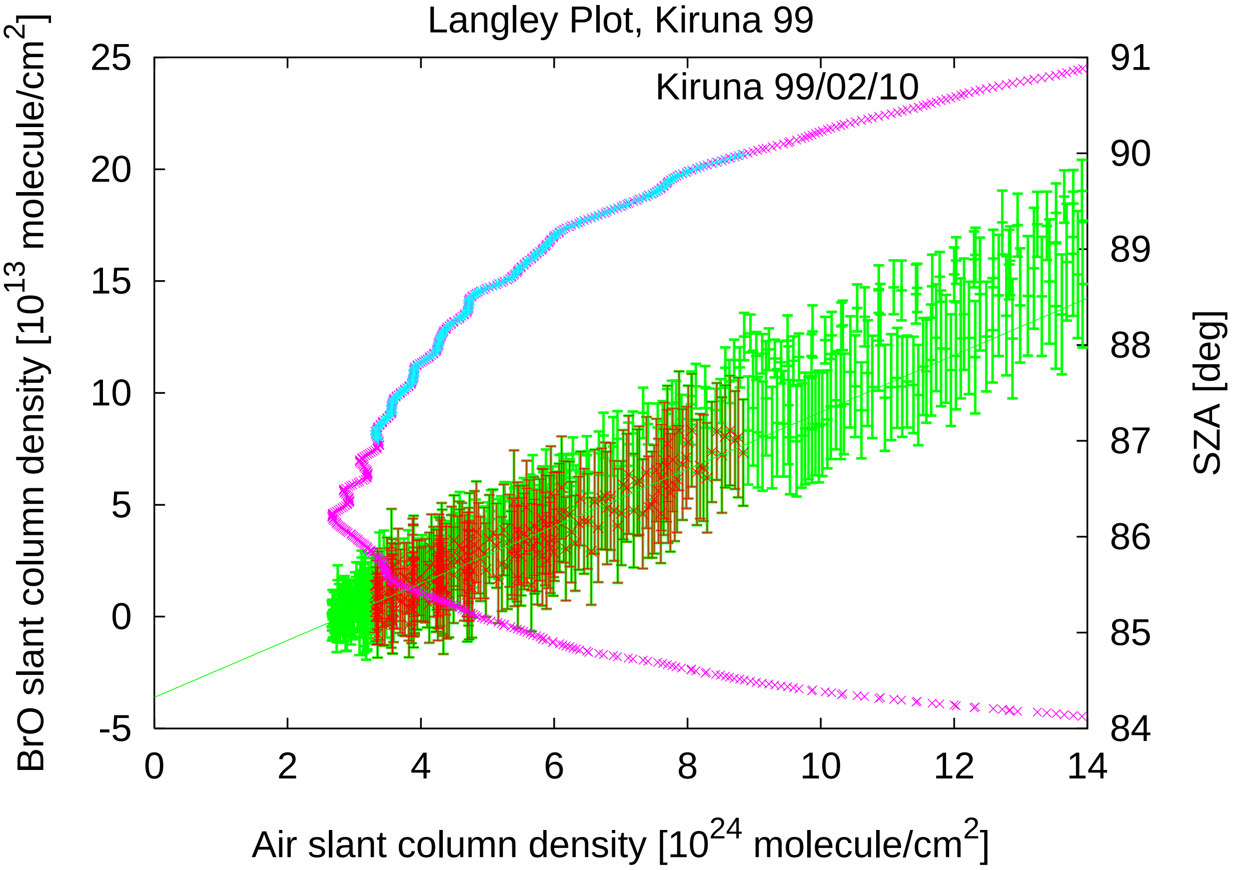

Figure 4.127: Langley plot for the flight at Kiruna 99 using the evening float SCDs for SZAs between 86^o and 90.0^o. The Fraunhofer reference spectrum is an average of 20 spectra measured at a balloon height of 28.5 km and a SZA of 85.9 − 86.1^o. The resulting SCD offset is $(3.6 \pm 0.5) \times 10^{13} \frac{molecule}{cm^2}$ and the mean mixing ratio above float (13 ± 2) ppt.

The BrO concentration and mixing ratio profiles are shown in Figure 4.128 and 4.129. In addition the SLIMCAT model profiles for the SZAs 82.9^o and 86.2^o are plotted in these figures. This is the SZA interval during which the ascent measurements were taken. So the photochemical change of BrO during the ascent of the balloon is almost negligible, especially when taking account of the measurement errors. The agreement between the measured and modelled profiles is very good above the concentration maximum, while the model tends to underestimate the BrO in the lower stratosphere.
The measured profile in the troposphere will be discussed in detail in the following chapter 5.

The model is again used to simulate the measurements during the flight. Figure 4.130 shows the photochemical BrO model field as a function of height and SZA for that flight. It is evident that we probed the daytime maximum only during the ascent measurements. During the occultation BrO is quickly converted to its nighttime reservoirs $BrONO_2$, $HOBr$ and - in this case of low NO_x and relatively high ClO_x - especially $BrCl$.

The comparison of modelled and measured BrO SCDs is shown in Figure 4.131 and 4.132. Again, we can observe a striking agreement of the modelled and measured BrO SCDs during the stratospheric part of the flight between 12:30 and 14:45 UT. In the lower stratosphere the model sees less BrO, which explains the underestimation of the BrO in the first part of the flight and also at the end of the flight

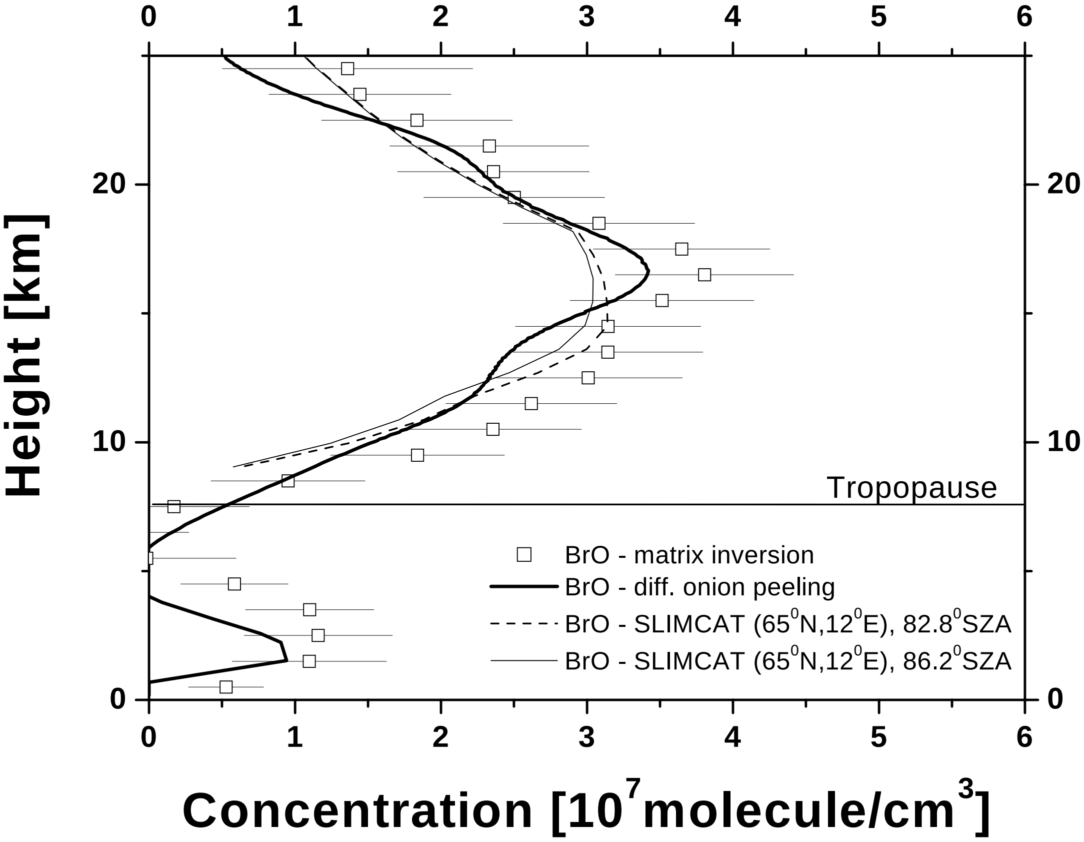

Figure 4.128: BrO concentration profile. The measured profile corresponds to a SZA range of $82.9 - 86.2^o$.

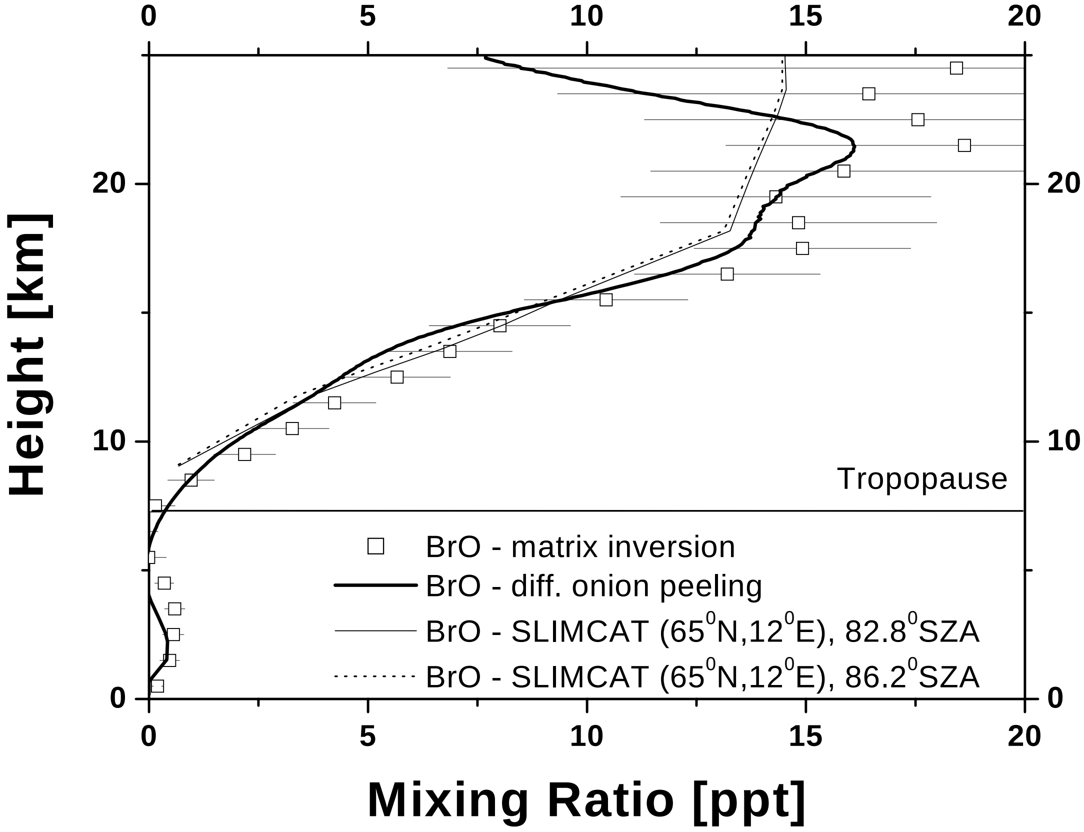

Figure 4.129: BrO mixing ratio profile. The measured profile corresponds to a SZA range of $82.9 - 86.2^o$.

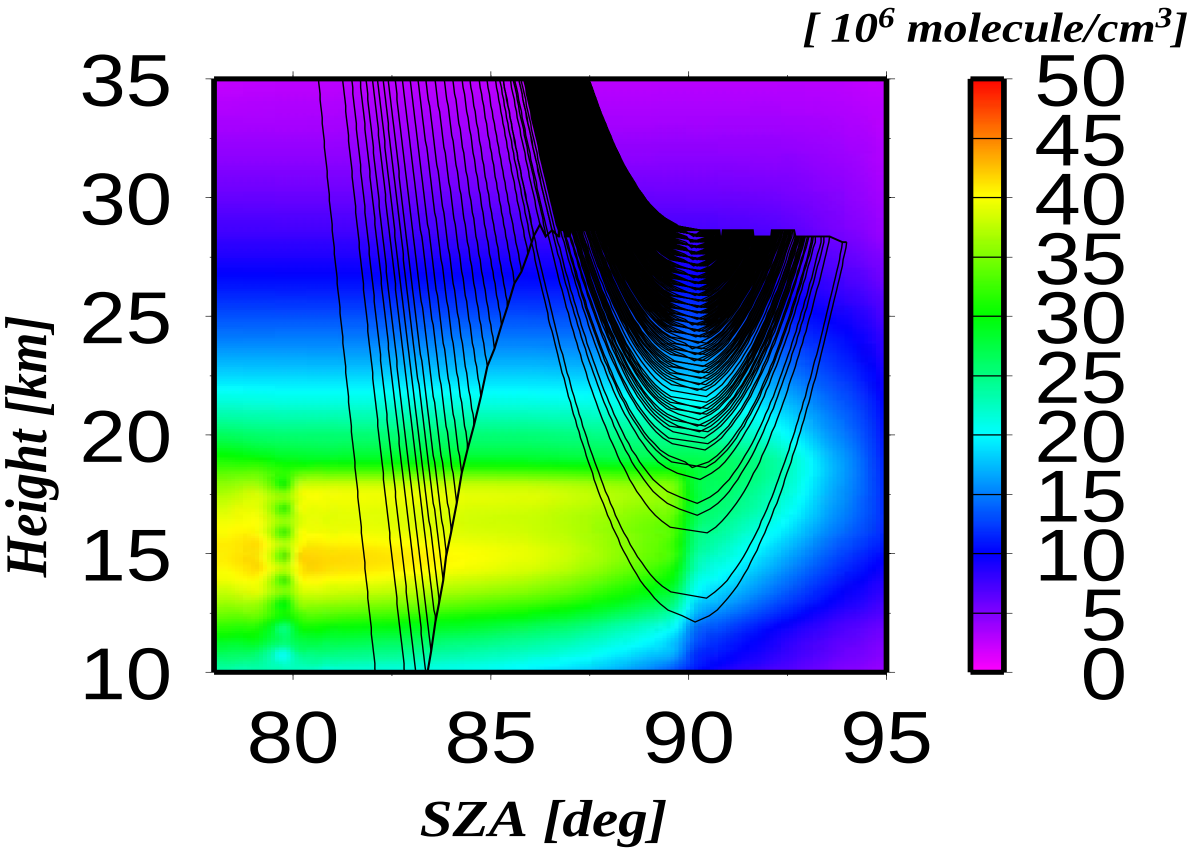

Figure 4.130: Modelling of BrO SCDs by integration of the concentration along the light path through the atmosphere. The model field for the measurements is color-coded as a function of height and SZA. Both the trajectory of the balloon (thick line) and the light rays from the sun (fine lines) reaching the balloon instrument are shown in the plot.

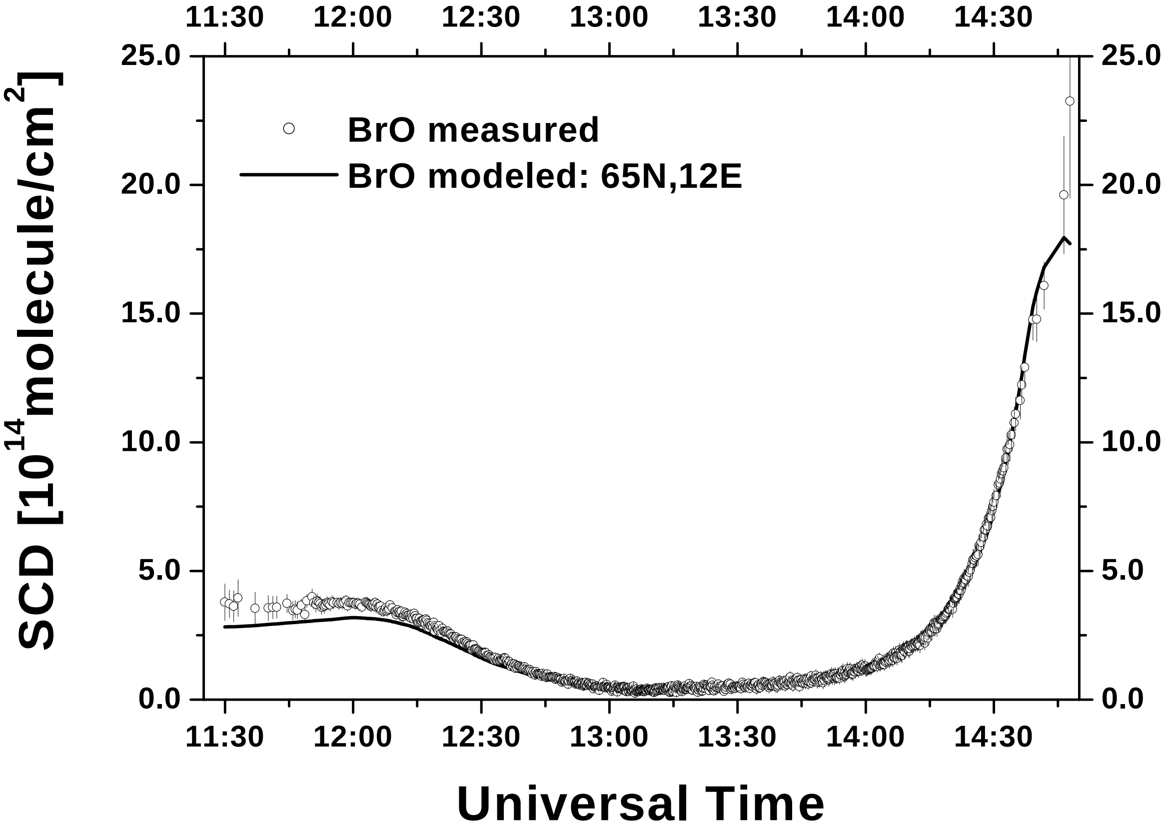

Figure 4.131: Time evolution of measured and modelled BrO SCDs for the Kiruna 99 flight on Feb. 10.

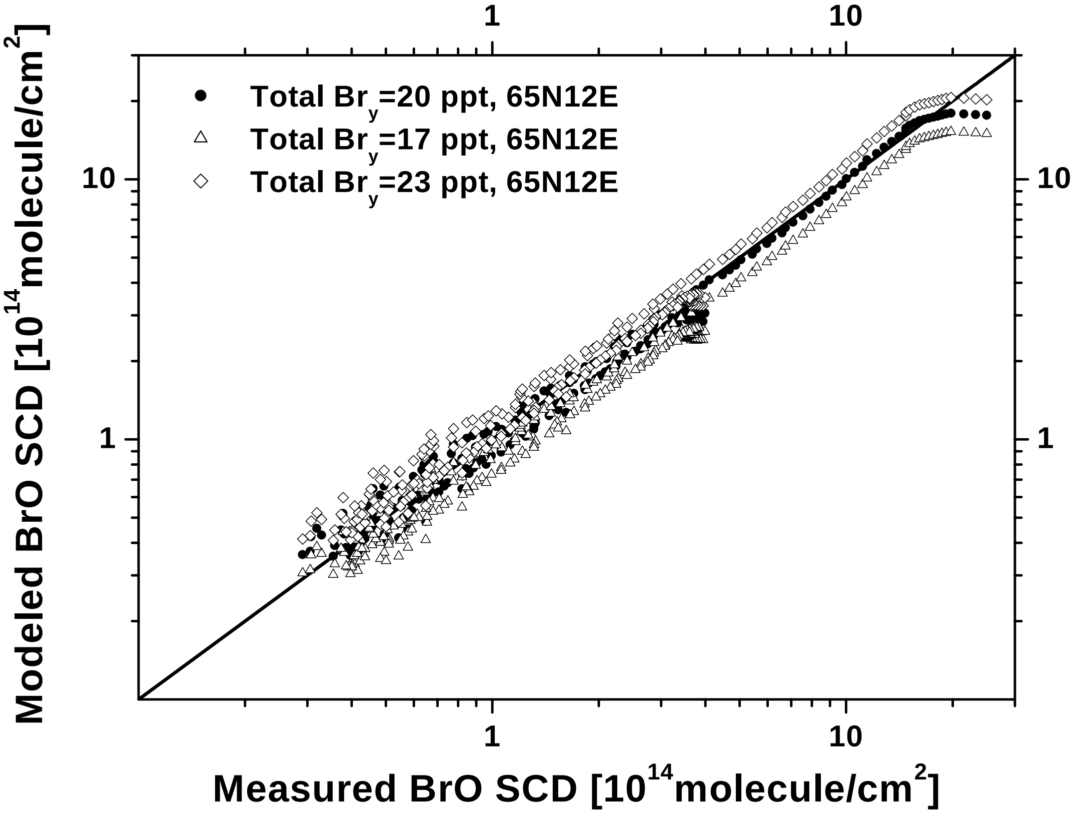

Figure 4.132: Correlation plot of modelled and measured BrO SCDs for the Kiruna 99 flight. The different model runs $(65N, 12E)$ with different total inorganic bromine contents are shown (Br_y = 17, 20 and 23 ppt).

(occultation), where the modelled SCDs tend to reach a plateau or even to decrease. This can also be explained by the underestimation of the model in the lower stratosphere, as the tangent points of the occultation measurements reach down to 10 km altitude for the last measurement points.

Figure 4.132 shows the correlation plot for the modelled and measured BrO SCDs for the three model runs with 17, 20 and 23 ppt total Br_y in the maximum. The best agreement with the measurement is being observed for 20 ppt total Br_y, which is in accordance with the comparisons done before. The correlation is no more linear in the case of the late occultation measurements - the largest SCDs - and for the tropospheric and lower stratospheric SCDs, where the SCDs are smaller modelled than measured.

Figure 4.133 shows the comparison of the integrated BrO VCDs measured by the balloon instrument, the ground-based zenith-scattered light DOAS spectrograph [Otten et al. 1997] and the satellite instrument GOME. The satellite (GOME) was measuring in the 320x40 km^2 area around Kiruna for a SZA of 82.1^o, which is nearly the same SZA encountered during the beginning of the balloon ascent. It is also clear that GOME is not only averaging over the whole pixel area but also over the different SZAs (the SZA change in this area is about 0.8^o). Obviously, there is again a striking discrepancy between the total vertical columns measured by GOME and the ground-based spectrograph on the one hand and the stratospheric BrO VCD measured by the balloon instrument on the other hand. This VCD difference is again an indirect evidence for a tropospheric BrO VCD of $(0.9-2.1)\times 10^{13}$molecule/cm^2. The gap between these measurements can be closed by the measured tropospheric BrO profile, which will be discussed in the next chapter.

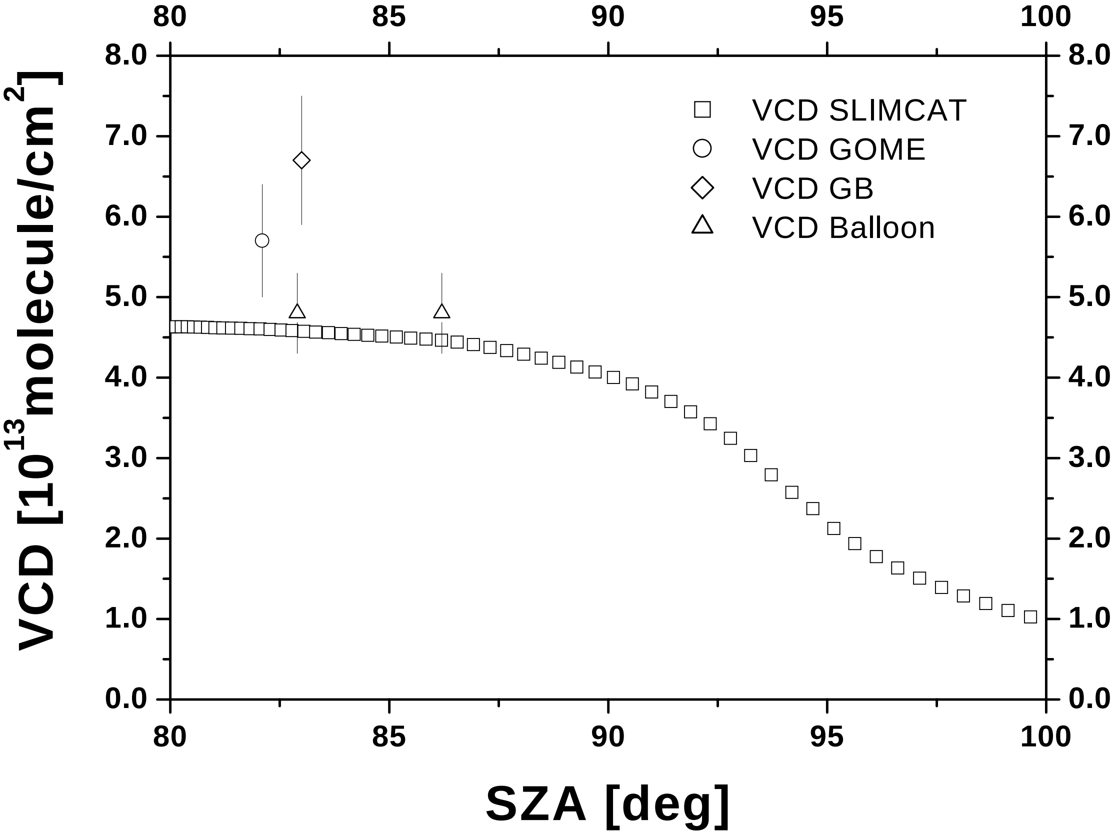

Figure 4.133: *BrO* VCD comparison between balloon-borne, ground-based and satellite-borne instruments (GOME). The VCD derived from the balloon profile belongs to a SZA range from 82.9 – 86.2^o, while the GOME measurement refers to SZA of 82.1^o and the ground-based VCD measurement took place at a SZA of 82^o.

4.6.2 *OClO* profile and SCD model comparison

The next Figures 4.134-4.135 display the retrieved concentration and mixing ratio profiles of *OClO* as they can be retrieved from the measured *OClO* SCDs during balloon ascent - evaluated in the *OClO* wavelength range. As the *OClO* is largely photolysed during daytime, the concentration is increasing dramatically during the occultation. That is why the different model profiles for the two SZAs at the beginning and the end of the balloon ascent measurements are also plotted in these figures. The model profile concentration maximum position agrees moderately with the measurements, while the lower part of the measured profile cannot be reproduced by the model. Here, the model concentration profiles are the ones calculated by the SLIMCAT model, while in the mixing ratio profile plot the profiles calculated by another 3-D CTM model (REPROBUS)[Lefévre et al. 1994] were included. Both models show the same profile structure, though the SLIMCAT model sees more *OClO*. The models take into account the same chemistry scheme, but use different meteorologies. SLIMCAT uses UKMO[7] meteorological data and REPROBUS uses ECMWF[8] data. Both consider heterogeneous chemistry on PSCs, which is mainly occurring in the heights of the modelled maximum. Here it is referred to chapter 7 of this thesis to deal with the question about this chlorine activation in detail.

As *OClO* is changing faster than *BrO* during the solar occultation, it is even more appropriate to calculate model SCDs from the 3-D CTM models and compare them directly to the measured SCDs. This is shown in Figure 4.136 together with the photochemical *OClO* field as a function of SZA and

---

[7] United Kingdom Meteorological Office

[8] European Centre for Medium-Range Weather Forecast, Reading

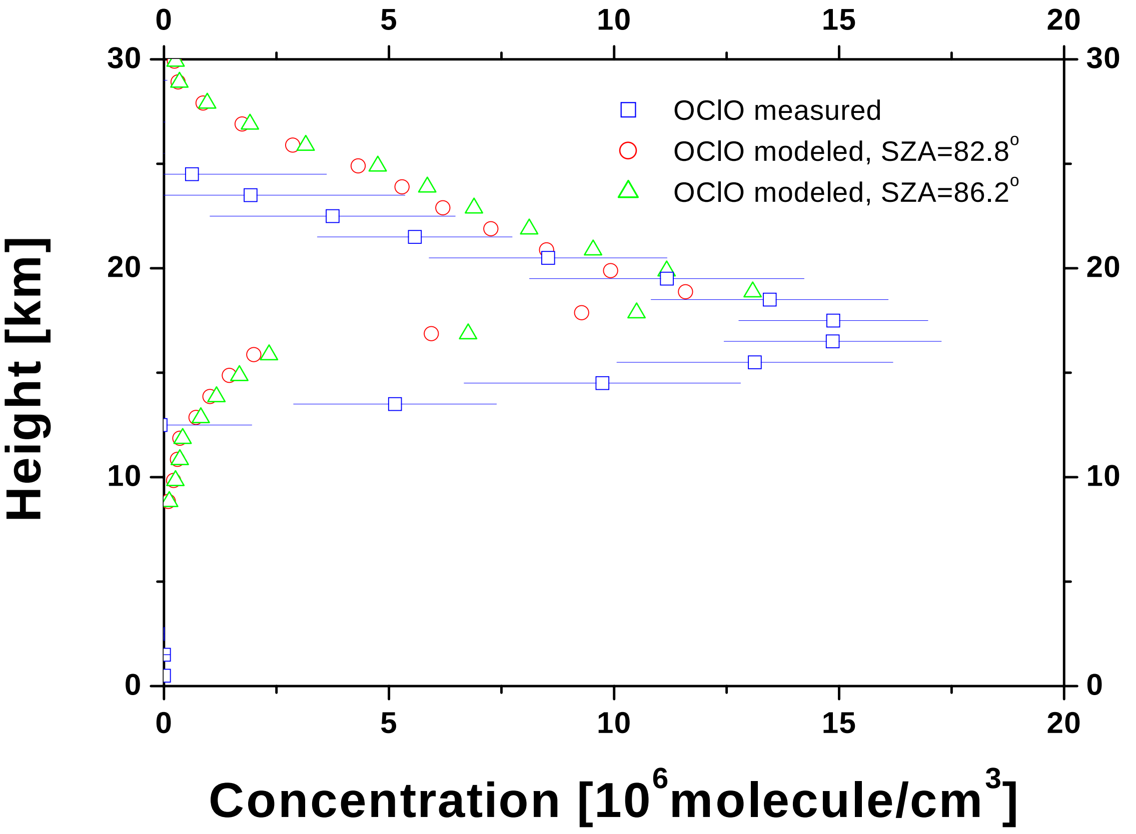

Figure 4.134: *OClO* concentration profile. The measured profile corresponds to a SZA range of $82.9 - 86.2^o$.

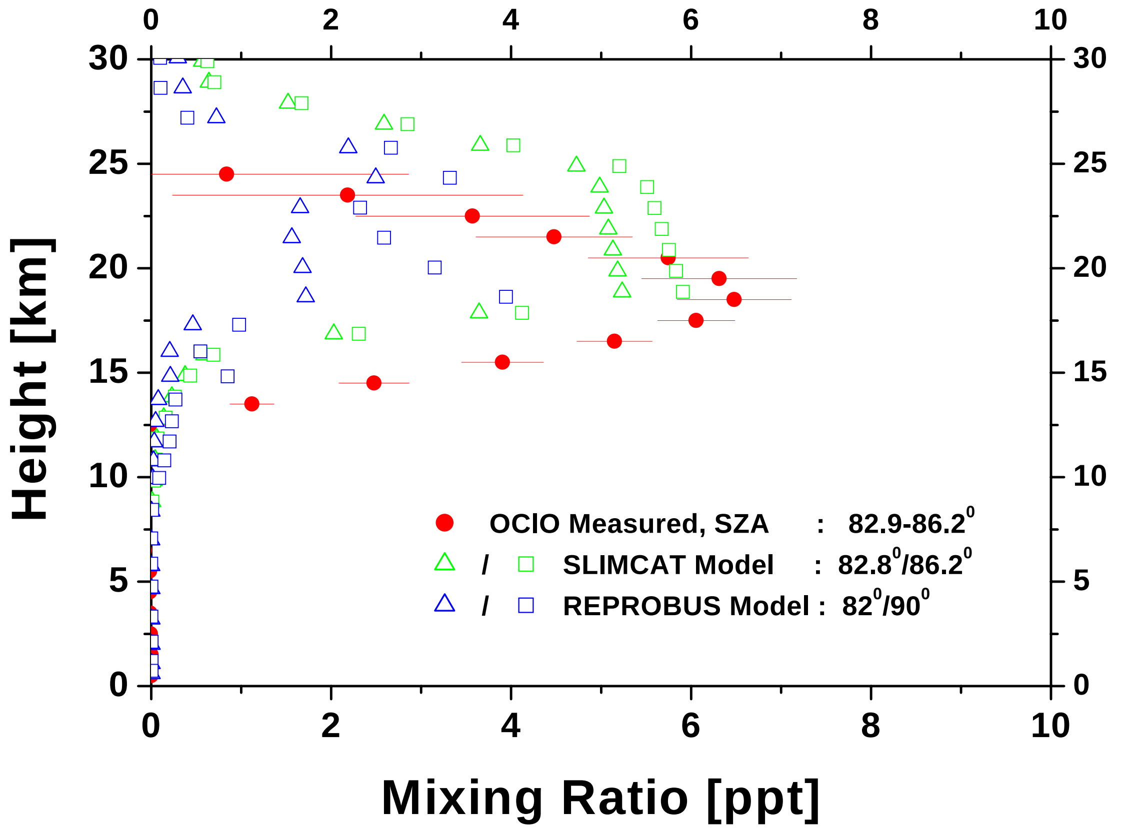

Figure 4.135: *OClO* mixing ratio profile. The measured profile corresponds to a SZA range of $82.9 - 86.2^o$.

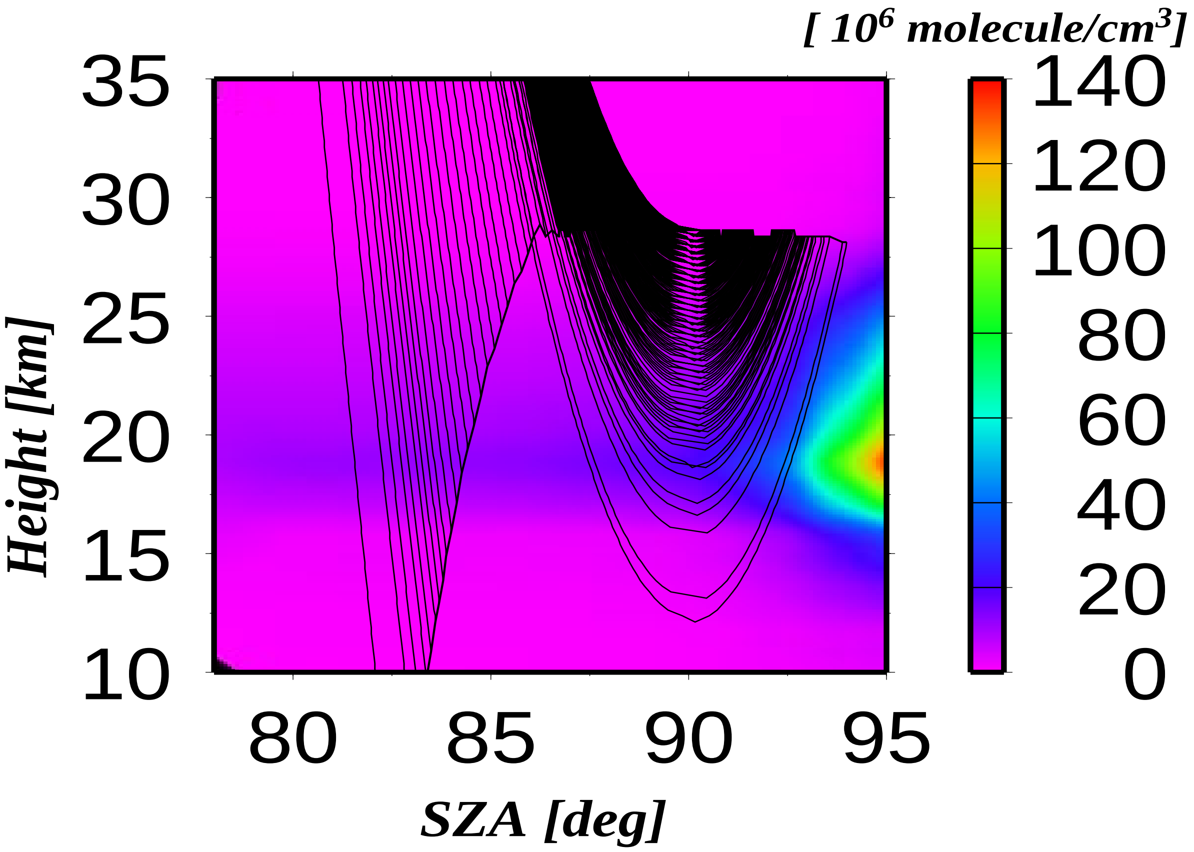

Figure 4.136: Modelling of *OClO* SCDs by integration of the concentration along the light path through the atmosphere. The model field for the measurements is colour-coded as a function of height and SZA. Both the trajectory of the balloon (thick line) and the light rays from the sun (fine lines) reaching the balloon instrument are shown in the plot.

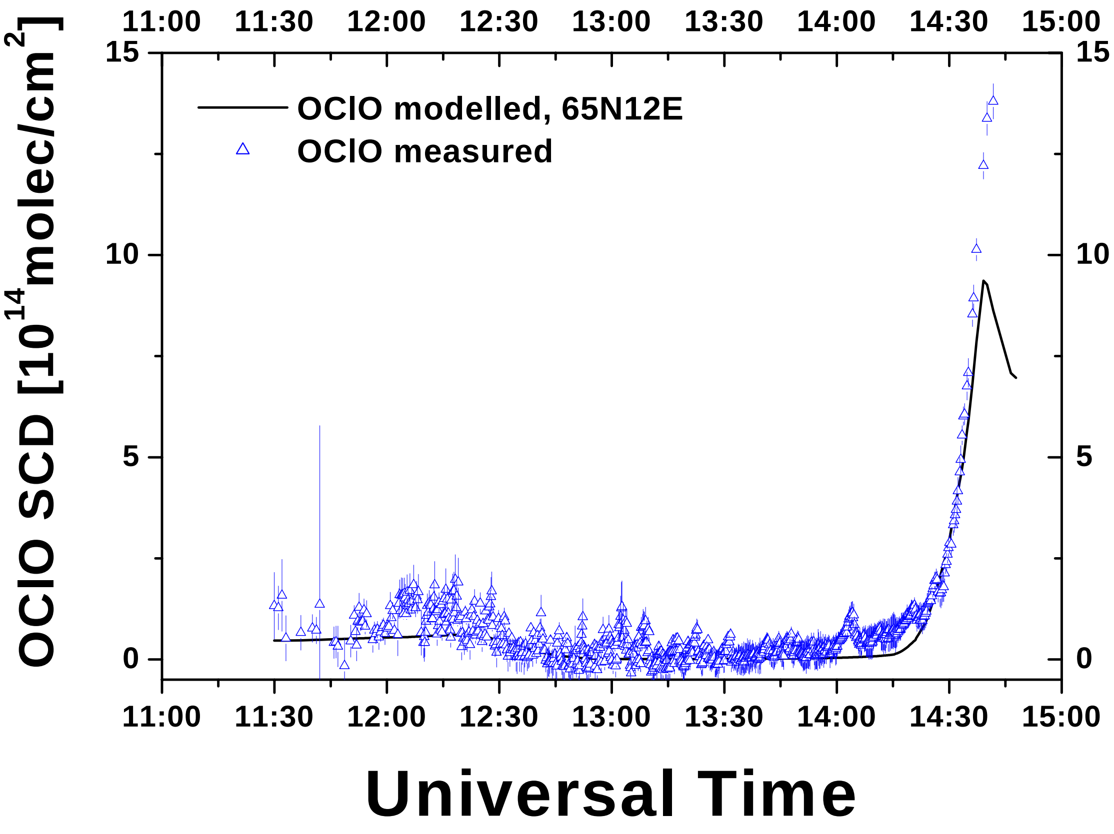

Figure 4.137: Time evolution of measured and modelled *OClO* SCDs for the Kiruna 99 flight on Feb.10.

height.
The comparison of modelled and measured *OClO* SCDs is shown in Figure 4.137 and 4.138. We can generally observe a striking agreement of the modelled and measured SCDs during the whole flight, as the SCDs during the ascent and the float of the balloon flight scatter very much. In the lower stratosphere the model sees less *OClO* compared to the average of the SCDs, which explains the underestimation of the *OClO* in the first part of the flight and also at the end of the flight (occultation), where the modelled SCDs begin to decrease. This can also explained by the underestimation of the model in the lower stratosphere, as the tangent points of the occultation measurements reach down to 10 km altitude for the last measurement points. During the first part of the occultation the measured SCDs increase faster than in the model.

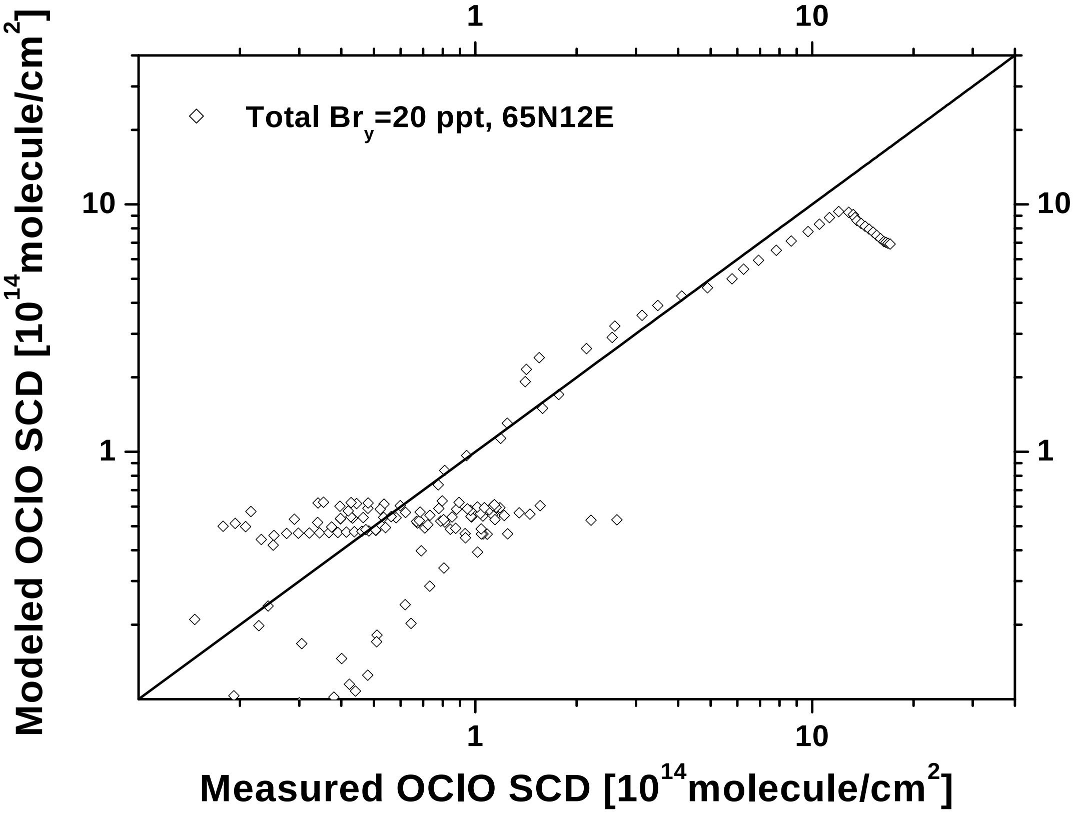

Figure 4.138: Correlation plot of modelled and measured *OClO* SCDs for the Kiruna 99 flight. The model run $(65N, 12E)$ was conducted with a total inorganic bromine content of $20\,ppt$.

The correlation plot between modelled and measured *OClO* SCDs again emphasizes the good agreement of model and measurement in the occultation part of the flight. During the ascent and the float the scatter of the SCDs hides the systematic difference between the model and measurement, which can be found in the profiles after averaging over the SCDs using a gaussian filter with 2-3 km filter width (σ).

4.7 The sunrise flight at Gap on June 25, 1999

Another issue of the HALOMAX[9] project was to study the mid-latitude stratosphere. That is why we conducted one more flight at mid-latitudes from Gap (France) in summer 1999. Because of the ground wind conditions in Gap during that time, it was only possible to launch a big stratospheric balloon during the night, when winds were less strong. That is why in summer only sunrise flights are possible starting from Gap.
In Figure 4.139 the trajectory of the balloon and the directions of the line of sight during the flight are plotted. While the balloon is moving in westerly direction the line of sight direction changes from north-east to south. During the sunrise the tangent points of the line of sight are moving towards the balloon in westerly direction.

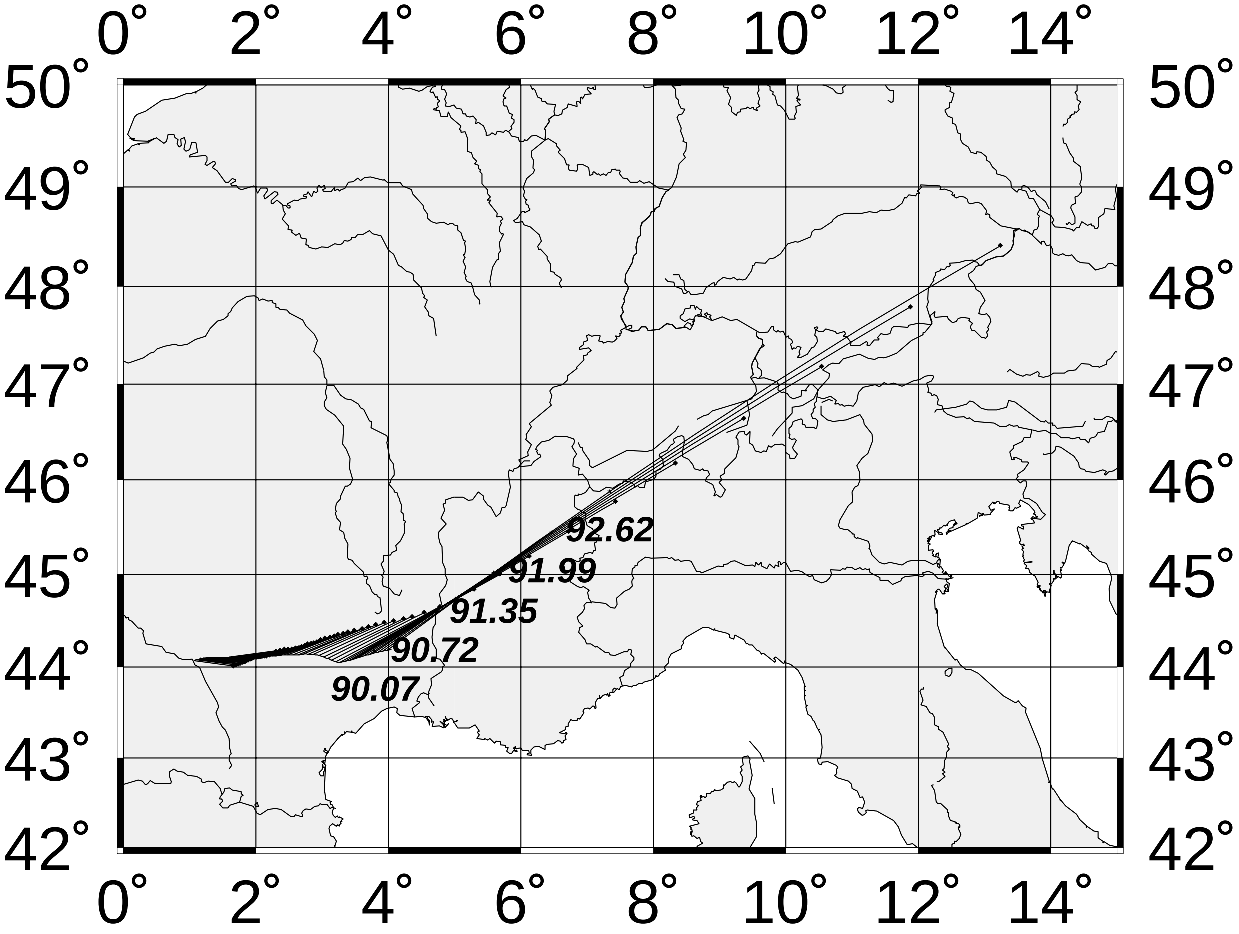

Figure 4.139: Balloon trajectory during the flight at Gap(France) on Jun. 25, 1999. The trajectory is the curved line towards the west, while the lines ending with a point denote the light rays for SZAs larger than 90^o and the end points show the location of the tangent points - that is the main area of atmospheric absorption during occultation.

In Figure 4.140 you can see the balloon height as a function of time as well as the SZA at the balloon position (latitude, longitude) during the time when measurements were taken. As the balloon is moving to the west during the sunrise the SZA is decreasing more slowly than if the position of the balloon was fixed.

---

[9] Mid and high latitude stratospheric distribution of long and short lived HALogen species during the MAXimum of the chlorine loading

The temperatures are well above the PSC formation temperatures and so chlorine activation does not play an important role during these measurements. After the sunrise the balloon cover was opened on the top (valve) to make the balloon descend slowly through the stratosphere. As the descend velocity was quite slow, the balloon did not descend further down than 20 km altitude before it had to be cut in the west of France - to be sure that the balloon was not moving across the Atlantic coast line.

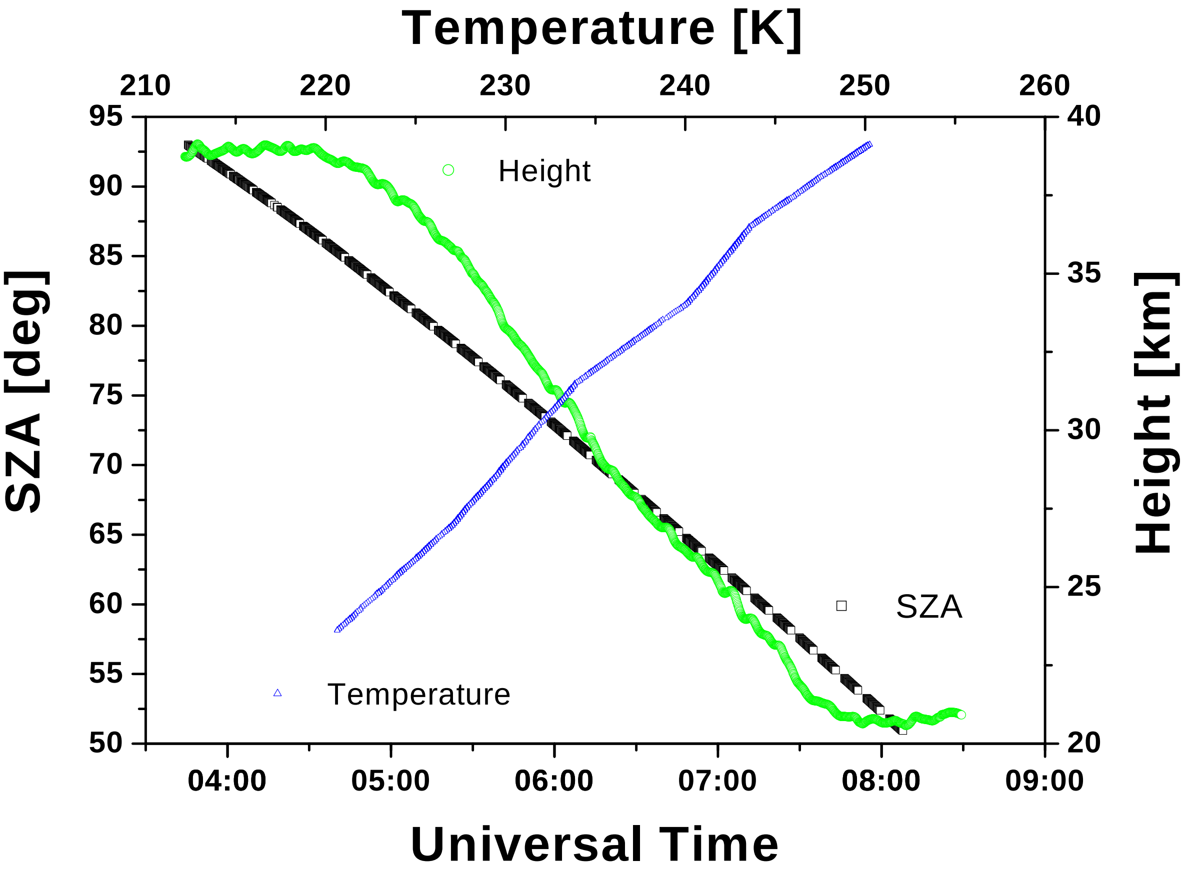

Figure 4.140: Balloon trajectory, temperature and SZA at balloon position (latitude, longitude) during the flight at Gap(France) on Jun. 25, 1999.

For the evaluation of the measured spectra the standard BrO retrieval wavelength window (346-360 nm) was used - as shown in an example in Figure 4.141. The BrO spectral signature can clearly be detected.

The time evolution of the measured species during the flight is shown in Figure 4.142-4.149. As the SZA is constantly decreasing the SCDs of all species are decreasing during the occultation part of the flight (sunrise). After the sunrise the balloon was opened to make the instrument descend. That is the part of the flight, when the SCDs are again slightly increasing. The O_3 and BrO SCDs are increasing more strongly than the O_4 and NO_2 SCDs, because the O_3 and BrO profile maxima are at lower altitudes than the NO_2 maximum and the O_4 mixing ratio is rather constant with height.
The wavelength shift of the spectrograph is comparable to the first Gap flight in 1997 ($\leq$0.002 nm) - again showing that the main part of the wavelength shifts occurs during the ascent of the balloon in the troposphere and lower stratosphere.

The Langley plot for the BrO SCDs is shown in Figure 4.150. The resulting SCD offset is $(0.5 \pm 0.5) \times 10^{13}$ molecule/cm^2 and the mixing ratio determined above float is (20 ± 5) ppt, which agrees reasonably well with the profile retrieved from the occultation SCDs, which will be shown in the following. The error of the Langley plot results are larger for the sunrise flights at Gap compared to

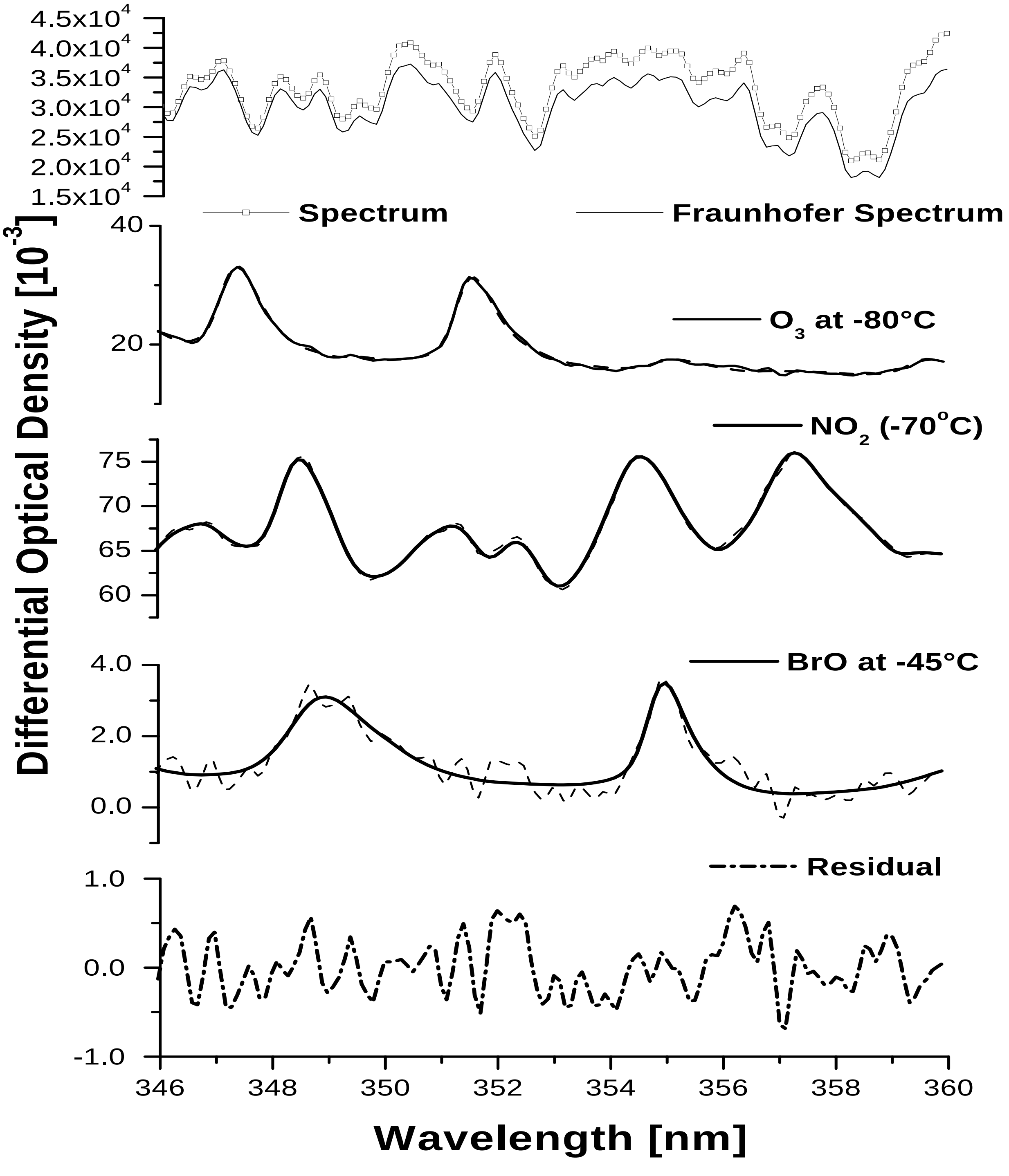

Figure 4.141: Typical DOAS evaluation in the BrO retrieval wavelength range (345-360 nm) for Gap 1999 for a spectrum measured in late occultation.The fit included O_3 at -80^oC and -20^oC(not shown), NO_2 at -70^oC (not shown), O_4(not shown), BrO at -45^oC and a polynomial of degree 3. The last spectrum is the residual of the fit which cannot be explained by the fit but is due partly to statistical noise and to systematic errors. All spectra have been filtered with a binomial filter of degree 3 before the fit.

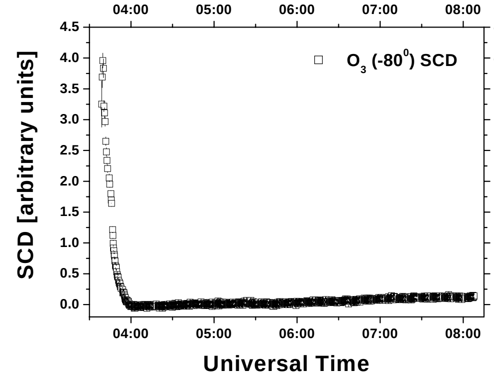

Figure 4.142: Time evolution of the $O_3(-80^oC)$ SCDs during the flight.

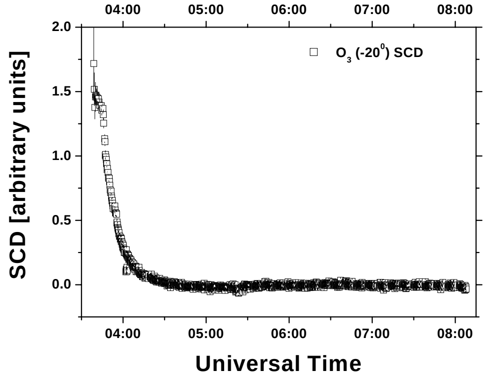

Figure 4.143: Time evolution of the $O_3(-20^oC)$ SCDs during the flight.

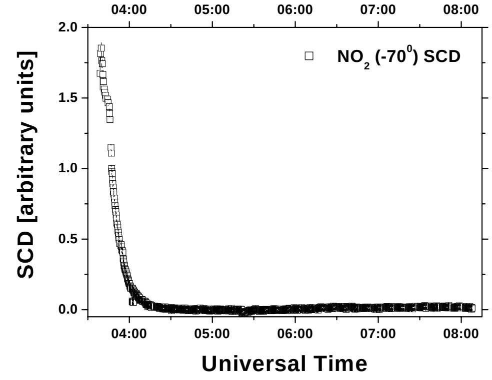

Figure 4.144: Time evolution of the $NO_2(-70^oC)$ SCDs during the flight.

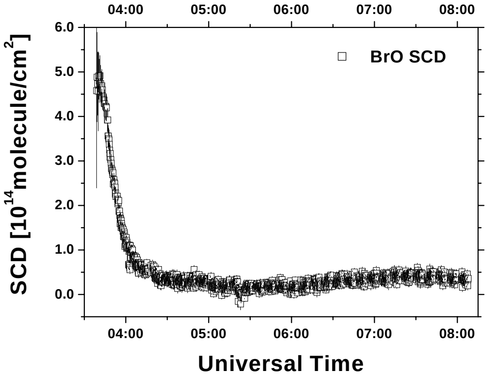

Figure 4.145: Time evolution of the $BrO(-45^oC)$ SCDs during the flight.

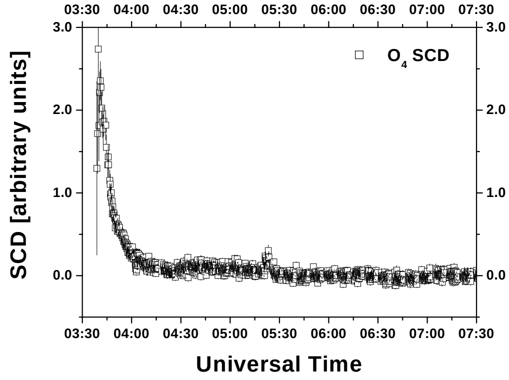

Figure 4.146: Time evolution of the O_4 SCDs during the flight.

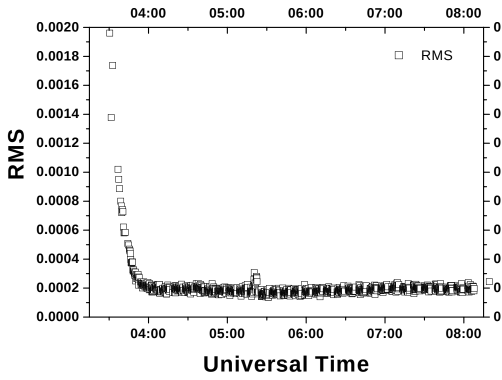

Figure 4.147: Time evolution of the RMS of the DOAS fit during the flight.

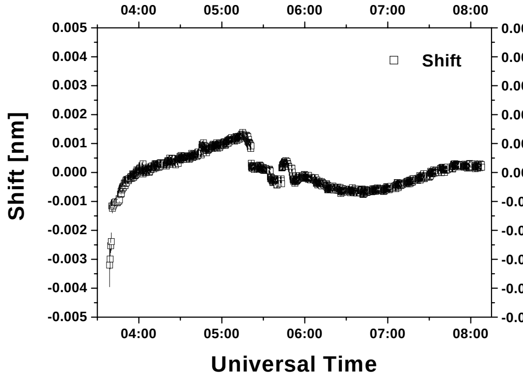

Figure 4.148: Time evolution of the shift of the reference spectra ensemble during the flight.

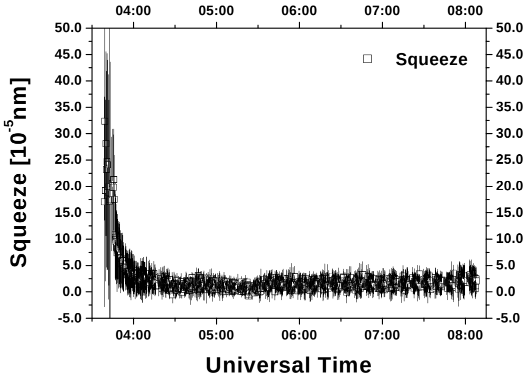

Figure 4.149: Time evolution of the squeeze of the reference spectra ensemble during the flight.

the mid/high latitude ascent flights, where the balloon float altitude is nearer to the maximum of the BrO concentration profile.

Again we retrieve a BrO occultation profile from the measured SCDs - see Figure 4.151 - still taking into account that we do not correct for the photochemical change of the species. As we know from the model comparison in 1997, the photochemical variation during the flight is tremendous, so that the occultation profile is only an approximation of the real profiles.

It is possible to generate a profile only using the SCDs measured during the solar occultation taking into account the SCDs for SZAs between 95 and 77^o. Secondly one can use the descent SCDs to extract a profile for the SZA range $77 - 47^o$ of the balloon flight.

The occultation profile can only reproduce profile values down to an altitude of 15 km, which is the lowest tangent height during the measurements. As the BrO concentration is increasing strongly with decreasing SZA the retrieved profile tends to show much more BrO above 30 km altitude, so that it is an average profile for different photochemical regimes. The same is only partly true for the descent profile, which was retrieved from the SCDs measured between $77-47^o$ SZA. Under these conditions the profile is already a factor of $2 - 3$ larger than at the beginning of the occultation. However, the profile retrieval tends to overrate the BrO amount in the 20-30 km altitude range, where the measurements took place, because we know that BrO cannot amount to more than the total inorganic bromine content of the stratosphere, which is 21 ± 2.5 ppt by that time. This is probably due to the bad SNR of the retrieved SCDs during the balloon descent, which is reflected in the large error bars of the profile. Still, it clearly shows that the BrO is strongly increasing with decreasing SZA and increasing time.

It can also be observed that the matrix inversion is not able to provide profile information above the highest altitude of the SCD measurements, where it states a constant concentration value leading to an artificial increase of the mixing ratio.

4.8 The sunset flight at Kiruna on February 18, 2000

During the THESEO 2000 - EuroSOLVE campaign[10] we conducted one flight at high latitudes from Kiruna, which took place within the highly activated polar vortex, when it was just above the launch site.

Figure 4.153 shows the trajectory of the balloon and the directions of the line of sight during the flight. While the balloon is moving in easterly direction the line of sight direction changes from south to south-west. During the sunset the tangent points of the light rays are moving away from the balloon in westerly direction. In colour the potential vorticity at the 475 K potential temperature level is shown (units of $10^{-6} K * m^2/(kg * s)$).

In Figure 4.154 the balloon height as a function of time can be seen as well as the SZA at the balloon position (latitude, longitude) during the time when measurements were taken. As the balloon is moving to the east during the sunset the SZA is increasing faster than if the position of the balloon was fixed.

The temperatures encountered during the flight are just above the PSC formation temperatures but there has been substantial chlorine activation observed during different other measurements in this winter. The TRIPLE experiment measured increased chlorine activation (up to 2 ppb ClO) in the PSC layer altitude range in early March compared to low activation at the end of January (up to 500 ppt ClO) [EORCU b]. During this winter also record ozone depletion of up to 70% for a 1 km thick region of the lower stratosphere has been measured by different measurement techniques (MATCH ozone sonde technique, ER-2 measurements, etc. [EORCU b]).

So it will again be interesting to search for $OClO$ signature in the measured spectra during the balloon flight to detect chlorine activation.

---

[10] THESEO 2000 is an European ozone measurement campaign that extends the 1997-99 THESEO campaign into winter/spring 1999/2000. There was close cooperation with the American NASA-led SOLVE campaign. See also

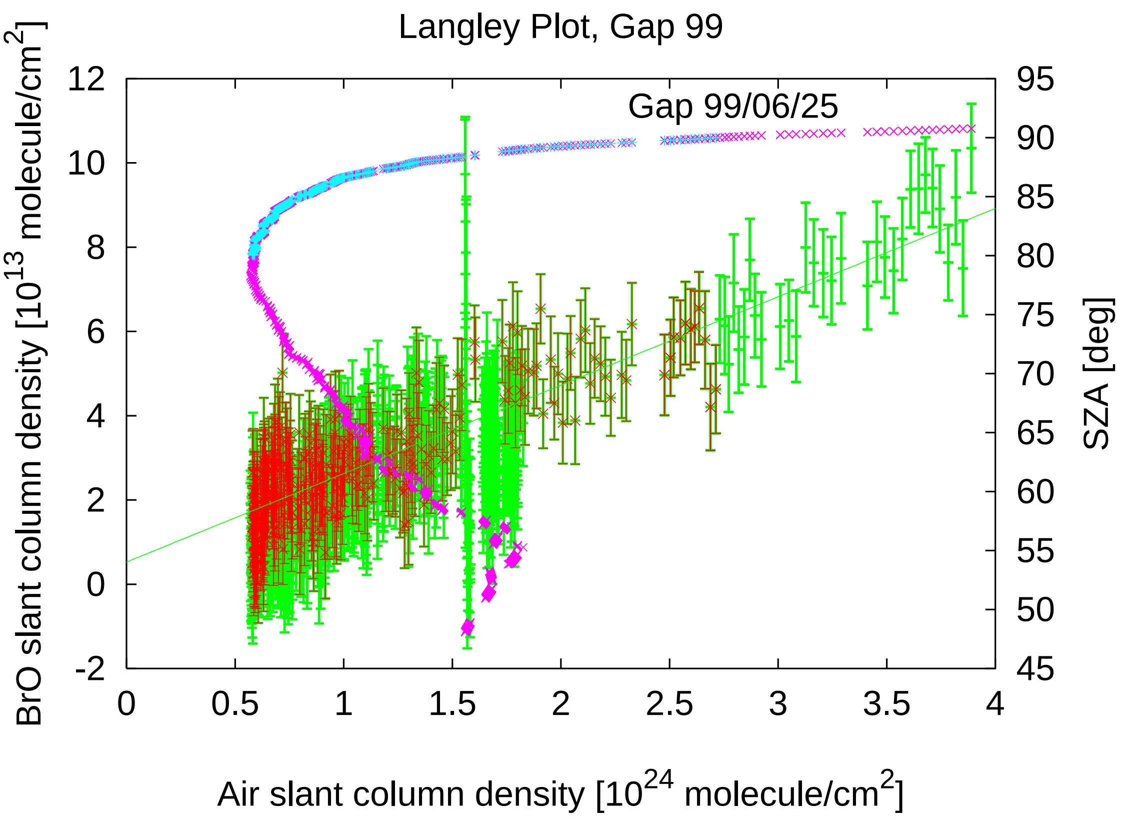

Figure 4.150: Langley plot for the flight at Gap 99 using the float SCDs for SZAs between 80^o and 90^o. The Fraunhofer reference spectrum is measured at a balloon altitude of 34.8 km and a SZA of 76^o. The resulting SCD offset is $(0.5 \pm 0.5) \times 10^{13}$ molecule/cm^2 and the mean mixing ratio above float (20 ± 5) ppt.

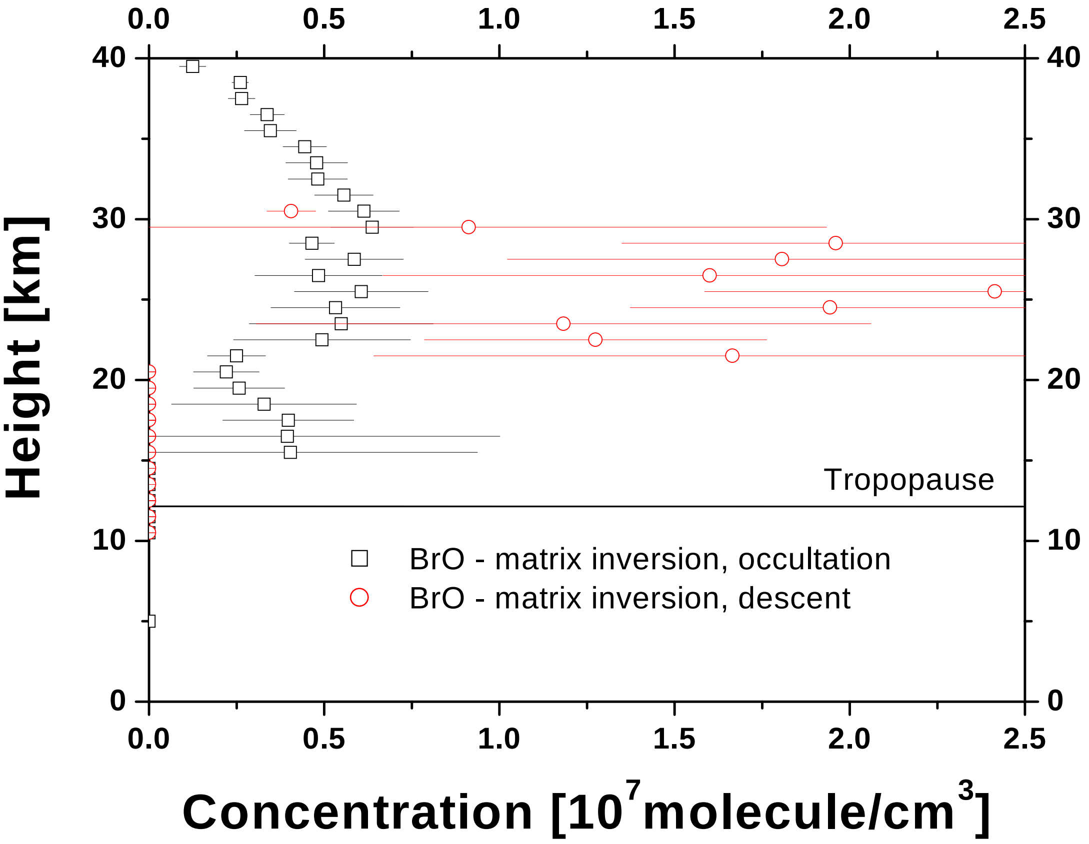

Figure 4.151: *BrO* concentration profile for the occultation part of the flight $(95 - 77^o$ SZA) and for the descent of the balloon $(77 - 47^o$ SZA).

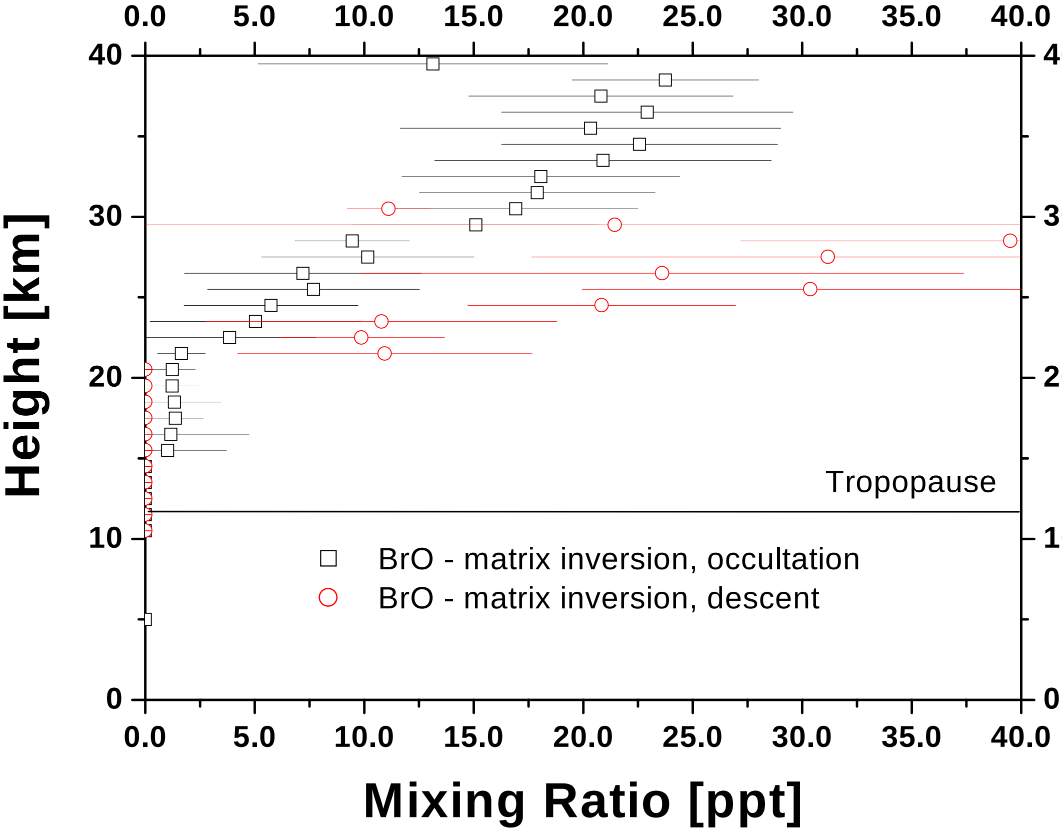

Figure 4.152: BrO mixing ratio profile for the occultation part of the flight ($95-77^o$ SZA) and for the descent of the balloon ($77-47^o$ SZA).

Figure 4.155 and 4.156 show typical DOAS evaluations in two different BrO retrieval ranges for that flight. The first wavelength range ($BrO\,range$) includes the two typically used BrO absorption lines (346-360 nm). In the second case ($BrO-OClO\,range$) one more $OClO$ absorption band is included in the fit to get a better signature of $OClO$ (346-368 nm) improving the residual. As we know from the $OClO$ evaluation of the Kiruna 99 flight, we can use the extended $BrO-OClO$ wavelength window to retrieve the absolute $OClO$ SCDs, because there is no big discrepancy expected compared to the $OClO$ range (362-390 nm). Unfortunately, it is not as easy to evaluate the spectra in the $OClO$ wavelength range for this flight, because the optical preanalyzer was changing its filtering characteristics during the flight leading to different exposure levels of the detector pixels within this wavelength range.

The change of the preanalyzer filtering function does also effect the retrieval of the O_4 fit coefficient within the two latter wavelength ranges, because there is a strong spectral correlation of O_4 with the polynomial used in the fit. As the polynomial tries to account for the change of broad band changes between the Fraunhofer spectrum and the measured spectrum, abrupt changes of the filtering function affect also the retrieval of O_4. This is especially true in the BrO wavelength range, while the correlation between O_4 is much less pronounced in the $BrO-OClO$ range. This is another reason, why to use the $OClO$ retrieved in the $BrO-OClO$ range for this flight, as the discrepancy of the $OClO$ time evolution for the two different ranges is well correlated with the different O_4 evolutions.
The time evolution of the measured species during the flight is shown in Figure 4.157-4.164. As the SZA is constantly increasing the SCDs of all species are increasing during the occultation part of the

---

http://www.nilu.no/projects/theseo2000.

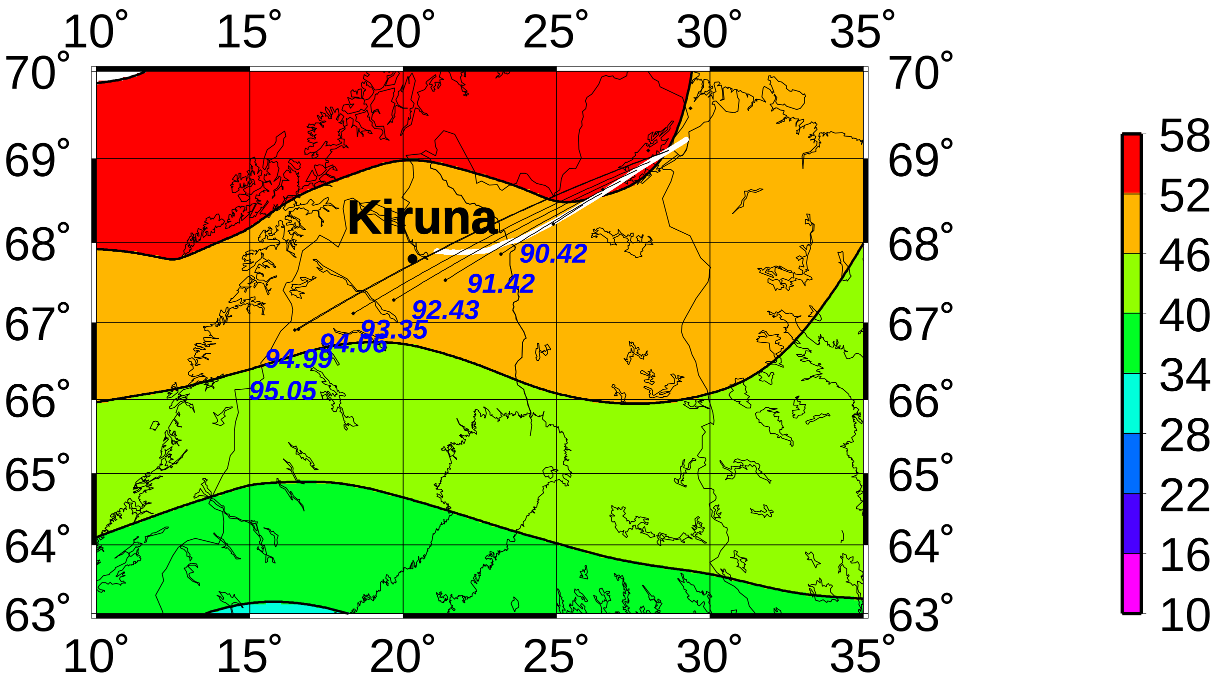

Figure 4.153: Balloon trajectory during the flight at Kiruna on Feb. 18, 2000. The trajectory is the white curved line towards the east, while the lines ending with a point denote the light rays for SZAs larger than 90^o and the end points show the location of the tangent points - that is the main area of atmospheric absorption during occultation. The potential vorticity is given in colour-code in units of $10^{-6} K * m^2/(kg * s)$.

flight. During the ascent of the balloon the SCDs with maximum concentrations in the lower and middle stratosphere are first increasing and then decreasing, while the O_4 SCDs - not shown here - are decreasing constantly proportional to the square of the observed airmass.
The wavelength shift of the spectrograph during the balloon ascent is largest in the troposphere, where the pressure differences between the measurements are the largest. In this flight the small leak of our spectrograph housing was larger than during the other flights, so that the shift between the first and the last measurements is larger (a factor of 2-3), than during the other ascent flights. That is why the RMS of the DOAS fits does not decrease to the statistical photoelectron noise level before the balloon reaching the float altitude.

4.8.1 BrO profile and SCD model comparison

The float of the flight is reached by the balloon quite late for a SZA of 89^o, so that there are only a few BrO SCDs available for the determination of the SCD offset using the Langley plot technique. That is why it was tried to evaluate the spectra of this flight using the Fraunhofer reference spectrum measured during the last winter flight at Kiruna in 1999. When we plot the resulting SCDs as a function of the originally retrieved SCDs we get a linear relation, where the offset determines the SCD offset difference between the two Fraunhofer reference spectra. This is shown in Figure 4.165 and the offset is $(1.6 \pm 0.2) \times 10^{13}$ molecule/cm^2 leading to a SCD offset of the Kiruna 2000 Fraunhofer spectrum of $(5.2 \pm 0.7) \times 10^{13}$ molecule/cm^2 - taking account of the SCD offset of the Kiruna 1999 Fraunhofer spectrum.

There is a nearly perfect linearity between the two evaluated SCD data sets and so the SCD offset retrieved using the two data sets will be applied.

The resulting concentration and mixing ratio profiles are shown in Figure 4.166-4.167 together

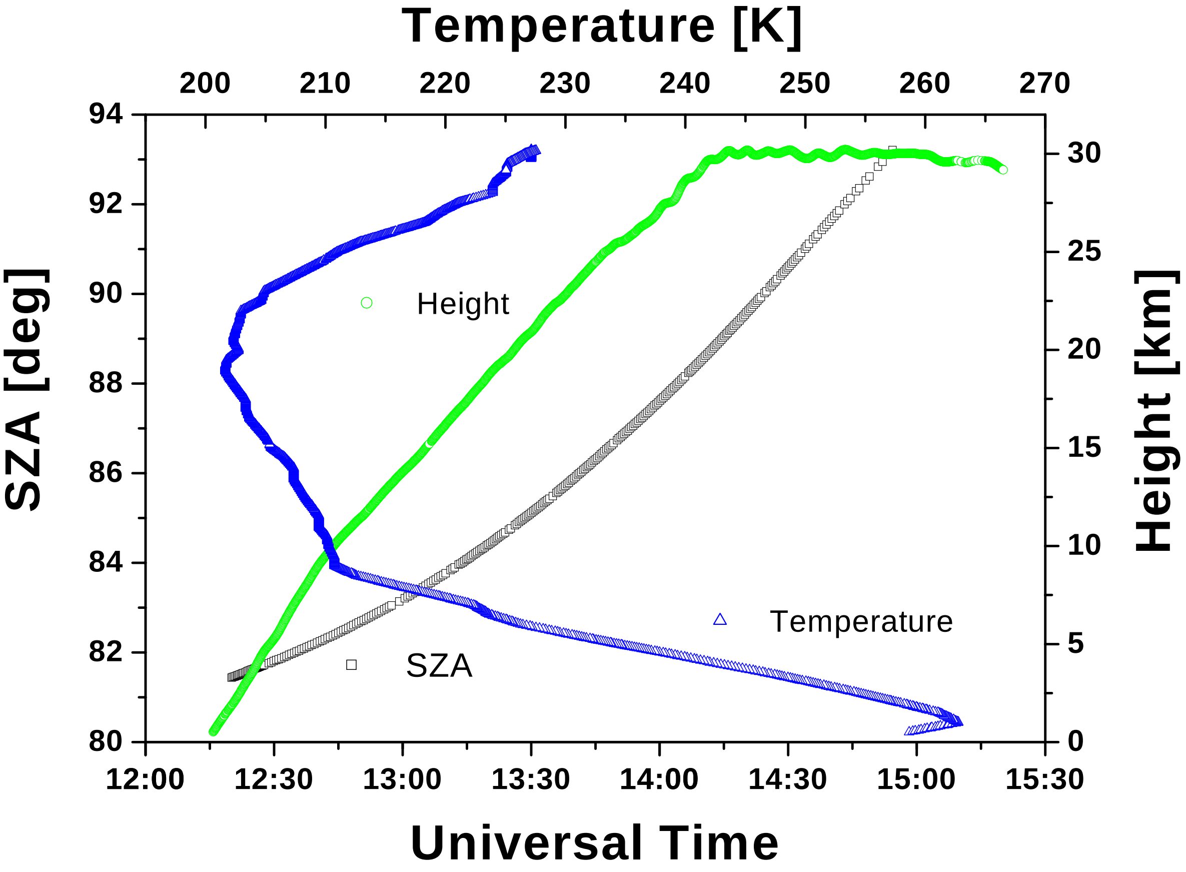

Figure 4.154: Balloon trajectory, temperature and SZA at balloon position (latitude, longitude) during the flight at Kiruna(Sweden) on Feb. 18, 2000.

with the modelled profiles (SLIMCAT[11]) for the two boundary SZAs 80.8 and 90^o. Generally a good agreement between the model and measurement can be observed below and above the concentration maximum, while the measured maximum is $10 - 20\%$ larger than modelled. As the photochemical change during this balloon ascent was quite substantial, the higher part of the profile belongs to larger SZAs and smaller profile values explaining the observed maximum in the mixing ratio.

It can be observed that the SLIMCAT model cannot describe BrO right in the lower stratosphere near to the tropopause. Below 12 km altitude the model underestimates the measured BrO significantly, probably by underestimating total Br_y in that altitude range.

In the middle stratosphere above 25 km the model and measurement are in quite good agreement taking into account the errors, especially when considering the difference between the two different profile retrieval methods.

The photochemical two-dimensional model field concentrations of the different chemical species as a function of height and SZA can be used again to generate modelled BrO SCDs, which can be compared then directly to our measurements, without manipulation of the measured data. Figure 4.168 shows the photochemical field of BrO - as modelled by SLIMCAT - and the line of sight through it during the balloon measurements.

When comparing the measured and modelled SCDs as a function of time - see Figure 4.169 - one can observe again a good agreement between model and measurement. The model describes the measurements very well in the float part and the late occultation of the flight, while it tends to

---

[11] It should be mentioned that the height levels in the SLIMCAT model have been changed from 12 to 24 in this new version available since spring 2000.

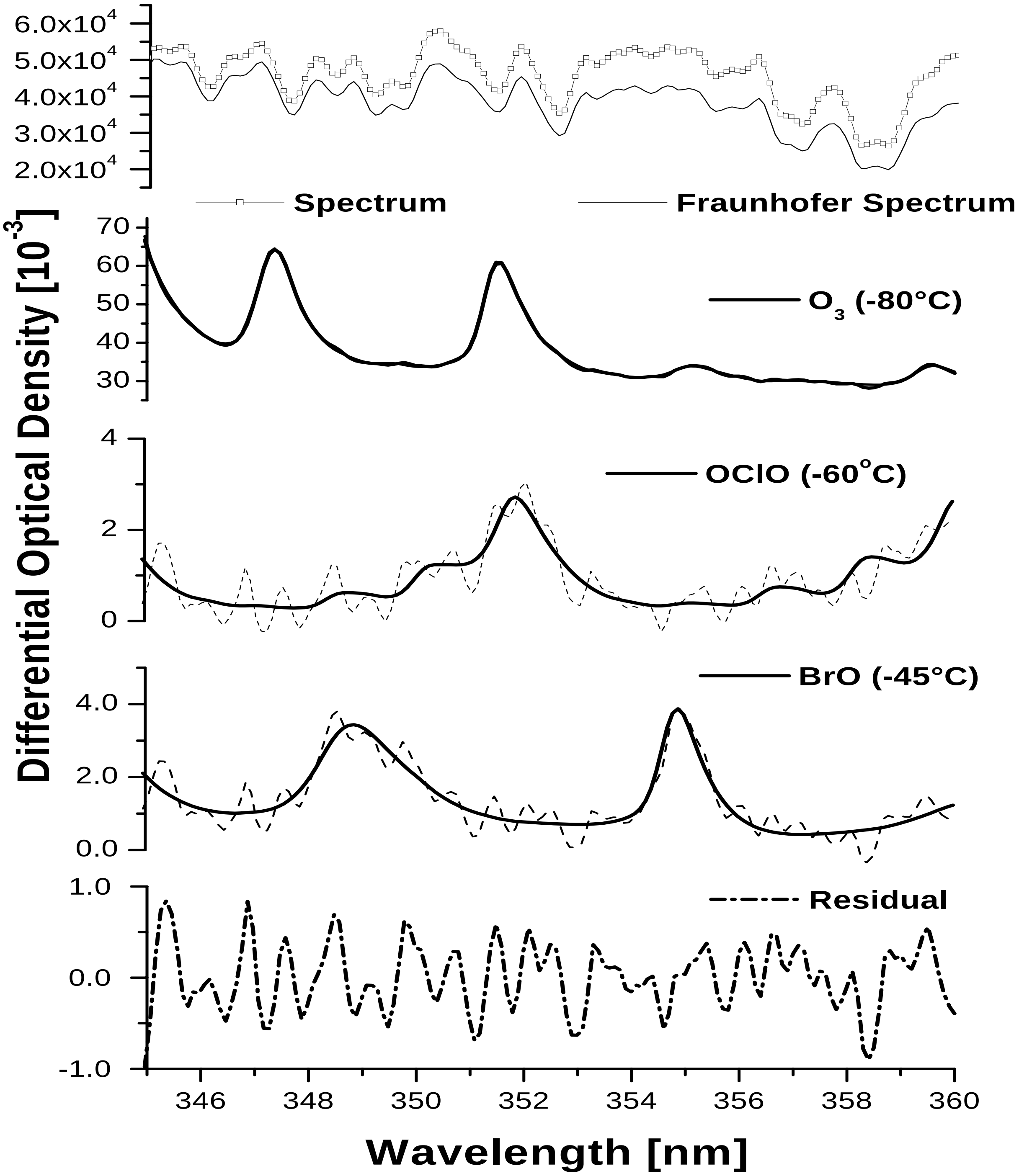

Figure 4.155: Typical DOAS evaluation in the BrO retrieval wavelength range (346-360 nm) for Kiruna 2000 for a spectrum measured at the tropopause. The fit included O_3 at -80^oC and -20^oC(not shown), NO_2 at -70^oC (not shown), O_4(not shown), BrO at -45^oC, $OClO$ at -60^oC and a polynomial of degree 3. The last spectrum is the residual of the fit which cannot be explained by the fit but is due partly to statistical noise and to systematic errors. All spectra have been filtered with a binomial filter of degree 3 before the fit.

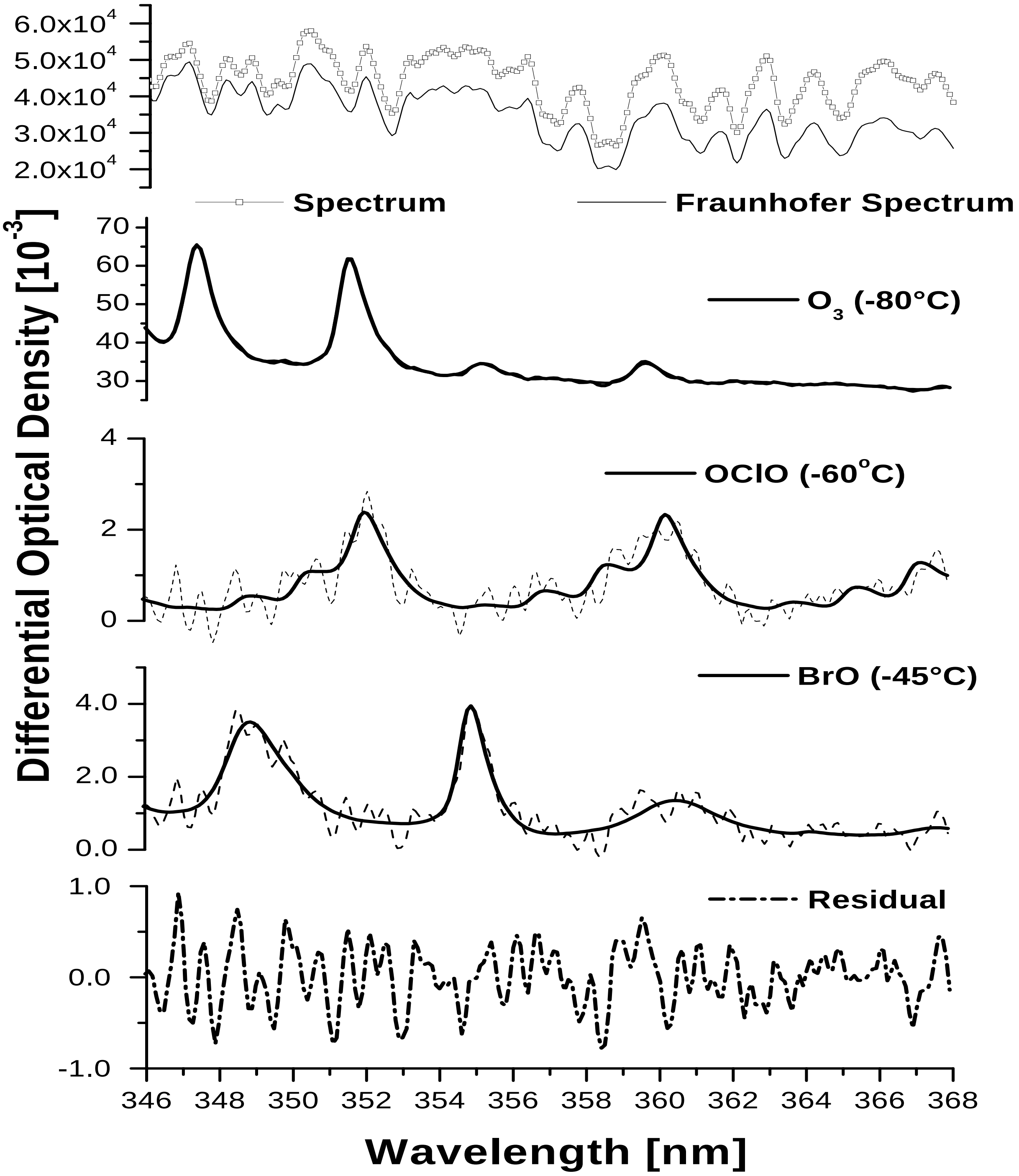

Figure 4.156: Typical DOAS evaluation in the $BrO-OClO$ retrieval wavelength range (346-368 nm) for Kiruna 2000 for a spectrum measured in late occultation. The fit included O_3 at -80^oC and -20^oC(not shown), NO_2 at -70^oC(not shown), O_4(not shown), BrO at -45^oC, $OClO$ at -60^oC and a polynomial of degree 5. The last spectrum is the residual of the fit which cannot be explained by the fit but is due partly to statistical noise and to systematic errors. All spectra have been filtered with a binomial filter of degree 3 before the fit.

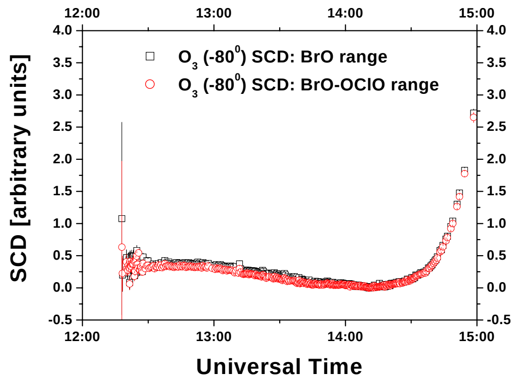

Figure 4.157: Time evolution of the $O_3(-80^oC)$ SCDs during the flight.

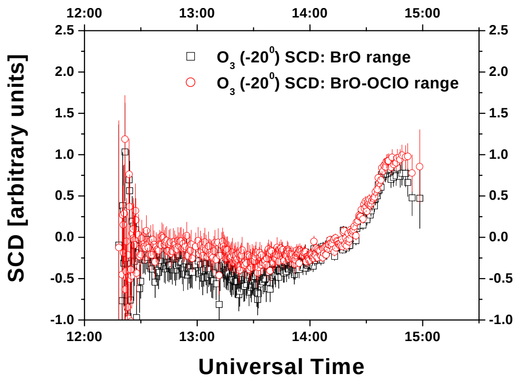

Figure 4.158: Time evolution of the $O_3(-20^oC)$ SCDs during the flight.

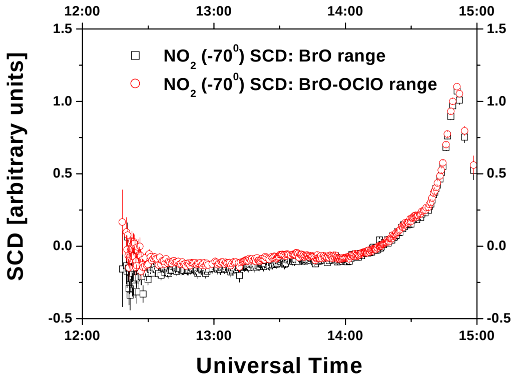

Figure 4.159: Time evolution of the $NO_2(-70^oC)$ SCDs during the flight.

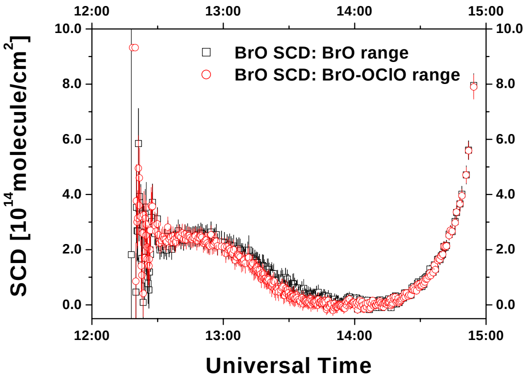

Figure 4.160: Time evolution of the $BrO(-45^oC)$ SCDs during the flight.

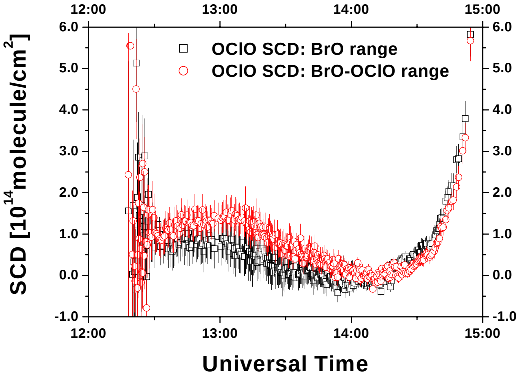

Figure 4.161: Time evolution of the $OClO$ SCDs during the flight.

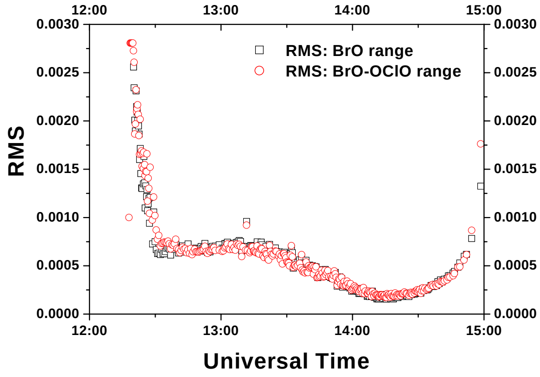

Figure 4.162: Time evolution of the RMS of the DOAS fit during the flight.

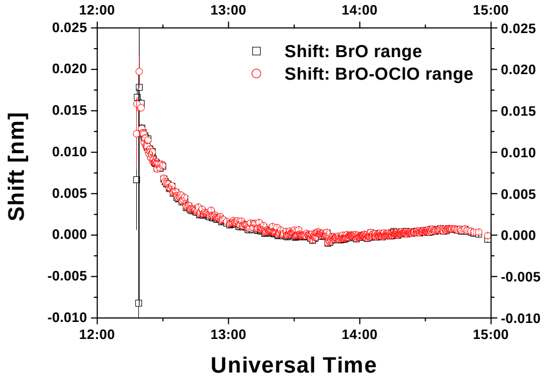

Figure 4.163: Time evolution of the shift of the reference spectra ensemble during the flight.

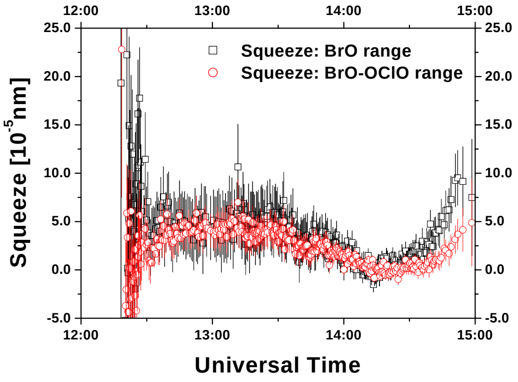

Figure 4.164: Time evolution of the squeeze of the reference spectra ensemble during the flight.

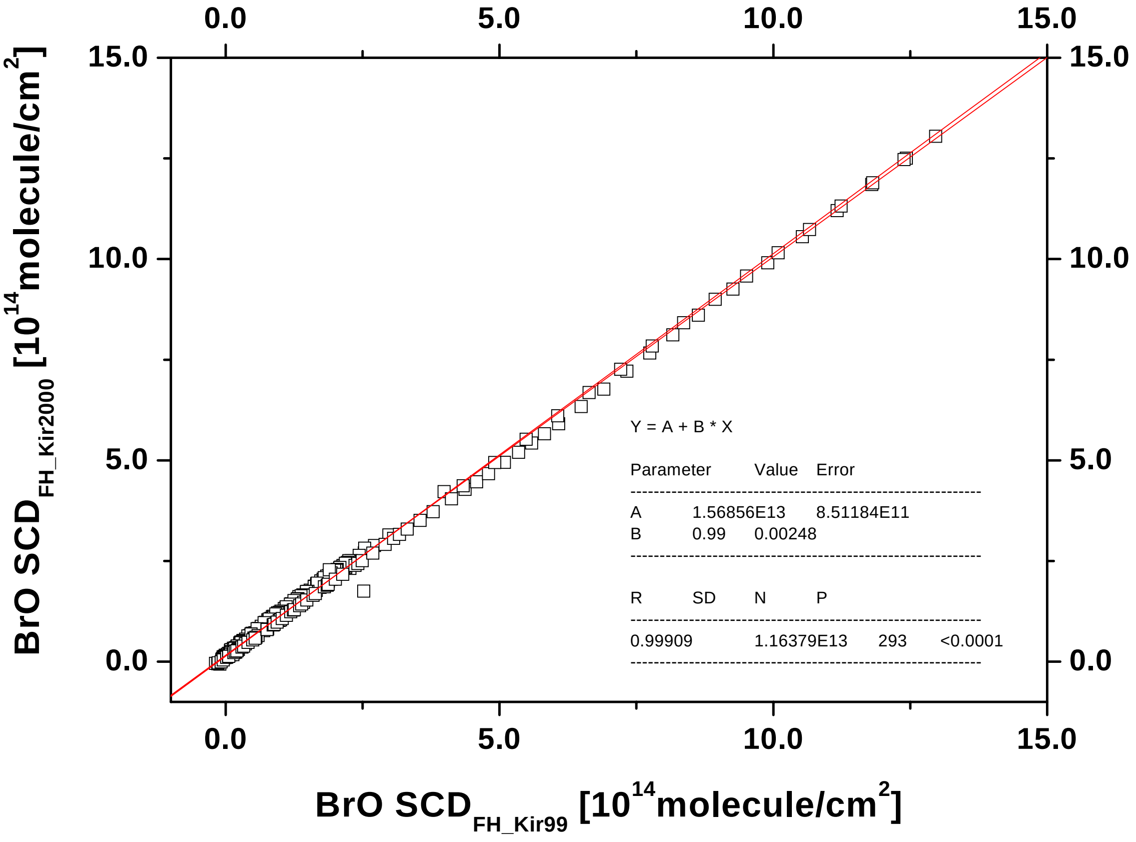

Figure 4.165: SCD offset comparison of the Kiruna 2000 and Kiruna 1999 Fraunhofer spectrum determined by evaluation of the measured spectra with both Fraunhofer spectra. The offset of the measured SCDs plotted against each other gives the difference - $1.6 \pm 0.2 \times 10^{13}$ molecule/cm^2.

underestimate the BrO during the ascent and the beginning of the occultation. That is why the Br_y=23 ppt simulation of the model seems to agree better with the measurements in the correlation plot of the modelled versus measured BrO SCDs - as shown in Figure 4.170. Wether this result can be interpreted as an indication of the increase in total stratospheric inorganic bromine will be discussed in chapter 6.

In comparison with the total atmospheric BrO VCD measurement by GOME and the ground-based DOAS instrument at IRF in Kiruna, the integrated balloon profile again shows $(1.5 - 2) \times 10^{13}$ molecule/cm^2 less BrO. That is this discrepancy is attributed once more to tropospheric BrO. Unfortunately it was not possible during this flight to measure well exposed spectra in the troposphere - mainly because of the cloudy sky, which prevented us from measuring below 4 km altitude.

4.8.2 *OClO* profile and SCD model comparison

Figure 4.172 and 4.173 display the $OClO$ ascent profiles retrieved for this flight and the modelled profiles for SZAs 80 and 90^o. The model sees the same increase of the $OClO$ profile above 12 km altitude with a concentration maximum around 18 km. But as the $OClO$ is increasing largely during the ascent of the balloon, each height segment of the profile belongs to another model profile or another SZA, so that the shift of the maximum position of the measured versus the modelled profiles can be explained by the increase of $OClO$. The main discrepancy between the model and measurement appears at higher altitudes than approximately 20 km, where the model sees much less $OClO$.
The $OClO$ concentrations are increasing muchly during the solar occultation, as can be observed in

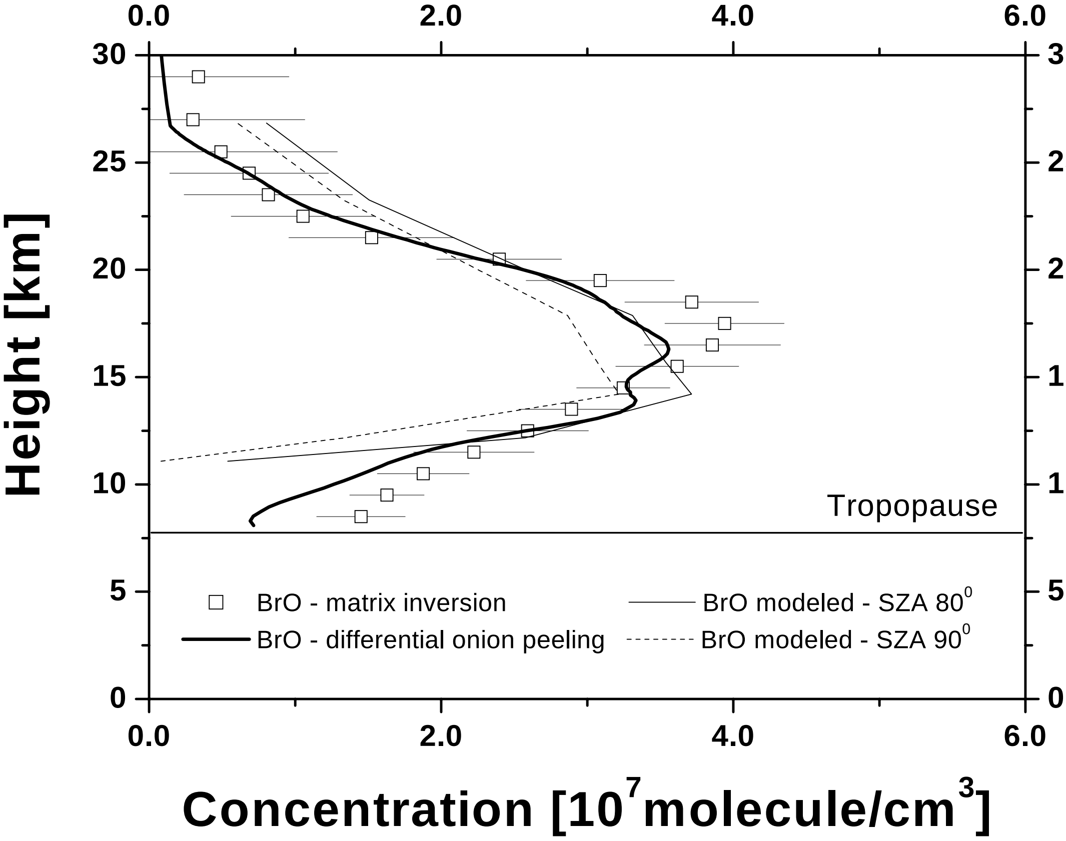

Figure 4.166: BrO concentration profile for the flight at Kiruna 2000 ($81.4-90^o$ SZA). For comparison, also the modelled profiles (SLIMCAT) are shown for the boundary SZAs 80.8^o and 90^o.

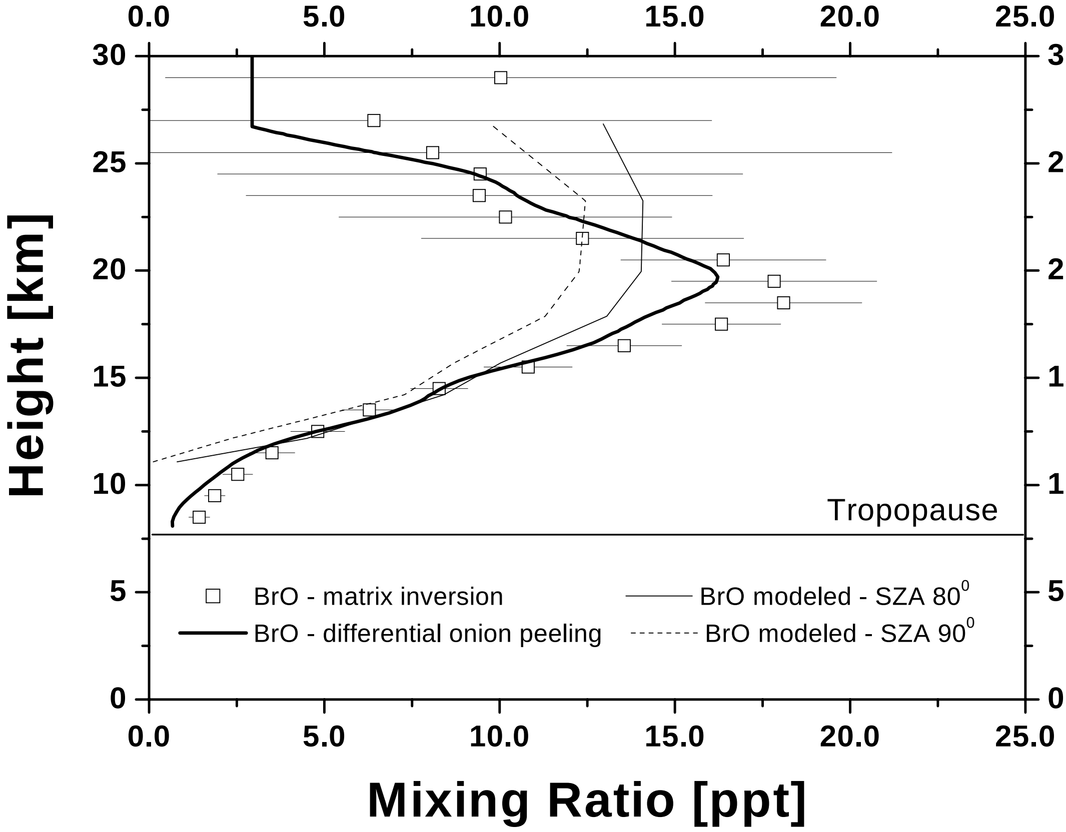

Figure 4.167: BrO mixing ratio profile for the flight at Kiruna 2000 ($81.4-90^o$ SZA). For comparison, also the modelled profiles by (SLIMCAT) are shown for the boundary SZAs 80.8^o and 90^o.

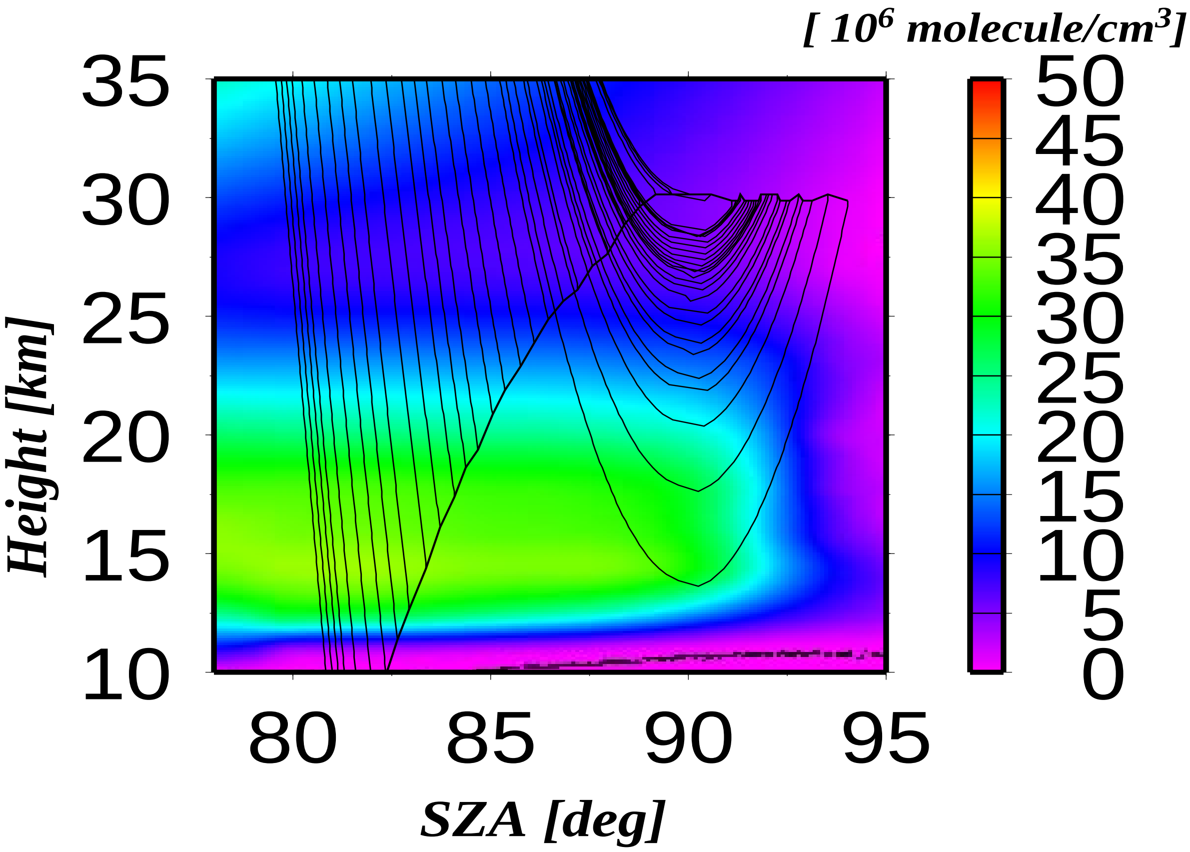

Figure 4.168: Modelling of BrO SCDs by integration of the concentration along the light path through the atmosphere. The model field for the measurements is colour-coded as a function of height and SZA. Both the trajectory of the balloon (thick line) and the light rays from the sun (fine lines) reaching the balloon instrument are shown in the plot.

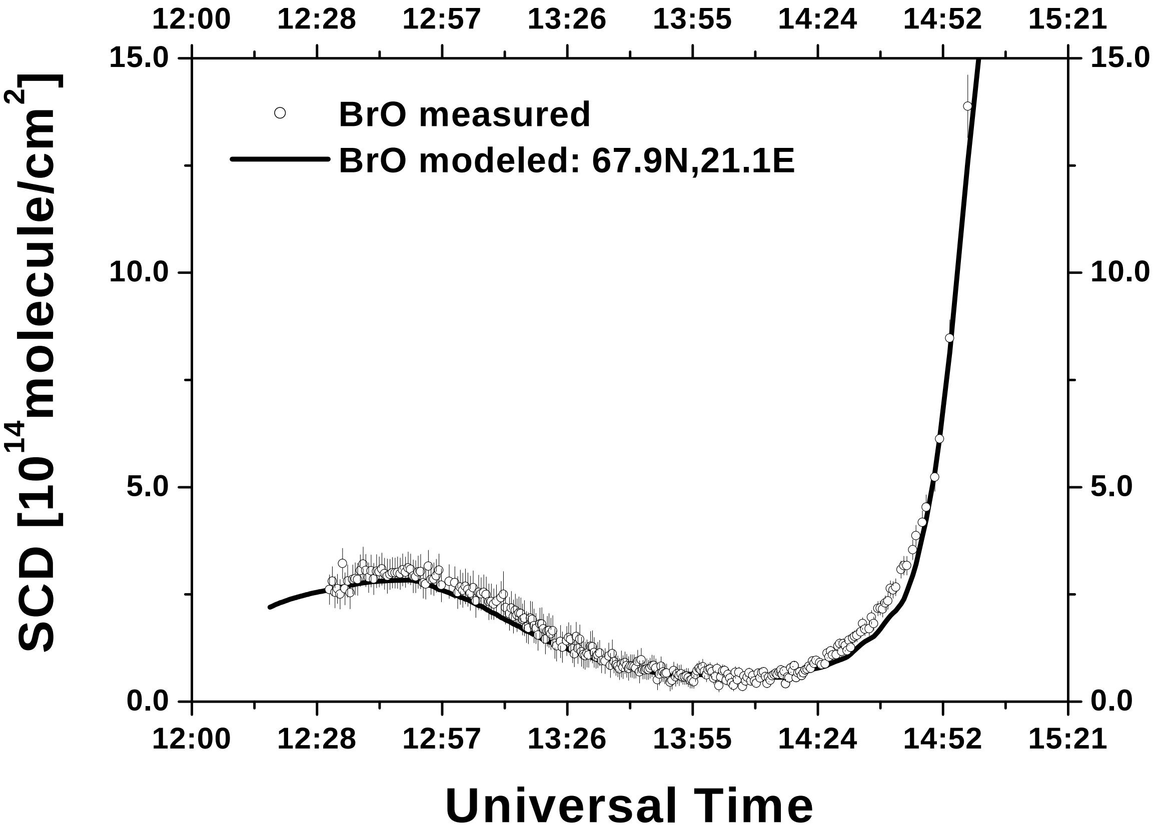

Figure 4.169: Time evolution of measured and modelled BrO SCDs for the Kiruna 2000 flight on Feb.18.

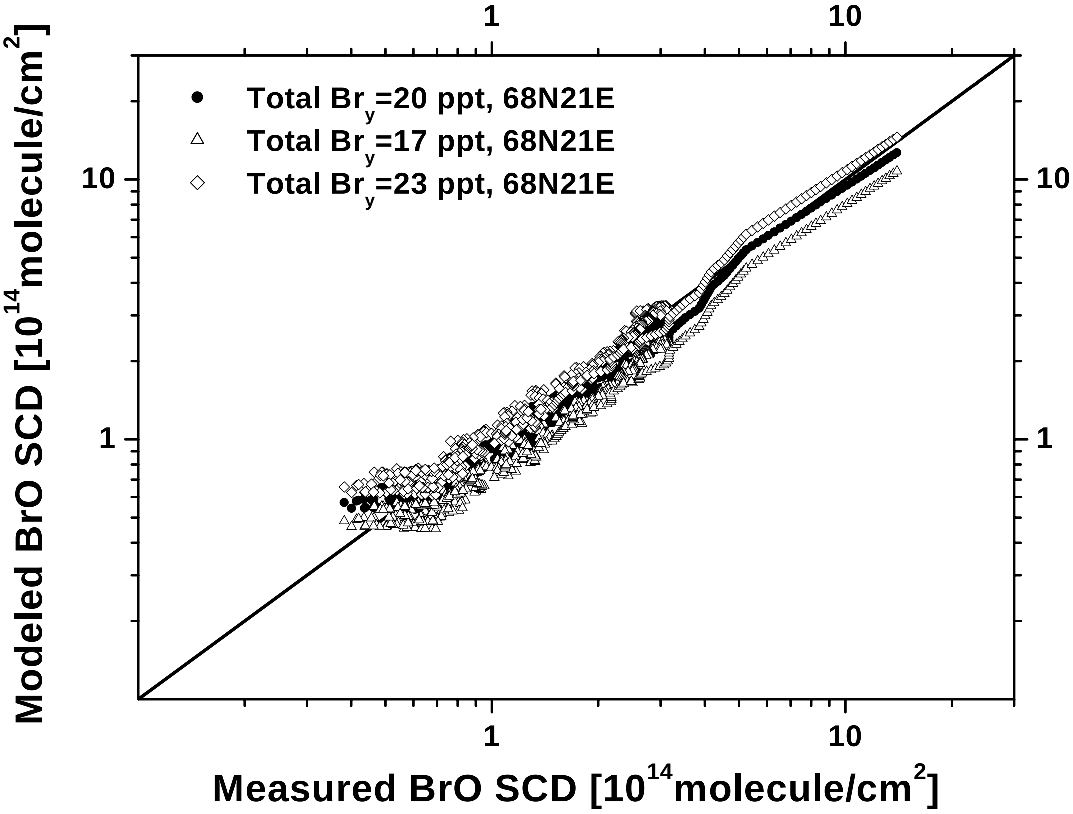

Figure 4.170: Correlation plot of modelled and measured BrO SCDs for the Kiruna 2000 flight. The different model runs $(68N, 21E)$ with different total inorganic bromine contents are shown $(Br_y = 17, 20$ and 23 ppt).

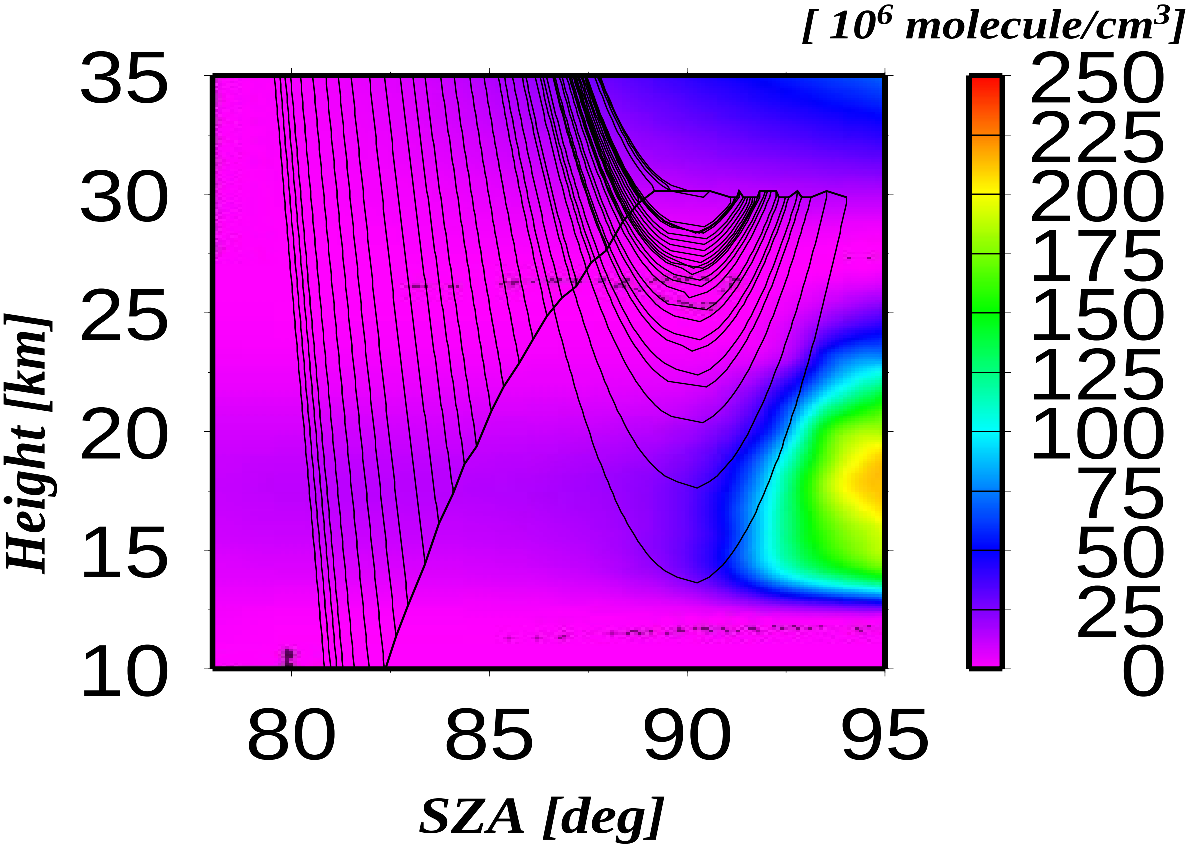

Figure 4.171: Modelling of $OClO$ SCDs by integration of the concentration along the light path through the atmosphere. The model field for the measurements is colour-coded as a function of height and SZA. Both the trajectory of the balloon (thick line) and the light rays from the sun (fine lines) reaching the balloon instrument are shown in the plot.

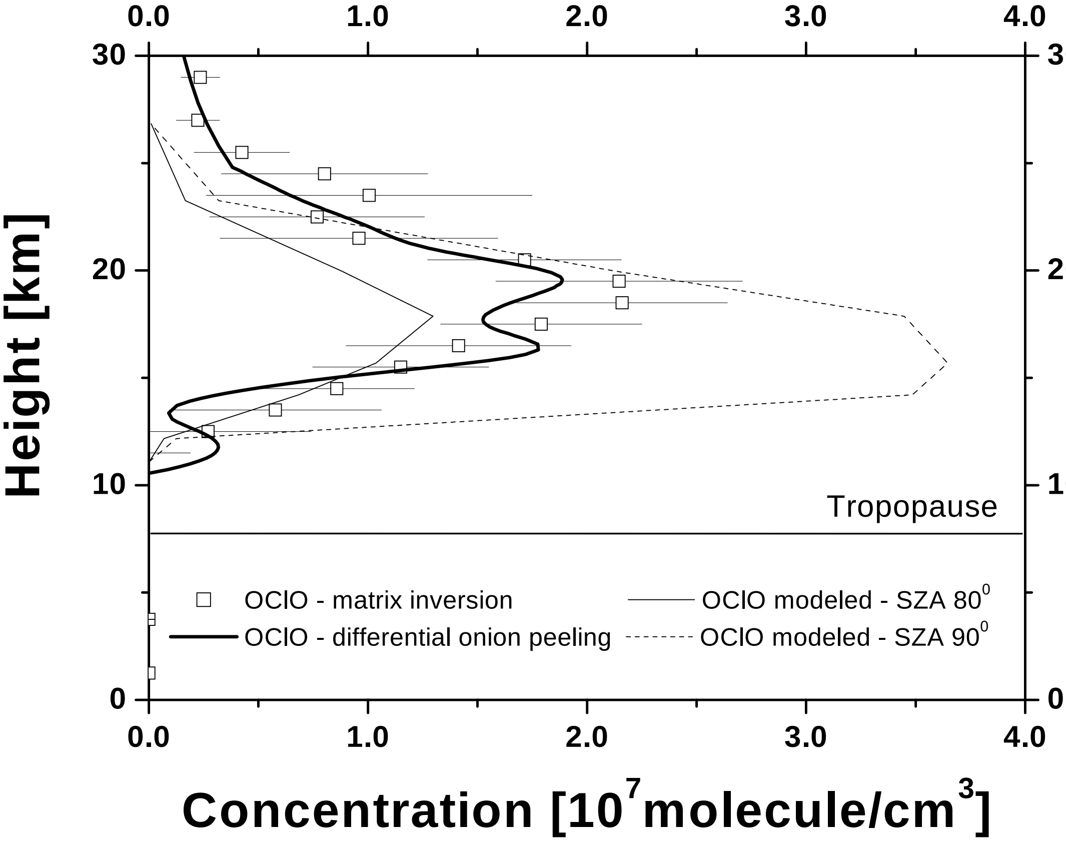

Figure 4.172: *OClO* concentration profile for the flight at Kiruna 2000 (81.4 − 90^o SZA). For comparison, also the modelled profiles (SLIMCAT) are shown for the boundary SZAs 80.8^o and 90^o.

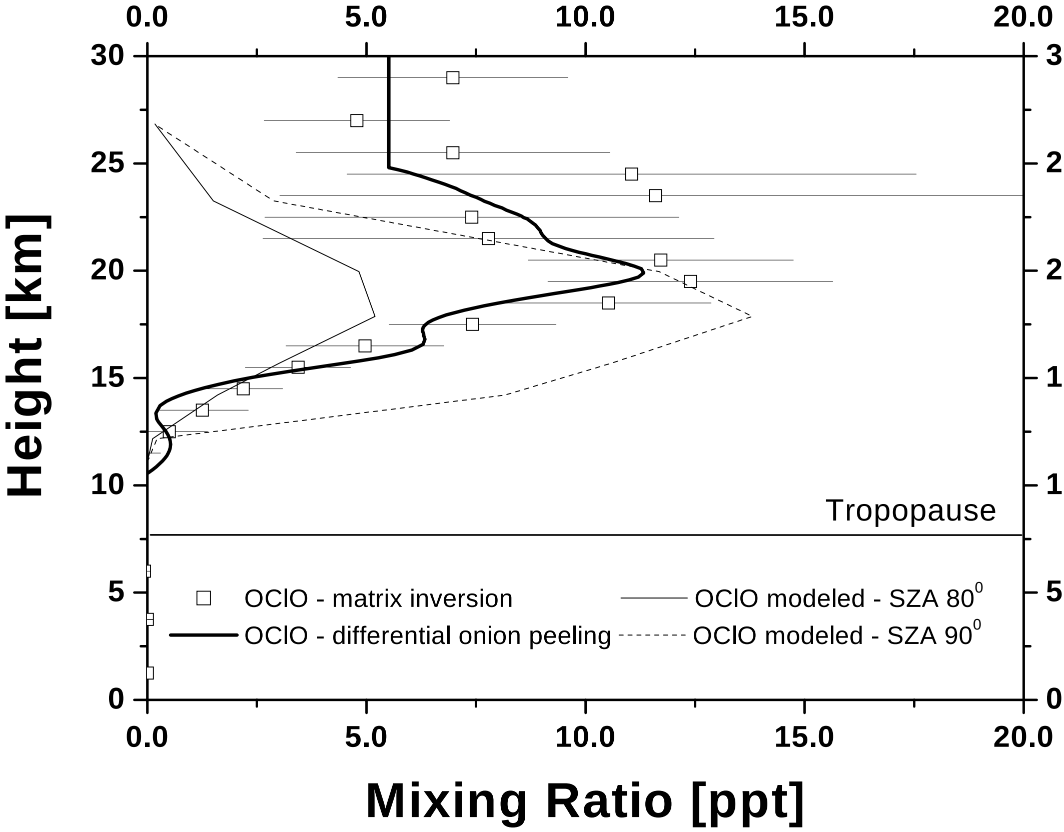

Figure 4.173: *OClO* mixing ratio profile for the flight at Kiruna 2000 (81.4−90^o SZA). For comparison, also the modelled profiles (SLIMCAT) are shown for the boundary SZAs 80.8^o and 90^o.

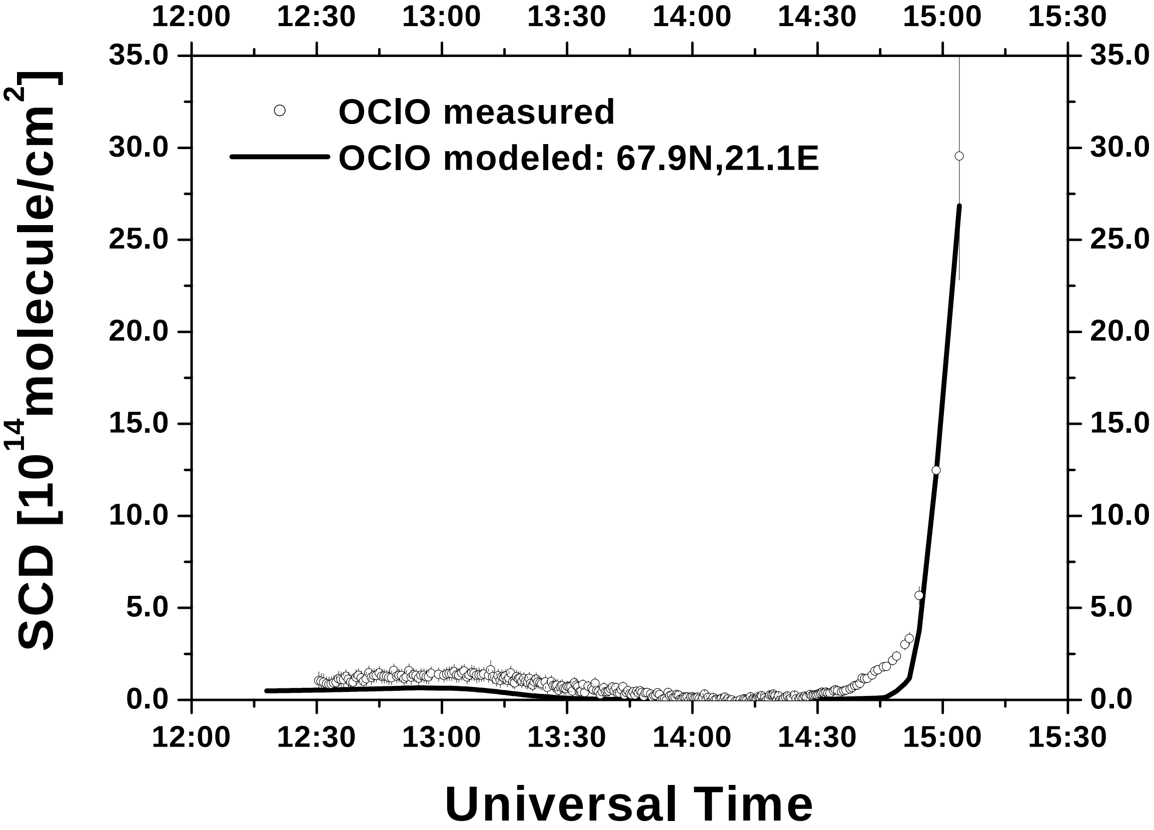

Figure 4.174: Time evolution of measured and modelled *OClO* SCDs for the Kiruna 2000 flight on Feb. 18.

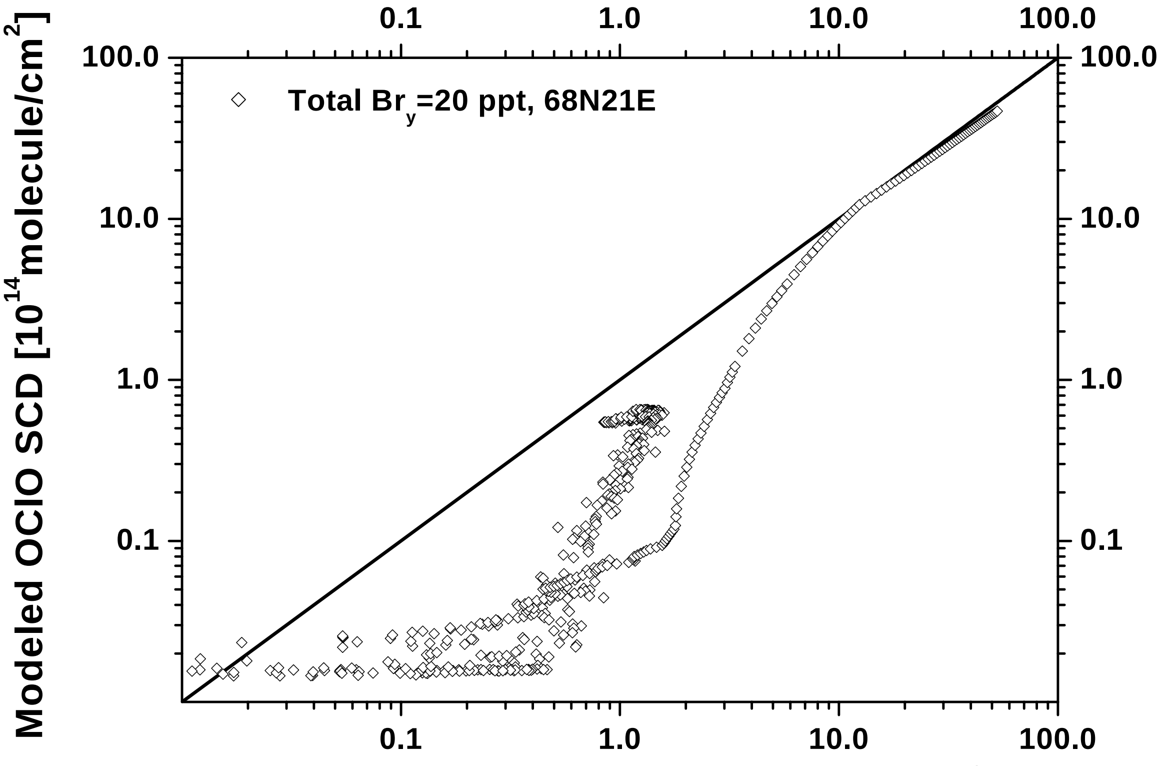

Figure 4.175: Correlation plot of modelled and measured *OClO* SCDs for the Kiruna 2000 flight. The model run $(68N, 21E)$ with a total inorganic bromine content of 20 ppt is shown.

Figure 4.171. It can only be observed in the 12-25 km altitude region, while it is nearly zero above and below. In this region PSC activation can play an important role, because the temperatures are low enough for them to form. Still it has to be noted that there were no PSCs directly observed in the light path and the temperatures in the airmasses next to the balloon were not lower than 200 K, well above the PSC formation temperatures. But chlorine activation could also have taken place during the days before the measurements, when the airmasses may have experienced lower temperatures.

The comparison of measured and modelled $OClO$ SCDs is shown in Figure 4.174. It can be seen, how the model is underestimating the measured $OClO$ SCDs during the ascent of the balloon and the beginning of the occultation. However, there seems to be a good agreement between the model and the measurement during the late occultation for large $OClO$ SCDs.

To interpret this finding, one could say that the model $OClO$ is not increasing fast enough during the twilight corresponding to a too fast $OClO$ photolysis or a too slow formation. On the other hand, one also has to take account of the profile form of $OClO$ when interpreting the SCD comparison, because the fact of too low $OClO$ concentrations above 25 km can also explain the observed discrepancy. This $OClO$ deficiency was already observed in the profile comparison between the balloon ascent profiles and the model profiles shown earlier in this section.

The correlation plot in Figure 4.175 underlines once more the underestimation of the $OClO$ concentration by the model.

4.9 Summary of BrO measurements during the eight LPMA/DOAS balloon flights

4.9.1 BrO profile measurements

Stratospheric BrO has been measured during eight balloon flights at mid and high latitudes during all seasons from November 1996 to February 2000. For all flights it was possible to measure high bromine activation - in the form of BrO - ranging from $50 - 70\%$ of total inorganic bromine.

Figure 4.176 shows a summary of all measurements of BrO until mid 1997. It includes in-situ measurements made by the chemical conversion/resonance fluorescence technique[Brune et al. 1989; Toohey et al. 1990; Avallone et al. 1995; McKinney et al. 1997]. As the in-situ instrument measures the resonance fluorescence of atomic Br - formed by the controlled reaction of BrO with NO - and as the sensitivity depends very much on pressure (Rayleigh scattering background signal, back reaction of Br with NO [Brune et al. 1989]), this technique is not well suited for measurements in the lower stratosphere and troposphere. The overall accuracy of this technique is 30-40% depending on the altitude level of the measurements. Unfortunately these measurements are sparse, quite limited with respect to space and time, and restricted to low ambient pressures. The in-situ profiles were recently revised (D.Toohey, priv. comm.). The first two ascent profiles measured by our balloon instrument are also shown as well as a profile measured by Pundt [1997] with a SAOZ[12] balloon sonde in the Arctic. The mixing ratio profiles measured by the remote sensing balloon instrument (DOAS + SAOZ) show the same structure for both mid-latitude autumn and high latitude winter. The profiles are only shifted by the altitude difference of the local tropopause.

The in-situ measurements are generally showing smaller bromine oxide values than the remote sensing measurements, when compared with the respective mid or high latitude profile. This can be explained by the increase of bromine loading of the stratosphere, which is 3-4 ppt Br_y from 1990 to 2000 [Engel 2000] - see also Figure 6.4.

---

[12] Systeme d'Analyse par Observation Zenitale

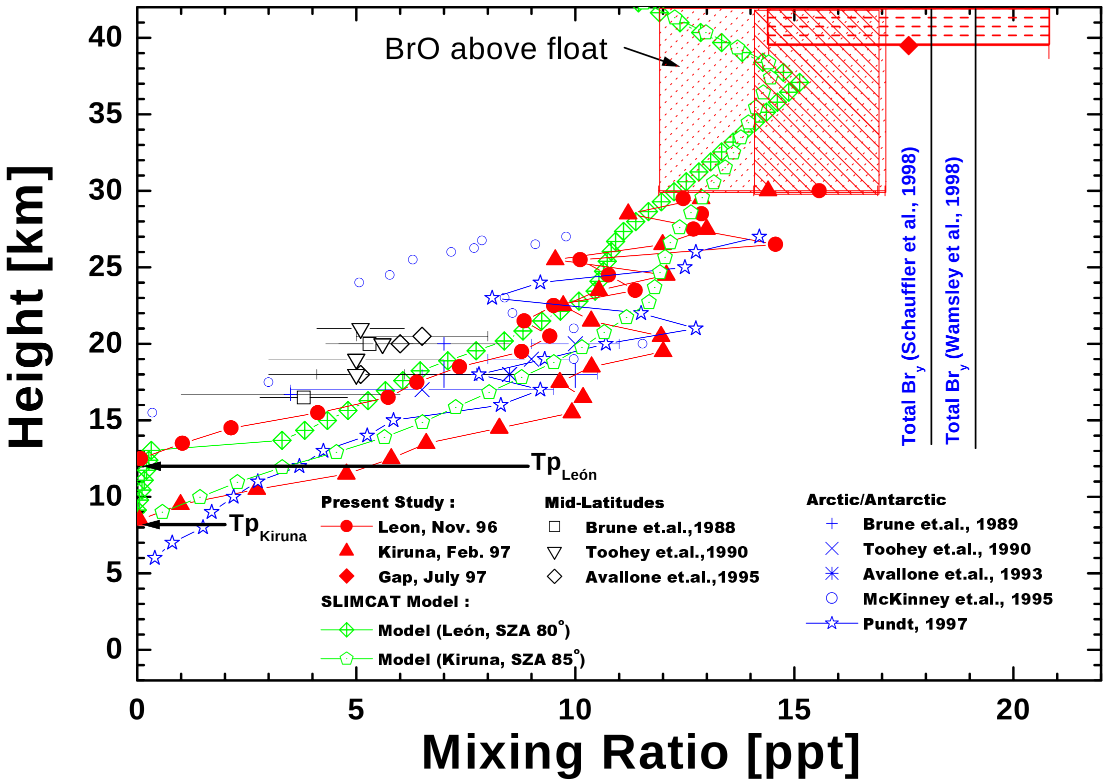

Figure 4.176: Comparison of measured stratospheric BrO profiles until mid 1997. The balloon profiles for our first two flights are included in the plot as well as the in-situ profiles measured by [Brune et al. 1989; Toohey et al. 1990; Avallone et al. 1995; McKinney et al. 1997]. For comparison modelled BrO profiles by SLIMCAT are also shown for our balloon flights. Adapted from [Harder et al. 1998].

Figure 4.177 shows a summary of the BrO profiles measured so far with our balloon-borne instrument. Only profiles retrieved from balloon ascent measurements are considered, because the photochemical variation is small during these measurements. Still it has to be noticed that the profiles refer to different SZA ranges - the profiles measured at León generally correspond to SZA ranges of $65/75 - 87^o$ and the Kiruna flight profiles were measured for SZAs of $82 - 88^o$; only the summer profile at Kiruna (1998) belongs to a larger SZA range: $75 - 88^o$.

The León profiles are shifted consistently to higher altitudes corresponding to a higher tropopause. But the bromine is shown to be activated - to be in the form of BrO - during all seasons and at all latitudes. Still there are minor differences in the BrO/Br_y ratio ranging from $0.5 - 0.7$ in mid-latitude summer and high latitude winter within the polar Arctic vortex, respectively. In the denoxified Arctic vortex the reservoir species $BrONO_2$ is less abundant than in summer at mid-latitudes.

The BrO SCD model-measurement inter comparison results in a total inorganic bromine amount (Br_y) of (20 ± 2.5)-(23 ± 2.5) ppt in the 1996-2000 stratosphere.

4.9.2 BrO VCD comparisons with satellite and ground-based instruments

Table 4.2 gives a summary of the BrO VCD comparison between the balloon-borne profile measurements and the VCD measurements by the GOME nadir looking satellite instrument, as well as the ground-based zenith-scattered light DOAS instrument located at Kiruna. For the flights, where it was possible to measure the total stratospheric BrO VCD - which is only possible for the six ascent flights

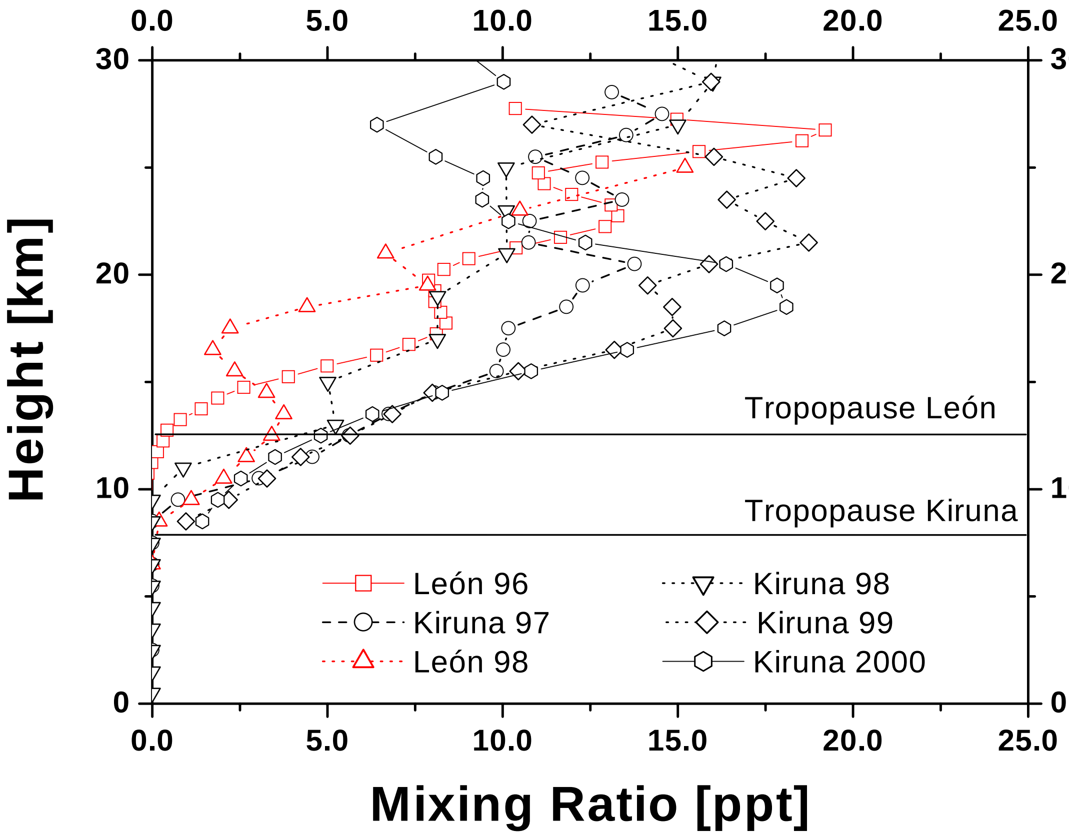

Figure 4.177: Comparison of measured stratospheric BrO profiles measured by balloon from 1996-2000. Only the profiles retrieved from balloon ascent are shown. It is important to notice that the profiles belong to different SZA ranges - see the text.

Overview of BrO VCDs for Balloon, Satellite(GOME) and Ground-based(GB) measurements							
Date	Location	SZA	Altitude	BrO VCD above Tropopause	BrO VCD GOME/GB	GOME SZA	BrO above float altitude
		[^{o}]	[km]	10^{13} molecule/cm^2		[^{o}]	[ppt]
23.11.96	León	$74 - 86.4$	$12 - 30.6$	2.3 ± 0.5	$4.3 \pm 0.8(GOME)$ $6.0 \pm 1(GOME)$	65.4	15.8 ± 3
14.02.97	Kiruna	$82.5 - 88.8$	$8 - 30$	4 ± 0.6	$6.8 \pm 0.8(GOME, 13.02)$ $6.4 \pm 2(GB)$	81.7	15.6 ± 3
20.06.97	Gap	$90 - 56$	$39.8 - 31$		$5.2 \pm 1(GOME)$	23.4	15.3 ± 3
19.03.98	León	$65 - 87$	$5 - 38.5$	2.0 ± 0.5	$4.4 \pm 0.5(GOME)$	45.5	12 ± 2
19./20.08.98	Kiruna	$74.8 - 87$	$2 - 38.5$	3.1 ± 0.5	$4.0 \pm 0.5(GOME)$ $3.6 \pm 0.8(GB)$	55.6	17 ± 3
		$94.5 - 84.7$	$33.3 - 27.6$		$4.0 \pm 0.5(GOME)$	56.0	15 ± 2
10.02.99	Kiruna	$82.9 - 86.2$	$0 - 28.2$	4.8 ± 0.5	$5.7 \pm 0.7(GOME)$ $6.7 \pm 0.8(GB)$	82.1	13 ± 2
25.06.99	Gap	$83.5 - 50$	$39.1 - 20.5$		$3.3 \pm 0.5(GOME)$	24.3	20 ± 5
18.02.00	Kiruna	$81.4 - 89.5$	$6 - 30.1$	3.8 ± 0.5	$5.5 \pm 0.7(GOME)$	82	17 ± 2

Table 4.2: Overview of measured BrO VCDs by the balloon-borne, satellite(GOME) and ground-based instruments(IRF,Kiruna). The GOME and the ground-based data are kindly provided by T.Wagner (IUP, Heidelberg).

- a consistent discrepancy between the integrated balloon profiles and the total atmospheric VCDs measured by the GOME and the ground-based instrument (GB) was found. Despite the scatter of the total atmospheric VCD measurements of GOME and the GB instrument, which can be explained by the different spatial areas probed by the instruments, there is a significant difference between the stratospheric BrO column and the total atmospheric BrO column (20-50%), which could only be explained by a tropospheric background of BrO. This tropospheric BrO background amounts up to $(1-2.5)\times10^{13}$ molecule/cm^2 corresponding to $1-2$ ppt, if distributed uniformly within the troposphere.

The next chapter will deal in detail with the observation, interpretation and consequences of the tropospheric BrO background observed by our instrument.

Chapter 5

The first measurement of a *BrO* profile in the free troposphere

One important result of the eight balloon flights is the consistent difference observed between the integrated balloon profile measurements of stratospheric *BrO* and the total atmospheric column measurements by the satellite instrument GOME and the zenith-sky ground-based instrument. The interpretation of this difference leads to the possible existence of tropospheric *BrO* during these flights. The question to be answered now is where resides the *BrO* in the troposphere [Fitzenberger et al. 2000].

Recent spectroscopic observations of tropospheric *BrO* could clearly establish the role inorganic bromine plays in the destruction of planetary boundary layer (PBL) ozone during polar spring. The detection of PBL *BrO* - with concentrations up to 100 ppt - was based on either ground-based long path absorption DOAS measurements [Hausmann and Platt 1994], aircraft-borne backscattering UV/Vis absorption measurements [McElroy et al. 1999], and/or satellite-borne spectroscopy (GOME) [Wagner and Platt 1998]. Also, recently our group recorded sizeable amounts of *BrO* [up to 80 ppt] from salt pans located at the Dead Sea, Israel [Hebestreit et al. 1999].

Speculations whether free tropospheric *BrO* may not only occur during these specific *BrO* events - and thus influence the chemistry of tropospheric ozone - were fed by a series of recent indirect evidences for *BrO* being possibly ubiquitous in the free troposphere (about 1 to 2 ppt, or (1-2)$\times 10^{13}$ molecule/cm^2 in total atmospheric column). These studies were essentially based on: (1) a comparison of collocated ground-based, balloon-borne, and satellite borne (GOME) *BrO* observations, where discrepancies between the integrated stratospheric *BrO* profiles (measured from balloons), and the total atmospheric *BrO* column (measured from the ground and/or satellite) were found ([Harder et al. 1998; Van Roozendael et al. 1999; Pundt 2000]), and (2) a comparison between measured ground-based *BrO* SCD, and model predictions (SLIMCAT) for stratospheric *BrO* where the model - accounting for 20 ppt of total stratospheric inorganic bromine ([Schauffler et al. 1998; Wamsley 1998; Harder et al. 2000; Pfeilsticker et al. 2000]) - significantly underestimated the total atmospheric *BrO* column amount measured around local noon in the Arctic [Friess et al. 1999]. Also in the Antarctic enhancements of *BrO* slant column densities have been found and attributed to tropospheric *BrO* events in the planetary boundary layer [Kreher 1996].

Here, first profile measurements of free tropospheric *BrO* are reported, that were performed by direct Sun DOAS spectroscopy from the azimuth angle controlled LPMA/DOAS balloon payload.

5.1 Methodology and Measurements

Since the detection of tropospheric BrO essentially relies on a subtraction of sequentially measured tropospheric and stratospheric BrO-SCDs during balloon ascent - after accounting for the photochemical change in the stratospheric BrO concentration and observation geometry (see below) - the method is only suitable if the resulting difference is larger than the combined uncertainties of both measured *BrO* SCDs. It is thus necessary to discuss thoroughly the uncertainties involved in the method.

Unfortunately only two LPMA/DOAS balloon flights so far performed are suitable for a search for tropospheric BrO. First, sunrise occultation measurements (flights 3, 7, second part of flight 5) are conducted from the balloon flying in the mid and upper stratosphere, and thus detection of tropospheric *BrO* is not possible. Second, strong tropospheric shear wind (flights 1, 2, and 4), technical problems and/or clouds (flight 8) prevented proper Sun pointing during the ascent in the troposphere. Third, the solar zenith angle (SZA) - and thus the airmass factor under which the comparably small tropospheric and much larger stratospheric *BrO* columns are observed - are too small for some of the flights (1 and 4) to separate the small tropospheric from the larger stratospheric column. Therefore, we think that flight 6 (from Kiruna on Feb. 10, 1999) - with the largest Signal-To-Noise ratio (SNR) - is most suitable for direct detection of the small tropospheric *BrO* concentrations. Still, despite its smaller SNR, flight 5 (from Kiruna on Aug. 19, 1998) provided almost continuously tropospheric spectra beginning at an altitude of 2.2 km.

For the flight of February 10, 1999, Figure 5.1 compares the measured and modelled BrO SCD as a function of flight time. As the balloon ascends through the troposphere into the lower stratosphere, the *BrO* SCDs remain nearly constant. Further on, the measured *BrO* SCDs decrease strongly, particularly when the balloon passes the maximum height of the *BrO* concentration profile and then ascends further to the balloon float altitude (at 28 - 29 km, and SZA=86.2^o). During solar occultation, the SCD values increase again, because the line of sight through the absorbing *BrO* layer becomes longer. The modelled *BrO* SCDs are obtained by integrating photochemically modelled stratospheric *BrO* concentrations along the line of sight of our observation. The modelled SZA-dependent *BrO* concentration field is taken from the SLIMCAT 3-D CTM model for the closest grid point to our measurement [Chipperfield 1999]. Clearly, the measured and modelled *BrO* SCDs compare excellently for the observation after 12:30 UT (above 20 km), while an increasing gap between measured and modelled *BrO* SCD opens with decreasing altitude. While a part of the gap is due to a shortcoming of the SLIMCAT model to correctly predict lowermost stratospheric *BrO* concentrations for that flight, another part of the gap may possibly point to tropospheric BrO. Since the next chapter - involving a comparison of total stratospheric bromine inferred from our *BrO* measurement, and a GC/MS analysis of total organic bromine in stratospheric air samples taken close to our flight - will address the model's underprediction of lower stratospheric *BrO* in detail, here the focus will be on the tropospheric contribution to this gap.

A zoom of the low altitude inter comparison is also shown in Figure 5.1. All three simulations (curves 1, 2, and 3) describe the amount of *BrO* SCD that would have been measured if there was only stratospheric *BrO* present. Curve 1 is a SLIMCAT simulation of stratospheric *BrO* for our flight. The curve 2 is calculated from the stratospheric *BrO* profile inferred from our stratospheric *BrO* measurements including no photochemical corrections. It has to be noted that assuming no photochemical change in stratospheric *BrO* during the course of the measurements slightly underpredicts the *BrO* SCD, mainly because during the course of the balloon ascent some of the stratospheric *BrO* (∼4 %) has already reacted into its nighttime reservoir species (mainly *BrCl* for this flight). In order to account for this photochemical loss in stratospheric BrO, a third simulation was carried out. Here we corrected our measured stratospheric *BrO* profile with the

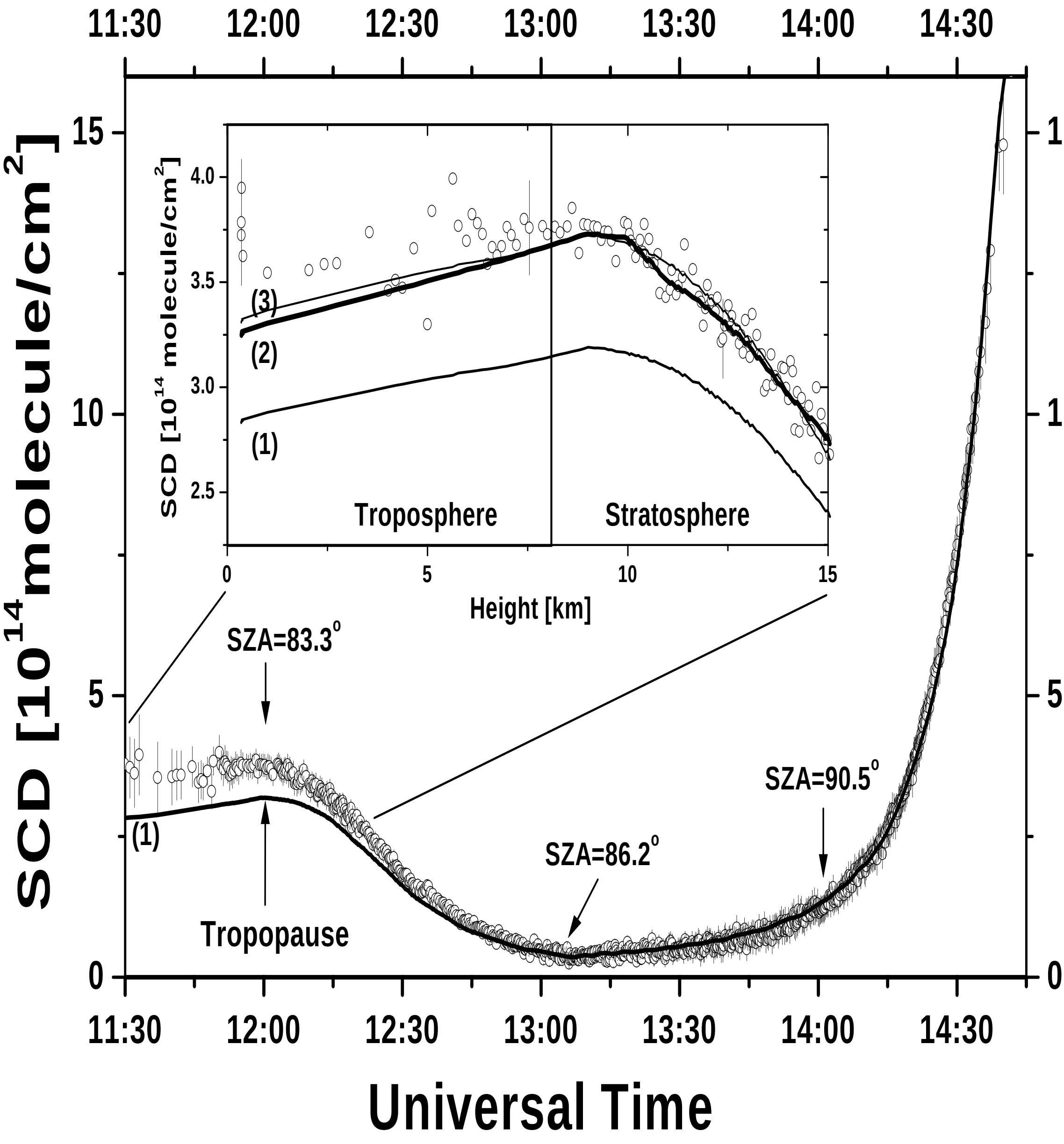

Figure 5.1: Comparison of measured and modelled BrO SCDs ($65^oN, 12^oE$) for the balloon flight from Kiruna ($67.9^0N, 21.1^0E$) on Feb. 10, 1999 as a function of flight time. The modelled curves are simulated line of sight BrO-SCDs for (1) stratospheric BrO predicted by SLIMCAT (curve 1), (b) the stratospheric BrO profile as measured by our instrument without photochemical correction (curve 2), and (c) as (b) but including the photochemical correction (curve 3) (for details see text).

model-predicted loss of stratospheric BrO during our measurements. The corrections are ~4 % for the total atmospheric column (see also Figure 5.2 for the model-predicted change in stratospheric BrO for the near ground and the lowermost stratospheric observations at SZA = 82.7^o, and 83.3^o, respectively).

To consolidate this result, we conducted a statistical test of the difference in measured and modelled BrO SCDs for the tropospheric observations (difference of the measured values to curve 3). The statistical test consists of calculating the error probability to reject the hypothesis $SCD_{model,curve3} = SCD_{meas}$ assuming a gaussian distribution of the measurements and investigating the random variable $Z = \frac{\overline{SCD_{meas}}-\overline{SCD_{model}}}{\sqrt{D(\overline{SCD_{meas}}-\overline{SCD_{model}})}}$, where Z is a normal random variable and $D(\overline{X}-\overline{Y}) = \frac{\sigma_x^2}{n}+\frac{\sigma_y^2}{n}$ [Bronstein and Semendjajew 1991]. It clearly shows that, the combined measured tropospheric BrO SCDs are on a 97.5 % significance level larger than the predicted values. Therefore, it is concluded that some BrO was present in the troposphere during this flight.

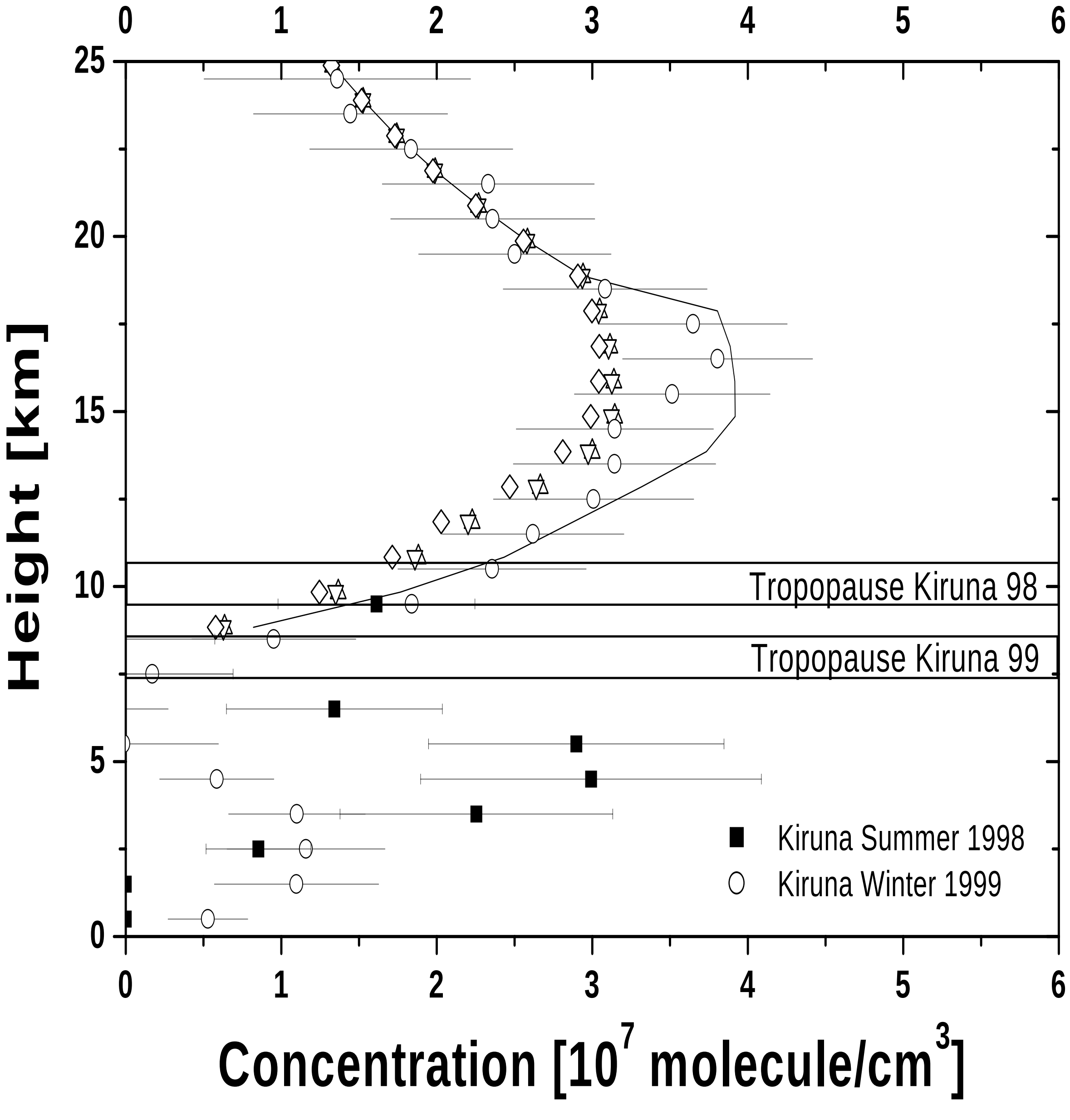

Figure 5.2: Atmospheric BrO profile for the balloon flight from Kiruna on Feb. 10, 1999. The measured BrO profile (open circle) is an average over $82.7^o \leq SZA \leq 86.2^o$ retrieved with the matrix inversion technique from the smoothed SCDs. The modelled SLIMCAT profiles for grid point (65°N,12°E) are for SZAs = 82.7^o (open upper triangle), = 83.3^o (open lower triangle), = 86.2^o (diamond), corresponding to lower tropospheric, tropopause and float altitude measurements, respectively. The solid line shows the observation-corrected modelled BrO profile for an average SZA = 83^o. In the troposphere is also shown the second measured profile of the flight at Kiruna on Aug. 19, 1998.

A further test for the presence of tropospheric BrO relies on a comparison of measured total

atmospheric BrO vertical column density (BrO VCD), and the integrated stratospheric profile. Our integrated stratospheric BrO profile yields (4.8±0.5)×10^{13} molecule/cm^2. The measured total BrO VCDs are taken from three sources: (1) the 4 combined BrO measurements - taken from the ground prior to the launch - result in a BrO VCD of (5.7±0.6)×10^{13} molecule/cm^2 for a SZA of 82.8^o, (2) GOME measured almost the same total atmospheric BrO VCD of (5.7±0.7)×10^{13} molecule/cm^2 for a similar SZA (= 82.2^o) as for our balloon measurement, and (3) our ground-based instrument located at Kiruna/Institutet för Rymdfysik (IRF), roughly 50 km from the balloon launch site, measured a BrO VCD of (6.7±0.8)×10^{13} molecule/cm^2 at a SZA = 82.2^o. Combining all three measurements, then the combined atmospheric BrO VCD ((5.9±0.4)×10^{13} molecule/cm^2) as well as each of the individual total BrO VCDs are significantly larger than the integrated stratospheric BrO profile. Finally, our integrated tropospheric profile results in a BrO column amount of (0.5±0.2)×10^{13} molecule/cm^2, a value being in reasonable agreement with the above difference in total combined atmospheric BrO-VCD ((0.2 to 2.0)×10^{13} molecule/cm^2), taking into account the errors. It should be noted that the tropospheric BrO VCD closely corresponds to the tropospheric BrO VCD that is required to bring the measured total atmospheric and modelled stratospheric BrO VCD into agreement for a comparison at the same location, and season, during 1995 [Friess et al. 1999]. Finally inspecting the inferred profile obtained for our balloon flight the tropospheric BrO maximizes at around 2-3 km altitude (0.6±0.2 ppt), and it is close to zero at the local tropopause.
As a second evidence we plotted also the retrieved tropospheric profile of the summer flight at Kiruna on Aug. 19, 1998 into Figure 5.2. Despite the smaller SNR of the measured BrO SCDs during that flight (smaller SZAs/AMFs) - for the comparison of the measured and modelled SCD time evolution see Figure 5.3 - it was possible to retrieve SCDs beginning at an altitude of 2.2 km. The profile form looks very similar to the one of the winter profile, while the larger maximum (2±0.8 ppt) lies higher up in the troposphere. Comparing the resulting VCDs - the total atmospheric, stratospheric and tropospheric VCD are (4.4±0.5),(3.2±0.5) and (1.2±0.4)10^{13} molecule/cm^2, respectively - we can find a fairly good agreement with the simultaneous ground-based measurements - (3.6±0.8)10^{13} molecule/cm^2- and the earlier GOME measurement (see Table 4.2).

To add to the already published comparisons of collocated measurements of BrO VCD and integrated stratospheric BrO profiles ([Harder et al. 1998; Van Roozendael et al. 1999; Pundt 2000]) Table 4.2 at the end of the last chapter summarizes our findings for the 8 LPMA/DOAS flights already conducted. The comparison reveals that tropospheric BrO - amounting to (0.6 to 3.7)×10^{13} molecule/cm^2, or 0.4 ppt to 2.3 ppt - if uniformly distributed within the troposphere - could have been present during all our balloon flights.

5.2 Discussion of the free tropospheric BrO measurements

It may be speculated on the possible source of tropospheric BrO. For our measurement conditions, it can be thought of two potential sources; (1) BrO ventilated into the free troposphere from BrO plumes known to occur in the PBL of both polar hemispheres in spring [Wagner and Platt 1998], or (2) BrO transported from the stratosphere or photochemically produced from the destruction of bromine-bearing organic precursors in the troposphere [Dvortsov 1998; Dvortsov et al. 1999]. At first glance, possibility 1 appears very appealing, because flight 6 was launched only about 400 km east of the Arctic Sea shores, and remnants of a BrO plume formed there could easily be transported to Kiruna by westerly winds. However, plumes of BrO in the Arctic PBL are known to occur later in the season (by mid March), usually when the Sun rises over the Arctic sea ice belt located much more northerly (1500 km) than the balloon trajectory [Wagner and Platt 1998]. Also, possibility 1 can hardly explain the evidence we, and others, found for tropospheric BrO occurrence at mid-latitudes (i.e., during fall, see flight 1) and in summer (flight 5). Possibility 2 also provides no straightforward explanation - especially when taking into account the minimum of the tropospheric BrO profile just

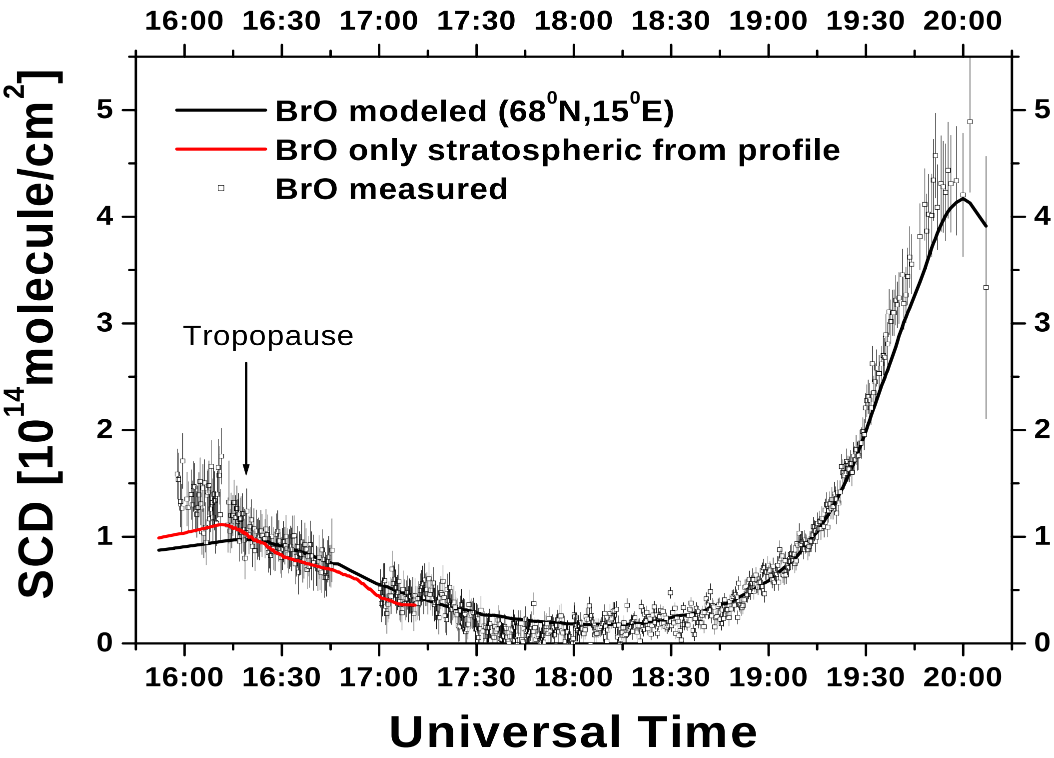

Figure 5.3: Time evolution of the BrO SCDs during the flight at Kiruna on Aug.19, 1998. The model prediction for the BrO is also shown as bold black line in the plot. In addition the red bold line, which ends at 17:10 UT denotes the SCD modelled by only using the stratospheric profile.

below the tropopause. Although it is evident that inorganic bromine may exist at a several ppt level in the free troposphere [Dvortsov 1998; Dvortsov et al. 1999], the gas phase bromine photochemistry, however, largely favours (by at least a factor of 10) the presence of HBr, $HOBr$, and $BrONO_2$ (through fast reactions of CH_2O, OH, HO_2, and NO_2 with BrO or Br), rather than BrO. Since there is no free tropospheric source known to provide inorganic bromine in excess of several ppt, an activation mechanism must exist therefore. We propose that in the sunlit troposphere BrO is produced by a heterogeneous activation of HBr, $HOBr$, and $BrONO_2$, possibly by reactions involving HCl taken up on tropospheric hydrometeors (ice crystals, water droplets) [Abbatt 1994; Abbatt and Nowak 1997; Erle et al. 1998; Disselkamp et al. 1999]. The subsequent release of $BrCl$, the fast $BrCl$ photolysis, and the reaction of Br atoms with ozone may then form BrO in the sunlit troposphere. If this mechanism occurs, then a small BrO background (some ppt at most) may exist ubiquitously in the free troposphere, preferentially in the wake of tropospheric clouds.
As pointed out by Dvortsov et al. [1999] the existence of free tropospheric Br_y depends essentially on the lifetime of the inorganic bromine species against rainout. If this lifetime is zero, then there is no Br_y available to form BrO. However, for lifetimes in the range of 10 days inorganic bromine can amount up to 1 ppt when including short-lived organic bromine species like bromoform ($CHBr_3$).

The possible consequences of free tropospheric BrO can be summarized as follows:

- NO_x chemistry: NO/NO_2 ratio is decreased through reaction of BrO with NO producing NO_2 and NO_x is decreased through heterogeneous reactions of $BrONO_2$ on aerosols.
- HO_x chemistry: HO_2 is decreased (BrO + HO_2 -> $HOBr$ + OH, subsequent photolysis of $HOBr$), thus the HO_2/OH ratio is reduced.

- Halogens: heterogeneous activation of chlorine via the reaction of $BrONO_2$ and HCl.

- Ozone production/destruction:

- The production rate of O_3 (via NO+HRO_2) is changed/reduced by the change in the NO/NO_2 ratio.

- Threshold for ozone production ($NO/O_3 = 1/4300$) is decreasing with free tropospheric BrO, because of the additional NO_2 production.

- Increased O_3 loss through catalytic ClO_x/BrO_x reaction cycles.

Chapter 6

Comparison of the inorganic and organic bromine budget for the Arctic lower stratosphere in winter 1998/1999

Stratospheric Br, currently assessed to 18-20 ppt, is the second most important halogen known to destroy the stratospheric ozone layer. At present its contribution to the total stratospheric ozone loss is estimated at about 25 % [WMO 1998]. Although much improvement in understanding the stratospheric budget and chemistry of Br has recently been achieved [Schauffler et al. 1998; Wamsley 1998; Harder et al. 2000] a major still unresolved issue is the impact of shorter-lived organic Br species on the photochemistry of the upper troposphere and lowermost stratosphere, where they are converted to reactive forms of Br [Dvortsov et al. 1999] and the amount of inorganic bromine influx from the troposphere into the stratosphere [Ko et al. 1997]. In-situ mass spectrometric analysis of aerosols at the tropopause suggests that ~1 ppt of Br is tied to the aerosol [Murphy and Thomson 2000], and recently our spectroscopic measurements suggested the presence of gaseous BrO in the free troposphere with mixing ratios possibly as large as several ppt [Fitzenberger et al. 2000]. Clearly, if transported through the tropopause that tropospheric inorganic Br may add to the organic Br input into the stratosphere [Ko et al. 1997].

During one of our eight balloon flights conducted so far, we had the unique possibility to compare our inorganic total stratospheric bromine determination method directly with the standard method based on the measurement of all organic precursor bromine species at the tropopause and in the lower stratosphere.

For the Arctic winter 1998/99 at Kiruna, in time closely measured vertical profiles (9-28 km) of all known major organic bromine species (CH_3Br, C_2H_5Br, CH_2BrCl, $CHBrCl_2$, CH_2Br_2, $CHBr_2Cl$, $CHBr_3$, $H1301$, $H1211$, $H1202$, $H2402$, and inferred total organic Br as a function of altitude (or age of the air)) are inter compared with total inorganic Br inferred from spectroscopic BrO observations that are corrected for the modelled stratospheric Br_y partitioning. Within the investigated altitude range, both total Br_y profiles differ less than the stated errors of each measurement. The good agreement suggests that the lower stratospheric budget and chemistry of Br are well understood for the probed condition. For early 1999, our data suggest an inorganic Br mixing ratio of 1.5 ppt in air just above the local tropopause (~8-9 km), and in 25 km (for 5.6 year old air) (18.4±1.8) ppt (inferred from the organic Br analyzed in the total air samples), and/or (21.5±3.0)ppt (inferred from the BrO measurements and photochemical modelling), respectively. Our study also suggests an inorganic Br influx of ((3.1±3.5)ppt) from the troposphere into the stratosphere [Pfeilsticker et al. 2000].

6.1 Methodology of the comparison

In order to assess more closely the present stratospheric budget of bromine, vertical profiles of almost simultaneously measured total organic and inferred $Br_y^{\texttt{org}}$, and inorganic $Br_y^{\texttt{in}}$ inferred from measured stratospheric BrO have been inter compared, for balloon flights conducted in the Arctic vortex in early 1999. The profile of $Br_y^{\texttt{org}}$ is obtained from the analyses of a suite of organic Br species in whole air samples, and the total inorganic Br is inferred from spectroscopic BrO measurements and corrected for the $BrO/Br_y^{\texttt{in}}$ ratio that is taken from photochemical modelling.

Within the framework of the European THESEO[1] campaign, balloon flights of the TRIPLE and the LPMA/DOAS gondola were conducted from Kiruna/Sweden (68^oN, 21^oE) on Feb. 6, 1999, and Feb. 10, 1999, respectively. By early February 1999, the Arctic vortex was located over Kiruna, dynamically unperturbed and the stratospheric temperatures just above PSC threshold (about 2 K) occurred. We probed the chemical composition of the vortex by conducting a series of balloon flights that were consecutively launched within 4 days (see below).

The in-situ TRIPLE gondola accommodates a total air sampler [Engel et al. 1997] - besides a Lyman α hygrometer, and a resonance fluorescence instrument for BrO/ClO measurements - of which the $CFC-11$ and the organic Br measurements are used in the present study. The remote-sensing LPMA/DOAS gondola carries two optical spectrometers that analyze the direct sunlight in almost the whole wavelength band ranging from the UV into the mid-IR.

In-situ N_2O and $CFC-11$ concentrations (and organic Br species as well, see below) were measured from total samples of stratospheric air using a balloon-borne cryosampler installed on TRIPLE. This technique condenses air into stainless steel vessels immersed in liquid neon [Engel et al. 1997]. After the flight the mixing ratios of N_2O, $CFC-11$, and other trace gases were determined in the laboratory of the University of Frankfurt using gas chromatography with electron capture detection. The precision of the analysis is in all cases better than 2%, the accuracy of the standard from NOAA/CMDL, e.g., [Elkins et al. 1993] is better than 2%.

N_2O was also measured with the FTIR spectrometer in the $2914.5/cm$ to $2915.3/cm$ wavenumber band during the ascent of the LPMA/DOAS gondola on Feb. 10, 1999. The processing of the FTIR interferograms has been described in several publications [Camy-Peyret et al. 1993; Payan et al. 1998]. The retrieval of the profiles from the LPMA spectra is performed using a global fit method which generates N_2O vertical mixing ratio profiles to an accuracy of 10% [Payan et al. 1998].

Organic Br compounds were measured - see Figure 6.1 for the Br_y speciation - in the total air samples of TRIPLE using a gas chromatograph/tri-sector mass spectrometer combination (Micromass VG Autospec GC-MS) operating in single ion mode. The halon gases were separated with a KCl-passivated alumina (PLOT) capillary column, and the other brominated compounds with a phenyl/methylpolysiloxane (DB5) capillary column. Detection limits were about 0.001 ppt for 800 ml air samples. Calibrations were made by gas phase static dilution for the halons [Fraser et al. 1999], by reference to air standards provided by the US National Atmospheric and Oceanic Administration for CH_3Br, and by liquid dilution and vaporisation for the other bromoalkanes [Carpenter et al. 1999]. Inter comparison studies with the NCAR laboratory (E. Atlas, personal communication 1999) showed within the errors of the measurements ($\sim$ 2%) a good agreement for CH_3Br, but for the other inter calibrated short-lived bromoalkanes deviations in the range of 14% to 43% occurred. Adjusting all of our concentrations to be compatible with those of NCAR increases estimates of total $Br_y^{\texttt{org}}$ by about 0.5 ppt (see below).

The partitioning of stratospheric bromine (and many other species) was calculated using a photochemical box model (with a timestep of 5 minutes), initialized with the 12:00 UT model output of a SLIMCAT 3-D model run [Chipperfield 1999]. The SLIMCAT model used prescribed meteorological fields (on 11 potential temperature levels distributed between $\theta = 350$ K and 2100 K with a horizontal resolution of 2.5° in latitude and 5.6° in longitude) of the United Kingdom Meteorological Office

---

[1] THird European Stratospheric Experiment on Ozone

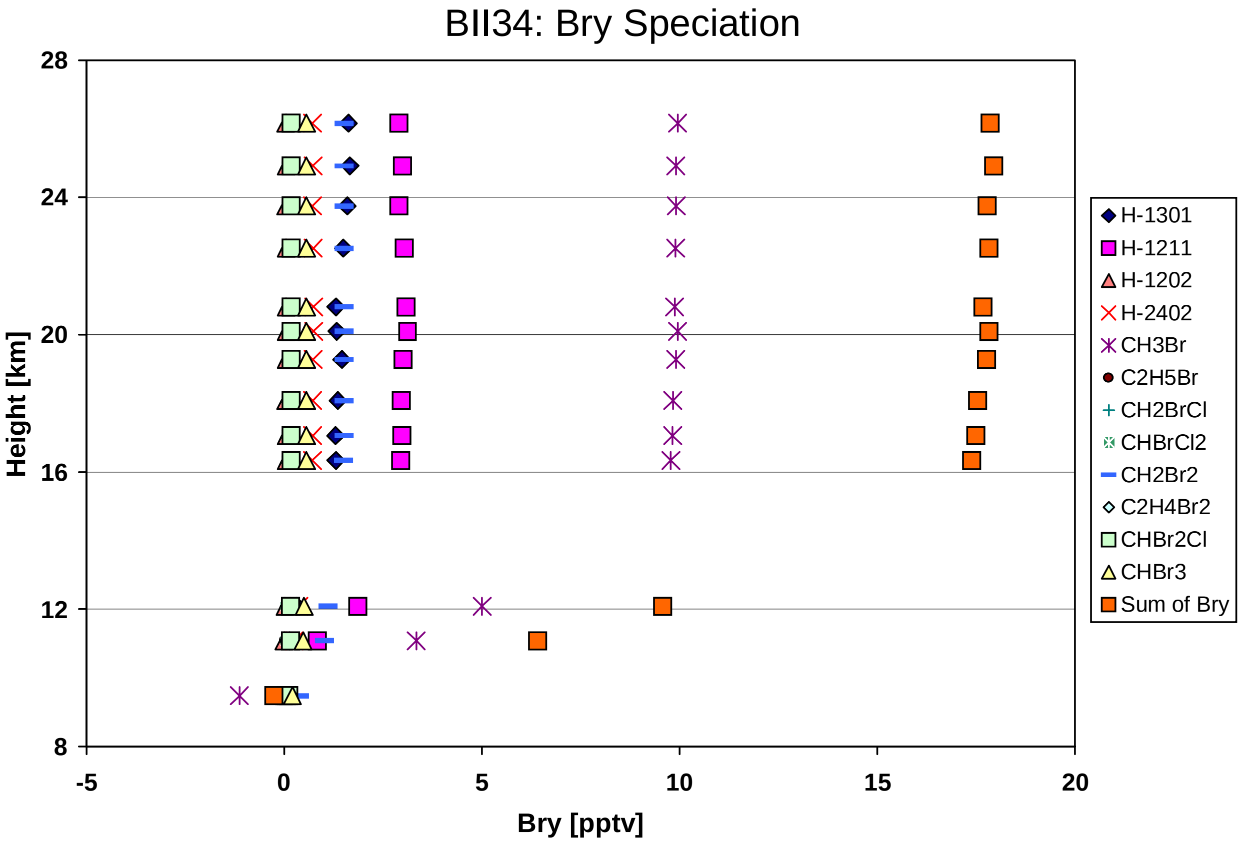

Figure 6.1: Inorganic bromine speciation for the TRIPLE balloon flight at Kiruna on Feb. 6, 1999 [Engel 2000].

(UKMO) analyses. Both the 3-D and photochemical box model run with a photochemical scheme based on the JPL-97 [DeMore et al. 1997] kinetic data and they include all known and relevant heterogeneous reactions. The 3-D model run was initialized as described in detail by [Chipperfield 1999] with the total stratospheric Br kept at 20 ppt. Mainly because of the existing uncertainties in the adopted chemical scheme (in particular for our conditions due to the uncertainty in the rate reaction coefficient $ClO + BrO$), in the following discussion we assume a 5% uncertainty in the modelled $BrO/Br_y^{\mathtt{in}}$ ($\sim$ 0.72) ratio. Accordingly, the uncertainty in $Br_y^{\mathtt{in}}$ inferred from BrO observations and the photochemical model is estimated at $\sim$ 15%.

6.2 Discussion of the comparison

Figure 6.2 shows the line of sight BrO SCD as a function of flight time measured by the DOAS instrument onboard the LPMA/DOAS gondola on Feb. 10, 1999. As the balloon ascends through the troposphere into the lower stratosphere, the measured BrO SCDs remain nearly constant, but further on the BrO SCDs decrease as the balloon passes the maximum height of the BrO profile and ascends further to the balloon float altitude (at about 28 km to 29 km, and SZA=86.2^o). During solar occultation, the BrO SCDs increase again, because the line of sight through the absorbing BrO layer is getting longer. Curve (1) describes the apparent slant column amount of the inferred total $Br_y^{\mathtt{org}}$ profile (see below) - taken along the observational line of sights. Curve (2) is calculated from curve (1) accounting for the modelled $BrO/Br_y^{\mathtt{in}}$ ratio by SLIMCAT. Our measured BrO is clearly larger than the expected BrO SCD (curve 2) but smaller than the apparent $Br_y^{\mathtt{org}}$ SCD values (curve 1). This finding indicates that, (1) stratospheric $Br_y^{\mathtt{in}}$ is larger than $Br_y^{\mathtt{org}}$ can account for, and (2)

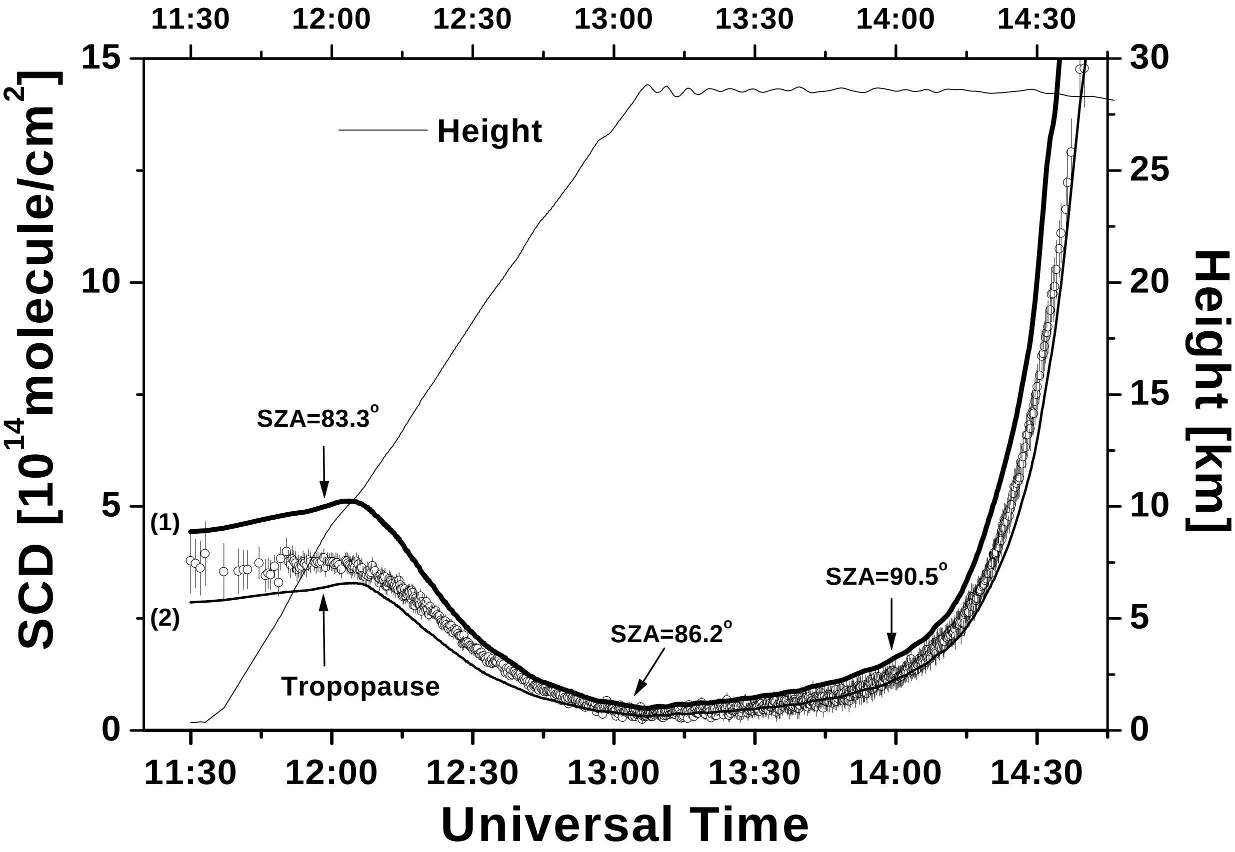

Figure 6.2: Comparison of measured and modelled BrO SCDs for the balloon flight from Kiruna (67.9^{o}N,21.1^{o}E) on Feb. 10, 1999 as a function of flight time and height. Curve (1) describes the BrO SCD if all inorganic Br - estimated from Br_y^{org} - resided in BrO (BrO/Br_y^{in} = 1). Curve (2) is like curve (1) but accounting for the modelled Br_y^{in} partitioning ($BrO/Br_y^{in} \sim 0.72$).

in the troposphere more BrO is measured than if there was only stratospheric BrO present. In the previous chapter it was thus concluded from finding (2) that, some BrO must have been present in the free troposphere, too.

Figure 6.3 shows the vertical profiles of all measured bromoalkanes (except CH_2BrCH_2Br that was also measured but is discarded in the analysis due to a missing reliable calibration) for the total air samples collected on Feb. 6, 1999. It is evident that due to photolytic destruction above the tropopause their mixing ratios rapidly decrease with height. The measured composition of the long-lived bromoalkanes compares well with previous observations conducted in the free and upper troposphere (8-17 km) of the 21^o-41^{o}N latitude band: $[CH_3Br]$=11.0/(9.95±0.46) ppt, $[H1211]$=4.1/(3.5±0.1) ppt, $[H1301]$=2.18/(2.3±0.18) ppt, $[H2402]$=0.37/(0.45±0.02) ppt, $[H1202]$=0.047 ppt/(no data) for our measurement versus Schauffler et al. [1999] including their reported standard mean deviation (s.d.) caused by the variability of the bromoalkanes in the troposphere (see Table 3 therein). For the short-lived gases the same comparison yields: $[CH_2Br_2]$=0.568/(0.76±0.21) ppt, $[C_2H_5Br]$=0.105/(no data) ppt, $[CH_2ClBr]$=0.098/(0.16±0.04) ppt, $[CHBrCl_2]$=0.071/(0.07±0.03) ppt, $[CHClBr_2]$=0.034/(0.09±0.03) ppt, and $[CHBr_3]$=0.121/(0.19±0.15) ppt, respectively. Adding up all bromine contained in the source gases, then our total upper tropospheric (at 8-9 km) Br_y^{org} =(21.1±0.5) ppt is at the larger end of the range 17.0-21.3 ppt found by Schauffler et al. [1999] for the 21^o-41^o N latitude band in 1996.

The stratospheric input of organic Br is calculated from adopting bromoalkane concentrations for the

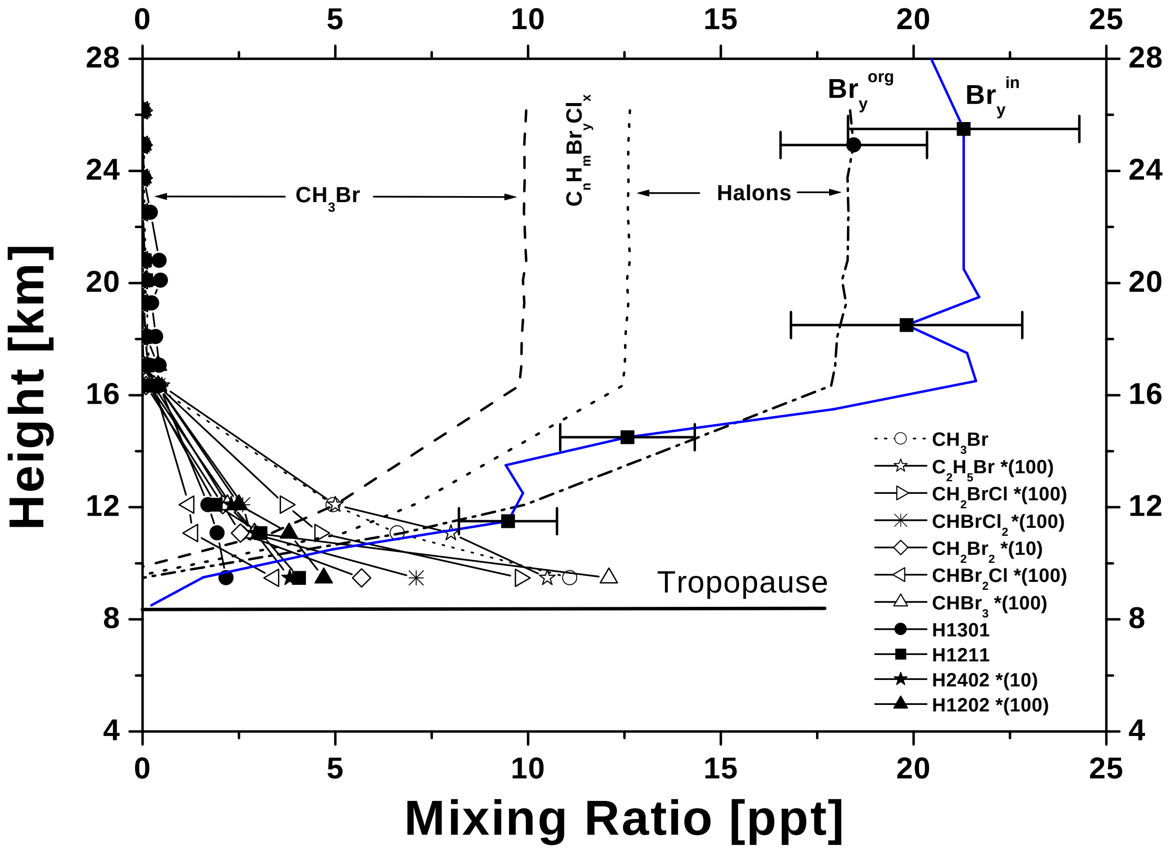

Figure 6.3: Vertical profiles of organic Br species for the TRIPLE flight on Feb. 6, 1999. The total Br_y^{org} , and the relative contributions of CH_3Br, $C_nH_mBr_yCl_x$, and the halons $H1301$, $H1211$, $H2402$, and $H1202$ to the total Br_y^{org} as a function of height. Total Br_y^{in} is calculated from measured BrO and the modelled BrO/Br_y^{in} ratio ($\sim$ 0.72).

time and location at entry into the stratosphere. It is assumed that (1) all gases, other than the halons, have exhibited no long term trends over the period of time represented by the stratospheric profile. For the halons (except $H1202$), the appropriate concentrations for the time at stratospheric entry were determined from third-order polynomial fits to tropospheric trends from Cape Grim, Tasmania [Fraser et al. 1999], after conversion to equivalent global mean concentrations based on an interhemispheric exchange time of 1.3 y [Maiss and Levin 1994]. (2) The following bromoalkane concentrations at the stratospheric entry are assumed: the upper tropospheric concentrations (including the s.d. variability) from Schauffler et al. [1999] for all gases are taken (except the halons, and C_2H_5Br - the latter was not measured by Schauffler et al. [1999]). For the halons (except H1202), the height dependent entry age of the probed stratospheric air was inferred from measured stratospheric C_2F_6, and SF_6 concentrations and the known atmospheric increase in C_2F_6 and SF_6 [Harnisch et al. 1996], c.f., the inferred C_2F_6 and SF_6-ages increase from 0 years at the local tropopause (8.5 km), to 2.4 y at 12 km, 4.5 y at 19.3km, and to maximal 6.2 y at 26.2km. For $H1202$ and C_2H_5Br stratospheric entry concentrations measured in our lowest altitude sample (at 9.5 km) were assumed.

Random uncertainties in calculated Br_y^{org} arise from uncertainty of the measured source gases and uncertainty of the entry level concentrations. The former was determined from root mean square propagation of all instrumental analytical errors for all measured species. The latter were similarly obtained from the reported s.d. [Schauffler et al. 1999], and in addition assuming a 50% uncertainty in the entry level concentrations of all gases other than the halons and CH_3Br. With all accountable uncertainties included, and adding the measurement errors, we obtained a $Br_y^{\mathtt{org}}$ value of 18.4 ppt at 25 km (for 5.6 year old air), with 1-σ error of ±1.8 ppt. This result is in excellent agreement with previous estimate made by Schauffler et al. [1999] and Wamsley [1998].

In Figure 6.3 the height dependent estimate of $Br_y^{\mathtt{org}}$ is compared with $Br_y^{\mathtt{in}}$ (calculated from the known $BrO/Br_y^{\mathtt{in}}$ partitioning and measured BrO and including all errors). It is found that within the errors of the measurements $Br_y^{\mathtt{in}}$ and $Br_y^{\mathtt{org}}$ reasonably compare, although $Br_y^{\mathtt{in}}$ is systematically larger than $Br_y^{\mathtt{org}}$. Since we have measured all known organic Br species (except ∼0.1 ppt from CH_2BrCH_2Br discarded), we think that discrepancy is most likely caused by an influx of inorganic Br ∼(3.1±3.5)ppt from the troposphere into the stratosphere. The inferred $Br_y^{\mathtt{in}}$ also suggests the presence of inorganic Br (∼ 1.5 ppt) in air just above the local tropopause, a result being in excellent agreement with 3-D model calculations [Dvortsov 1998].

Finally, we calculate the lower stratospheric relations of $Br_y^{\mathtt{org}}$ and $Br_y^{\mathtt{in}}$ to $CFC-11$ (TRIPLE) and N_2O (TRIPLE and LPMA/DOAS). For the TRIPLE flight the in-situ measured $Br_y^{\mathtt{org}}$ (given in ppt) relates to N_2O (given in ppb) by

$$\begin{aligned}[Br_y^{\mathtt{org}}] &= 18.12 + 0.036 \cdot [N_2O] - 5.84 \cdot 10^{-4} \cdot [N_2O]^2 \\ &\quad +3.73 \cdot 10^{-6} \cdot [N_2O]^3 - 8.98 \cdot 10^{-9} \cdot [N_2O]^4 \end{aligned} \tag{6.1}$$

and to $CFC-11$ (given in ppt) by

$$\begin{aligned}[Br_y^{\mathtt{org}}] &= 18.92 - 0.01877 \cdot [CFC-11] + 3.42 \cdot 10^{-4} \cdot [CFC-11]^2 \\ &\quad -2.49 \cdot 10^{-6} \cdot [CFC-11]^3 + 1.368 \cdot 10^{-9} \cdot [CFC-11]^4 \end{aligned} \tag{6.2}$$

which are valid for stratospheric N_2O and $CFC-11$ concentrations larger than 10 ppb, and 25 ppt, respectively. The same relation calculated from inferred $Br_y^{\mathtt{in}}$ and spectroscopically measured N_2O onboard the LPMA/DOAS gondola yields

$$\begin{aligned}[Br_y^{\mathtt{org}}] &= 18.78 + 0.075 \cdot [N_2O] - 5.47 \cdot 10^{-4} \cdot [N_2O]^2 \\ &\quad +1.39 \cdot 10^{-6} \cdot [N_2O]^3 - 3.07 \cdot 10^{-9} \cdot [N_2O]^4 \end{aligned} \tag{6.3}$$

Note that our relations are somewhat different from that found by Wamsley [1998] for fall 1994, primarily because since then stratospheric N_2O slightly augmented and $CFC-11$ already started to decline, but $Br_y^{\mathtt{org}}$ or $Br_y^{\mathtt{in}}$ were still increasing (by about ∼1.64 ppt since 1994), and an inorganic bromine influx into the stratosphere has not been considered previously.

In summary, this study reveals that, in early 1999 stratospheric bromine was speciated like this : ∼45 % from CH_3Br (of which probably the same amounts are due to natural and anthropogenic sources [WMO 1998]), ∼13 % from naturally released short-lived bromoalkanes, ∼28% from anthropogenically emitted halons ($H1301$, $H1211$, $H2402$, and $H1202$), and ∼14% from inorganic Br transported from the troposphere into the stratosphere. Our almost simultaneous $Br_y^{\mathtt{org}}$ and $Br_y^{\mathtt{in}}$ observations thus set a limit, but it does not exclude an influx ((3.1±3.5)ppt) of inorganic bromine from the troposphere into the stratosphere. In concluding, it is estimated that the man-made Br species have a share of ∼43/50 % in the total stratospheric Br burden (assuming (1) a 2:1 share in natural and anthropogenic CH_3Br sources [Yokouchi et al. 2000] or (2) that either the upper tropospheric $Br_y^{\mathtt{in}}$ is completely due to natural sources or of the same share as stratospheric $Br_y^{\mathtt{in}}$, respectively) that was close to 20 ppt in early 1999.

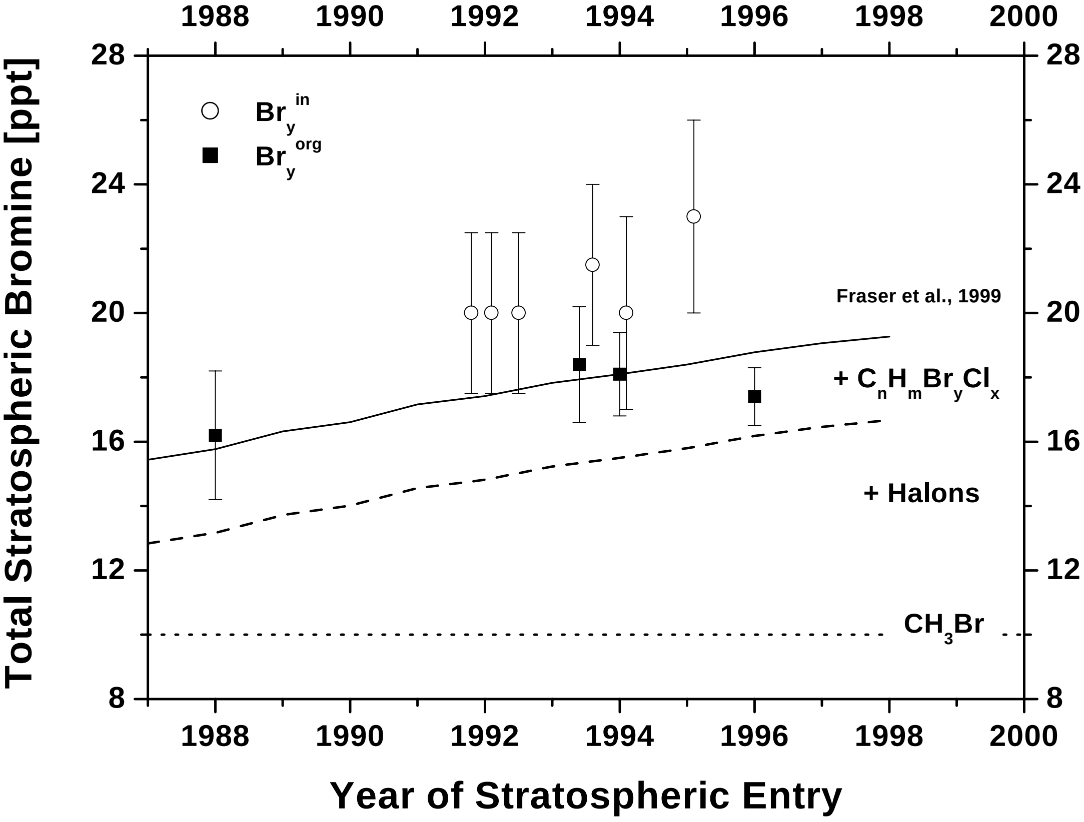

Figure 6.4: Time evolution of organic and inorganic stratospheric bromine from 1988-2000. The organic bromine data are taken from [Fraser et al. 1999] and [Wamsley 1998]. Methyl bromide is assumed constant over the presented time range [WMO 1998].

6.3 A recent history of total organic and inorganic stratospheric bromine

Combining all the available information published recently, it is now possible to reconstruct a recent history of stratospheric burden of bromine. The basic idea beyond this reconstruction is to put together the inferred stratospheric bromine and the air age information from the simultaneous measurements of CO_2, SF_6 or $CFC-11$ - using the knowledge of the temporal trend of these species in the troposphere.

Figure 6.4 displays all the measurements done so far. The total stratospheric bromine inferred with the organic bromine method closely follows the measured trend of the tropospheric bromine bearing source gases - except for the Schauffler et al. [1999] value for 1996, where only a proxy for the stratospheric bromine content was used. The inorganic bromine inferred from our balloon borne spectroscopic measurements follow this trend - taking into account the error bars - but they are consistently 1-3 ppt larger than the organic bromine input to the stratosphere. This can only be explained by an influx of tropospheric inorganic bromine into the stratosphere in accordance with previous studies ([Ko et al. 1997; WMO 1998; Harder et al. 2000; Fitzenberger et al. 2000; Pfeilsticker et al. 2000]).

As the time range covered by our balloon borne measurements is only a four year interval, the trend in stratospheric inorganic bromine is not as clearly visible as in the organic high precision measurements, but one has also to take into account that the organic measurements are in-situ measurements and the inorganic method relies on remote sensing measurements, so that the agreement is still very surprising and convincing at the same time, but more measurements are needed to investigate the probable influx of tropospheric Br_y into the stratosphere in more detail - especially to search for the global source regions of this input, which are expected to be in the tropics.

Chapter 7

Lagrangian case studies for the interpretation of enhanced *OClO* measurements at mid and high latitudes

During the winter flights in the Arctic vortex it was expected to find *OClO* as an indicator for chlorine activation within the vortex. That is why the search for *OClO* signatures primarily in the data retrieved from these flights was performed. In this chapter the measurements of *OClO* made during a relatively 'warm' stratospheric Arctic winter (1998/99) will be shown and a Lagrangian trajectory box model will be presented to interpret these measurements in comparison with the model results of the SLIMCAT 3-D CTM model. Furthermore a case, where *OClO* could be measured also at mid-latitudes - especially during the solar occultation - will be investigated and this finding will be compared with the model output of the different models.
The first part of this chapter contains a description of the specially designed Lagrangian trajectory box model LABMOS[1]. It will show the program structure and the photochemical input used to generate model output, which can directly be compared to our SCD measurements.
In the second part the comparison of the measurements and the model outputs of both models for the different geophysical conditions, where *OClO* could be measured, will be presented.

7.1 The Lagrangian trajectory box model LABMOS

The model uses ECMWF[2] airmass trajectories calculated on 7 isentropic levels [Knudsen and Carver 1994] - which are the 350, 380, 400, 435, 475, 550 and 675 K potential temperature level. The trajectories are based on the 6 hourly ECMWF T213 initialized analysis data. They are calculated 10 days back in time, but become increasingly unreliable because of the accumulating errors. The calculations are linear in space and time using a 1.5x1.5 degree latitude-longitude grid and a second order Runge-Kutta integration scheme with a timestep of 1 hour. The pressure at an isentropic level is calculated by assuming that T varies linearly with log(p). The trajectory calculations stop prematurely when the air parcels move south of 3N or above 10 mbar.
The PV along the trajectory is calculated using a centred difference scheme except between the two upper levels (10 and 30 mbar) of the ECMWF model. The PV values differ a little from the PV values in the 'isentrop' directories on the NILU[3] database due to a difference in the distance between the gridpoints used in the calculations. PV varies a lot along a trajectory primarily due to the coarse vertical interpolations and unreal small-scale structures in the ECMWF analysis. This PV variation

---

[1] LAgrangian Box MOdel for the Stratosphere

[2] European Centre for Medium-Range Weather Forecasts, http://www.nilu.no

[3] NILU: Norwegian Institute for Air Research, *http://www.nilu.no*

can be reduced a little by averaging PV along the trajectories (for example over 24 hours).
There has been some discussion recently about the accuracy of the ECMWF trajectories - as well as other meteorological models - after comparing them to long duration balloon flight measurements of the meteorological parameters [Pommereau 2000]. The main biases in comparison with trajectory calculations using different meteorological analysis can be observed in the 5-30 mbar region, but this discrepancy could be resolved by including more pressure levels in the meteorological model ECMWF (old:31, new:50). Still for the model calculations shown in this thesis the old version trajectories were used, because the interesting altitude range for the measurement of BrO and $OClO$ is below 30 km ($p \geq 30$ mbar).
The model also provides the possibility to use trajectories calculated by the NASA[4] GSFC[5] Trajectory Model [Schoeberl and Sparling 1994]. The trajectory data can be retrieved by using the Goddard Automailer [Lait et al. 1996]. The GSFC model uses NMC[6] data from NMC analyses using balance-equation-computed winds. If the NMC analyses are not available then forecast fields are used. Using these trajectories does not change the principle results retrieved using the ECMWF trajectories, why here only the latter model trajectories are used.

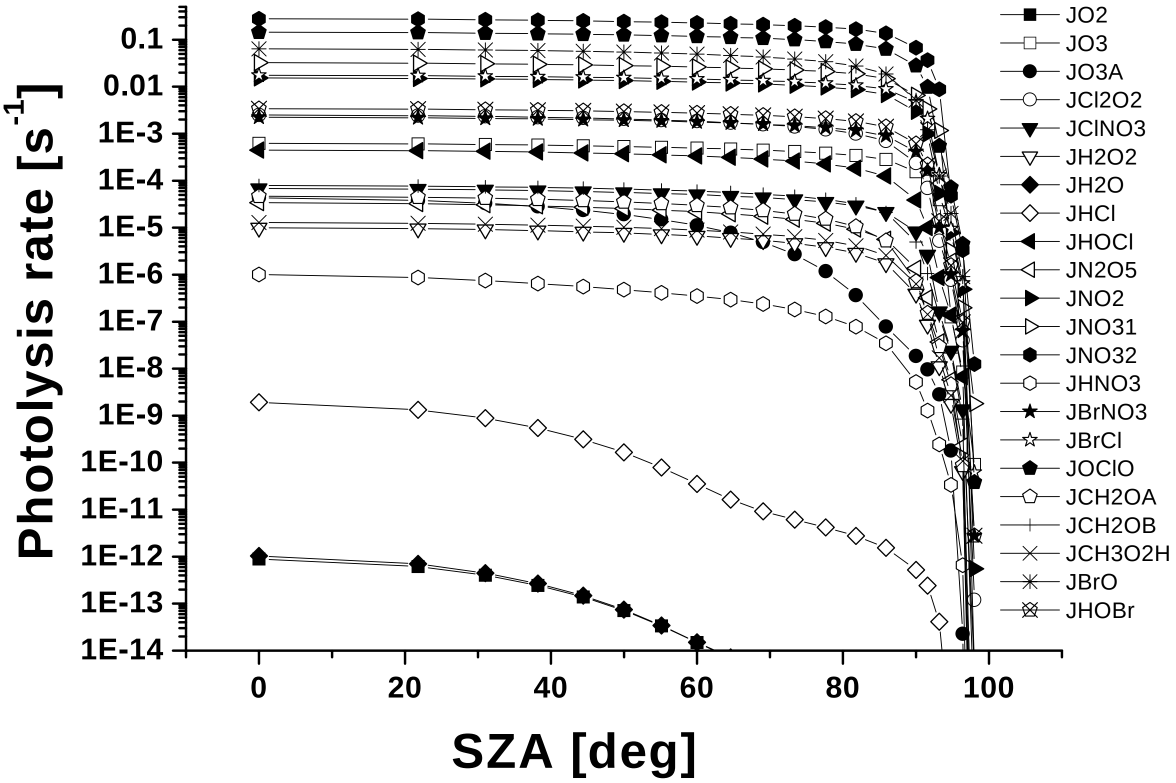

Figure 7.1: SLIMCAT photolysis rates used in the model LABMOS for 49.4 mbar, 200 K and 1.575 O_3 scaling factor. All available photolysis rates are shown in this plot. There are no J values for Br_2, because the model - like SLIMCAT - assumes that these species are instantaneously dissociated in the sunlit stratosphere.

The chemical model is based on a zero dimensional box model [Müller et al. 1994; Helmling 1994; Erle 1999] using chemical kinetics data of the JPL-97 and the updated JPL-2000 database [DeMore

---

[4] National Aeronautics and Space Administration

[5] Goddard Space Flight Center

[6] National Meteorological Center

et al. 1997; Sander et al. 2000]. It includes the full NO_x, HO_x, ClO_x and BrO_x chemistry with a total of 68 gas phase reactions, 29 photolytical reactions and 7 heterogeneous reactions on the liquid background sulphate aerosols using the framework presented by Hanson et al. [1994] - for details see Section 2.4.1. As the SLIMCAT 3-D CTM model, the Lagrangian model uses a precompiled lookup table of photolysis rates based on [Lary and Pyle 1991], where the actual photolysis rates are given as a function of pressure, temperature, SZA and a so called O_3 scaling factor, which is between 0 and 2. An O_3 scaling factor of 1 corresponds to a standard O_3 profile and the more O_3 is available the less UV light enters the lower stratosphere reducing the photolysis rates of the species absorbing in that wavelength region. The photolysis rates for 49.4 mbar, 200 K and 1.575 O_3 scaling factor are shown in Figure 7.1 as a function of SZA - for a definition of the photolysis rate, please see Appendix B.
The organization structure of the Lagrangian model is shown in Figure 7.2. First the trajectory data are read in together with the photolysis rate table and then the meteorological values are interpolated on a 5 min grid. Then the SZA is precalculated using the trajectory data and the photolysis rates are interpolated with respect to the SZA. All theses interpolations are cubic spline interpolations, while during the chemical model integration of the differential equations the meteorological parameters and the SZA are interpolated linearly. The integration of all differential equations is done with the process and chemical reaction modeller FACSIMILE[7]. Besides photochemical variations of the concentrations also changes because of the pressure change on the isentropic surfaces are taken into account. During the integration of the chemical reactions a time accuracy of $10^{-4} sec$ is chosen and the output is generated every 5 min. The runtime of the 10 day model run on one isentropic level on a AMD K6 200 MHz PC is about 5-6 min.

7.2 Case study of the in-vortex flight at Kiruna on February 10, 1999

As could be seen in chapter 4, the flight from Kiruna on Feb.10, 1999 was within the polar Arctic vortex and the temperatures were well above the different PSC formation thresholds. Still it was possible to observe significant amounts of $OClO$ and the question now is, how could this observation be interpreted in terms of chlorine activation during that time, because it is well known on the other hand that there was nearly no O_3 depletion observed in this winter at northern latitudes [Goutail et al. 2000] - less than 5% by mid March.
Figure 7.3 shows the 10-day backward airmass trajectories for 6 of the seven available potential temperature levels. They are all ending at the grid point Kiruna $(67.9N, 21.1E)$ at 12:00UT on the day of the measurements. In the plots the trajectory output of the two different meteorological models ECMWF(∘) and GSFC(⋄) are shown and the colour code gives the time of each trajectory point in hours before the endpoint. It is obvious that the trajectory calculations deviate tremendously for times earlier than 5 days, but they converge more and more when reaching the endpoint and higher altitudes or higher potential temperature levels, respectively. Still they show both that the airmasses encountered during the measurements are all of polar origin. Overall it can be shown that the results of the model do not depend very much on the choice of the trajectory model - in this case.

When having a look at the meteorological parameters on the different trajectories - Figure 7.4 shows the meteorology and the evolution of the bromine species on the 475 K potential temperature level - it is obvious that the air masses were not seeing much sunlight during the last 10 days before the encounter. That is why heterogeneous chemistry on the background aerosol becomes very important for the speciation of the chemical species measured. The temperatures were in the beginning of the 10 day period above 200 K, but reached after 100 hours down to 196 K and rose again a few days before the endpoint.

Table 7.1 gives the chemical and aerosol initialization values used during the standard run

---

[7] AEA Technology, FACSIMILE RELEASE 3.05 DATE 23/12/93 FROM FORTRAN FILE facsim_big.f

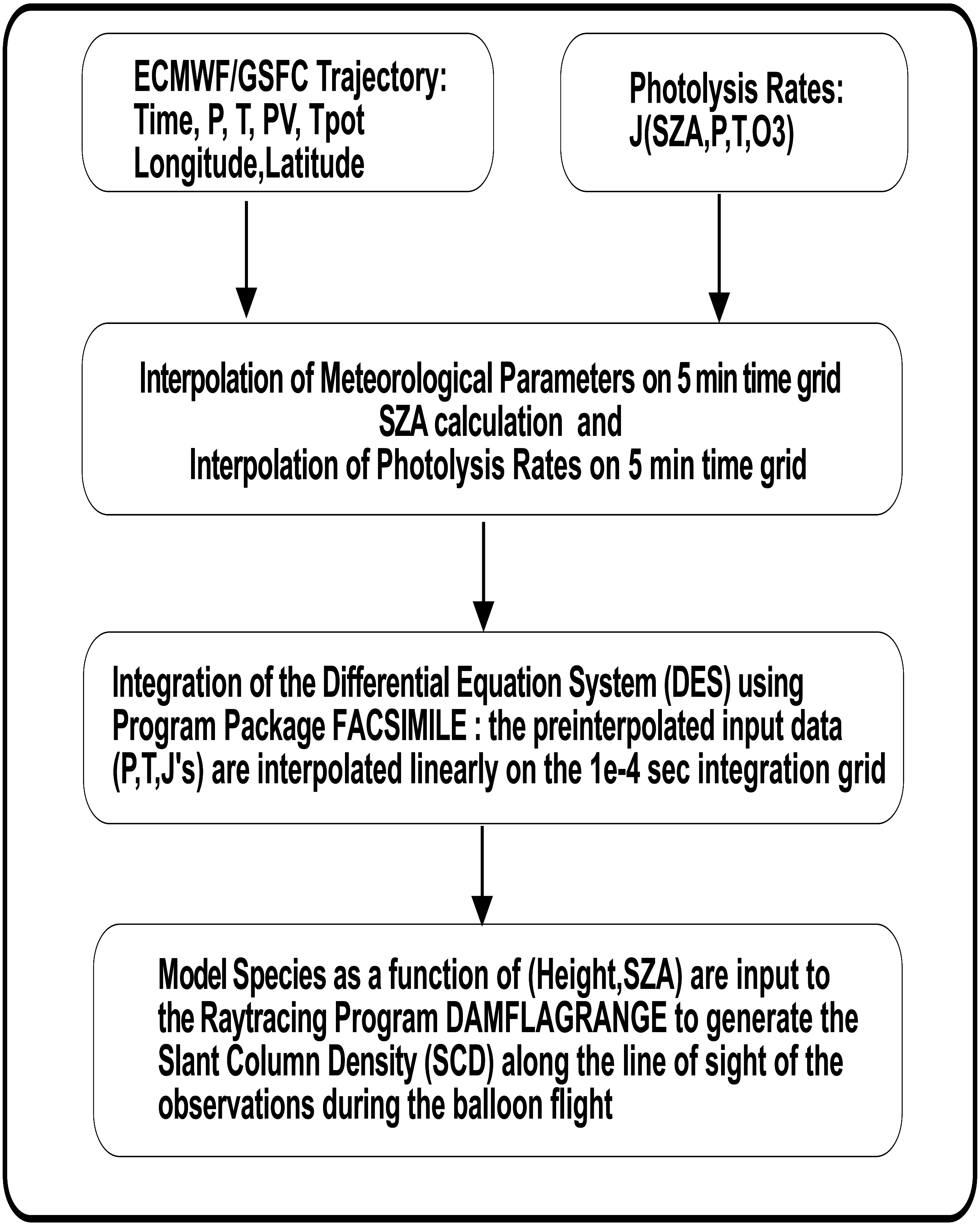

Figure 7.2: Organization chart of the Lagrangian trajectory box model LABMOS. The trajectory input data can be chosen from the ECMWF or GSFC model. For details see text.

of the Lagrangian model. The aerosol surface values are taken from the measurements of the LMD(Laboratoire de Meteorologie Dynamique, France) optical particle counter [Engel 2000] installed

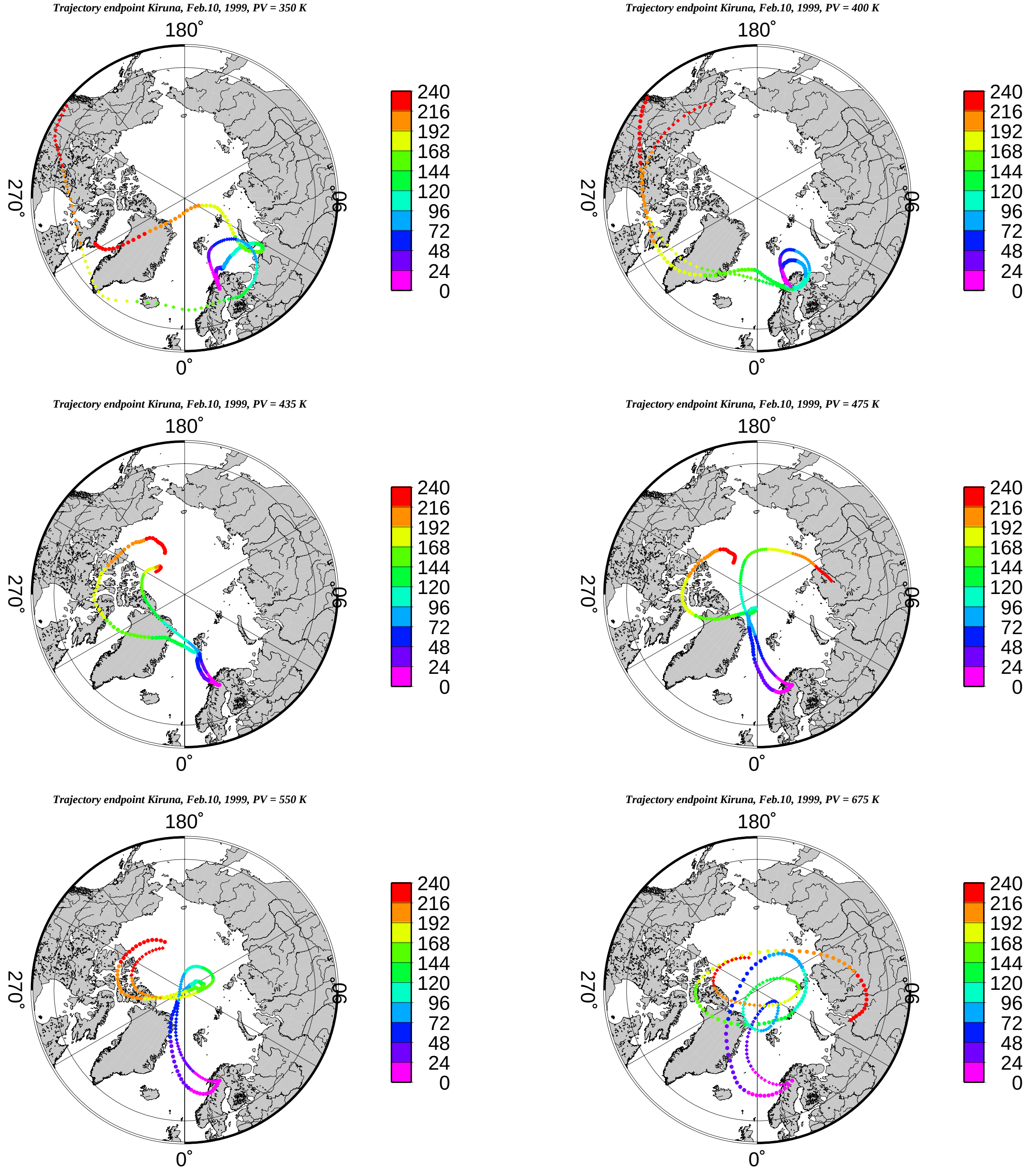

Figure 7.3: 10-day backward airmass trajectories for the different isentropic potential temperature levels: 350 K, 400 K, 435 K, 475 K, 550 K, 675 K. These potential temperatures correspond at the endpoint Kiruna at 12:00UT to altitudes of 12 km, 16 km, 18.1 km, 20.9 km, 24.5 km, 29.7 km. The ECMWF/GSFC trajectories are denoted by $\circ$, $\diamond$, respectively. The time of each trajectory point is given in color code and in units of hours before reaching the endpoint.

LABMOS Standard Model Run Initialization							
T_{pot} [K]	350	380	400	435	475	550	675
Height$_{endpoint}$ [km]	11.7	14.3	16	18.1	20.9	24.5	29.7
Aerosol surface[$\mu m^2 cm^{-3}$]	6	5	4	3	2	1.1	0.5
Aerosol mean radius [μm]	0.15	0.15	0.15	0.15	0.15	0.15	0.15
NO_x [ppt]	10	20	20	30	30	40	50
NO_y [ppb]	1.75	3.95	6.34	9.65	13.11	17.24	12.9
ClO_x [ppt]	75	120	320	350	390	440	480
Cl_y [ppt]	693	1370	1920	2400	2990	3140	3680
Br_y [ppt]	8.6	12.0	17.2	20.0	21.5	21.5	21.5

Table 7.1: Summary of the physical-chemical initialization of the standard Lagrangian trajectory model run. The trajectories all start for SZAs larger than 90^0.

on the TRIPLE gondola, which flew within the vortex from Kiruna only four days before our LPMA/DOAS balloon experiment. As this counter only measured particles with diameters larger than 0.35 μm and the measured height profiles for particles of this size did not differ very much from winter 1994/95 to winter 98/99 - taking into account the variability between the two profiles measured during the same winter 98/99 - the aerosol surface density profiles measured by the SAGE[8] II satellite experiment [Thomason and Poole 1997] for the years 1994-96 were assumed, when the aerosol loading reached again background levels after the large eruption of Mount Pinatubo in June 1991. The model starts with a denoxified stratosphere like it was measured during several balloon flights of the THESEO campaign and also during our measurements. The NO_y and the Cl_y were taken from the LPMA/DOAS measurements, where the retrieved Cl_y coincides very well with the TRIPLE results from the in vortex flight four days before. The Br_y used is the total bromine determined by our own measurements in accordance with the organic bromine precursor measurements on the TRIPLE gondola - see chapter 6 - but the larger value of 21.5 ppt total inorganic bromine in the maximum was used.

Figure 7.4 shows the evolution of nearly all bromine species involved in the inorganic bromine chemistry - only Br, Br_2 and $BrONO$ are missing, but these species are much less abundant than the others. The time, when the airmasses are sunlit varies largely and BrO only shows up, when photochemistry sets in, while $BrONO_2$ is converted to $HOBr$ and subsequently to $BrCl$ during the polar night and $HOBr$ produces BrO and OH in the morning, which is reacting with ClO to generate $OClO$, $ClOO$ and $BrCl$ - especially during the sunset. This increase of $BrCl$ is clearly seen, even though most of the chlorine monoxide is converted to $OClO$. When the airmasses are sunlit again, the BrO shows up, as $BrCl$ is photolysed very rapidly and also $BrONO_2$ forms by the reaction of BrO with NO_2. It can also be observed that the more sunlight is reaching the airmasses the more important become $HOBr$ and $BrONO_2$ as nighttime reservoirs. At the beginning of the night $BrONO_2$ is a more important reservoir than $HOBr$, while in the morning most of the bromine nitrate has been converted heterogeneously to $HOBr$, which is photolysed faster than $BrONO_2$ leading to the morning/evening asymmetry observed in the BrO concentrations. The bromine reservoir species HBr is initialized with a constant mixing ratio of 1.5 ppt for the upper 6 potential temperature levels - according to the recent measurements of HBr [Carlotti et al. 1995; Nolt et al. 1997] - and 2.0 ppt on the lowest isentropic level. From the gas phase chemistry it is clear that the HBr/Br_y ratio should increase significantly towards the tropopause. Also, the BrO measurements itself confirm this increase, because the Br_y profile is known from the organic precursor measurements, as well as our Br_y calculation. Otherwise the BrO mixing ratio is overestimated dramatically on the lowest model level. The HBr mixing ratio stays constant during the 10-day period, as the only relevant destruction processes via the OH and $O(^3P)$ channels are insignificant. Also the production from atomic bromine does not play an important

---

[8] Stratospheric Aerosol and Gas Experiment - a successor for SAGE II is planned for launch in 2000/2001.

role, as there is only a small amount of Br.

The chlorine chemistry during this 10-day period is shown in Figure 7.5 for the 475 K potential temperature level. ClO, Cl_2O_2 and $OClO$, as well as $BrCl$ are the photochemically most active species and vary complementarily to each other from day to night, while the other species do not change very much. Only $HOCl$ increases significantly during the long time from 175 h to 60 h before the endpoint because of the heterogeneous reaction of $ClONO_2$ with H_2O. 60 h before the endpoint the sunlit time becomes longer as well as the ClO daytime maximum concentration becomes larger. $OClO$ is nearly constant during the night at an 60-100 ppt level.

Most of the nitrogen species - except $ClONO_2$ which can be seen in the previous figure - are displayed in Figure 7.6. The active NO_x species NO and NO_2 do only appear in the sunlit phases of the trajectory, while NO_3 is most abundant - less than 1 ppt - throughout the night, when there has been some NO_x activation before. During the long polar night NO_3 is consumed by the reaction with NO_2 to N_2O_5. Also the reaction of HNO_3 with OH is triggered by sunlight - as the OH is maximal for smallest SZA producing directly NO_3.

Figure 7.7 shows the evolution of the oxygen species for the 10 days before the measurements. O_3 is slightly decreasing, when the airmasses are sunlit again approximately 3 days before the endpoint. During the long night before the O_3 mixing ratio remains nearly constant; but at the end of the time - when the airmasses are sunlit again - the O_3 mixing ratios are decreasing at a rate of $\approx 10 ppb/day$. In this figure also the pressure of the airmass is plotted against time, which is behaving the same way as the temperature as a consequence of the isentropic trajectory model.

The next Figure 7.8 shows the comparison of measured and modelled LABMOS as well as SLIMCAT BrO profiles. The measured BrO mixing ratio profile falls in between the two models in the lower stratosphere, where the main difference between the model results stems from the different Br_y initialisations. The Lagrangian model LABMOS uses the actually measured Br_y, while SLIMCAT only initializes the maximum Br_y mixing ratio in the middle stratosphere and determines the lower stratospheric Br_y profile from the photolysis of the organic bromine precursors referenced to CH_3Br. The 3-D CTM SLIMCAT underestimates the lower stratospheric BrO either because there is too less Br_y in the lower stratosphere or because the partitioning of BrO is not modelled right. The LABMOS model studies show that - once the Br_y is fixed by the measurements - the modelled BrO depends very much on the HBr put into the model. The HBr does not change during the model time, but it determines the difference available for transformation into active bromine.

Together with the BrO the Br_y and the BrO/Br_y profiles are displayed in the same plot. The Br_y profile is the same as input into the Lagrangian (LABMOS) study during the initialization, because there is no process in the model removing inorganic bromine. The BrO/Br_y ratio is about 0.55-0.6 at 4 km above the local tropopause, which is at 8 km altitude, and increases to 0.7 in the middle stratosphere. As we are comparing profiles measured between 82.7 and 86^o SZA, we can expect the BrO to amount up to 75-80% during times, when the airmasses are sunlit with smaller SZAs.

Figure 7.9 contains the comparison of measured and modelled $OClO$ profiles. While there is a quite good agreement between model and measurement in the middle atmosphere above 18 km altitude, the measured lower stratospheric $OClO$ values cannot be reproduced by either model. But it turns out that the measured profile form can be better reproduced by the Lagrangian model, which only accounts for heterogeneous chlorine activation on the background sulphate aerosols, while the 3-D CTM SLIMCAT - also taking into account the heterogeneous activation on PSC ice/NAT/ternary solution particles - seems to be dominated by the PSC activation, which normally takes place above 18 km at the measurement location. From the LABMOS studies it is also obvious that the amount of $OClO$ in the model depends strongly on the aerosol content of the stratosphere, while the BrO is nearly insensitive to the aerosol loading.

To further investigate the model/measurement comparison, it is salutary to model the measured SCDs of BrO and $OClO$ - as it is described in the previous chapters. When looking at Figure 7.10 one can see again the good agreement between the measured and modelled BrO SCDs in the occultation part

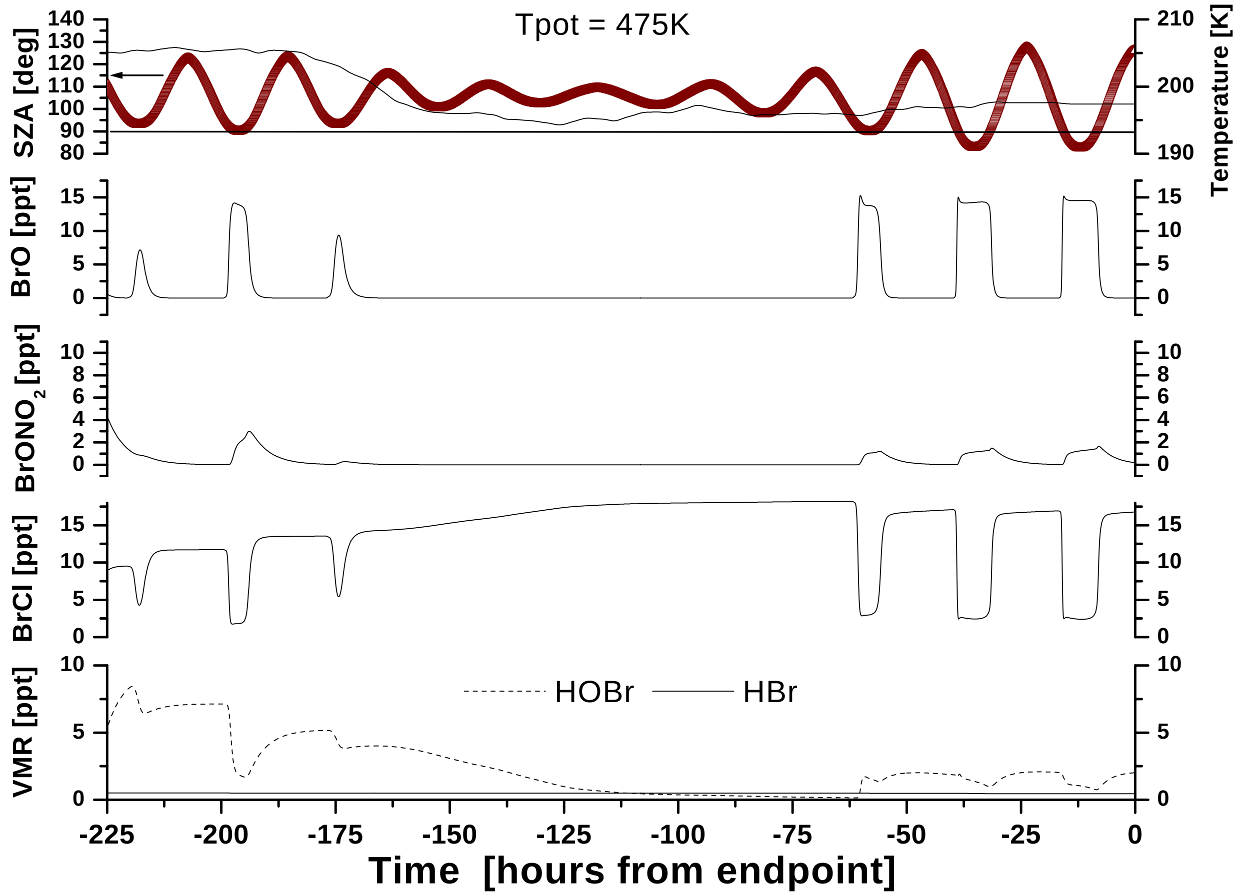

Figure 7.4: Time evolution of the bromine species on the 475K potential temperature isentropic level. Also the SZA and temperature evolution is displayed.

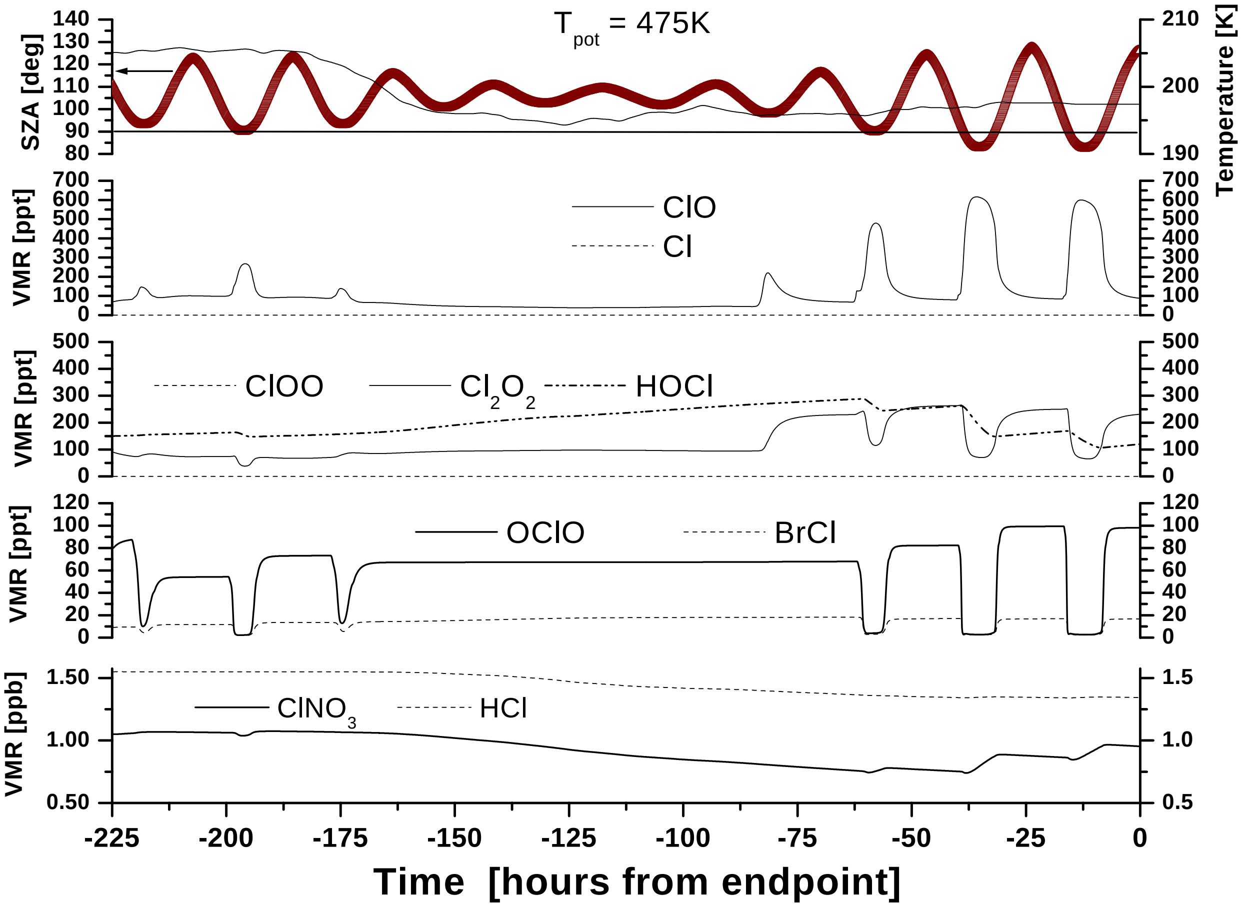

Figure 7.5: Time evolution of the chlorine species on the 475K potential temperature isentropic level. Also the SZA and temperature evolution is displayed.

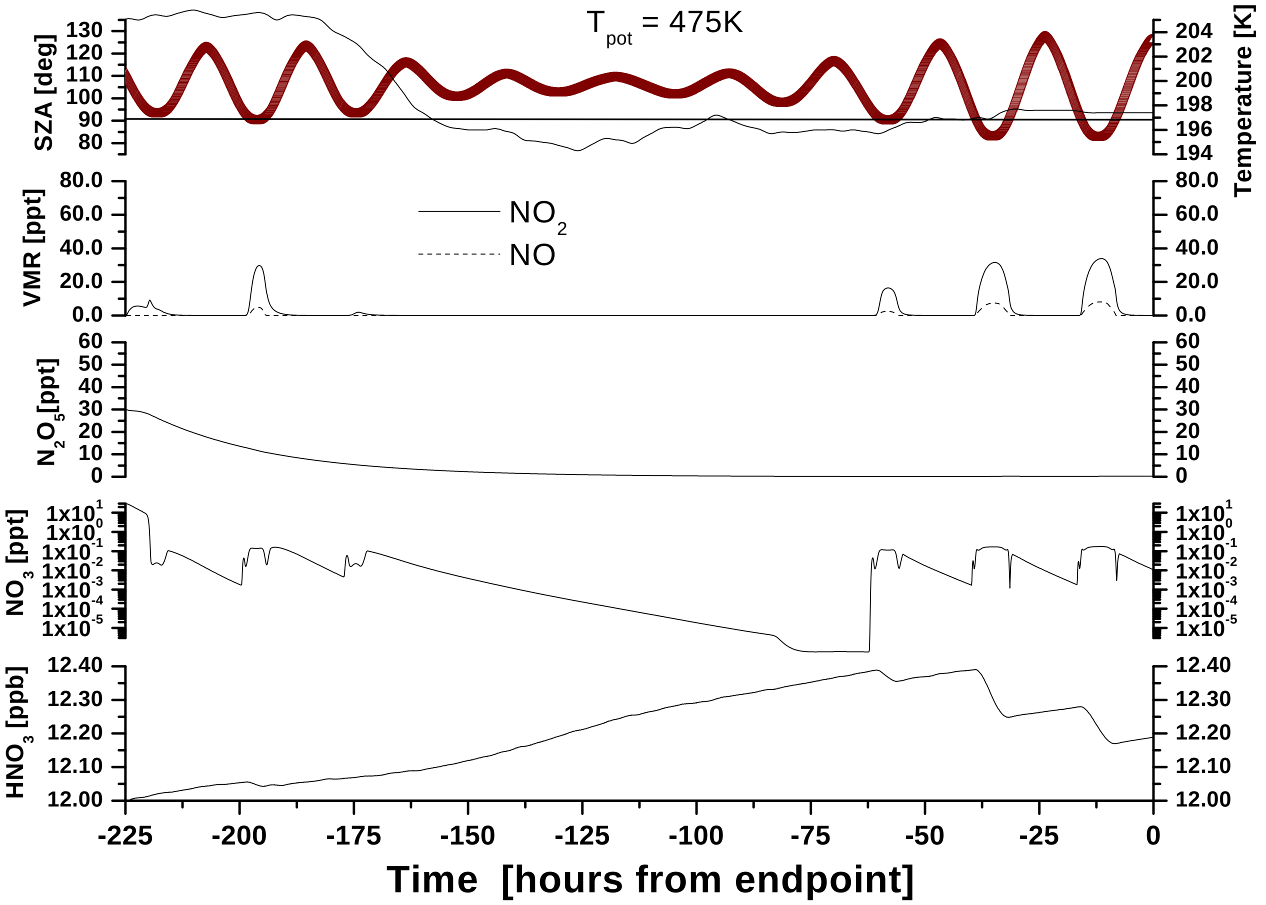

Figure 7.6: Time evolution of the nitrogen species on the 475K potential temperature isentropic level. Also the SZA and temperature evolution is displayed.

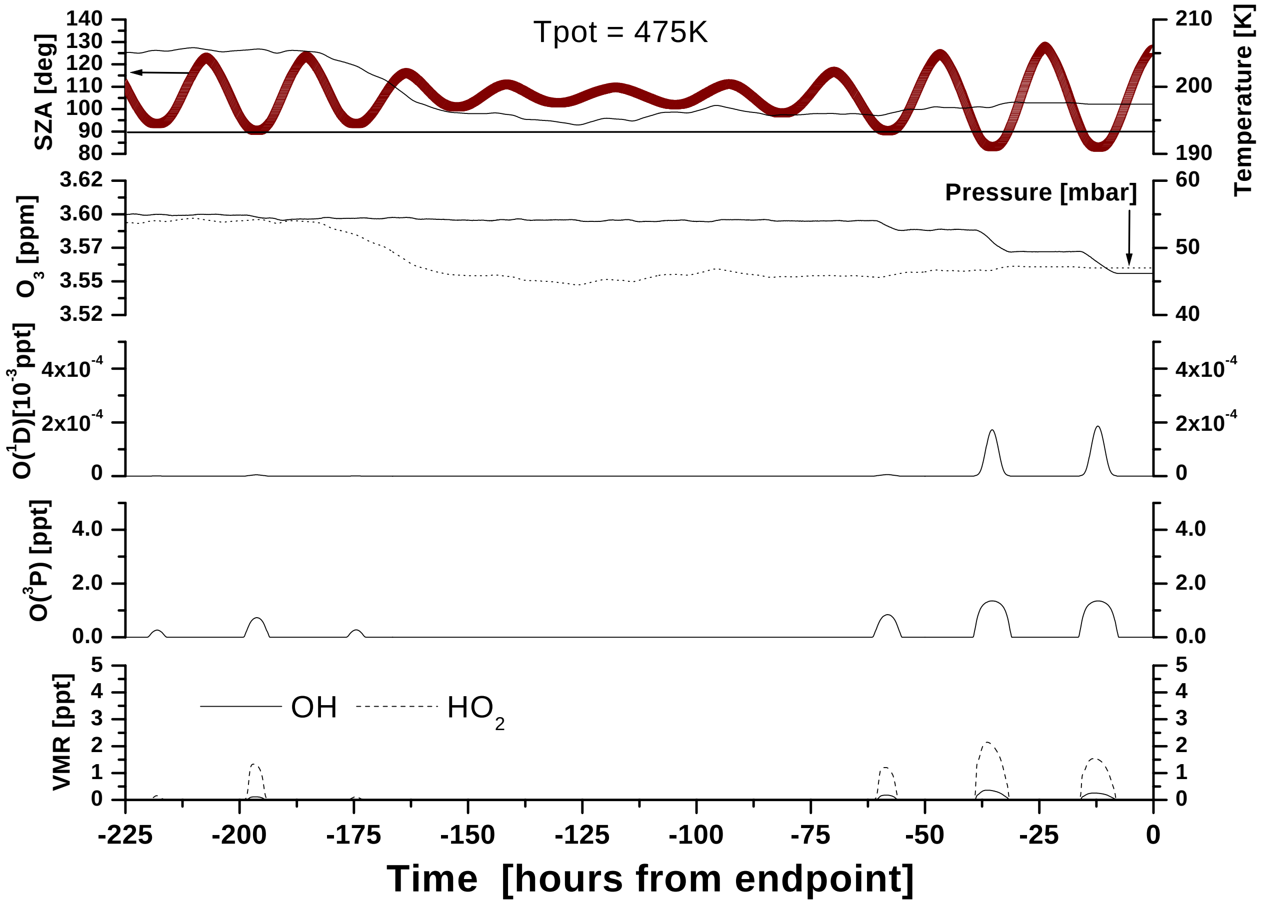

Figure 7.7: Time evolution of the oxygen species on the 475K potential temperature isentropic level. Also the SZA and temperature evolution is displayed.

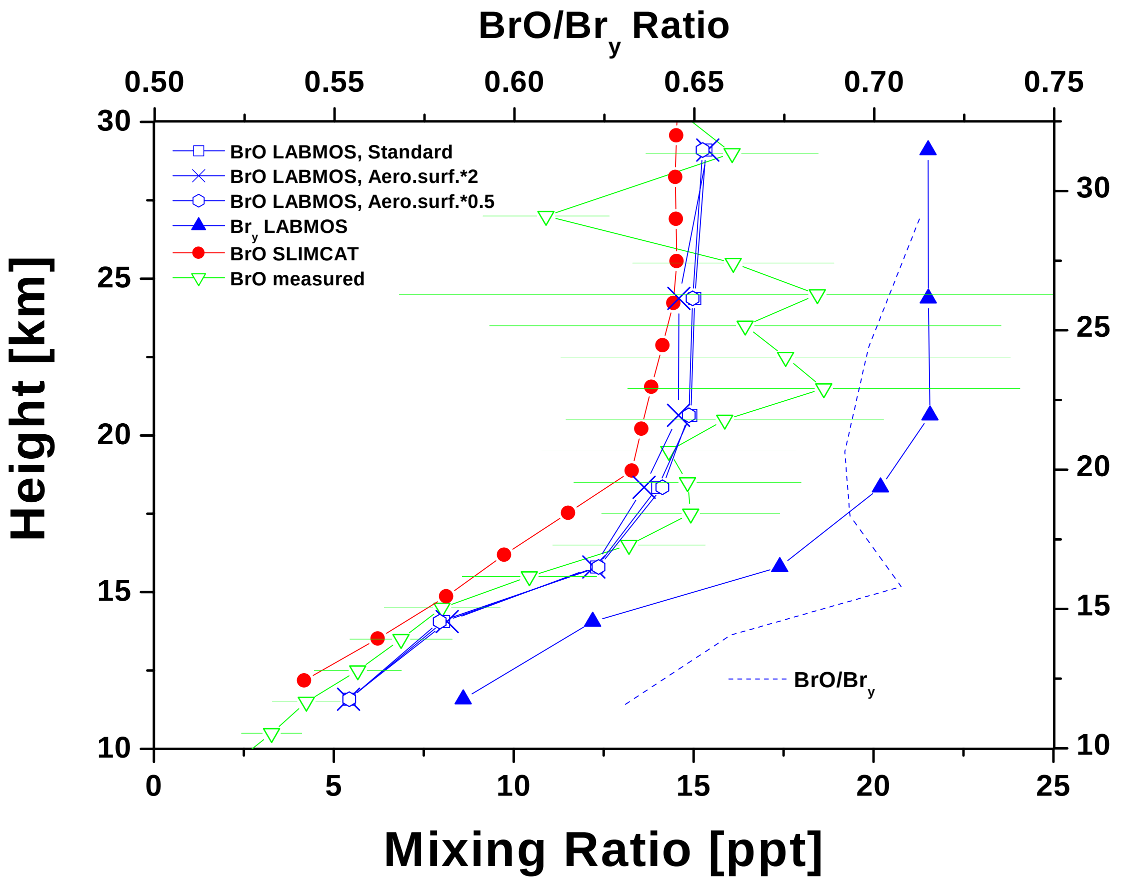

Figure 7.8: Measured and modelled - SLIMCAT and LABMOS - BrO profiles. Also the Br_y profile as well as the BrO/Br_y ratio is shown in the plot.

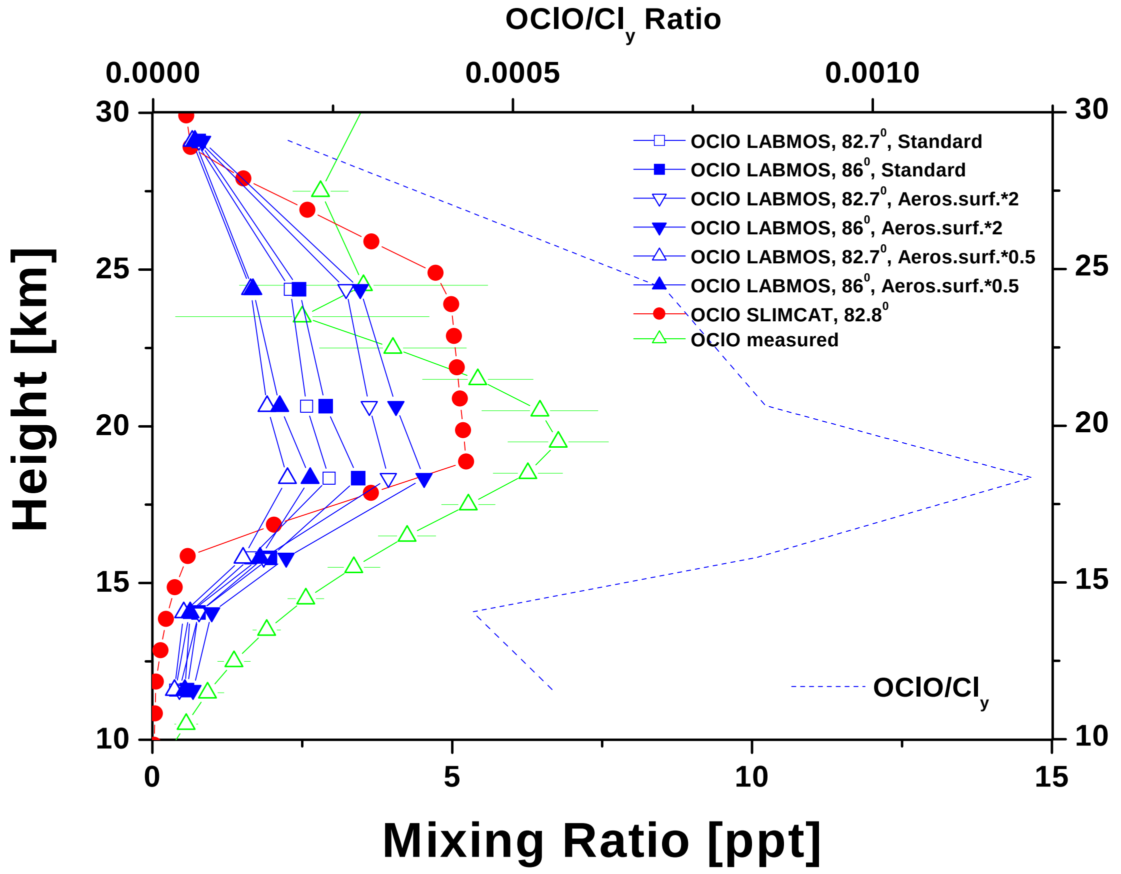

Figure 7.9: Measured and modelled - SLIMCAT and LABMOS - $OClO$ profiles. Also $OClO/Cl_y$ ratio profile is shown in the plot. The different LABMOS profiles for the two SZAs $(82.8, 86^0)$ at the beginning and the end of the ascent measurements refer to three different model runs: with standard, double and half aerosol loading.

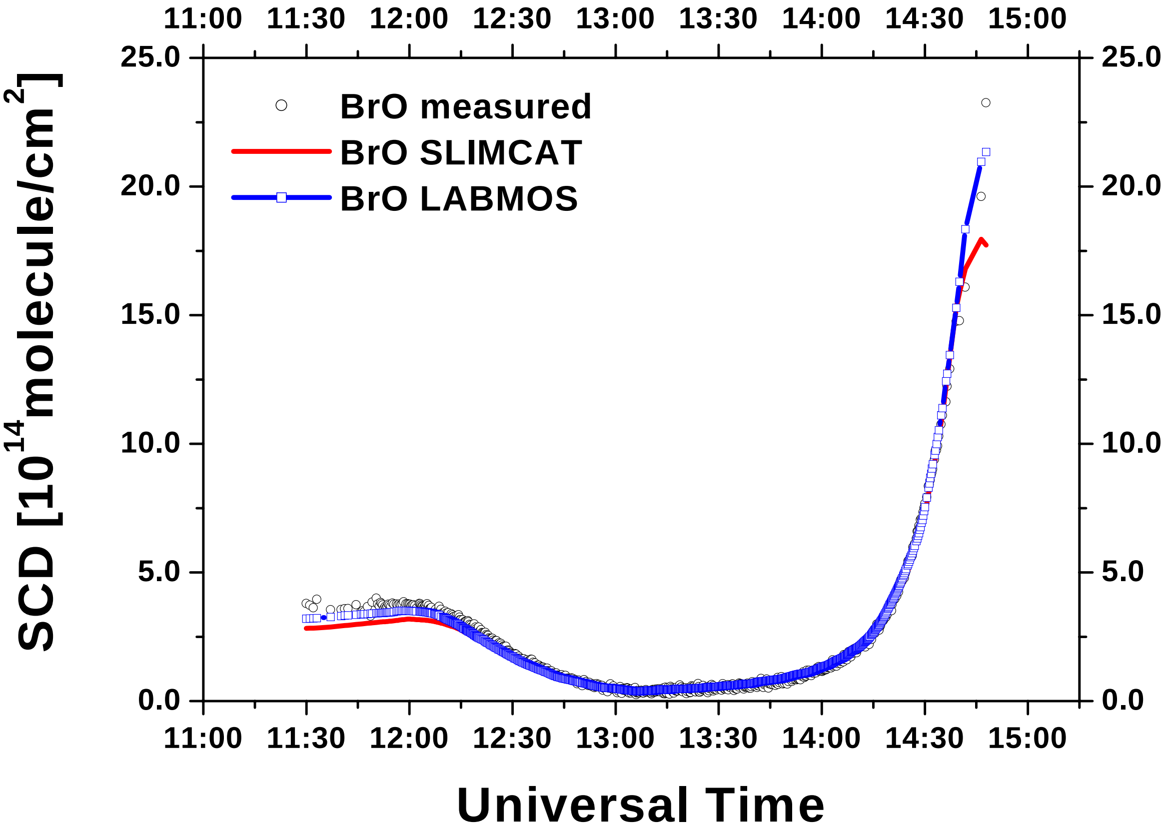

Figure 7.10: Measured and modelled - SLIMCAT and LABMOS - *BrO* SCD time evolutions.

of the flight, both for the 3-D CTM model SLIMCAT and the Lagrangian trajectory model LABMOS. During the ascent of the balloon in the lower stratosphere the SLIMCAT model underestimates the SCDs in accordance with the profile comparison. This discrepancy is more pronounced in the SCDs, because the same mixing ratio difference produces a larger column difference in the lower stratosphere than in the middle stratosphere. This is also the reason for the LABMOS model SCDs better following the measured SCD trend at the end of the occultation, where the SLIMCAT SCDs deviate.

Figure 7.11 displays the resulting modelled and measured *OClO* SCD time evolutions during the flight. As seen in the profile comparison, both models underestimate the *OClO* SCDs slightly in the lower stratosphere. The underestimation is nearly the same in both models, because SLIMCAT sees more *OClO* in the PSC altitude range and less *OClO* in the lower stratosphere than the LABMOS model. The occultation SCDs are better modelled by LABMOS - especially when taking into account the strong dependence on the aerosol loading of the stratosphere - while the SLIMCAT model SCDs deviate for very large SZAs ($\geq 93^o$), when the tangent point altitude is in the lower stratosphere (down to 10 km). Overall it can be said that the increase with SZA for SZAs larger than 90^o is very much dependent on the photolysis rate of *OClO*, which is the reason, why the increase looks quite similar in both models - using the same photolysis rates. As the measured SCDs increase in this SZA region faster than in the model, either the photolysis rates are too large or the rate reaction coefficient for the *OClO* production is too small.

To investigate this *OClO* discrepancy further, a model run with halved photolysis rates of *OClO* was conducted. The result is also shown in Figure 7.11. The small triangles connected by line denote this model run. As expected the increase of *OClO* during the occultation goes faster - even faster than measured for largest SZAs - but at the beginning of the occultation the increase is slower than

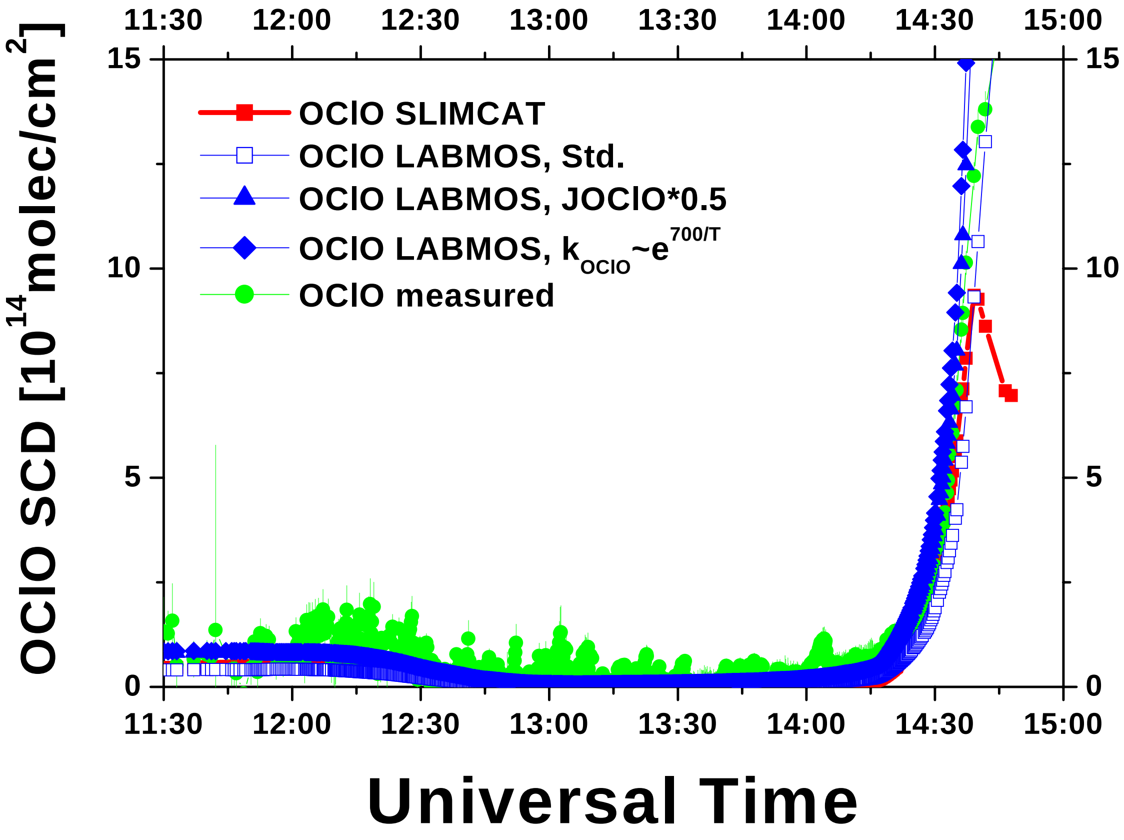

Figure 7.11: Measured and modelled - SLIMCAT and LABMOS - $OClO$ SCD time evolutions. The standard LABMOS model runs are shown, as well as a run with halved J_{OClO} and one with decreased *activation temperature* ($k \approx e^{700/T}$).

measured and during the ascent the modelled $OClO$ is also significantly smaller. As the photolysis rates are expected to be much better known than with an uncertainty of 50% - the absorption cross section is measured with 10% uncertainty, the quantum yield is measured to be nearly unity [DeMore et al. 1997] and the actinic flux is also known with better accuracy - it is reasonable not to expect the photolysis rate to be the major cause of the observed discrepancy. That is why also a model run with increased rate reaction coefficient for the formation of $OClO$ (from $ClO + BrO$) was conducted - the *activation temperature* E/R of the second-order reaction is decreased from -550 to $-700K$. This is reasonable, because the stated uncertainty factor at room temperature ($298K$) is 1.25 and this uncertainty is increasing for other temperatures [Sander et al. 2000]. The results of this run are included in the figure, too. Increasing the rate reaction coefficient to the upper limit has the same effect as decreasing the photolysis rates by a factor of 2. It is also possible that the major uncertainty of the $OClO$ simulations stems from the aerosol surface density used in the Lagrangian model, because the aerosol size distribution has only been measured in the long-tail region above 0.35 μm and the variability of the number density in this region is well pronounced for the conditions probed [Engel 2000]. Doubling or halving the aerosol content increases or reduces the modelled SCDs by $30-40\%$.

From the comparison of the two different models (SLIMCAT and LABMOS) it is clear that the 3-D CTM model - which includes heterogeneous chemistry on PSCs - shows heterogeneous chlorine activation on PSCs, while this is not possible for the LABMOS model, which only takes account of heterogeneous reactions taking place on the background aerosols. Still the Lagrangian model can reproduce the measured SCDs as well as the profile structure. Also, observations of PSCs made by multiwavelength LIDAR[9] located at FMI Sodankylä (Finland) suggest that there were no PSCs over Northern-Finland in January-February 1999, despite the almost continuous LIDAR operation in the absence of tropospheric clouds [EORCU a]. No PSCs were observed by balloon-borne backscatter sondes launched from Kiruna in early February even though temperatures below PSC existence temperatures were encountered [EORCU a].

Except for a brief period in mid-December, the french satellite instrument POAMIII made regular observations in the latitude band $64 - 67^o$N throughout the winter. The only unambiguous PSC observations occurred between 1-3 December, 1998 and were sighted near Scandinavia, centred in the altitude range 24-25km. From February 8-13, 1999 there were a few observations of enhanced aerosol between longitudes $30 - 40^o$E. The small amount of enhancement makes it questionable whether these were PSCs, but the enhancement did occur at the altitude (approximately 20km) where temperatures were at or below the NAT existence point [EORCU a].

Remote sensing measurements by the ASUR (sub-mm radiometer, 605-662GHz) instrument onboard the DLR[10] aircraft *Falcon* between January 22 and February 8 over Northern Scandinavia showed a weak but significant chlorine activation at altitudes between 18 km and 26 km inside or across the edge of the polar vortex on several occasions, although temperatures inside the polar vortex had been too high for PSC formation since the middle of December 1998 [Bremer 2000]. The highest chlorine activation of about 300 ppt to 400 ppt was observed on January 22. Those high values of ClO at the beginning of the measurement period could be attributed to the persistence of the chlorine activation of early December. In-situ ClO measurements of the ClO/BrO monitor on the TRIPLE balloon gondola on Feb. 6, 1999 show no significant chlorine activation ($ClO \leq 200ppt$) pointing to the absence of any recent activation in agreement with the temperature history of the observed airmasses.

Finally it can be said that the chlorine activation in the arctic winter 98/99 in total was very small compared to previous winters and ozone depletion in the sunlit stratosphere did not surmount 5% of the total column [EORCU a].

7.3 Case study of the out-of-vortex flight at León on November 23, 1996

In this section Lagrangian model studies are presented to investigate the appearance of $OClO$ enhancements observed during the occultation part of the mid-latitude flight at León on Nov.23, 1996. This is not the only out-of-vortex flight, where some $OClO$ could be detected, but it is a flight, where significant $OClO$ amounts are found - see also Section 4.1. There, the comparison with $OClO$ values modelled by the 3-D CTM model SLIMCAT showed that $OClO$ SCDs are underestimated in the model by a factor of up to 10. Here the Lagrangian model LABMOS will be used to investigate the most important uncertainties in the model concerning $OClO$ in further detail to try to understand these observations.

Figure 7.12 displays the airmass trajectories of the two meteorological models ECMWF and GSFC for that day and the endpoint Madrid (ECMWF) and 42^oN, 355^oE(GSFC). The ECMWF trajectories from the NILU database can only be retrieved for fixed locations and the next one to our measurement site was Madrid, while the GSFC model automailer provides the possibility to choose any location. Despite the small differences of the endpoint coordinates almost all of the isentropic trajectories deviate only little - compared to the large scales of the stratospheric circulation - during 5 days before the measurements. It can also be seen that the winds were quite strong in the stratosphere a few days before and during our balloon flight (up to 80 km/h). That is why the balloon flight did not last as long as the sun measurements were possible, because the balloon was drifting away very fast. It is also interesting to note that the trajectories are almost all within a latitudinal belt (40-60^{o}N) and did not

---

[9] LIDAR: LIght Detection And Ranging

[10] Deutsches Zentrum für Luft- und Raumfahrt

reach polar regions - at least during the 5 days before the endpoint, where the trajectory models are most reliable.
Using the different trajectory models does not change the principal results of this section that is why again the model results obtained with ECMWF trajectories are presented.

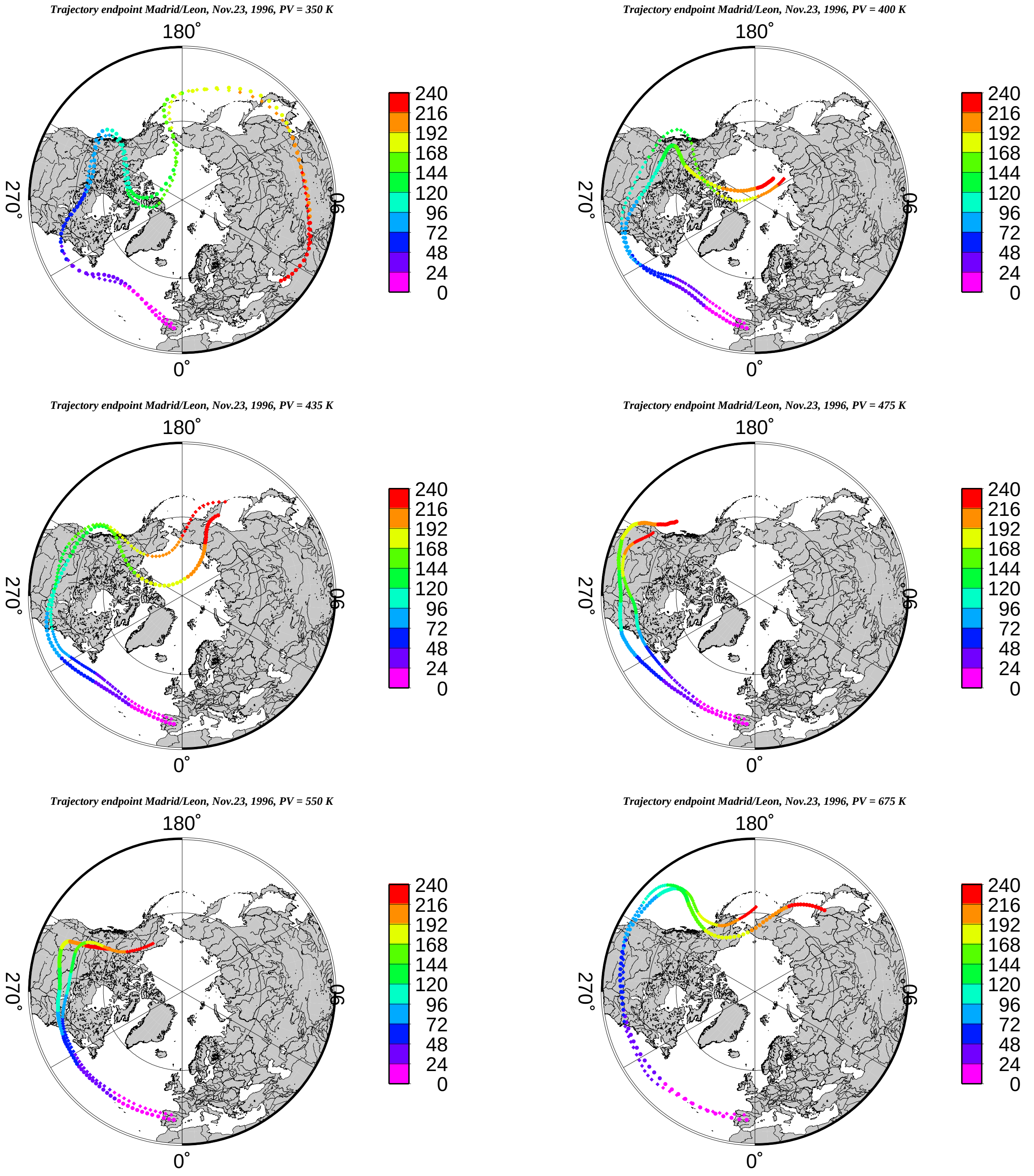

Figure 7.12: 10-day backward airmass trajectories for the different isentropic potential temperature levels: 350 K, 400 K, 435 K, 475 K, 550 K, 675 K. These potential temperatures correspond at the endpoint Madrid at 12:00UT to altitudes of 13.4 km, 15.8 km, 18.4 km, 19.6 km, 22.7 km and 26.7 km. The ECMWF/GSFC trajectories are denoted by ∘, ⋄, respectively. The time of each trajectory point is given in color code and in units of hours before reaching the endpoint.

When looking at the meteorological parameters on the different trajectories - Figure 7.13 shows the meteorology and the evolution of the bromine species on the 475 K potential temperature level - it is obvious that the airmasses experienced sunlight during each of the last 10 days before the encounter. That is why a non-optimal initialization is quickly changed to the equilibrium state of the chemical system. The temperatures were constantly around 210 K for the 10 day period. On the other isentropic levels the time evolution may look different. But at the end of the trajectories, when the trajectories are converging, the behaviour becomes more and more equal.

LABMOS Standard Model Run Initialization							
T_{pot} [K]	350	380	400	435	475	550	675
Height$_{endpoint}$ [km]	13.4	14.8	15.8	18.4	19.6	22.7	26.7
Aerosol surface[$\mu m^2 cm^{-3}$]	5	5	4	3	2	1	0.5
Aerosol mean radius [μm]	0.15	0.15	0.15	0.15	0.15	0.15	0.15
NO_x [ppt]	3	11	1.5	1.5	402	654	2260
NO_y [ppb]	0.7	2	2.6	5.75	8.3	9	14
ClO_x [ppt]	2	12	12	12.5	11.5	12.5	40
Cl_y [ppt]	900	1025	1280	1673	2170	2850	3190
Br_y [ppt]	4.9	7.4	9.0	13.3	17.2	19.5	20.2

Table 7.2: Summary of the physical-chemical initialization of the standard Lagrangian trajectory model run. The trajectories all start for SZAs larger than 90^0.

Table 7.2 shows the chemical and aerosol loading initialization of the Lagrangian 10-day model run. Total chlorine and nitrogen is taken from measurements of the LPMA interferometer during the León 96 flight itself and the MIPAS measurements at the same location in July 1997 [Pfeilsticker 1999]. The total chlorine and nitrogen loading - no denoxification is assumed in both cases - is known to change only little during these eight months and under undisturbed conditions - as it was the case for both measurements. The background aerosol loading is the same like for the Kiruna 99 model study. It is in accordance with the surface density derived from SAGE II measurements for the year 1996 at 40-60^{o}N [Thomason and Poole 1997].

Figure 7.13 displays the inorganic bromine species during the 10 days of the trajectory. As the SZA evolution is always the same and the temperature does not change very much, BrO comes out of its nighttime reservoir species $BrONO_2$ and $HOBr$ around sunrise faster than it disappears during sunset. The explanation for this behaviour is the larger photolysis rate of $HOBr$, which increases during the night by the hydrolysis of $BrONO_2$ on the background aerosol. $BrCl$ is not existent in appreciable amounts like in the polar Arctic case study, because it is continuously photolysed during the day. The HBr initialized with 1.5 ppt is disappearing within 4-5 days as a result of the OH and atomic oxygen attack at this isentropic level. $BrONO_2$ is the most important bromine reservoir during the daytime. Its daytime variation can be explained by the increase of NO_2 throughout the day and its photolysis. At sunrise it forms nearly simultaneously with BrO, but is reduced by the photolysis. It reaches a minimum before noon and increases afterwards again, as NO_2 is increasing, too. During the night it is heterogeneously converted to $HOBr$ on the background aerosol. In the morning the photolysis of $HOBr$ constitutes an additional OH source, which is depleting ozone.

The time evolution of the chlorine species is shown in Figure 7.14 for the 475 K isentropic model level. ClO is appearing at dawn from zero nighttime values. It stems from the photolysis of the reservoir species $ClONO_2$, $HOCl$ and HCl and the subsequent reaction of atomic chlorine with ozone. Also $HOCl$ shows a strong enhancement during the day, as it is formed mainly by the reaction of HO_2 with ClO. HO_2 itself comes from the fast reaction of OH with O_3. $OClO$ and $BrCl$, which result from the reaction of BrO with ClO, appear almost only during the night because of their large photolysis rates. As the yield of $OClO$ at 210 K temperature is eight times larger than that one of $BrCl$, it is much more abundant than $BrCl$ and in comparison with $BrCl$ it reaches its nighttime maximum very early. $BrCl$ on the other hand increases throughout the night, because of the heterogeneous reaction of $BrONO_2$ with HCl forming additional $BrCl$. It can also be observed that $ClONO_2$ is decreasing and HCl is increasing as a consequence of the heterogeneous reactions taking place on the sulphate aerosols.

In Figure 7.15 the nitrogen species time evolution is plotted during the standard model run. NO is only appearing during the day, when it is directly produced by the photolysis of NO_2 and NO_3. Both latter nitrogen species have a maximum at dusk, just when the photolysis ends to be dominant. NO_2 is decreasing then throughout the night, while NO_3 stays constant for the longest part of the darkness. This is because NO_2 not only is in thermal equilibrium with N_2O_5 and NO_3, but it is also reduced when reacting with O_3 to form NO_3. Nitric acid is increasing during the night as is N_2O_5 as a result of the heterogeneous reactions of $ClONO_2$, N_2O_5 and $BrONO_2$. The weak long-term oscillation on the HNO_3 mixing ratio can be explained by the equilibration of the differential equation system, because NO_x is increasing as HNO_3 decreases and vice versa. In principal it should only increase in the long run, because of the heterogeneous production of HNO_3, but the system is equilibrating with a long time constant of a few days.

The time evolution of the oxygen species is shown in Figure 7.16. Ozone is constantly decreasing at an approximate rate of 3 ppb/day - which is a factor of 3 smaller than the rate observed during the winter case study presented before. The atomic oxygen, OH and HO_2 mixing ratios are both maximal around noon everyday. In comparison with the winter case study it can be observed that the HO_2/OH ratio changed from 5:1 to 10:1, because direct photolytical production of HO_2 is larger in mid-latitude autumn than in high latitude winter. During the day HO_2 exhibits the same behaviour like NO_2: it increases dramatically when photolysis sets in and has a minimum between the photolytical peak and the noon maximum. The peak at dawn is due to the fast photolysis of $HOBr$ producing additional OH, which forms nearly instantaneously HO_2 by reaction with O_3.

The profile comparison of measured and modelled BrO can be found in Figure 7.17. Both models underestimate the BrO amounts above 20 km altitude, while SLIMCAT tends to overestimate the lower stratospheric BrO just above the tropopause more than LABMOS. As stated in Chapter 4, this overestimation can be a result of the Br_y initialization in that altitude range, because SLIMCAT only takes into account CH_3Br and not the halons, which have longer lifetimes against photolysis than methyl bromide. When using the Br_y profile retrieved during the Kiruna 1999 flight - after a suitable correction of the altitude shift of the tropopause and stratosphere - the LABMOS model results show a good agreement in the lower stratosphere with the measured values - especially when not considering the oscillation of the measured profile, which stems from the matrix inversion as it is not observed in the onion peeling profile after smoothing the SCDs slightly. From the NO_2 profile comparison - see Figure 7.19 - it is also evident that the more heterogeneous reaction on the background aerosols take place, i.e. the more background aerosol there is, the less NO_2 can be observed in the model. This can be easily understood, as more heterogeneous activation of halogens and hydrolysis of N_2O_5 leads to enhancements of HNO_3, whose photolysis rate is much smaller than the one of $ClONO_2$, $BrONO_2$ and N_2O_5[11], so that there is less production of NO_2 during the day. Also the thermal equilibrium between N_2O_5, NO_2 and NO_3 responds to a reduction of N_2O_5 by an enhanced consumption of NO_2. Since SLIMCAT sees less NO_2 than the measurements and almost the same amount of NO_2 like LABMOS, it is not clear, why the SLIMCAT BrO is smaller in the altitude range (550 K, 675 K), where NO_2 is maximal.

The BrO/Br_y ratio is nearly constant on the isentropic levels considered by this case study. It is between 0.4 and 0.6 - nearly 30-50% smaller than in the winter case study with a denoxified stratosphere. The minimal BrO/Br_y ratio can be observed in the altitude region, where the effect of heterogeneous chemistry is maximal - which can be seen in the scatter of the profile values for the different model runs assuming different aerosol loadings.

The $OClO$ occultation profile comparison - see Figure 7.18 - reveals a dramatic underestimation of

---

[11] $J_{BrONO_2} > J_{ClONO_2} \gg J_{HNO_3}$

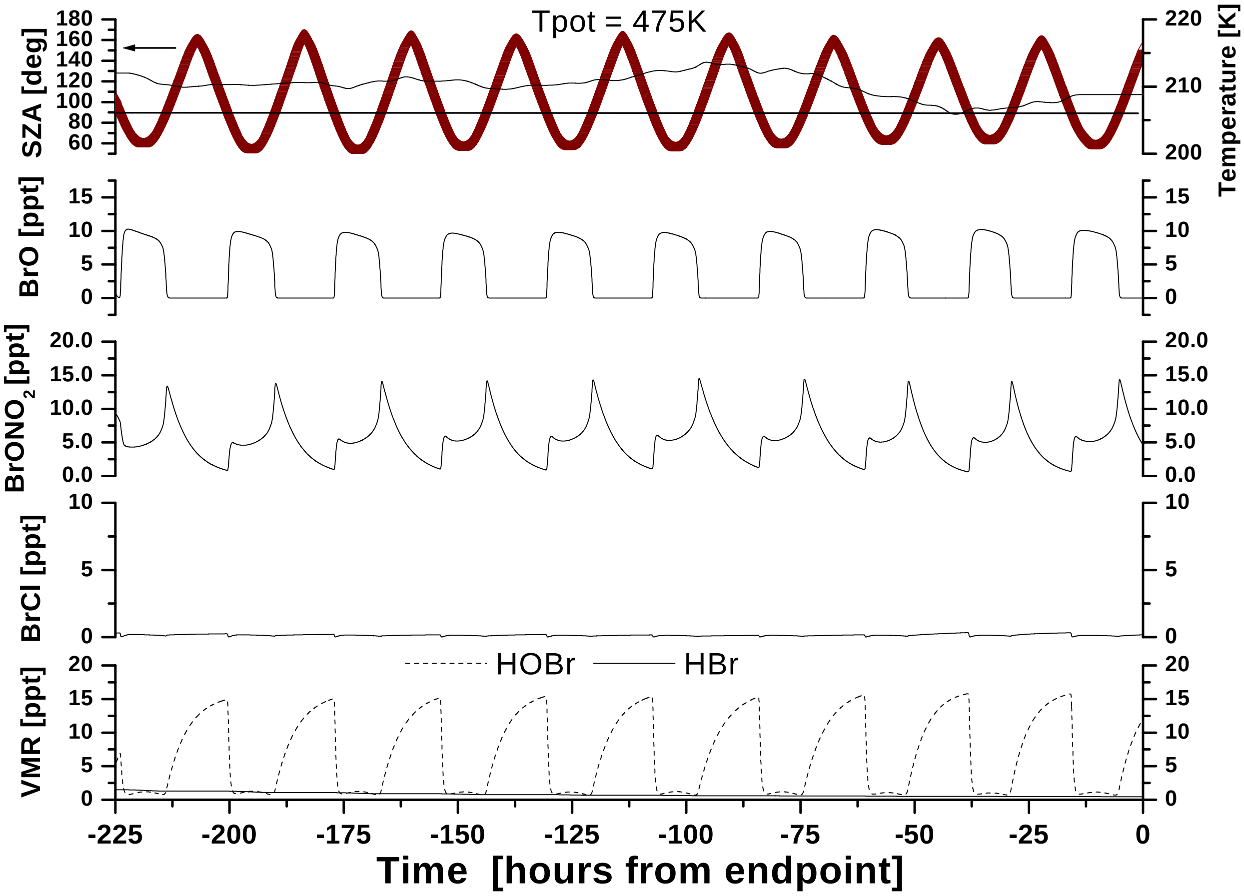

Figure 7.13: Time evolution of the bromine species on the 475K potential temperature isentropic level. Also the SZA and temperature evolution is displayed.

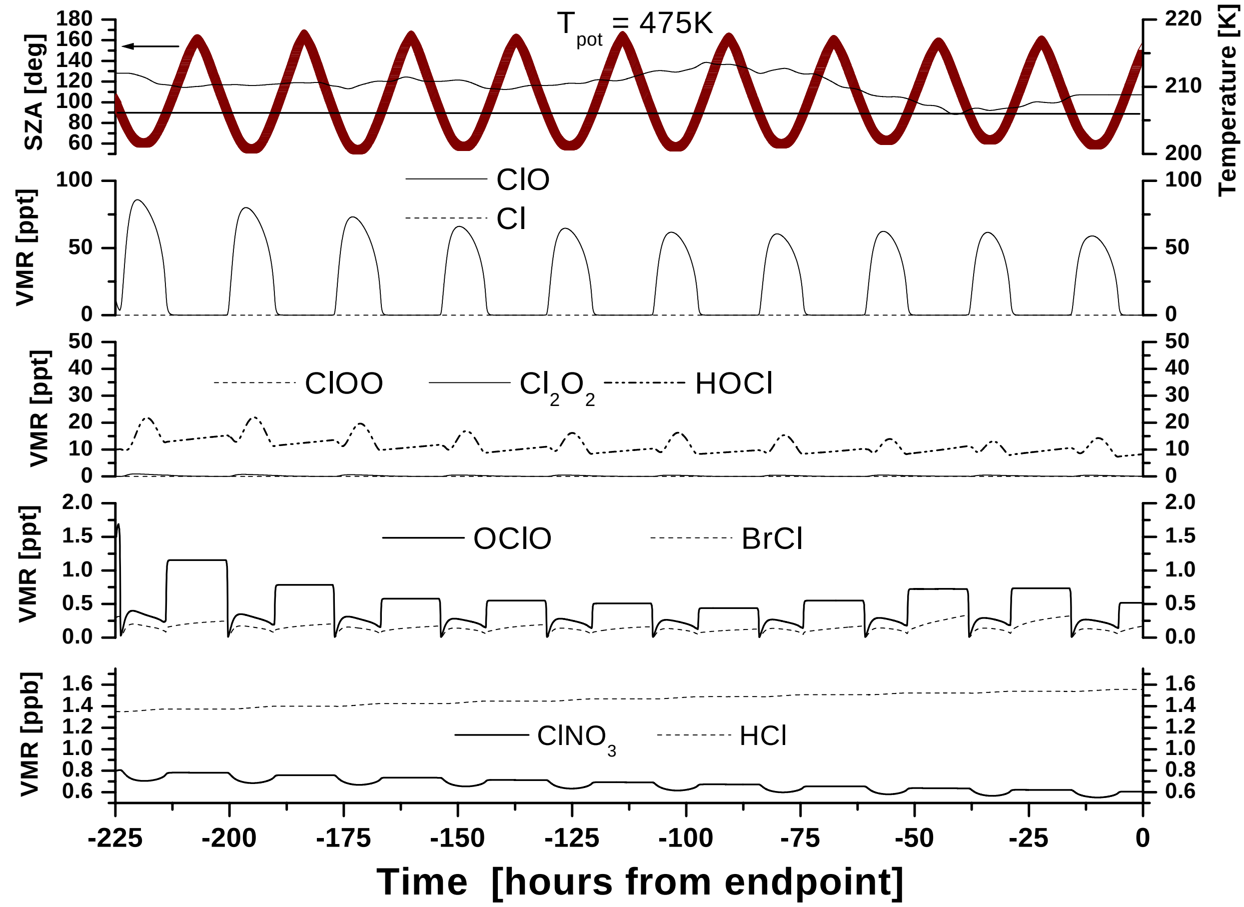

Figure 7.14: Time evolution of the chlorine species on the 475K potential temperature isentropic level. Also the SZA and temperature evolution is displayed.

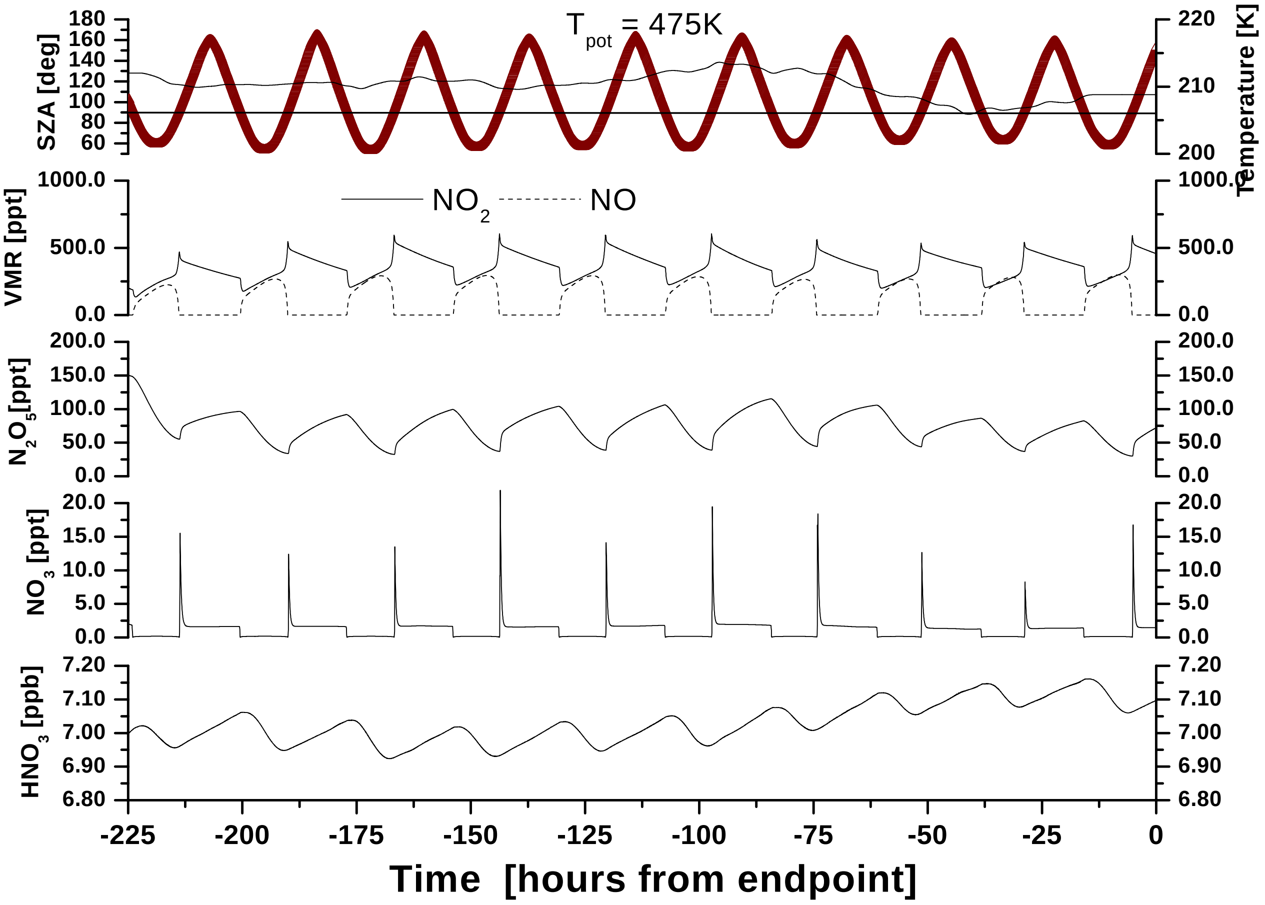

Figure 7.15: Time evolution of the nitrogen species on the 475K potential temperature isentropic level. Also the SZA and temperature evolution is displayed.

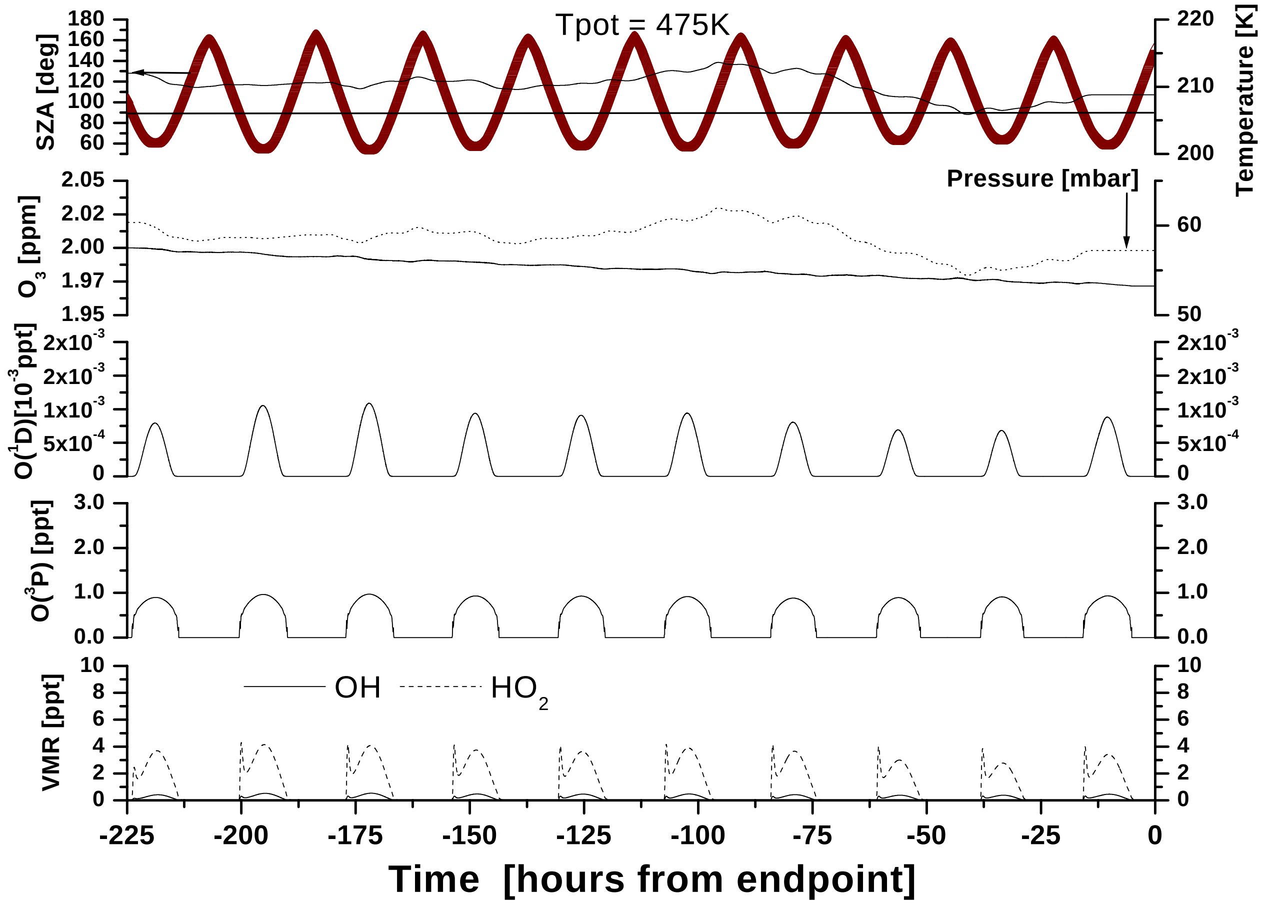

Figure 7.16: Time evolution of the oxygen species on the 475K potential temperature isentropic level. Also the SZA and temperature evolution is displayed.

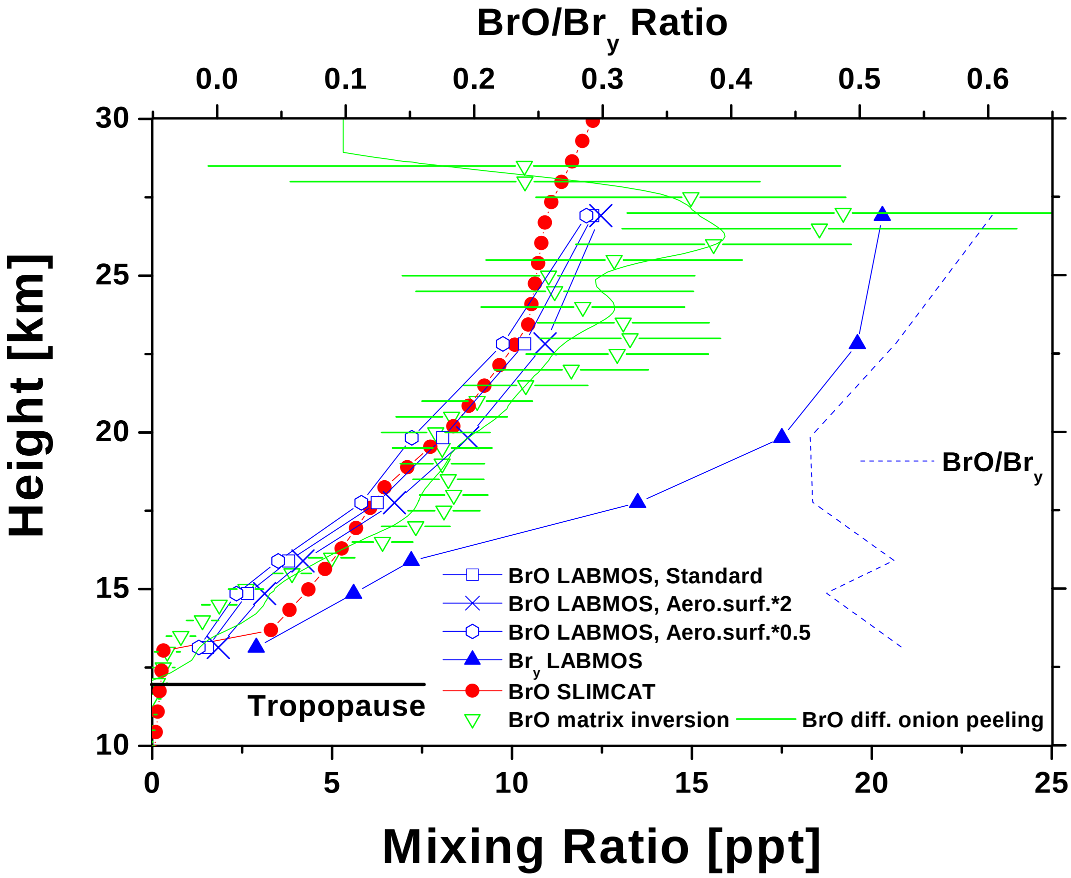

Figure 7.17: Measured and modelled - SLIMCAT and LABMOS - BrO profiles. Also the Br_y profile as well as the BrO/Br_y ratio is shown in the plot. The measurements took place between 74 and 86.4^0 SZA.

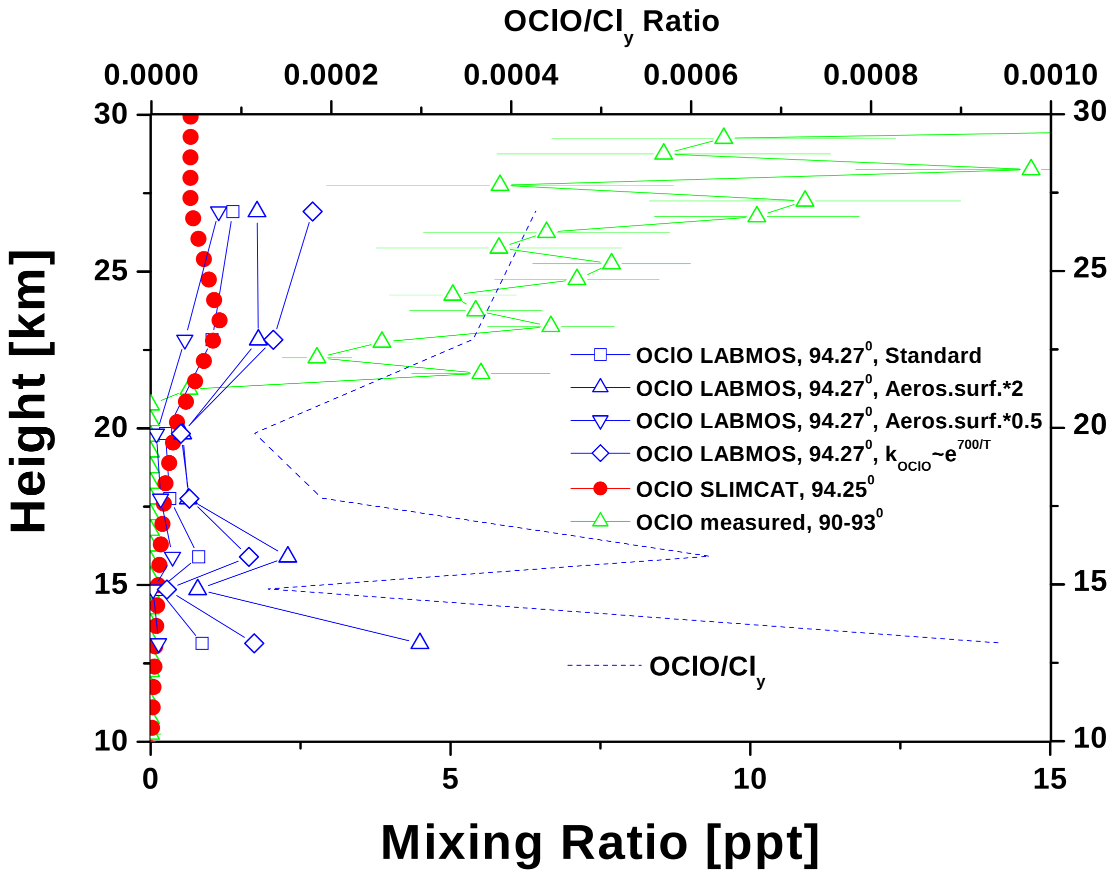

Figure 7.18: Measured and modelled - SLIMCAT and LABMOS - $OClO$ profiles. The measured profile is an occultation profile, where no photochemically related change is considered. Also $OClO/Cl_y$ ratio profile is shown in the plot. The different LABMOS profiles for SZA 94.25^0 refer to three different model runs: with standard, double and half aerosol loading.

the twilight $OClO$ by both the SLIMCAT and LABMOS model during these conditions. On the other hand, the LABMOS model seems to get the $OClO$ profile structure better, even though it is necessary to mention that the occultation profile retrieval did not take into account photochemical variations of the species. Still, because the $OClO$ appears very fast for approximately 94^o SZA and stays constant during the night, the occultation profile is a good estimate of the real nighttime profile. The LABMOS $OClO$ shows a lower stratospheric enhancement, which is very sensitive to the aerosol loading. This is caused by very low temperatures (around 205 K) during two days before the measurements.
The measured and modelled NO_2 profiles compare quite well, as can be seen in Figure 7.19. Both models have a slight tendency to underestimate the NO_2 amounts just below the NO_2 maximum, which is at approximately 35 km altitude. This underestimation can be related to the underestimation of the NO_x/NO_y ratio and a wrong $NO_y - N_2O$ correlation in the models, which has been stated recently for high latitudes by a series of publications [Gao 1999; Bösch et al. 1999; Pfeilsticker et al. 2000].

The BrO SCD comparison - see Figure 7.20 - looks more or less the same for both models and is in total agreement with the profile comparison shown before. The modelled SCDs are smaller during the ascent and the float of the balloon, while the occultation SCDs fit better. But it is interesting to notice that the LABMOS SCDs tend to be smaller during the begin of the occultation measurements, where the $OClO$ is formed mainly. In the late occultation the models are better describing the measured SCDs then.

As can be seen in Figure 7.21 the $OClO$ SCDs are underestimated by both models by a factor of 10-40. This discrepancy is mostly dependent on the relative change of ClO and the photolysis rate of $OClO$ itself. For a SZA of 90^o, the photolytic (≈ 0.048 s^{-1} at 675 K) destruction rate of $OClO$ is nearly as large as the production rate of $OClO$ molecules ($ClO \approx 4.8 \cdot 10^7$, $BrO \approx 6.2 \cdot 10^6$ and $OClO \approx 7.9 \cdot 10^4$ molecule/cm^3): $Prod_{OClO} = 3.9 \cdot 10^3 \frac{molecule}{cm^3 * sec} \approx Dest_{OClO} = 3.8 \cdot 10^3 \frac{molecule}{cm^3 * sec}$. That is why the nighttime $OClO$ amount is not very sensitive to changes of the photolysis rate of $OClO$ and the ClO or BrO amount. Therefore, the only possible - perhaps speculative - conclusions to try to explain the observations at least qualitatively could be:

- assumption of a much larger aerosol loading - which is not in accordance with the measurements
- assumption of a much smaller photolysis rate of $OClO$ - which is not probable, as the absorption cross section is well known (10%), the quantum yield is approximately 1.0 [DeMore et al. 1997] and the actinic flux in the stratosphere is also quite well understood in the stratosphere [Schneider 1997; Bösch 2000].
- assumption of much lower temperatures compared to the ones given by the trajectory models - which was not observed
- assumption of another chlorine activation mechanism at mid-latitudes, which is not in accordance with the good agreement of modelled and measured ClO
- assumption of a new or formerly neglected source of $OClO$ - especially effective for higher NO_x loadings of the stratosphere at mid-latitudes

There are also other measurements indicating a stratospheric $OClO$ background during times with low or no chlorine activation and no denoxification. The ground-based ZSL DOAS measurements of Wagner [2000] of $OClO$ at Kiruna show an offset even during summer, when no denoxification or chlorine activation can be expected and temperatures are higher than needed for effective heterogeneous activation on the background aerosol. Although the Signal-To-Noise Ratio of these summer measurements by ZSL is much smaller, as the ZSL AMF is $\leq$10 and the direct sunlight AMF at the tangent point is between 50 and 200, the VCD calculated from the occultation measurements ($VCD_{Balloon} \approx 4 \cdot 10^{14}/(50 - 200) \frac{molecule}{cm^2} \approx (5 \pm 3) \cdot 10^{12} \frac{molecule}{cm^2}$) agrees reasonably well with the VCD estimate from

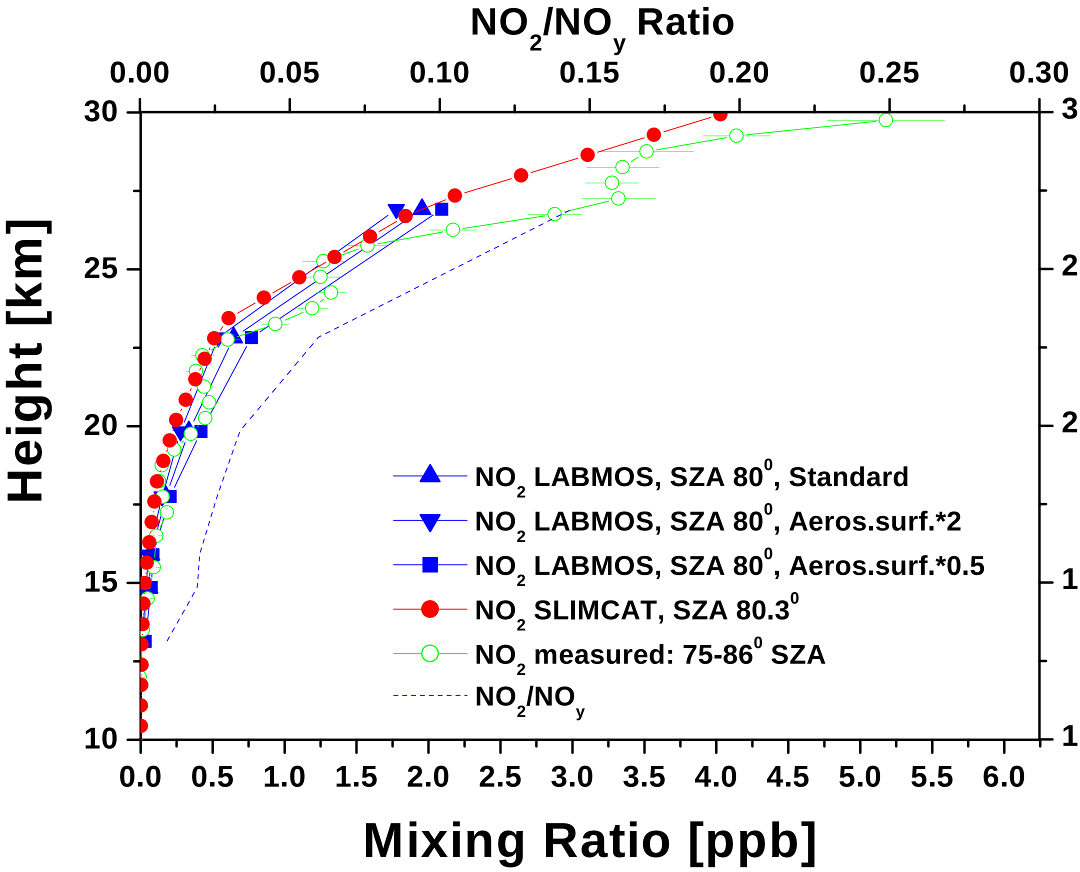

Figure 7.19: Measured and modelled - SLIMCAT and LABMOS - NO_2 profiles. Also the NO_y profile as well as the NO_2/NO_y ratio is shown in the plot. The measurements took place between 74 and 86.4^0 SZA.

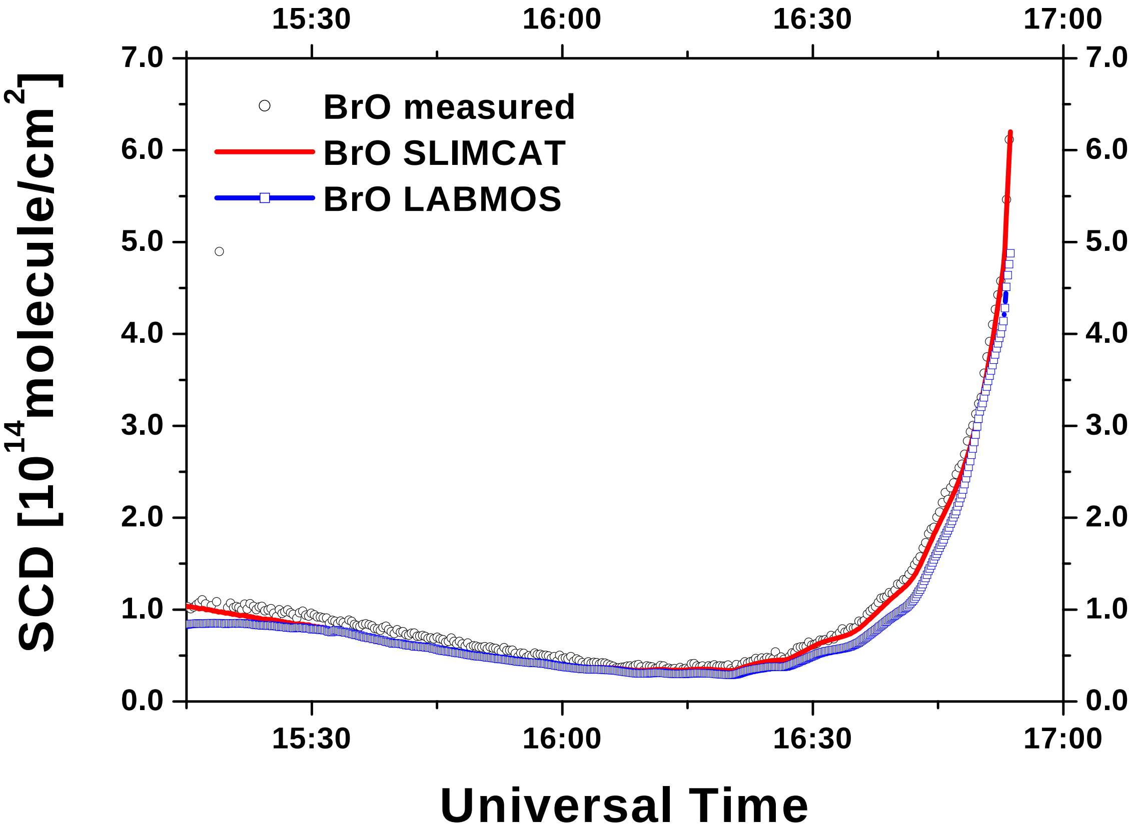

Figure 7.20: Measured and modelled - SLIMCAT and LABMOS - BrO SCD time evolutions.

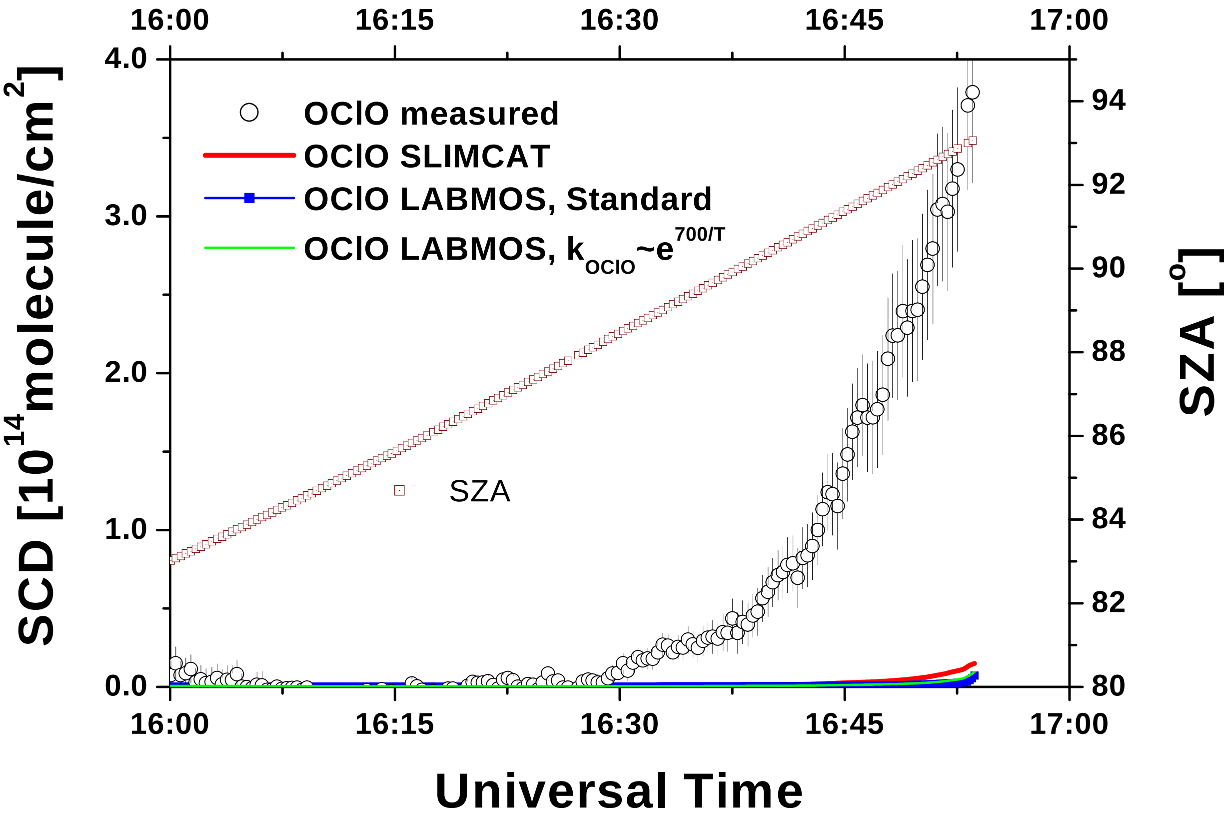

Figure 7.21: Measured and modelled - SLIMCAT and LABMOS - $OClO$ SCD time evolutions.

this summer background ($VCD_{ground-based} = 2 \cdot 10^{13}/(5-10)\frac{molecule}{cm^2} = (3 \pm 2) \cdot 10^{12}\frac{molecule}{cm^2}$) [Wagner 1999].

Chapter 8

Conclusions and Outlook

This thesis analyzes optical absorption signatures of BrO, $OClO$, O_3, NO_2 and some other species recorded in direct sunlight during 8 stratospheric LPMA/DOAS balloon flights under different geophysical conditions quantitatively to deduce vertical profiles of these species.

The good performance of the balloon-borne DOAS instrument could be demonstrated during all these flights. It was possible to increase the accuracy of the measurements by the inclusion of a GPS receiver and a more precise pressure sensor. With a newly developed stray light correction method, the residual structures of the DOAS fit could be minimized. This new method suggests that the optical prism preanalyzer system could be removed during the next flights to increase the UV detector signal by a factor of 4-5 - especially when measuring in the troposphere and during occultation. Also, the addition of a separate sun tracker for the DOAS instrument with larger light entrance telescopes should be considered to increase the sensitivity of the instrument in the UV significantly. The DOAS evaluation of the measured raw spectra was found to be best in the least-square sense when using laboratory reference spectra taken with the same instrument and not convoluted literature spectra, even when the latter were corrected for the solar I_0 effect. This behaviour is most likely explained by interpolation errors during the 'shifts' and 'squeezes' of the spectra during the DOAS evaluation and the convolution process. Therefore, it is advisable to record again new laboratory reference spectra before each balloon flight, especially when a new instrument will be employed.

This thesis contributes to the understanding of the importance of stratospheric gas phase and heterogeneous chemistry under different geophysical conditions between 1996 and 2000. It was possible to measure BrO profiles during all six ascent flights and the evolution of BrO during occultation for all eight flights. It could be shown that inorganic bromine is always activated to a large degree - the active species being principally BrO - depending mainly on the NO_x loading of the stratosphere. During undisturbed conditions like in spring, summer, and autumn at mid-latitudes, the BrO/Br_y ratio is about 0.5, while it increases in the winter Arctic stratosphere up to a ratio of about 0.7. It could be verified during the six ascent flights that the increase of the BrO mixing ratio profile in the lower stratosphere is almost the same under all probed conditions. The profiles only differ because of the shift of the tropopause height between the different flights. Based on model studies it could be shown that the increase of BrO in the lower stratosphere is mainly determined by the Br_y profile in that region, which is also independent of the location of the measurement. In a concerted cluster flight, balloon-borne in-situ measurements of organic bromine precursors provided a Br_y estimate, which could be directly compared to the Br_y profile deduced from our BrO measurements together with the modelled BrO/Br_y ratio at each altitude. A good agreement of the Br_y profiles in the lower stratosphere was found, while the maximum value of the inorganic Br_y profile was consistently larger (about 2-3 ppt or 10-15%) than the estimate from the organic precursor measurements [Fitzenberger et al. 2000; Pfeilsticker et al. 2000; Harder et al. 2000]. This observation - together with the

comparison of the Br_y derived from our measurements of BrO over a 4 year period with the organic Br_y estimates - raises the issue of an additional inorganic Br_y source in the stratosphere. One possible source could be tropospheric BrO which could be measured at least during two flights directly in the free troposphere with levels reaching between 0.6 and 2 ppt [Fitzenberger et al. 2000]. Despite the temporal and spatial sparsity of these measurements, it could be possible that inorganic bromine - most probably in the form of HBr or BrO - could cross the tropopause and add to the inorganic bromine generated by the photolysis of organic precursors.
This is also supported by a recent report of ionic bromine found in upper tropospheric and lower stratospheric aerosol measurements [Murphy and Thomson 2000], which can amount up to 1-2 ppt. But it is still an open question, how much of this bromine is coming out of the aerosols.

As a part of this thesis new DOAS algorithms for the detection of $OClO$ were implemented differing from each other in relation to the wavelength range. A good agreement of the $OClO$ occultation measurements in the different wavelength ranges is found. But, as the Fraunhofer structures are very strong in the $OClO$ range, the smallest residuals can be achieved in an extended BrO window.
$OClO$ could be measured during several flights in the Arctic winter where different cases of chlorine activation could be encountered in the stratosphere. Three-D CTM model (SLIMCAT) and lagrangian trajectory box model (LABMOS) studies showed that these $OClO$ enhancements could be basically understood by heterogeneous chemistry taking place on PSCs or background sulphate aerosols. There were also measurements of enhanced levels of $OClO$ at mid-latitudes in autumn, when chlorine activation was quite low. These observations cannot be reproduced by either of the models and it is not clear where such a twilight $OClO$ production under chemically unperturbed conditions could originate from.

The balloon-borne LPMA/DOAS measurements shall be continued in the future for the validation of different satellite instruments (ODIN[1], SCIAMACHY[2]) extending the knowledge about the evolution of the stratosphere in the Arctic and mid-latitude stratosphere during the next years.

---

[1] ODIN is a Swedish small satellite project for astronomical and atmospheric research. The main astronomical objective is to perform detailed studies of the physics and the chemistry of the interstellar medium by observing emission from key species. And the atmospheric research will address scientific problem areas in the stratosphere and mesosphere by making measurements of various trace species, *http://www.ssc.se/ssd/ssat/odin.html*

[2] SCanning Imaging Absorption SpectroMeter for Atmospheric CHartographY (SCIAMACHY) will be launched in 2001 - as successor of the very successful GOME experiment - on the European ENVISAT satellite together with two other Earth observing instruments: MIPAS and GOMOS. For details, please visit: *http://www.iup.physik.uni-bremen.de/ifepage/SCIA/SCIAMACHY.htm*

Appendix A

Appendix

A.1 Meteorological Definitions

A.2 Potential Temperature

The potential temperature (θ) is a measure for the sum of potential and internal energy of an air parcel (P, T). It is defined as the temperature, that an air parcel would have when being brought adiabatically to normal pressure ($P_0 = 1013 mbar$) starting from a temperature T and pressure p. θ is therefore a conservative property in any adiabatic air parcel displacement, and is sometimes used to evaluate air parcel trajectories - see chapter 7.

$$\theta = T \times (\frac{P_0}{P})^{(c_p - c_v)/c_p} = T \times (\frac{P_0}{P})^{\kappa} \tag{A.1}$$

Here c_p, c_v is the specific heat of air at constant pressure/volume and $\kappa = R/c_p = 0.286$ is the exponent in the laws for adiabatic processes for air (external heating $Q = 0$, first law of thermodynamics: $c_p \frac{dT}{dt} - \frac{1}{\rho}\frac{dp}{dt} = Q$). Introducing the potential temperature in the first law of thermodynamics provides a convenient simplification:

$$\frac{d\theta}{dt} = \left[\frac{P_0}{P}\right]^{\kappa} \frac{Q}{c_p} \tag{A.2}$$

and allows for ready evaluation of the influence of external heating (Q) on θ. There is an unambiguous relation between potential temperature and entropy meaning that surfaces of equal potential temperature are identical with isentropic surfaces ($dS = Q/T$).

A.3 Ertl´s potential vorticity

The natural measure representing the vorticity of horizontal air flow is the vertical component of the rotation vector of the velocity vector $\vec{v}$: $\zeta = rot_z \vec{v}$. Combining this relative vorticity with the vorticity resulting from the Earth rotation relative to an inertial system, we add the component of the Earth´s angular velocity perpendicular to the ground surface:

$$\eta = \zeta + f = rot_z \vec{v} + 2\Omega sin(\phi) \tag{A.3}$$

where Ω is the angular velocity of the Earth. This we call the absolute vorticity. Ertl´s potential vorticity PV is defined by

$$PV = \frac{\nabla\theta}{\rho}(2\vec{\Omega} + rot_z \vec{v}) \tag{A.4}$$

and it is conserved for baroclinic air flow, where the air parcels change their thermodynamic state variables adiabatically and there is no friction. Using the barometric relation $dp = -\rho g dz$ we get the definition applied often in meteorological models

$$PV = -g\frac{d\theta}{dp} \times (2\Omega sin(\phi) + rot_z\vec{v}) \tag{A.5}$$

The PV is normally expressed in units of PVU ($PVU = 1 \times 10^{-6} Km^2 kg^{-1} s^{-1}$).

A.4 Geopotential Height

In dynamical meteorology it is convenient to introduce the geopotential Φ defined as the work required to raise a unit mass to height z from mean sea level:

$$\Phi = \int_0^z g(z', \phi) dz' \tag{A.6}$$

Using this definition we can build the geopotential height, defined as

$$h(z, \phi) = \frac{1}{g_0} \int_0^z g(z', \phi) dz' \tag{A.7}$$

where $g_0 = 9.80 m/s^2$ is a constant gravitational acceleration reference. On normal isohypses (surfaces of equal geometrical height) there can be a gravitational acceleration, while on geopotential isohypses the gravitational acceleration can be neglected and the pressure gradient force is only influenced by the pressure difference on surfaces of equal geopotential. Perturbations by planetary wave activity can lead to geopotential differences on an isobaric level along a certain latitude belt, generating waves of distinct wavenumbers.

Appendix B

Chemical Reaction Rate Constants

For all reactions the newest available [DeMore et al. 1997; Sander et al. 2000] rate reaction coefficients are used.

B.1 Bimolecular Gas Phase Reactions

A direct or concerted bimolecular reaction - also called second-order reactions - is one in which the reactants A and B proceed to products C and D without the intermediate formation of an AB adduct that has appreciable bonding, i.e., there is no bound intermediate; only the transition state $(AB)^{\neq}$ lies between reactants and products. Very useful correlations between the expected structure of the transition state and the A-Factor of the reaction rate constant can be made, especially in reactions that are constrained to follow a well-defined approach of the two reactants in order to minimize energy requirements in the making and breaking of bonds. The rate constants for these reactions are well represented by the Arrhenius expression $k = Aexp(-E/RT)$ (units: $cm^3 molecule^{-1} s^{-1}$) in the 200-300K temperature range. These rate constants are not pressure dependent. The indirect or nonconcerted class of bimolecular reactions is characterized by a more complex reaction path involving a potential well between the reactants and products, leading to a bound adduct $[AB]^*$ A and B. The intermediate $[AB]^*$ is different from the transition state $(AB)^{\neq}$, in that it is a bound molecule which can, in principle, be isolated. Reactions of the nonconcerted type can have a more complex temperature dependence and can exhibit a pressure dependence if the lifetime of $[AB]^*$ is comparable to the rate of collisional deactivation of $[AB]^*$. This arises because the relative rate at which $[AB]^*$ goes to products C + D vs. reactants A + B is a sensitive function of its excitation energy. Thus, in reactions of this type, the distinction between the bimolecular and trimolecular classification becomes less meaningful, and it is especially necessary to study such reactions under the temperature and pressure conditions in which they are to be used in model calculation, or, alternatively, to develop a reliable theoretical basis for extrapolation of data.

* Oxygen reactions :
k = 8.0E-12*EXP(-2060/TEMP) : O + O3 = ;
k = 2.2E-10 *O1D : H2O = OH + OH ;
k = 1.5E-10*0.75 *CH4 *O1D : = CH3 + OH ;
k = 1.5E-10*0.20 *CH4 *O1D : = CH3O + HO2;
k = 1.5E-10*0.05 *CH4 *O1D : = CH2O + H2 ;
k = 4.8E-13*EXP(700/TEMP) : HO2 + CLO = HOCL ;
k = 3.0E-11*EXP(200/TEMP) : O + HO2 = OH + O2 ;
k = 4.8E-11*EXP(250/TEMP) : HO2 + OH = H2O ;
k = 1.5E-12*EXP(-880/TEMP) : OH + O3 = HO2 ;
k = 7.4E-12*EXP(270/TEMP) : OH + CLO = HO2 + CL ;

k = 3.2E-13*EXP(320/TEMP) : OH + CLO = O2 + HCL ;
k = 3.5E-12*EXP(250/TEMP) : HO2 + NO = OH + NO2 ;
k = 2.0E-14*EXP(-680/TEMP) : HO2 + O3 = OH ;
k = 2.3E-13*EXP(600/TEMP) : HO2 + HO2 = H2O2 ;
k = 2.9E-11*EXP(-160/TEMP) : H2O2+ OH = HO2 + H2O ;

* Chlorine/Bromine/Nitrogen reactions :
k = 2.3E-12*EXP(260/TEMP) : BRO + CLO = BR + CLOO ;
k = 9.5E-13*EXP(550/TEMP) : BRO + CLO = BR + OCLO ;
k = 4.1E-13*EXP(290/TEMP) : BRO + CLO = BRCL ;
k = 3.0E-11*EXP(-2450/TEMP) : CLO + CLO = CLOO + CL ;
k = 3.5E-13*EXP(-1370/TEMP) : CLO + CLO = CL + OCLO ;
k = 1.0E-12*EXP(-1590/TEMP) : CLO + CLO = CL2 ;
k = 9.6E-12*EXP(-1360/TEMP) *CH4 : CL = HCL ;
k = 0.80*4.7E-13 : CLO + NO3 = CLOO + NO2 ;
k = 0.20*4.7E-13 : CLO + NO3 = OCLO + NO2 ;
k = 2.4E-12*EXP(40/TEMP) : BRO + BRO = BR + BR ;
k = 1.7E-11*EXP(-800/TEMP) : BR + O3 = BRO ;
k = 2.3E-11*EXP(-200/TEMP) : CL + O3 = CLO ;
k = 3.0E-11*EXP(70/TEMP) : CLO + O = CL ;
k = 6.4E-12*EXP(290/TEMP) : CLO + NO = CL + NO2 ;
k = 1.2E-13*EXP(-2450/TEMP) : NO2 + O3 = NO3 ;
k = 5.6E-12*EXP(180/TEMP) : NO2 + O = NO ;
k = 3.0E-12*EXP(-1500/TEMP) : NO + O3 = NO2 ;
k = 1.8E-11*EXP(170/TEMP) : CL + HO2 = HCL ;
k = 2.6E-12*EXP(-350/TEMP) : HCL + OH = H2O + CL ;
k = 3.0E-12*EXP(-500/TEMP) : HOCL + OH = CLO + H2O ;
k = 1.7E-13 : HOCL + O = CLO + OH ;
k = 1.9E-11*EXP(230/TEMP) : BRO + O = BR ;
k = 2.2E-11 : BRCL + O = BRO + CL ;
k = 8.8E-12*EXP(260/TEMP) : BRO + NO = BR + NO2 ;
k = 3.4E-12*EXP(540/TEMP) : BRO + HO2 = HOBR ;
k = 2.6E-11*EXP(-1300/TEMP) : BR + OCLO = BRO + CLO ;
k = 1.2E-10*EXP(-430/TEMP) : HOBR + O = BRO + OH ;
k = 7.5E-11 : BRO + OH = BR + HO2 ;
k = 1.7E-33*MCOLL*EXP(1000/TEMP) : HO2 + HO2 = H2O2 ;
k = 1.8E-11*EXP(225/TEMP) : BRNO3 + O = BRO + NO3 ;

*Organic HBR production :
k = 1.5E-13*(1+0.6*PRESS/1023) : OH + CO = HO2 + CO2 ;
k = 1.0E-11*EXP(0/TEMP) : OH + CH2O = CO + HO2 + H2O ;
k = 2.7E-12*EXP(200/TEMP) : OH + CH3O2H = CH3O2 + H2O ;
k = 1.1E-12*EXP(200/TEMP) : OH + CH3O2H = CH2O + OH + H2O ;
k = 6.7E-12*EXP(-600/TEMP) : OH + CH3OH = CH2O + HO2 ;
k = 3.8E-13*EXP(800/TEMP) : HO2+ CH3O2 = CH3O2H ;
k = 3.0E-12*EXP(280/TEMP) : CH3O2 + NO = CH3O + NO2 ;
k = 2.5E-14*EXP(190/TEMP) : CH3O2 + CH3O2= CH3O2CH3 ;
k = 7.5E-14*EXP(190/TEMP) : CH3O2 + CH3O2= CH3O + CH3O ;
k = 1.5E-13*EXP(190/TEMP) : CH3O2 + CH3O2= CH2O + CH3OH ;
k = 3.9E-14*EXP(-900/TEMP) : CH3O = CH2O + HO2 ;

k = 9.1E-12 : CH2OH = CH2O + HO2 ;
k = 2.45E-12*EXP(-1775/TEMP) : CH4 + OH = CH3 + H2O ;

* BR2 reactions :
k = 2.8E-14*EXP(860/TEMP) : BRO + BRO = BR2 ;
k = 4.2E-11 : BR2 + OH = HOBR + BR ;
k = 1.6E-11 : BR + NO3 = BRO + NO2 ;

* HBR reactions :
k = 1.7E-11*EXP(-800/TEMP) : BR + CH2O = HBR + HCO ;
k = 3.5E-12*EXP(140/TEMP) : HCO = CO + HO2 ;
k = 1.1E-11 : HBR + OH = BR + H2O ;
k = 5.8E-12*EXP(-1500/TEMP) : HBR + O = BR + OH ;
k = 1.5E-11*EXP(-600/TEMP) : BR + HO2 = HBR ;
k = 1.0E-12 : BR + CH3OH= CH2OH + HBR;

B.2 Trimolecular Gas Phase Reactions

Rate constants for third order reactions of the type

$$A + B \Longleftrightarrow [AB]^* \overset{M}{\Longrightarrow} AB \tag{B.1}$$

are given in the form

$$k_0(T) = k_0^{300} \times \{\frac{T}{300}\}^{-n} cm^6 molecule^{-2} s^{-1} \tag{B.2}$$

(where k_0^{300} has been adjusted for air as the third body), together with a recommended value of n. Where pressure fall-off corrections are necessary, an additional entry gives the limiting high-pressure rate constant in a similar form:

$$k_{\inf}(T) = k_{\inf}^{300} \times \{\frac{T}{300}\}^{-m} cm^3 molecule^{-1} s^{-1} \tag{B.3}$$

To obtain the effective second-order rate constant for a given condition of temperature and pressure (altitude), the following formula is used:

$$k_f([M],T) = \frac{k_0(T)[M]}{1 + \frac{k_0(T)[M]}{k_{\inf(T)}}} \times 0.6^{\left(1+\left[log_{10}\left(\frac{k_0(T)[M]}{k_{\inf(T)}}\right)\right]^2\right)^{-1}} \tag{B.4}$$

The fixed value 0.6 that appears in this formula fits the data for all listed reactions adequately, although in principle this quantity may be different for each reaction, and also temperature dependent.

K0 = 6E-34*(300/TEMP)@2.4;
k = K0*MCOLL *O2 : O = O3;

K1 = 1.8E-11*EXP(110/TEMP)*MCOLL*.78;
K2 = 3.2E-11*EXP(70/TEMP)*O2;
O1D = J3A * O3 / (K1 + K2) ;

```
    K0 = 2.0E-30*(300/TEMP)@4.4;
Kinf = 1.4E-12*(300/TEMP)@0.7;
AUX = K0*MCOLL/Kinf;
Khin = Kinf*AUX/(1.+AUX)*0.6@(1/(1+LOG10(AUX)**2)) ;
k = Khin : NO2 + NO3 = N2O5;
Kequ = 3.0E-27*EXP(10991/TEMP);
k = Khin/Kequ : N2O5 = NO2 + NO3;

    K0 = 2.4E-14*EXP( 460/TEMP);
K2 = 2.7E-17*EXP(2199/TEMP);
K3 = 6.5E-34*EXP(1335/TEMP);
Khin = K0 + ( K3*MCOLL / (1 + K3*MCOLL/K2 ) );
k = Khin : HNO3 + OH = NO3 + H2O ;

    K0 = 2.4E-30*(300/TEMP)@3.1;
Kinf = 1.7E-11*(300/TEMP)@2.1;
AUX = K0*MCOLL/Kinf;
Khin = Kinf*AUX/(1.+AUX)*0.6@(1/(1+LOG10(AUX)**2));
k = Khin : OH + NO2 = HNO3;

    K0 = 5.2E-31*(300/TEMP)@3.2;
Kinf = 6.9E-12*(300/TEMP)@2.9;
AUX = K0*MCOLL/Kinf;
Khin = Kinf*AUX/(1.+AUX)*0.6@(1/(1+LOG10(AUX)**2));
k = Khin : BRO + NO2 = BRNO3;

    K0 = 4.2E-31*(300/TEMP)@2.4;
Kinf = 2.7E-11*(300/TEMP)@0.0;
AUX = K0*MCOLL/Kinf;
Khin = Kinf*AUX/(1.+AUX)*0.6@(1/(1+LOG10(AUX)**2));
k = Khin : BR + NO2 = BRNO2;

    K0 = 1.8E-31*(300/TEMP)@3.4;
Kinf = 1.5E-11*(300/TEMP)@1.9;
AUX = K0*MCOLL/Kinf;
Khin = Kinf*AUX/(1.+AUX)*0.6@(1/(1+LOG10(AUX)**2));
k = Khin : CLO + NO2 = CLNO3;

    K0 = 2.2E-32*(300/TEMP)@3.1;
Kinf = 3.4E-11*(300/TEMP)@1.0;
AUX = K0*MCOLL/Kinf;
Khin = Kinf*AUX/(1.+AUX)*0.6@(1./(1.+LOG10(AUX)**2)) ;
k = Khin :CLO + CLO = CL2O2;
Kequ = 1.27E-27*EXP(8744/TEMP);
k = Khin/Kequ :CL2O2 = CLO + CLO;

    K0 = 2.7E-33*(300/TEMP)@1.5;
Khin = K0*MCOLL;
k = Khin *O2 : CL = CLOO ;
Kequ = 5.7E-25*EXP(2500/TEMP);
```

k = Khin/Kequ : CLOO = Cl ;

K0 = 4.5E-31*(300/TEMP)@3.0;
Kinf = 1.8E-12*(300/TEMP)@1.7;
AUX = K0*MCOLL/Kinf;
Khin = Kinf*AUX/(1.+AUX)*0.6@(1/(1+LOG10(AUX)**2));
k = Khin : CH3 = CH3O2;

B.3 Photochemical reactions

The photolytic destruction rate is defined as follows :

$$\frac{d[X]}{dt} = J_X \times [X] \tag{B.5}$$

with the photolysis rates J_X calculated from the actinic flux $A(\lambda)$, the absorption cross section $\sigma(\lambda)$ and the quantum yield $q(\lambda)$:

$$J_X = \int_{\lambda_0}^{\lambda_1} A(\lambda)\sigma(\lambda)q(\lambda)d\lambda \tag{B.6}$$

where the actinic flux itself is defined by

$$A(\lambda) = \int_{\Omega} I(\lambda, \Omega)d\Omega = \int_{\theta}\int_{\phi} I(\lambda, \theta, \phi)sin(\theta)d\theta d\phi \tag{B.7}$$

k = J2 *O2 : = O + O ;
k = J3 : O3 = O ;
k = J3A : O3 = O ;
k = JCL2 : CL2 = CL + CL ;
k = JCL2O2 : CL2O2= CL + CLOO;
k = JCLNO3 : CLNO3= CL + NO3 ;
k = JH2O2 : H2O2 = OH + OH ;
k = JH2O : H2O = OH + H ;
k = JHCL : HCL = CL + HO2 ;
k = JHOCL : HOCL = OH + CL ;
k = JN2O5 : N2O5 = NO2+ NO3 ;
k = JNO2 : NO2 = NO + O ;
k = JNO3A : NO3 = NO ;
k = JNO3B : NO3 = NO2+ O ;
k = JHNO3 : HNO3 = OH + NO2 ;
k = 0.29*JBRNO3 : BRNO3= BR + NO3 ;
k = 0.71*JBRNO3 : BRNO3= BRO + NO2 ;
k = JBRNO3 : BRNO2= BR + NO2 ;
k = JBRCL : BRCL = BR + CL ;
k = JHOBR : HOBR = BR + OH ;
k = JOCLO : OCLO = CLO+ O ;
k = JBR2 : BR2 = BR +BR ;
k = JBRO : BRO = BR + O ;
k = JCH2OA : CH2O = HO2 + HCO ;
k = JCH2OB : CH2O = H2 + CO ;

```
k = JCH3O2H : CH3O2H= CH3O+ OH ;
```

B.4 Heterogeneous reactions

The diffuso-reactive heterogeneous reactions used in the model are treated according to the parameters given by Hanson et al. [1994].

```
    LPH2O = LOG(PRESS*H2O/MCOLL);
AUX2 = 44.777+1.3204*LPH2O-0.19988*TEMP;
WPsulf = ((-14.458+0.62456*LPH2O)*TEMP+3565.)/AUX2;

    GAMMA1 = 10@(1.86-0.0747*WPsulf);
vCLNO3 = sqrt( (8.*k*TEMP)/(pi*mCLNO3) );
lg1 = 0.031*10@(0.074*WPsulf)*1.e-7*sqrt(TEMP);
q1 = Aradi/lg1;
GAMMA1= GAMMA1 * ((exp(q1)+exp(-q1))/(exp(q1)-exp(-q1)) -1./q1);
Khet1 = GAMMA1 * vCLNO3 * Asulf / 4.;
k = Khet1/H2O : CLNO3 + H2O = HOCL + HNO3;

    GAMMA2 = 0.1;
vN2O5 = sqrt( (8.*k*TEMP)/(pi*mN2O5 ) );
Khet2 = GAMMA2 * vN2O5 * Asulf / 4.;
k = Khet2/H2O : N2O5 +H2O = HNO3 + HNO3;

    PHCL = 0.001*PRESS*HCL/MCOLL;
HHCL = PHCL * 10@(15.514-0.1791*WPsulf);
GAMMA3 = 0.018*sqrt(TEMP*HHCL);
lg3 = 1.e4*100.*1.e-8/GAMMA3*4.*0.082*TEMP/vCLNO3;
q3 = Aradi/lg3;
GAMMA3= GAMMA3 * ((exp(q3)+exp(-q3))/(exp(q3)-exp(-q3)) -1./q3);
Khet3 = GAMMA3 * vCLNO3 * Asulf / 4.;
k = Khet3/HCL : CLNO3 +HCL = HNO3 + CL2;

    AUX3 = (15+3*(60-WPsulf));
GAMMA4 = 0.023*sqrt(TEMP*PHCL*10@(15.514-0.1791*WPsulf))*AUX3;
lg4 = 1.e4*sqrt(1.e-8/1.e5/HHCL);
q4 = Aradi/lg4;
GAMMA4= GAMMA4 * ((exp(q4)+exp(-q4))/(exp(q4)-exp(-q4)) -1./q4);
vHOCL = sqrt( (8.*k*TEMP)/(pi*mHOCL ) );
Khet4 = GAMMA4 * vHOCL * Asulf / 4.;
k = Khet4/HCL : HOCL +HCL = H2O + CL2;

    vBRNO3 = sqrt( (8.*k*TEMP)/(pi*mBRNO3 ) );
GAMMA5 = 4.*1.e4*0.082*TEMP*SQRT(1.e8*1.e-8*HHCL)/vBRNO3;
lg5 = 1.e4*1.e4*1.e-8/GAMMA5*4*0.082*TEMP/vBRNO3;
q5 = Aradi/lg5;
GAMMA5= GAMMA5 * ((exp(q5)+exp(-q5))/(exp(q5)-exp(-q5)) -1./q5);
Khet5 = GAMMA5 * vBRNO3 * Asulf / 4.;
```

```
k = Khet5/HCL : BRNO3 + HCL = BRCL + HNO3;

   vHOBR = sqrt( (8.*k*TEMP)/(pi*mHOBR ) );
GAMMA6 = 4.*1.e6*0.082*TEMP*SQRT(1.e5*1.21e-8*HHCL)/vHOBR;
lg6 = 1.e4*1.e6*1.21e-8/GAMMA6*4*0.082*TEMP/vHOBR;
q6 = Aradi/lg6;
GAMMA6= GAMMA6 * ((exp(q6)+exp(-q6))/(exp(q6)-exp(-q6)) -1./q6);
Khet6 = GAMMA6 * vHOBR * Asulf / 4.;
k = Khet6/HCL : HOBR + HCL = BRCL + H2O;

   G7help = AMAX (0.05 , 0.78-(0.0413*(WPsulf-65.22)));
GAMMA7 = AMIN (0.78 , G7help);
Khet7 = GAMMA7 * vBRNO3 * Asulf / 4.;
k = Khet7/H2O : BRNO3 + H2O = HOBR + HNO3;
```

B.5 Concentration change because of changing volume along the trajectory

The concentration change because of the changing pressure/volume change is calculated in the lagrangian model - using the ideal gas law - according to

$$\frac{d[X]}{dt} = \frac{d[X]}{dV}\frac{dV}{dt} = \frac{d(N_X/V)}{dV}\frac{d(\nu RT/p)}{dt} = ... = -\frac{[X]}{T/P}\frac{d(T/P)}{dt} \tag{B.8}$$

Bibliography

Abbatt, J. (1994). Heterogeneous reaction of hobr with hbr and hcl on ice surfaces at 228 k. *Geophys. Res. Lett. 21*, 665–668.

Abbatt, J. and J. Nowak (1997). Heterogeneous interactions of hbr and hocl with cold sulfuric acid solutions : Implications for arctic boundary layer bromine chemistry. *J. Phys. Chem. A 101*, 2,131–2,137.

Aliwell, S., R. Jones, and D. Fish (1997). Mid-latitude observations of the seasonal variation of bro, 1. zenith-sky measurements. *Geophys. Res. Lett.* (24), 1195.

Anderson, J., W.H.Brune, and M.H.Proffitt (1989). Ozone destruction by chlorine radicals within the antarctic vortex: The spatial and temporal evolution of $clo - o_3$ anticorrelation based on in situ er-2 data. *J.Geophys.Res.* (94), 11,465–11479.

Avallone, L. M., D. W. Toohey, S. Schauffler, W. Pollock, L. Heidt, and E. Atlas (1995). In-situ measurements of bro during aase ii. *Geophys. Res. Lett. 22*, 831.

Avallone, L. M., D. W. Toohey, S. M. Schauffler, L. E. H. W. H. Pollock, and E. L. Atlas (1993). In-situ measurements of *clo* at mid-latitudes: Is there an effect from mt.pinatubo. *Geophys. Res. Lett. 20*, 2519–2522.

Bates, D. and M. Nicolet (1950). Atmospheric hydrogen. *Publ.Astron.Soc.Pac.* (62), 106–110.

Bauer, N. (1997). Charakterisierung des doas-ballon-spektrographen zur bestimmung stratosphärischer spurenstoffe. Diplomarbeit, Institut für Umweltphysik, Universität Heidelberg.

Boeker, E. and R. van Grondelle (1995). *Environmental Physics.* John Wiley Sons.

Bösch, H., e. a. (2000). Comparison of measured and modelled stratospheric photolysis frequencies of $\mathrm{no_2}$ ($\mathrm{j(no_2)}$) at large solar zenith angles. *Geophys. Res. Lett.(submitted).*

Bösch, H., C. Camy-Peyret, M.P.Chipperfield, R.Fitzenberger, H.Harder, R.Huppert, S.Payan, D.Perner, U.Platt, and K.Pfeilsticker (1999). Measurements of stratospheric trace gas profiles at different latitudes and seasons using a new balloon-borne doas-instrument. In *Proceedings : 14th ESA Symposium on European Rocket and Balloon Programmes and Related Research*, pp. 347.

Brasseur, G. Atmospheric chemistry and global change. draft.

Brasseur, G. and C. Granier (1992). Mount pinatubo aerosols, chlorofluorocarbons, and ozone depletion. *Science* (257), 1239–1242.

Brasseur, G. and S. Solomon (1986). *Aeronomy of the middle atmosphere.* Dordrecht: D. Reidel Publishing Company.

Bremer, H. e. a. (2000). Stratospheric ozone decrease observed by asur during the arctic winter 1999/2000.

Brewer, A. (1949). Evidence for a world circulation provided by the measurements of helium and water vapour distribution in the stratosphere. *Q.J.R.Meteorol.Soc.* (75), 351–363.

Bronstein, I. and K. Semendjajew (1991). *Taschenbuch der Mathematik.* B.G.Teubner Verlagsgesellschaft.

Brune, W., J. Anderson, and K. Chan (1989, November). In situ observations of bro over antarctica: Er-2 aircraft results from 54 s to 72 s latitude. *J. Geophys. Res. 94*(D14), 16639–16647.

Burrows, J., A.Dehn, B. Deters, S.Himmelmann, A.Richter, S.Voigt, and J. Orphal (1998). Atmospheric remote-sensing reference data from gome: Temperature-dependent absorption cross sections of no_2 in the $231 - 794$ nm range. *Journal of Quantitative Spectroscopy and Radiative Transfer 60*, 1025–1031.

Bussemer, M. (1993). Der ring-effekt: Ursachen und einflu"s auf die spektroskopische messung stratosph"arischer spurenstoffe. Diplomarbeit, Institut für Umweltphysik, Universität Heidelberg.

Butler, J. H., S. A. Montzka, A. D. Clarke, J. M. Lobert, and J. W. Elkins (1998). Growth and distribution of halons in the atmosphere. *J. Geophys. Res. 103*(D1), 1503–1511.

Camy-Peyret, C., Flaud, A.Perrin, C. Rinsland, A. Goldman, and F. Murcray (1993). Stratospheric n$_2$o$_5$, ch$_4$, and n$_2$o profiles from ir solar occultation spectra. *J. Atmos. Chem. 16*, 31–40.

Camy-Peyret, C., P. Jeseck, T. Hawat, G. Durry, G. Berubeé, L. Rochette, and D. Huguenin (1995). The lpma ballon-borne ftir spectrometer for remote sensing of atmospheric constituents. In *Proceedings 12th ESA Symposium on Rocket and Balloon Programmes and Related Research*, pp. 323–328.

Carlotti, M., P.A.R.Ade, B.Carli, P.Ciarpallini, U.Cortisi, M.J.Griffin, G.Lepri, F.Mencaraglia, A.G.Murray, I.G.Nolt, J.H.Park, and J.V.Radostitz (1995). Measurement of stratospheric hbr using high resolution far infrared spectroscopy. *Geophys.Res.Lett. 22*(23), 3207–3210.

Carpenter, L., W. Sturges, S. Penkett, P. Liss, B. Alicke, K. Hebestreit, and U. Platt (1999). Observations of short-lived alkyl iodides and bromides at mace head, ireland: links to biogenic sources and halogen oxide production. *J. Geophys. Res. 104*, 1,679–1,689.

Carslaw, K., M.Wirth, A.Tsias, B.P.Luo, A.Dörnbrack, M.Leutbecher, H.Volkert, W.Renger, J.T.Bacmeister, E.Reimer, and T.Peter (1998). Increased stratospheric ozone depletion due to mountain-induced atmospheric waves. *Nature* (391), 675–678.

Carslaw, K., T. Peter, and J. B. S. Eckermann (1999). Widespread solid particle formation by mountain-waves in the arctic stratosphere. *J. Geophys. Res. 104*(D1), 1827–1836.

Chapman, S. (1930). On ozone and atomic oxygen in the upper atmosphere. *Philos. Mag.* (10), 369–383.

Chipperfield, M. (1999). Multiannual simulations with a three-dimensional chemical model. *J.Geophys. Res.* (1104), 1.781–1.806.

Chipperfield, M. P., D. E. Shallcross, and D. J. Lary (1997, December). A model study of the potential role of the reaction bro + oh in the production of stratospheric hbr. *Geophys. Res. Lett. 24*(23), 3025–3028.

Cornu, A. (1879). Observation de la limite ultraviolette du spectre solaire à diverses altitudes. *C.R.Hebd.Seances Acad.Sci.* (89), 808.

Crutzen, P. (1970). The influence of nitrogen oxide on the atmospheric ozone content. *Q.J.R. Meteorol.Soc.* (96), 320–327.

Crutzen, P. (1974). Photochemical reactions initiated by and influencing ozone in unpolluted tropospheric air. *Tellus* (26), 47–57.

Crutzen, P. and F. Arnold (1986). Nitric acid cloud formation in the cold antarctic stratosphere: A major cuase for the springtime "ozone hole". *Nature* (324), 651–655.

Cunnold, D., F.Alyea, N.Phillips, and R.G.Prinn (1975). A three-dimensional dynamical-chemical of atmospheric ozone. *J.Atmos.Sci.* (32), 170.

Danilin, M. and J. McConnell (1995). Stratospheric effects of bromine activation on/in sulfate aerosol. *J.Geophys.Res.* (100), 11.237–11.243.

DeMore, W. B., S. P. Sander, D. M. Golden, R. F. Hampson, M. J. Kurylo, C. J. Howard, A. R. Ravishankara, C. E. Colb, and M. J. Molina (1997). Chemical kinetics and photochemical data for use in stratospheric modeling. Technical Report Evaluation number 12, NASA/JPL publication 97-4.

Disselkamp, R., E. Chapman, W. Barchet, S. Colson, and C. Howd (1999). Brcl production in nabr/nacl/hno$_3$/o$_3$ solutions representative of sea-salt aerosols in the marine boundary layer. *Geophys. Res. Lett. 26*, 2,183–2,186.

Dobson, G. (1930). Observations of the amount of ozone in the earth's atmosphere and its relation to other geophysical conditions. *Pro.R.Soc.London Ser.A.*(129), 411.

Dobson, G. (1968). Forty years' research on atmospheric ozone at oxford: A history. *Appl.Opt.* (7), 387–405.

Dvortsov, V. (1998). *Atmospheric distribution of* ^{222}*Rn and bromine species as simulated with 3-D and 2-D transport with convection.* Ph. D. thesis, University of New York at Stony Brook, USA.

Dvortsov, V., M. A. Geller, S. Solomon, S. M. Schauffler, E. L.Atlas, and D. R. Blake (1999). Rethinking reactive halogen budget in the midlatitude stratosphere. *Geophys. Res. Lett.*, 1.699 – 1.702.

Dvortsov, V., S. Solomon, R. Portmann, R. Garcia, J. Austin, B. Steil, C. Brühl, P. Crutzen, and E. Manzini.

ECMWF (1999). Ecmwf (european center for medium-range weather forecasts) temperature and potential vorticity analyses. Technical report, Danish Meteorol. Inst., Kobenhavn.

Elkins, J., D. Fahey, J.M.Gilligan, G. Dutton, T.J.Baring, C.M.Volk, R. Dunn, R.C.Myers, S.A.Montzka, P.R.Wamsley, A.H.Hayden, J.H.Butler, T.M.Thompson, T.H.Swanson, E.J.Dlugokencky, P.C.Novelli, D.F.Hurst, J.M.Lobert, S.J.Ciciora, R.J.McLaughlin, T.L.Thompson, R.H.Winkler, P.J.Fraser, L.P.Steele, and M.P.Lucarelli (1996). Airborne gas chromatograph for in situ measurements of long-lived species in the upper troposphere and lower stratosphere. *Geophys.Res.Lett.* (23), 347–350.

Elkins, J., T. Thompson, T. Swanson, J.H.Butler, B.D.Hall, S.O.Cummings, D. Fisher, and A. Raffo (1993). Decrease in the growth rates of atmospheric chlorofluorocarbons 11 and 12. *Nature* (364), 780–783.

Engel, A. (2000). Final report of the project: Mid and high latitude stratospheric distribution of long and short lived halogen species during the maximum of the chlorine loading. Technical report, CEC contract ENV4-97-0524.

Engel, A., U. Schmidt, and R. Stachnik (1997). Partitioning between chlorine reservoir species deduced from observations in the arctic winter stratosphere. *J. Atmos. Chem. 27*, 107–126.

EORCU. The northern hemisphere stratosphere in the winter of 1998/99. European Ozone Research Coordinating Unit, preliminary.

EORCU. The northern hemisphere stratosphere in the winter of 1999/2000. European Ozone Research Coordinating Unit, preliminary.

Erle, F. (1999). *Untersuchungen zur Halogenaktivierung der winterlichen arktischen Stratosphäre anhand flugzeuggestützter spektroskopischer Messungen.* Ph. D. thesis, University of Heidelberg.

Erle, F., A. Grendel, D. Perner, U. Platt, and K. Pfeilsticker (1998). Evidence of heterogeneous bromine chemistry on cold stratospheric sulphate aerosols. *Geophys. Res. Lett. 25*, 4,329–4,332.

Fabry, C. and M. Buisson (1913). L'absorption de l'ultraviolet par l'ozone et la limite du spectre solaire. *J. Phys.* (3), 196–206.

Fahey, D., S.R.Kawa, E.L.Woodbridge, P.Tin, J.C.Wilson, H.H.Jonasson, J.E.Dye, D.Baumgardner, S.Borrmann, D.W.Toohey, L.M.Avalone, M.H.Proffitt, J.Margitan, M.Loewenstein, J. Podolske, R.J.Salawitch, S.C.Wofsy, M.K.W.Ko, D.E.Anderson, M.R.Schoeberl, and K.R.Chan (1993). In situ measurements constraining the role of sulphate aerosols in midlatitude ozone depletion. *Nature* (363), 509–514.

Farman, J. C., G. Gardiner, and J. D. Shanklin (1985). Large losses of total ozone in antarctica reveal seasonal clo_x and no_x interaction. *Nature 315*, 207–210.

Ferlemann, F. (1998). *Ballongestützte Messung stratosphärischer Spurengase mit differentieller optischer Absorptionsspektroskopie.* Ph. D. thesis, University of Heidelberg, Germany.

Ferlemann, F., N. Bauer, R.Fitzenberger, H.Harder, H.Osterkamp, D.Perner, U.Platt, M.Schneider, P.Vradelis, and K.Pfeilsticker (2000). A new doas-instrument for stratospheric balloon-borne trace gas studies. *J.Appl.Optics 39*(15), 2377–2386.

Fish, D. J. and R. L. Jones (1995). Rotational raman scattering and the ring effect in zenit-sky spectra. *Geophys. Res. Lett. 22*(7), 811–814.

Fitzenberger, R., H.Bösch, C.Camy-Peyret, M.P.Chipperfield, H.Harder, S. Payan, U.Platt, B.-M.Sinnhuber, and K.Pfeilsticker (2000). Balloon-borne doas measurements of bromine oxide in the stratosphere and troposphere. In I. O. Commission (Ed.), *Proceedings of the Quadrennial Ozone Symposium - Sapporo 2000*, pp. 373. NASDA.

Fitzenberger, R., H.Bösch, C.Camy-Peyret, M.P.Chipperfield, H.Harder, U.Platt, B.-M.Sinnhuber, T.Wagner, and K.Pfeilsticker (2000). First profile measurement of tropospheric bro. *Geophys. Res. Lett. 27*(18), 2921–2924.

Fraser, P., D. Oram, C. Reeves, and S. Penkett (1999). Southern hemispheric halon trends (1978-1998) and global halon emissions. *J. Geophys. Res. 104*, 15,985–15,999.

Friess, U., M.P.Chipperfield, H.Harder, C.Otten, U.Platt, J.Pyle, T.Wagner, and K.Pfeilsticker (1999). Intercomparison of measured and modelled bro slant column amounts for the arctic winter and spring 1994/95. *Geophys.Res.Lett. 26*(13), 1861–1864.

Gao, R. e. a. (1999). A comparison of observations and model simulations of no_x/no_y in the lower stratosphere. *Geophys. Res. Lett. 26*, 1153–1156.

Garcia, R. R. and S. Solomon (1994). A new numerical model of the middle atmosphere: 2. ozone and related species. *J. Geophys. Res. 99*(D6), 12937–12951.

Gilles, M. . A. T., J. Burkholder, and A. Ravishankara (1997). A study of the br+io $\longrightarrow$ i+bro and the reverse reaction. *Chem. Phys. Lett. 272*, 75–82.

Gomer, T., T. Brauers, F. Heintz, J. Stutz, and U. Platt (1996). *MFC User Manual, Vers. 1.98.* Institut für Umweltphysik, Universität Heidelberg.

Goutail, F., C.Deniel, F.Lefevre, J.P.Pommereau, A.Sarkissian, and L.Denis (2000). Ozone loss in the arctic and mid-latitudes stratosphere from 1993 to 2000. In *Proceedings of the Quadrennial Ozone Symposium - Sapporo 2000.*

Greenblatt, G., J. Orlando, J. Burkholder, and A. Ravishankara (1990, October). Absorption measurements of oxygen between 330 and 1140 nm. *J. Geophys. Res. 95*(D11), 18577–18582.

Haagen-Smit, A., C. Bradley, and M. Fox (1952). Formation of ozone in los angeles smog. *Proc.Second Nat.Air Pollut.Symp.*, 54–56.

Hamamatsu Photonics (1995, December). *Thermoelectrically-cooled N-MOS linear image sensors S5930, S5931 series.*

Hanson, D., A.R.Ravishankara, and E.R.Lovejoy (1996). Reaction of $brono_2$ with h_2o on submicron sulfuric acid aerosol and the implications for the lower stratosphere. *J.Geophys.Res.* (101), 9063–9069.

Hanson, D., A.R.Ravishankara, and S.Solomon (1994). Heterogeneous reactions in sulfuric acid aerosols: A framework for model calculations. *J.Geophys.Res.* (99), 3615–3629.

Hanson, D. and K. Mauersberger (1988). Laboratory studies of the nitric acid trihydrate: Implications for the south polar stratosphere. *Geophys.Res.Lett. 15*(8), 855–858.

Hanson, D. and A. Ravishankara (1995). Heterogeneous chemistry of bromine species in sulfuric acid under stratospheric conditions. *Geophys.Res.Lett.* (22), 385–388.

Harder, H. (1999). *Messung und Modellierung stratosphärischer Spurenstoffprofile zur Abschätzung des anorganischen Gesamt-Brom-Budgets.* Ph. D. thesis, University of Heidelberg, Germany.

Harder, H., H. Bösch, C. Camy-Peyret, M. Chipperfield, R. Fitzenberger, S. Payan, D. Perner, U. Platt, B.-M. Sinnhuber, and K. Pfeilsticker (2000). Comparison of measured and modeled stratospheric bro: Implications for the total amount of stratospheric bromine. *Geophys. Res. Lett. (in press).*

Harder, H., C. Camy-Peyret, F. Ferlemann, R. Fitzenberger, T. Hawat, H. Osterkamp, M. Schneider, D. Perner, U. Platt, P. Vradelis, and K. Pfeilsticker (1998). Stratospheric bro profiles measured at different latitudes and seasons: Atmospheric observations. *Geophys.Res.Lett.* (25), 3843–3846.

Harnisch, J., R. Borchers, P. Fabian, and M. Maiss (1996). Tropospheric trends for cf_4 and c_2f_6 since 1982 derived from sf_6 dated stratospheric air. *Geophys. Res. Lett. 23*, 1,099–1,102.

Hartley, W. (1880). On the probable absorption of solar radiation by atmospheric ozone. *Chem.News* (42), 268.

Hausmann, M. and U. Platt (1994, December). Spectroscopic measurement of bromine oxide and ozone in the high arctic during polar sunrise experiment 1992. *J. Geophys. Res. 99*(D12), 25399–25413.

Hawat, T., C. Camy-Peyret, P. Jeseck, and R. Torguet (1995). Desription and performances of a balloon-borne heliostat for solar absorption measurements. In *Proceedings 12th ESA Symposium on Rocket and Balloon Programmes and Related Research.*

Hebestreit, K., J. Stutz, D. Rosen, V. Matveiv, M. Peleg, M. Luria, and U. Platt (1999). Doas measurements of tropospheric bromine oxide in mid-latitudes. *Science 283*, 55–57.

Helmling, M. (1994). Modellierungen von photochemischen prozessen entlang von luftmassentrajektorien im arktischen frühjahr. Master's thesis, Institut für Umweltphysik, Universität Heidelberg.

Huppert, R. (2000). Theoretische und experimentelle untersuchungen zum solaren i_0 effekt. Master's thesis, University of Heidelberg, Germany.

Johnston, P. (1996). Making uv/vis cross sections reference fraunhofer and synthetic spectra. priv.comm.

Johnston, P., R.L.McKenzie, J.G.Keys, and W.A.Matthews (1992). Observations of depleted stratospheric no_2 following the pinatubo volcanic eruption. *Geophys.Res.Lett.* (19), 211–213.

Kanzawa, H., C.Camy-Peyret, Y. Kondo, and N.Papineau (1997). Implementation and first scientific results of the ilas validation balloon campaign at kiruna-esrange in february-march 1997. *European Space Agency Spec. Publ.*, 211–215.

Knudsen, B. and G. Carver (1994). Accuracy of the isentropic trajectories calculated for the easoe campaign. *Geophys.Res.Lett. 21*(13), 1199–1202.

Ko, M., N. Sze, C. Scott, and D. Weisenstein (1997). On the relation between chlorine/bromine loading and short-lived tropospheric source gases. *J. Geophys. Res. 102*, 25,507 – 25,517.

Koop, T. and K. Carslaw (1996). Melting of $h_2so_4 \cdot 4h_2o$ particles upon cooling: Implications for polar stratospheric clouds. *Science 272*, 1638–1641.

Kreher, K. (1996). *Spectroscopic Measurements of Atmospheric OClO, BrO and NO_2 and their Relation to Antarctic Ozone Depletion.* Dissertation, Institut für Umweltphysik, Universität Heidelberg.

Kromminga, H., S. Voigt, J. Orphal, and J. P. Burrows (1999). Uv-visible ft spectra of oclo at atmospheric temperature. *Proceedings of the 1st European Symposium on Atmospheric Measurements from Space, ESA Special Publication.*

Kurucz, R., I.Furenlid, J.Brault, and L. Testerman (1984). *Solar flux atlas from 296 to 1300 nm, National Solar Observatory Atlas No.1.* National Solar Observatory.

Lait, L., P.A.Newman, and M.R.Schoeberl (1996). Using the goddard automailer. Technical report, NASA Goddard Space Flight Center.

Lary, D. (1996, January). Gas phase atmospheric bromine photochemistry. *J. Geophys. Res. 101*(D1), 1505–1516.

Lary, D. (1998). Atmospheric fluorine chemistry. *submitted to J. Geophys. Res.*.

Lary, D., M. Chipperfield, R. Toumi, and T. Lenton (1996, January). Heterogeneous atmospheric bromine chemistry. *J. Geophys. Res. 101*(D1), 1489–1504.

Lary, D. and J. Pyle (1991). Diffuse radiation, twilight and photochemistry. *J. Atmos. Chem 13*, 373–392.

Lefêvre, F., G. P. Brasseur, I. Folkins, A. K. Smith, and P. Simon (1994). Chemistry of the 1991-1992 stratospheric winter: three-dimensional model simulations. *J. Geophys. Res. 99*, 8183–8195.

Levin, I. and V. Hesshaimer (1996). Refining of atmospheric transport model entries by the globally observed passive tracer distributions of ^{86}kr and sulfur hexafluoride. *J.Geophys.Res.* (101), 16745–16755.

Lipson, J., M.J.Elrod, T. Beiderhase, L.T.Molina, and M. Molina (1997). Temperature dependence of the rate constant and branching ratio for the $oh + clo$ reaction. *J.Chem.Soc.Faraday Trans.* (93), 2665–2673.

Maiss, M. and I. Levin (1994). Global increase of sf_6 observed in the atmosphere. *Geophys. Res. Lett. 21*, 569–572.

McCormick, M., H. Steele, P.Hamill, W. Chu, and T. Swissler (1982). Polar stratospheric cloud sightings by sam ii. *J.Atmos.Sci.* (39), 1387–1397.

McElroy, C., C. McLinden, and J. McConnell (1999). Evidence for bromine monoxide in the free troposphere during the arctic polar sunrise. *Nature 397*, 338–341.

McElroy, M. B., R. J. Salawitch, S. C. Wofsy, and J. A. Logan (1986). Reductions of antarctic ozone due to synergistic interactions of chlorine and bromine. *Nature 321*, 759–762.

McKinney, K. A., J. M. Pierson, and D. W. Toohey (1997). A wintertime in situ profile of bro between 17 and 27 km in the arctic vortex. *Geophys. Res. Lett. 24*, 853–856.

Molina, L. and M. Molina (1987). Production of cl_2o_2 from the self-reaction of the clo radical. *J.Phys.Chem.* (91), 433–436.

Molina, M. and F. Rowland (1974). Stratospheric sink for chlorofluoromethanes: Chlorine atom catalyzed destruction of ozone. *Nature* (249), 812–820.

Montzka, S. A., J. H. Butler, R. C. Myers, T. M. Thompson, T. H. Swanson, A. D. Clarke, L. T. Lock, and J. W. Elkins (1996). Decline in the tropospheric abundance of halogen from halocarbons: Implications for stratospheric ozone depletion. *Science 272*, 1318–1322.

Mozurkewich, M. and J. Calvert (1988). Reaction probability of n_2o_5 on aqueous aerosols. *J.Geophys.Res.* (93), 15,889–15,896.

Müller, R., T. Peter, P.J.Crutzen, H.Oelhaf, G.P.Adrian, T.v.Clarmann, A.Wegner, U.Schmidt, and D.Lary (1994). Chlorine chemistry and the potential for ozone depletion in the arctic stratosphere in the winter of 1991/92. *Geophys.Res.Lett. 21*, 1427–1430.

Murphy, D. and D. Thomson (2000). Halogen ions and no^+ in mass spectra of aerosols in the upper troposphere and lower stratosphere. *Geophys. Res. Lett., submitted.*

Newman, P., J.G.Gleason, R.D.McPeters, and R.S.Solarski (1997). Anomalously low ozone over the arctic. *Geophys.Res.Lett.* (24), 2689–2692.

Nolt, I. G., P. A. R. Ade, F. Alboni, B. Carli, M. Carlotti, U. Cortesi, M. Epifani, M. J. Griffin, P. A. Hamilton, C. Lee, G. Lepri, F. Mencaraglia, A. G. Murray, J. H. Park, K. Park, P. Raspollini, M. Ridolfi, and M. D. Vanek (1997, February). Stratospheric hbr concentration profile obtained from far-infrared emission spectroscopy. *Geophys. Res. Lett. 24*(3), 281–284.

Noxon, J. (1975). Nitrogen dioxide in the stratosphere and troposphere measured by ground-based absorption spectroscopy. *Science 189*, 547–549.

Noxon, J. (1979). Stratospheric no_2 2: Global behavior. *J.Geophys.Res.* (84), 5067.

Otten, C., F. Ferlemann, U. Platt, T. Wagner, and K. Pfeilsticker (1997). Groundbased doas uv/visible measurements at kiruna (sweden) during the sesame winters 1993/94 and 1994/95.

Pawson, S. and B. Naujokat (1999). The cold winters of the middle 1990s in the northern lower stratosphere. *J.Geophys.Res. 104*(D12), 14,209–14,222.

Payan, S., C.Camy-Peyret, P. Jeseck, T.Hawat, and G.Durry (1998). First direct simultaneous *hcl* and $clono_2$ profile measurements in the arctic vortex. *Geophys.Res.Lett. 25*(14), 2663–2666.

Perner, D. and U. Platt (1979). Detection of nitrous acid in the atmosphere by differential optical absorption. *Geophys.Res.Lett.* (7), 1053–1056.

Pfeilsticker, K. (1999). Final report of the eu-sponsored project: Balloon-borne profile measurements and modeling for studying the chemistry of the lower stratosphere (short title chelosba). Technical report, CEC contract ENV4-95-0178.

Pfeilsticker, K., H. Bösch, C.Camy-Peyret, M.Chipperfield, R.Fitzenberger, H.Harder, F.Lefevre, S.Payan, and B.-M.Sinnhuber (2000). Testing of the $\mathrm{no}_x/\mathrm{no}_y$ ratio in the high latitude summer stratosphere by inter comparison of measurements with model calculations. In *Proceedings of the Quadrennial Ozone Symposium - Sapporo 2000 - Hokaido University, Sappro, Japan, 3-8 July 2000*, pp. 587.

Pfeilsticker, K., W. Sturges, H.Bösch, C.Camy-Peyret, M.P.Chipperfield, A. Engel, R.Fitzenberger, M.Müller, S.Payan, and B.-M.Sinnhuber (2000). Lower stratospheric organic and inorganic bromine budget for the arctic winter 1998/99. *Geophys.Res.Lett. 27*(20), 3305.

Platt, U. (1994). Differential optical absorption spectroscopy (doas). In M. W. Sigrist (Ed.), *Air Monitoring by Spektroscopic Techniques*, Volume 127. New York: John Wiley & Sons, Inc.

Platt, U., L. Marquard, T. Wagner, and D. Perner (1997). Corrections for zenith scattered light doas. *Geophys.Res.Lett. 24*(14), 1759–1762.

Plumb, R., D. Waugh, and M. Chipperfield (1999). The effects of mixing on tracer relationships in the polar vortices. *submitted to J. Geophys. Res.*.

Pommereau, J. e. a. (2000). Investigation of ozone loss related processes from long duration balloon flights in the arctic vortex: The theseo-lagrangian experiment. In *Proceedings of the Quadrennial Ozone Symposium - Sapporo 2000 - Hokaido University, Sapporo, Japan, 3-8 July 2000*, pp. 247–248.

Portmann, R., S.Solomon, R.R.Garcia, L.W.Thomason, L.R.Poole, and M.P.McCormick (1996). Role of aerosol variations in anthropogenic ozone depletion in the polar regions. *J.Geophys.Res.* (101), 22,991–23,006.

Press, W. H., S. A. Teukolsky, W. T. Vetterling, and B. P. Flannery (1995). *Numerical Recipes in C; The Art of Scientific Computing.* Cambridge: University Press.

Pundt, I. (1997). *Étude de la distribution verticale des oxydes d'iode et de brom dans la basse stratosphère à l'aide de la sonde SAOZ-ballon.* Dissertation, Université Paris VI.

Pundt, I., J.-P. Pommereau, C. Phillips, and E. Lateltin (1998). Upper limit of iodine oxide in the lower stratosphere. *J. Atmos. Chem. 30*, 173–185.

Pundt, I. e. a. (2000). Simultaneous uv-vis measurements of bro from balloon, satellite and ground: Implications for tropospheric bro. In *Air Pollution Research Report, Polar Stratospheric Ozone 1999, Proc. 5th European Symp., (in press).*

Pyle, J., J. Austin, M. Chipperfield, R. Cox, J.C.Farman, L. Gray, N.R.P.Harris, R.L.Jones, A. McCulloch, S. Penkett, C.E.Reeves, H.K.Roscoe, K.P.Shine, R.Toumi, and A. Webb (1999). *Stratospheric Ozone 1999.* Department of Environment, Transport and Regions.

Richter, A., M.Eisinger, A.Ladstätter-Wei, and J.P.Burrows (1999). Doas zenith sky observations: 2. seasonal variation of bro over bremen(53^on) 1994-1995. *J.Atmos.Chem.* (32), 83–99.

Rodriguez, J., M.K.W.Ko, and N.D.Sze (1991). Role of heterogeneous conversion of n_2o_5 on sulphate aerosols in global ozone loss. *Nature* (352), 134–137.

Roedel, W. (1992). *Physik unserer Umwelt: Die Atmosphäre.* Berlin Heidelberg: Springer Verlag.

Rowland, F. and M. Molina (1975). Chlorofluoromethanes in the environment. *Rev.Geophys.* (13), 1–35.

Sander, S., R.R.Friedl, W. B. DeMore, D. M. Golden, R. F. Hampson, M. J. Kurylo, R. Hampson, R.E.Huie, A. R. Ravishankara, C. E. Kolb, M. J. Molina, and G.K.Moortgat (2000). Chemical kinetics and photochemical data for use in stratospheric modeling: Supplement to evaluation 12: Update of key reactions. Technical Report Evaluation number 13, NASA/JPL publication 00-3.

Sanders, R., S. Solomon, M. Caroll, and A.L.Schmeltekopf (1989). Visible and near-ultraviolet spectroscopy at mcmurdo station antarctica, 4. overview and daily measurements of no_2, o_3 and $oclo$ during 1987. *J.Geophys.Res.* (94), 11381–11491.

Schauffler, S., E. Atlas, D. Blake, F. Flocke, R. Lueb, J. Lee-Taylor, V. Stroud, , and W. Travnicek (1999). Distribution of brominated organic compounds in the upper troposphere and lower stratosphere. *J. Geophys. Res. 104*, 21,513–21,535.

Schauffler, S. M., E. L. Atlas, F. Flocke, R. A. Lueb, V. Stroud, and W. Travnicek (1998). Measurement of bromine-containing organic compounds at the tropical tropopause. *Geophys. Res. Lett. 25*(3), 317–320.

Schmidt, U. and A. Khedim (1991). In situ measurements of carbon dioxide in the winter arctic vortex and at mid-latitudes: An indicator of the age of stratospheric air. *Geophys.Res.Lett.* (18), 763–766.

Schneider, M. (1997). Gleichzeitige, ballongestützte messungen von o_3, no_2 der photolysefrequenz von no_2 in der stratosphäre. Diplomarbeit, Institut für Umweltphysik, Universität Heidelberg.

Schoeberl, M. and L. Sparling (1994). Trajectory modelling. In *Diagnostic Tools in Atmospheric Physics, Proc.S.I.F.Course CXVI.*

Schreiner, J., C. Voigt, A. Kohlmann, F. Arnold, K. Mauersberger, and N. Larsen (1999). Chemical analysis of polar stratospheric cloud particles. *Science 283*(5404), 968–970.

Schulte, M. (1996). Damf v1.22 direct light air mass factors. Scientific project work, Institut für Umweltphysik, University of Heidelberg.

Sessler, J., M. Chipperfield, J.Pyle, and R. Toumi (1995). Stratospheric $oclo$ measurements as a poor quantitative indicator of chlorine activation. *Geophys.Res.Lett.* (22), 687–690.

Sinnhuber, B.-M. and M. Chipperfield (2000). Study of the impact of total bromine loading in the global stratosphere. personal communication.

Slusser, J., D.J.Fish, E.K.Strong, R.L.Jones, H.K.Roscoe, and A.Sarkissian (1997). Five years of no_2 vertical column measurements at faraday(65^os): Evidence for the hydrolysis of $brono_2$ on pinatubo aerosols. *J.Geophys.Res.* (102), 12,987–12,993.

Solomon, S. (1999). Stratospheric ozone depletion: A review of concepts and history. *Reviews of Geophysics 37*(3), 275–316.

Solomon, S., R. Garcia, and A. Ravishankara (1994, October). On the role of iodine in ozone depletion. *J. Geophys. Res. 99*(D10), 20491–20499.

Solomon, S., G.H.Mount, R.W.Sanders, and A.L.Schmeltekopf (1987). Visible spectroscopy at mcmurdo station antarctica, 2, observations of $oclo$. *J.Geophys.Res.* (92), 8329–8338.

Solomon, S., R.R.Garcia, F.S.Rowland, and D.J.Wuebbles (1986). On the depletion of antarctic ozone. *Nature* (321), 755–758.

Solomon, S., R.W.Portmann, R. Garcia, L.W.Thomason, L.R.Poole, and M.P.McCormick (1996). The role of aerosol variations in anthropogenic ozone depletion at northern midlatitudes. *J.Geophys.Res.* (101), 6713–6727.

Solomon, S., R.W.Portmann, R. Garcia, W.Randel, F.Wu, R.Nagatani, J.Gleason, L.Thomason, L.R.Poole, and M.P.McCormick (1998). Ozone depletion at midlatitudes: Coupling of volcanic aerosols and temperature variability to anthropogenic chlorine. *Geophys.Res.Lett.* (25), 1871–1874.

Solomon, S., R.W.Sanders, R. Jakoubek, K.H.Arpag, S.L.Stephens, J.G.Keys, and R. Garcia (1996). Visible and near-ultraviolet spectroscopy at mcmurdo station, antarctica, 10. reductions of stratospheric no_2 due to pinatubo aerosols. *J.Geophys.Res.* (99), 3509–3516.

Sonett, C., M. Giampapa, and M. Matthews (1991). *The sun in time.* The University of Arizona Press.

Staehelin, J., A. Renaud, J.Bader, R.McPeters, P.Viatte, B.Hoegger, V.Bugnion, M.Giroud, and H.Schill (1998). Total ozone series at arosa (switzerland): Homogenization and data comparison. *J.Geophys.Res.* (103), 5827–5841.

Stolarski, R. and R. Cicerone (1974). Stratospheric chlorine: A possible sink for ozone. *Can.J.Chem.* (52), 1610–1615.

Stroh, F. (1999). Sunset photochemistry of clo and bro in the arctic stratosphere from in-situ measurements during halomax. *Fifth European Workshop on Stratospheric Ozone, St.Jean-de-Luz, France*.

Strunk, M., A. Engel, U.Schmidt, C.M.Volk, T.Wetter, I.Levin, and H.Glatzel-Mattheier (2000). co_2 and sf_6 as stratospheric age tracers: consistency and the effect of mesopheric loss. *Geophys.Res.Lett.* (27), 341–344.

Stutz, J. and U. Platt (1996, Oktober). Numerical analysis and estimation of the statistical error of differential optical absorption spectroscopy measurements with least-squares methods. *Applied Optics 35*(30), 6041–6053.

Sze, N., M.K.W.Ko, D.K.Weisenstein, J.M.Rodriguez, R.S.Stolarski, and M.R.Schoeberl (1989). Antarctic ozone hole: Possible implications for ozone trends in the southern hemisphere. *J.Geophys.Res.* (94), 11,521–11,528.

Tabazadeh, A., O. Toon, B. Gary, J. Bacmeister, and M. Schoeberl (1996). Observational constraints on the formation of type ia polar stratospheric clouds. *Geophys.Res.Lett.* (23), 2109–2112.

Tabazadeh, A., O. Toon, and P. Hamill (1995). Freezing behaviour of stratospheric sulfate aerosol inferred from trajectory studies. *Geophys.Res.Lett.* (22), 1725–1728.

Thomason, L. and L. Poole (1997). A global climatology of stratospheric aerosol surface area density deduced from stratospheric aerosol and gas experiment ii measurements: 1984-1994. *J.Geophys.Res. 102*(D7), 8967–8976.

Tie, X.-X. and G. Brasseur (1996). The importance of heterogeneous bromine chemistry in the lower stratosphere. *Geophys.Res.Lett.* (23), 2505–2508.

Tolbert, M., M.J.Rossi, and D.M.Golden (1988). Antarctic ozone depletion chemistry: Reactions of n_2o_5 with h_2o and hcl on ice surfaces. *Science* (240), 1018–1021.

Toohey, D. W., J. G. Anderson, W. H. Brune, and K. R. Chan (1990). In-situ measurements of bro in the arctic stratosphere. *Geophys. Res. Lett. 17xx*, 513–516.

Toon, O., P.Hamill, R.P.Turco, and J.Pinto (1986). Condensation of hno_3 and hcl in the winter polar stratosphere. *Geophys.Res.Lett.* (13), 1284–1287.

Toumi, R. (1994). Reaction of clo with no_3: $oclo$ formation and night-time o_3 loss. *Geophys.Res.Lett.* (21), 1487–1490.

Tung, K., M. Ko, J. Rodriguez, and N. Sze (1986). Are antarctic ozone variations a manifestation of dynamics or chemistry. *Nature* (333), 811–814.

Van Roozendael, M. and C. Fayt (2000). *WinDOAS 2.1, Software User Manual.* Belgium Institut for Space Aeronomy (BIRA/IASB).

Van Roozendael, M., C. Fayt, J.-C. Lambert, I. Pundt, T. Wagner, A. Richter, and K. Chance (1999). Development of a bromine oxide product from gome. *Proc. ESAMS99-European Symposium on Atmospheric Measurements from Space, ESTEC, Noordwijk, The Netherlands, 18-22 January 1999, WPP-161*, 543–547.

Vradelis, P. (1998). Verbesserung der ballon-doas-messungen durch streulichtunterdrückung und numerische untersuchungen des auswerteprozesses. Diplomarbeit, Institut für Umweltphysik, Universität Heidelberg.

Wagner, T. (1999). *Satellite Observations of Atmospheric Halogen Oxides.* Ph. D. thesis, University of Heidelberg.

Wagner, T. (2000). Dsd comparison (90^o-80^o sza) for kiruna ground-based zsl measurements. personal communication.

Wagner, T. and C. Leue (1999). Global maps of gome data, iup heidelberg. http://giger.iup.uni-heidelberg.de/maps/index.html.

Wagner, T. and U. Platt (1998). Satellite mapping of enhanced bro concentrations in the troposphere. *Nature 395*, 486–490.

Wahner, A., A. Ravishankara, S. Sander, and R. Friedl (1988, November). Absorption cross section of bro between 312 and 385 nm at 298 and 223 k. *Chem. Phys. Lett. 152*(6), 507–512.

Wahner, A., G. Tyndall, and A. Ravishankara (1987). Absorption cross sections for oclo as a function of temperature in the wavelength range 240-480 nm. *J. Phys. Chem. 91*(11), 2734–2738.

Wamsley, P. R. e. a. (1998). Distribution of halon-1211 in the upper troposphere and lower stratosphere and the 1994 total bromine budget. *J. Geophys. Res. 103*, 1,513–1,526.

Waschevsky, G. and J. Abbatt (1999). $hobr$ in sulfuric acid solutions: solubility and reactions with hcl as a function of temperature and concentration. *J.Phys.Chem.submitted.*

Waugh, D., R. Plumb, R.Atkinson, M.Schoeberl, L.Lait, P.Newman, M.Loewenstein, D.Toohey, M.Avallone, C.Webster, and R.May (1994). Transport of material out of the stratospheric arctic vortex by rossby wave breaking. *J.Geophys.Res.* (99), 1071–1088.

Wilmouth, D., T.F.Janisco, N.M.Donahue, and J.G.Anderson (1999). Fourier transform ultraviolet spectroscopy of the $a\,^2\pi_{3/2} \longleftarrow x\,^2\pi_{3/2}$ transition of bro. *J.Phys.Chem.,A 103*, 8935–8945.

WMO (1998). *Scientific Assessment of ozone depletion: 1998.* Geneva, Switzerland: World Meteorological Organization (WMO), Global Ozone Observing System(GO_3OS).

Wofsy, S., M. McElroy, and Y. Yung (1975). The chemistry of atmospheric bromine. *Geophys. Res. Lett. 2*, 215–218.

Yokouchi, Y., T. Machida, L. Barrie, D. Toom-Sauntry, Y. Nojiri, Y. Fujinuma, Y. Inuzuka, H.-J. Li, H. Akimoto, and S. Aoki (2000). Latitudinal distribution of atmospheric methyl bromide: measurements and modeling. *Geophys.Res.Lett. 27*(5), 697–700.

Yung, Y. L., J. P. Pinto, R. T. Watson, and S. P. Sander (1980). Atmospheric bromine and ozone perturbations in the lower stratosphere. *J. Atm. Sci. 37*, 339–353.

Zhang, R., M.-T. Leu, and M. Molina (1996). Formation of polar stratospheric clouds on preactivated background aerosols. *Geophys.Res.Lett. 23*, 1669–1672.

Appendix C

Danksagung

Schließlich will ich all denjenigen danken, die zum Zustandekommen und Erfolg dieser Arbeit beigetragen haben.

Herrn Prof. U. Platt danke ich für die Möglichkeit, diese interessante Thematik bearbeiten und an fünf der acht präsentierten Ballonmeßkampagnen teilnehmen zu können. Weiterhin ist die große wissenschaftliche Freiheit hervorzuheben, mit der am Institut für Umweltphysik gearbeitet werden konnte und kann.

Herrn Prof. K. Mauersberger danke ich für die Begutachtung meiner Dissertation.

Herrn Priv.Doz. Klaus Pfeilsticker danke ich für die intensive Betreuung zwischen und während der Ballonmeßkampagnen, die zum Entstehen vieler der hier präsentierten Ideen und Ergebnisse beigetragen hat.

Meinen Vorgängern Dr.Frieder Ferlemann und Dr.Hartwig Harder bin ich sehr dankbar für die gute Einweisung in das tolle Experiment und das Arbeitsgebiet am Anfang meiner Doktorandenzeit und für das weitergehende Interesse an der Arbeit nach ihrem Verlassen des Instituts. Hartmut Bösch, Rüdiger Huppert und Paul Vradelis danke ich für die Hilfe bei den gemeinsam durchgeführten Ballonmeßkampagnen und die immer vorhandene Bereitschaft zur Diskussion der Ergebnisse. Dr. Frank Erle bin ich sehr für die Einführung in die Modellierung mit FACSIMILE dankbar.

Für das Korrekturlesen dieser Arbeit danke insbesondere Hartmut, Klaus, Thomas, Kai, Gerd, Irene, Christiane und Bernd, die dabei halfen, grobe sprachliche Fehler und Ungereimtheiten zu beseitigen, so daß sich dieses Werk nun hoffentlich besser lesen lässt.

Dr.Claude Camy-Peyret, Dr.Sebastian Payan, Dr.Pascal Jeyseck, Yao Te und Isabelle Pepin (LPMA, Universite Pierre et Marie Curie, Paris) danke ich für die freundliche und effektive Zusammenarbeit während der gemeinsamen Ballonmeßkampagnen, bei denen sie uns viel Verständnis entgegengebracht haben und immer eine Hilfe waren, wenn Not am Mann/Frau war. Weiterhin bin ich dem Ballonteam der CNES um Jean Evrard zu Dank verpflichtet, ohne deren Erfahrung die Ballonflüge nicht hätten so erfolgreich durchgeführt werden können.

Die gute Zusammenarbeit mit Dr. M.P. Chipperfield und Dr. B.-M. Sinnhuber (beide University of Leeds (SLIMCAT)) sollte hier auch nicht unerwähnt bleiben, die mich mit aktuellen SLIMCAT Modelldaten versorgt haben, ohne die diese Arbeit in dieser Form nicht hätte zustandekommen können.

Dank geht natürlich auch an M. van Roozendaal und C. Fayt, den Entwicklern von WINDOAS, die uns freundlicherweise diese Auswertesoftware zur Verfügung gestellt haben, mit der es möglich war, die Genauigkeit der Messungen zu erhöhen.

Auch will ich hier meiner Arbeitsgruppe Luftchemie am Institut für Umweltphysik danken, deren freundschaftliche und kooperative Atmosphäre für die Arbeit sehr positiv und wichtig war.

Schlußendlich gilt mein aufrichtiger Dank meiner Mutter und meinen Brüdern, die mich während meines Studiums und der Doktorarbeit immer mit Interesse und Vertrauen unterstützt haben.

Diese Arbeit wurde gefördert durch die Europäische Union (EU Projekte: CHELOSBA, THESEO(HALOMAX) und THESEO2000(EuroSolve)).